BEILSTEIN JOURNAL OF NANOTECHNOLOGY

Advanced atomic force microscopy techniques II

Edited by Thilo Glatzel and Thomas Schimmel

Imprint

Beilstein Journal of Nanotechnology
www.bjnano.org
ISSN 2190-4286
Email: journals-support@beilstein-institut.de

The *Beilstein Journal of Nanotechnology* is published by the Beilstein-Institut zur Förderung der Chemischen Wissenschaften.

Beilstein-Institut zur Förderung der Chemischen Wissenschaften
Trakehner Straße 7–9
60487 Frankfurt am Main
Germany
www.beilstein-institut.de

BEILSTEIN JOURNAL OF NANOTECHNOLOGY

Advanced atomic force microscopy techniques II

Thilo Glatzel*[1], Ricardo Garcia[2] and Thomas Schimmel[3]

Editorial

Open Access

Address:
[1]Department of Physics, University of Basel, Klingelbergstrasse 82, 4056 Basel, Switzerland, [2]Instituto de Microelectronica de Madrid, CSIC Isaac Newton 8, 28760 Tres Cantos, Madrid, Spain and [3]Institute of Nanotechnology (INT), Karlsruhe Institute of Technology (KIT), 76021 Karlsruhe, Germany

Email:
Thilo Glatzel* - thilo.glatzel@unibas.ch

* Corresponding author

Keywords:
AFM

Beilstein J. Nanotechnol. **2014,** *5,* 2326–2327.
doi:10.3762/bjnano.5.241

Received: 21 November 2014
Accepted: 25 November 2014
Published: 03 December 2014

This article is part of the Thematic Series "Advanced atomic force microscopy techniques II".

Editor-in-Chief: T. Schimmel

Surface science and nanotechnology are inherently coupled because of the increased surface-to-volume ratio at the nanometer scale. Most of the exciting and astonishing properties of nanoscale materials are related to certain surface reconstructions and nanoscale geometries. New functionality is achieved by combinations of nanoscale materials or by structuring their surfaces. The unrivaled tools for measurements of all kind of nanoscale properties are scanning probe microscopy (SPM) techniques, which were triggered by the invention of the scanning tunneling microscope (STM) in 1982 [1-3] and of the atomic force microscope (AFM) in 1986 [4]. These tools opened a huge field of nanoscale studies, from metal surfaces and clusters, molecular structures, insulators to liquid and electrochemical environments and even allowed the integration of various SPM techniques into biological and chemical experiments.

The second volume of the Thematic Series “Advanced atomic force microscopy techniques”, which is presented here, compiles again exciting developments in nanoscale research based on SPM techniques addressed by the scientific community within the last years. Similar to the first volume [5], the development of advanced techniques and their application is the focus of this Thematic Series. Contributions related to energy conversion and storage systems have been addressed, e.g., the analysis of cathodes of lithium–sulfur batteries for a comparison of their nanoscale electrical, electrochemical, and morphological properties [6] or the analysis of CdS quantum dots on TiO_2 by a combination of AFM and X-ray photoelectron spectroscopy [7]. The folding and rupture of graphene on SiC analyzed by non-contact AFM and Kelvin probe force microscopy [8] are presented as well as molecular structures such as the self-assembly of multidentate organothiols onto Au(111), which were studied in situ by using scanning probe nanolithography and time-lapse AFM [9]. Patterns of thiol-based self-assembled monolayers for the site-selective growth of metal-organic frameworks have been created and analyzed by a nanografting technique by using an AFM as a structuring tool [10]. The effect of Cu intercalation at the interface of self-assembled monolayers and a Au(111)/mica substrate was analyzed by STM [11] as well as the growth behavior of PTCDA islands [12].

Furthermore, the analysis of mechanical properties of either nanoparticles [13] or biological systems [14-16] is covered by several articles and reviewed by Cohen and co-workers [17].

Especially the application of advanced SPM techniques in biology provides exciting new results and clearly shows a route for development for the next years. All of the new applications and experiments are strongly dependent on theoretical and technical developments. Virtual AFMs used to simulate AFM measurements [18-20] and to deconvolute complex correlations between various surface properties [21] are based on the implementation of proportional-integral controllers to give realistic feedback behaviours. Stirling proposed a theoretical model for studying the SPM feedback in the context of control theory providing the possibility to understand and model the performance from SPM systems with real parameters [22]. Furthermore, technical contributions discuss the impact of thermal frequency drift of quartz-based force sensors at low temperatures to the accuracy of the force measurements [23] and the trade-offs in sensitivity and sampling depth in bimodal and trimodal AFM [24]. The examples mentioned give a first impression of this collection of high quality research provided to the Beilstein Journal of Nanotechnology, the open-access journal for publication and dissemination of nanoscience research results. We are convinced that the articles presented here will stimulate new ideas in the research field.

We would like to thank all of the authors for their excellent contributions and the referees for their comprehensive and valuable reports, sustaining a journal that is attractive for contributors. Finally, we would also like to thank the team at the Beilstein-Institut for their excellent support and acknowledge the open-access policy of the Beilstein Journal of Nanotechnology, which provides the professional framework and support allowing the collection, review, publishing, and distribution of research results in an easy and excellent way.

Thilo Glatzel, Ricardo Garcia & Thomas Schimmel

November 2014

References

1. Binnig, G.; Rohrer, H.; Gerber, C.; Weibel, E. *Phys. Rev. Lett.* **1982,** *49,* 57. doi:10.1103/PhysRevLett.49.57
2. Binnig, G.; Rohrer, H.; Gerber, C.; Weibel, E. *Appl. Phys. Lett.* **1982,** *40,* 178. doi:10.1063/1.92999
3. Binnig, G.; Rohrer, H. *Helv. Phys. Acta* **1982,** *55,* 726–735.
4. Binnig, G.; Quate, C. F.; Gerber, C. *Phys. Rev. Lett.* **1986,** *56,* 930. doi:10.1103/PhysRevLett.56.930
5. Glatzel, T.; Hölscher, H.; Schimmel, T.; Baykara, M. Z.; Schwarz, U. D.; Garcia, R. *Beilstein J. Nanotechnol.* **2012,** *3,* 893–894. doi:10.3762/bjnano.3.99
6. Hiesgen, R.; Sörgel, S.; Costa, R.; Carlé, L.; Galm, I.; Cañas, N.; Pascucci, B.; Friedrich, K. A. *Beilstein J. Nanotechnol.* **2013,** *4,* 611–624. doi:10.3762/bjnano.4.68
7. Ghazzal, M. N.; Wojcieszak, R.; Raj, G.; Gaigneaux, E. M. *Beilstein J. Nanotechnol.* **2014,** *5,* 68–76. doi:10.3762/bjnano.5.6
8. Temmen, M.; Ochedowski, O.; Kleine Bussmann, B.; Schleberger, M.; Reichling, M.; Bollmann, T. R. J. *Beilstein J. Nanotechnol.* **2013,** *4,* 625–631. doi:10.3762/bjnano.4.69
9. Tian, T.; Singhana, B.; Englade-Franklin, L. E.; Zhai, X.; Lee, T. R.; Garno, J. C. *Beilstein J. Nanotechnol.* **2014,** *5,* 26–35. doi:10.3762/bjnano.5.3
10. Ladnorg, T.; Welle, A.; Heissler, S.; Wöll, C.; Gliemann, H. *Beilstein J. Nanotechnol.* **2013,** *4,* 638–648. doi:10.3762/bjnano.4.71
11. Shen, C.; Buck, M. *Beilstein J. Nanotechnol.* **2014,** *5,* 258–267. doi:10.3762/bjnano.5.28
12. Zebari, A. A. A.; Kolmer, M.; Prauzner-Bechcicki, J. S. *Beilstein J. Nanotechnol.* **2013,** *4,* 927–932. doi:10.3762/bjnano.4.104
13. Maharaj, D.; Bhushan, B. *Beilstein J. Nanotechnol.* **2014,** *5,* 822–836. doi:10.3762/bjnano.5.94
14. Guzman, H. V.; Garcia, R. *Beilstein J. Nanotechnol.* **2013,** *4,* 852–859. doi:10.3762/bjnano.4.96
15. Tatlybaeva, E. B.; Nikiyan, H. N.; Vasilchenko, A. S.; Deryabin, D. G. *Beilstein J. Nanotechnol.* **2013,** *4,* 743–749. doi:10.3762/bjnano.4.84
16. Ramos, J. R.; Pabijan, J.; Garcia, R.; Lekka, M. *Beilstein J. Nanotechnol.* **2014,** *5,* 447–457. doi:10.3762/bjnano.5.52
17. Cohen, S. R.; Kalfon-Cohen, E. *Beilstein J. Nanotechnol.* **2013,** *4,* 815–833. doi:10.3762/bjnano.4.93
18. Nony, L.; Baratoff, A.; Schär, D.; Pfeiffer, O.; Wetzel, A.; Meyer, E. *Phys. Rev. B* **2006,** *74,* 235439. doi:10.1103/PhysRevB.74.235439
19. Polesel-Maris, J.; Gauthier, S. *J. Appl. Phys.* **2005,** *97,* 044902. doi:10.1063/1.1841462
20. Canova, F. F.; Foster, A. S. *Nanotechnology* **2011,** *22,* 045702. doi:10.1088/0957-4484/22/4/045702
21. Elias, G.; Glatzel, T.; Meyer, E.; Schwarzman, A.; Boag, A.; Rosenwaks, Y. *Beilstein J. Nanotechnol.* **2011,** *2,* 252–260. doi:10.3762/bjnano.2.29
22. Stirling, J. *Beilstein J. Nanotechnol.* **2014,** *5,* 337–345. doi:10.3762/bjnano.5.38
23. Pielmeier, F.; Meuer, D.; Schmid, D.; Strunk, C.; Giessibl, F. J. *Beilstein J. Nanotechnol.* **2014,** *5,* 407–412. doi:10.3762/bjnano.5.48
24. Eslami, B.; Ebeling, D.; Solares, S. D. *Beilstein J. Nanotechnol.* **2014,** *5,* 1144–1151. doi:10.3762/bjnano.5.125

License and Terms

Beilstein Journal of Nanotechnology

AFM as an analysis tool for high-capacity sulfur cathodes for Li–S batteries

Renate Hiesgen*[1], Seniz Sörgel[2], Rémi Costa[2], Linus Carlé[2], Ines Galm[1], Natalia Cañas[2], Brigitta Pascucci[1,2] and K. Andreas Friedrich[2]

Full Research Paper

Open Access

Address:
[1]Faculty of Basic Science, University of Applied Sciences Esslingen, Esslingen, Germany, and [2]Institute of Technical Thermodynamics, Electrochemical Energy Technology, German Aerospace Center, Stuttgart, Germany

Email:
Renate Hiesgen* - renate.hiesgen@hs-esslingen.de

* Corresponding author

Keywords:
conductive AFM; high capacity; lithium-sulfur batteries; material-sensitive AFM; sulfur cathode

Beilstein J. Nanotechnol. **2013,** *4,* 611–624.
doi:10.3762/bjnano.4.68

Received: 10 April 2013
Accepted: 11 September 2013
Published: 04 October 2013

This article is part of the Thematic Series "Advanced atomic force microscopy techniques II".

Guest Editors: T. Glatzel and U. D. Schwarz

Abstract

In this work, material-sensitive atomic force microscopy (AFM) techniques were used to analyse the cathodes of lithium–sulfur batteries. A comparison of their nanoscale electrical, electrochemical, and morphological properties was performed with samples prepared by either suspension-spraying or doctor-blade coating with different binders. Morphological studies of the cathodes before and after the electrochemical tests were performed by using AFM and scanning electron microscopy (SEM). The cathodes that contained polyvinylidene fluoride (PVDF) and were prepared by spray-coating exhibited a superior stability of the morphology and the electric network associated with the capacity and cycling stability of these batteries. A reduction of the conductive area determined by conductive AFM was found to correlate to the battery capacity loss for all cathodes. X-ray diffraction (XRD) measurements of Li_2S exposed to ambient air showed that insulating Li_2S hydrolyses to insulating LiOH. This validates the significance of electrical ex-situ AFM analysis after cycling. Conductive tapping mode AFM indicated the existence of large carbon-coated sulfur particles. Based on the analytical findings, the first results of an optimized cathode showed a much improved discharge capacity of 800 mA·g(sulfur)$^{-1}$ after 43 cycles.

Introduction

Lithium rechargeable batteries with high capacity are a key technology for the widespread implementation of battery-powered cars. The specific energy of existing lithium batteries needs further improvement to enable acceptable driving ranges of electric vehicles. Moreover, this is also important for portable applications. Besides efficiency and energy density, numerous other requirements have to be fulfilled, which include industrial scalability and the capability for mass-production. In the last few decades, lithium–sulfur batteries have attracted increasing attention due to their high theoretical

energy density (2500 $Wh \cdot kg^{-1}$) and theoretical capacity (1672 $mA \cdot g^{-1}$), which are based on the electrochemical reaction 16 Li + $S_8 \rightleftarrows 8\ Li_2S$ [1,2]. In addition, these batteries have the advantage of having sulfur-based cathodes, which are cheap, abundant, and environmentally friendly. However, these batteries suffer from much lower realised capacities and lifecycles, which is mainly due to:

(1) the low electrical conductivity of sulfur (5×10^{-30} $S \cdot cm^{-1}$ at 25 °C), which leads to a poor electrochemical accessibility and a low utilisation of sulfur,

(2) the electrochemical irreversibility due to the loss of sulfur active-material and parasitic reactions of dissolved polysulfides at the Li electrode and

(3) the morphological and volumetric changes of the cathode material upon cycling [3,4].

The redox reaction of the sulfur cathode can only occur when the sulfur is in contact with the carbon because of the insulating nature of sulfur. In this regard, an ideal cathode would be composed of a continuous, electronically conductive carbon network coated with a monolayer of sulfur. The contact between the carbon–sulfur composite and the current collector is also a very important parameter for the performance of the Li–S battery, which depends mainly on the type of binder that is used [5-7].

Related to the morphology and volume changes of the cathodes, it was found that the sulfur cathodes expand while discharging and shrink while charging. The thickness change of the electrode was measured to be approximately 22% [8]. Capacity fading due to structural and volume changes was reported in several publications [4,9-13]. Therefore, to achieve a high performance Li–S battery, it is necessary to restrict the changes in the morphology and volume of the cathode. Recent advances with graphene–sulfur composite materials demonstrated reasonably high and stable specific capacities of up to 600 $mA \cdot g(sulfur)^{-1}$ over more than 100 cycles [13,14]. One way to suppress the polysulfide shuttle mechanism and to enhance the sulfur retention is to coat the electrodes. This can be performed by physical vapour deposition of a nickel layer or by coating with Nafion [15,16]. To obtain a superior capacity and reversible cycle performance, the production of thin and porous sulfur cathodes or the use of foam-like structures as current collectors have been shown to be advantageous [9,17,18]. Recent studies have shown that the use of highly ordered mesoporous carbon with a bimodal pore structure with a high specific area and a large pore volume is beneficial. It traps a part of the polysulfides for a certain time before release, thereby reduces the electrochemical irreversibility and can lead to a very high and stable capacity of approximately 1000 $mA \cdot g(sulfur)^{-1}$ [19,20]. Another approach is based on vertically aligned carbon nanotubes (CNTs) grown on a nickel foil without any binder. To date, these binder-free CNT cathodes contain the highest published total ratio of sulfur (90%) in an electrode [21]. The advantage of a stable three-dimensional conductive network achieved by the introduction of carbon nanofibres has also been demonstrated [22]. Besides these more sophisticated approaches the introduction of a porous carbon/polytetrafluorethylen (PTFE) containing material, which is used as a gas diffusion layer in fuel cells (GDL), positioned in front of the cathode has led to capacities, in dependence on the discharge rate, of 1000–1200 $mA \cdot g(sulfur)^{-1}$ [23].

In this work, the aim is to investigate the electrical and morphological stability of lithium–sulfur cathodes manufactured by suspension spraying or doctor blading in order to improve the performance of these electrodes. Results from recent XRD studies were used that clarified a complete chemical reaction of the non-conductive Li_2S layer to an also insulating LiOH layer. This layer was stable in air and enabled an AFM study of the conductive area [24]. Polyvinylidene fluoride (PVDF) and carboxymethyl cellulose (CMC) binders were used to test the influence of the binders on the battery performance. The suspension-spraying technique is advantageous because it can be used in mass production processes. In a first step the focus was on the preparation of a porous, homogeneous, thin, and agglomeration-free cathode, which exhibited reduced structural changes during the discharge–charge cycles. Morphological changes and the stability of the electronic conductivity of the sulfur cathodes upon cycling were detected by means of SEM, material-sensitive AFM and conductive tapping mode AFM. We aim to demonstrate that a direct correlation exists between the cycling stability and the properties on the nanometre scale, and that AFM analysis can disclose the morphology of the carbon–sulfur interface. Based on the analytical results of the nanoscale analysis an optimized preparation technique was introduced which lead to an enhanced battery performance.

Results and Discussion

Li–S batteries with different preparation and composition

Figure 1 shows a comparison of the discharge capacity of the first batteries containing differently prepared cathodes over 50 cycles.

Although the battery, whose cathode was coated by hand (doctor-blade coated, referred to as DBC-PVDF), has a high initial discharge capacity (872 $mAh \cdot g^{-1}$), the capacity decreases significantly upon cycling. After 50 cycles, the remaining

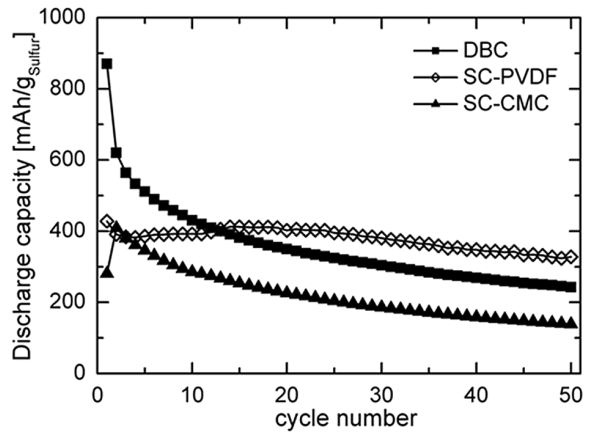

Figure 1: Comparison of the cycling performances of non-optimised Li–S batteries prepared with different binders. The batteries were tested in the range of 2.8–1.5 V vs Li/Li$^+$ at a current density of 533 mA·g^{-1} sulfur.

capacity is only 242 mAh·g^{-1}. This behaviour is quite typical for the Li–S cathodes [3,12,25,26].

In contrast to the DBC-PVDF sample, battery cathodes with the same composition but prepared by a home-made suspension spraying device (suspension coated, referred to as SC-PVDF) show a substantial reversible capacity of 330 mAh·g^{-1} after 50 cycles (see Figure 1). The degradation of the capacity after 100 cycles is only 25%, which demonstrates a good electrochemical reversibility. The better performance of the sprayed cathode can be attributed to the porous and homogeneous carbon–sulfur network-structure, which is mostly stable upon cycling, as proofed by SEM and AFM measurements (see below).

The sprayed cathodes prepared with carboxymethyl cellulose (CMC) binders (SC-CMC) show discharge capacities of 136 mAh·g^{-1} after 50 cycles, which is inferior to other values (Figure 1). One of the reasons for the low initial discharge capacity compared to the theoretical capacity (1672 mAh·g^{-1}) could be the bad contact between sulfur and carbon black, so that not all of the sulfur in the cathode is reduced (low sulfur utilisation). Another reason could be the non-ideal penetration of the electrolyte into the cathode. If the cathode is not ideally porous, or if the cathode is too thick, and if the amount of electrolyte is insufficient to fill the pore volume, sulfur is only partially reduced. It is therefore of interest to optimise the amount of electrolyte as a function of the free volume available within the porous cathode. Concerning the capacity fading observed on the tested cathodes, several hypotheses can be proposed:

(1) During battery discharge, elemental sulfur (S_8) is first broken down to form a chain-like polysulfide anion (S_8^{2-}), which combines with Li^+ ions to yield high-order lithium polysulfides (Li_2S_x, $x \geq 4$). These high-order polysulfides are soluble in the organic electrolytes and therefore the viscosity of the electrolyte increases [27]. In this case, Li^+ ion diffusion and penetration into the inner parts of the cathode decrease. Therefore, most of the reduction reactions take place on the surface of the cathode.

(2) Some of the reduction products, Li_2S_2 and Li_2S, which are low-order polysulfides, are insoluble in the electrolyte and stay on the surface of the cathode to form a dense film [9,13,28-30]. During these processes the carbon–sulfur network is subject to modification. Therefore, the electronic percolation is partially reduced, which results in the formation of electrochemically inactive areas. For this reason, low-order polysulfides cannot be oxidised back to high-order polysulfides within these areas. Additionally, these low-order polysulfides block the pores of the cathode upon cycling and the electrolyte cannot penetrate properly into the cathode structure. Therefore, Li^+ ion diffusion is reduced and further electrochemical reactions are restricted. All of these phenomena result in degradation of the capacity.

(3) Some of the high-order polysulfides migrate through to the anode side due to the shuttle mechanism and react with Li^+ ions on the surface of the anode [31,32]. This time, low-order polysulfides form and settle down on the surface of the lithium anode. They cannot be oxidised back and therefore block the active sites of the anode surface [31].

As shown in Figure 2c and Figure 2d, the morphological changes upon cycling of the SC-PVDF cathode are much less than those of the DBC-PVDF (Figure 2a and Figure 2b) or SC-CMC cathodes (Figure 2e and Figure 2f). The porous structure of the SC-PVDF cathode is preserved after 50 discharge/charge cycles. In this way, further electrochemical reactions are possible.

Although the SC-CMC samples were prepared by spraying, it was not possible to obtain a reversible capacity, which is most likely due to the formation of a crust-like layer on the cathode surface upon cycling (Figure 2f). As one can see in Figure 2e, the application of a CMC binder in a sulfur cathode caused the formation of loose particles and also led to a bad contact between carbon black and the sulfur particles. Therefore, the carbon–sulfur network structure was not stable upon cycling and changes of morphology and volume were observed. A proper binder should have a high adhesion between the electrode materials and the current collector and should form a good network between the active material and the conductive carbon. In this way, the electron transport as well as the diffusion of the lithium ions is facilitated [33].

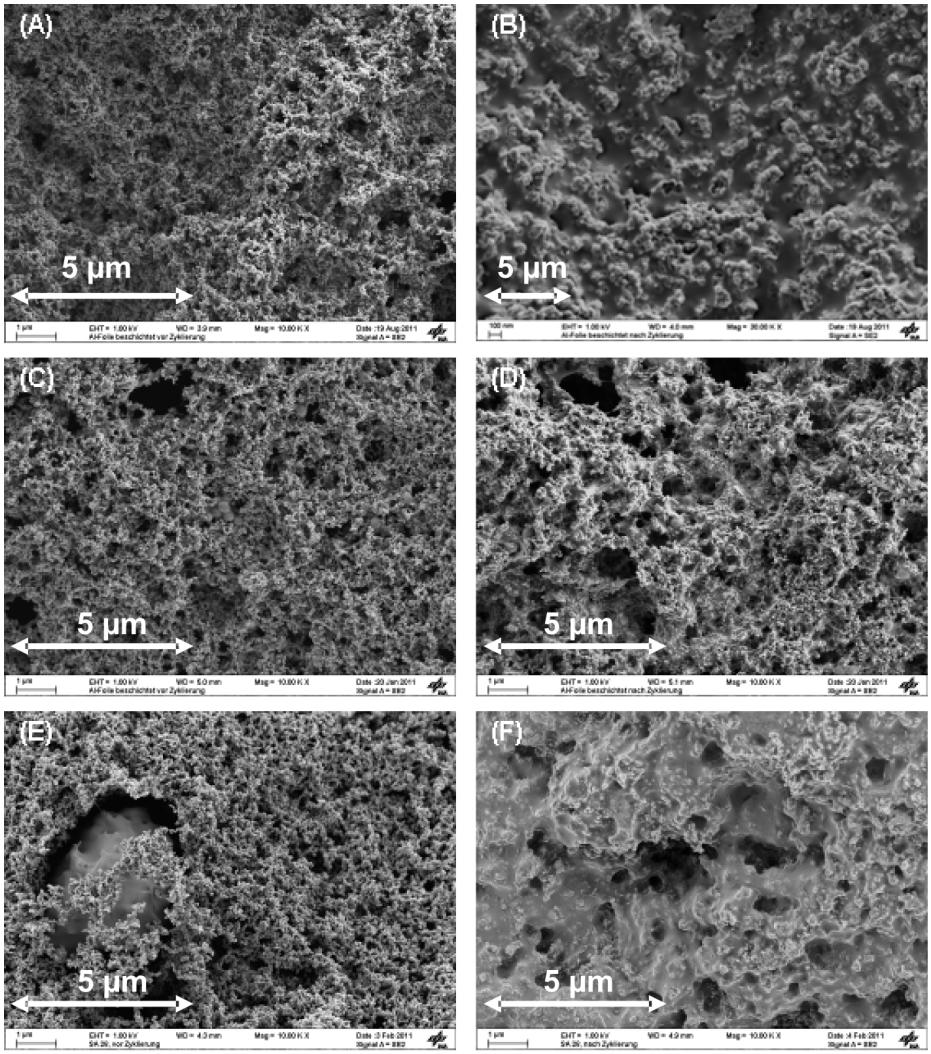

Figure 2: SEM images of (a) DBC-PVDF before cycling, (b) DBC-PVDF after the 50th discharge, (c) SC-PVDF before cycling, (d) SC-PVDF after the 50th discharge, (e) SC-CMC before cycling, (f) SC-CMC after the 50th discharge.

X-Ray diffraction

Lithium containing components like the cathodes after cycling in a battery are sensitive to ambient air. Water as well as nitrogen and oxygen reacts with the lithium and change surface and bulk composition. Therefore AFM analysis of battery materials, which contain lithium, has been performed in situ in a glove-box [11]. Upon cycling a reduction of the conductive area was observed that was attributed to the formation of a non-conductive Li_2S layer. The stability of Li_2S in air was analysed by means of XRD. Li_2S powder was exposed to air, and the subsequent reaction was measured in a time-dependent sequence. Figure 3 shows the X-ray patterns of the Li_2S sample before (a) and after (b) approximately 25 min of contact with air. In air, lithium sulfide easily hydrolyses and reacts to form hydrogen sulfide and lithium hydroxide ($Li_2S + 2\ H_2O \rightarrow 2\ LiOH + H_2S$). It can be observed that the integrated intensity of the peaks of Li_2S decreased significantly, while the peak intensity of LiOH increased. Instead of the insulating Li_2S layer an also insulating LiOH layer was formed, which was stable in air. Measurements during exposure to air were also made by using AFM imaging. No significant differences in stiffness and in conductivity were detected. However, changes may have already happened during the transfer procedure. Therefore, an ex-situ analysis by using AFM allowed for retrieval of significant results on the percentage of the remaining conductive area after cycling. Details of these measurements can be found in [24].

Atomic force microscopy

AFM of basic components

In order to calibrate the AFM for the material-sensitive analysis, an evaluation of the properties of the basic materials, which

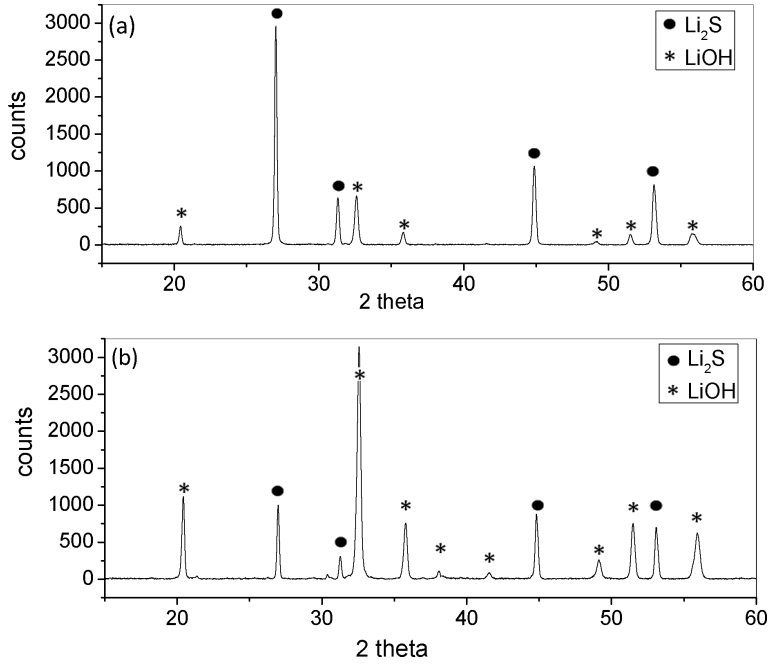

Figure 3: X-ray pattern of the Li_2S sample before (a) and after (b) approximately 25 min in contact with air.

were used for the cathode preparation, was performed. Therefore, pellets were prepared from powder at a pressure of 10 kN and imaged separately by AFM (Figure 4).

As shown in Figure 5, the DMT modulus (stiffness) differs significantly. The highest values were measured for sulfur and a very small stiffness was measured for carbon, which was the

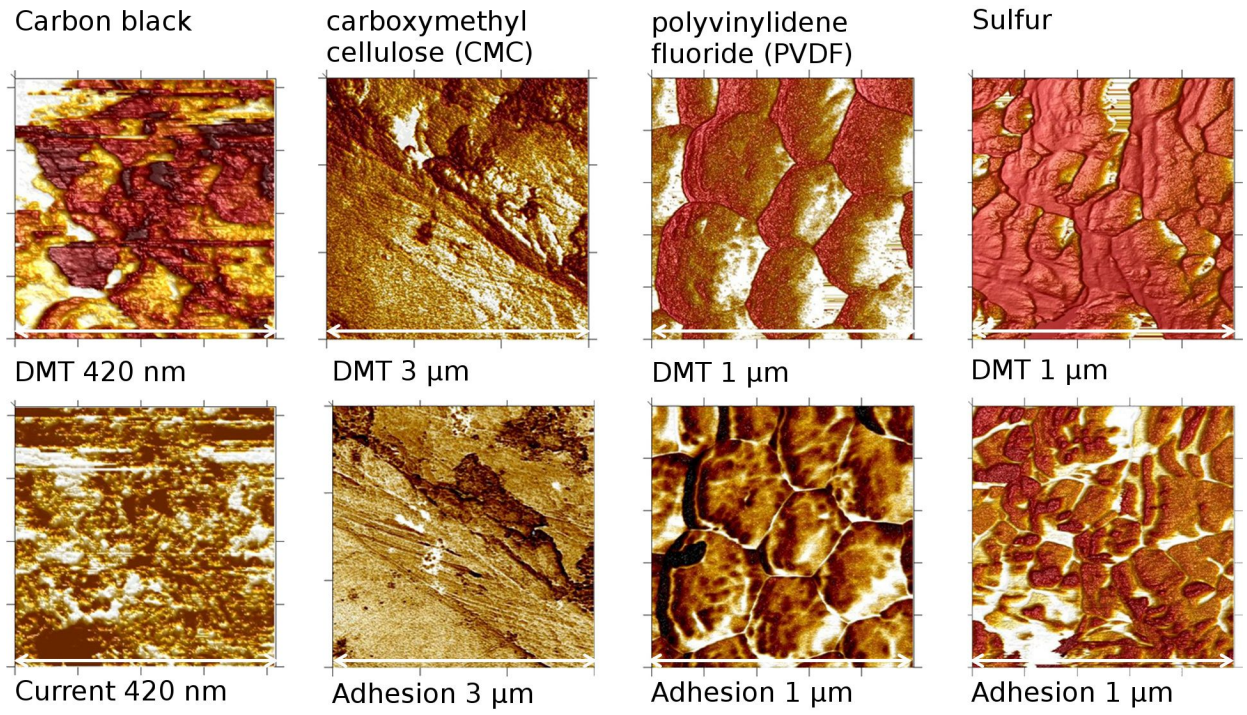

Figure 4: Mapping of DMT modulus and current/adhesion of basic materials used for cathode preparation from AFM, brighter colours indicate higher values. The size of the scale bar is given below each image.

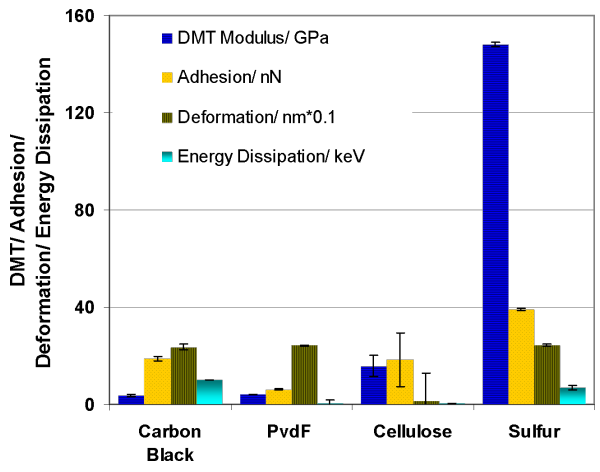

Figure 5: Statistical evaluation of mechanical properties of the basic materials used for preparing the cathodes.

only conductive sample in this series. In the other properties, sulfur differed slightly from carbon black and binder with a smaller energy dissipation and a slightly increased adhesion. It is noted, that the measured DMT modulus has values out of the recommended range for this type of tip. Therefore, the accuracy of those values is not very high. However, the large differences allowed a good differentiation from carbon. No significant differences were found for the deformation values with the exception of cellulose as a binder material. The adhesion force was smallest for the fluorine containing PVDF binder. For the identification of sulfur the stiffness values were used. During the stiffness measurements the tip puts a pressure on the surface and a subsurface volume is involved. Thereby, even if coated with a thin layer of other material, sulfur can be identified with high certainty. The identification of carbon is performed by measuring its conductivity.

In Figure 6 AFM images of the SC-PVDF sample are shown. All AFM images measure 3 µm × 3 µm. The topography is displayed together with the simultaneously measured mapping of deformation, adhesion force, DMT modulus (stiffness), TUNA™ current, and peak current. The different properties of image areas allowed for a distinction of different surface materials, which is not possible with the topography image only.

For all other samples these properties were measured and used for the analysis. However, for simplicity, only the topography images, together with stiffness and current images, recorded by conductive PeakForce-QNM™ (see section Experimental), are displayed. The surface is rough, consistent with the SEM images of Figure 2, with height differences of 750 nm on a 3 µm scale. A large part of the surface exhibits a comparably hard/elastic material with high DMT modulus (brighter colours indicate areas with higher stiffness). These regions concurrently exhibit a lower deformation. The adhesion force is higher

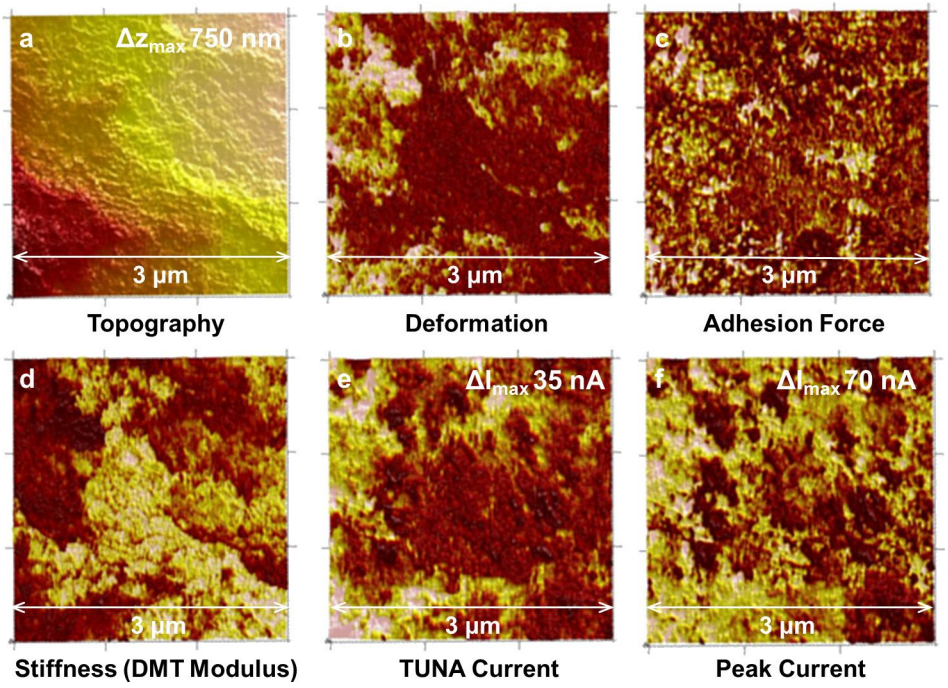

Figure 6: AFM images of an SC-PVDF sample before cycling. a) topography, b) deformation, c) adhesion, d) DMT modulus (stiffness), e) PeakForce-TUNA™ current, f) PeakForce QNM™ current (brighter colours are higher values).

at those parts of the surface where the stiffness values are smaller. In the centre of the TUNA current image in Figure 6, the current density has lower intensities, whereas the corresponding stiffness is especially high. Deformation values, on the other hand, are relatively low. Due to the insulating nature of sulfur, it can be expected that areas of high sulfur content exhibit low current density; however, they should have a high stiffness compared to carbon-rich areas (see Figure 5). It can therefore be concluded that a heterogeneous chemical distribution is present in this area, with a sulfur-rich region in the centre. No indication of this heterogeneity is visible in the topographical images. As observed in the recording of the TUNA™ current (where the average steady state current is displayed, Figure 6e), little or no steady current flow was measured at the parts of the surface with high stiffness (DMT). In contrast, a peak current (Figure 6f) was present in this area. The peak current signal gives the current flow at maximal pressure of the AFM tip ($\Delta t \approx 0.001$ s). In this time domain, transient (capacitive) currents can be detected and were present in most parts of the surface with high stiffness. These transient currents indicated surface regions where fast charging processes occurred even before contact of that sample to lithium species. Therefore, the transients were not associated with an ionic charging process. An electronic charge transfer is present and a charging of carbon agglomerates on insulating sulfur particles (indicated by the high stiffness of this region) with the tip is assumed. The size of the underlying sulfur particles retrieved from the high stiffness region is about 0.5 µm and presumably they are too large for a high utilization of sulfur. In the peak current image, several black spots indicate regions where no current was measured and concurrently displayed highest stiffness. By comparing the size of the carbon particles with the particles in the range of a few ten nanometers as reported by [34], the resulting coverage of large sulfur particles by the much smaller carbon is expected.

After cycling the SC-PVDF sample, the grains are more defined and larger than before cycling (Figure 7a). Although, in this image the roughness is larger (Δz = 1.5 µm) than before cycling, no general difference in roughness before and after cycling could be detected for this sample (see Figure 9 below). A coarsening of the finer surface structures is also visible in the SEM images (Figure 2d). A few isolated grains exhibit a high stiffness. This harder surface area is also not conductive. In general, most of the conductive regions exhibit high energy dissipation (not shown) and are quite ductile. The magnitude of the current (QNM™ current) decreased from approximately 30 nA before cycling to less than 1.5 nA (average values). In the adhesion image (not shown), three different magnitudes are distinguishable: a very high adhesion, a medium value for most of the surface and a few grains with a very small adhesion. Areas of high adhesion were non-conductive and high stiffness indicates the presence of sulfur-rich grains at the surface (see Figure 5).

In Figure 7b, topography, stiffness, and QNM™ current of the DBC-PVDF sample that was coated by the doctor blade technique are displayed. Before cycling, the height differences are larger than in the SC-PVDF sample. However, the highest current of 1.7 nA is much smaller than the 30 nA measured at the SC-PVDF sample. Most of the surface has similar hardness and low energy dissipation values. Higher currents were measured at regions with higher stiffness. Because it is not averaged, the PeakForce QNM™ current is comparable to the peak current of the PeakForce-TUNA™ mode, and thereby includes transient as well as steady-state current. Conductivity measured in stiff areas is not expected due to low conductivity of sulfur. When capacitive currents are detected, this indicates a conductive or electrochemically active layer on top of a harder sulfur grain, as shown in Figure 6. Following the results of calibration with the base materials (Figure 4 and Figure 5) and the observation of the previous measurement of SC-PVDF, the combination of high stiffness and conductivity indicates the presence of carbon-coated sulfur at the surface. The surface areas with a high energy dissipation and a low current exhibit mostly high adhesion. In the adhesion image (not shown), several small grains of approximately 50 nm size and with a very low adhesive force are visible, which appear to be very soft. These grains may consist of PVDF binder which should be soft, non-conductive, and exhibit small adhesion.

After cycling (Figure 7c), some large crystalline-like grains with lengths of approximately 2–3 µm are visible, which possess a high hardness, no conductivity, and show low deformation and energy dissipation. The region in between these crystallites exhibits a finite but very small conductivity, one order of magnitude smaller than before cycling. Here, several small conductive soft grains with low adhesion, high deformation and high energy dissipation are visible, which could be due to the presence of PVDF binder particles.

The SC-CMC sample (Figure 7d) was prepared with a different binder (carboxymethyl cellulose) and consisted of grains with approximately 100 nm size arranged in several terrace-like layers. The softer particles are quite homogeneously distributed and most of the surface is stiffer. The more ductile grains are conductive, have small adhesion, high energy dissipation and high deformation. Due to their properties, this material is most likely carbon or carbon-rich. One larger non-conductive grain at the bottom right is much harder than the surrounding regions and had high adhesion. Therefore, it is most likely a sulfur-rich particle.

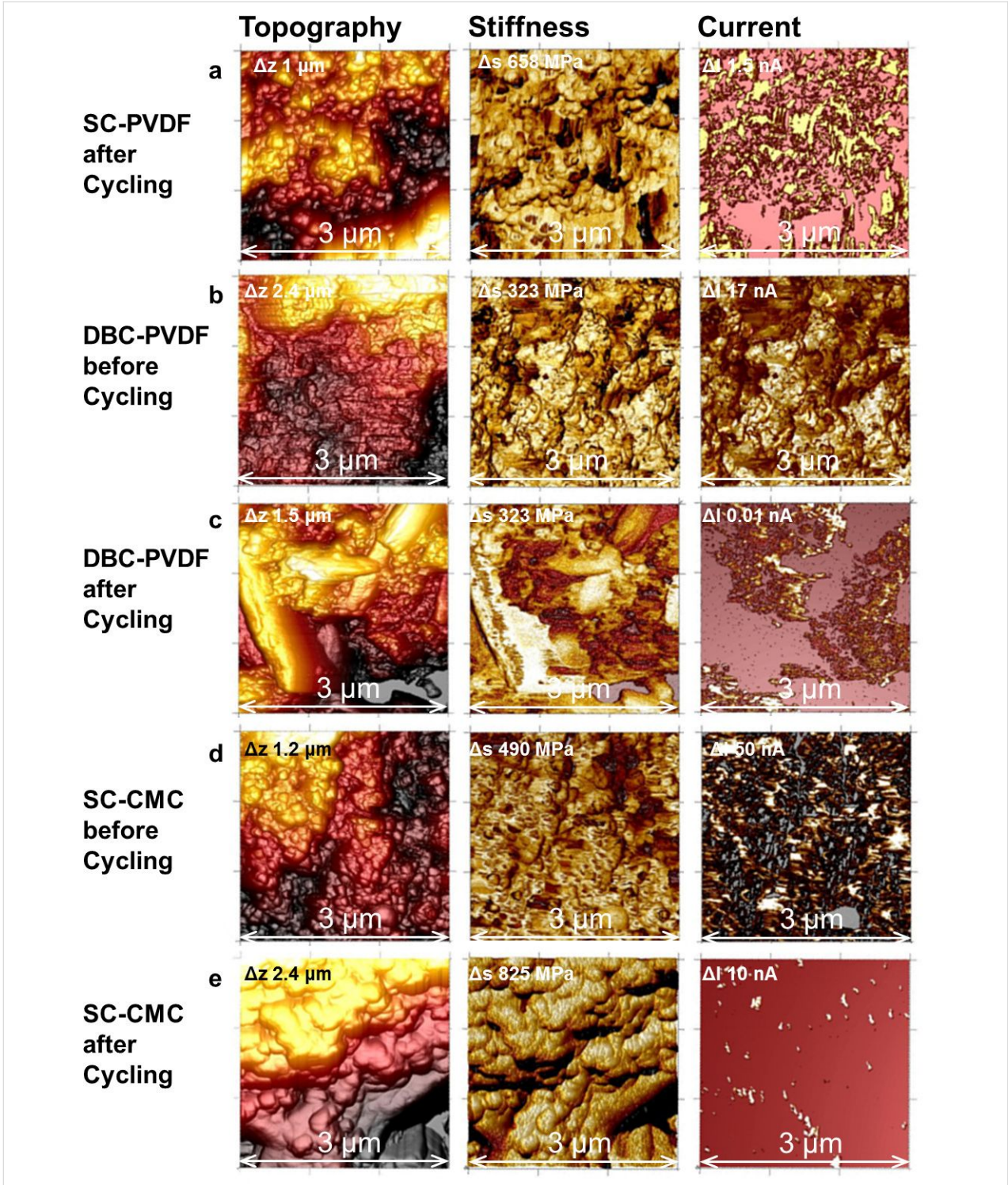

Figure 7: AFM image of topography, DMT modulus, and QNM™ current of a) SC-PVDF after cycling b) DBC-PVDF before cycling, c) DBC-PVDF after cycling, d) SC-CMC before cycling and e) SC-CMC after cycling. The scale bar is given as a value in the image.

After cycling (Figure 7e) the grains are enlarged, the surface is much smoother, finer particles are lost, and flat terraces are visible in the topography image. However, the total height difference has not changed significantly. The steep (almost vertical) borders of these terraces can hardly be measured by AFM and are visible as black regions. These steep and smooth features most likely represent large carbon particles with even layers visible at the borders. The surface layer stiffness is quite

homogeneous. The stiffness scale of the displayed area is larger after cycling although on average the stiffness has decreased. The current decreases by more than one order of magnitude after cycling and only very small spots are still conductive. These conductive spots have higher energy dissipation and adhesion and mark some of the terrace borders.

A statistical evaluation of the mean conductive area before and after battery cycling is displayed in Figure 8. For all samples the total conductive area was always reduced upon cycling. A similar reduction of the conductive area was also reported from in situ conductive AFM measurements by Auerbach et al. [11]. This is proof for composition changes, which take place upon cycling. The smallest reduction of the conductive area was found for the SC-PVDF sample, which was in accordance with the best battery cycling performance. Much larger relative reduction is visible for DBC-PVDF and the SC-CMC samples, and for the latter an almost complete loss of the conductive area was measured. The improvement of the cycle life in SC-PVDF samples may therefore be attributed to the good electrical path and structural stability given by a well-distributed sulfur-carbon composite network.

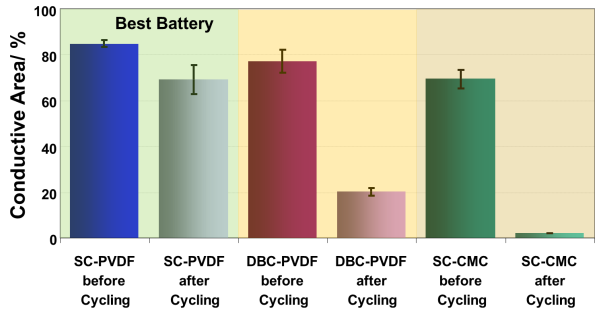

Figure 8: Conductive area during image acquisition under identical conditions at the cathodes before and after 50 cycles; area 3 µm × 3 µm, U = 0.5 V with same AFM tip.

In Figure 9 a comparison of the mean stiffness and the roughness of the different cathodes before and after cycling is presented. Energy dissipation indicates a non-elastic deformation of the material and is larger in the SC-CMC cathode prepared with the carboxymethyl cellulose binder compared to the cathodes containing polyvinylidene fluoride binder. The energy dissipation of the samples containing PVDF binder did not change at all. The samples with CMC binder have significantly different properties. They are much more ductile from the beginning and even after a decrease in cycling, energy dissipation is still higher for the PVDF containing samples. From the

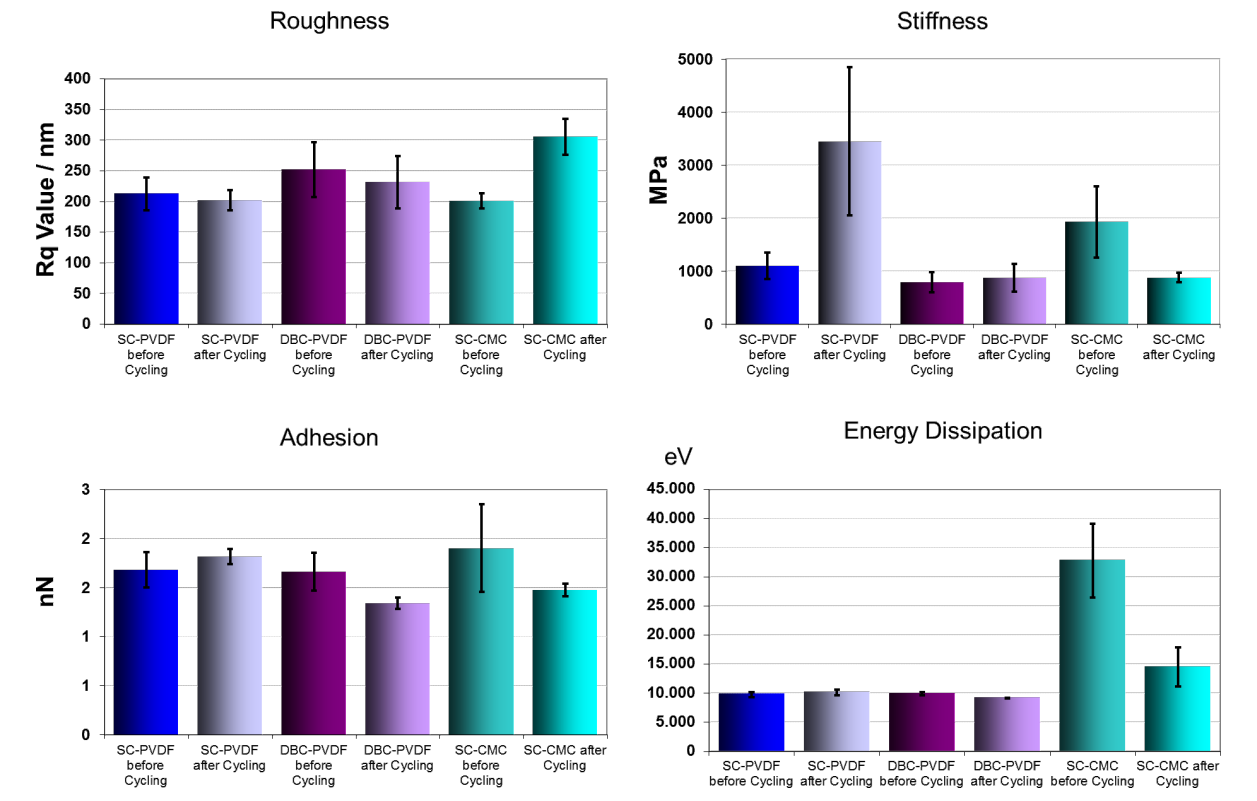

Figure 9: Comparison of mean values of roughness, adhesion, energy dissipation, and stiffness, from statistical evaluation of AFM images measured under identical conditions at the cathodes before and after 50 cycles; the imaged area is 3 µm × 3 µm with the same AFM tip.

analysis of compounds it can be concluded that carbon leads to the highest energy dissipation values. As a consequence, high values indicate an initial carbon-rich surface and the reduction of energy dissipation values after cycling indicates a loss of carbon after cycling. The adhesion force is quite sensitive to the properties of a thin surface layer. A difference in surface hydrophobicity is visible in the adhesion force, which has been shown previously with other fluorine-containing materials and is expressed here in the low adhesion force of pure PVDF. Here, only small adhesion force changes are visible. A small increase in adhesion of SC-PVDF samples may point to an enrichment of PVDF after cycling but is not significantly large [35].

The differences in stiffness in the basic materials are most significant for discerning the components. The mean stiffness of the surface increased largely for the SC-PVDF sample and did not change upon cycling for the doctor-bladed PVDF-containing sample. An increased stiffness indicates an enrichment of the sulfur-containing material at the surface, which has very high stiffness values compared to pure material. In contrast, for the SC-CMC cathode with the carboxymethyl cellulose binder, the surface stiffness decreased, which indicates a fading of the initial stiff sulfur species from the surface and an enrichment of softer species. Taking into account the almost complete loss of the conductive area (Figure 8), these soft species are most likely not carbon, which would be conductive. As shown by XRD, Li_2S_2/Li_2S species, which are known to form an insoluble crust at the surface, are not existent after the exposure to air. Instead, they have likely reacted to LiOH, which may still form a crust-like layer at the surface.

Although the roughness in individual images before and after cycling was different, the average roughness of the PVDF-containing samples did not change upon cycling. However, it did increase significantly in the samples prepared with CMC binder, which indicates a severe morphology change.

Li–S battery with optimized cathode

From the morphology analysis the existence of large sulfur particles partly coated with a thin carbon layer was deduced. This is the reversed composition of the advantageous morphology. Therefore an additional milling step with a pearl mill to gain a finer dispersion of the superior SC-PVDF cathode material was introduced, and performance increased significantly as shown in Figure 10. The optimized battery has an initial discharge capacity of 1030 mAh·g^{-1} and after 43 cycles with a discharge rate of 533 mAh·g(sulfur)$^{-1}$ (C/3) the capacity still measures about 800 mAh·g^{-1}. SEM measurements showed finer particles and a more homogeneous surface of the samples. Further results will be reported in a forthcoming paper.

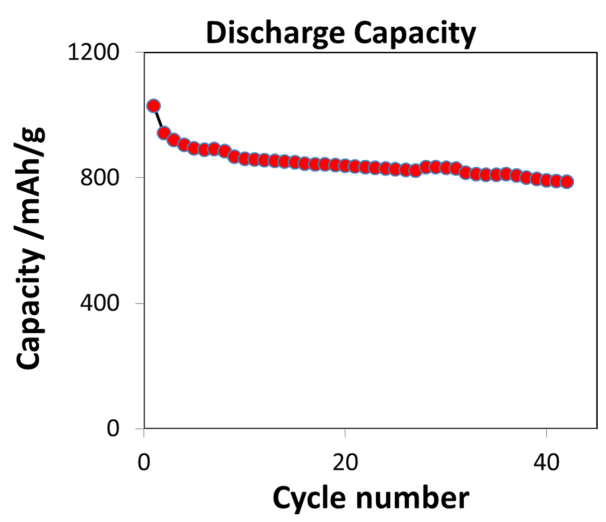

Figure 10: Discharge capacity of the optimized Li–S battery in the range of 2.8–1.5 V vs Li/Li$^+$ at a current density of 533 mA·g(sulfur)$^{-1}$.

Conclusion

In this study, it was shown that the microstructural aspects of the cathodes strongly impact the battery cycle life and the performance of the battery. SEM and AFM results confirmed a morphological change upon battery cycling, which was dependent mostly on the binder (PVDF or CMC). The superior sprayed cathode containing PVDF binder was observed to have a porous and homogeneous carbon–sulfur network structure that was the most stable upon cycling. The preparation and the nature of the binder had a significant influence on the degradation of the cathodes. Improvement of the cycle life of the sprayed cathode that contained PVDF binder could be attributed to the good electrical path and structural stability given by the well-distributed sulfur-carbon composite network. In a first approach a reversible capacity value of approximately 330 mAh·g^{-1} was retained for up to 100 cycles. After 50 cycles batteries prepared with PVDF binder showed a much better performance in accordance with a small change of the conductive area. Preparation by spray coating resulted in a significantly smaller loss of the conductive area in accordance with better battery cycling performance. Therefore, suspension spraying was proven to have the potential to be used as a high performance cathode production technique suitable for mass production.

XRD measurements showed that upon the reaction of insulating Li_2S to LiOH, an ex-situ conductivity analysis allows the retrieval of meaningful results on the conductive surface. The ex-situ analysis is much easier in comparison to previously reported AFM measurements in a glove-box [11]. It is also very difficult to exclude small levels of water vapour, even for scrupulously performed experiments, which can endanger the

reproducibility and repeatability of tests. Generally, for all samples the conductivity changed significantly upon 50 cycles as measured by AFM. Differences in transient current and steady-state current indicate the existence of disadvantageously large sulfur particles with thin carbon layers on top. An incomplete wetting of sulfur particles by carbon was also observed by AFM. Another observation was that the change of the conductive area correlated with the loss in battery performance upon cycling. The reduction of the conductive area was found to be largest for the CMC sample, only a percentage of 2.9% of the initial value was left on average, compared to 81% for the SC-PVDF sample. No correlation was found with the magnitude of current values measured by AFM. High current values correspond to highly conductive, most likely carbon-rich, areas that are not sufficient for a good battery. The surface structure changed differently for the studied samples, e.g., the sample with PVDF lost only the finer structures upon cycling, whereas for the inferior sample with CMC the overall roughness also increased. In this case, larger grains were visible and flat terraces appeared. The surface composition also changed differently upon cycling; harder grains with no conductivity were frequently observed to be present in PVDF-containing samples, and these were most likely sulfur-rich particles.

The inferior CMC-containing samples developed a carbon-rich surface after cycling. The initial stiff sulfur species were likely lost at the surface and replaced with non-conductive species, the most likely of which was LiOH, which had formed from the reaction of Li_2S/Li_2S_2 in humid air.

Based on the principle advantage of the SC-PVDF preparation technique with an advantageous stability of the electronic network but too large sulfur particles, an additional milling step to get a finer dispersion was introduced in the preparation. First experiments exhibited a significant increase of the battery performance with a remaining discharge capacity of 800 $mA{\cdot}g(sulfur)^{-1}$ after 43 cycles.

These results from battery performance confirm the importance of a firm and lasting sulfur–carbon network, which depends on the nature of the binder, and the need for optimal dispersion of particles and the importance of adequate material dispersion. We could also show that advanced material-sensitive and conductive AFM techniques with their potential to analyse microstructural changes, particle size, and even chemical nature are useful to optimize battery materials.

Experimental

Cathode preparation

Suspensions were prepared by mixing sulfur (100 mesh, 99.5%, Alfa Aesar), carbon black Super P conductive (99%, Alfa Aesar), polyvinylidene fluoride (PVDF) binder (Aldrich) with dimethyl sulfoxide (DMSO) (≥99.9%, Aldrich) and ethanol (99.5%, VWR) 50/50 vol %. After the suspensions were thoroughly mixed for 24 h, they were sprayed on aluminium current collectors (99.45%, Alfa Aesar, thickness: 0.025 mm) by using an air-atomising internal mixing nozzle (LECHLER GmbH) piloted by a 3D axis robot. The coating was performed by spraying four layers to minimise the roughness. The thicknesses of the spray-coated cathodes were approximately 30 μm. For comparison, the cathodes were also prepared by doctor-blade coating. The spray- and hand-coated cathodes (5 cm × 5 cm) were dried under vacuum at 50 °C for 24 h. The resulting cathodes consisted of 50 wt % sulfur, 40 wt % carbon black and 10 wt % PVDF. In a similar way, cathodes containing 10 wt % carboxymethyl cellulose binder (CMC, Aldrich) were also prepared. This time, the suspension contained a 50/50 vol % ethanol/water mixture to be able to dissolve the CMC binder. Circular discs of 10 mm diameter were cut from the cathode films. The stainless-steel Swagelok® type lithium–sulfur batteries were assembled in an Ar-filled glove box by stacking together 10 mm diameter discs of lithium metal foil (99.9%, Alfa Aesar, thickness: 1.5 mm), 12 mm diameter discs of polyethylene separator (Entek, thickness: 20 μm), and the prepared cathodes. 14 μL of 1 mol/L lithium hexafluorophosphate ($LiPF_6$) (99.99%, Aldrich) in tetra(ethylene glycol) dimethyl ether (TEGDME) (99.9%, Aldrich) was used as an electrolyte.

Cathode analysis

The charge/discharge performance of the lithium–sulfur batteries was investigated by using a Zahner IM6 electrochemical workstation with a battery cycling software. The batteries were cycled galvanostatically between 1.5 V and 2.8 V vs Li/Li^+ at a current density of 533 $mA{\cdot}g^{-1}$ at room temperature. The morphology of the samples was investigated by SEM with a LEO Gemini (Zeiss) and AFM with a Multimode 8 Bruker system.

XRD measurement of Li_2S in air

X-ray diffractograms (Figure 3) were measured in reflection mode with an X-ray diffractometer (D8 Discover GADDS) equipped with a VÅNTEC-2000 areal detector. Exposures were made with an accelerating voltage of 45 kV and a tube current of 0.650 mA. The total exposure time was 12 min [24].

AFM analysis

For the AFM measurements, cathodes were demounted in a reduced state and fixed with conductive silver paste onto a conductive sample holder. A Multimode 8 (Bruker Corp.) was used that is equipped with a special tapping mode, the "Quantitative Nanomechanical Peak Force" (QNM™) mode, where the

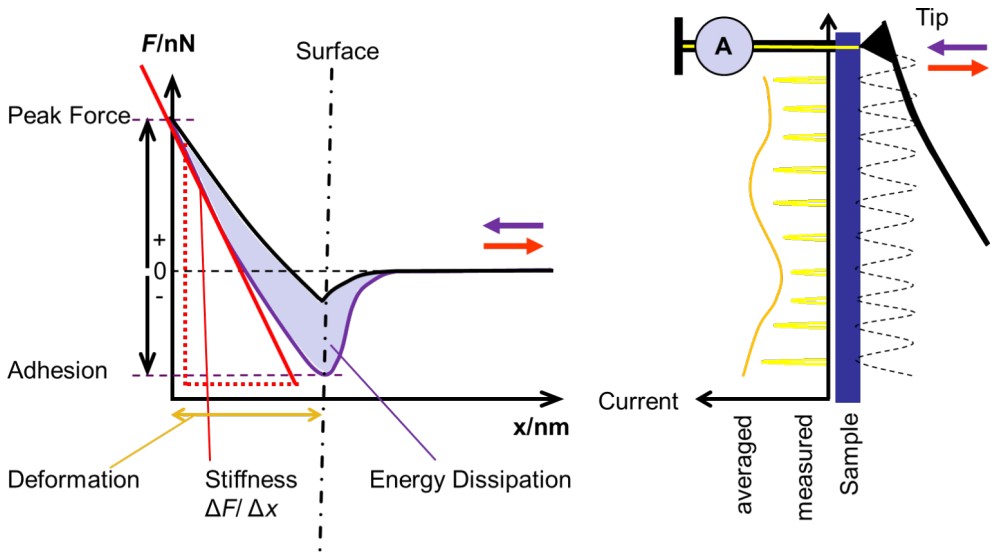

Figure 11: Force separation curve with scheme of evaluation of mechanical properties by AFM (left) and scheme of current measurement with time averaged signal (right) [36].

force–separation curve is recorded at every image point and the topography mechanical properties (e.g., adhesion force, energy dissipation, deformation, DMT modulus or stiffness, peak force, phase shift) are simultaneously evaluated. In case of a conductive tip, the current during the contact of the tip with the sample can be recorded. A scheme of a force–distance curve is given in Figure 11 [21].

In each measurement the mapping of the pre-chosen mechanical properties is recorded. The current measurement needs to be performed with a conductive tip. In tapping mode the current flow is not continuous and a lock-in amplifier is used to derive a time averaged current (PeakForce-TUNA™ mode was used (Bruker Corp.). Two different signals were used as current output, the first of which is the averaged steady state current, named the PeakForce-TUNA™-current. The second current output is the peak current, which is recorded with a short acquisition time during the highest contact pressure and delivers higher current values due the inclusion of transient currents (acquisition time on the order of 0.001 s) [35,37]. By comparing these two current signals, transient currents can be distinguished from steady state current flow. Because the PeakForce-QNM™ current (without the use of a lock-in-amplifier) is not averaged, these results also include transient (capacitive) currents and are comparable to the peak current signal in PeakForce-TUNA™ mode. Previously, we measured conductivity in contact mode, which was associated with a significant pressure on the sample surface with the risk of surface deformation or even damage [31,32,38]. The samples were not exposed to electrolyte before cycling. The samples were investigated without an additional cleaning after cycling to preserve the surface. We also investigated the influence of contact to the electrolyte, but could reproduce the initial conductivity values afterwards. Statistical evaluation of the properties of each image was performed, yielding a histogram of the occurrence of the pixel values for a specific property. The peak occurrence value from a histogram was taken as the mean value of this property in one image. To determine the conductivity, the total conductive area in one image was evaluated. A mean value including error bars was calculated from all images measured with the same size. From five images of the same size from two different spots, at least 1 mm apart, a general average value was calculated, including the corresponding error for one standard deviation. All images used for evaluation of sample properties were recorded with an equal image size (3 µm length) and an identical AFM tip (PPP-NCHPt, NanoAndMore GmbH, spring constant: 30–50 N/m). Images measured in PeakForce-TUNA™ mode were not included in the statistical evaluations. The stiffness values of sulfur base-materials were out of the range recommended for analysis with the tip. Nevertheless, a measurement was possible and delivered a value, although a higher uncertainty can be assumed. For a differentiation of sulfur from the other components it was sufficient.

Acknowledgements

The authors gratefully acknowledge the financial support from the project “Elektrochemie für Elektromobilität - Verbund Süd”. We are also grateful for a Forschungsaversum by the State Ministry for Research and Education of Baden-Württemberg as part of the project “Brennstoffzellen- und Batterieallianz Baden-Württemberg”. We would like to thank Bruker Corp. for providing the PeakForce-TUNA™ module.

References

1. Ji, X.; Lee, K. T.; Nazar, L. F. *Nat. Mater.* **2009,** *8,* 500–506. doi:10.1038/nmat2460
2. Scrosati, B.; Garche, J. *J. Power Sources* **2010,** *195,* 2419–2430. doi:10.1016/j.jpowsour.2009.11.048
3. Yuan, L.; Yuan, H.; Qiu, X.; Chen, L.; Zhu, W. *J. Power Sources* **2009,** *189,* 1141–1146. doi:10.1016/j.jpowsour.2008.12.149
4. Jeon, B. H.; Yeon, J. H.; Chung, I. J. *J. Mater. Process. Technol.* **2003,** *143–144,* 93–97. doi:10.1016/S0924-0136(03)00327-3
5. Choi, Y.-J.; Kim, K.-W.; Ahn, H.-J.; Ahn, J.-H. *J. Alloys Compd.* **2008,** *449,* 313–316. doi:10.1016/j.jallcom.2006.02.098
6. Huang, Y.; Sun, J.; Wang, W.; Wang, Y.; Yu, Z.; Zhang, H.; Wang, A.; Yuan, K. *J. Electrochem. Soc.* **2008,** *155,* A764–A767. doi:10.1149/1.2967191
7. Kim, N.-I.; Lee, C.-B.; Seo, J.-M.; Lee, W.-J.; Roh, Y.-B. *J. Power Sources* **2004,** *132,* 209–212. doi:10.1016/j.jpowsour.2003.12.028
8. He, X.; Ren, J.; Wang, L.; Pu, W.; Jiang, C.; Wan, C. *J. Power Sources* **2009,** *190,* 154–156. doi:10.1016/j.jpowsour.2008.07.034
9. Cheon, S.-E.; Choi, S.-S.; Han, J.-S.; Choi, Y.-S.; Jung, B.-H.; Lim, H. S. *J. Electrochem. Soc.* **2004,** *151,* A2067–A2073. doi:10.1149/1.1815153
10. Wang, Y.; Huang, Y.; Wang, W.; Huang, C.; Yu, Z.; Zhang, H.; Sun, J.; Wang, A.; Yuan, K. *Electrochim. Acta* **2009,** *54,* 4062–4066. doi:10.1016/j.electacta.2009.02.039
11. Elazari, R.; Salitra, G.; Talyosef, Y.; Grinblat, J.; Scordilis-Kelley, C.; Xiao, A.; Affinito, J.; Aurbach, D. *J. Electrochem. Soc.* **2010,** *157,* A1131–A1138. doi:10.1149/1.3479828
12. Choi, Y.-J.; Chung, Y.-D.; Baek, C.-Y.; Kim, K.-W.; Ahn, H.-J.; Ahn, J.-H. *J. Power Sources* **2008,** *184,* 548–552. doi:10.1016/j.jpowsour.2008.02.053
13. He, G.; Ji, X.; Nazar, L. *Energy Environ. Sci.* **2011,** *4,* 2878–2883. doi:10.1039/C1EE01219C
14. Wang, H.; Yang, Y.; Liang, Y.; Robinson, J. T.; Li, Y.; Jackson, A.; Cui, Y.; Dai, H. *Nano Lett.* **2011,** *11,* 2644–2647. doi:10.1021/nl200658a
15. Hassoun, J.; Agostini, M.; Latini, A.; Panero, S.; Sun, Y.-K.; Scrosati, B. *J. Electrochem. Soc.* **2012,** *159,* A390–A395. doi:10.1149/2.039204jes
16. Schneider, H.; Garsuch, A.; Panchenko, A.; Gronwald, O.; Janssen, N.; Novák, P. *J. Power Sources* **2012,** *205,* 420–425. doi:10.1016/j.jpowsour.2011.12.061
17. Cheon, S.-E.; Ko, K.-S.; Cho, J.-H.; Kim, S.-W.; Chin, E.-Y.; Kim, H.-T. *J. Electrochem. Soc.* **2003,** *150,* A800–A805. doi:10.1149/1.1571533
18. Barchasz, C.; Mesguich, F.; Dijon, J.; Leprêtre, J. C.; Patoux, S.; Alloin, F. *J. Power Sources* **2012,** *211,* 19–26. doi:10.1016/j.jpowsour.2012.03.062
19. Schuster, J.; He, G.; Mandlmeier, B.; Yim, T.; Lee, K. T.; Bein, T.; Nazar, L. F. *Angew. Chem.* **2012,** *124,* 3651–3655. doi:10.1002/ange.201107817
20. Evers, S.; Nazar, L. F. *Chem. Commun.* **2012,** *48,* 1233–1235. doi:10.1039/c2cc16726c
21. Hagen, M.; Dörfler, S.; Althues, H.; Tübke, J.; Hoffmann, M. J.; Kaskel, S.; Pinkwart, K. *J. Power Sources* **2012,** *213,* 239–248. doi:10.1016/j.jpowsour.2012.04.004
22. Rao, M.; Song, X.; Liao, H.; Cairns, E. J. *Electrochim. Acta* **2012,** *65,* 228–233. doi:10.1016/j.electacta.2012.01.051
23. Su, Y.-S.; Manthiram, A. *Nat. Commun.* **2012,** *3,* 1166. doi:10.1038/ncomms2163
24. Cañas, N. A.; Wolf, S.; Wagner, N.; Friedrich, K. A. *J. Power Sources* **2013,** *226,* 313–319. doi:10.1016/j.jpowsour.2012.10.092
25. Roduner, E.; Hiesgen, R. Fuel Cells – Proton-Exchange Membrane Fuel Cells – Membranes: Spatially Resolved Measurements. In *Encyclopedia of Electrochemical Power Sources;* Garche, J.; Dyer, C.; Moseley, P.; Ogumi, Z.; Rand, D.; Scrosatti, B., Eds.; Elsevier: Amsterdam, 2009; pp 775–786. doi:10.1016/B978-044452745-5.00938-2
26. Hiesgen, R.; Haiber, J. Measurement Methods – Structural Properties: Atomic Force Microscopy. In *Encyclopedia of Electrochemical Power Sources;* Garche, J.; Dyer, C.; Moseley, P.; Ogumi, Z.; Rand, D.; Scrosatti, B., Eds.; Elsevier: Amsterdam, 2009; pp 696–717. doi:10.1016/B978-044452745-5.00073-3
27. Zhang, Y.; Wu, X.; Feng, H.; Wang, L.; Zhang, A.; Xia, T.; Dong, H. *Int. J. Hydrogen Energy* **2009,** *34,* 1556–1559. doi:10.1016/j.ijhydene.2008.12.006
28. Zheng, W.; Liu, Y. W.; Hu, X. G.; Zhang, C. F. *Electrochim. Acta* **2006,** *51,* 1330–1335. doi:10.1016/j.electacta.2005.06.021
29. Kolosnitsyn, V. S.; Karaseva, E. V. *Russ. J. Electrochem. Soc.* **2008,** *44,* 506–509. doi:10.1134/S1023193508050029
30. Cheon, S.-E.; Ko, K.-S.; Cho, J.-H.; Kim, S.-W.; Chin, E.-Y.; Kim, H.-T. *J. Electrochem. Soc.* **2003,** *150,* A796–A799. doi:10.1149/1.1571532
31. Hiesgen, R.; Wehl, I.; Aleksandrova, E.; Roduner, E.; Bauder, A.; Friedrich, K. A. *Int. J. Energy Res.* **2010,** *34,* 1223–1238. doi:10.1002/er.1661
32. Ryu, H.-S.; Ahn, H.-J.; Kim, K.-W.; Ahn, J.-H.; Lee, J.-Y. *J. Power Sources* **2001,** *153,* 360–364. doi:10.1016/j.jpowsour.2005.05.037
33. Zhang, Z.; Zeng, T.; Qu, C.; Lu, H.; Jia, M.; Lai, Y.; Li, J. *Electrochim. Acta* **2012,** *80,* 440–444. doi:10.1016/j.electacta.2012.07.054
34. Gnanamuthu, R. M.; Lee, C. W. *Mater. Chem. Phys.* **2011,** *130,* 831–834. doi:10.1016/j.matchemphys.2011.08.060
35. Mikhaylik, Y. V.; Akridge, J. R. *J. Electrochem. Soc.* **2004,** *151,* A1969–A1976. doi:10.1149/1.1806394
36. Hiesgen, R.; Helmly, S.; Galm, I.; Morawietz, T.; Handl, M.; Friedrich, K. A. *Membranes* **2012,** *2,* 783–803. doi:10.3390/membranes2040783
37. Zhang, S.; Yuan, X.-Z.; Hiesgen, R.; Friedrich, K. A.; Wang, H.; Schulze, M.; Haug, A.; Li, H. *J. Power Sources* **2012,** *205,* 290–300. doi:10.1016/j.jpowsour.2012.01.031
38. Derjaguin, B. V.; Muller, V. M.; Toporov, Yu. P. *J. Colloid Interface Sci.* **1975,** *53,* 314–326. doi:10.1016/0021-9797(75)90018-1

Beilstein Journal of Nanotechnology

Routes to rupture and folding of graphene on rough 6H-SiC(0001) and their identification

M. Temmen[1], O. Ochedowski[2], B. Kleine Bussmann[2], M. Schleberger[2], M. Reichling[1] and T. R. J. Bollmann[*1]

Full Research Paper

Open Access

Address:
[1]Fachbereich Physik, Universität Osnabrück, Barbarastraße 7, 49076 Osnabrück, Germany and [2]Fakultät für Physik and CeNIDE, Universität Duisburg-Essen, 47048 Duisburg, Germany

Email:
T. R. J. Bollmann[*] - tbollman@uni-osnabrueck.de

* Corresponding author

Keywords:
graphene; Kelvin probe force microscopy (KPFM), local contact potential difference (LCPD); non-contact atomic force microscopy (NC-AFM); SiC

Beilstein J. Nanotechnol. **2013,** *4,* 625–631.
doi:10.3762/bjnano.4.69

Received: 05 May 2013
Accepted: 12 September 2013
Published: 07 October 2013

This article is part of the Thematic Series "Advanced atomic force microscopy techniques II".

Guest Editors: T. Glatzel and T. Schimmel

Abstract

Twisted few layer graphene (FLG) is highly attractive from an application point of view, due to its extraordinary electronic properties. In order to study its properties, we demonstrate and discuss three different routes to in situ create and identify (twisted) FLG. Single layer graphene (SLG) sheets mechanically exfoliated under ambient conditions on 6H-SiC(0001) are modified by (i) swift heavy ion (SHI) irradiation, (ii) by a force microscope tip and (iii) by severe heating. The resulting surface topography and the surface potential are investigated with non-contact atomic force microscopy (NC-AFM) and Kelvin probe force microscopy (KPFM). SHI irradiation results in rupture of the SLG sheets, thereby creating foldings and bilayer graphene (BLG). Applying the other modification methods creates enlarged (twisted) graphene foldings that show rupture along preferential edges of zigzag and armchair type. Peeling at a folding over an edge different from a low index crystallographic direction can result in twisted BLG, showing a similar height as Bernal (or AA-stacked) BLG in NC-AFM images. The rotational stacking can be identified by a significant contrast in the local contact potential difference (LCPD) measured by KPFM.

Introduction

Since its discovery in 2004 [1], graphene, the 2D crystal with a honeycomb lattice of sp^2-bonded carbon atoms, has been shown to have unique properties such as high mechanical strength and elasticity, a very high electrical and thermal conductivity, the impermeability to gases, and many others [2]. All of them make it highly attractive for numerous applications, and a most promising candidate for advanced microelectronics technology [3], in which especially bilayer graphene (BLG) is of interest, as its band gap can be tuned [4]. Although the electronic properties of AB-stacked (Bernal) BLG is of special interest due to its tunable bandgap, rotationally stacked or twisted BLG is more attractive from an application point of view due to its

angle-dependent electronic properties [4-10]. Twisted few layer graphene (FLG) exhibits electronic properties ranging from Dirac cones found for single layer graphene (SLG) for rotation angles over 15° where the layers are effectively decoupled, to a Fermi velocity renormalization for smaller rotation angles [8-11]. For very small rotation angles, $\theta \leq 2°$, the electronic properties are found to be coupled to the resulting moiré spots for twisted BLG [10].

In order to study these properties experimentally, (few layer) graphene can be produced in various ways. The growth of graphene on metals followed by transfer to another substrate as well as epitaxial growth on SiC, both have a potential for mass production if technological shortcomings can be overcome. However, exfoliation from graphite still results in graphene flakes of highest quality [1,2], which then can be modified in situ to create (twisted) FLG. In comparison to the well known epitaxial growth of graphene on SiC [12-14], here we study mechanically exfoliated graphene on 6H-SiC(0001) to produce large sheets of high quality. Defects are first created by swift heavy ions (SHI). The unique controllability of SHI irradiation, by tuning the incident angle with respect to the crystallographic directions of graphene as well as the range and the energy loss mechanism, makes it a viable route for one-dimensional controlled defect creation relevant for future applications [15,16]. By the use of ions having kinetic energies in the range of 100 MeV impinging under grazing incidence, it has already been shown that SLG flakes can be ruptured in a controlled process by highly localized energy deposition [15]. This results in foldings that are BLG sheets produced in the vicinity of the ion track. Foldings can also be produced by line scanning the sample with an AFM tip in the contact mode, in which the tip forces are capable of rupturing the sheet [17]. Here, we report that also severe heating is able to create foldings on SLG, deposited under ambient conditions. The modification method making use of SHI irradiation is further on referred to as method (i), contacting and line scanning, as method (ii), and severe heating, as method (iii), respectively. The combination of the latter two is further on referred to as *post-preparation treatment*. Note that in some cases the origin of the foldings can not be uniquely identified as method (ii) or (iii) as AFM imaging involves strong tip–sample interactions.

Rupture and folding result in a system where we can study and compare properties of graphene in several thicknesses, sheet orientations, edges [18,19] and stackings. To discriminate the different BLG stackings, we investigate the topography by non-contact atomic force microscopy (NC-AFM) combined with measuring the local contact potential differences (LCPD) using Kelvin probe force microscopy (KPFM).

Experimental

Graphene is exfoliated from a HOPG crystal (Momentive Performance Materials, Columbus, OH, USA) under ambient conditions on an as delivered Si-rich 6H-SiC(0001) substrate (Pam-XIAMEN, Xiamen, China) applying a well known recipe [1]. After preparation, the sample is taken in ambient atmosphere to the IRRSUD beamline of the Grand Accélérateur National d'Ions Lourds GANIL (Caen, France) for SHI irradiation with 81 MeV Ta^{24+} ions under 1.5° grazing incidence. The ion fluence is adjusted to 5–10 ions/μm^2.

Irradiated samples are initially inspected by tapping mode atomic force microscopy performed under ambient conditions using a Dimension 3100 AFM (Veeco Metrology, Santa Barbara, CA, USA) and NCHR cantilevers (Nanosensors, Neuchatel, Switzerland). NC-AFM images are obtained using a well characterized [20-22] UHV 750 NC-AFM system (RHK Technology, Troy, MI, USA) in an ultra-high vacuum chamber with a base pressure well below 5×10^{-11} mbar. Force sensors used are NCH Si cantilevers (Nanosensors, Neuchatel, Switzerland) with the exception of the measurements presented in Figure 7a, in which a Vistaprobe T-300 cantilever (Vistaprobe, Phoenix, AZ, USA) was used. Both cantilevers have a fundamental eigenfrequency $f_0 \approxeq 300$ kHz. To obtain correct height measurements, KPFM [23,24] imaging is performed simultaneously by applying an AC voltage of 1 V amplitude at a frequency of 1.2 kHz added to the DC bias regulated to minimize electrostatic forces. To remove volatile surface contaminants that can significantly influence LCPD measurements [25], the sample is heated in UHV to 500 K prior to measurements. All images in this paper are presented without filtering or smoothing. The topographic images are compensated for piezo creep and drift as well as for scanner bow using common plane subtraction and (facet) leveling algorithms of the Gwyddion software package [26].

Results and Discussion

Graphene flake characterization

After mechanically exfoliating graphene on the 6H-SiC(0001) substrate, a flake is selected that has a width of 2–3 μm and a length of ≈40 μm. The flake shows straight parallel edges and the apparent thickness of the SLG flake is 0.7 ± 0.4 nm. Since a thickness measurement of SLG flakes is not straightforward and thickness values reported in literature range from 0.35 nm to ≈1 nm [1,27-29], we use a LabRAM HR micro-Raman spectrometer (Horiba, Kyoto, Japan) to confirm the identity as SLG using its 2D band [30,31]. Figure 1 shows the Raman spectrum measured for the 6H-SiC(0001) substrate and the SLG covered substrate. The sharpness and symmetry of the 2D band around 2650 cm^{-1} combined with the quality of the single Lorentzian fit are characteristic for the presence of SLG [30,31].

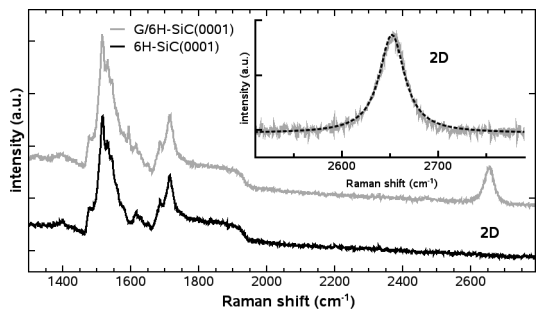

Figure 1: Micro-Raman spectrum for both, the substrate and the SLG flake introduced in Figure 3. The inset shows the 2D Raman peak and its Lorentzian fit.

Mechanically exfoliated graphene is known to adapt to its substrate like a carpet [32]. The Kelvin-compensated NC-AFM topography measurements taken on SLG reflect the substrate step structure with its bilayer step height of 0.33 ± 0.10 nm [13]. A representative line profile is shown in the inset of Figure 2. To determine whether the roughness on the SLG reflects the contours of the underlying substrate, we determine the height distribution on both, the bare substrate and the graphene covered substrate in 70 × 70 nm^2 areas free of steps. The roughness can be characterized by the standard deviation σ of the height distribution [32] shown in Figure 2. For the exfoliated SLG sheet we find a roughness that is about 60% of the substrate roughness, indicating that graphene adapts to its underlying substrate closely but removes part of its roughness.

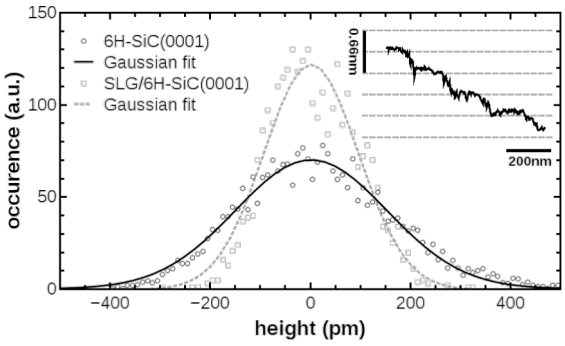

Figure 2: Roughness analysis of NC-AFM images taken on a single terrace within 70 × 70 nm^2 on the 6H-SiC(0001) substrate (standard deviation σ = 304 pm) and on the SLG (σ = 189 pm). The inset shows a line profile taken on the SLG flake perpendicular to substrate step edges measured by Kelvin-compensated NC-AFM.

Methods for rupture and folding of graphene

To create FLG including layers with twisted stacking, the exfoliated graphene is exposed to SHI irradiation (i) followed by a combination of line scanning the sample with an AFM tip (ii) and severe heating (iii). The tapping mode AFM survey image shown in Figure 3a exhibits a representative part of the flake comprising all phenomena discussed in this paper, rupture and folding of various origin, labeled by (i), (ii) and (iii), respectively. The tapping mode AFM survey image shown in Figure 3b, has been taken right after SHI irradiation where the SLG shows foldings at an angle of 58.0 ± 1.2° with respect to the flakes edge. The properties of such foldings related to the ion track have been described in more detail elsewhere [15]. Defects created by method (i) can be used as a seed for further rupture created by methods (ii) and (iii). The dimensions of the tip-induced foldings (ii) are similar to the ones reported in literature and can be created without defects of type (i) [17]. Severe heating results in the opening at locations of existing rupture, creating type (iii) structures. For this type of modification, the interfacial layer residing between the substrate and the SLG flake due to its exfoliation in ambient, is anticipated to play a major role. Thin water films resulting from exfoliation in ambient have been recognized in literature as an important feature determining the sheet properties [33-39]. The structures of type (iii) might act as a pressure release for heated water confined at the interface. The dashed box in Figure 3a shows the same region as the dashed box in Figure 3b after heating to 700 K. The onset of the heating effect is found at about 500 K.

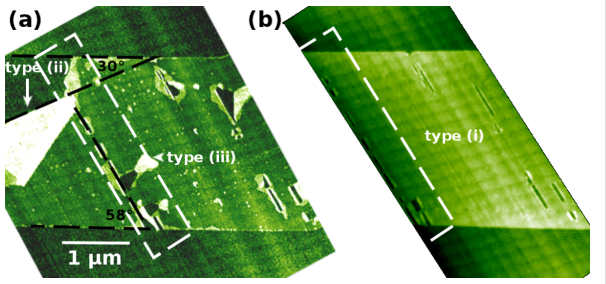

Figure 3: Tapping mode AFM image (a) of an exfoliated SLG flake on 6H-SiC(0001) showing examples of rupture and folding by the use of SHI, type (i), modification by AFM tip contacting and linescanning (ii), and severe heating (iii). Tapping mode AFM image (b) showing the modifications of SLG solely due to SHI irradiation, type (i), namely foldings aligned with the ion track. The dashed box in Figure 3(a) exhibiting modifications of type (ii) and (iii) added later, corresponds to the dashed box in Figure 3(b) prior to post-preparation treatment.

Discriminating graphene stackings by their surface potential

Next, we investigate the graphene layer, its rupture, foldings and stacking in more detail by Kelvin compensated NC-AFM imaging, demonstrating the identification of (twisted) FLG. To study the properties of rupture and foldings in the SLG originating from treatment with methods (i), (ii) and (iii) in detail, we analyze images taken in the areas A, B and C marked by the boxes in Figure 4.

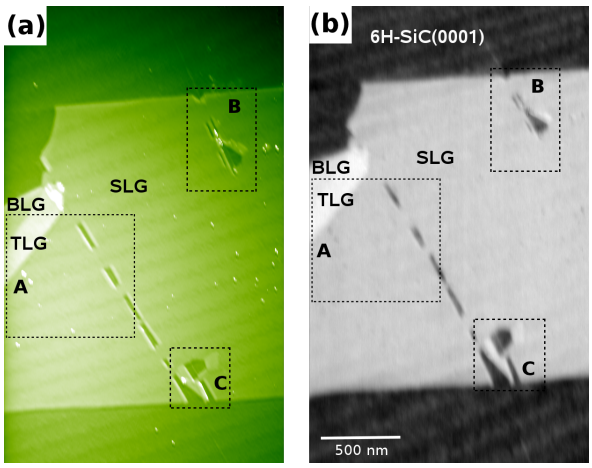

Figure 4: NC-AFM image (a) of an exfoliated SLG flake on 6H-SiC(0001), irradiated with SHI and subjected to post-preparation treatment, and its corresponding LCPD image (b). Folding structures, which result from post-preparation treatment labeled by A, B and C are analyzed in detail in Figure 5, Figure 6 and Figure 7.

The folding marked by A in Figure 4 is a typical example of a type (ii) folding, in which the folding over 30° with respect to the SLG flakes edge (see also Figure 3), results in large Bernal-stacked (or energetically unfavorable AA-stacked) areas of BLG and trilayer graphene (TLG). Figure 5a shows a detailed KPFM image of region A, the corresponding height profile in Figure 5b, and CPD histogram in Figure 5c performed in the white square shown in Figure 5a, from which the LCPD of BLG and TLG with respect to SLG can be determined. The LCPD between SLG and BLG is found to be 137 mV, which is in agreement with the LCPD found in a previous study [16,40] as well as for epitaxially grown SLG and BLG [12]. Between BLG and TLG, the LCPD is determined to be 43 mV. From the line profile in the topography, the interlayer distance between SLG and BLG (0.37 ± 0.10 nm) and BLG and TLG (0.36 ± 0.10 nm) are determined, in agreement with the interlayer distance found for graphite stacking [41-43]. A similar result is found for the folding marked by B, where the respective image is shown in Figure 6.

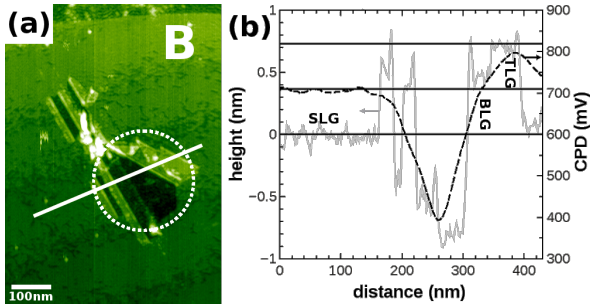

Figure 6: (a) NC-AFM image of the region marked by B in Figure 4, where post-preparation treatment resulted in the folding encircled by the dashed line. Line profiles (b) reveal the height (solid gray line) of BLG (limited accuracy due to areal size and spatial resolution) and TLG (+0.72 nm with respect to SLG) in agreement with the interlayer distance (marked by horizontal full lines) found for graphite stacking. From the LCPD line profile (dashed black line), the LCPD of the different foldings can not be discriminated due to the limited spatial resolution.

Figure 6a shows a detailed topographic image, in which the folding structure that results from SHI irradiation and post-preparation treatment is encircled. The edges of folding structures have angles of 30°, 90° and 120° with respect to the SLG flake edges reflecting the six-fold symmetry of the graphene lattice combined with the two most stable edge configurations, namely zigzag and armchair [18,19]. From the line profile (grey dashed line) in Figure 6b, the interlayer distance between SLG and TLG (0.72 nm) is determined, again in agreement with the interlayer distance found for graphite stacking [41-43]. For this folding, the areas for BLG and TLG are too small in size and too close to each other to be spatially resolved by KPFM.

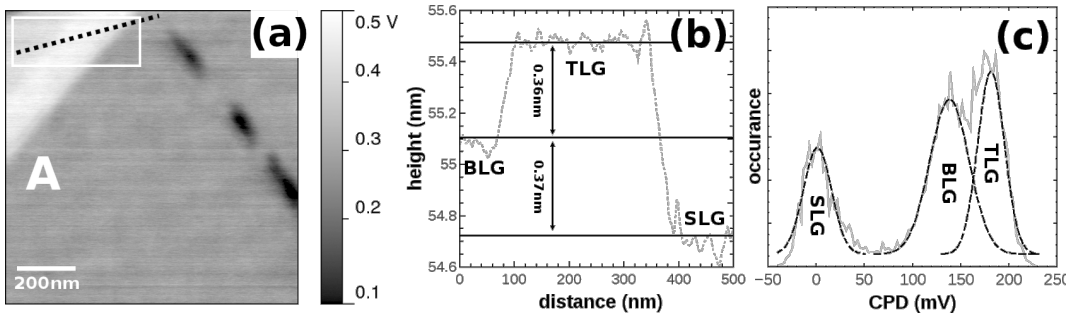

Figure 5: (a) LCPD image of the folding marked by A in Figure 4. (b) The profile taken in the corresponding NC-AFM image reveals the height of BLG and TLG in agreement with the interlayer distance (marked by horizontal full lines) found for graphite stacking. (c) From the CPD histogram performed in the square marked in Figure 5a, the LCPD between SLG and BLG (137 ± 40 meV) and BLG and TLG (43 ± 27 meV) can be identified by normal distributions, in which the error is one standard deviation (σ).

Therefore, the foldings can not be discriminated in the LCPD line profile (black full line) shown in Figure 6b.

Figure 7a shows a detailed topographic image of region C right after SHI bombardment and slight heating, which results in foldings that are BLG sheets aligned with the ion track. Figure 7b shows the same region C after applying post-preparation treatment, which results in enlarged foldings left and right of the region already opened by the SHI impact. In contrast to the situation right after SHI irradiation, foldings appear ruptured along characteristic angles with respect to the flake edges. As can be seen from the comparison of Figure 7a and Figure 7b, the post-preparation treatment of a SLG sheet, which has been folded, can be interpreted as peeling the folding away from the region already opened by the SHI impact as illustrated in Figure 7d [44]. Due to the high elasticity of graphene, when peeling the folding by applying the post-preparation methods, the SLG detaches from the substrate and folds back onto itself, thereby extending the folding and enlarging the opened region. Peeling at an angle can result in a twisted BLG sheet with rupturing along preferential directions as demonstrated below.

To understand the role of the preferential directions of rupture, we start by identifying the edge of the large SLG flake, marked by the white line at the bottom of the image. The edge resulting from exfoliation is expected to have a preferential direction being either a zigzag or an armchair edge. Therefore, the vast majority of edges formed by rupture due to post-preparation treatment are found to be aligned at 30° and 60° with respect to the SLG flake edge, exemplified at the bottom of Figure 7b. Considering the symmetry of the graphene lattice, these ruptures can, therefore, be identified as either zigzag or armchair edges.

Assigning the SLG flake edge, being of either zigzag or armchair structure, the dashed lines enclosing an angle of 30° with the SLG flake edge, therefore, correspond to the other type edges. However, the edge over which the folding on the right took place, marked by the arrow in Figure 7b, has an angle of about 70° with respect to the SLG flake edges as a result of peeling under an angle by applying the post-preparation treatment. One might, therefore, expect a twisted or rotational stacking for the attached BLG. Note that, although peeling at a slight angle on the existing folding results in a twisted stacking, the (preferential) directions of rupture are unaffected by this. Comparing the height of this folding with the one on the left side of the SHI track as shown in Figure 7e does, however, not reveal any significant difference in height. The height found

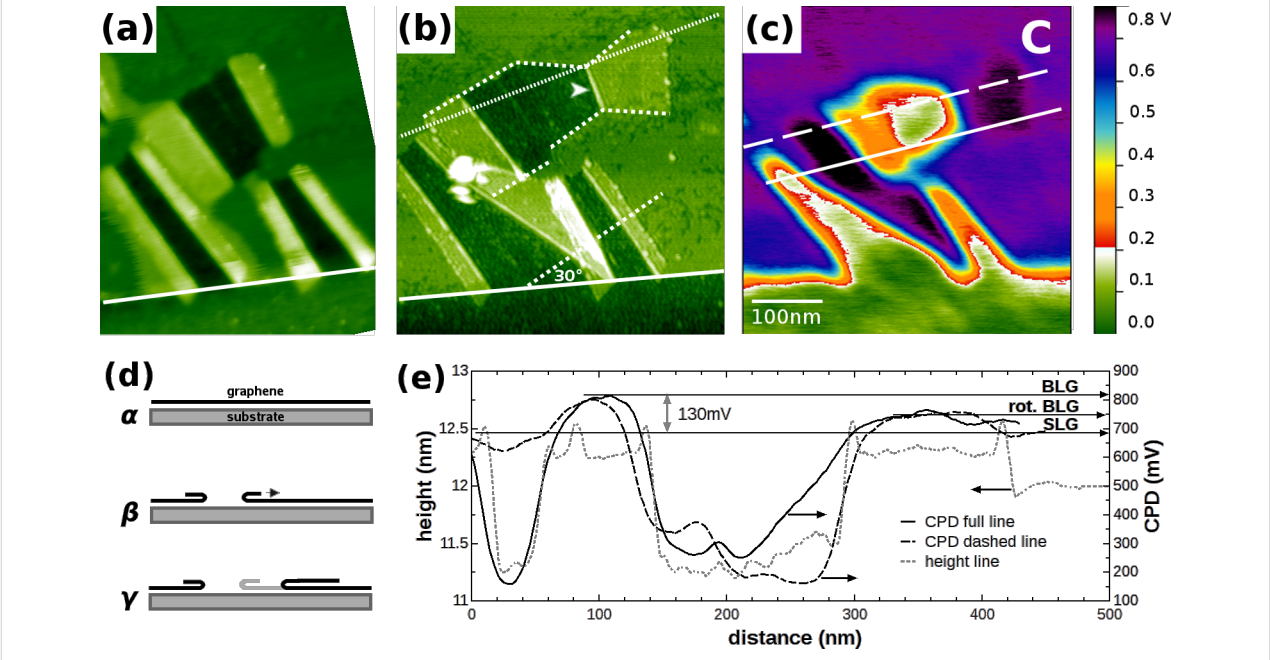

Figure 7: NC-AFM image of the region marked C in Figure 4 with foldings due to SHI impact on the left and right of the ion track prior to (a) and after (b) post-preparation treatment. (b) Large folding created by post-preparation treatment, where the identified edges, zigzag and armchair, are labeled by (white) full and dashed lines and make angles of 30° with respect to each other as exemplified at the bottom. (c) LCPD image taken at the same position but extracted from a different image. (d) Cartoons of the graphene exfoliated on the substrate (α), after SHI irradiation creating BLG (β), followed by applying post-preparation methods where the direction of peeling the folding on the right is marked by the arrow (γ). (e) Line profiles taken in frames (b) and (c) reveal the same height but a significant difference in the LCPD for the two foldings. The LCPD difference is attributed to the stacking difference as expected from the misalignment of the right folding with respect to the low index crystallographic directions of the SLG flake.

for both foldings is in agreement with the values found in Figure 5 and Figure 6. Within the error of several angstroms for the height measurement, we are unable to discriminate between the AA- and AB-stacking interlayer distance difference of 10% [42,45-47].

However, by the use of KPFM, one is able to clearly discriminate between different rotational stackings. In Figure 7c, we show the LCPD of the large BLG foldings on the left and right of the ion track. As a striking observation, we note that the two BLG foldings show a slight but significant difference in their LCPD. Care has to be taken by comparing the LCPD for the two foldings due to the influence of the substrate steps on the LCPD measurement. In this case, however, both foldings are on the same terrace and quite far away from any step edge. The line profiles drawn in Figure 7e, in the center and within close vicinity to the step edge, show identical behavior for the two foldings. The LCPD measured for the left (810 ± 5 mV) and for the right (754 ± 13 mV) folding, enables us to discriminate twisted BLG by ≈55 mV which is well above the variation in LCPD on a SLG or BLG sheet. The reduced potential of the twisted folding on the right is in between that of SLG and Bernal- (or energetically unfavourable AA-) stacked BLG.

Conclusion

In summary, we demonstrate different routes to rupture and folding of SLG on a 6H-SiC(0001) substrate as well as experimental techniques to identify and discriminate the resulting (twisted) BLG and TLG structures. Rupture and folding of SLG on a 6H-SiC(0001) can be induced by scanning and contacting with an AFM tip and by severe heating resulting in foldings with (AA- or) Bernal-stacking and twisted stacking. SLG sheets rupture along preferential edges of zigzag and armchair type, even when peeling an existing folding is performed under an angle resulting in a twisted stacking. While the (AA- or) Bernal-stacked BLG and twisted BLG can not be discriminated by their height, they can clearly be distinguished by the difference in their LCPD.

Acknowledgements

The authors are grateful to B. Ban d'Etat and H. Lebius, at the IRRSUD beamline of the Grand Accélérateur National d'Ions Lourds GANIL (Caen, France) for assistance in sample preparation. This work was supported by the SPP 1459 and by the SFB 616 of the Deutsche Forschungsgemeinschaft and by the European Community in the framework of the Integrating Activity Support of Public and Industrial Research Using Ion Beam Technology (SPIRIT) under EC contract no. 227012. M.T. gratefully appreciates support from the Hans-Mühlenhoff-Stiftung.

References

1. Novoselov, K. S.; Geim, A. K.; Morozov, S. V.; Jiang, D.; Zhang, Y.; Dubonos, S. V.; Grigorieva, I. V.; Firsov, A. A. *Science* **2004,** *306,* 666–669. doi:10.1126/science.1102896
2. Soldano, C.; Mahmood, A.; Dujardin, E. *Carbon* **2010,** *48,* 2127–2150. doi:10.1016/j.carbon.2010.01.058
3. Novoselov, K. S.; Fal'ko, V. S.; Colombo, L.; Gellert, P. R.; Schwab, M. G.; Kim, K. *Nature* **2012,** *490,* 192–200. doi:10.1038/nature11458
4. Zhang, Y.; Tang, T.-T.; Girit, C.; Hao, Z.; Martin, M. C.; Zettl, A.; Crommie, M. F.; Shen, Y. R.; Wang, F. *Nature* **2009,** *459,* 820. doi:10.1038/nature08105
5. Lopes dos Santos, J. M. B.; Peres, N. M. R.; Castro Neto, A. H. *Phys. Rev. Lett.* **2007,** *99,* 256802. doi:10.1103/PhysRevLett.99.256802
6. Hass, J.; Varchon, F.; Millán-Otoya, J. E.; Sprinkle, M.; Sharma, N.; de Heer, W. A.; Berger, C.; First, P. N.; Magaud, L.; Conrad, E. H. *Phys. Rev. Lett.* **2008,** *100,* 125504. doi:10.1103/PhysRevLett.100.125504
7. Li, G.; Luican, A.; Lopes dos Santos, J. M. B.; Castro Neto, A. H.; Reina, A.; Kong, J.; Andrei, E. Y. *Nat. Phys.* **2010,** *6,* 109–113. doi:10.1038/nphys1463
8. Mele, E. J. *J. Phys. D: Appl. Phys.* **2011,** *45,* 23.
9. Luican, A.; Li, G.; Reina, A.; Kong, J.; Nair, R. R.; Novoselov, K. S.; Geim, A. K.; Andrei, E. Y. *Phys. Rev. Lett.* **2011,** *106,* 126802. doi:10.1103/PhysRevLett.106.126802
10. Landgraf, W.; Shallcross, S.; Türschmann, K.; Weckbecker, D.; Pankratov, O. *Phys. Rev. B* **2013,** *87,* 075433. doi:10.1103/PhysRevB.87.075433
11. Suárez Morell, E.; Pacheco, M.; Chico, L.; Brey, L. *Phys. Rev. B* **2013,** *87,* 125414. doi:10.1103/PhysRevB.87.125414
12. Filleter, T.; Emtsev, K. V.; Seyller, T.; Bennewitz, R. *Appl. Phys. Lett.* **2008,** *93,* 133117. doi:10.1063/1.2993341
13. Held, C.; Seyller, T.; Bennewitz, R. *Beilstein J. Nanotechnol.* **2012,** *3,* 179–185. doi:10.3762/bjnano.3.19
14. Kageshima, H.; Hibino, H.; Tanabe, S. *J. Phys.: Condens. Matter* **2012,** *24,* 314215. doi:10.1088/0953-8984/24/31/314215
15. Akcöltekin, S.; Bukowska, H.; Peters, T.; Osmani, O.; Monnet, I.; Alzaher, I.; Ban d'Etat, B.; Lebius, H.; Schleberger, M. *Appl. Phys. Lett.* **2011,** *98,* 103103. doi:10.1063/1.3559619
16. Ochedowski, O.; Bussmann, B. K.; Ban d'Etat, B.; Lebius, H.; Schleberger, M. *Appl. Phys. Lett.* **2013,** *102,* 153103. doi:10.1063/1.4801973
17. Carozo, V.; Almeida, C. M.; Ferreira, E. H. M.; Cançado, L. G.; Achete, C. A.; Jorio, A. *Nano Lett.* **2011,** *11,* 4527–4534. doi:10.1021/nl201370m
18. Jia, X.; Hofmann, M.; Meunier, V.; Sumpter, B. G.; Campos-Delgado, J.; Romo-Herrera, J. M.; Son, H.; Hsieh, Y.-P.; Reina, A.; Kong, J.; Terrones, M.; Dresselhaus, M. S. *Science* **2009,** *323,* 1701–1705. doi:10.1126/science.1166862
19. Girit, C. O.; Meyer, Ç. Ö.; Erni, R.; Rossell, M. D.; Kisielowski, C.; Yang, L.; Park, C.-H.; Crommie, M. F.; Cohen, M. L.; Louie, S. G.; Zettl, A. *Science* **2009,** *323,* 1705–1708. doi:10.1126/science.1166999
20. Lübbe, J.; Tröger, L.; Torbrügge, S.; Bechstein, R.; Richter, C.; Kühnle, A.; Reichling, M. *Meas. Sci. Technol.* **2010,** *21,* 125501. doi:10.1088/0957-0233/21/12/125501
21. Lübbe, J.; Doering, L.; Reichling, M. *Meas. Sci. Technol.* **2012,** *23,* 045401. doi:10.1088/0957-0233/23/4/045401
22. Lübbe, J.; Temmen, M.; Rode, S.; Rahe, P.; Kühnle, A.; Reichling, M. *Beilstein J. Nanotechnol.* **2013,** *4,* 32–44. doi:10.3762/bjnano.4.4

23. Nonnenmacher, M.; O'Boyle, M. P.; Wickramasinghe, H. K. *Appl. Phys. Lett.* **1991,** *58,* 2921–2923. doi:10.1063/1.105227
24. Weaver, J. M. R.; Abraham, D. W. *J. Vac. Sci. Technol., B: Microelectron. Nanometer Struct.–Process., Meas., Phenom.* **1991,** *9,* 1559–1561. doi:10.1116/1.585423
25. Bukowska, H.; Meinerzhagen, F.; Akcöltekin, S.; Ochedowski, O.; Neubert, M.; Buck, V.; Schleberger, M. *New J. Phys.* **2011,** *13,* 063018. doi:10.1088/1367-2630/13/6/063018
26. Nečas, D.; Klapetek, P. *Cent. Eur. J. Phys.* **2012,** *10,* 181–188. doi:10.2478/s11534-011-0096-2
27. Ishigami, M.; Chen, J. H.; Cullen, W. G.; Fuhrer, M. S.; Williams, E. D. *Nano Lett.* **2007,** *7,* 1643–1648. doi:10.1021/nl070613a
28. Nemes-Incze, P.; Osváth, Z.; Kamarás, K.; Biró, L. P. *Carbon* **2008,** *46,* 1435–1442. doi:10.1016/j.carbon.2008.06.022
29. Akcöltekin, S.; El Kharrazi, M.; Köhler, B.; Lorke, A.; Schleberger, M. *Nanotechnology* **2009,** *20,* 155601. doi:10.1088/0957-4484/20/15/155601
30. Malard, L. M.; Pimenta, M. A.; Dresselhaus, G.; Dresselhaus, M. S. *Phys. Rep.* **2009,** *473,* 51–87. doi:10.1016/j.physrep.2009.02.003
31. Ferrari, A. C.; Basko, D. M. *Nat. Nanotechnol.* **2013,** *8,* 235–246. doi:10.1038/nnano.2013.46
32. Lui, C. H.; Liu, L.; Mak, K. F.; Flynn, G. W.; Heinz, T. F. *Nature* **2009,** *462,* 339–341. doi:10.1038/nature08569
33. Xu, K.; Cao, P.; Heath, J. R. *Science* **2010,** *329,* 1188–1191. doi:10.1126/science.1192907
34. Cao, P.; Xu, K.; Varghese, J. O.; Heath, J. R. *Nano Lett.* **2011,** *11,* 5581–5586. doi:10.1021/nl2036639
35. He, K. T.; Wood, J. D.; Doidge, G. P.; Pop, E.; Lyding, J. W. *Nano Lett.* **2012,** *12,* 2665–2672. doi:10.1021/nl202613t
36. Komurasaki, H.; Tsukamoto, T.; Yamazaki, K.; Ogino, T. *J. Phys. Chem. C* **2012,** *116,* 10084–10089. doi:10.1021/jp301402u
37. Lee, M. J.; Choi, J. S.; Kim, J.-S.; Byun, I.-S.; Lee, D. H.; Ryu, S.; Lee, C.; Park, B. H. *Nano Res.* **2012,** *5,* 710–717. doi:10.1007/s12274-012-0255-9
38. Shim, J.; Lui, C. H.; Ko, T. Y.; Yu, Y.-J.; Kim, P.; Heinz, T. F.; Ryu, S. *Nano Lett.* **2012,** *12,* 648–654. doi:10.1021/nl2034317
39. Verdaguer, A.; Segura, J. J.; López-Mir, L.; Sauthier, G.; Fraxedas, J. *J. Chem. Phys.* **2013,** *138,* 121101. doi:10.1063/1.4798941
40. Bussmann, B. K.; Ochedowski, O.; Schleberger, M. *Nanotechnology* **2011,** *22,* 265703. doi:10.1088/0957-4484/22/26/265703
41. Bernal, J. D. *Proc. R. Soc. London, Ser. A* **1924,** *106,* 749–773. doi:10.1098/rspa.1924.0101
42. Baskin, Y.; Meyer, L. *Phys. Rev.* **1955,** *100,* 544. doi:10.1103/PhysRev.100.544
43. Chung, D. D. L. *J. Mater. Sci.* **2002,** *37,* 1475–1489. doi:10.1023/A:1014915307738
44. Shi, X.; Yin, Q.; Wei, Y. *Carbon* **2012,** *50,* 3055–3063. doi:10.1016/j.carbon.2012.02.092
45. Ziambaras, E.; Kleis, J.; Schröder, E.; Hyldgaard, P. *Phys. Rev. B* **2007,** *76,* 155425. doi:10.1103/PhysRevB.76.155425
46. Lebègue, S.; Harl, J.; Gould, T.; Ángyán, J. G.; Kresse, G.; Dobson, J. F. *Phys. Rev. Lett.* **2010,** *105,* 196401. doi:10.1103/PhysRevLett.105.196401
47. Alam, M. S.; Lin, J.; Saito, M. *Jpn. J. Appl. Phys.* **2011,** *50,* 080213. doi:10.1143/JJAP.50.080213

License and Terms

Beilstein Journal of Nanotechnology

Site-selective growth of surface-anchored metal-organic frameworks on self-assembled monolayer patterns prepared by AFM nanografting

Tatjana Ladnorg[1], Alexander Welle[2], Stefan Heißler[1], Christof Wöll[1] and Hartmut Gliemann[*1]

Full Research Paper

Open Access

Address:
[1]Institute of Functional Interfaces (IFG), Karlsruhe Institute of Technology (KIT), Hermann-von-Helmholtz-Platz 1, 76344 Eggenstein-Leopoldshafen, Germany and [2]Institute for Biological Interfaces 1 (IBG1), Karlsruhe Institute of Technology (KIT), Hermann-von-Helmholtz-Platz 1, 76344 Eggenstein-Leopoldshafen, Germany

Email:
Hartmut Gliemann[*] - hartmut.gliemann@kit.edu

* Corresponding author

Keywords:
atomic force microscopy (AFM); metal-organic frameworks; nanografting; nanoshaving; SURMOF

Beilstein J. Nanotechnol. **2013,** *4,* 638–648.
doi:10.3762/bjnano.4.71

Received: 29 May 2013
Accepted: 17 September 2013
Published: 11 October 2013

This article is part of the Thematic Series "Advanced atomic force microscopy techniques II".

Guest Editors: T. Glatzel and T. Schimmel

Abstract

Surface anchored metal-organic frameworks, SURMOFs, are highly porous materials, which can be grown on modified substrates as highly oriented, crystalline coatings by a quasi-epitaxial layer-by-layer method (liquid-phase epitaxy, or LPE). The chemical termination of the supporting substrate is crucial, because the most convenient method for substrate modification is the formation of a suitable self-assembled monolayer. The choice of a particular SAM also allows for control over the orientation of the SURMOF. Here, we demonstrate for the first time the site-selective growth of the SURMOF HKUST-1 on thiol-based self-assembled monolayers patterned by the nanografting technique, with an atomic force microscope as a structuring tool. Two different approaches were applied: The first one is based on 3-mercaptopropionic acid molecules which are grafted in a 1-decanethiolate SAM, which serves as a matrix for this nanolithography. The second approach uses 16-mercaptohexadecanoic acid, which is grafted in a matrix of an 1-octadecanethiolate SAM. In both cases a site-selective growth of the SURMOF is observed. In the latter case the roughness of the HKUST-1 is found to be significantly higher than for the 1-mercaptopropionic acid. The successful grafting process was verified by time-of-flight secondary ion mass spectrometry and atomic force microscopy. The SURMOF structures grown via LPE were investigated and characterized by atomic force microscopy and Fourier-transform infrared microscopy.

Introduction

Metal organic frameworks (MOFs) are highly crystalline three-dimensional micro- and mesoporous materials that consist of metal ions or metal-oxo units (serving as nodes) interconnected by organic linkers. In conventional synthesis the MOFs are formed in a solvothermal process, and the reaction products precipitate in the form of crystalline powders [1,2]. One of the best-known MOFs is HKUST-1, first introduced by Chui et al. [3]. This MOF consists of "paddle wheels" formed by attaching 1,3,5-benzenetricarboxylate linkers to a Cu^{2+}-dimer (see Figure 1a). Meanwhile several thousands of different MOF structures are documented in the literature [4]. The high variety of the nodes and linkers as well as the huge number of possible combinations allows, in principle, the preparation of an almost infinite number of different MOF structures with different chemical and/or physical and geometrical properties (e.g., pore size and pore structure, etc.), which can be tailored for the corresponding application.

As a particulate system this class of material is already applied in the field of nanotechnology, e.g., for gas storage and gas separation [6-8], catalysis [9], delivery of therapeutic agents [10-12] and sensor devices [13]. Presently, more advanced applications are discussed, in particular in medicine and technology. For many of the more advanced applications the MOF materials need to be deposited on a solid substrate. Several methods have been introduced to create MOF-based coatings (for a recent review see [14]). One possible procedure is the so called in-situ synthesis, which was introduced by Bein et al. [15]. In this synthesis the MOF crystals are grown by dipping a gold coated substrate, which is terminated with a thiol-based self-assembled monolayer (SAM), into a solution containing a mixture of the metal nodes and the organic linkers. As a result, the MOF crystal growth is started by a substrate-induced nucleation process. Many of the methods developed to deposit MOFs on solid substrates suffer from the fact that the resulting MOF layer has a polycrystalline character due to the random orientation of the crystals on the substrate. In the field of catalysis, for example, this polycrystalline character might hinder or even suppress the free diffusion of molecules or reaction products into or out of the MOF layer. To overcome these limitations, which result from the highly polycrystalline nature of the MOF-coatings, a novel method was recently developed that produces very smooth, homogeneous MOF-coatings. These surface anchored metal–organic frameworks (SURMOFs) exhibit a uniform layer thickness and are fabricated using a novel layer-by-layer (LBL) method [16-20]. This procedure is schematically shown in Figure 1b. First, a gold coated substrate is modified by the deposition of a thiol-based SAM, that carries either an –OH, a –COOH or a pyridine unit. The SAM, and in particular its surface termination, plays a crucial role in this context

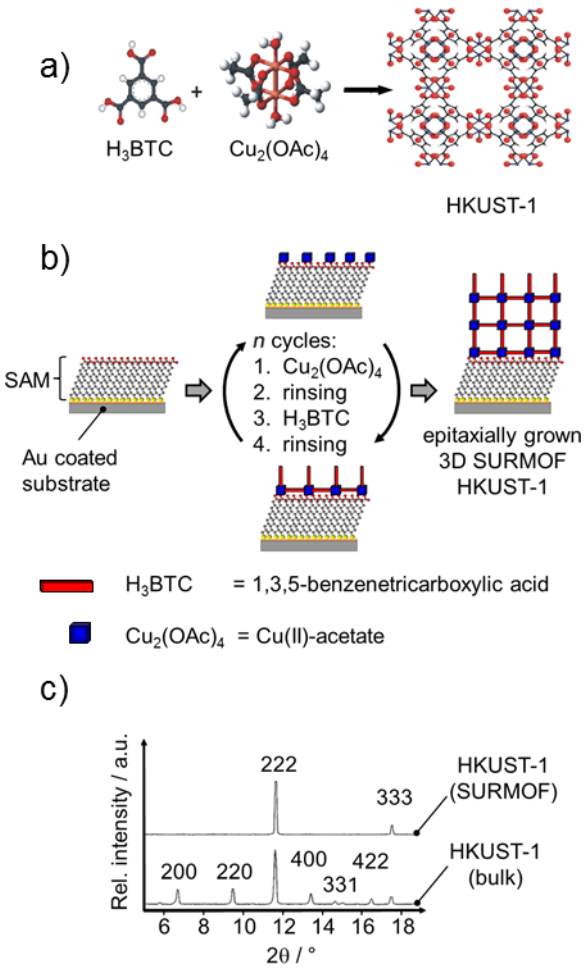

Figure 1: (a) Building units for the growth of MOF HKUST-1 and the unit cell of HKUST-1. (b) The principle of the layer-by-layer growth of a surface anchored MOF. (c) XRD results for a polycrystalline particulate HKUST-1 sample and the corresponding SURMOF. The oriented growth of the SURMOF material is clearly proven by the two reflexes of the SURMOF in the [111] direction [5].

and also determines the growth direction of the SURMOF [14,15]. On a CH_3-terminated SAM no deposition takes place [16]. Subsequent to SAM deposition the substrate is immersed into a solution of the metal node, rinsed, dipped in the linker solution and rinsed again. After this procedure the first layer of the SURMOF is deposited and the SURMOF thickness can be precisely and reproducibly controlled by the number of cycles [21]. The size of the pores within this crystalline periodic material can be controlled by the length and the size of the organic ligands [22-24]. As SURMOFs grow in an oriented way and the layers are oriented parallel to the substrate molecules can diffuse from the surface of the SURMOF to the supporting substrate without hindrance. Therefore, SURMOFs can be used as model systems to gain a detailed understanding of, e.g., the

kinetics of sorption/desorption processes or as active sites for sensor systems [16]. The high degree of orientation and the high structural quality of a SURMOF are evidenced by the XRD data. Figure 1c shows a comparison of recorded data of a polycrystalline powder MOF and of the corresponding SURMOF, both for the case of HKUST-1. While the powder MOF shows all reflexes of different orientations of the crystal, in the case of the SURMOF produced by the LBL method, in the out-of-plane XRD data only the [111] direction is detected. This is a direct proof that the LBL preparation results in a highly oriented SURMOF with (111)-layers grown parallel to the surface. A particular advantage of using thiol-based SAMs as a templating surface for the deposition of SURMOF structures on solid substrates is the availability of a large number of processes for the lateral structuring of SAMs, e.g., micro contact printing (μCP) [25]. With the application of these methods the selective deposition of SURMOFs is straightforward, as was shown recently for the case of HKUST-1 grown on a 16-mercaptohexadecanoic acid- (MHDA-) based SAM pattern created by μCP [18,21]. The feature sizes that can be achieved with this method, however, are limited and the preparation of sub-micrometer sized patterns is challenging or even impossible for μCP. The fabrication of structures within SAMs [26] of higher resolution can be obtained by nanoshaving and nanografting [27] or other methods based on scanning probe microscopy techniques, e.g., atomic force microscopy (AFM) [28,29]. Both lithography methods allow for lateral structuring with resolutions down to several nanometers. They are based on the cleavage of the bond between the thiolate species and the Au-substrate by an AFM tip. Depending on the applied force this cleavage can be carried out without scratching the substrate. Another advantage of the nanoshaving technique is the possibility to perform it in liquid or in air, depending on the system which should be modified. Nanoshaving in air or in a clean solvent always results in a removal of defined molecules [30] while nanografting [27] is usually performed in an organothiol containing solution, enabling the site-selective substitution of the removed SAM molecules by other SAM molecules which are present in the solution (Figure 2). The use of nanografting and nanoshaving for the fabrication of nanometer-sized structures, which consist of MOF material will be of interest for many applications. An area of potential interest are biological studies. It is known that cell adhesion depends strongly on both the chemical functionalization of the surface as well as on the distribution of the chemical functionalities [31,32].

In this work we demonstrate the successful growth of micrometer sized HKUST-1 structures on patterns inside thiolate-based SAMs by using the AFM as nanografting tool. ToF-SIMS analyses were carried out to demonstrate the successful SAM patterning by nanografting, while FT-IR microscopy and AFM were used to verify the SURMOF growth on the patterned substrate.

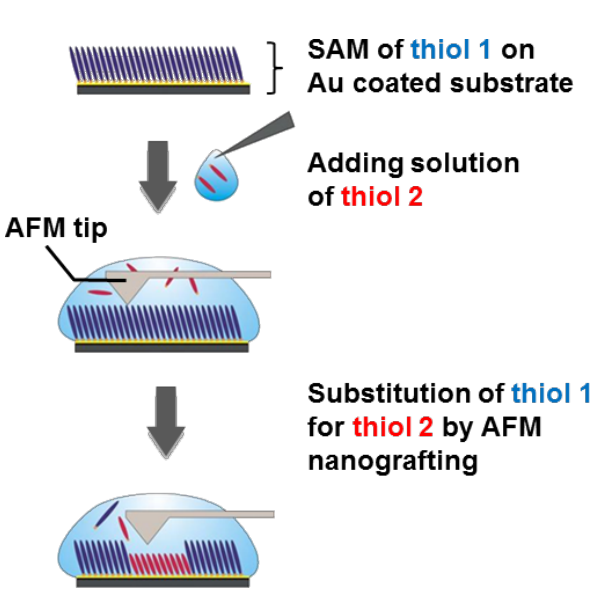

Figure 2: Scheme of the nanografting process.

Results and Discussion

The in-situ nanografting process includes two processes: (1) shaving of the original SAM made from the first thiol followed by (2) the refill of the shaved areas with the second thiol, which occurs instantaneously during the shaving as the shaving is carried out in a solution of the second thiol. Before doing the actual grafting, the parameters for the nanografting process (vertical force applied by the AFM tip to the substrate, scan speed, etc.) were optimized.

HKUST-1 SURMOF on MPA nanografted structures

To obtain a patterned deposition of HKUST-1, nanografting was first carried out within a SAM matrix made of 1-decanethiol (DT). A pattern was created by shaving with the AFM tip and the removed 1-decanethiolates were substituted by 3-mercaptopropionic acid (MPA) molecules present in the supernatant ethanol (Figure 3a). Figure 3b and Figure 3c show the AFM-topography and AFM-phase images, respectively, immediately after the areas of four MPA rectangles were grafted into the DT matrix SAM with the AFM tip. The height difference between the DT SAM and the grafted MPA coated features was determined from the cross section in Figure 3d along the red line in Figure 3b. The measured height difference of 1.7 ± 0.2 nm is in good agreement with the theoretical length difference between the two thiols (DT and MPA) of 1.5 nm. In addition, the phase contrast data shown in Figure 3c reveal the

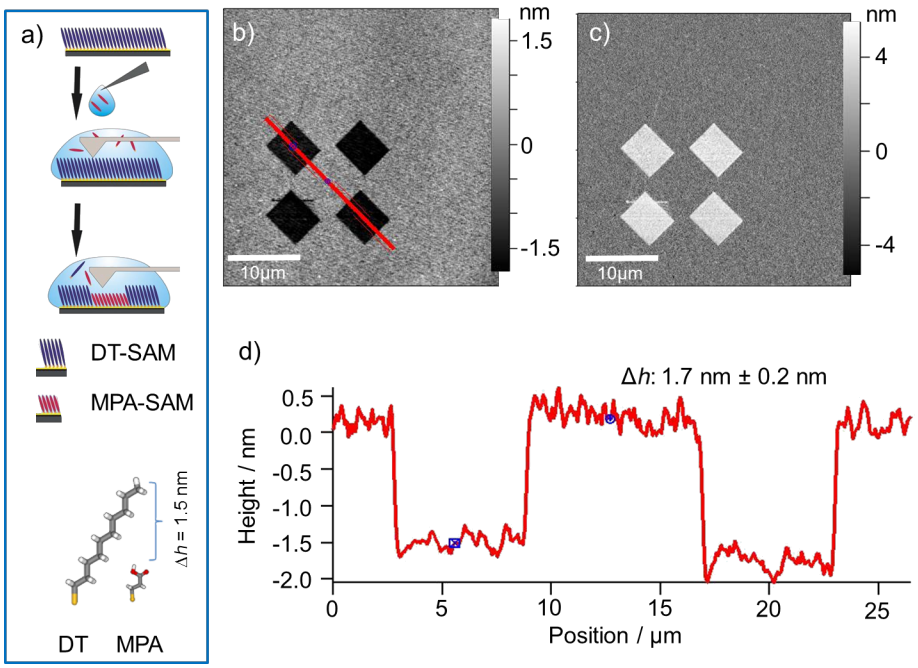

Figure 3: (a) Scheme of the grafting experiment and used SAM molecules (without H-atoms). AFM-topography (b) and -phase (c) image of MPA structures grafted in a DT SAM matrix. (d) Cross section along the red line in (b).

presence of two different materials inside and around the grafted areas. These findings directly demonstrate the success of the grafting experiment.

In addition to the AFM investigations, which provided information about topography and material contrast of the grafted sample, a chemical characterization was carried out by time-of-flight secondary ion mass spectrometry (ToF-SIMS). For that purpose a sample with grafted rectangular structures of 10 µm × 12 µm was prepared. The corresponding AFM-phase image is shown in Figure 4a. According to the results in Figure 3c, the grafted rectangular MPA coated structures show a significantly different phase shift compared to the 1-decanethiolate matrix SAM. The result of the negative polarity total secondary ion mapping is shown in Figure 4b. High mass resolution spectra, obtained with very short Bi^+ primary ion pulses (1 ns), "high current bunched mode", allowed for the detection of several very characteristic cluster ion peaks. Most importantly, the corresponding Au cluster ion of DT $[AuSC_{10}H_{22}]^-$ at *m*/*z* 371 (Figure 4c) and the Au cluster ion of MPA $[Au_2SC_3H_5O_2]^-$ at *m*/*z* 499 (Figure 4d) were detected as characteristic peaks. While this spectrometry mode allows for an unambiguous chemical assignment, the lateral resolution of the analysis is limited due to a primary ion beam spot diameter of approx. 5 µm. To obtain higher lateral resolutions, imaging was performed with a non-bunched primary ion pulse without chromatic aberration, thus providing nominal mass resolution. This analysis showed the expected pattern of MPA fragments, e.g., $[C_3H_3O_2]^-$ and $[C_3H_5SO_2]^-$ (Figure 4e). As strong peaks of fragmented ions provide the highest contrast, the sum of O^- and OH^- secondary ions is shown in Figure 4f which was produced by imaging 256 × 256 pixels in a 65 µm × 65 µm field of view.

After characterizing the nanografted features in some detail, the nanografted patterns were used as a substrate for the SURMOF deposition. Figure 5a shows the AFM topography images of a surface area, which was first patterned by grafting three squares of MPA into a DT SAM layer, followed by the layer-by-layer growth of HKUST-1 SURMOF using the spray method. The SURMOF structures in Figure 5a correspond to the elevated structures. The micrographs demonstrate that the SURMOF growth is strictly limited to the grafted areas and no unspecific deposition of the HKUST-1 can be recognized outside of the squares. When the lithography program for the grafting experiment starts, the AFM tip moves to its initial position, while the tip is still in contact with the surface. This results in the grafting of the MPA SAM into the DT matrix SAM along this trace. Therefore, a line consisting of HKUST-1, which connects the big square with one of the small squares can be recognized beside the laminar SURMOF structures in Figure 5a. This line was used to determine the height of the grown SURMOF layer, because the laminar structures show an inhomogeneous height

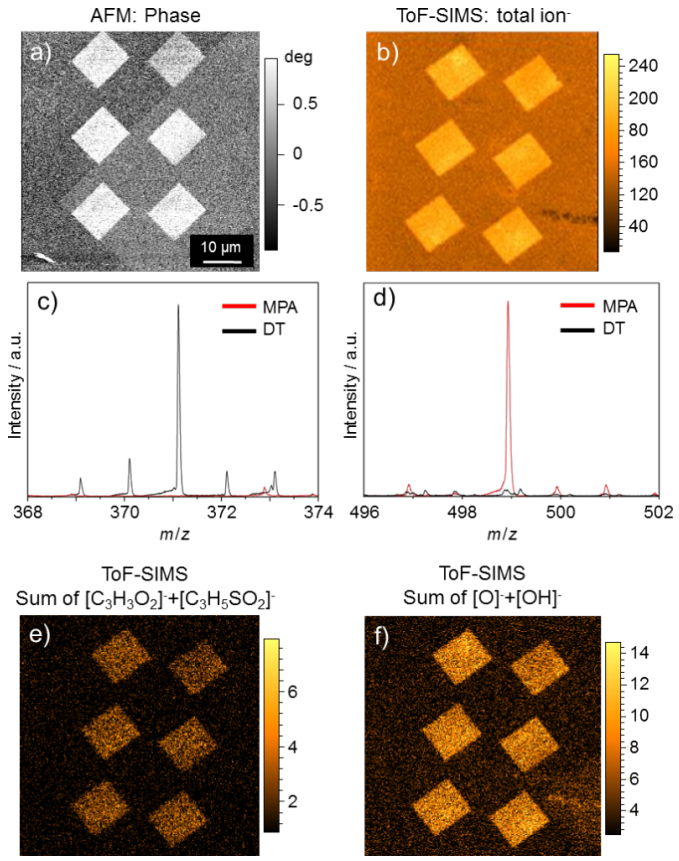

Figure 4: (a) AFM phase contrast image of six rectangles consisting of MPA grafted into a DT matrix SAM. (b) Negative polarity total secondary ion mapping. (c) High mass resolution SIMS data for DT (black line) and MPA (red line), the peak at *m*/*z* 371 in (c) is attributed to $[AuSC_{10}H_{22}]^-$, the Au cluster ion of DT, (d) as (c) the peak at *m*/*z* 499 is assigned to $[Au_2SC_3H_5O_2]^-$, the Au cluster ion of MPA. Other characteristic peaks are found at *m*/*z* 105, $[C_3H_5SO_2]^-$, and *m*/*z* 301, $[AuSC_3H_4O_2]^-$. (e) Local distribution of MPA fragments $[C_3H_3O_2]^-$ and $[C_3H_5SO_2]^-$, (f) local distribution of $[O]^-$ and $[OH]^-$.

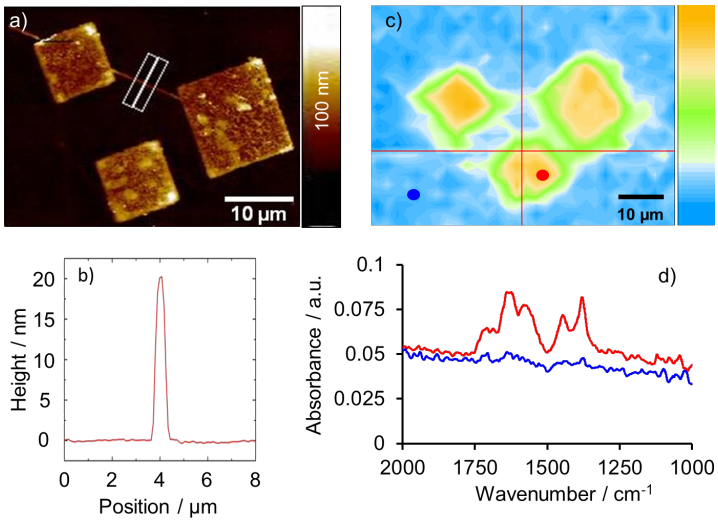

Figure 5: (a) AFM-topography image of HKUST-1 structures, prepared by spray coating after grafting squared areas of MPA into the DT matrix thiol. (b) Cross section along the white line of (a). (c) FT-IR imaging of the wavenumber region between 1510 cm^{-1} and 1780 cm^{-1}. (d) FT-IR spectra representing the area inside the squares (red line in (d) corresponding to red dot in (c)) and outside of the structures (blue line in (d), according to the blue dot in (c)).

distribution. The evaluation of the cross section of this SURMOF line (Figure 5b) along the white line in Figure 5a yields a height of 20 nm which is, according to the height scale, comparable to the height of those SURMOF areas grown with a lower layer thickness. From Figure 5a it can be clearly seen that there are some areas, which are significantly higher than 20 nm.

To demonstrate that the deposited material consists of HKUST-1, FT-IR imaging of the surface area was carried out using an ATR FT-IR microscope. Figure 5c shows the lateral distribution of the band intensities between 1510 cm^{-1} and 1780 cm^{-1}, which includes the typical region for the asymmetric stretching vibrations of carboxylate groups. It is obvious that the highest intensity can be recognized on the grafted areas as expected. Figure 5d shows two spectra, which represent the grafted areas (red spot in Figure 5c and red line in Figure 5d) and the surrounding area (blue spot in Figure 5c and blue line in Figure 5d) after the growth of HKUST-1, respectively. The typical bands of the asymmetric –COO stretching vibrations of the carboxylate groups can be detected between 1610 cm^{-1} and 1550 cm^{-1}, while the bands between 1420 cm^{-1} and 1300 cm^{-1} represent the symmetric –COO vibration bands of the deprotonated linker [33,34]. The band at 1446 cm^{-1} corresponds to the C–C vibration of the aromatic ring of the linker molecule [35]. The bands between 1730 cm^{-1} and 1680 cm^{-1} can be assigned to the stretching vibration of the –CO group and the C–OH group of the protonated SAM and some residual BTC linker molecules in the SURMOF structures. These findings demonstrate the selective growth of HKUST-1 SURMOF on the grafted areas.

HKUST-1 SURMOF on MHDA nanografted structures

As a second thiol supporting the selective growth of SURMOF structures, 16-mercaptohexadecanoic acid (MHDA), was used and grafted into a matrix SAM made from 1-octadecanethiol (ODT, Figure 6a). In this case ODT was used because the back bone length of this thiol is comparable to that of the grafted MHDA. A matrix SAM consisting of the significantly shorter 1-decanethiol (DT), as it was used for the grafting of 3-mercaptopropionic acid (MPA), would be spontaneously substituted by the longer MHDA molecules over time.

In Figure 6b and Figure 6c the AFM topography and AFM phase contrast images of the MHDA structures grafted into the ODT SAM are displayed, respectively. The grafted regions appear as dark areas in the topography image, indicating a depression. The significant phase contrast is a hint that the grafted areas are coated with molecules, which have a chemical termination different from that of the surrounding SAM regions. According to the cross section of Figure 6d measured along the red line in Figure 6b, the average height difference between the matrix SAM and the grafted MHDA area amounts to about 0.2 nm. This value is in good agreement with the theoretical length difference of approx. 0.2 nm between the MHDA and the ODT molecule.

To characterize the chemical composition of the structured areas, ToF-SIMS measurements were carried out. Characteristic ions of ODT and MHDA are detected at *m/z* 483, $[AuSC_{18}H_{38}]^-$, *m/z* 679, $[Au_2SC_{18}H_{37}]^-$, and *m/z* 681,

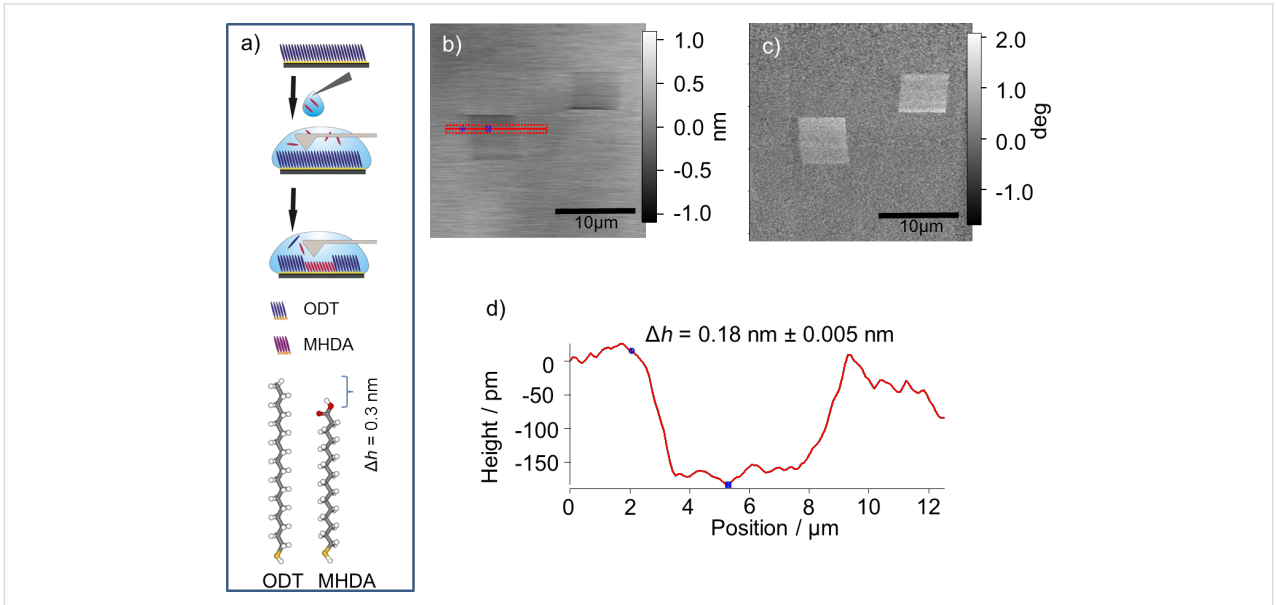

Figure 6: (a) Scheme of the grafting experiment and used SAM molecules. AFM-topography (b) and -phase (c) images of the MHDA areas grafted into an ODT matrix SAM. (d) Cross section along the red line in (b).

$[Au_2SC_{16}H_{31}O_2]^-$. Apart from these characteristic pseudomolecular peaks the comparison of small fragments providing strong SIMS signals allows for differentiation between the two thiols. The results of this investigation are summarized in Figure 7a, in which the ToF-SIMS spectra of the matrix thiol (ODT) and the grafted thiol (MHDA) are superimposed. In case of MHDA (red line) the following peaks are identified: *m*/*z* 41, $[C_2HO]^-$, *m*/*z* 58, $[C_2H_2O_2]^-$, and *m*/*z* 71, $[C_3H_3O_2]^-$. In addition there are several $[(CH_2)_nC_3H_3O_2]^-$ fragments with n = 1–8 (*m*/*z* 85, 99, 113, 127, 141, 155, 169, 183), as well as $[O]^-$ and $[OH]^-$. In case of the ODT SAM, peaks marked with *m*/*z* 64, 80, and 97 in the ODT spectrum can be assigned to $[SO_2]^-$, $[SO_3]^-$, $[SO_4H]^-$, respectively. These ions can be found for some thiol SAMs with oxidized thiol groups [36]. The extraordinary high ionization yield of these ions results in strong SIMS signals but provides no quantitative information. A mapping of the lateral distribution of the characteristic masses of MHDA and ODT results in Figure 7b and Figure 7c, respectively. The high intensity of the *m*/*z* 41 fragments (which are assigned to $[C_2HO]^-$) in Figure 7b demonstrates that the grafting was successfully carried out.

After demonstrating the successful grafting of MHDA, the deposition of the HKUST-1 SURMOF was carried out again by employing the spray method. In Figure 8a the structure of the layers are displayed schematically. The corresponding AFM topography image of the rectangular SURMOF structures is presented in Figure 8b. According to the cross section in Figure 8c along the red line of Figure 8b, the average height of the SURMOF structures amount to about 63 nm. Interestingly, this value is significantly larger than that measured for the SURMOF-structures grown on the MPA grafted areas (Figure 5). Note that in both cases the same number of deposition cycles (40) has been applied.

From the more detailed AFM-topography images of Figure 8d and Figure 8f, a particulate-like growth of the SURMOF material can be observed on top of both the MHDA-terminated, grafted areas and the matrix SAM. A higher density of crystallites can be found at the MHDA terminated surface areas. This is in contrast to the findings for the selective SURMOF grown on the MPA-terminated areas grafted in the DT SAM where no particulate material can be detected on the OD SAM (Figure 5). A roughness (RMS) of 28.9 ± 3.9 nm was determined for the MHDA-based structures, which is slightly rougher than the surrounding ODT SAM based areas with a roughness of 24.3 ± 3.1 nm. The cross sections in Figures 8e (along the red line in Figure 8d) and 8g (along the red line in Figure 8f) exhibit a comparable height of the crystals irrespective of the SAM on which they grew. The fact that the growth of crystals can be observed on the ODT SAM is a hint that a spontaneous exchange between the ODT and the MHDA took place locally,

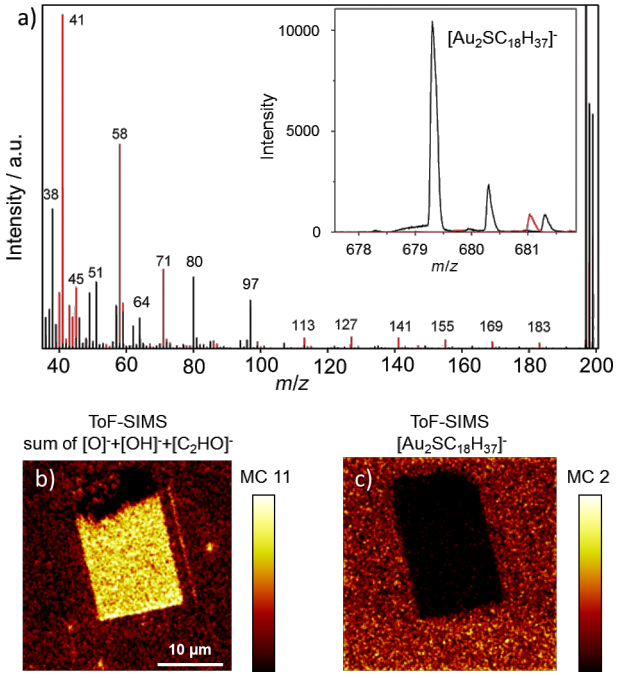

Figure 7: (a) ToF-SIMS spectra of ODT (black) and MHDA (red) SAMs on gold substrates. The inset shows the $[Au_2SC_{18}H_{37}]^-$ peak at *m*/*z* 679 characteristic for ODT. In (b) and (c) the mapping of the $[O]^-$ + $[OH]^-$ + $[C_2HO]^-$ and the $[Au_2SC_{18}H_{37}]^-$ (*m*/*z* 679) fragments, respectively, are shown, demonstrating the successful grafting of MHDA into the ODT SAM.

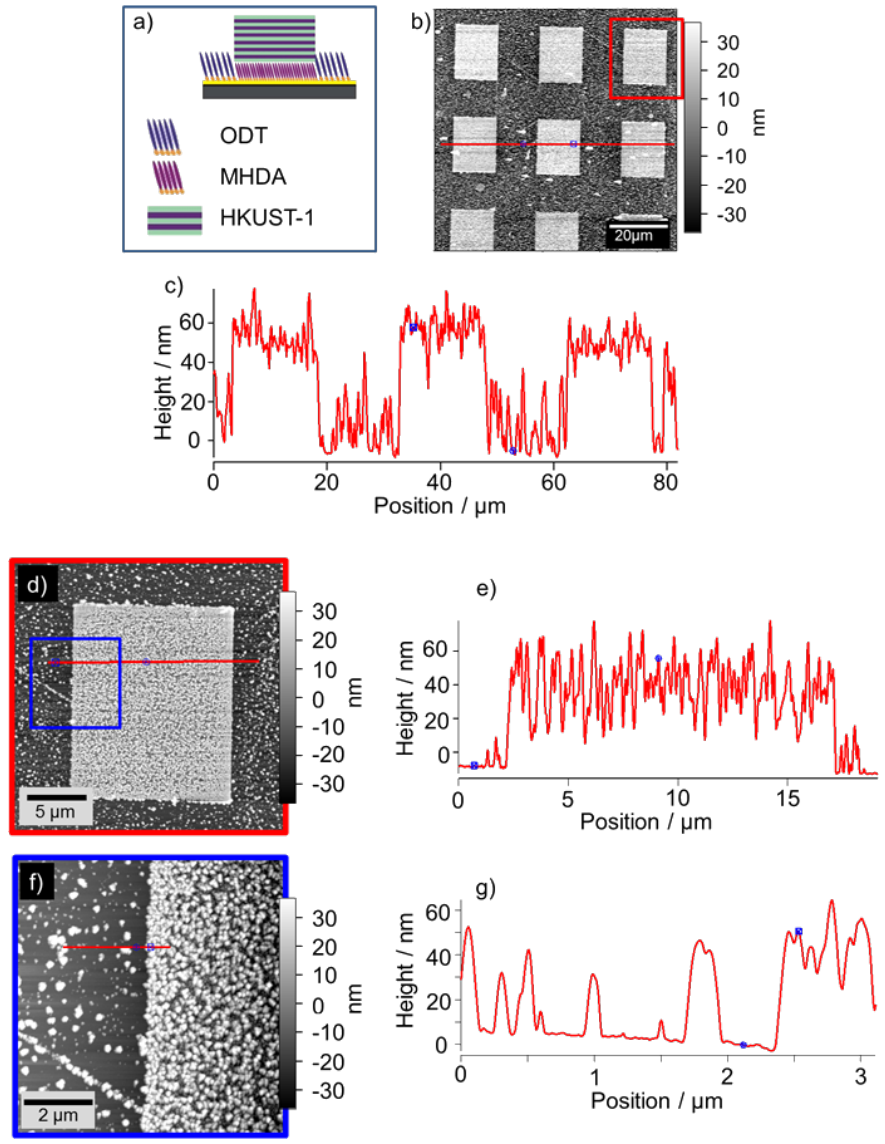

Figure 8: (a) Scheme of the layer cross-section of the AFM topography image of rectangular HKUST-1 structures site-selectively grown on the grafted MHDA areas. (b) AFM topography image of an array of rectangular HKUST-1 structures, grown on the MHDA terminated areas. (c) Cross section along the red line in (b). (d) and (f) detailed AFM topography images of the structure shown in (b) with the corresponding cross sections in (e) and (g), respectively.

and that this thiol combination is not as advantageous as the grafting of MPA into a matrix SAM of DT.

Conclusion

In the present proof-of-concept study it has been demonstrated that the selective growth of micro- and sub-microsized MOF-structures can be achieved by combining layer-by-layer growth with AFM-based nanografting. As the amount of available SURMOF structures is limited by the applied nanografting method and the structure dimensions are in the micrometer-range, the oriented growth of this structures has not yet been proven (e.g., by XRD). This will be a future challenge. The results also show, that an appropriate combination of thiols that activate the SURMOF growth and thiols that set up the matrix must be figured out, in order to avoid an undesirable and uncontrolled growth of SURMOF crystallites on the non-grafted areas. (This was observed for the SURMOFs based on MHDA grafted into an ODT matrix SAM.) Nevertheless the availability of such MOF-structures opens a wide range of opportunities to create three-dimensional structures of highly porous materials, which offer a high flexibility with regard to the geometrical shape, size and height. It has been demonstrated in previous works that the direction of the oriented growth of the SURMOFs can be influenced by the chemical termination of

the supporting SAM [14,15] and that the orientation of the SURMOF structures in turn influences the adsorption of guest molecules in the MOF host-structure [37]. To create a pattern with differently oriented SURMOF structures on the same substrate, which will be interesting for biological application, would require a technique, which allows the patterning of the substrate with different SAMs. Although usual structuring methods, such as micro contact printing or e-beam lithography, can be used for SAM patterning as well, those techniques reach a limit when patterns with differently terminated SAMs on the same substrate have to be prepared. This is because either the samples have to be removed from the UHV and/or a realignment of the sample as well as the recovery of the formerly prepared pattern becomes necessary, before the next structuring step can be carried out. By contrast, in the case of AFM nanografting the sample stays in the liquid cell and differently terminated SAM structures can be written just by exchanging the supernatant thiol solution. Although the grafting technique will not be suitable for a high throughput and large scale preparation of substrates, it has the power as scientific tool to prepare highly specific substrates for basic research.

Experimental

Sample preparation

For substrate preparation and surface functionalization we followed a previously described route [38]. Briefly, Au coated substrates for the nanografting experiments were prepared by depositing a 5 nm layer of titanium and subsequently 130 nm of gold onto polished [100] silicon wafers (Siegert Wafer, Germany) using a Leybold Univac evaporator (Leybold Optics, Germany). Metal deposition was done at room temperature at a base pressure of 10^{-7} bar. For the preparation of the initial SAMs on the gold covered silicon wafer 1-octadecanethiol (ODT) or 1-decanethiol (DT) were used. The SAM was produced by immersing the substrate in a 1 mM ethanolic solution of ODT or DT for 12 h.

Nanografting and AFM characterization

All AFM investigations were carried out with a MFP-3D Bio AFM (Asylum Research, Mannheim). Grafting experiments and AFM investigation of the surface were performed in a polystyrene petri dish (BD falcon, VWR, Germany) mounted on the scanner of the MFP-3D Bio. For grafting experiments the "B" tips of NSC-35 cantilever chips (Micromash, Germany) with the nominal force constant of 16 N/m were used. Both the nanografting of 3-mercaptopropionic acid (MPA) in a DT SAM and the nanografting of 16-mercaptohexadecanoic acid (MHDA) in ODT SAM were performed in a 0.2 mM ethanolic solution of the corresponding acid. In both cases 10% (v/v) glacial acetic acid was added to the grafting solutions. The nanografting in the case of MPA/DT was performed in contact mode with a loading force of 345 nN, while for MHDA/ODT a loading force of 303 nN was used to remove thiols out of the existing matrix SAM. All AFM surface analysis experiments were carried out in the intermittent contact mode and the AFM tip was scanned at an angle of 90° relative to the longitudinal axis of the cantilever in several scan ranges. The AFM was used in a closed loop on all three axes. AFM images were evaluated with the IGOR software.

SURMOF preparation

For the preparation of the SURMOF on the grafted areas a new, recently published LBL spray method was used [39]. In Figure 9 the scheme of the spray method for SURMOF preparation is shown. The horizontally mounted sample is subsequently sprayed (1) with the ethanolic Cu acetate solution (c = 1.0 mM / 10 s spraying time / 20 s waiting time), (2) with pure ethanol for rinsing (3 s spraying time / 1 s waiting time), (3) with the linker solution consisting of an ethanolic solution of 1,3,5-benzenetricarboxylic acid (c = 0.1 mM / 15 s spraying time / 20 s waiting time) and (4) finally again with pure ethanol (3 s spraying time / 1 s waiting time). This procedure is repeated 40 times. At the end of this process the sample was rinsed again with pure ethanol for 2 s.

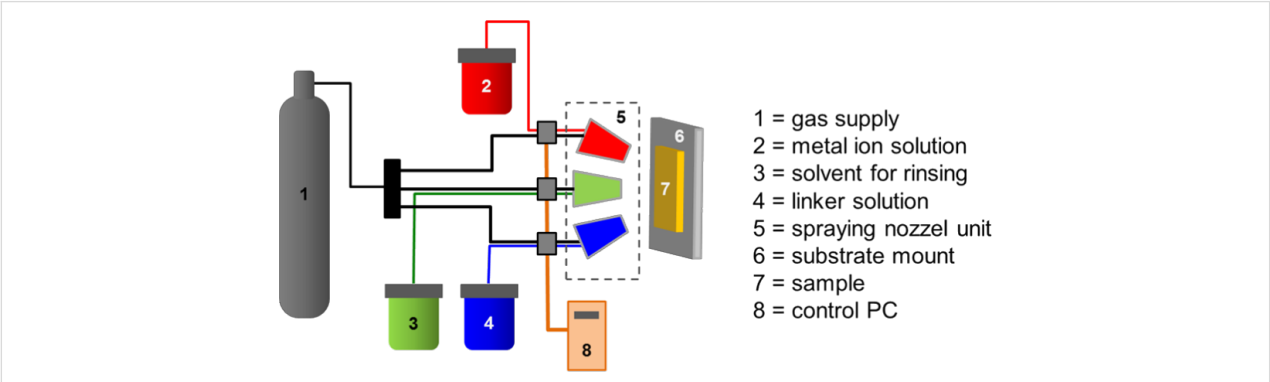

Figure 9: Setup employed for the fabrication of MOF thin films with the spray method [39].

FT-IR-imaging

FT-IR-imaging was performed on a Bruker Hyperion 3000 FT-IR (Bruker Optics, Ettlingen, Germany) imaging system equipped with a 20× ATR objective with a Ge-Crystal tip. A 64 × 64 pixel FPA detector sensitive to a range of 900–3800 cm^{-1} was used. 4096 spectra were aquired in one measurement over a field of view of 32 × 32 µm, 4 × 64 scans were collected over an area of 64 × 64 µm with a spectral resolution of 4 cm^{-1}.

ToF-SIMS

Time-of-flight secondary ion mass spectrometry was performed on a TOF-SIMS 5 instrument from ION-TOF GmbH, Münster, Germany. This instrument is equipped with a Bi cluster liquid metal ion source and a reflectron type time-of-flight analyzer. For spectrometry short primary ion pulses (<1 ns) of Bi_1^+ and Bi_3^+ at an energy of 25 keV were applied providing high mass resolution secondary ion spectra with a moderate spot size of about 5 mm (bunched mode). Spectrometry was performed in static SIMS mode by limiting the primary ion dose to $<10^{11}$ ions/cm^2. High lateral resolution images were acquired in a primary ion source mode providing a lateral resolution of about 200 nm with nominal mass resolution (burst alignment mode). No charge compensation was required. Spectra were calibrated on omnipresent C^-, CH^-, CH_2^-, Au^-, and molecular peaks.

Acknowledgements

The authors thank the DFG (SPP 1362) for financial support.

References

1. Zacher, D.; Shekhah, O.; Wöll, C.; Fischer, R. A. *Chem. Soc. Rev.* **2009,** *38,* 1418–1429. doi:10.1039/b805038b
2. Zacher, D.; Yusenko, K.; Bétard, A.; Henke, S.; Molon, M.; Ladnorg, T.; Shekhah, O.; Schüpbach, B.; de los Arcos, T.; Krasnopolski, M.; Meilikhov, M.; Winter, J.; Terfort, A.; Wöll, C.; Fischer, R. A. *Chem.–Eur. J.* **2011,** *17,* 1448–1455. doi:10.1002/chem.201002381
3. Chui, S. S.-Y.; Lo, S. M.-F.; Charmant, J. P. H.; Orpen, A. G.; Williams, I. D. *Science* **1999,** *283,* 1148–1150. doi:10.1126/science.283.5405.1148
4. Furukawa, H.; Cordova, K. E.; O'Keeffe, M.; Yaghi, O. M. *Science* **2013,** *341,* No. 6149. doi:10.1126/science.1230444
5. Gliemann, H.; Wöll, C. *Mater. Today* **2012,** *15,* 110–116. doi:10.1016/S1369-7021(12)70046-9
6. Wang, X.-S.; Ma, S. Q.; Forster, P. M.; Yuan, D. Q.; Eckert, J.; López, J. J.; Murphy, B. J.; Parise, J. B.; Zhou, H.-C. *Angew. Chem., Int. Ed.* **2008,** *47,* 7263–7266. doi:10.1002/anie.200802087
7. Furukawa, H.; Ko, N.; Go, Y. B.; Aratani, N.; Choi, S. B.; Choi, E.; Yazaydin, A. Ö.; Snurr, R. Q.; O'Keeffe, M.; Kim, J.; Yaghi, O. M. *Science* **2010,** *329,* 424–428. doi:10.1126/science.1192160
8. Mueller, U.; Schubert, M.; Teich, F.; Puetter, H.; Schierle-Arndt, K.; Pastré, J. *J. Mater. Chem.* **2006,** *16,* 626–636. doi:10.1039/b511962f
9. Czaja, A. U.; Trukhan, N.; Müller, U. *Chem. Soc. Rev.* **2009,** *38,* 1284–1293. doi:10.1039/b804680h
10. Bauer, S.; Stock, N. *Chem. Unserer Zeit* **2008,** *42,* 12–19. doi:10.1002/ciuz.200800434
11. Horcajada, P.; Serre, C.; Maurin, G.; Ramsahye, N. A.; Balas, F.; Vallet-Regí, M.; Sebban, M.; Taulelle, F.; Férey, G. *J. Am. Chem. Soc.* **2008,** *130,* 6774–6780. doi:10.1021/ja710973k
12. McKinlay, A. C.; Morris, R. E.; Horcajada, P.; Férey, G.; Gref, R.; Couvreur, P.; Serre, C. *Angew. Chem., Int. Ed.* **2010,** *49,* 6260–6266. doi:10.1002/anie.201000048
13. Lu, G.; Hupp, J. T. *J. Am. Chem. Soc.* **2010,** *132,* 7832–7833. doi:10.1021/ja101415b
14. Shekhah, O.; Liu, J.; Fischer, R. A.; Wöll, C. *Chem. Soc. Rev.* **2011,** *40,* 1081–1106. doi:10.1039/c0cs00147c
15. Biemmi, E.; Scherb, C.; Bein, T. *J. Am. Chem. Soc.* **2007,** *129,* 8054–8055. doi:10.1021/ja0701208
16. Shekhah, O.; Wang, H.; Kowarik, S.; Schreiber, F.; Paulus, M.; Tolan, M.; Sternemann, C.; Evers, F.; Zacher, D.; Fischer, R. A.; Wöll, C. *J. Am. Chem. Soc.* **2007,** *129,* 15118–15119. doi:10.1021/ja076210u
17. Shekhah, O.; Wang, H.; Zacher, D.; Fischer, R. A.; Wöll, C. *Angew. Chem., Int. Ed.* **2009,** *48,* 5038–5041. doi:10.1002/anie.200900378
18. Zhuang, J. L.; Friedel, J.; Terfort, A. *Beilstein J. Nanotechnol.* **2012,** *3,* 570–578. doi:10.3762/bjnano.3.66
19. Witters, D.; Vermeir, S.; Puers, R.; Sels, B. F.; De Vos, D. E.; Lammertyn, J.; Ameloot, R. *Chem. Mater.* **2013,** *25,* 1021–1023. doi:10.1021/cm400216m
20. Münch, A. S.; Mertens, F. *J. Mater. Chem.* **2012,** *22,* 10228–10234. doi:10.1039/c2jm15596f
21. Munuera, C.; Shekhah, O.; Wang, H.; Wöll, C.; Ocal, C. *Phys. Chem. Chem. Phys.* **2008,** *10,* 7257–7261. doi:10.1039/b811010g
22. Rosi, N. L.; Eddaoudi, M.; Kim, J.; O'Keeffe, M.; Yaghi, O. M. *CrystEngComm* **2002,** 401–404. doi:10.1039/b203193k
23. Rowsell, J. L. C.; Yaghi, O. M. *Microporous Mesoporous Mater.* **2004,** *73,* 3–14. doi:10.1016/j.micromeso.2004.03.034
24. Kumar, A.; Whitesides, G. M. *Appl. Phys. Lett.* **1993,** *63,* 2002–2004. doi:10.1063/1.110628
25. Liu, J. X.; Lukose, B.; Shekhah, O.; Arslan, H. K.; Weidler, P.; Gliemann, H.; Bräse, S.; Grosjean, S.; Godt, A.; Feng, X. L.; Müllen, K.; Magdau, I. B.; Heine, T.; Wöll, C. *Sci. Rep.* **2012,** *2,* No. 921. doi:10.1038/srep00921
26. Bain, C. D.; Whitesides, G. M. *Angew. Chem., Int. Ed. Engl.* **1989,** *28,* 506–512. doi:10.1002/anie.198905061
27. Liu, M.; Amro, N. A.; Liu, G. Y. *Annu. Rev. Phys. Chem.* **2008,** *59,* 367–386. doi:10.1146/annurev.physchem.58.032806.104542
28. Obermair, C.; Kress, M.; Wagner, A.; Schimmel, T. *Beilstein J. Nanotechnol.* **2012,** *3,* 824–830. doi:10.3762/bjnano.3.92
29. Obermair, C.; Wagner, A.; Schimmel, T. *Beilstein J. Nanotechnol.* **2011,** *2,* 659–664. doi:10.3762/bjnano.2.70
30. Liu, G. Y.; Xu, S. *Abstr. Pap. - Am. Chem. Soc.* **1997,** *214,* 29–IEC.
31. Hanke, M.; Arslan, H. K.; Bauer, S.; Zybaylo, O.; Christophis, C.; Gliemann, H.; Rosenhahn, A.; Wöll, C. *Langmuir* **2012,** *28,* 6877–6884. doi:10.1021/la300457z
32. Kalinina, S.; Gliemann, H.; López-García, M.; Petershans, A.; Auernheimer, J.; Schimmel, T.; Bruns, M.; Schambony, A.; Kessler, H.; Wedlich, D. *Biomaterials* **2008,** *29,* 3004–3013. doi:10.1016/j.biomaterials.2008.04.003

33. Seo, Y.-K.; Hundal, G.; Jang, I. T.; Hwang, Y. K.; Jun, C.-H.; Chang, J.-S. *Microporous Mesoporous Mater.* **2009,** *119,* 331–337. doi:10.1016/j.micromeso.2008.10.035
34. Borfecchia, E.; Maurelli, S.; Gianolio, D.; Groppo, E.; Chiesa, M.; Bonino, F.; Lamberti, C. *J. Phys. Chem. C* **2012,** *116,* 19839–19850. doi:10.1021/jp305756k
35. Wang, F.; Guo, H.; Chai, Y.; Li, Y.; Liu, C. *Microporous Mesoporous Mater.* **2013,** *173,* 181–188. doi:10.1016/j.micromeso.2013.02.023
36. Cooper, E.; Leggett, G. J. *Langmuir* **1998,** *14,* 4795–4801. doi:10.1021/la9802567
37. Liu, B.; Tu, M.; Fischer, R. A. *Angew. Chem., Int. Ed.* **2013,** *52,* 3402–3405. doi:10.1002/anie.201207908
38. Grunwald, C.; Eck, W.; Opitz, N.; Kuhlmann, J.; Wöll, C. *Phys. Chem. Chem. Phys.* **2004,** *6,* 4358–4362. doi:10.1039/b405543h
39. Arslan, H. K.; Shekhah, O.; Wohlgemuth, J.; Franzreb, M.; Fischer, R. A.; Wöll, C. *Adv. Funct. Mater.* **2011,** *21,* 4228–4231. doi:10.1002/adfm.201101592

License and Terms

Beilstein Journal of Nanotechnology

Atomic force microscopy recognition of protein A on *Staphylococcus aureus* cell surfaces by labelling with IgG–Au conjugates

Elena B. Tatlybaeva[1], Hike N. Nikiyan[*2,3], Alexey S. Vasilchenko[2,4] and Dmitri G. Deryabin[1,5]

Full Research Paper

Open Access

Address:
[1]Department of Microbiology, Orenburg State University, Pobedy Ave, 13, 460018, Orenburg, Russia, [2]Department of Biochemical Physics, Orenburg State University, Pobedy Ave, 13, 460018, Orenburg, Russia, [3]Institute of micro- and nanotechnologies of Orenburg State University, Pobedy Ave, 13, 460018, Orenburg, Russia, [4]Institute of Cellular and Intracellular Symbiosis, RAS, Pionerskaya str., 11, 460000, Orenburg, Russia and [5]All-Russian Research Institute of Beef Cattle, RAA, 9 Yanvarja str, 29, 460000, Orenburg, Russia

Email:
Hike N. Nikiyan[*] - nikiyan@yahoo.com

* Corresponding author

Keywords:
atomic force microscopy; IgG–gold nanoparticle conjugates; protein A; *Staphylococcus aureus*

Beilstein J. Nanotechnol. **2013,** *4,* 743–749.
doi:10.3762/bjnano.4.84

Received: 12 July 2013
Accepted: 21 October 2013
Published: 11 November 2013

This article is part of the Thematic Series "Advanced atomic force microscopy techniques II".

Guest Editors: T. Glatzel and T. Schimmel

Abstract

The labelling of functional molecules on the surface of bacterial cells is one way to recognize the bacteria. In this work, we have developed a method for the selective labelling of protein A on the cell surfaces of *Staphylococcus aureus* by using nanosized immunogold conjugates as cell-surface markers for atomic force microscopy (AFM). The use of 30-nm size Au nanoparticles conjugated with immunoglobulin G (IgG) allowed the visualization, localization and distribution of protein A–IgG complexes on the surface of *S. aureus*. The selectivity of the labelling method was confirmed in mixtures of *S. aureus* with *Bacillus licheniformis* cells, which differed by size and shape and had no IgG receptors on the surface. A preferential binding of the IgG–Au conjugates to *S. aureus* was obtained. Thus, this novel approach allows the identification of protein A and other IgG receptor-bearing bacteria, which is useful for AFM indication of pathogenic microorganisms in poly-component associations.

Introduction

The development of fast and sensitive methods for bacterial recognition remains an important problem in microbiology. In some cases the recognition includes the labelling of cells with different kinds of markers, which is followed by microscopy. In optical microscopy, immunochemical or immunofluorescent labels are used [1]. In the case of electron microscopy, specific

antibodies are conjugated with electron-dense particles, such as colloidal gold [2]. Significant progress in microscopic techniques has been reached with the invention of the atomic force microscope (AFM) [3]. However, appropriate approaches for the utilization of AFM in revealing markers are still being developed.

Compared to traditional methods of visualization – scanning electron and optical microscopy – AFM offers important benefits: a high spatial resolution, a real quantitative data acquisition in three dimensions, a relatively simple and nondestructive sample preparation procedure and a flexibility in ambient operating conditions [4]. These benefits allow for the development of highly sensitive high-resolution methods for the detection of individual structures or labels on the surface of microorganisms. These, in turn, open wide prospects for the estimation of the exact quantity of bound markers, their topology on the surface and other kinds of immune and substrate-specific activity analyses. The prospective AFM approach uses a functionalized tip in order to obtain force curves for the protein-coated substrate and to measure the specific interaction forces [5,6]. The main restriction of this method is the requirement to use a liquid cell, which complicates the scanning process and often leads to the appearance of artefacts in the recorded images. AFM recognition of microorganisms can also include the detection of specific antigen/antibody (Ag/Ab) complexes on the surface of the cell wall. In this case, the detection process consists of a comparison of size distribution histograms of antigen molecules before and after their interaction with specific and nonspecific antibodies [7]. The application of this approach, however, is complicated by the existence of "noise" in the images caused by nonspecific interactions. These circumstances indicate the relevance of the development of a simple, sensitive and reproducible AFM recognition method that is available both for routine studies and for unambiguous interpretation of the AFM results. In order to increase the reliability of the complex detection on bacterial cell surfaces, specific proteins are conjugated with nanodimensional labels that are easily resolved by AFM and also have a distinct structure [7]. It, in turn, allows for the identification of interactions and the quantitative determination of the localization of resultant complexes. In order to evolve this technique of AFM recognition, our attention was also drawn to the possibility of identifying not only antigens, but also functional cell-surface receptors that bind host proteins and, therefore, are significant in the pathogenesis of infectious diseases. In particular, it is important to distinguish the cells that carry immunoglobulin-binding receptors on their surface: protein A produced by *Staphylococcus aureus* [8] and protein G expressed in group C and G *Streptococcus* bacteria [9]. These protein–protein interactions also lead to the formation of specific complexes on the cell surface, in which IgG molecules are bound in the wrong orientation (in relation to normal antibody function). Thus, bacteria are disrupted by opsonization [10] and phagocytosis [11].

In this regard, the aim of our work was the development of an AFM method to specifically label *Staphylococcus aureus*, which bears protein A, with IgG–Au conjugates by using the direct visualization of the labels on the bacterial cell surface as a criterion for identification.

Results

In the first step of our experimental procedure, IgG–Au conjugates were imaged. In Figure 1a, the results of these measurements are shown. Morphometric analysis showed that the average size (diameter) value of the observed structures was 80 ± 12 nm and had a small dispersion (Figure 1b). Considering the broadening effect caused by the tip, it can be concluded that conjugates are found on the mica surface both in single form and as aggregates composed of 2–3 conjugates. Taking into account the broadening effect of the tip, the observed size was significantly greater than the size of IgG that was estimated in [12]. This indicates that the conjugate size is mainly defined by gold nanoparticle dimensions. Under these experimental conditions, there was no aggregation of conjugates as indicated in [13]. These results were used as background for the following labelling and recognition of IgG–Au conjugates on the bacterial surfaces.

As visualized in the second step of the study, intact *S. aureus* cells appeared on the mica surface as grape-like clusters of round cocci. These formations occurred because of cells that remained attached to one another after dividing and were promoted by protein A, which induces bacterial aggregation in liquid media [14]. The diameter of cells observed in clusters (Figure 1c) varied from 600 to 1040 nm (Figure 1d); the average value was 800 ± 120 nm and was typical for this microorganism.

Analysis of the mean-square roughness (R_q) of the *S. aureus* surface suggested that the bacteria have a relatively smooth surface (R_q = 1.03 ± 0.45 nm), typical for noncapsulated Staphylococcus cells [15]. The lack of a capsule is an important condition for the subsequent successful visualization of complexes of IgG–Au conjugates with protein A that is anchored to the peptidoglycan pentaglycine bridges in *Staphylococcus*.

The third step of the study included imaging *S. aureus* cells incubated with the IgG–Au conjugates. Formations with dimensions in the same range as the previously defined IgG–Au

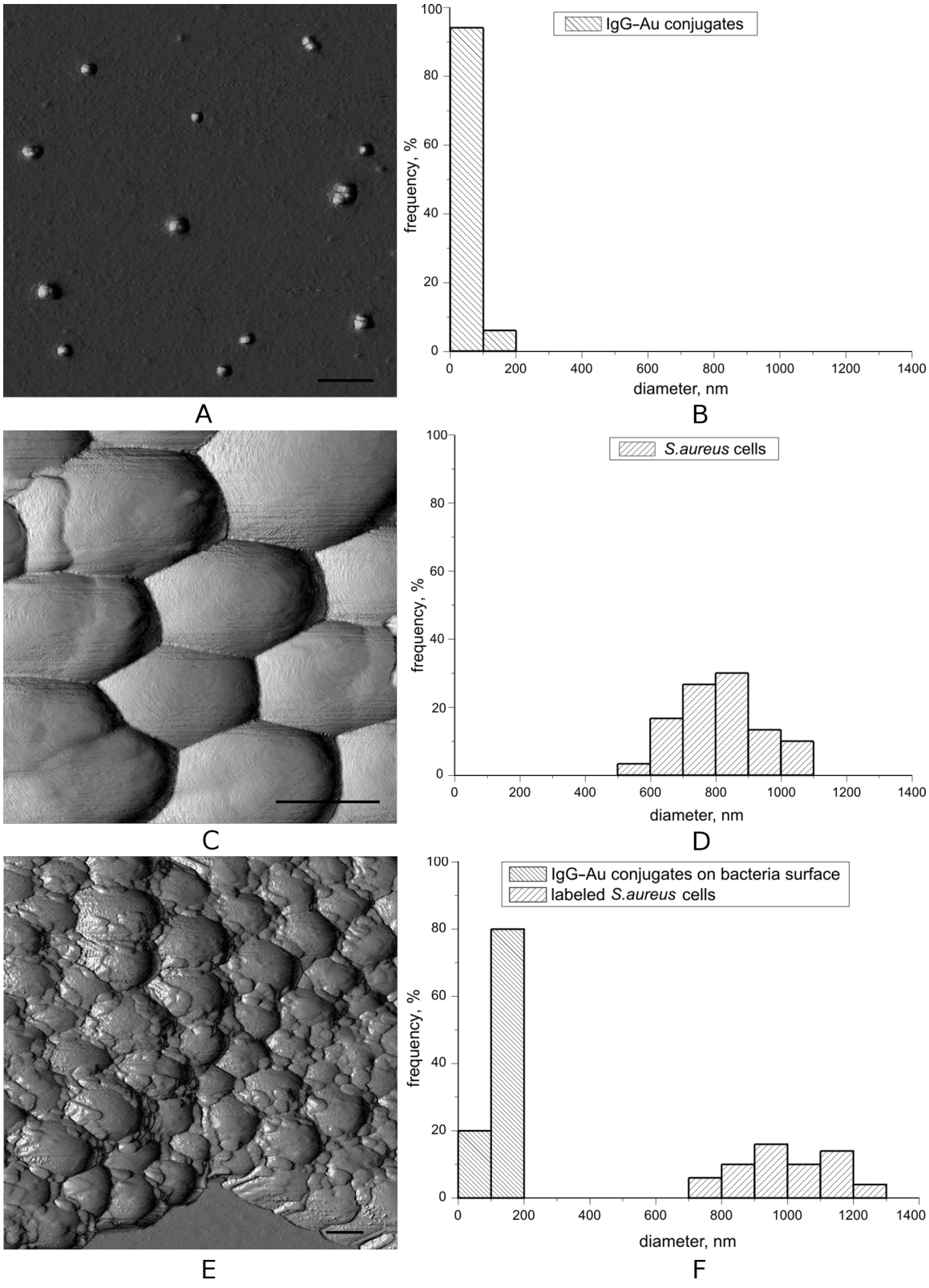

Figure 1: Topographic AFM images of the IgG–Au conjugates (a), *S. aureus* cells before (c) and after (e) contact with conjugates. Scale bar is 500 nm in all panels. (b), (d), (f) - Size (diameter) distribution histograms of corresponding structures. Information for each histogram was collected from several scans.

conjugates (100–253 nm) were identified on the cell surface (Figure 1e). However, the comparisons of the size distributions of the conjugates and the mentioned formations (Figure 1f) indicated a difference in the average values. The average diameter of aggregates observed on the bacteria was 140 ± 40 nm.

The size distribution histogram in Figure 1f shows that the formation of the complexes led to an increase in the cell diameters of *Staphylococcus*. The average diameter of the observed cells was 990 ± 140 nm and differed from intact cells with a high reliability ($P < 0.0001$). Roughness of the cell surface was higher values this time (R_q = 2.60 ± 2.23 nm).

An irregular distribution of IgG–Au conjugates on the cellular surfaces was established. We defined three ways of orientation of the IgG–Au labels according to binding area (Figure 2a): 1 - on top of the cell (90–60º angle range), 2 - on one side (60–30º) and 3 - at the bottom (30–0º) as shown in Figure 2a. The analysis of over 200 labels showed that the majority of particles (78%) were located in the second zone, 19% of particles were in the first, and only 3% of the total number of particles were located in the third zone (Figure 2b).

After contact with IgG–Au conjugates structures on the surface of *S. aureus* were detected, which showed size characteristics that corresponded to to initial IgG–Au conjugates. We consider this as demonstration for the affinity of staphylococcal protein A (SpA) to bind in the Fc region of IgG. At the same time, the observed result was comparable to the immunolabelling methodology based on the affinity of SpA for IgG, which is applicable to either immunofluorescence observation using light microscopy or immunogold detection with electron microscopic techniques [16] on the one hand, and corresponds to conceptions of IgG preferentially binding to protein A-rich zones on the other [17].

To confirm the selectivity of conjugates for *Staphylococcus* cells, mixes of bacteria that contained *S. aureus* and *B. licheniformis* incubated without and with IgG–Au conjugates were prepared. According to the shape, the type of cells can be easily distinguished in these mixes (Figure 3a). *Bacillus licheniformis* are rod-shaped bacteria 2.02 ± 0.12 μm in length and 0.91 ± 0.16 μm in width. In contrast to *S. aureus*, no protein A or other Fc receptors can be found on the surface of *B. licheniformis* [18], which suggests their inability of protein–protein interaction through the Fc region.

The result of co-incubation of *S. aureus* and *B. licheniformis* after the interaction with IgG–Au is shown in Figure 3b. After treatment with the conjugates, these bacterial cells were morphologically distinct and at the same time were differently labelled. On the surface of the *S. aureus* bacteria, IgG–Au conjugates were clearly visible (Figure 3b) and had the same size and arrangement as in the previous experimental series. However, the surface of *B. licheniformis* was clear or had a small quantity of particles bordering on the staphylococci area.

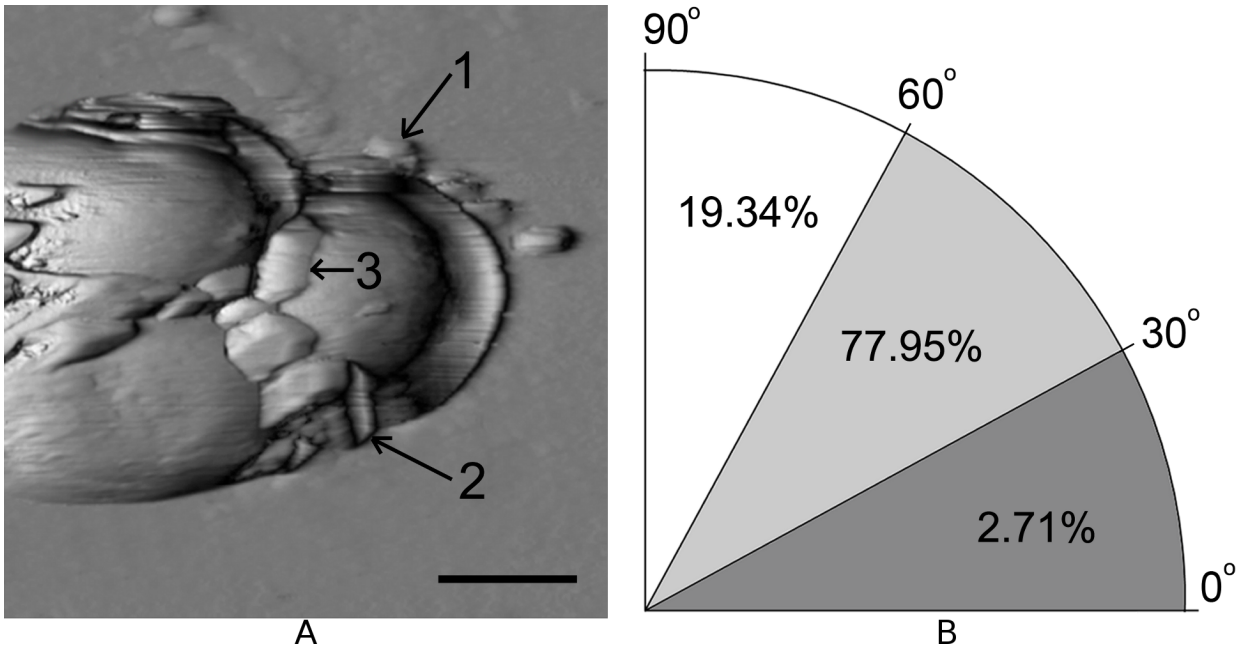

Figure 2: Distribution of IgG–Au conjugates on *S. aureus* cells: AFM image (a) and allocation of aggregates on a cellular surface according to binding area (b). Scale bar is 500 nm.

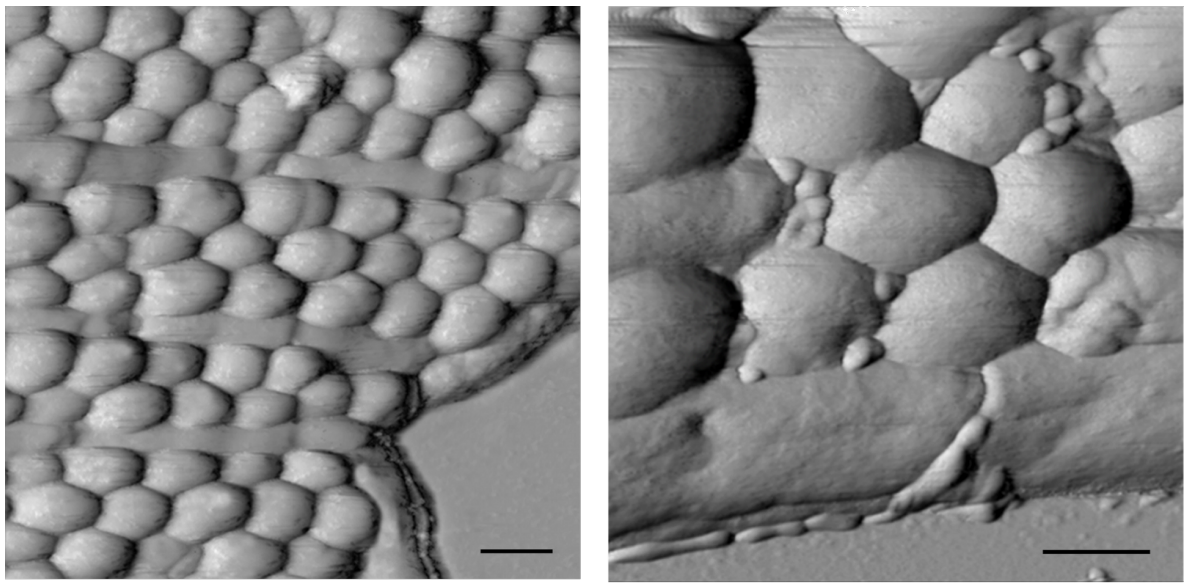

Figure 3: Topographic AFM images of *S. aureus* and *B. licheniformis* mixture before (a) and after (b) interaction with IgG–Au conjugates. Scale bar is 500 nm for both panels.

The distribution of conjugates along these bacterial surfaces was then analysed. The majority of particles (66%) observed in the scan area were localized on the staphylococci surface, 5% were observed on the substrate, 19% were in the areas between the cells, and only 10% of the particles were observed on the surface of bacilli.

Thus, the preferable binding of IgG–Au conjugates to the surface of the protein A-positive *S. aureus* in contrast to the protein A-negative *B. licheniformis* was shown. However, absolute selectivity of binding was not established, which reduces the efficiency of differentiation and requires further research.

Discussion

The use of immunogold labels as cell-surface markers for atomic force microscopy was already offered during the early stages of the development of the method [19]. Meanwhile, even though the use of AFM is growing rapidly in microbiology and a number of different AFM techniques enable the study of biomaterials [4,20], gold labelling is still not a routine procedure. We are sure that the development of methods of nanogold synthesis with precise dimensional characteristics and shape [21], and also their conjugation with various functional proteins, is a key to the effective use of AFM for studying the interactions between single molecules, which includes protein–protein interactions and recognition, and also for solving specific cellular discrimination and AFM imaging problems. In this paper, we described the use of IgG–Au conjugates for marking *S. aureus* cells that bear protein A on the surface, which functions as an Fc receptor for immunoglobulins [22,23]. The essence of this suggested approach was the application of AFM to detect protein A–IgG complexes on the bacterial cell surfaces by using colloidal gold nanoparticles as labels (Figure 4a).

A moderate heterogeneity of the dimensional characteristics of the IgG–Au conjugates was revealed by AFM image analysis. Thus, conjugates were found both as single, spherically shaped objects, 80 ± 12 nm in size, and partially as aggregates composed of 2–3 particles. The registered size of the conjugates was defined by the size of nanogold particles and it was significantly larger than that of single, unlabeled IgG proteins that were estimated by X-ray diffraction analyses (14.2 nm) [13]. Because of their typical shape and size, these structures were easily distinguished by AFM and were very convenient for the use as labels.

The binding of individual IgG–Au conjugates to *S. aureus* bacterial cell walls led to the formation of aggregates on the cell surface. A further analysis showed an uneven distribution of aggregates over the staphylococcal surface, which can be explained by the deposition of protein A at discrete locations in the envelope [18]. It was a very promising result that confirmed the possible use of IgG–Au conjugates for protein A marking. Moreover, it provided an opportunity to detect bacterial cells that bear the protein, the estimation of the distribution of protein A on the surface, and, potentially, also for evaluating its quantity in a cellular wall.

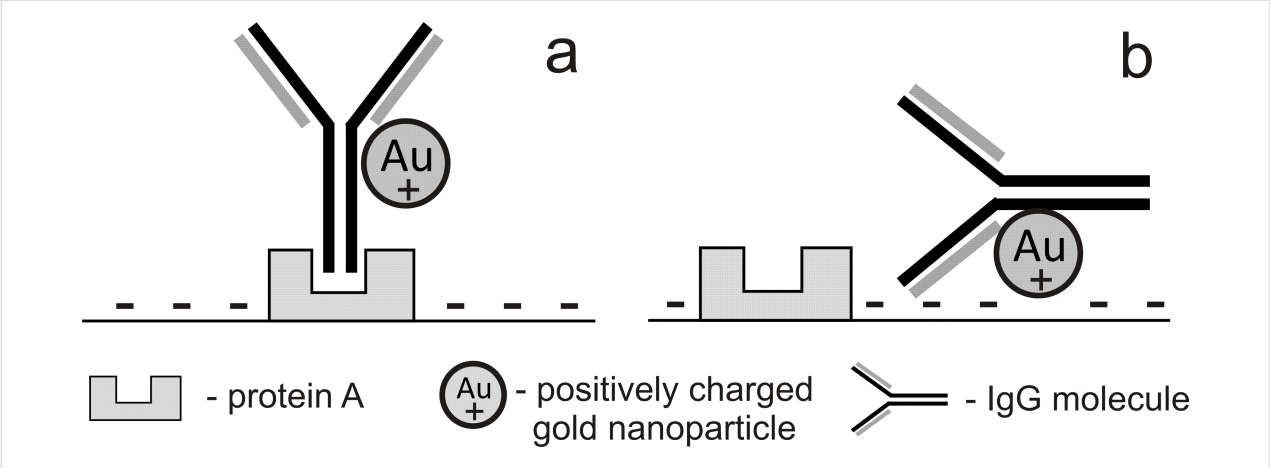

Figure 4: Two types of conjugate interactions with bacterial cell surfaces: selective binding of the Fc region of IgG in a non-antigenic way to protein A (a); non-selective electrostatic binding of colloidal gold to membrane (b).

To prove the selectivity of IgG–Au conjugates to only bind cells that bear to protein A, a mixture of *S. aureus* and *B. licheniformis* cells, which differed in shape and size was made. *B. licheniformis*, besides strong differences in morphology to *S. aureus*, have no protein A or other Fc receptors on the surface, which should allow for a clear distinction because of the IgG–Au conjugates only binding to *S. aureus* surfaces.

The obtained results indicated a preferential, but not exclusive (66% of the particles), binding of IgG to *S. aureus*, which was in accordance with the initial hypothesis. For 24% of the IgG–Au conjugates, the result was not clear as they were not bound to a cellular surface or were localized at the border between *S. aureus* and *B. licheniformis*. Some of the observed labels (10%) were found on bacilli surfaces, which was undesirable for the selective labelling and discrimination of protein A-positive and -negative cells. We suppose that this was a nonspecific binding that can be explained by electrostatic interactions between negatively charged cell surfaces [24] and positively charged particles of colloidal gold [25], as shown in Figure 4b. This result partially limits the use of nanogold particles in cell suspensions with a negative zeta-potential on the surface. Further research requires an improvement of label properties, in particular by neutralization of the surface charges of the gold nanoparticle by anionoid compounds.

Conclusion

We herein present a method to recognise protein A-bearing *Staphylococcus aureus* by using IgG–Au conjugates as cell-surface markers and an AFM technique for their detection on bacterial surfaces. Because of the typical shape and size of colloidal gold nanoparticles, the localization of labels and their distribution on the bacterial surfaces can be studied. The prevalence of IgG–Au conjugates at cell division zones was demonstrated as well as their preferential binding to protein A-bearing *S. aureus* surfaces contrary to protein A-deficient *B. licheniformis* cells in the mixtures. Thus, in comparison with previously developed methods, this method, which is based on the direct observation of labelled cell surfaces, may be a new approach for the identification of microorganisms in complex bacterial mixtures.

Experimental

Bacteria preparation

Two bacterial strains were used: *Staphylococcus aureus* (FDA 209P, ATCC 6538) possessing a high level of protein A [26] and *Bacillus licheniformis* (ATCC 2336), which has a cell wall devoid of protein A. Both the microorganisms are Gram positive, which allows them to be processed and investigated in the same conditions; however, they differ in form and size, sufficient for their morphological differentiation.

Bacterial strains were cultured on LB agar (Sigma-Aldrich, USA) at 37 °C for 24 h and then washed with distilled water. Cells were harvested by centrifugation (1700*g*, 7 min) of the bacterial suspension and were subsequently diluted with distilled water to produce about 10^9 viable cells per mL. Bacterial concentration was determined by measuring the A_{640} of the culture.

Immunolabelling and AFM sample preparation

Mouse monoclonal immunoglobulin G (IgG) antibodies against a genus-specific antigen of Chlamydia species conjugated with gold nanoparticles (IgG–Au conjugates, VedaLab, France) were used for bacterial cell labelling. These antibodies did not cross react with *S. aureus* or *B. licheniformis*, therefore, their binding was specific for protein A. The IgG–Au conjugates were mixed

with a suspension of *Staphylococcus aureus 209 P* or a mixture of *Bacillus licheniformis* cells at a ratio of 1:2 and incubated for 1 h at 37 °C with constant stirring on a thermostatic orbital shaker ST-3 (“Elmi”, Latvia). The labelled suspensions were then centrifuged for 5 min at 1700*g*, and the supernatant was discarded. The unbound IgG–Au conjugates were additionally washed twice through consecutive resuspensions with distilled water. Along with the test samples, IgG–Au conjugates, intact cells of *Staphylococcus aureus 209 P* and the mixture of *Bacillus licheniformis* were incubated and processed in the same conditions and used as a control samples. For the imaging of dried samples, a 2.5-μL droplet of bacterial suspension was applied to a freshly cleaved mica surface and left to dry in a humidity-controlled environment at 93% according to [27]. The mica surface is most commonly used for protein AFM imaging because of its hydrophilic character, its atomically flatness and the high affinity for proteins [28].

Atomic force microscopy imaging

Images were collected by using an SMM-2000 atomic force microscope (JSC "Proton-MIET Plant", Russia) operated in contact mode. V-shaped silicon nitride cantilevers MSCT-AUNM from Veeco Instruments Inc. with a spring constant of 0.01 N/m were used. The typical radius of the MSCT-AUNM tip is approx. 10 nm, which is comparable to the size of the gold conjugates utilized in immunolabelling experiments.

Acknowledgements

This work was supported by grant RFBR No 13-04-97054 from the Russian Foundation of Basic Research.

References

1. Ramos-Vara, J. A. *Vet. Pathol.* **2005,** *42,* 405–426. doi:10.1354/vp.42-4-405
2. Kuo, J., Ed. *Electron Microscopy (Methods and Protocols);* Humana Press: Totowa NJ, 2007.
3. Binning, G.; Quate, C. F.; Gerber, C. *Phys. Rev. Lett.* **1986,** *56,* 930–933. doi:10.1103/PhysRevLett.56.930
4. Dufrêne, Y. F.; Hinterdorfer, P. *Eur. J. Physiol.* **2008,** *256,* 237–245. doi:10.1007/s00424-007-0413-1
5. Lv, Z.; Wang, J.; Chen, G.; Deng, L. *Nanoscale Res. Lett.* **2010,** *5,* 1032–1038. doi:10.1007/s11671-010-9598-x
6. Creasey, R.; Sharma, S.; Gibson, C. T.; Craig, J. E.; Ebner, A.; Becker, T.; Hinterdorfer, P.; Voelckera, N. H. *Ultramicroscopy* **2011,** *111,* 1055–1061. doi:10.1016/j.ultramic.2011.03.008
7. Maluchenko, N. V.; Agapov, I. I.; Tonevitsky, A. G.; Moisenovich, M. M.; Savvateev, M. N.; Tonevitsky, E. A.; Bykov, V. A.; Kirpichnikov, M. P. *Biofizika* **2004,** *49,* 1008–1014.
8. Graille, M.; Stura, E. A.; Corper, A. L.; Sutton, B. J.; Taussig, M. J.; Charbonnier, J.-B.; Silverman, G. J. *Proc. Natl. Acad. Sci. U. S. A.* **2000,** *97,* 5399–5404. doi:10.1073/pnas.97.10.5399
9. Sjöbring, U.; Björck, L.; Kastern, W. *J. Biol. Chem.* **1991,** *266,* 399–405.
10. Bukharin, O. V.; Deryabin, D. G.; Brudastov, Yu. A. *Bull. Exp. Biol. Med.* **1994,** *117,* 643–645. doi:10.1007/BF02444343
11. Foster, T. Staphylococcus. In *Medical Microbiology,* 4th ed.; Baron, S., Ed.; Galveston (TX): University of Texas Medical Branch at Galveston, 1996; Chapter 12. http://www.ncbi.nlm.nih.gov/books/NBK8448/
12. Yu, Y. G.; Xu, R. X.; Jiang, X. D.; Ke, Y. Q. *Chin. J. Traumatol. (Engl. Ed.)* **2005,** *8,* 277–282.
13. Chen, Y.; Cai, J.; Xu, Q.; Chen, Z. W. *Mol. Immunol.* **2004,** *41,* 1247–1252. doi:10.1016/j.molimm.2004.05.012
14. Merino, N.; Toledo-Arana, A.; Vergara-Irigaray, M.; Valle, J.; Solano, C.; Calvo, E.; Lopez, J. A.; Foster, T. J.; Penadés, J. R.; Lasa, I. *J. Bacteriol.* **2009,** *191,* 832–843. doi:10.1128/JB.01222-08
15. Tollersrud, T.; Berge, T.; Andersen, S. R.; Lund, A. *APMIS* **2001,** *109,* 541–545.
16. Forsgren, A.; Sjöquist, J. *J. Immunol.* **1966,** *97,* 822–827.
17. Spratt, B. G. *Proc. Natl. Acad. Sci. U. S. A.* **1975,** *72,* 2999–3003.
18. DeDent, A. C.; McAdow, M.; Schneewind, O. *J. Bacteriol.* **2007,** *189,* 4473–4484. doi:10.1128/JB.00227-07
19. Putman, C. A. J.; de Grooth, B. G.; Hansma, P. K.; van Hulst, N. F.; Greve, J. *Ultramicroscopy* **1993,** *48,* 177–182. doi:10.1016/0304-3991(93)90180-6
20. Liu, S.; Wang, Y. *Scanning* **2010,** *32,* 61–73. doi:10.1002/sca.20173
21. Barnard, A. S.; Young, N. P.; Kirkland, A. I.; van Huis, M. A.; Xu, H. *ACS Nano* **2009,** *3,* 1431–1436. doi:10.1021/nn900220k
22. Frank, M. B. Antibody Binding to Protein A and Protein G beads. In *Molecular Biology Protocols;* Frank, M. B., Ed.; Oklahoma City, 2001.
23. Boyle, M. D. P. *Bacterial Immunoglobulin-binding Proteins;* Academic Press, 1989; Vol. 1, p 409.
24. Dickson, J. S.; Koohmaraie, M. *Appl. Environ. Microbiol.* **1989,** *55,* 832–836.
25. Leff, D. V.; Brandt, L.; Heath, J. R. *Langmuir* **1996,** *12,* 4723–4730. doi:10.1021/la960445u
26. Gross, G. N.; Rehm, S. R.; Toews, G. B.; Hart, D. A.; Pierce, A. K. *Infect. Immun.* **1978,** *21,* 7–9.
27. Nikiyan, H.; Vasilchenko, A.; Deryabin, D. *Int. J. Microbiol.* **2010,** 704170. doi:10.1155/2010/704170
28. Ouerghi, O.; Touhami, A.; Othmane, A.; Ouada, H. B.; Martelet, C.; Fretigny, C.; Jaffrezic-Renault, N. *Biomol. Eng.* **2002,** *19,* 183–188. doi:10.1016/S1389-0344(02)00046-1

License and Terms

Beilstein Journal of Nanotechnology

Dynamic nanoindentation by instrumented nanoindentation and force microscopy: a comparative review

Sidney R. Cohen*[1] and Estelle Kalfon-Cohen[1,2]

Review

Open Access

Address:
[1]Department of Chemical Research Support, Weizmann Institute of Science, POB 26, Rehovot, ISRAEL 76100 and [2]School of Engineering and Applied Science, Harvard University, Cambridge, MA 02138, USA

Email:
Sidney R. Cohen* - Sidney.cohen@weizmann.ac.il

* Corresponding author

Keywords:
atomic force microscopy; loss modulus; nanoindentation; storage modulus; viscoelasticity

Beilstein J. Nanotechnol. **2013,** *4,* 815–833.
doi:10.3762/bjnano.4.93

Received: 13 July 2013
Accepted: 25 October 2013
Published: 29 November 2013

This article is part of the Thematic Series "Advanced atomic force microscopy techniques II".

Guest Editors: T. Glatzel and T. Schimmel

Abstract

Viscoelasticity is a complex yet important phenomenon that drives material response at different scales of time and space. Burgeoning interest in nanoscale dynamic material mechanics has driven, and been driven by two key techniques: instrumented nanoindentation and atomic force microscopy. This review provides an overview of fundamental principles in nanoindentation, and compares and contrasts these two techniques as they are used for characterization of viscoelastic processes at the nanoscale.

Review

Introduction

Understanding and controlling mechanics at the nanometer level is the key to a wide range of cutting-edge topics in science and technology, which range from engineered devices to biological organisms and include novel materials. A number of impressive technologies have been employed in such studies that include, but are not limited to, optical tweezers [1], surface force apparatus [2,3], nanomanipulators [4], electron and other microscopy techniques. Two techniques which have made great advances in the studies of nanomechanics are instrumented nanoindentation and scanning probe microscopy. The versatility and utility of these techniques lies in their capability to measure mechanical response at precise sample locations, in very small volumes and at shallow depths, while monitoring time, depth and force response. The high spatial resolution allows for the determination of local mechanical properties on nanosized objects, and for seeing heterogeneities at the nanoscale, as well as local effects which occur due to a vertical polymer confinement [5]. The time dimension is of particular

use in determining the viscoelastic response, which cannot be neglected in analysis of many polymers, biomaterials, and other soft matter.

In the following, we compare and contrast these two point-probe nanomechanical testing techniques. Following a brief review of nanoindentation, we concentrate on the influence and measurement of viscoelastic phenomena. Both experimental and theoretical considerations are included. Finally, a few demonstrative experiments are reported in order to illustrate and critically evaluate the topics reviewed.

A brief history of point-probe nanomechanical testing

The behavior of materials under controlled stress has enjoyed wide attention over the years. The elastic model developed by Boussinesq [6] and by Hertz [7] is still used today even at the nanoscale under certain limiting constraints. This theory was extended to a range of indenter geometries by Sneddon [8]. However, the pure Hertzian model does not consider surface energies and related adhesion forces, which become significant and may even dominate the overall force behavior at the nanoscale. Several groups considered the effects of adhesion under various contact mechanics models in the 1970s [9-13]. These models analyze the changing contact shapes and stresses that occur when the surface energy and the adhesive forces in the vicinity of the contact are significant. The Johnson–Kendall–Roberts (JKR) theory is appropriate for characterizing contacts of compliant samples with high surface energies, i.e., when there is strong adhesive contact between the tip and the sample [12]. This model balances the elastic energy with the surface energy, expressed as adhesion within the contact zone. It was followed by the Derjaguin–Muller–Toporov (DMT) model, which is applicable for stiffer samples and a lower but non-negligible surface energy, probed by a comparably sharp tip [11]. The DMT model accounts for forces outside the contact zone. These two extreme cases are delineated using the Tabor parameter [10], while the intermediate regime is covered by the work of Maugis [14]. An analytical model has been presented that encompasses all three of these models including the transition region [15].

These, and other important early works [16-19] paved the way for two new point-probe nanomechanical testing devices which were developed in the 1980s – instrumented nanoindentation (INI, also known as depth-sensing instrumentation) [19,20] and atomic force microscopy (AFM, also known by the more general term of scanning probe microscopy, SPM) [21]. These developments facilitated the measurement of mechanical properties of very small volumes of materials, opening new avenues of research. Reducing dimensions to the nanoscale gave birth to new paradigms in mechanical measurements and interpretation: In addition to the increased importance of surface effects such as friction and surface energy, dropping to the sub-optical regime made optical determination of the contact geometry impossible. This led to the need to determine the contact region size from force–displacement curves.

Fundamental equations and their limitations

The estimation of the elastic modulus from force–deformation curves alone was determined for the Hertzian case by Doerner and Nix who presumed a flat punch geometry to estimate the contact area [22]. The theory was subsequently refined to account for the changing contact area at different points in the unloading curve by Oliver and Pharr (O&P) [23]. The latter developed a nanoindentation model and measurement protocol to quantitatively deduce the elastic modulus and the hardness of materials by loading an axisymmetric indenter into a sample while recording the applied force and displacement. The indenter "area function" is determined by performing this experiment on a well-known material, typically fused quartz. The principle quantities derived from a nanoindentation experiment are elastic modulus and hardness. The former is a fundamental property of the material, which, in principle, can be calculated from bond stiffness, and the latter in turn can be related to shearing bond strengths. The modulus, which was formally defined as the ratio between stress/strain (σ/ε), can be directly computed from a nanoindentation load/deformation curve with the aid of an analytical model such as the widely used O&P approach [23]. This approach uses relations that were derived by Sneddon [8] in order to extract the indentation modulus from the slope of the unloading curve according to Equation 1 [23,24]

$$E_{\mathrm{r}} = \frac{\sqrt{\pi}S}{2\sqrt{A}} \tag{1}$$

where S is stiffness, given by the slope dF/dh of the unloading curve, and A the contact area between the indenter and the sample. E_{r} is the reduced modulus which accounts for both sample and indenter Poisson ratio and modulus – υ_{s}, E_{s} and υ_{i}, E_{i} respectively:

$$\frac{1}{E_{\mathrm{r}}} = \frac{1-\upsilon_{\mathrm{i}}^2}{E_{\mathrm{i}}} + \frac{1-\upsilon_{\mathrm{s}}^2}{E_{\mathrm{s}}} \tag{2}$$

Several depth sensing indentation methods were developed to evaluate A [23-25], which allow for evaluation of hardness and modulus without imaging the indentation impression. This model is applicable for flat, homogeneous and isotropic

samples, without nonidealities such as adhesion [11,12], pile-up [26-28], and time-dependent effects [29-35].

In practice, this fundamental equation has been extended to samples which do not, in principle, meet the basic requirements. For instance, in heterogeneous materials, sub-micron sized domains can be treated by this analysis when using an indenter with nanometric radius and small indentation depths. Thin, soft films on hard substrates also are well-described by this equation when the indentation depth is limited [36-39].

Whereas limiting indentations to the nanoscale justifies ignoring some types of inhomogeneities, the influence of small, intrinsic adhesion forces is enhanced. The presence of capillary and adhesive forces changes the contact profile and modifies the force acting between indenter and sample during pull-out. This behavior is highlighted by a significant attraction between tip and surface upon pull-out seen as a hysteretic negative unloading force (Figure 1). Accordingly, the contact radius depends on the thermodynamic work of adhesion, $\Delta\gamma$, considered in the JKR theory.

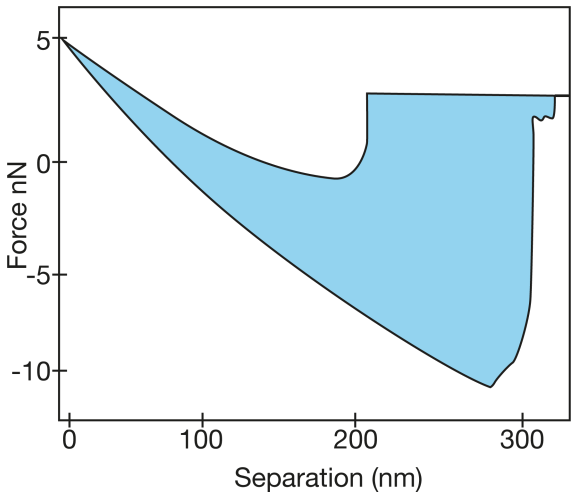

Figure 1: Adhesion-induced hysteretic negative unloading force observed on indenting PDMS (4% cross-linked) by AFM with a pyramidal silicon nitride tip of force constant 0.05 N/m. The colored area represents the hysteresis between ingoing- and outgoing traces and defines the energy loss.

Ebenstein and Wahl examined several ways of calculating the modulus for real experimental data, in order to handle the inaccessibility of some necessary parameters. For instance, since the true contact area is rarely known, for the JKR relation [40]:

$$E_{\mathrm{r}} = \frac{-3RP_{\mathrm{adh}}}{a_0^3} \tag{3}$$

The contact radius at zero net force, a_0 as well as the adhesive force P_{adh} can be found by curve fitting. Typically unloading curves are preferably taken for analysis to avoid the plastic deformation that is present during loading. In AFM this procedure may lead to erroneous results: Since the AFM experiment does not control the load, but rather the displacement, the tip–surface system has an additional degree of freedom because of a compliance of the cantilever, which leads to a more stable contact during unloading. Hence, the fit to the JKR model, which presumes load control, is invalidated [41].

For the DMT model the interaction is described by:

$$E_{\mathrm{r}} = {}^{3}\!/_{4}\, P_{\mathrm{tot}} R^{-1/2} \delta^{-3/2} \tag{4}$$

where P_{tot} is the total force, including P_{adh}, and δ the sample deformation.

The Tabor parameter, which is used to distinguish between JKR and DMT conditions is given by [10,40]:

$$\mu = \left(\frac{R\Delta\gamma^2}{E_{\mathrm{r}}^2 z_{\mathrm{o}}^2} \right)^{1/2} \tag{5}$$

When μ is less than 0.1, the DMT theory is applied and when μ is greater than 5, the JKR theory is used [40]. The intermediate regime between these two extremes is covered by the work of Maugis [14]. The choice of the model (JKR, DMT or Hertz), that is used for the reduced modulus calculation then requires some a-priori knowledge of the material or preliminary investigations as will be further developed below.

Instrumentation

Schematics of INI and AFM instruments are shown in Figure 2. Table 1 gives a comparison of their capabilities and characteristics. For INI, a calibrated force is applied to the indenter tip, which in turn is constrained with a vertical spring. The lateral spring constant can be considered infinite in the standard configuration, and the indenter motion is confined to the plane perpendicular to the sample. The vertical indenter displacement is measured independently, providing nm-level sensitivity. The accurate determination of the contact point then allows for a direct determination of the indentation depth. Indentation placement is directed by an optical view, or in some cases the indenter tip itself is used to make a higher resolution profiling scan of the surface to enable a placement in the tens of nm range.

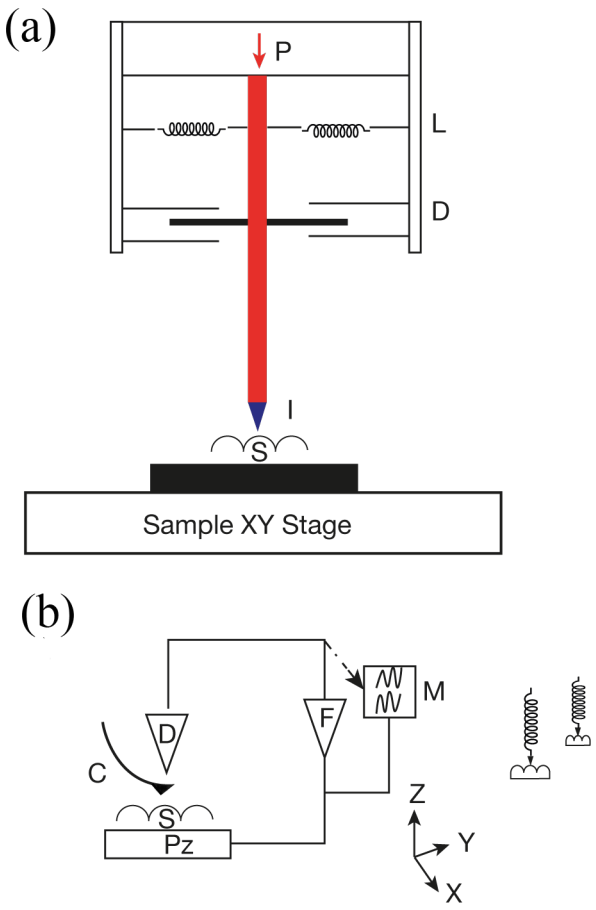

Figure 2: (a) Schematic of instrumented nanoindenter, including P - calibrated force; L - support springs; D - Position sensor; I - indenter tip supported by shaft; S - sample. (b) Schematic of AFM showing Pz - piezoelectric motion transducer; S -sample; C - integrated cantilever and tip; D - cantilever motion detector; F - feedback; M - monitor for display. To right the working of AFM is shown schematically: extension of spring changes before and after applying load. From [42].

For AFM/SPM the situation is somewhat different. A calibrated displacement is applied to the base of the probe or to the sample, and this motion is transduced into force by a flexing of the cantilever beam that holds the probing tip. The degree of flexure is measured, usually by optical means, and the force is obtained with knowledge of the cantilever stiffness and of the measured degree of bending. The sample–tip motion is actuated by piezoelectric elements, which can be linearized by closed-loop control. The cantilever beam is usually oriented at an angle to the surface, which results in some tangential force being applied in addition to the normal force. A tangential motion along the long cantilever axis can lead to additional flexural bending [43], while a force orthogonal to this direction results in a sideways torsion with the ultimate torque being moderated by the tip length [44]. Thus, the choice between INI and AFM typically involves a trade-off between a more reliable characterization of force and a larger dynamic force range for the former and a better force and displacement sensitivity and a superior imaging/placement for the latter [45-47]. For soft materials, in which an insensitivity to the initial contact can lead to a severe underestimation of the contact depth in INI, the enhanced sensitivity of the AFM carries some distinct advantages. However, even though AFM has been successfully used to probe mechanical properties on the nanoscale, there are a number of drawbacks, which make the quantification of the mechanical properties challenging. Many of the factors discussed in previous reviews over the past decade are still issues today [48-51]. Most notable of these are the implicit assumptions of linear elasticity, which require the contact radius and the indentation depth to be much smaller than the indenter radius, and the absence of tangential stress so that forces are restricted to the surface normal – all these are difficult to maintain in AFM.

Table 1: Comparison between instrumented nanoindentation (INI) and atomic force microscopy (AFM).[a]

characteristic	INI	AFM
vertical spring constant	100 N/m	from <0.01 N/m to over 500 N/m
lateral spring constant	10^5 N/m	10–1000 N/m[b]
lowest fundamental resonance	20–500 kHz	several thousand kHz
displacement sensitivity	1 nm	0.05 nm or better
load sensitivity	10 nN	<0.05 nN[c]
dynamic range of force	10^8	10^3
nm-scale imaging	nonexistent to fair	excellent
bandwidth	0.001–100 Hz	1 Hz – several kHz
temporal stability[d]	good	fair

[a]Parameters given here are typical and may vary from instrument to instrument, [b]Typically 2 orders of magnitude greater than flexural (normal) spring constant, [c]Depends on cantilever used in measurement. [d]Sensitive to instrumental design: environmental control can improve this.

Dynamic nanoindentation

Background and relevant models

Time-dependent phenomena, i.e., when the material strain is not synchronous with the force or displacement applied to the perturbation stress, have a strong influence on the load-vs-deformation curves. Since there is a time lag between a change in applied stress and the response of the material, the deformation response still "remembers" the increase in stress during a hold at peak load or even during unloading. This leads to a "nose" in the curve (as shown in Figure 3) and, in extreme cases, to an apparent negative stiffness. This phenomenon will depend on the rate of change of the force. Computational approaches exist that modify the Sneddon contact mechanics model to remove the time-dependent effects of viscoelastic materials [52,53]. Time-dependent compliance is ubiquitous and can appear even in quite hard ceramics as result of the rearrangement of point defects [54]. Under some conditions, the nose can be due to viscoplasticity [55]. By choosing working conditions that avoid viscoplastic deformation during unloading, it may be possible to apply the O&P model with consistent results [56]. However, there is still a need to utilize analytical approaches that are directly suited for viscoelastic materials. Many examples of such work can be found in the literature. Since the classical solutions assume equilibrium conditions, which do not strictly hold when there is a viscoelastic response, numerical approaches have been developed [57,58]. The variety of analytical approaches can be justified by different considerations that must be made for different classes of materials as has been recently reviewed [59].

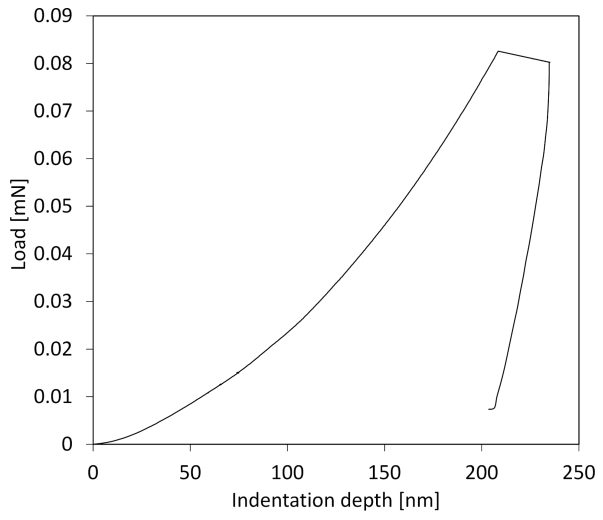

Figure 3: Load-vs-displacement curve taken by nanoindentation with a Berkovich indenter tip on a polyurethane sample showing negative stiffness, seen as the outward bulging of the curve, which develops in the unloading (right branch) of the curve, because of creep.

The wide variation in experimental protocols that is applied for dynamic studies is a natural outcome of their diversity. In order to put some order to these methods, it is necessary to understand the basics behind the physical phenomena. Here, we will limit the discussion to linear viscoelastic behavior, which means that the strain depends only on time and not on the magnitude of stress. This holds when the stress is kept small. The dynamics can be experimentally studied by several means, the most common being summarized here [60]:

1. creep relaxation, in which the indenter is rapidly brought to a given force/stress and the change in strain required to maintain this situation is monitored.
2. stress relaxation where the indenter is brought to a given deformation/strain and the stress required to maintain it is monitored.
3. periodic variation of stress, usually sinusoidal, at a given frequency f, equivalent to a transient experiment at time $t = 1/2\pi f = 1/\omega$.

To formulate the time response in terms of well-understood mechanical elements, the viscous component is modeled most simply as a combined spring and dashpot either in parallel (Voigt model) or in series (Maxwell model), shown in Figure 4a and Figure 4b. A comparison of these two models, as well as the resulting constitutive equations can be found in the book of Shaw and MacKnight [61]. These models address the fact that the mechanical behavior of a viscoelastic material cannot be described by either a simple spring or by a viscous element. In general, the Maxwell model is more appropriate to a viscoelastic fluid and the Voigt model a viscoelastic solid. In comparison, these models yield the same results, except that the Voigt model cannot describe a stress relaxation experiment because the dashpot would develop a singularity in force with step change of strain.

To illustrate these differences, for load control as it is used in INI creep relaxation, the Voigt model, Figure 4a, can be applied, but for nanoindentation stress relaxation as it is conveniently done in AFM, the Maxwell model (Figure 4b) is more appropriate. Whereas these simplistic models give a general means to quantify the physical phenomena, they do not encompass the complexity inherent in a real system. Therefore, combinations of Voigt and Maxwell components are often used to better approximate reality. These could be a series of constitutive elements connected in parallel, or in series, depicted in Figure 4c and 4d, respectively. A combination of Voigt elements connected in series is known as the Voigt–Kelvin model. This model and its modifications are widely used for nanoindentation creep relaxation analysis due to the suitability of the Voigt model for solids as mentioned above [62-64].

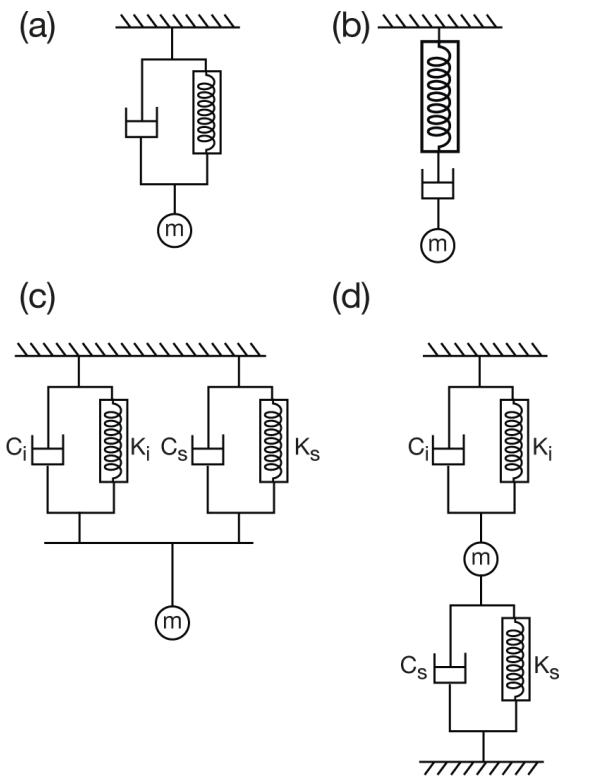

Figure 4: Fundamental models for a viscoelastic mechanical system. (a) Voigt model (b) Maxwell model (c) Generalized Voigt model with 2 components (d) Voigt–Kelvin model.

Combinations of the different models are also used. A comparison of three different models (Maxwell, Voigt–Kelvin, and combined Maxwell and Voigt–Kelvin) revealed that the latter gave the best fit to experimental data and also displayed a predictive power for experimentally-obtained indentation curves [65].

Classically, in the DMS (dynamic mechanical spectroscopy) technique, a macroscopic sample is subjected to a modulated stress and the strain is recorded [66]. The energy released by the relaxation of a polymeric chain generates a phase shift between the harmonic stress and strain, which is in turn used to express the dynamic elastic moduli as defined above. This shift is frequency-dependent, as the various modes of internal friction of the polymer are excited at distinct characteristic times. In order to probe the viscoelasticity at the nanoscale analogous techniques are applied. An interpretation should consider that the measured phenomena could be different at the nanoscale for the general reasons already discussed and more specific properties of polymers such as issues of confinement [5,67].

We first consider the modulation experiment for which either the stress or the strain could be modulated. In this case, stress and strain will exhibit a phase difference designated as angle δ and the modulus can be now expressed as complex modulus E^*:

$$\begin{aligned} E'_\omega &= \left|E^*\right|\cos\delta \\ E''_\omega &= \left|E^*\right|\sin\delta \\ E^* &= E' - iE'' \\ \left|E^*\right| &= \sqrt{E'^2 + E''^2} \end{aligned} \tag{6}$$

Here, E' is the storage modulus, which measures the energy stored during one oscillation cycle, and E'' is the loss modulus, which measures the energy dissipated during an oscillation cycle.

The phase lag, referred to as loss tangent (tan δ), arises from any of a number of molecular-level lossy processes such as entanglement, slip or friction between the monomer units. Although the phase lag is not amenable to a direct theoretical interpretation, it is relatively easy to be determined accurately and provides useful qualitative information. Furthermore, tan δ takes on characteristic values, e.g., approximately 1 for amorphous polymers in the transition zone, and 0.1 for glassy and crystalline polymers [60]. Most importantly, it does not require any knowledge of the contact area and it can be used to clearly identify phase transitions.

At the micro-level, the thermodynamic state of the polymer can be related to a molecular motion at different hierarchical levels – from the cooperative motion of entire chains through short hops of individual segments and finally to internal rotations and vibrations of the component molecules. Polymers exhibit several phase transitions that can be correlated with the relaxation at characteristic frequencies [66]. The loss modulus will vary over a wide range of frequencies and show peaks at specific temperatures and frequencies that correspond to phase changes. These changes can be effected both mechanically by a change of frequency, and also through internal thermal motion. A related approach to understand the molecular dynamics is thus by varying the temperature [68,69]. The correspondence between temperature and frequency is embodied in the temperature–time superposition [70]. In general, increasing the temperature induces a molecular relaxation that leads to an increased phase lag between stress and strain. The loss modulus, which reflects the viscous damping of the sample, then increases with temperature. Concomitantly, the storage modulus is reduced since molecular relaxation loosens the molecular bonds.

Experimental aspects of the dynamic response measurement

Some caveats should be applied in comparing experiments made under different conditions: The creep response depends on the tip shape, and results obtained by using the common Berkovich indenter show an apparently more compliant sample than a spherical tip [35,71]. Investigation of dynamic elastic contacts showed that the frequency of oscillation strongly influences the contact radius [33]. Furthermore, the creep compliance and the time-dependent shear modulus can vary with the ultimate force applied because of a deviation from linear viscoelastic behavior [30].

Because of their small size and the fine control over force and displacement, the point probes are particularly amenable to dynamic loading, in which a small modulation of several nanometers is superimposed on the quasistatic loading curve, and the displacement amplitude and phase angle between the applied modulated force and the corresponding modulated displacement are measured continuously at a given excitation frequency [72]. Detailed explanations of force modulation techniques and analyses can be found in the literature [20,73]. Briefly, the modulated force $P = P_0 \sin(\omega t)$, results in a displacement oscillation at the same frequency expressed by $h(t) = h_0 \sin(\omega t - \varphi)$. The dynamic in-phase and out-of-phase equations can be re-written in terms of experimental observables as follows [74]:

$$E'_\omega = \frac{P_0}{h_0}\frac{\sqrt{\pi}}{2\beta\sqrt{A}}(1-\nu^2)\cos\delta \tag{7}$$

$$E''_\omega = \frac{P_0}{h_0}\frac{\sqrt{\pi}}{2\beta\sqrt{A}}(1-\nu^2)\sin\delta \tag{8}$$

where P_0 is the steady-state modulated load amplitude, h_0 is the resulting modulated displacement amplitude, and δ as defined above is the angular phase shift between the applied force and the measured displacement. The contact area A is not an observable, but can be derived by calibrating the indenter. It has been noted that these relations hold strictly only for shear between two parallel plates and the application to nanoindentation experiments should be used with caution [75].

By using the dynamic model shown in Figure 4c, an analytical solution for the resulting displacement amplitude, h_0, and the phase shift, δ, can be derived. In AFM, the modulation may be applied at the tip or at the sample, which will lead to different analytical solutions [63]. Here, the solution is given for force modulation applied to the tip, as is typical for INI [64,73]. Thus, the measured displacement amplitude h_0 induced by the modulated force amplitude P_0 is:

$$h_0 = \frac{P_0}{\sqrt{\left(k - m\omega^2\right)^2 + (c\omega)^2}} \tag{9}$$

and the measured phase shift between the applied force and measured displacement is related to sample and instrumental parameters by:

$$\tan\delta = \frac{c\omega}{k - m\omega^2} \tag{10}$$

$$k = k_\mathrm{i} + k_\mathrm{s}; \qquad c = c_\mathrm{i} + c_\mathrm{s} \tag{11}$$

where c_i, c_s are the damping coefficients of the air gap in the displacement transducer and sample, respectively, k_i and k_s instrumental and sample stiffness, and m the indenter mass. Typically, no correction is made for the additional moving mass of the contact since it is insignificant relative to the indenter construct. In the case where this assumption would no longer be valid, an effective mass should be used in the equations together with effective k and c in order to avoid an overestimation of c and hence of E".

After calibration to determine m, c_i, and k_i, the sample-specific values for E' and E'' can be obtained as shown in Equation 12. These equations also illustrate how the damping coefficient can be understood as the out-of-phase counterpart to the in-phase stiffness giving the storage modulus. This leads naturally to expression of tan δ as the ratio of E''/E'.

$$E' = \frac{k_\mathrm{s}\sqrt{\pi}}{2\sqrt{A}}; \quad E'' = \frac{c_\mathrm{s}\omega\sqrt{\pi}}{2\sqrt{A}}; \quad \delta = \tan^{-1}\left(\frac{c_\mathrm{s}\omega}{k_\mathrm{s}}\right) \tag{12}$$

Despite the fact that for the configuration of nanoindentation experiments, the basic assumptions that underlie such models are not strictly satisfied, they yield reasonable results relative to classic rheological studies and other macroscopic measurements [35,75-78].

Creep relaxation, which was introduced in the previous section, is also used to determine time-dependent phenomena. Although most studies invoke the loss modulus E'' and a viscosity coefficient η, Yang et al. assign three contributions to the creep [79]: the elastic deformation, analogous to the deformation used in Equation 1, the viscoelastic deformation controlled by an exponential term, and the viscous component η.

In the creep experiment, the probe tip is pushed into the material at a fixed load P_I and an initial depth h_I. The force is held constant by the system feedback throughout the creep time and the creep is detected as change in position required to compensate for the relaxation and to maintain constant force. Relaxation of the viscoelastic material then results in an increased indentation depth. In principle, the creep displacement can be directly read from the experimental displacement curves. For INI this would be the displacement sensor reading of the indenter position. For AFM it would be the *z*-piezo extension, which is ideally monitored by a linearized sensor. However, thermal drift and piezo creep can also contribute to the apparent displacement, thus they must be minimized and/or measured and corrected for. This can present a challenge, particularly in AFM, which largely relies on piezoelectric motion transducers. It should be noted that a *z*-sensor, which is used to linearize the *z*-motion, cannot distinguish between creep and thermal drift. In light of this discussion, additional differences between AFM and INI can be added to those mentioned above: the time resolution of the measurement, which is related to the inertia of the system, and the drift/creep characteristics. These are noted in Table 1 as bandwidth and temporal stability.

For a given creep time t, the corresponding displacement into the surface $h(t)$ is measured experimentally. The creep behavior can then be modeled following [79] and [80]:

$$J(t)=\frac{A_I h(t)}{P_I h_I} = \frac{1}{E_\infty}-\sum_1^3 \frac{E_i}{(E_i+E_\infty)E_\infty} exp\left(\frac{-E_i E_\infty}{\eta_i (E_i+E_\infty)} t\right) \quad (13)$$

with h_I being the initial indentation and $h(t)$ the indentation at time t. A_I (initial contact area) and P_I are known or measured; Such curves are then related to different relaxation modes of polymers and the frequency spectrum of internal modes by models such as Voigt–Kelvin, for which the model in Figure 4d is extended to n intrinsic units. The applicability of different mechanical models to a unique mechanical system is an established mathematical concept that was recognized in the interpretation of polymer systems (see [60], pp 16 and 17). Sun and Walker applied the Zener model, with these elements connected in parallel, to model creep in a number of different polymer systems. They found that 1–3 elements were required depending on the polymer studied. Ideally, each such element, with its characteristic time, represents a given transition in the polymer. As usual, over-interpretation should be avoided, and one should always recall that the simplified or even complex mechanical models are describing a substantially more complex molecular system.

Dynamic AFM probe nanoindentation

Boasting the advantage of wider bandwidth, smaller inertia of the system, better lateral resolution and more sensitive force detection, AFM provides some interesting opportunities for monitoring the dynamics in nanoindentation. Operating the AFM under dynamic mode has distinct advantages in reducing the sample damage, particularly for delicate samples [81,82]. Also, the volume needed for probing is reduced even further, which allows for the analysis of small areas and thin films down to a single monolayer [83]. A recent example is the application of AFM imaging together with the mechanical measurement to give a detailed insight on cellular membrane mechanics, which is only meaningful when the viscoelastic response is accounted for [84]. The bandwidth advantage has been extended to the MHz range, allowing an access to higher harmonics [85-89]. This provides several advantages: Higher harmonics can be exploited to separate the mechanical measurement from the topographic feedback, the signal-to-noise ratio can be improved, and the accessible dynamic force range is enhanced since each harmonic is associated with its own characteristic spring constant. Investigation of a material over a wide range of frequencies also gives a sharper topographic contrast since some materials, which may yield under the tip force, are unable to respond at high modulation frequencies and thus appear to be stiffer. The inclusion of multiple, higher frequencies, also allows for a full characterization of the highly nonlinear cantilever dynamics [81,90]. Nonetheless, the application of such techniques still requires the knowledge of contact geometry, an assumption of some contact model and/or force potential, and in some cases the input of some parameters of the material. Thus the inherent fundamental limitations of quantitative nanomechanical testing must be accounted for. New noncontact techniques allow for the monitoring of the entire force profile while starting at noncontact positions. The deconvolution implemented to convert the experimentally observed frequency shift/amplitude change to a force can also introduce some uncertainty [91]. Single-frequency techniques are still more readily accessible in most laboratories. Dynamic imaging modes that are commonly used in AFM provide the phase information, typically as an image channel measured and displayed simultaneously with the topographic image. The phase shift is interpreted as giving an estimate, generally qualitative, of the energy dissipation [92,93]. Nonetheless, there are many contributions to such phase contrast including the changing tip–surface contact area as the tip scans the sample. Each case must be modeled differently.

Theoretical studies exploit phase and amplitude data together to identify and quantitatively measure the different dissipation processes [82,94]. One caveat arising from the modulation techniques is that the phase lag signal carries information on add-

itional dissipative processes other than viscoelastic energy dissipation, such as surface adhesion and capillary forces [95]. "On-the-fly" measurements of dissipation, which integrate the area under the hysteretical force–distance curves as depicted by the blue-shaded region in Figure 1 can also include these effects of adhesion and thus cannot be unequivocally assigned to viscoelastic processes in the material. Such effects are critical issues for polymers. For this reason, equating phase contrast with a viscoelastic effect would be misleading in many cases. Calculations by Garcia and coworkers succeeded in separating and quantitatively reproducing different contributions to dissipation [96]. This work underscores the importance of including the contribution of the oscillating cantilever to the overall mechanical response.

Eastman and Zhu show that the adhesion forces depend strongly on the surface energy of the tip, and on the wettability of the tip surface in a humid environment [97]. In ambient conditions, the surface of a polymer is likely to be covered by a thin layer of water that is sufficient for increasing the capillary and possibly van der Waals interaction. Any additional adhesion will act to increase the hysteresis in the force–distance curve and thus complicate the application of simple mechanical models.

In addition to these environmental effects, the instrumental contribution to damping must be accounted for. These inherent instrumental properties include those of the spring (cantilever), of the electronics, and of the piezoelectric transducer. For INI, careful calibration protocols have been described to account for these [64,73]. For SPM there is no unified approach to this procedure, yet. Such calibration requires knowledge of the frequency-dependent amplitude and phase shift and is critical for accurately evaluating the stiffness and damping coefficient of the tested material. For dynamic INI, the modulation is applied at the tip–sample contact. In dynamic AFM operation the displacement may be applied to the base of the cantilever or to the base of the sample, in which case the cantilever spring acts in series with the tip–surface compliance [20,73]. A very different response is obtained when the modulation is applied at the tip–sample contact [98]. Burnham et al., in an analysis of the mechanics of dynamic AFM contact, described the various modes, in which the AFM can be used to study energy dissipation [63]. They split the possible operation modes into three categories: force modulation, sample modulation and tip modulation. They found that a proper choice of measurement category and associated frequencies is needed for different types of samples.

The system response for a typical AFM measurement can be calculated from Equation 12, following the setup of Figure 4d. In this case the total stiffness K and damping C differ from Equation 11 as follows:

$$K = \frac{k_\mathrm{i}k_\mathrm{s}}{k_\mathrm{i}+k_\mathrm{s}}\ ;\ C = \frac{c_\mathrm{i}c_\mathrm{s}}{c_\mathrm{i}+c_\mathrm{s}} \tag{14}$$

The instrumental contributions to stiffness and damping, k_i and c_i respectively, are determined by an independent calibration. Then, from the measured system response, the stiffness and damping of the sample can be extracted. Clearly, this procedure entails a careful calibration of the instrumental damping both for INI and AFM.

Researchers have wrestled with the best way to measure the dynamics for two decades. One of the earliest attempts to measure the dynamic modulus by AFM was performed by applying a modulation directly to the sample z-piezo [99]. In this early work, the instrumental phase shift was removed by conducting a comparative measurement on a stiff, clean surface. By modifying the AFM setup, Hutter et al. induced small oscillations to the deflection signal by inserting the modulation directly to the feedback loop to generate a compensatory oscillation of the sample z-piezo [100]. This approach is proposed as easy to implement, and allows for the measurement of the dynamic modulus while imaging the sample. This setup provided a quantitative measurement of the viscoelastic properties of PVA fibers. Also here, the instrumental phase response was assessed by a measurement of a perfectly rigid sample. McGuiggan and Yarusso calibrated the instrumental phase shift on a hard surface. They pointed out that this method ignores slip that may occur at the surface [101]. They furthermore note that most models do not include adhesion hysteresis, an unknown tip shape, and other factors. They chose to report their data as tan δ since the ratio between loss and storage modulus cancels out the unknown terms.

Minary-Jolandan and Yu also related to the potential errors when the instrumental phase shift is measured on a hard surface and noted that it may lead to large errors on rather compliant samples, which exhibit only small phase shifts [102]. They proposed a method to remove the offset phase directly on the sample of interest at zero contact force, which provides an accurate in-situ calibration of the instrument. This method accounts for all factors contributing to the phase shift except for those caused by the compression of the sample under the tip. Therefore, this method would not work on a soft polymer brush with ill-defined interface.

For the resonance modes, system response and phase shift are non-negligible in air. Yuya et al. removed the internal beam

damping by evaluating its behavior suspended in air [103]. A known reference was used for calibration, allowing them to measure storage and loss modulus with an ultrasonic contact technique utilizing the first three flexural modes. For measurements in any fluid, including air, there will be a drag force on the bulk cantilever. In liquid, this drag force is very significant. Mahaffy et al. recorded this force in an aqueous environment as the tip approached the surface, but before it made contact and thus comprised a noncontact measurement of the phase shift [104]. A combination of the two corrections was made in a study of viscoelastic behavior of cells [105]. In this work, the hydrodynamic drag of the cantilever was measured at varying heights above the surface, and in addition, the phase response of the AFM piezo was measured in contact with a stiff cantilever probe on a hard surface in air. These few examples prove that there is no accepted standardized protocol for the characterization of the intrinsic phase shift, even though the use of a rigid substrate as reference is quite widely used.

The point-probe techniques also lend themselves to measurements that are not necessarily based on AC methods for the characterization of viscoelastic materials. In many dynamic processes it is found that more energy is required to separate two surfaces than is released when they come into contact. This is usually manifested as a hysteresis between the loading and the unloading curves in force measurements. The fine resolution can be achieved with noncontact AFM allows for a quantitative detection of dissipation that involves the formation and the breakage of weak intermolecular bonds in an organic molecule [106]. However, for many practical cases, the separation entails energy dissipation in the bulk material – generally a viscoelastic/plastic deformation, as well as capillary and adhesive forces.

The analysis of AFM force–distance curves of polydimethylsiloxane (PDMS) showed a strong influence of the measurement conditions such as the loading–unloading rate and the dwell time, as well as intrinsic material properties like the crosslinking density and chemical surface modifications [80,107-109]. The viscoelastic response has been studied both through hysteresis in the loading–unloading portion of the curve [110,111], and in the adhesive pull-off segment [80,109]. Analyzing the results in this fashion allows one to distinguish between the bulk relaxation (observed in the temporal dependence of adhesion-induced indentation upon tip extension) and relaxation at the tip–surface interface (observed in the temporal dependence of the retraction curve). The distinction between the mechanical response of a bulk polymer and its surface is one important goal of all point-probe measurements and has also been achieved by using dynamic INI [67].

Current status

Evidently a multitude of experiments and protocols are described in the literature for extracting the viscoelastic properties of soft polymers by using dynamic INI and AFM nanoindentation. The need to develop standard methods in dynamic nanoindentation has been shown to be crucial for the reliability and repeatability of the experiments. Such a standardized method should include a clear protocol for the modulation, the calibration process of the instrument, the reference materials and the frequency ranges. Some efforts have been made in this direction, but there is no consensus on the matter yet [51]. Nonetheless, it is anticipated that under the action of ISO TC164 SC3 accepted protocols will be decided upon [112].

When these two point probe techniques are used to measure the same surface, the divergence between INI and AFM is apparent. As indicated above, there are notable differences between what, and how they measure. The comparison between instrumented nanoindentation and AFM probe nanoindentation provided here has emphasized some of these differences.

Demonstration of the concepts

By way of demonstrating some of these issues, an experimental comparison between AFM and instrumented dynamic nanoindentation for assessing the viscoelasticity in polymers is presented below. Simple approaches were chosen to demonstrate that meaningful data can be obtained with relative ease, and also to point out the resultant inaccuracies. In order to highlight the issues that are discussed in this review, particular attention is given to the calibration of the instrument. The dynamic moduli of two polymers are estimated on the basis of Equation 12.

Nanoindentation experiments were performed on isotactic polypropylene (iPP, 127,000 g/mol) by using instrumented nanoindentation (Agilent DCM) and AFM tip based nanoindentation (NTMDT NTEGRA). A typical INI load-vs-displacement curve is displayed in Figure 5A. The modulation results (continuous stiffness measurement CSM^{TM}, modulation amplitude 5 nm) displayed in Figure 5B reflect the modulus value, which is determined by the instrument software by using standard O&P analysis [23]. The curve in Figure 5B starts at high E values and rapidly decreases down to an indentation depth of about 60 nm, after which it settles to an asymptotic value. This is due to surface effects in addition to the unreliability of the area function at very small depths and a relatively large amplitude of oscillation compared to the deformation at low depths. Averaged over 20 tests, the asymptotic reduced storage modulus is 2.7 ± 0.2 GPa. After adjusting for a Poisson ratio of 0.45, the resultant value of 2.15 GPa compares well with literature data that report a Young's modulus of 1.8 GPa at this

frequency [113]. The data in Figure 5 represent the storage modulus. In order to measure the smaller loss component, dynamic analysis was performed by using the relations summarized in this review, and reported below.

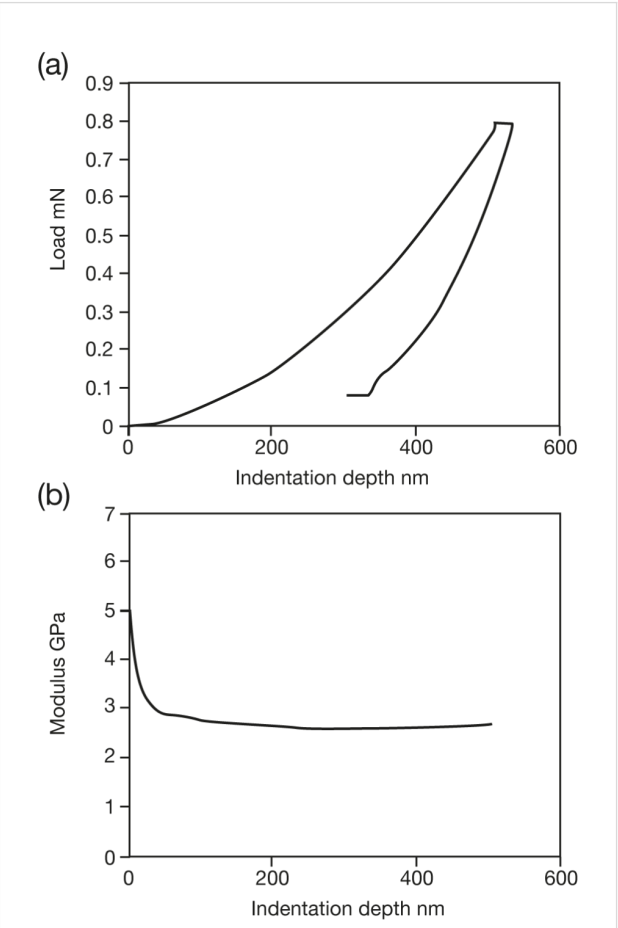

Figure 5: Modulus measurements on polypropylene (A) Load-vs-deformation curve (B) Reduced storage modulus determined using continuous stiffness measurement vs depth. CSM modulation amplitude 5 nm at 45 Hz.

Dynamic instrumented nanoindentation

In order to extract the storage and the loss modulus from dynamic testing, the instrument response must be characterized and corrected for. The introduction of a frequency specific phase lock amplifier in the continuous stiffness measurement (CSM) induces a frequency-dependent phase shift. Consequently, a correction of the phase shift is required. The calibration is made according to the protocol described by Herbert et al. [64]: With the indenter tip hanging in free space the stiffness and the damping of the instrument are measured as a function of the frequency by using Equations 9–11 above.

The calibration revealed a significant variation in damping with the frequency (Figure 6).

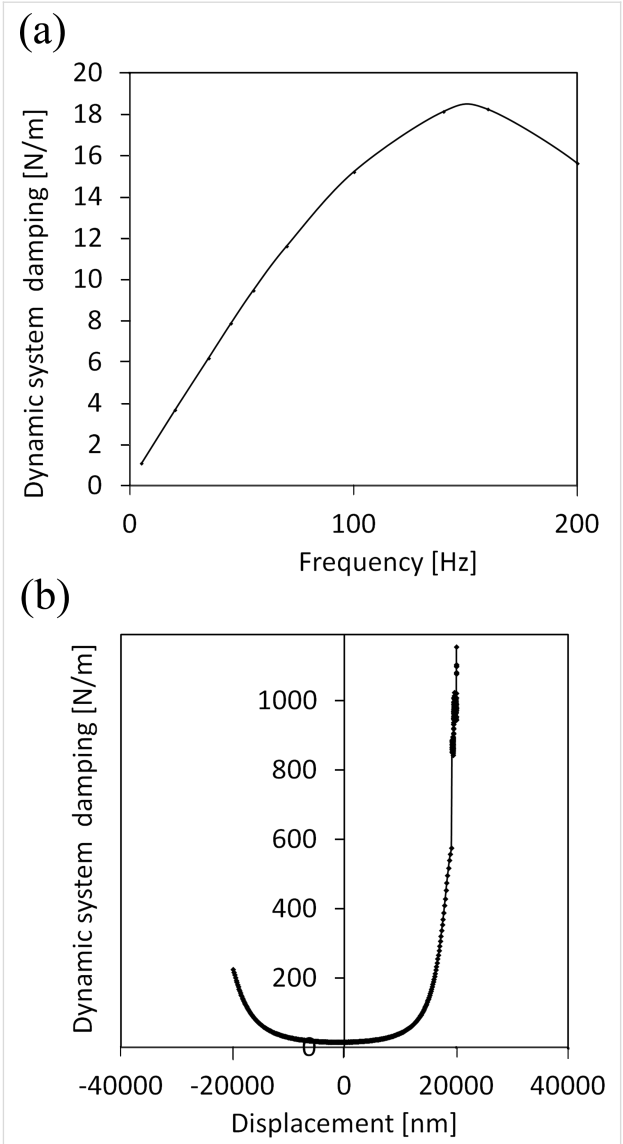

Figure 6: Calibration of the system damping for INI. The damping was computed for each frequency at different vertical extensions of the indenter over a range of ± 30 µm. The damping is computed by using Equations 9–11 and is reported here as $C_i\omega$. (a) System damping as a function of the frequency for a displacement near 0. (b) System damping as a function of the displacement of the indenter head at 200 Hz frequency.

Figure 7 shows the variation of the loss moduli and loss tangent with the modulation frequency ($\omega/2\pi$) at a depth of 1000 nm for the iPP films. As mentioned previously, tan δ is particularly suited for detecting dissipative processes such as friction [60,114]. The progressive increase of the loss tangent with the frequency can be attributed to the increase of internal chain friction at higher frequencies [66]. In comparison to the storage modulus, the values of loss modulus observed in Figure 7 contribute little to the magnitude of the complex modulus, so the careful calibration procedure is essential to get accurate data.

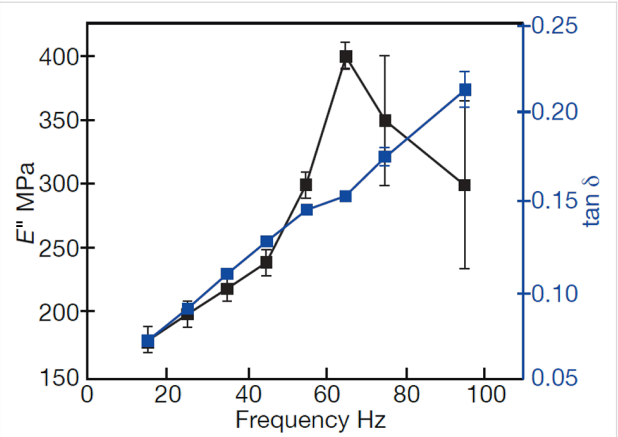

Figure 7: Dynamic INI of iPP as a function of the frequency. The error bars indicate the standard deviation calculated for at least five measurements in three different places.

AFM-based modulation

In this experiment, the tip was first indented to a depth of 50 nm into the sample in the AFM (Bruker, multimode). Prior to the experiment, the cantilever spring constant and the deflection sensitivity were determined with the Nanoscope software (former from the thermal noise and the latter by measuring the deflection of the cantilever with the displacement on a hard surface). The tip radius for various depths was estimated from a sample of known modulus by using the DMT relation and quantitative mechanical mapping (QNM®) mode (Bruker). A modulation was then applied at several frequencies in the range of 5–300 Hz. A digital lock-in amplifier was used to detect the amplitude and the phase of the cantilever oscillation relative to the drive signal. The modulation was conducted by using two oscillatory modes. In the first method, called *z*-modulation here, a sinusoidal signal is added to the *z*-voltage of the piezoelectric tube [99,115]. This leads to a modulated deflection of the cantilever of 5–10 nm and thus a variation of the force between tip and sample. This modulated amplitude is fed into a lock-in amplifier and the output of the lock-in amplifier is recorded as amplitude vs time. Because of the mechanical and instrumental response, the amplitude and phase of the instrumental contribution depend on the frequency. For a quantitative analysis of the data it is therefore necessary to correct for the response with the apparatus transfer function by using an incompressible sample. In the second mode, tip modulation, the cantilever base is modulated via the tip holder. Here the contribution of the instrument damping is isolated by vibrating the cantilever in air and the loss modulus of the sample is calculated by using Equation 11 and Equation 12.

The subtraction of instrumental damping is less straightforward in AFM than in INI. It has been suggested that for frequencies well below resonance, modulating the tip in air will give a negligible phase shift [102]. In our system, a small but observable shift can be detected as shown in Figure 8a. The phase lag rose slightly with the modulation frequency, from 0.5° at 5 Hz to 2.5° at 300 Hz. When the tip was brought in contact with the sample, the phase lag jumped to 180° as a direct consequence of the contact. After nulling this phase jump, the phase lag recorded on a hard surface was indeed larger than that recorded with the tip being suspended in air, and the phase lag increased from 2° to 10° in the frequency range from 5 to 300 Hz.

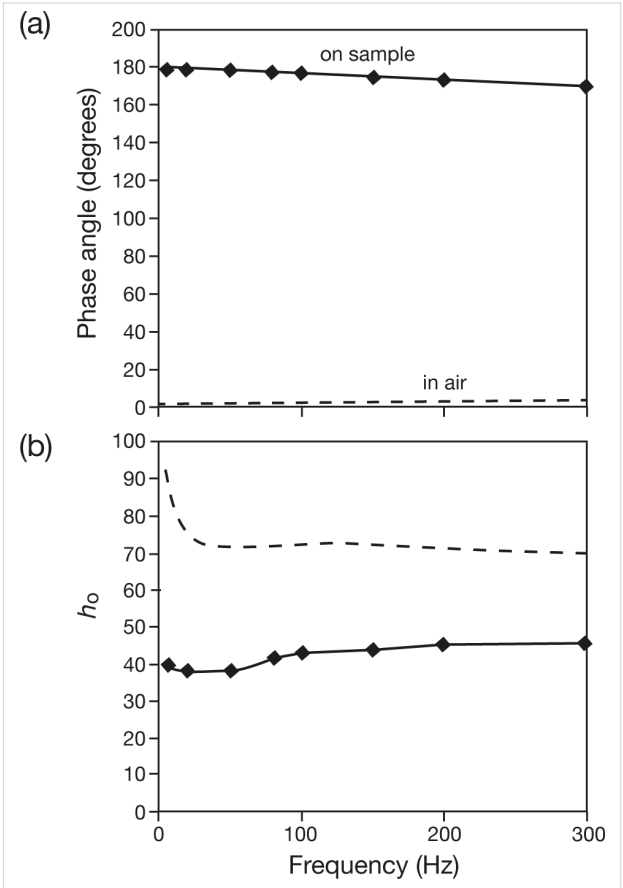

Figure 8: AFM tip modulation: (a) Phase shift and (b) amplitude in air (dashed line) and on sample (solid line).

Variations in the loss modulus and in tan δ with the modulation frequency were obtained from the AFM results for iPP according to Equation 12. The results are displayed in Figure 9. Increases of both the loss modulus and the loss tangent are observed. The comparison of both absolute values obtained in dynamic INI vs AFM and the change of E″ and tan δ with the frequency are favorable. The differences will be discussed below.

Creep measurements

Creep tests were performed on 1-mm thick polymethyl methacrylate (PMMA, M_w = 350,000) films. The tests were

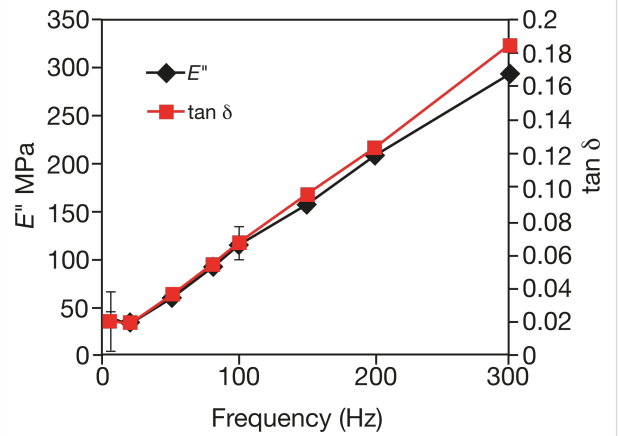

Figure 9: Dynamic AFM measurements of iPP as a function of the frequency. The measurements were made at a depth h = 50 nm by using a probe with a spring constant k = 33 N/m and a nominal tip radius of 50 nm. The oscillation amplitude was maintained at 10 nm.

performed by using an AFM (NTEGRA, NT-MDT). The AFM probe was indented to an initial depth of 50 nm into the surface, then held at a constant load while monitoring the change in the z-sensor over a creep time of 10 s. The sensitivity of the detector was previously calibrated to compute the deformation variation with time $h(t)$. During the creep test, the contact area between the tip and the sample increases with the displacement of the probe into the sample. The contact area is estimated as an approximately conical shape for depths of 25 nm and beyond, by using the manufacturer value for the half-angle of the tip.

The resulting curves were fit to Equation 13 to obtain E_∞, the storage modulus at steady state conditions, as well as viscosity η_i and modulus E_i at characteristic times τ_i. The latter is calculated from the relationship $\tau_i = \eta_i/E_i$. Single, double, and triple exponential fits were attempted: the triple exponential fit was not significantly better than the double exponential fit. The following values are obtained: Asymptotic storage modulus, E_∞ = 6.25 GPa; E_1 = 1.53 GPa, η_1 = 42 MPa·s, τ_1 = 0.027 s; E_2 = 2.08 GPa, η_2 = 71 MPa·s, τ_2 = 1.01 s.

As a comparison, the dynamic nanoindentation of PMMA gives E' = 3.89 GPa and E'' = 0.537 GPa at 45 Hz and E’ = 3.4 GPa and E” = 0.33 GPa at 1 Hz. A recent study about the elastic and viscoelastic properties of PLLA/HA films that also used a biexponential fit found relaxation times of this order [116]. When the creep time is increased, plastic yielding occurs as seen in Figure 10. The graph deviates from the asymptotical behavior and E_∞ increases (i.e., for t = 100 s, E_∞ = 7.2 GPa).

Discussion

The brief summary of the experimental analyses highlights the different factors that can influence the final results. The correlation between INI and AFM results should include a discussion of the dynamic testing protocol, surface effects, and calibration issues. In the following section, the data presented above will serve as a support for the comparison of the techniques, in terms of protocol and source of errors.

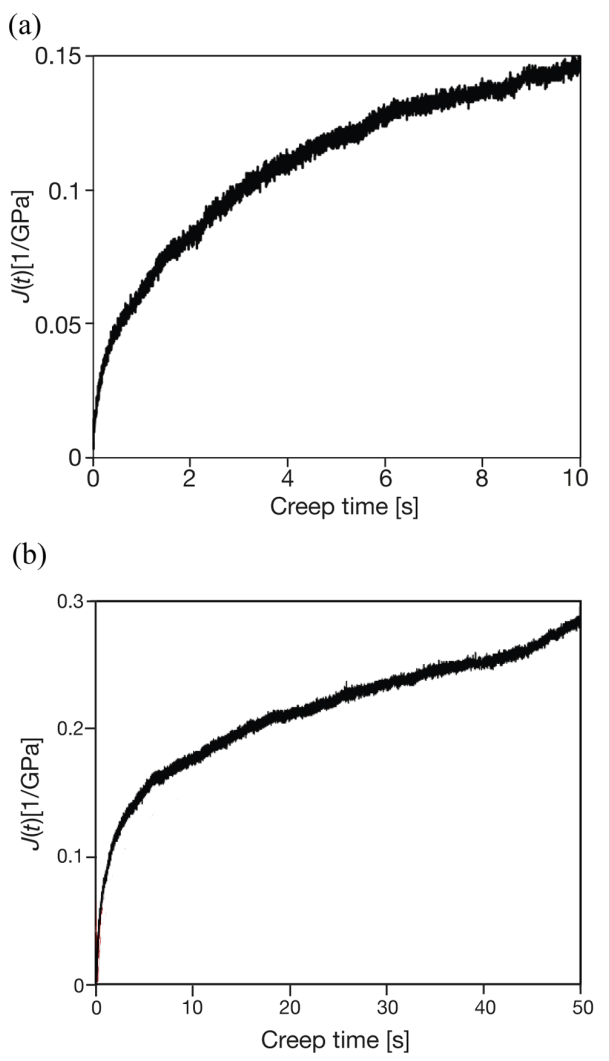

Figure 10: AFM probe creep test showing the creep compliance calculated using Equation 11 for PMMA. (a) A 10 second creep test. (b) Longer time showing effect of plastic yield (see text), in deviation of curve at long times.

Evaluation of the methods

Instrument calibration

In INI a calibrated force is applied along the surface normal. The load is controlled by electromagnetic or electrostatic actuators, the displacement is measured independently and the indenter head is supported by springs, in our case with a vertical stiffness of approximately 100 $N \cdot m^{-1}$ and a lateral stiffness of 10000 $N \cdot m^{-1}$ [64]. This strong asymmetry in compliance confines the motion to the surface normal in accordance with

the Voigt model applied here. A key issue in dynamic nanoindentation is to successfully evaluate the instrumental contribution to the measured stiffness and damping. As previously noted, the frequency response of the instrument is controlled by the magnitude of the moving mass, the stiffness of the support springs and the damping of the head. Here INI has some advantages over AFM, for instance the widely used capacitive or electrostatic sensing of the indenter motion is stable over time and thus accurate for low frequencies, which allows for an access to frequencies usually used in rheological studies (0.1–1000 Hz).

Contrary to INI, among the various studies made on dynamic AFM, there is no consensus for quantifying the instrumental damping so that a number of different calibration methods exist. Most literature reports make use of a rigid substrate, such as sapphire or a silicon wafer as a reference sample. Since the substrate displays a purely elastic response, any phase shift observed can then be attributed to the instrument damping. As noted in [102], the use of a rigid sample is not accurate for materials that display small phase lags on the same order of that of the reference sample.

The modulation source

In the classical dynamic test at the macroscale the phase lag is measured from the strain response to a sinusoidal tensile/flexural stress. In contrast the phase lag in nanoindentation is controlled by the displacement response of the indenter to sinusoidal loading. The combined response of the instrument and the sample is described in the case of dynamic INI by two springs in parallel. The parallel model describes a configuration, in which equal forces are applied on both sample and indenter tip. This is in line with AFM, where a displacement, rather than a force is applied, typically at the base of the cantilever so the two springs (sample and instrument) are in series. The fact that the force is not restricted to the surface normal in AFM has been discussed above and also widely in the literature [63,64,117]. Lateral forces can arise because of the angle between the cantilever and the sample owing to the instrumental configuration. But this can be compensated for by controlling the angular path of the loading curve [118].

Even with such a correction the cantilever may twist during the indentation, especially at the start of the indentation, because of a torque arising from the imperfect vertical loading of the tip owing to the sample roughness, and the alignment of sample or tip. This can lead to either a flexural or a torsional force. The former will be detected in an optical-lever-based AFM system as normal force. The latter may, or may not, influence the detected normal force signal depending on the extent of cross-talk, but it will certainly influence the overall force balance. The torsional force could be significant in magnitude, considering the much larger magnitude of the torsional spring constant, which for a rectangular cantilever is related to the normal spring constant with a proportionality constant of [cantilever length/tip height]^2. For typical Si single crystal micromachined cantilevers this factor ranges between 30–1000 [44]. Edwards et al. developed a correction factor for both rectangular and v-shaped cantilevers, which encompasses the tilt and the torque of the cantilever and extracts the pure normal force [119]. The correction also accounts for different tip geometries.

Surface effect-surface detection

The ability of these nanoscale techniques to probe the outer few nm of the surface presents an opportunity and a challenge: Firstly, a proper location on the surface requires great precision. The pitfalls in improper surface detection have been highlighted by Deuschle et al. [120]. In that work, the detection of the surface by triggering on a rise in the force above a noise threshold was compared to changes in contact stiffness that were derived from the amplitude of the modulation, P_0/h_0. For a PDMS sample with a modulus of 1 MPa, the surface was "missed" by 580 nm when using the former method with a resulting error in the computation of the modulus of 400%, whereas for a dynamic approach the overshoot was only 30 nm and the error in modulus only 10%. Various extrapolation methods can be used to determine the contact point [41,121,122] and it may be done by fitting the approach curves to an appropriate model [34,123]. Surface effects dictate the mechanical response in many nanoscale problems. Furthermore, surface properties can be quite different than those of the bulk. On the other hand, limiting the analyses to only a few nm presents a few more problems – firstly, discrete atomic/molecular events may be important, and the models that are used in general and are covered in this review are all continuum models. Secondly, getting knowledge of the contact geometry is much more difficult at this scale: Presumptions of a smooth surface and a geometrically ideal axiosymmetric indenter do not hold. In addition, the effects already discussed, which involve the influence of adhesion, etc., become dominant at this scale. For example, one dynamic study on an epoxy surface found that it was necessary to penetrate the surface by 130 nm in order to overcome the surface roughness and get representative results [124]. Monitoring the convergence of the CSM values with depth as shown in Figure 5 helps to estimate the depth at which surface geometric effects are overcome. Recently, accurate measurements of the modulus for several polymers at depths of only several nanometers was shown to be possible by properly accounting for adhesion, carefully characterizing the tip shapes, and limiting the maximum stress [125]. Surface effects also influence the models chosen, both because the linear elastic regime is exceeded at relatively small loads and depths, and

because the tip geometry is hard to track over the different size scales. Sometimes, this depth cannot be controlled, for instance when the adhesive force is large (see Figure 1) and even at zero external loading force the depth can be significant.

Sources of error and internal calibration

Internal calibration and errors are perhaps the most critical aspect of nanoindentation. Here too, there is a divergence between the emphasis in AFM and in INI.

Spring stiffness and instrument compliance

For INI the force is applied directly to the tip through a calibrated transducer: This force is the same as that on the sample. Thus, over a wide range of sample moduli, the stiffness of the spring is independent of the stiffness of the studied material. In contrast, AFM is controlled by displacement. The total displacement is split into cantilever bending and deformation, so that the ultimate force that can be applied on the sample is dependent on the cantilever spring stiffness [126]. The choice of a particular cantilever fixes the spring constant and hence ultimate deformation of the sample. If the deformation is too small, there will be sensitivity problems, and if it is too large, the assumptions on contact area, deformation mode, and even linear elasticity may be violated. In general, one cantilever probe can test a limited (approximately 2 orders of magnitude) span of elastic moduli. A useful rule of thumb for choosing an appropriate spring may be estimated from the contact stiffness for a Hertzian contact $S = 2aE^*$ [20].

There are a number of ways to calibrate the cantilever spring constant, covered in a review by Sader [127], and even careful calibration will generally result in a relative uncertainty on the order of 10%. The forces in INI are generally factory calibrated, although most manufacturers provide for some on-site calibration. Standard procedures for good working practice strongly recommend 1% tolerance for both force and displacement [128]. Instrument compliance must also be included in the determination of the sample deformation. For polymers that have elastic moduli of a few GPa or less, the precise calibration of this value is not expected to contribute significantly to the results.

Contact area

A main shortcoming of nanoindentation is the inability to optically view the indentation area in real time, or directly upon load release as in microindentation. Rather, the contact area is calculated based on the knowledge of the accurate indenter geometry, which in turn yields the projected contact area at each depth. This is only possible for a well-defined tip. The INI community developed several methods to accurately estimate the shape of the tip. One method is based on an AFM scan of the tip, which gives the real geometry of the indenter [129]. But this requires removing the tip from the head for each such measurement. For small depths, as they are used in nanoindentation, the shape at the end of the tip is critical and this geometry can change significantly over the course of a day's work [130,131]. Some attempts have also been made to image the imprint of the indenter left in the sample by AFM scanning [57,129]. Another possibility is to use the INI indenter tip as a probe scanner to scan a sample with very sharp features as it is widely done for AFM tip radius calibration [132,133].

Blind reconstruction is attractive since it only requires the data obtained from the topographical scan that was performed during the routine course of the experiment [132]. However, this technique does not give the complete area function of the tip, rather only for those parts that come into contact with the sample during such a scan [134]. When deeper depths are accessed in the indentation cycle, the relevant data needed about the tip profile may not be available. For this reason, reference-based techniques have become attractive, in a fashion quite similar to that adapted in the O&P method for INI, in which a standard sample of known modulus is used to estimate the tip shape in AFM [134,135]. Recently, AFM tip areas were determined by first applying a large tip that could be characterized optically using INI, then using that value as a reference for determining the AFM tip size by Hertzian analysis [136]. The objective of tip-shape calibration is to estimate the cross-section area of the indenter tip as a function of the distance from the apex. Although most procedures make such tip calibration on one sample, calibrating the area function on two different materials (for instance, sapphire and fused quartz) further increases the accuracy of the area function [122].

In contrast to INI, AFM probes are consumables and often several tips may be used in the course of a measurement, so extensive calibrations are not practical. One should keep in mind that those calibrations still depend on the reliability of the internal calibration (deflection sensitivity, spring constant, validity of analytical model, topography). They also depend on the reliability of the analytical model used to back-calculate the tip area from a known modulus. In this context, it is worth noting that the determination of the loss factor, tan δ, does not require a determination of the area thus removing a major source of uncertainty [137].

Deflection sensitivity

The force applied to the cantilever results in a flexure, characterized by the deflection angle in an optical beam setup. The deflections must be kept within the linear response regime of both cantilever spring and optical system. This linear response is calibrated by pressing the tip on a non-deforming surface.

Although simple to perform, care is required to obtain a meaningful result: The displacement calibration can vary with the tip velocity [138] and the alignment of the cantilever. The calibration is also prone to artifacts, such as those due to friction at the tip–surface contact that can introduce systematic errors to the value [139].

Conclusion

This review has outlined the considerations which should be made in the nanomechanical testing of viscoelastic materials by using point probes. It should be clear from the reading that there are still many loose ends to tie up in order to discover the best way to make such measurements. However, both the INI and AFM techniques have the means and technology in place to push the field forward. Great strides have been made in ensuring the reliability and usefulness of the data. The advances, both on the technical and the conceptual level, thus work in unison to forge new levels of understanding of viscoelastic processes at the nanoscale.

References

1. Ashkin, A.; Dziedzic, J. M.; Bjorkholm, J. E.; Chu, S. *Opt. Lett.* **1986,** *11,* 288–290. doi:10.1364/OL.11.000288
2. Tabor, D.; Winterton, R. H. S. *Proc. R. Soc. London, Ser. A* **1969,** *312,* 435–450. doi:10.1098/rspa.1969.0169
3. Israelachvili, J. N.; Tabor, D. *Proc. R. Soc. London, Ser. A* **1972,** *331,* 19–38. doi:10.1098/rspa.1972.0162
4. Xie, H.; Onal, C.; Régnier, S.; Sitti, M. In *Atomic Force Microscopy Based Nanorobotics;* Siddlano, B.; Khatib, O., Eds.; Springer-Verlag: Berlin, Heidelberg, 2012; pp 87–143. doi:10.1007/978-3-642-20329-9
5. Zhou, J.; Komvopoulos, K. *J. Appl. Phys.* **2006,** *100,* 114329. doi:10.1063/1.2398797
6. Boussinesq, J. *Applications des Potentiels a l'etude de equilibre et du mouvement des solides elastiques;* Gauthier-Villars: Paris, 1885.
7. Hertz, H. *J. Reine Angew. Math.* **1882,** *92,* 156–171. doi:10.1515/crll.1882.92.156
8. Sneddon, I. N. *Int. J. Eng. Sci. (Oxford, U. K.)* **1965,** *3,* 47–57. doi:10.1016/0020-7225(65)90019-4
9. Johnson, K. L. *Contact Mechanics;* Cambridge Univ. Press: Cambridge, 1985. doi:10.1017/CBO9781139171731
10. Tabor, D. *J. Colloid Interface Sci.* **1977,** *58,* 2–13. doi:10.1016/0021-9797(77)90366-6
11. Derjaguin, B. V.; Muller, V. M.; Toporov, Yu. P. *J. Colloid Interface Sci.* **1975,** *53,* 314–325. doi:10.1016/0021-9797(75)90018-1
12. Johnson, K. L.; Kendall, K.; Roberts, A. D. *Proc. R. Soc. London, Ser. A* **1971,** *324,* 301–313. doi:10.1098/rspa.1971.0141
13. Barthel, E. *J. Colloid Interface Sci.* **1998,** *200,* 7–18. doi:10.1006/jcis.1997.5309
14. Maugis, D.; Barquins, M. *J. Phys. D* **1978,** *11,* 1989–2023. doi:10.1088/0022-3727/11/14/011
15. Schwarz, U. D. *J. Colloid Interface Sci.* **2003,** *261,* 99–106. doi:10.1016/S0021-9797(03)00049-3
16. Bulychev, S. I.; Alekhin, V. P.; Shorshorov, M. K.; Ternovskii, A. P.; Shnyrev, G. D. *Zavod. Lab.* **1975,** *41,* 1137–1140.
17. Ternovskii, A. P.; Alekhin, V. P.; Shorshorov, M. K.; Khrushchov, M. M.; Skvortsov, V. N. *Zavod. Lab.* **1974,** *39,* 1242–1247.
18. Loubet, J. L.; Georges, J. M.; Marchesini, O.; Meille, G. *J. Tribol.* **1984,** *106,* 43–48. doi:10.1115/1.3260865
19. Pethica, J. B.; Hutchings, R.; Oliver, W. C. *Philos. Mag. A* **1983,** *48,* 593–606. doi:10.1080/01418618308234914
20. Pethica, J. B.; Oliver, W. C. *Phys. Scr.* **1987,** *T19,* 61–66. doi:10.1088/0031-8949/1987/T19A/010
21. Binning, G.; Quate, C. F.; Gerber, C. *Phys. Rev. Lett.* **1986,** *56,* 930–933. doi:10.1103/PhysRevLett.56.930
22. Doerner, M. F.; Nix, W. D. *J. Mater. Res.* **1986,** *1,* 601–609. doi:10.1557/JMR.1986.0601
23. Oliver, W. C.; Pharr, G. M. *J. Mater. Res.* **1992,** *7,* 1564–1583. doi:10.1557/JMR.1992.1564
24. Oliver, W. C.; Pharr, G. M. *J. Mater. Res.* **2004,** *19,* 3–20. doi:10.1557/jmr.2004.19.1.3
25. Pharr, G. M.; Oliver, W. C.; Brotzen, F. R. *J. Mater. Res.* **1992,** *7,* 613–617. doi:10.1557/JMR.1992.0613
26. Miyake, K.; Fujisawa, S.; Korenaga, A.; Ishida, T.; Sasaki, S. *Jpn. J. Appl. Phys.* **2004,** *43,* 4602–4605. doi:10.1143/JJAP.43.4602
27. Beegan, D.; Chowdhury, S.; Laugier, M. T. *Surf. Coat. Technol.* **2005,** *192,* 57–63. doi:10.1016/j.surfcoat.2004.02.003
28. Poole, W. J.; Ashby, M. F.; Fleck, N. A. *Scr. Mater.* **1996,** *34,* 559–564. doi:10.1016/1359-6462(95)00524-2
29. Overney, R. M.; Leta, D. P.; Pictroski, C. F.; Rafailovich, M. H.; Liu, Y.; Quinn, J.; Sokolov, J.; Eisenberg, A.; Overney, G. *Phys. Rev. Lett.* **1996,** *76,* 1272–1275. doi:10.1103/PhysRevLett.76.1272
30. Vanlandingham, M. R.; McKnight, S. H.; Palmese, G. R.; Eduljee, R. F.; Gillespie, J. W., Jr.; McCulough, R. L. *J. Mater. Sci. Lett.* **1997,** *16,* 117–119. doi:10.1023/A:1018533708655
31. Asif, S. A.; Colton, R. J.; Wahl, K. J. Nanoscale Surface Mechanical Property Measurements: Force Modulation Techniques Applied to Nanoindentation. In *Interfacial Properties on the Submicron Scale;* Frommer, J.; Overney, R., Eds.; ACS Books, 2000.
32. Odegard, G. M.; Gates, T. S.; Herring, T. M. *Exp. Mech.* **2005,** *45,* 130–136. doi:10.1007/BF02428185
33. Greenwood, J. A.; Johnson, K. L. *J. Colloid Interface Sci.* **2006,** *296,* 284–291. doi:10.1016/j.jcis.2005.08.069
34. Han, L.; Frank, E. H.; Greene, J. J.; Lee, H.-Y.; Hung, H.-H. K.; Grodzinsky, A. J.; Ortiz, C. *Biophys. J.* **2011,** *100,* 1846–1854. doi:10.1016/j.bpj.2011.02.031
35. vanLandingham, M. R.; Chang, N.-K.; Drzal, P. L.; White, C. C.; Chang, S.-H. *J. Polym. Sci., Part B: Polym. Phys.* **2005,** *43,* 1794–1811. doi:10.1002/polb.20454
36. Gao, H.; Chiu, C.-H.; Lee, J. *Int. J. Solids Struct.* **1992,** *29,* 2471–2492. doi:10.1016/0020-7683(92)90004-D
37. Hay, J.; Crawford, B. *J. Mater. Res.* **2011,** *26,* 727–738. doi:10.1557/jmr.2011.8
38. Chen, X.; Vlassak, J. J. *J. Mater. Res.* **2001,** *16,* 2974–2982. doi:10.1557/JMR.2001.0408
39. Xu, H.; Pharr, G. M. *Scr. Mater.* **2006,** *55,* 315–318. doi:10.1016/j.scriptamat.2006.04.037
40. Ebenstein, D. M.; Wahl, K. J. *J. Colloid Interface Sci.* **2006,** *298,* 652–662. doi:10.1016/j.jcis.2005.12.062
41. Notbohm, J.; Poon, B.; Ravichandran, G. *J. Mater. Res.* **2011,** *27,* 229–237. doi:10.1557/jmr.2011.252
42. Cohen, S. R. *Heterog. Chem. Rev.* **1994,** *2,* 135–144.

43. Aimé, J. P.; Elkaakour, Z.; Gauthier, S.; Michel, D.; Bouhacina, T.; Curély, J. *Surf. Sci.* **1995,** *329,* 149–156. doi:10.1016/0039-6028(95)00122-0
44. Liu, Y.; Wu, T.; Evans, D. F. *Langmuir* **1994,** *10,* 2241–2245. doi:10.1021/la00019a035
45. Bhushan, B.; Koinkar, V. N. *Appl. Phys. Lett.* **1994,** *64,* 1653–1655. doi:10.1063/1.111949
46. Withers, J. R.; Aston, D. E. *Adv. Colloid Interface Sci.* **2006,** *120,* 57–67. doi:10.1016/j.cis.2006.03.002
47. Cohen, S. R.; Apter, N.; Jesse, S.; Kalinin, S.; Barlam, D.; Peretz, A. I.; Ziskind, D.; Wagner, H. D. *Isr. J. Chem.* **2008,** *48,* 65–72. doi:10.1560/IJC.48.2.65
48. Unertl, W. N. *J. Vac. Sci. Technol., A* **1999,** *17,* 1779–1786. doi:10.1116/1.581890
49. VanLandingham, M. R. *J. Res. Natl. Inst. Stand. Technol.* **2003,** *108,* 249–265. doi:10.6028/jres.108.024
50. VanLandingham, M. R.; Villarrubia, J. S.; Guthrie, W. F.; Meyers, G. F. *Macromol. Symp.* **2001,** *167,* 15–44. doi:10.1002/1521-3900(200103)167:1<15::AID-MASY15>3.0.CO;2-T
51. Butt, H.-J.; Cappella, B.; Kappl, M. *Surf. Sci. Rep.* **2005,** *59,* 1–152. doi:10.1016/j.surfrep.2005.08.003
52. Briscoe, B. J.; Fiori, L.; Pelillo, E. *J. Phys. D: Appl. Phys.* **1998,** *31,* 2395–2405. doi:10.1088/0022-3727/31/19/006
53. Feng, G.; Ngan, A. H. W. *J. Mater. Res.* **2002,** *17,* 660–668. doi:10.1557/JMR.2002.0094
54. Korobko, R.; Kim, S. K.; Kim, S.; Cohen, S. R.; Wachtel, E.; Lubomirsky, I. *Adv. Funct. Mater.* **2013,** in press. doi:10.1002/adfm.201301536
55. Moeller, G. *J. Polym. Sci., Part B: Polym. Phys.* **2009,** *47,* 1573–1587. doi:10.1002/polb.21758
56. Jakes, J. J.; Lakes, R. S.; Stone, D. S. *J. Mater. Res.* **2012,** *27,* 463–474. doi:10.1557/jmr.2011.363
57. Attard, P. *Phys. Rev. E* **2001,** *63,* 061604. doi:10.1103/PhysRevE.63.061604
58. Attard, P. *Langmuir* **2001,** *17,* 4322–4328. doi:10.1021/la010086p
59. Oyen, M. L.; Cook, R. F. *J. Mech. Behav. Biomed. Mater.* **2009,** *2,* 396–407. doi:10.1016/j.jmbbm.2008.10.002
60. Ferry, J. D. *Visoelastic properties of Polymers;* Wiley: NY, 1980.
61. Shaw, M. T.; MacKnight, W. J. *Introduction fo Polymer Viscoelasticity,* 3rd ed.; John Wiley & Sons: Hoboken, New Jersey, 2005. doi:10.1002/0471741833
62. Wahl, K. J.; Asif, S. A. S.; Greenwood, J. A.; Johnson, K. L. *J. Colloid Interface Sci.* **2006,** *296,* 178–188. doi:10.1016/j.jcis.2005.08.028
63. Burnham, N. A.; Gremaud, G.; Kulik, A. J.; Gallo, P.-J.; Oulevey, F. *J. Vac. Sci. Technol., B* **1996,** *14,* 1308–1312. doi:10.1116/1.589086
64. Herbert, E. G.; Oliver, W. C.; Pharr, G. M. *J. Phys. D: Appl. Phys.* **2008,** *41,* 074021–074029. doi:10.1088/0022-3727/41/7/074021
65. Vandamme, M.; Ulm, F.-J. *Int. J. Sol. Struct.* **2006,** *43,* 3142–3165. doi:10.1016/j.ijsolstr.2005.05.043
66. Sperling, L. H. *Introduction to Physical Polymer Science,* 4th ed.; Wiley, Hoboken: New Jersey, 2005; pp 362–414.
67. Chakravartula, A.; Komvopoulos, K. *Appl. Phys. Lett.* **2006,** *88,* 131901. doi:10.1063/1.2189156
68. Cappella, B.; Kaliappan, S. K.; Sturm, H. *Macromolecules* **2005,** *38,* 1874–1881. doi:10.1021/ma040135f
69. Loubet, J. L.; Oliver, W. C.; Lucas, B. N. *J. Mater. Res.* **2000,** *15,* 1195–1198. doi:10.1557/JMR.2000.0169
70. Williams, M. L.; Landel, R. F.; Ferry, J. D. *J. Am. Chem. Soc.* **1955,** *77,* 3701–3707. doi:10.1021/ja01619a008
71. Sakharova, N. A.; Fernandes, J. V.; Antunes, J. M.; Oliveira, M. C. *Int. J. Solids Struct.* **2009,** *46,* 1095–1104. doi:10.1016/j.ijsolstr.2008.10.032
72. Lucas, B. N.; Oliver, W. C.; Swindeman, J. E. In *Mater. Res. Soc. Symp. Proc.;* Moody, N. R.; Gerberich, W. W.; Burnham, N.; Baker, S. P., Eds.; San Francisco, 1998; Vol. 522, pp 3–14. doi:10.1557/PROC-522-3
73. Asif, S. A. S.; Wahl, K. J.; Colton, R. J. *Rev. Sci. Instrum.* **1999,** *70,* 2408–2413. doi:10.1063/1.1149769
74. Herbert, E. G.; Oliver, W. C.; Lumsdaine, A.; Pharr, G. M. *J. Mater. Res.* **2009,** *24,* 626–637. doi:10.1557/jmr.2009.0089
75. White, C. C.; VanLandingham, M. R.; Drzal, P. L.; Chang, N. K.; Chang, S.-H. *J. Polym. Sci., Part B: Polym. Phys.* **2005,** *43,* 1812–1824. doi:10.1002/polb.20455
76. Tranchida, D.; Kiflie, Z.; Acierno, S.; Piccarolo, S. *Meas. Sci. Technol.* **2009,** *20,* 095702. doi:10.1088/0957-0233/20/9/095702
77. Tsukruk, V. V.; Gorbunov, V. V.; Huang, Z.; Chizhik, S. A. *Polym. Int.* **2000,** *49,* 441–444. doi:10.1002/(SICI)1097-0126(200005)49:5<441::AID-PI240>3.3.CO;2-L
78. Huang, G.; Wang, B.; Lu, H. *Mech. Time-Depend. Mater.* **2004,** *8,* 345–364. doi:10.1007/s11043-004-0440-7
79. Yang, S.; Zhang, Y.-W.; Zeng, K. *J. Appl. Phys.* **2004,** *95,* 3655–3666. doi:10.1063/1.1651341
80. Sun, Y.; Walker, G. C. *Langmuir* **2005,** *21,* 8694–8702. doi:10.1021/la050448j
81. Gannepalli, A.; Yablon, D. G.; Tsou, A. H.; Proksch, R. *Nanotechnology* **2011,** *22,* 355705. doi:10.1088/0957-4484/22/35/355705
82. Garcia, R.; Herruzo, D. T. *Nat. Nanotechnol.* **2012,** *7,* 217–226. doi:10.1038/nnano.2012.38
83. Tirosh, E.; Benassi, E.; Pipolo, S.; Mayor, M.; Valášek, M.; Frydman, V.; Corni, S.; Cohen, S. R. *Beilstein J. Nanotechnol.* **2011,** *2,* 834–844. doi:10.3762/bjnano.2.93
84. Medalsy, I. D.; Müller, D. J. *ACS Nano* **2013,** *7,* 2642–2650. doi:10.1021/nn400015z
85. Gotsmann, B.; Seidel, C.; Anczykowski, B.; Fuchs, H. *Phys. Rev. B* **1999,** *60,* 11051–11061. doi:10.1103/PhysRevB.60.11051
86. Stark, M.; Stark, R. W.; Heckl, W. M.; Guckenberger, R. *Proc. Natl. Acad. Sci. U. S. A.* **2002,** *99,* 8473–8478. doi:10.1073/pnas.122040599
87. Rabe, U. Atomic Force Acoustic Microscopy. In *Applied Scanning Probe Methods Vol II;* Fuchs, H.; Bhushan, B., Eds.; Springer: Berlin, 2006; pp 37–90.
88. Sahin, O.; Magonov, S.; Su, C.; Quate, C. F.; Solgaard, O. *Nat. Nanotechnol.* **2007,** *2,* 507–514. doi:10.1038/nnano.2007.226
89. Guo, S.; Solares, S. D.; Mochalin, V.; Neitzel, I.; Gogotsi, Y.; Kalinin, S. V.; Jesse, S. *Small* **2012,** *8,* 1264–1269. doi:10.1002/smll.201101648
90. Jesse, S.; Kalinin, S. V.; Proksch, R.; Baddorf, A. P.; Rodriguez, B. J. *Nanotechnology* **2007,** *18,* 435503. doi:10.1088/0957-4484/18/43/435503
91. Welker, J.; Illek, E.; Giessibl, R. J. *Beilstein J. Nanotechnol.* **2012,** *3,* 238–248. doi:10.3762/bjnano.3.27
92. Cleveland, J. P.; Anczykowski, B.; Schmid, A. E.; Elings, V. B. *Appl. Phys. Lett.* **1998,** *72,* 2613–2615. doi:10.1063/1.121434
93. Scott, W. W.; Bhushan, B. *Ultramicroscopy* **2003,** *97,* 151–169. doi:10.1016/S0304-3991(03)00040-8
94. Garcia, R. *Amplitude Modulation Atomic Force Microscopy;* Wiley-VCH Verlag GmbH & Co. KgaA: Weinheim, Germany, 2010.

95. Friedenberg, M. C.; Mate, M. C. *Langmuir* **1996,** *12,* 6138–6142. doi:10.1021/la960331i
96. Garcia, R.; Gómez, C. J.; Martinez, N. F.; Patil, S.; Dietz, C.; Magerle, R. *Phys. Rev. Lett.* **2006,** *97,* 16103. doi:10.1103/PhysRevLett.97.016103
97. Eastman, T.; Zhu, D.-M. *Langmuir* **1996,** *12,* 2859–2862. doi:10.1021/la9504220
98. Xu, X.; Koslowski, M.; Raman, A. *J. Appl. Phys.* **2012,** *111,* 54303. doi:10.1063/1.3689815
99. Radmacher, M.; Tillmann, R. W.; Gaub, H. E. *Biophys. J.* **1993,** *64,* 735–742. doi:10.1016/S0006-3495(93)81433-4
100. Yang, N.; Wong, K. K. H.; de Bruyn, J. R.; Hutter, J. L. *Meas. Sci. Technol.* **2009,** *20,* 025703. doi:10.1088/0957-0233/20/2/025703
101. McGuiggan, P. M.; Yarusso, D. J. *J. Mater. Res.* **2004,** *19,* 387–395. doi:10.1557/jmr.2004.19.1.387
102. Minary-Jolanadan, M.; Yu, M. F. *Ultramicroscopy* **2008,** *108,* 821–825. doi:10.1016/j.ultramic.2008.01.005
103. Yuya, P. A.; Hurley, D. C.; Turner, J. A. *J. Appl. Phys.* **2008,** *104,* 074916. doi:10.1063/1.2996259
104. Mahaffy, R. E.; Park, S.; Gerde, E.; Käs, J.; Shih, C. K. *Biophys. J.* **2004,** *86,* 1777–1893. doi:10.1016/S0006-3495(04)74245-9
105. Smith, B. A.; Tolloczko, B.; Martin, J. G.; Grütter, P. *Biophys. J.* **2005,** *88,* 2994–3007. doi:10.1529/biophysj.104.046649
106. Lange, M.; van Vörden, D.; Möller, R. *Beilstein J. Nanotechnol.* **2012,** *3,* 207–212. doi:10.3762/bjnano.3.23
107. Choi, G. Y.; Kim, S.; Ulman, A. *Langmuir* **1997,** *13,* 6333–6338. doi:10.1021/la970525d
108. Kim, S.; Choi, G. Y.; Ulman, A.; Fleischer, C. *Langmuir* **1997,** *13,* 6850–6856. doi:10.1021/la970649q
109. Sun, Y.; Akhremitchev, B.; Walker, G. C. *Langmuir* **2004,** *20,* 5837–5845. doi:10.1021/la036461q
110. Gillies, G.; Prestidge, C. A.; Attard, P. *Langmuir* **2002,** *18,* 1674–1679. doi:10.1021/la011461g
111. Vakarelski, I. U.; Toritani, A.; Nakayama, M.; Higashitani, K. *Langmuir* **2001,** *17,* 4739–4745. doi:10.1021/la001588q
112. http://www.iso.org/iso/home/standards_development/list_of_iso_technical_committees/iso_technical_committee.htm?commid=53558.
113. Brun, C.; Delobelle, P.; Fromm, M.; Berger, F.; Chambaudet, A.; Jaffiol, F. *Mater. Sci. Eng., A* **2001,** *315,* 63–69. doi:10.1016/S0921-5093(01)01200-X
114. Ashby, M. F. *Acta Metall.* **1989,** *37,* 1273–1293. doi:10.1016/0001-6160(89)90158-2
115. Maivald, P.; Butt, H. J.; Gould, S. A. C.; Prater, C. B.; Drake, B.; Gurley, J. A.; Elings, V. B.; Hansma, P. K. *Nanotechnology* **1991,** *2,* 103–106. doi:10.1088/0957-4484/2/2/004
116. Üzüm, C.; Hellwig, J.; Madaboosi, N.; Volodkin, D.; von Klitzing, R. *Beilstein J. Nanotechnol.* **2012,** *3,* 778–788. doi:10.3762/bjnano.3.87
117. Braithwaite, G. J. C.; Luckhan, P. F. *J. Colloid Interface Sci.* **1999,** *218,* 97–111. doi:10.1006/jcis.1999.6298
118. Cannara, R. J.; Brukman, M. J.; Carpick, R. W. *Rev. Sci. Instrum.* **2005,** *76,* 053706. doi:10.1063/1.1896624
119. Edwards, S. A.; Ducker, W. A.; Sader, J. E. *J. Appl. Phys.* **2008,** *103,* 064513. doi:10.1063/1.2885734
120. Deuschle, J.; Enders, S.; Arzt, E. *J. Mater. Res.* **2007,** *22,* 3107–3119. doi:10.1557/JMR.2007.0394
121. Lin, D. C.; Dimitriadis, E. K.; Horkay, F. *J. Biomech. Eng.* **2007,** *129,* 430–440. doi:10.1115/1.2720924
122. Cabibbo, M.; Ricci, P.; Cecchini, R.; Chudoba, T.; Rymuza, Z.; Sullivan, J.; Dub, S.; Cohen, S. *Micron* **2012,** *43,* 215–222. doi:10.1016/j.micron.2011.07.016
123. Notbohm, J.; Poon, B.; Ravichandran, G. *J. Mater. Res.* **2012,** *27,* 229–237. doi:10.1557/jmr.2011.252
124. Zhang, Y.-R.; Bai, S.-L.; Yang, D.-Y.; Zhang, Z.; Kao-Walter, S. *J. Polym. Sci., Part B: Polym. Phys.* **2008,** *46,* 281–288. doi:10.1002/polb.21365
125. Dokukin, M. E.; Sokolov, I. *Macromolecules* **2012,** *45,* 4277–4288. doi:10.1021/ma202600b
126. Vanlandingham, M. R.; McKnight, S. H.; Palmese, G. R.; Elings, J. R.; Huang, X.; Bogetti, T. A.; Eduljee, R. F.; Gillespie, J. W., Jr. *J. Adhes.* **1997,** *64,* 31–59. doi:10.1080/00218469708010531
127. Sader, J. Calibration of Atomic Force Microscope Cantilevers. In *Encyclopedia of Surface and Colloid Science;* Hubbard, A. T., Ed.; Marcel Dekker: NY, 2002.
128. ISO-14557-2 Metallic materials — Instrumented indentation test for hardness and materials parameters —Part 2 Verification and calibration of testing machines, 2009.
129. Takagi, S. *J. Mater. Res.* **2012,** *27,* 294–301. doi:10.1557/jmr.2011.300
130. Chiu, Y. L.; Ngan, A. H. W. *Acta Mater.* **2002,** *50,* 1599–1611. doi:10.1016/S1359-6454(02)00025-3
131. Bull, S. J. *Z. Metallkd.* **2002,** *93,* 870–874.
132. Villarrubia, J. S. *J. Res. Natl. Inst. Stand. Technol.* **1997,** *102,* 425–454. doi:10.6028/jres.102.030
133. Markiewicz, P.; Cohen, S. R.; Efimov, A.; Ovchinnikov, D. V.; Bukharaev, A. A. *Probe Microsc.* **1999,** *1,* 355–364.
134. Clifford, C. A.; Seah, M. P. *Appl. Surf. Sci.* **2005,** *252,* 1915–1933. doi:10.1016/j.apsusc.2005.08.090
135. Young, T. J.; Monclus, M. A.; Burnett, T. L.; Broughton, W. R.; Ogin, S. L.; Smith, P. A. *Meas. Sci. Technol.* **2011,** *22,* 125703. doi:10.1088/0957-0233/22/12/125703
136. Griepentrog, M.; Krämer, G.; Capella, B. *Polym. Test.* **2013,** *32,* 455–460. doi:10.1016/j.polymertesting.2013.01.011
137. Hayes, S. A.; Goruppa, A. A.; Jones, F. R. *J. Mater. Res.* **2004,** *19,* 3298–3306. doi:10.1557/JMR.2004.0437
138. Rutland, M. W.; Tyrrell, J. W. G.; Attard, P. *J. Adhes. Sci. Technol.* **2004,** *18,* 1199–1215. doi:10.1163/1568561041581324
139. Pratt, J. R.; Shaw, G. A.; Kumanchik, L.; Burnham, N. A. *J. Appl. Phys.* **2010,** *107,* 44305. doi:10.1063/1.3284957

Beilstein Journal of Nanotechnology

Peak forces and lateral resolution in amplitude modulation force microscopy in liquid

Horacio V. Guzman and Ricardo Garcia*

Full Research Paper

Open Access

Address:
Instituto de Ciencia de Materiales de Madrid, CSIC, Sor Juan Ines de la Cruz 3, 28049 Madrid, Spain

Email:
Ricardo Garcia* - r.garcia@csic.es

* Corresponding author

Keywords:
force microscopy; lateral resolution; nanomechanics; peak force

Beilstein J. Nanotechnol. **2013,** *4,* 852–859.
doi:10.3762/bjnano.4.96

Received: 10 October 2013
Accepted: 20 November 2013
Published: 06 December 2013

This article is part of the Thematic Series "Advanced atomic force microscopy techniques II".

Guest Editors: T. Glatzel and T. Schimmel

Abstract

The peak forces exerted on soft and rigid samples by a force microscope have been modeled by performing numerical simulations of the tip motion in liquid. The forces are obtained by using two contact mechanics models, Hertz and Tatara. We present a comparison between the numerical simulations and three analytical models for a wide variety of probe and operational parameters. In general, the forces derived from analytical expressions are not in good quantitative agreement with the simulations when the Young modulus and the set-point amplitude are varied. The only exception is the parametrized approximation that matches the results given by Hertz contact mechanics for soft materials and small free amplitudes. We also study the elastic deformation of the sample as a function of the imaging conditions for materials with a Young modulus between 25 MPa and 2 GPa. High lateral resolution images are predicted by using both small free amplitudes (less than 2 nm for soft materials) and high set-point amplitudes.

Introduction

The high-resolution imaging of heterogeneous materials, in particular soft materials in liquid, by amplitude modulation atomic force microscopy (AM-AFM) is an active area of research in nanotechnology [1-11]. In AM-AFM, a sharp tip is attached at the end of a microcantilever that oscillates at or near its resonant frequency. When the tip is in close proximity to the sample, the amplitude and the phase shift of the oscillation change with the strength of the interaction force. The determination of the tip–sample interaction force is a major issue in dynamic AFM because the force gives access to the materials properties of the sample; nonetheless the force is not a direct observable. Therefore, several methods have been proposed to reconstruct the force in dynamic AFM [12-18]. However, the use of force inversion methods has not been generalized in AM-AFM because the accuracy of some of the above methods is still under study. On the other hand, numerical simulations

have been used to determine the maximum repulsive interaction forces, which are referred to as peak forces hereafter [19-23]. An analytical scaling law has been deduced to calculate the peak forces in air [21]. This method has been applied to determine the force on viral capsids in liquid [24]. However, the above expressions are often constrained to a specific interaction force model, such as Hertzian mechanics and thus their application range is somehow limited.

Numerical simulations have supported the development of AM-AFM by predicting several properties of the tip motion [25-27]. Those simulations provide the standards against which new experimental or analytical methods should be compared [28]. Recently, we have provided a broader numerical insight into the interaction forces in AM-AFM [19] by considering elastic, viscoelastic, electrostatic double layer and van der Waals interactions.

Here, we perform an extensive computational study of AM-AFM to obtain the peak forces of soft (50 MPa) and relatively rigid (2 GPa) materials for two different models of contact mechanics, namely Hertz [29] and Tatara [30-32]. We also provide a comparison between the numerical simulations and three analytical expressions [21,33,34]. The dependence of the peak force on a wide range of tip–microcantilever properties, operational parameters and mechanical properties of the sample is analyzed. The Young modulus (E_s) ranges from 25 MPa to 2 GPa; the tip radius (R_t) is varied between 5 and 10 nm; the free amplitude (A_0) goes from 1 to 10 nm and the set-point amplitude (A_{sp}) is within the $0.65A_0$ to $0.95A_0$ range.

The numerical results are compared to three analytical models, the parametrized [21], the average [33] and the linear one [34]. The numerical simulations show significant differences from the results given by the analytical approximations, although the parametrized expression is in good agreement with the Hertzian mechanics. The average model follows the trend of the Tatara model for the peak forces when varying the set-point amplitude for soft samples. For soft materials, the indentation of the tip could be higher than A_{sp}. Thus the tip and the sample are in permanent contact during the whole oscillation cycle. In fact, the ability of exerting small forces and imaging materials in a non-invasive manner can be jeopardized because of the effect of a static deflection component when A_{sp}/A_0 decreases. We have also studied the relationship among peak forces, lateral resolution and sample properties for soft (50 MPa) and rigid (2 GPa) samples. We deduce a rule to image soft materials with a lateral resolution below 3 nm that involves the application of forces in the sub-100 pN regime, the use of cantilevers with force constants below 0.1 N/m, free amplitudes below 2 nm and relative sharp tips ($R_t \leq 5$nm). AM-AFM operation at relatively high amplitudes can also lead to tip blunting [35,36]. The estimation of the peak force prior to performing the experiment could prevent tip damage.

Results and Discussion

Tip motion and contact time for soft and relatively rigid materials

In AM-AFM the equation of motion for the microcantilever–tip system is approximated by using the point-mass model [25],

$$m\ddot{z}(t) = -kz(t) - \frac{m\omega_0}{Q}\dot{z}(t) + F_{ts}(d) + F_0\cos\omega t \qquad (1)$$

where m is the effective cantilever mass that includes the added mass of the fluid, and ω_0, Q, k and F_{ts} are, respectively, angular resonant frequency, quality factor, spring constant and tip–sample interaction force. The point-mass model is suitable if the contribution of higher modes to the cantilever motion is negligible [37]. This could be the case in liquid for small free amplitudes, say below 1.5 nm [38]. At higher amplitudes, the tip–surface force generates higher harmonics components, which could lead to the momentary excitation of higher eigenmodes, in particular the second eigenmode [7]. To account for those effects we also describe the microcantilever–tip system by using an extended Euler–Bernoulli equation [39]. This model considers the cantilever as a continuous and uniform rectangular beam under the action of external forces,

$$\begin{aligned} &EI\frac{\partial}{\partial x^4}\left[w(x,t) + a_1\frac{\partial w(x,t)}{\partial t}\right] + \rho bh\frac{\partial^2 w(x,t)}{\partial t^2} \\ &= -a_0\frac{\partial w(x,t)}{\partial t} + \delta(x-L)\left[F_0\cos\omega t + F_{ts}(d)\right] \end{aligned} \qquad (2)$$

where E is the Young modulus of the cantilever, I the area moment of inertia, a_1 the internal damping coefficient, ρ the mass density; b, h and L are, respectively, the width, height and length of the cantilever; a_0 is the hydrodynamic damping; $w(x,t)$ is the time dependent vertical displacement of the differential element of the beam placed at the x position, and F_{ts} tip–sample interaction force.

Equations 1 and 2 are numerically solved by using a fourth-order Runge–Kutta algorithm [40]. One should note that the use of Equations 1 and 2 in environments of low Q are valid for directly excited cantilevers, such as magnetic [41-43] or photothermal excitations [44,45]. The tip–sample interaction forces are modelled by using two different contact mechanics models, Hertz [29] and Tatara [30-32]. The widely used Hertz model gives the force as

$$F_{\text{Hertz}} = \frac{4}{3} E_{\text{eff}} \sqrt{R_{\text{t}}}\, \delta^{3/2} \tag{3}$$

The Tatara contact mechanics has two key differences with respect to Hertzian mechanics. First it includes the finite size of the sample and second it also considers that the sample deformation happens symmetrically at both the tip–sample and the sample–substrate interfaces. Thus the vertical and lateral displacements are part of the contact force computed with this model.

$$F_{\text{Tatara}} = \frac{n}{2^{3/2}} \delta^{3/2} + \frac{3n^2}{8n_{\text{c}}} \delta^2 + \frac{15n^3}{2^{11/2} n_{\text{c}}^2} \delta^{5/2} \tag{4}$$

where

$$\frac{1}{E_{\text{eff}}} = \frac{1-\nu_{\text{t}}^2}{E_{\text{t}}} + \frac{1-\nu_{\text{s}}^2}{E_{\text{s}}} \tag{5}$$

$$n = \frac{4}{3} \sqrt{R_{\text{eff}}}\, E_{\text{eff}} \tag{6}$$

$$n_{\text{c}} = \frac{4\pi E_{\text{t}} R_{\text{t}} E_{\text{s}} R_{\text{s}}}{6 + \nu_{\text{t}} - 2\nu_{\text{t}}^2 + \nu_{\text{s}} - 2\nu_{\text{s}}^2} \tag{7}$$

$$\frac{1}{R_{\text{eff}}} = \frac{1}{R_{\text{t}}} + \frac{1}{R_{\text{s}}} \tag{8}$$

The subindexes “t” and “s” stand, respectively, for tip and sample. In the above equations, δ is the indentation depth, ν is the Poisson coefficient (ν_{t} = 0.3 and ν_{s} = 0.4) and E the Young modulus with E_{t} = 170 GPa. Each contact mechanics model is particularly suited for some types of deformations or strains. Hertz contact mechanics is used to deal with small deformations at the region of contact between tip and sample. Large deformations and finite object sizes are not well described by Hertz contact mechanics [32]. As a consequence, the Tatara model allows a maximum vertical deformation equal to R_{eff} and is particularly suited to describe large deformations (with respect to the original size) of relatively soft matter, in which a vertical force generates both vertical and lateral deformations. To apply contact mechanics models in conditions that do not meet the model assumptions will lead to unadequate numerical estimations.

We have not found significant differences in the calculation of peak forces by using the point-mass model and the continuous beam for free amplitudes below 2 nm. For that reason, the data for A_0 = 1 nm has been obtained with the point-mass model while for A_0 = 10 nm we have used the extended Euler–Bernoulli model.

Figure 1 shows one period of the tip oscillation and the corresponding force. The peak force is defined as the maximum force point in the dashed line curves. The curves show a purely repulsive interaction, which starts as soon as the mechanical contact is established. The tip–sample interface according to Tatara (Figure 1a) or Hertz (Figure 1b) is also shown. Both contact mechancis models have been applied to describe the response of soft (50 MPa) and relatively rigid (2 GPa) surfaces. Figure S1 of Supporting Information File 1 shows the instantaneous force for a variable set-point amplitude.

Simulated and analytical peak forces values: Dependence on the Young modulus and the set-point amplitude

Hu and Raman [21], Kowalewski and Legleiter [34] and Rodriguez and Garcia [33] have derived some analytical scaling laws to determine the interaction forces in AM-AFM. Hu and

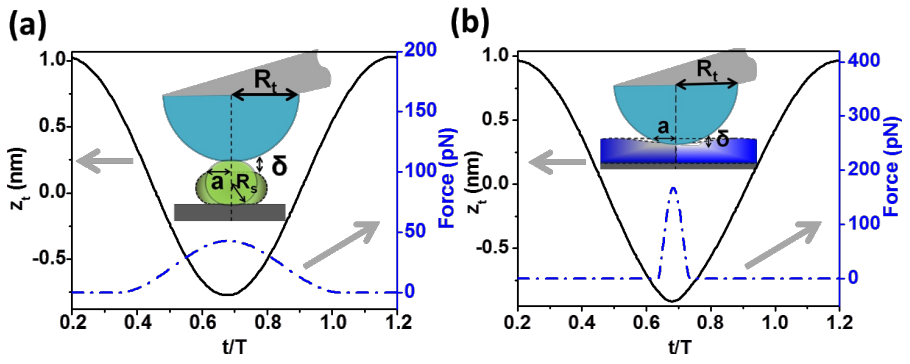

Figure 1: Peak forces, tip motion and contact time for two materials. (a) Soft sample (E_{s} = 50 MPa) simulated with the Tatara interaction force (Equation 4). (b) Rigid sample (E_{s} = 2 GPa) simulated with the Hertz interaction force (Equation 3). Simulation inputs: k = 0.1 N/m, f_0 = 25 kHz, Q = 2, A_0 = 1 nm, R_{t} = 5 nm, R_{s} = 4 nm and A_{sp} = 0.9 A_0.

Raman parametrized the peak force (repulsive) by using a nonlinear asymptotic theory [46] and Hertz contact mechanics,

$$F_{\text{par}} = 2^{1/8}\left(\frac{\pi^3}{3}\right)^{1/4}\left[\frac{k^3}{Q^3}E_{\text{eff}}\sqrt{R_{\text{t}}}\right]^{1/4}\left(A_{\text{sp}}A_0^2 - A_{\text{sp}}^3\right)^{3/8} \quad (9)$$

Rodriguez and Garcia, by using the virial-dissipation method [39,47,48], deduced the following expression for the mean value of the force during an oscillation,

$$F_{\text{average}} = \frac{kA_0}{2Q}\left[1-\left(\frac{A_{\text{sp}}}{A_0}\right)^2\right]^{1/2} \quad (10)$$

In the absence of long-range attractive forces, the average force can provide an estimation of the peak force.

Kowalewski and Legleiter proposed an extension of the Hooke law to determine the force in AM-AFM [34]. In this expression the force depends linearly on the amplitude reduction,

$$F_{\text{linear}} = \frac{k\left(A_0 - A_{\text{sp}}\right)}{2Q} \quad (11)$$

Figure 2 shows a comparison between the analytical expressions in Equations 9–11 and the numerical results (Hertz and Tatara). The comparison covers a range of the Young modulus from 25 to 2000 MPa. Hu and Raman parametrized force matches the numerical results derived from the Hertz model in some conditions. The parametrized model overestimates the peak forces in the case of very soft materials with a maximum error of 11%. On the other hand, for stiffer materials the force is underestimated with a maximum deviation of 16%. Numerical simulations performed with the Tatara model give smaller peak force values than those obtained from the Hertz model [19,49]. This is because in Tatara contact mechanics the deformation happens at both the tip–sample and the sample–substrate interfaces. The linear and average expressions fail to capture the trend of the numerical simulations because those expressions have been exclusively deduced from the dynamic properties of the tip motion and do not consider any influence of the materials properties of the sample. Additional comparisons by varying the tip radius are presented in Figure S2 of Supporting Information File 1.

In Figure 3, the reduction of A_{sp} from $0.95A_0$ to $0.65A_0$ produces an increase of the peak force. This trend is reported by all the approximations and simulations. However, the linear approximation give values that are smaller by a factor of 5–100 compared with the numerical simulations. As a consequence, the linear approximation should not be used to estimate the peak force in AM-AFM. The average model gives values close to the Tatara model for soft materials (25–50 MPa). However, it fails to reproduce the data for stiffer surfaces. The average model gives the mean value of the forces, attractive and repulsive, acting on the tip during an oscillation period. Consequently, whenever the forces change significantly with the distance (stiff materials) this approximation will fail to give a good estimation of the peak force. The parametrized model gives a good numerical description of the peak forces derived from the Hertz model for relatively soft materials.

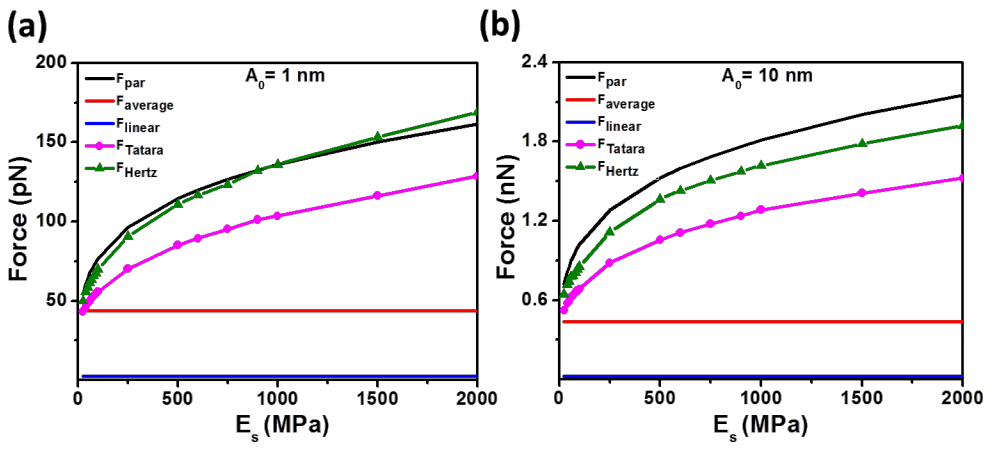

Figure 2: Peak force dependence on the Young modulus of the sample for different numerical simulations (Hertz and Tatara) and force analytical approximations (parametrized, average and linear). (a) A_0 = 1 nm, R_t = 5 nm and (b) A_0 = 10 nm, R_t = 5 nm. Other simulation inputs are: k = 0.1 N/m, f_0 = 25 kHz, Q = 2, R_s = 4 nm, and A_{sp} = 0.9 A_0.

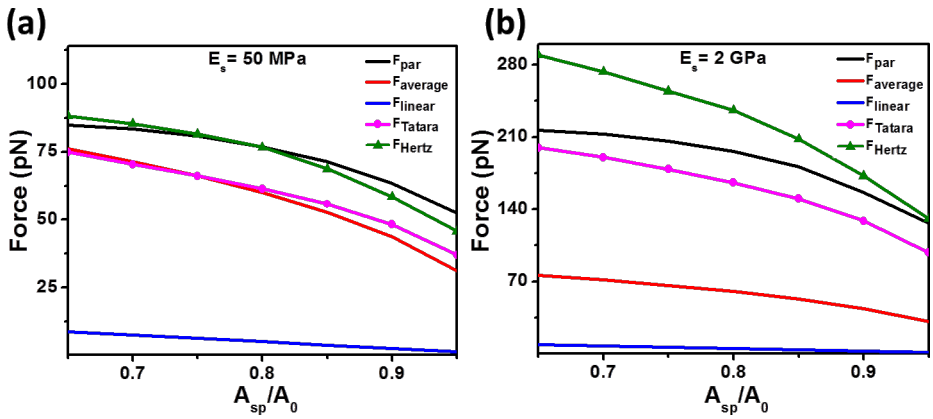

Figure 3: Dependence of the peak force on the set-point amplitude for different numerical simulations (Hertz and Tatara) and force analytical approximations (parametrized, average and linear). (a) A_0 = 1 nm and E_s = 50 MPa. (b) A_0 = 1 nm and E_s = 2 GPa. Simulation inputs are: k = 0.1 N/m, f_0 = 25 kHz, Q = 2, R_t = 5 nm, and R_s = 4 nm.

Sample deformation in terms of E_s, A_0, and R_t

The deformation (indentation) exerted by the tip can be considered as an indicator of the degree of invasiveness of the technique. The dependence of the indentation on the Young modulus for Hertz and Tatara models is shown in Figure 4. The indentation values are computed and normalized by the free amplitude for two values, 1 and 10 nm, and two tip radii, 5 and 10 nm, respectively. The two-colour curve separates the operational parameters in which the deformation is smaller than the set-point amplitude from those in which the deformation is larger. As expected, the indentation increases by decreasing the Young modulus of the sample. Remarkably, for soft materials (i.e., those with E_s < 100 MPa) the indentation values are close to or even larger than the set-point amplitude. This means that the tip and the sample are in permanent contact during the whole oscillation. This result was observed experimentally by Raman et al. [6] while imaging cells. Hertz contact mechanics gives smaller indentations than Tatara. In addition, these results underline the relevance of the contribution from the static deflection, which cannot be neglected in liquid while imaging soft materials [19]. However, the above effect decreases, for the same ratio A_{sp}/A_0, when increasing the free amplitude as shown in Figure 4b.

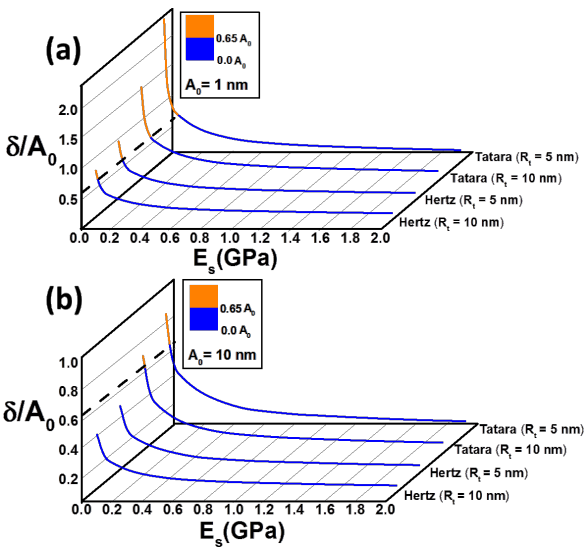

Figure 4: Normalized indentation as a function of the Young modulus of the sample for the Hertz and Tatara models. The indentation was normalized to the set-point amplitude: (a) A_0 = 1 nm and (b) A_0 = 10 nm. In the data above the dashed line indicates the point from which the whole oscillation is performed in contact to the material. Simulation inputs: k = 0.1 N/m, f_0 = 25 kHz, Q = 2, A_{sp} = 0.65A_0, R_s = 4 nm, and two different R_t of 5 and 10 nm, respectively.

Lateral resolution at small peak forces

Imaging at high-spatial resolution demands a compromise between probe, operational parameters and sample properties. Figure 5 shows the lateral resolution as given by Hertz and Tatara models for two materials, respectively, E_s = 50 MPa and 2 GPa. The lateral resolution is defined as the contact diameter between tip and sample. In Figure 5 we visualize the interplay between the free oscillation amplitude and set-point amplitude with the lateral resolution and peak forces. For a fixed A_{sp}/A_0 ratio the contact diameter increases with A_0, which reduces the lateral resolution. Lowering the A_{sp}/A_0 ratio down to the range between 0.65 and 0.95 also reduces the lateral resolution. In any situation the Tatara model gives a better lateral resolution than the Hertz model. This result can be traced back to the observation that, for the same operational conditions and probe values, the Tatara model gives smaller peak forces than the Hertz model. The lateral resolution also depends on the elastic response of the sample. As a general rule, the stiffer the sample

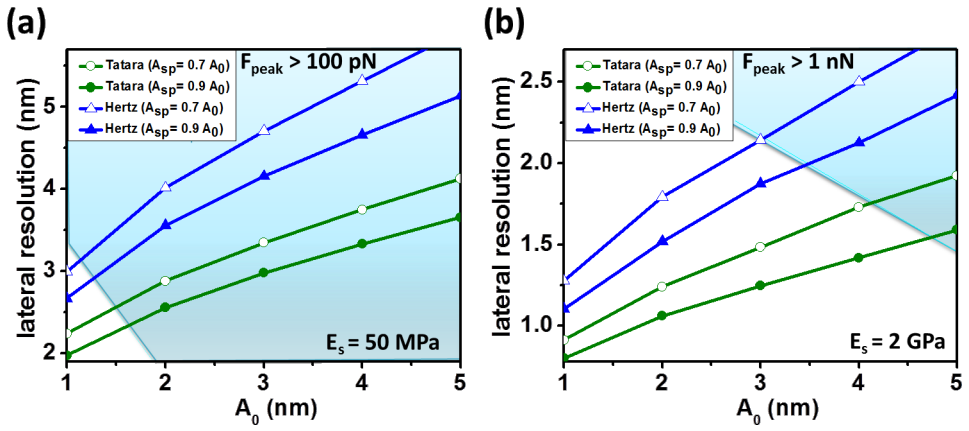

Figure 5: Lateral resolution maps for Hertz and Tatara contact mechanics. (a) E_s = 50 MPa. (b) E_s = 2 GPa. Filled symbols for $A_{sp} = 0.9A_0$; empty symbols for $A_{sp} = 0.7A_0$. Circles for Tatara and triangles for Hertz. Simulation inputs: k = 0.1 N/m, f_0 = 25 kHz, Q = 2, $A_{sp} = 0.65A_0$, R_t = 5 nm, R_s = 4 nm, and two different A_{sp} of 0.9 and $0.7A_0$, respectively.

the better the lateral resolution. Sub-nanometric resolution can be achieved by using small A_0 and maintaining a relatively high A_{sp}/A_0 ratio for soft materials and rigid materials. It has been reported that, in some special situations, also for low A_{sp}/A_0 ratios a high resolution can obtained experimentally [28,50]. We note that for soft materials (E_s = 50 MPa) and in the best case scenario (Tatara model) a lateral resolution below 1 nm could only be reached by using a free amplitude below 0.5 nm. We have separated the plots into regions, for soft materials (Figure 5a) a small sub-100 pN force value is used; while for rigid materials (Figure 5b) a sub-1 nN reference value is considered.

Conclusion

The numerical simulation of the tip motion in amplitude modulation AFM provides a comprehensive description of the factors that control the peak force and the lateral resolution in liquid. We have simulated the peak force for two contact mechanics models, Tatara and Hertz, and we have calculated three analytical approximations, linear, average and parametrized. The linear approximation fails to describe qualitatively and quantitatively the peak forces. The average model captures the peak force behaviour with the operational parameters but the quantitative agreement is poor. The parametrized model resembles the results given by Hertz for soft materials and small free amplitudes but its quantitative accuracy decreases by increasing the Young modulus. The results show that the discrepancy between the analytical and calculated values tends to decrease with smaller Young moduli and higher ratio A_{sp}/A_0. The spatial resolution depends on the operational parameters, the elastic response of the sample, the peak force, and the contact mechanics model. The conditions to achieve a high spatial resolution become more demanding for lower Young moduli of the samples. A high spatial resolution in liquid requires the use of rather small oscillation amplitudes. Sub-1 nm lateral resolutions for a soft material of a Young modulus of 50 MPa will require the use of a free amplitude of 0.5 nm or less. Lowering the free amplitude of the oscillation improves the lateral resolution in liquid. The resolution increases in line with the Young modulus of the sample, while keeping the operational parameters constant. The lateral resolution depends on the contact mechanics model used to characterize the sample deformation. In the Tatara model the sample is finite, consequently the stress is relaxed both vertically and laterally, which, for the same indentation, provides smaller forces and consequently a better resolution that the result given by Hertz model.

The results presented here provide a good estimation of the peak force values experienced by the samples observed with an AFM in liquid. However, the simulations have been performed without considering hydration layers or viscoelastic effects that arise either from the sample or the hydration layer. Those effects could modify the peak force values reported here, although we do not expect significant changes for the data acquired under the conditions for a high spatial resolution (sub-5 nm).

Supporting Information

Supporting Information File 1

Additional experimental details.
[http://www.beilstein-journals.org/bjnano/content/supplementary/2190-4286-4-96-S1.pdf]

Acknowledgements

This work was funded by the Ministerio de Economía y Competitividad (Consolider Force-For-Future, CSD2010-00024, MAT2009-08650) and European Union Seventh Framework Programme [FP7/2007-2013] under grant agreement no. 280772, project iONE-FP7 and the Cost Action TD1002.

References

1. Gan, Y. *Surf. Sci. Rep.* **2009,** *64,* 99–121. doi:10.1016/j.surfrep.2008.12.001
2. Uchihashi, T.; Iino, R.; Ando, T.; Noji, H. *Science* **2011,** *333,* 755–758. doi:10.1126/science.1205510
3. Garcia, R.; Magerle, R.; Perez, R. *Nat. Mater.* **2007,** *6,* 405–411. doi:10.1038/nmat1925
4. Voïtchovsky, K.; Kuna, J. J.; Contera, S. A.; Tosatti, E.; Stellacci, F. *Nat. Nanotechnol.* **2010,** *5,* 401–405. doi:10.1038/nnano.2010.67
5. Dong, M. D.; Husale, S.; Sahin, O. *Nat. Nanotechnol.* **2009,** *4,* 514–517. doi:10.1038/nnano.2009.156
6. Raman, A.; Trigueros, S.; Cartagena, A.; Stevenson, A. P. Z.; Susilo, M.; Nauman, E.; Contera, S. A. *Nat. Nanotechnol.* **2011,** *6,* 809–814. doi:10.1038/nnano.2011.186
7. Xu, X.; Melcher, J.; Basak, S.; Reifenberger, R.; Raman, A. *Phys. Rev. Lett.* **2009,** *102,* 060801. doi:10.1103/PhysRevLett.102.060801
8. Ando, T.; Uchihashi, T.; Fukuma, T. *Prog. Surf. Sci.* **2008,** *83,* 337–437. doi:10.1016/j.progsurf.2008.09.001
9. Martinez-Martin, D.; Herruzo, E. T.; Dietz, C.; Gomez-Herrero, J.; Garcia, R. *Phys. Rev. Lett.* **2011,** *106,* 198101. doi:10.1103/PhysRevLett.106.198101
10. Rico, F.; Su, C.; Scheuring, S. *Nano Lett.* **2011,** *11,* 3983–3986. doi:10.1021/nl202351t
11. Herruzo, E. T.; Asakawa, H.; Fukuma, T.; Garcia, R. *Nanoscale* **2013,** *5,* 2678–2685. doi:10.1039/c2nr33051b
12. Sader, J. E.; Uchihashi, T.; Higgins, M. J.; Farrell, A.; Nakayama, Y.; Jarvis, S. P. *Nanotechnology* **2005,** *16,* S94–S101. doi:10.1088/0957-4484/16/3/018
13. Legleiter, J.; Park, M.; Cusick, B.; Kowalewski, T. *Proc. Natl. Acad. Sci. U. S. A.* **2006,** *103,* 4813–4818. doi:10.1073/pnas.0505628103
14. Hölscher, H. *Appl. Phys. Lett.* **2006,** *89,* 123109. doi:10.1063/1.2355437
15. Lee, M.; Jhe, W. *Phys. Rev. Lett.* **2006,** *97,* 036104. doi:10.1103/PhysRevLett.97.036104
16. Hu, S.; Raman, A. *Nanotechnology* **2008,** *19,* 375704. doi:10.1088/0957-4484/19/37/375704
17. Katan, A. J.; van Es, M. H.; Oosterkamp, T. H. *Nanotechnology* **2009,** *20,* 165703. doi:10.1088/0957-4484/20/16/165703
18. Platz, D.; Forchheimer, D.; Tholén, E. A.; Haviland, D. B. *Nat. Commun.* **2013,** *4,* 1360. doi:10.1038/ncomms2365
19. Guzman, H. V.; Perrino, A. P.; Garcia, R. *ACS Nano* **2013,** *7,* 3198–3204. doi:10.1021/nn4012835
20. San Paulo, A.; Garcia, R. *Phys. Rev. B* **2002,** *66,* 041406. doi:10.1103/PhysRevB.66.041406
21. Hu, S.; Raman, A. *Appl. Phys. Lett.* **2007,** *91,* 123106. doi:10.1063/1.2783226
22. Xu, X.; Melcher, J.; Raman, A. *Phys. Rev. B* **2010,** *81,* 035407. doi:10.1103/PhysRevB.81.035407
23. Solares, S. D.; Chang, J.; Seog, J.; Kareem, A. U. *J. Appl. Phys.* **2011,** *110,* 094904. doi:10.1063/1.3657940
24. Xu, X.; Carrasco, C.; de Pablo, P. J.; Gomez-Herrero, J.; Raman, A. *Biophys. J.* **2008,** *95,* 2520–2528. doi:10.1529/biophysj.108.132829
25. Garcia, R.; San Paulo, A. *Phys. Rev. B* **1999,** *60,* 4961–4967. doi:10.1103/PhysRevB.60.4961
26. Rodriguez, T. R.; Garcia, R. *Appl. Phys. Lett.* **2004,** *84,* 449–451. doi:10.1063/1.1642273
27. Solares, S. D.; Chawla, G. *Meas. Sci. Technol.* **2010,** *21,* 125502. doi:10.1088/0957-0233/21/12/125502
28. Santos, S.; Barcons, V.; Christenson, H. K.; Billingsley, D. J.; Bonass, W. A.; Font, J.; Thomson, N. H. *Appl. Phys. Lett.* **2013,** *103,* 063702. doi:10.1063/1.4817906
29. Butt, H. J.; Kappl, M. *Surface and interfacial forces;* Wiley-VCH Verlag GmbH & Co. KGaA: Weinheim, 2010; pp 120–125.
30. Tatara, Y. *JSME Int. J., Ser. A* **1993,** *36,* 190–196.
31. Tatara, Y. *J. Eng. Mater. Technol.* **1989,** *111,* 163–168. doi:10.1115/1.3226449
32. Ikai, A.; Afrin, R.; Sekiguchi, H. *Curr. Nanosci.* **2007,** *3,* 17–29. doi:10.2174/157341307779940535
33. Rodriguez, T. R.; Garcia, R. *Appl. Phys. Lett.* **2003,** *82,* 4821. doi:10.1063/1.1584790
34. Kowalewski, T.; Legleiter, J. *J. Appl. Phys.* **2006,** *99,* 064903. doi:10.1063/1.2175473
35. Santos, S.; Guang, L.; Souier, T.; Gaderlab, K.; Chiesa, M.; Thomson, N. H. *Rev. Sci. Instrum.* **2012,** *83,* 043707. doi:10.1063/1.4704376
36. Vahdat, V.; Grierson, D. S.; Turner, K. T.; Carpick, R. W. *ACS Nano* **2013,** *7,* 3221–3235. doi:10.1021/nn305901n
37. Rodriguez, T. R.; Garcia, R. *Appl. Phys. Lett.* **2002,** *80,* 1646–1648. doi:10.1063/1.1456543
38. Voitchovsky, K. *Phys. Rev. E* **2013,** *88,* 022407. doi:10.1103/PhysRevE.88.022407
39. Lozano, J. R.; Garcia, R. *Phys. Rev. B* **2009,** *79,* 014110. doi:10.1103/PhysRevB.79.014110
40. Garcia, R. *Amplitude Modulation Atomic Force Microscopy;* Wiley-VCH: Weinheim, Germany, 2010. doi:10.1002/9783527632183
41. Florin, E.-L.; Radmacher, M.; Fleck, B.; Gaub, H. E. *Rev. Sci. Instrum.* **1994,** *65,* 639. doi:10.1063/1.1145130
42. O'Shea, S. J.; Welland, M. E.; Pethica, J. B. *Chem. Phys. Lett.* **1994,** *223,* 336–340. doi:10.1016/0009-2614(94)00458-7
43. Han, W.; Lindsay, S. M.; Jing, T. *Appl. Phys. Lett.* **1996,** *69,* 4111–4113. doi:10.1063/1.117835
44. Umeda, N.; Ishizaki, S.; Uwai, H. *J. Vac. Sci. Technol., B* **1991,** *9,* 1318. doi:10.1116/1.585187
45. Ramos, D.; Tamayo, J.; Mertens, J.; Calleja, M. *J. Appl. Phys.* **2006,** *99,* 124904. doi:10.1063/1.2205409
46. Sanders, J. A.; Verhulst, F. *Averaging Methods in Nonlinear Dynamical Systems;* Springer, 1985.
47. San Paulo, A.; Garcia, R. *Phys. Rev. B* **2001,** *64,* 193411. doi:10.1103/PhysRevB.64.193411
48. Lozano, J. R.; Garcia, R. *Phys. Rev. Lett.* **2008,** *100,* 076102. doi:10.1103/PhysRevLett.100.076102
49. Santos, S.; Verdaguer, A.; Chiesa, M. *J. Chem. Phys.* **2012,** *137,* 044201. doi:10.1063/1.4737516
50. Ebeling, D.; Solares, S. D. *Nanotechnology* **2013,** *24,* 135702. doi:10.1088/0957-4484/24/13/135702

Beilstein Journal of Nanotechnology

STM tip-assisted engineering of molecular nanostructures: PTCDA islands on Ge(001):H surfaces

Amir A. Ahmad Zebari, Marek Kolmer and Jakub S. Prauzner-Bechcicki*

Full Research Paper

Open Access

Address:
Research Centre for Nanometer-scale Science and Advanced Materials (NANOSAM), Institute of Physics, Jagiellonian University, Reymonta 4, 30-059 Krakow, Poland

Email:
Jakub S. Prauzner-Bechcicki* - jakub.prauzner-bechcicki@uj.edu.pl

* Corresponding author

Keywords:
molecular nanostructures; scanning tunneling microscopy; tip-induced processes

Beilstein J. Nanotechnol. **2013,** *4,* 927–932.
doi:10.3762/bjnano.4.104

Received: 10 October 2013
Accepted: 10 December 2013
Published: 18 December 2013

This article is part of the Thematic Series "Advanced atomic force microscopy techniques II".

Guest Editors: T. Glatzel and T. Schimmel

Abstract

Islands composed of perylene-3,4,9,10-tetracarboxylic dianhydride (PTCDA) molecules are grown on a hydrogen passivated Ge(001):H surface. The islands are studied with room temperature scanning tunneling microscopy and spectroscopy. The spontaneous and tip-induced formation of the top-most layer of the island is presented. Assistance of the scanning probe seems to be one of the factors that facilitate and speed the process of formation of the top-most layer.

Introduction

On-surface engineering of molecular nanostructures is one of the key elements for many forthcoming technologies. A wide range of possibilities is explored to search for an efficient, precise and cheap strategy for the fabrication of various organic nanostructures. Recently, there has been an increasing interest in the field of molecular self-assembly-based processes as a means of organic nanostructure formation [1-3]. As such, self-assembly allows for obtaining nanowires, two dimensional lattices, molecular islands, and molecular mono- and multilayers with a high yield. The resulting structures are often stable and almost perfect. The implementation of bottom-up self-assembly-based methods in an industrial process may require, however, the reshaping and tailoring of the structure with precise top-down methods to obtain the desired shape and properties. Scanning tip induced processes may serve as such a step to adjust the final form of the molecular nanostructure.

The design and formation of a molecular device is a key element of its successful operation. However, the desired properties of the device may be severely hampered by its environment, e.g., dangling bonds of a semiconducting substrate surface or electrical contact with a metallic substrate. There have been developed several strategies to minimize or even eliminate the influence of the underlying substrate on a molecular nanostructure on-top of it [4]. From an industrial perspective, a very promising approach is to cover the chosen substrate

by an additional ultra-thin buffer layer, i.e., either a few monolayers of an insulator (e.g., NaCl on metal surfaces [5-13] or KBr on InSb [14,15]) or even a single layer of an atomic or molecular species (e.g., passivation of Si or Ge surfaces [16-19]). Such an extremely thin interlayer not only electronically decouples on-top adsorbed molecular species, but additionally may dramatically enhance the mobility of the molecules and increase their chances to self-assemble and form molecular nanocrystals [9-11,20]. For the purpose of the present study it is very convenient to focus on the hydrogen passivation of Si and Ge surfaces. It has been shown in case of Si(001) [17], Si(111) [18] and Ge(001) [19] surfaces that such a passivating layer electronically decouples the molecule from the substrate and increases their mobility.

In this article, high-resolution scanning tunneling microscope (STM) measurements of self-assembled perylene-3,4,9,10-tetracarboxylic dianhydride (PTCDA) molecular islands on a hydrogen passivated germanium surface, Ge(001):H, are presented. The application of bias voltage pulses in STM allows for the modification of the islands. We found that the presence of a scanning tip of the tunneling microscope facilitates and speeds the formation of a new full top-layer of the island.

Results and Discussion

Due to the presence of a passivating hydrogen layer on the Ge(001) surface, molecule–substrate interactions are significantly weakened and molecules are extremely mobile. The imaging of a single molecule at room temperature is impossible. At the high coverage, however, the accumulation of the PTCDA molecules is dominated by molecule–molecule interactions and molecular islands are formed. The islands grow in the Volmer–Weber mode. The density of the islands is 2.5×10^9 cm^{-2} for coverage of 0.7 ML. Approximately 60% of the islands exhibit a strip-like hexagonal shape with two long edges and four short ones. It is noteworthy that molecular islands quite often extend in one direction over 100 nm and more, traversing several substrate terraces without any influence to their structure. It is possible to achieve high-resolution images on top of the islands in rt STM (see Figure 1a). These images show that the islands have crystalline character, and the top-most layer closely resembles the herringbone structure found for the (102) plane of PTCDA bulk crystal [21,22]. Similar arrangements have been reported for the Si(001):H/PTCDA system [20]. Most of the islands have a height of 2.1 nm, what corresponds to 6 molecular layers.

Insight into the electronic structure of the studied system is obtained by rt STS measurements (see Figure 1b). For a bare germanium surface a band gap of ≈0.2 eV is obtained, in fair agreement with literature data [23-25]. A hydrogen passivated

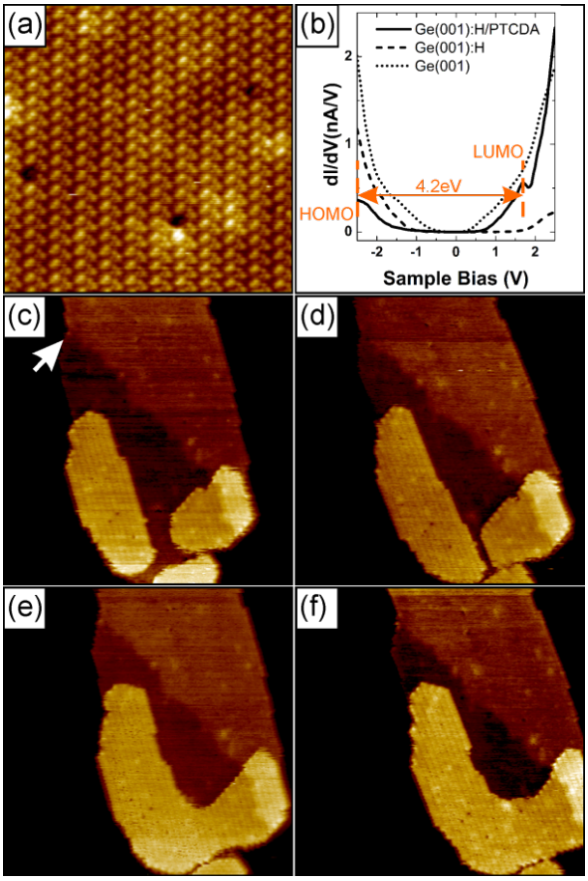

Figure 1: (a) High resolution STM image on top of a PTCDA island, 25 nm × 25 nm, showing the herringbone structure. (b) STS curves for Ge(001), Ge(001):H and PTCDA molecular island. (c)–(f) Four successive scans of the same area to illustrate the gradual growth of top layer, scan size 100 nm × 100 nm. White arrow marks the change in contrast on the island attributed to the underlying step-edge of the Ge(001):H substrate. For each STM image ((a) and (c)–(f)) the scanning parameters are I = 10 pA, U = +2 V.

surface exhibit a band gap of ≈0.85 eV, similarly to a recently reported value obtained from low temperature measurements [25]. The energy gap between the highest occupied molecular orbital (HOMO) and the lowest unoccupied molecular orbital (LUMO) of a PTCDA island on Ge(001):H is measured as 4.2 eV. The latter value corresponds well with results reported for thick films (>5 nm) [26-29]. The electronic properties of the PTCDA islands are very different from the underlying passivated germanium, and there are no other features in the bias window from −2.5 V to 1.7 V (corresponding to the semiconducting energy gap of PTCDA molecules) of the STS curves. This means that the electronic structure of PTCDA is unperturbed by the electronic properties of the underlying substrate.

Figure 1c–f show a set of four consecutive scans of the same area on top of the PTCDA island. The change of the contrast in

the middle of each of the scans (see white arrow in Figure 1c) originates from the step-edge of the underlying Ge(001):H surface. It may serve as a reference point for the observed evolution of the top-most layer. Every scan took 9 minutes (taking one image from the top to the bottom includes forward and backward scans). In the first scan from the set (Figure 1c) one can see that the starting structure of the top-most layer of the molecular island was composed of separate features, each of which has a height of one monolayer. On a subsequent scan (Figure 1d) one can observe a gradual growth of these features, eventually leading to their coalescence into one object (Figure 1e) that continues to gradually grow (Figure 1f). Typically, the morphology of PTCDA islands are stable during a STM/STS characterization. We assume that the presented evolution of the top-most molecular layer was probably unintentionally induced during a "cleaning" procedure of the scanning probe, i.e., by application of high voltage pulses.

To investigate the initiation of growth of the top-most layer of an island by well-defined conditions we applied a bias voltage pulse of 5 V for 25 ms in the middle of the island (Figure 2a). As a consequence we observed a hole at the position of the pulse, and ad-molecules gathered around (Figure 2b). Consecutive scans (Figure 2c–h) show a gradual growth of the top-most layer. In the course of time a new full top layer is formed with the pulse-made hole remaining unhealed. The speed of the growth of the top-most layer is approximately 124 nm^2/min.

The edges of the hole play the role of nucleation sites for the created layer. Energy barriers at the rim of the hole, i.e., Ehrlich–Schwoebel barriers, are too high to be crossed by diffusing molecules at rt, even in the presence of the field created by the scanning tip, and the molecules prefer to diffuse laterally within the same layer instead of moving downward to fill in the hole [30]. The height of the island changes by 0.35 nm, as can be inferred from a comparison of the cross-section profiles of the island before and after the top-most layer was formed (Figure 2i). The observed change in the height corresponds well to the distance between molecular planes in the [102] direction of the PTCDA bulk molecular crystal [20]. The edges of lower laying molecular sheets are a plausible source of molecules for the newly formed top-most layer. The edges observed on the scans are quite often fuzzy and change their shape during the manipulation (Figure 2). Moreover, after the adlayer formation the island considerably decreased its lateral dimension (Figure 2i).

In both discussed examples the island was continuously scanned during formation of the top-most layer. To shed some light on the role of the scanning tip in the process we performed a follow-up experiment. We applied a bias voltage pulse on top of an island (7 V, 25 ms). In Figure 3a we present the image of the island immediately after the pulse. Then, we retracted the tip for 10 minutes. After that time only a small increase in the size of the newly formed top-most layer was observed (Figure 3b). Thereafter, we retracted the tip again, this time for 20 minutes. Similarly, only a slight change in the size of the new adlayer was recorded (Figure 3c). We decided to retract the tip once more, for 30 minutes. And again, a minor change in the size was observed. In Figure 3d we present the image of the top-most layer of the island 130 minutes after the pulse. The total time elapsed from the pulse includes 60 min when tip was retracted and 70 min spent on scanning. From the inspection of the cross-section height profiles in Figure 3e it is clear that there was only a single-layer-height structure formed on the top of the island that did not exceed over the whole island. The overall

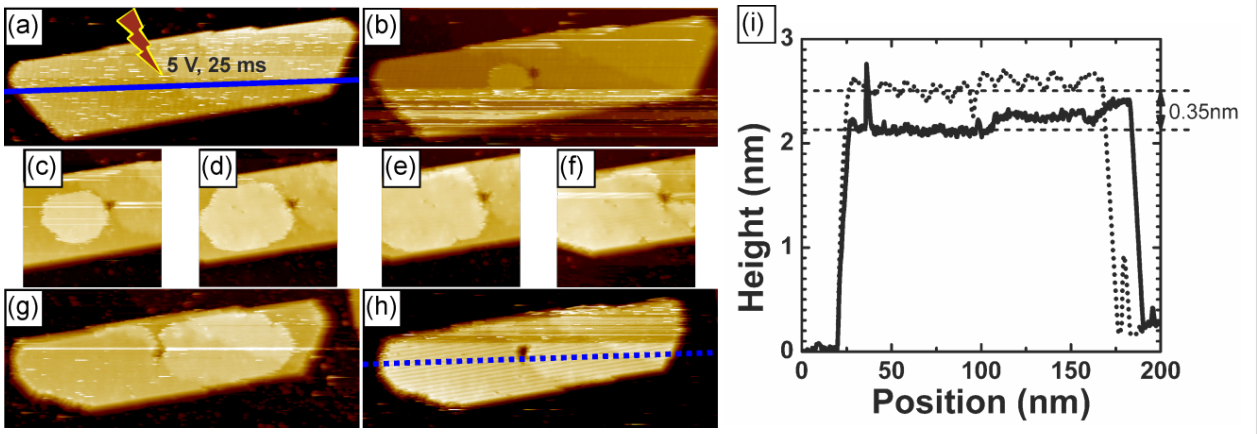

Figure 2: (a)–(h) A sequence of scans showing tip-initiated growth of the top-most layer of the PTCDA molecular island. Size of images:(a),(b),(g),(h) 70 nm × 180 nm, (c)–(f) 70 nm × 70 nm. Scanning parameters are I = 10 pA, U = +2 V. Blue solid and dotted lines mark positions at the cross-section height profiles. (i) The cross-section height profiles of the same island before and after the completion of the top-most layer indicated by solid and dotted lines (see (a) and (h) for position), respectively.

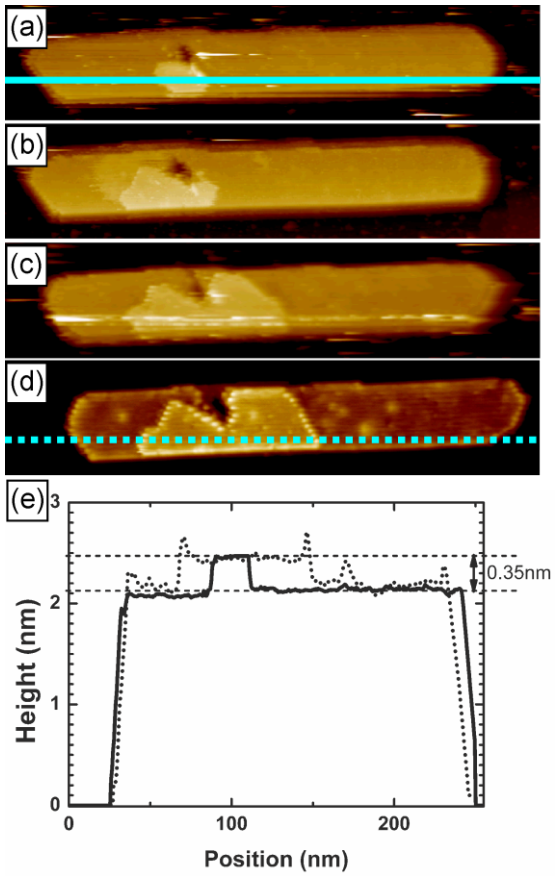

Figure 3: (a)–(d) A sequence of scans showing a partial growth of the top-most layer without continuous presence of the scanning tip. The light blue solid and dotted lines mark the positions of the cross-section height profiles. Scan size: 50 nm × 250 nm. Scanning parameters are I = 3 pA, U = +2 V. Scan (d) is taken 2 h later than scan (a). (e) The cross-section height profiles of the same island before and after the formation of the top-most layer indicated by solid and dotted lines (see (a) and (d) for positions), respectively.

average speed of growth of the observed structure in this case is approximately 13 nm^2/min.

Most probably, the three dimensional mesa-like shape of the PTCDA crystalline nanoislands grown on Ge(001):H surface results from an efficient ascending interlayer transport. The configuration of molecules in a layer is determined, to some extent, by strain in the layer. Roughly speaking, the less strained a layer is the more relaxed molecules are in it. Yet, the amount of stress encountered by the molecules in the layer depends on the distance from the island–substrate interface. Thus, the further away from the interface the layer is, the less strain it experiences [31]. Consequently, binding energies on the edges of lower lying layers are smaller than binding energies on the edges of higher lying layers. Therefore, molecules attached to the edges of lower lying layers prefer to ascend and attach to more favorable sites on higher laying layers. Due to the applied bias voltage pulses we created new edges on the top-most layer offering convenient adsorption sites with high binding energies. Thus, we expect that an ascending interlayer transport is responsible for the newly grown top-most layer. The presence of the scanning tip seems to enhance that kind of process. Most probably, the presence of the electric field generated by a biased STM probe efficiently decreases the corresponding energy barriers for an ascending interlayer molecular transport. Hence, a continuous scanning of the island after pulsing allows for formation of the top-most layer roughly one order of magnitude faster than has been observed for intermittent scanning (compare results presented in Figure 2 and Figure 3). We would like to stress that this result is of qualitative character only, as many different parameters (e.g., tip composition/geometry, current set-point, bias voltages, sample temperature, etc.) may play a role in setting the final growth rate.

It is rather expected that in our experiment the scanning probe is coated with molecular material. One could then argue that the direct deposition from the tip should also significantly contribute to the observed growth of the top-most layer. However, if such a mechanism was the main source of the material it would usually lead to unstable imaging conditions. On the contrary, we observe growth of the top-most layer without disturbances typically associated with scanning tip modifications. Additionally, the direct deposition from the tip would not necessarily result in changes in the lateral dimensions of the islands, which is seen in each of the analyzed events of the growth (see for example cross-section height profiles in Figures 2i and 3e).

Conclusion

We presented a rt STM/STS study of PTCDA crystalline nanoislands on a Ge(001):H surface. The high-resolution measurements revealed that the top-most layer has a structure closely resembling the herringbone structure found for the (102) plane of PTCDA bulk crystal. Spectroscopic data showed no influence of the substrate on the electronic properties of the islands. The crystalline nanostructures can be easily modified by the scanning probe, and the presence of the tip seems to be one of the factors that facilitate and speed formation of the top-most layer of the island. This feature may be a suitable supplementary step for self-assembly-based methods to fine-tune the final form of the molecular nanostructures of interest.

Experimental

The experiments were carried out in a multi-chamber ultra-high vacuum system equipped with variable temperature STM (Omicron GmbH). The base pressure in the system was in the low 10^{-10} mbar range, with the exception of the microscope chamber where the pressure was 4–5 × 10^{-11} mbar. Atomically

flat Ge(001) surfaces were prepared by a few cycles of simultaneous annealing of the samples at 780 °C (as measured by infrared pyrometer) and ion beam bombardment (1 keV Ar^+, at 45° off-normal) for 20 minutes. The ion current density was approximately 0.3 μA/cm^2. The samples were held to slowly cool down to room temperature at a rate of 0.1 A/min. To obtain a passivated surface the Ge(001) samples were exposed to hydrogen atoms provided by a homebuilt hydrogen cracker. The partial hydrogen pressure in the chamber was kept at 4–5 × 10^{-7} mbar for 2.5 hours, and the sample was kept at 200 °C. The PTCDA molecules were deposited with the use of a standard effusion cell (Kentax GmbH) at 310 °C on the sample, which was kept at room temperature. The molecular flux was controlled by a quartz-microbalance. STM measurements were carried out in constant current mode at room temperature (rt) by means of electrochemically etched tungsten tips as probes. Scanning tunneling spectroscopy (STS) measurements were carried out at rt. The STS data were averaged over 2500 curves taken from a grid covering a 10 × 10 nm^2 surface area. The differential tunneling conductance (dI/dV) as a function of the sample bias V was obtained numerically from the I–V curves.

Acknowledgements

The authors are grateful to Prof. M. Szymonski for his helpful advice and encouragement. The authors acknowledge helpful comments by S. Godlewski on the experimental procedures. This work was supported by a grant from Switzerland through the Swiss Contribution to the enlarged European Union (Joint Polish-Swiss Research Program) no PSPB-085/2010 "Molecular assemblies on semiconductors and insulating surfaces" (http://www.molsurf.eu).

References

1. Otero, R.; Gallego, J. M.; Vázquez de Parga, A. L.; Martin, N.; Miranda, R. *Adv. Mater.* **2011,** *23,* 5148–5176. doi:10.1002/adma.201102022
2. Palma, C.-A.; Cecchini, M.; Samori, P. *Chem. Soc. Rev.* **2012,** *41,* 3713–3730. doi:10.1039/c2cs15302e
3. Tait, S. L. *ACS Nano* **2008,** *2,* 617–621. doi:10.1021/nn800207w
4. Prauzner-Bechcicki, J. S.; Godlewski, S.; Szymonski, M. *Phys. Status Solidi A* **2012,** *209,* 603–613. doi:10.1002/pssa.201127623
5. Gross, L.; Moll, N.; Mohn, F.; Curioni, A.; Meyer, G.; Hanke, F.; Persson, M. *Phys. Rev. Lett.* **2011,** *107,* 086101. doi:10.1103/PhysRevLett.107.086101
6. Repp, J.; Meyer, G.; Stojković, S. M.; Gourdon, A.; Joachim, C. *Phys. Rev. Lett.* **2005,** *94,* 026803. doi:10.1103/PhysRevLett.94.026803
7. Liljeroth, P.; Repp, J.; Meyer, G. *Science* **2007,** *317,* 1203–1206. doi:10.1126/science.1144366
8. Abel, M.; Clair, S.; Ourdjini, O.; Mossoyan, M.; Porte, L. *J. Am. Chem. Soc.* **2011,** *133,* 1203–1205. doi:10.1021/ja108628r
9. Wang, Y.; Kröger, J.; Berndt, R.; Tang, H. *J. Am. Chem. Soc.* **2010,** *132,* 12546–12547. doi:10.1021/ja105110d
10. Bombis, C.; Kalashnyk, N.; Xu, W.; Lægsgaard, E.; Besenbacher, F.; Linderoth, T. R. *Small* **2009,** *5,* 2177–2182. doi:10.1002/smll.200900301
11. Rossel, F.; Pivetta, M.; Patthey, F.; Ćavar, E.; Seitsonen, A. P.; Schneider, W.-D. *Phys. Rev. B* **2011,** *84,* 075426. doi:10.1103/PhysRevB.84.075426
12. Bombis, C.; Ample, F.; Lafferentz, L.; Yu, H.; Hecht, S.; Joachim, C.; Grill, L. *Angew. Chem., Int. Ed.* **2009,** *48,* 9966–9970. doi:10.1002/anie.200904645
13. Ramoino, L.; von Arx, M.; Schintke, S.; Baratoff, A.; Güntherodt, H. J.; Jung, T. A. *Chem. Phys. Lett.* **2006,** *417,* 22–27. doi:10.1016/j.cplett.2005.10.006
14. Such, B.; Goryl, G.; Godlewski, S.; Kolodziej, J. J.; Szymonski, M. *Nanotechnology* **2008,** *19,* 475705. doi:10.1088/0957-4484/19/47/475705
15. Godlewski, S.; Goryl, G.; Kolodziej, J. J.; Szymonski, M. *Appl. Surf. Sci.* **2010,** *256,* 3746–3752. doi:10.1016/j.apsusc.2010.01.018
16. Mayne, A. J.; Riedel, D.; Comtet, G.; Dujardin, G. *Prog. Surf. Sci.* **2006,** *81,* 1–51. doi:10.1016/j.progsurf.2006.01.001
17. Bellec, A.; Ample, F.; Riedel, D.; Dujardin, G.; Joachim, C. *Nano Lett.* **2009,** *9,* 144–147. doi:10.1021/nl802688g
18. Gruyters, M.; Pingel, T.; Gopakumar, T. G.; Néel, N.; Schütt, C.; Köhler, F.; Herges, R.; Berndt, R. *J. Phys. Chem. C* **2012,** *116,* 20882–20886. doi:10.1021/jp3058433
19. Godlewski, S.; Kolmer, M.; Kawai, H.; Such, B.; Zuzak, R.; Saeys, M.; de Mendoza, P.; Echavarren, A. M.; Joachim, C.; Szymonski, M. *ACS Nano* **2013,** *7,* 10105–10111. doi:10.1021/nn404254y
20. Vaurette, F.; Nys, J. P.; Grandidier, B.; Priester, C.; Stievenard, D. *Phys. Rev. B* **2007,** *75,* 235435. doi:10.1103/PhysRevB.75.235435
21. Ogawa, T.; Kuwamoto, K.; Isoda, S.; Kobayashi, T.; Karl, N. *Acta Crystallogr., Sect. B* **1999,** *55,* 123–130. doi:10.1107/S0108768198009872
22. Forrest, S. R. *Chem. Rev.* **1997,** *97,* 1793–1896. doi:10.1021/cr941014o
23. Radny, M. W.; Shah, G. A.; Schofield, S. R.; Smith, P. V.; Curson, N. J. *Phys. Rev. Lett.* **2008,** *100,* 246807. doi:10.1103/PhysRevLett.100.246807
24. Nakatsuji, K.; Takagi, Y.; Komori, F.; Kusuhara, H.; Ishii, A. *Phys. Rev. B* **2005,** *72,* 241308. doi:10.1103/PhysRevB.72.241308
25. Kolmer, M.; Godlewski, S.; Kawai, H.; Such, B.; Krok, F.; Saeys, M.; Joachim, C.; Szymonski, M. *Phys. Rev. B* **2012,** *86,* 125307. doi:10.1103/PhysRevB.86.125307
26. Tautz, F. S. *Prog. Surf. Sci.* **2007,** *82,* 479–520. doi:10.1016/j.progsurf.2007.09.001
27. Hill, I. G.; Kahn, A.; Soos, Z. G.; Pascal, R. A., Jr. *Chem. Phys. Lett.* **2000,** *327,* 181–188. doi:10.1016/S0009-2614(00)00882-4
28. Tsiper, E. V.; Soos, Z. G.; Gao, W.; Kahn, A. *Chem. Phys. Lett.* **2002,** *360,* 47–52. doi:10.1016/S0009-2614(02)00774-1
29. Zahn, D. R. T.; Gavrila, G. N.; Gorgoi, M. *Chem. Phys.* **2006,** *325,* 99–112. doi:10.1016/j.chemphys.2006.02.003
30. Yim, S.; Kim, K.-i.; Jones, T. S. *J. Phys. Chem. C* **2007,** *111,* 10993–10997. doi:10.1021/jp0715272
31. Zhong, D. Y.; Hirtz, M.; Wang, W. C.; Dou, R. F.; Chi, L. F.; Fuchs, H. *Phys. Rev. B* **2008,** *77,* 113404. doi:10.1103/PhysRevB.77.113404

Beilstein Journal of Nanotechnology

Surface assembly and nanofabrication of 1,1,1-tris(mercaptomethyl)heptadecane on Au(111) studied with time-lapse atomic force microscopy

Tian Tian[1], Burapol Singhana[2], Lauren E. Englade-Franklin[1], Xianglin Zhai[1], T. Randall Lee[2] and Jayne C. Garno[*1,§]

Full Research Paper

Open Access

Address:
[1]Department of Chemistry, Louisiana State University, 232 Choppin Hall, Baton Rouge, LA 70803, USA and [2]Department of Chemistry and the Texas Center for Superconductivity, University of Houston, Houston, Texas 77204-5003, USA

Email:
Jayne C. Garno[*] - jgarno@lsu.edu

* Corresponding author
§ Fax: 225-578-3458

Keywords:
liquid AFM; multidentate; nanografting; nanolithography; self-assembly

Beilstein J. Nanotechnol. **2014,** *5,* 26–35.
doi:10.3762/bjnano.5.3

Received: 16 August 2013
Accepted: 20 December 2013
Published: 09 January 2014

This article is part of the Thematic Series "Advanced atomic force microscopy techniques II".

Guest Editors: T. Glatzel and T. Schimmel

Abstract

The solution self-assembly of multidentate organothiols onto Au(111) was studied *in situ* using scanning probe nanolithography and time-lapse atomic force microscopy (AFM). Self-assembled monolayers (SAMs) prepared from dilute solutions of multidentate thiols were found to assemble slowly, requiring more than six hours to generate films. A clean gold substrate was first imaged in ethanolic media using liquid AFM. Next, a 0.01 mM solution of multidentate thiol was injected into the liquid cell. As time progressed, molecular-level details of the surface changes at different time intervals were captured by successive AFM images. Scanning probe based nanofabrication was accomplished using protocols of nanografting and nanoshaving with *n*-alkanethiols and a tridentate molecule, 1,1,1-tris(mercaptomethyl)heptadecane (TMMH). Nanografted patterns of TMMH could be inscribed within *n*-alkanethiol SAMs; however, the molecular packing of the nanopatterns was less homogeneous compared to nanopatterns produced with monothiolates. The multidentate molecules have a more complex assembly pathway than monothiol counterparts, mediated by sequential steps of forming S–Au bonds to the substrate.

Introduction

Multidentate thiol-based adsorbates attach to gold surfaces through multiple bonds that provide enhanced stability to self-assembled monolayers (SAMs) [1,2]. Although detailed investigations of monodentate thiol-based SAMs have been widely reported, relatively few studies of SAMs derived from bidentate or tridentate thiol adsorbates are available. One might predict that the bulkier headgroups of multidentate adsorbates would strongly influence the kinetics, stability, and surface

organization when compared to analogous monodentate *n*-alkanethiol adsorbates. The synthesis of custom-designed multidentate thiol-based adsorbates offers opportunities for generating interfaces having well-defined structure and composition based on either bidentate or tridentate thiol groups, a crosslinked junction, and tailgroups of tunable chemical composition [3-6].

The nature of the headgroup, junctions, hydrocarbon backbone, and tailgroups of SAMs enable designs of complex architectures for applications and surface patterning [7-9]. The stability of organosulfur-based adsorbates on noble metal surfaces is a consideration for applications of SAMs, which impacts the reliability and durability of the related products [10-17]. To realize the full potential of patterning surfaces for manufacturing processes, challenges need to be addressed for designing robust surface coatings that resist damage. Multidentate molecules provide a model surface that will resist self-exchange and surface migration, and enable further steps of chemical reactions with high fidelity. Degradation of alkanethiol SAMs on metal surfaces is caused by UV exposure, thermal desorption, and oxidation [18,19]. It has been reported that SAMs designed with longer chain lengths are more thermally stable than those with shorter chains [19-22]. Multidentate thiols have been investigated as a means to improve the overall stability of alkanethiol SAMs, by forming multiple bonds between a molecule and the surface [2,23]. Several new classes of multidentate alkanethiols have been synthesized that have two or three legs and a binding moiety at each end of the legs [3-6,23]. By appropriate design of the anchoring point, multidentate alkanethiols can be engineered to bind to multiple sites on a noble metal surface. The trend in thermal stability is tridentate alkanethiol > bidentate alkanethiol > *n*-alkanethiol [3,17]. Multidentate adsorbates form stable films that resist desorption and exchange and also resist diffusion across the surface of gold, offering opportunities to generate robust surface nanopatterns.

While the kinetics and mechanisms of film growth of SAMs derived from *n*-alkanethiols have been well-studied [24-28], analogous scanning probe investigations of the surface self-assembly of tridentate alkanethiols on Au(111) have yet to be reported. Within a liquid environment, studies of surface reactions can be accomplished using time-lapse atomic force microscopy (AFM). To understand more completely the surface structure and self-assembly process for multidentate thiols, we chose a tridentate molecule, 1,1,1-tris(mercaptomethyl)heptadecane (TMMH) for in situ AFM studies. The orientation of TMMH on the surface was investigated using approaches with liquid imaging and scanning probe lithography. By using a liquid sample cell for AFM studies, fresh reagents can be introduced to the system for monitoring step-wise changes of a surface over time, such as before and after nanofabrication steps. Side-by-side comparisons of the surface structures of multidentate adsorbates versus *n*-alkanethiol SAMs were accomplished using nanografting to give a local measurement of film thickness, referencing the well-known dimensions of *n*-alkanethiols as a baseline.

Results and Discussion

Liquid environments expand the capabilities for scanning probe protocols to provide insight for dynamic processes at the nanoscale [29]. For example, studies of the elastic modulus of SAMS and protein films was accomplished in liquid media using force modulation AFM [30]. Liquid imaging often has advantages for AFM studies, particularly for conducting in situ investigations of chemical or biochemical reactions. Liquid media has benefits for improving resolution, since the amount of force applied between the tip and sample can be reduced [31]. Surface changes after immersion in different liquids can be investigated using time-lapse AFM imaging. Investigations of surfaces throughout the course of chemical self-assembly reactions have been monitored with AFM in liquid media [27]. Further, by injecting new molecules into the sample cell, AFM-based nanofabrication can be accomplished using protocols of nanoshaving and nanografting [32,33]. Of course, the solvents chosen for AFM liquid experiments should be optically transparent, and must have a relatively slow rate of evaporation (e.g., water, ethanol, butanol, or hexadecane).

Surface self-assembly of TMMH. A liquid AFM study was accomplished using time-lapse imaging to investigate the self-assembly of TMMH molecules on template-stripped gold (Figure 1). The surface was imaged in ethanol before injecting the TMMH solution (Figure 1a). The image reveals relatively flat domains bordered by several cracks and scars; the sites of the defects furnish reference landmarks for in situ imaging. After injecting a solution of TMMH in ethanol (0.01 mM) into the liquid cell, small changes were observed during the first hour. At this concentration, a few adsorbates became apparent after 1 h (Figure 1b). Increases in surface coverage were detected as time progressed. Time-lapse images after 2, 2.5, and 3 h are presented in Figure 1c–e with a distinct arrangement of surface landmarks to anchor the location for acquiring successive images. However, as the surface coverage of TMMH increased, the landmarks became indistinguishable (Lateral force images corresponding to the topography frames of Figure 1 are provided in the Supporting Information File 1, Figures S1, S2, and S3). To continue the experiment, a square region was shaved clean to provide a reference location for further time points (Figures S3 and S4 in the Supporting Information File 1). For nanoshaving, a higher force was applied to the AFM tip during scans to sweep away TMMH molecules

from the gold surface (Figure 1e). The experiment was terminated after 6 h before the surface reached saturation coverage (Figure 1f).

With higher magnification, the thickness of the adsorbates can be measured more precisely (Figure 2). The initial bright structures (Figure 2a) appear to attach preferentially to the edges of gold terraces; at this magnification, however, it is difficult to clearly resolve the smallest adsorbates. There are multiple overlapping terraces throughout the areas of the substrate, so evidence of a mobile phase is not conclusive. Several heights are apparent for the adsorbates ranging from 0.5 to 2.2 nm. The shortest structures correspond approximately to the thickness of an alkyl chain with a side-on orientation. The 0.5 nm measurement concurs with the height expected for a physisorbed phase with the backbone of the molecule oriented parallel to the substrate [27]. The tallest heights measured 2.2 nm, and this thickness corresponds to a standing upright configuration of the TMMH, which has a theoretical length of 2.3 nm. A distribution of intermediate heights ranging from 0.8 to 2.0 nm were measured for the adsorbates in Figure 2, which suggests a complex self-assembly pathway for TMMH.

When considering a possible surface assembly model for the observations of Figure 1 and Figure 2, it appears that the initial orientation of the molecule is arranged with a side-on configuration, with the alkyl backbone aligned parallel to the substrate. It is likely that one sulfur of the tridentate molecule attaches to the surface in the initial molecular adsorption step. As time progresses, a second sulfur attached to the surface with rearrangement to a canted orientation, in which the backbone is lifted from the surface to adopt a tilted configuration. The adsorbates with thickness values between 0.8 and 2.0 nm correspond to the transition from a lying-down phase. Over a longer time interval, eventually the molecule rearranges to an upright orientation (2.2 nm), which likely has all three sulfur

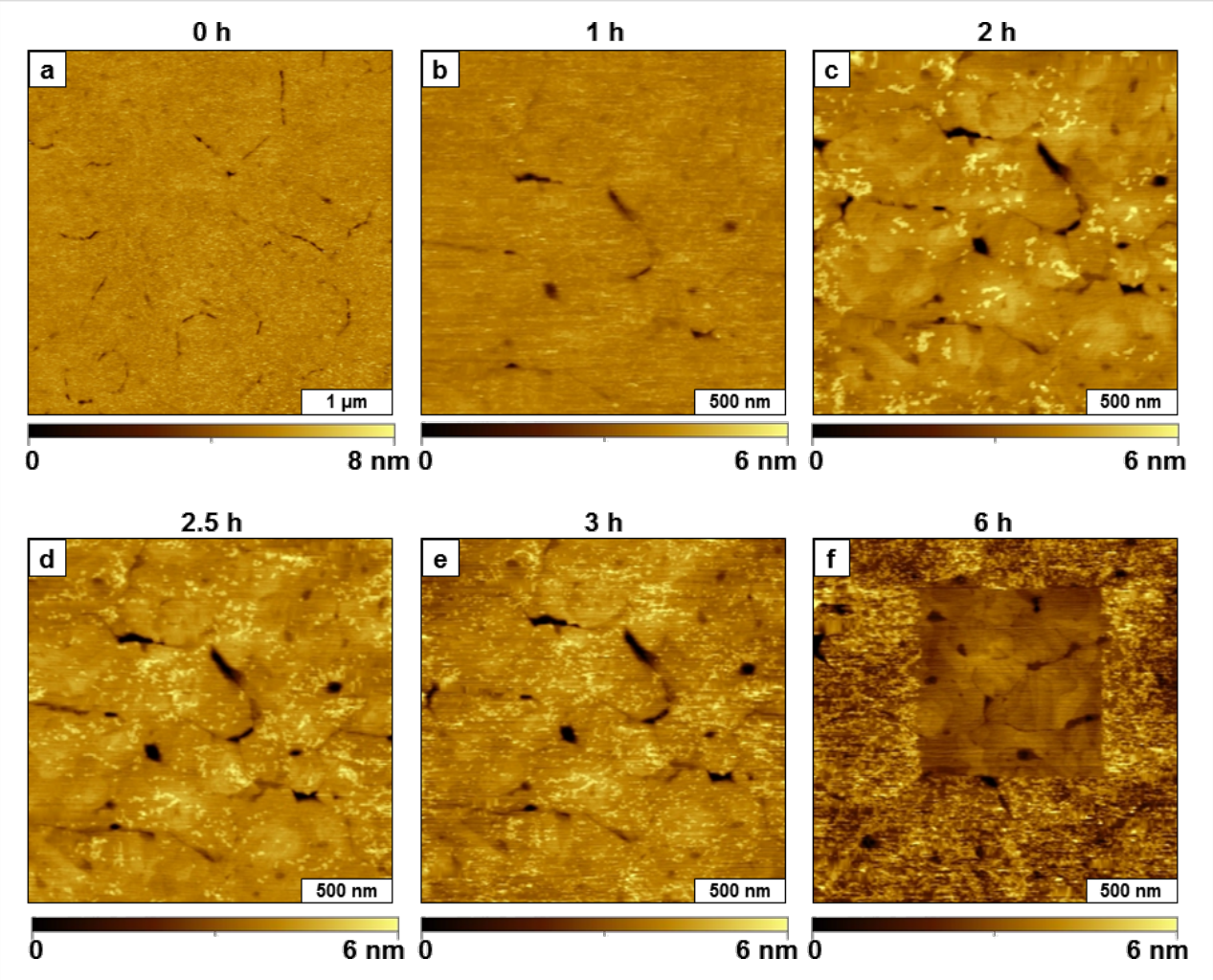

Figure 1: Solution self-assembly of TMMH on gold viewed by time-lapse AFM. Topography images (contact-mode in liquid) acquired after (a) 0 h; (b) 1 h; (c) 2 h; (d) 2.5 h; (e) 3 h; (f) 6 h after injection of TMMH solution.

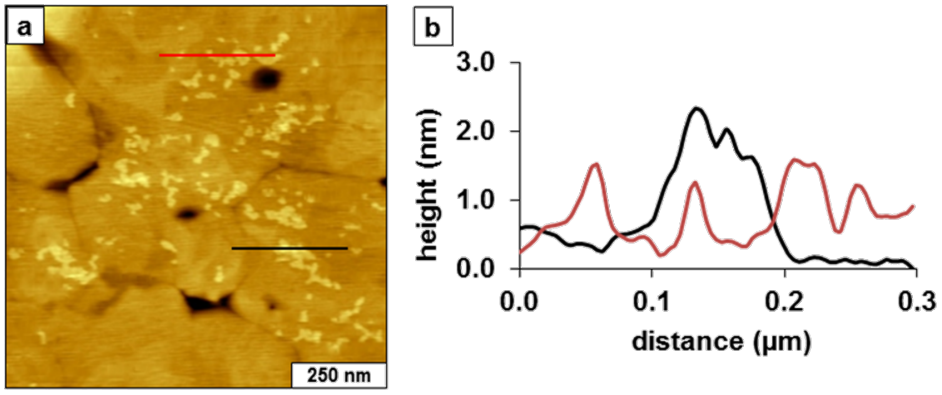

Figure 2: Representative cursor profiles of the side-on and standing phases of TMMH measured after 2 h of immersion.

groups attached to the surface. Although we have no direct evidence of the numbers of sulfur groups attached to the substrate using AFM characterizations, the range of intermediate height measurements of Figure 2 suggest a step-wise attachment of the sulfur moieties.

Kinetic trends for the surface-assembly of the taller phase of TMMH are plotted in Figure 3. The binding of TMMH is relatively slow at this concentration. At higher concentrations, multilayers of TMMH were formed through dithiol bonds; therefore dilute conditions were used to slow the rate of surface deposition [27]. As shown by the surface coverage estimates in Figure 3, the rate of surface adsorption of TMMH increased after 2 h, suggesting that interactions between neighboring molecules as surface density increased influenced the rate of surface attachment. The data for Figure 3 were constructed from analyzing the surface area of regions containing TMMH adsorbates and are a composite of lying-down, standing and multilayer adsorbates. After TMMH bound to surface sites, molecules began to associate and attach to the surface more quickly. Incomplete monolayers were observed for brief immersion steps, and mature, densely packed SAMs were formed after at least 24 h immersion. The initial studies with tridentate TMMH molecules reveal slow adsorption >6 h to reach a standing configuration with dilute conditions of 0.01 mM solution.

Nanoshaving of a TMMH film on gold. A convenient way to measure locally the thickness of an organothiol film with liquid AFM is to shave away a small area of the film by applying a higher force to the AFM probe and sweeping. An example of nanoshaving is shown in Figure 4 for a 200 × 200 nm^2 area of gold that was uncovered by the AFM tip. Some of the molecules are deposited at the left and right sides of the nanopattern, indicated by the bright edges. However, most of the molecules dissolved in the liquid media or are swept away by the scanning action of the AFM tip. A possible concern when increasing the force to the AFM tip is that the probe might become dull or break. However, for this example the tip retains its sharpness because the pinhole defects and contours of the step edges of the underlying gold beneath the SAM of TMMH (Figure 4a) can be resolved, even after the tip was used for fabrication steps. In comparison to the example of nanoshaving in

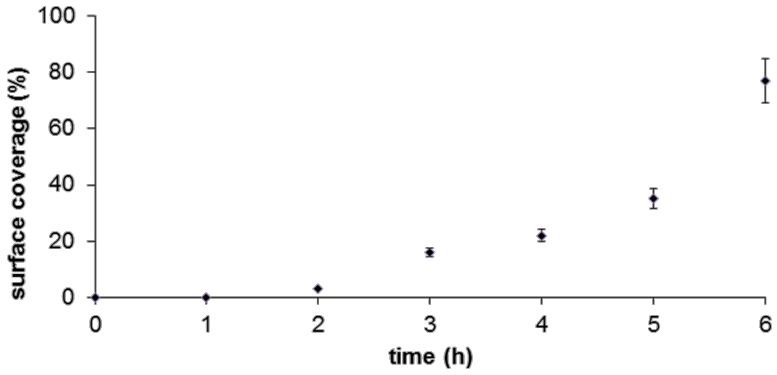

Figure 3: Gradual increase in surface coverage of the taller (standing) phase of TMMH as time progressed.

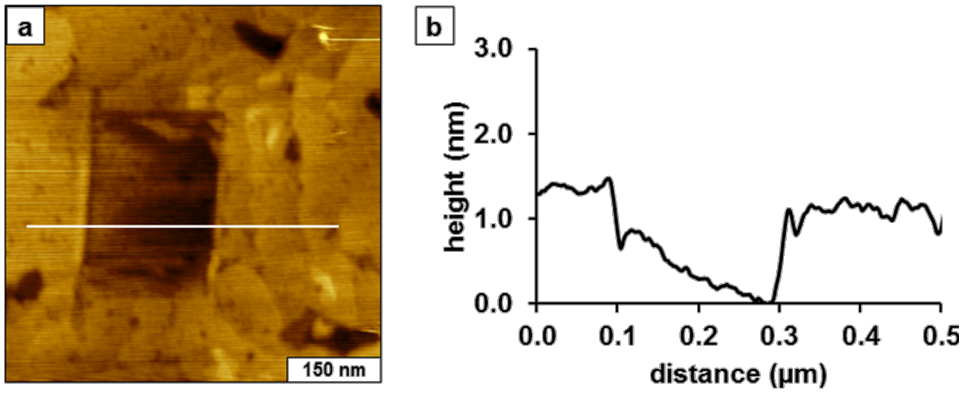

Figure 4: Nanoshaved square within a SAM of TMMH. (a) Topography image acquired in ethanol; (b) Line profile across the square pattern.

Figure 1f, the SAM is more densely packed after 30 h immersion in TMMH (see Figure 4). The thickness of the SAM is 1.0 ± 0.2 nm measured at the right edge of the nanopattern. The baseline within the nanoshaved area has a slope due to the nature of the substrate. The left side has a hill of adsorbates from the material scraped to the side by the nanoshaving process and is unreliable for measuring the thickness.

Nanografting of *n*-alkanethiols within TMMH. By injecting new molecules into the sample cell, AFM-based nanofabrication can be accomplished using nanoshaving and nanografting protocols [32,33]. Approaches with nanolithography enable side-by-side comparisons of the surface structures of multidentate adsorbates versus *n*-alkanethiol monolayers (i.e., film thickness, morphology). Our experimental strategies rely on using a liquid sample cell for AFM studies, since fresh reagents can be introduced to the system, and stepwise changes of the surface before and after nanofabrication can be monitored in situ. For experiments in liquid media, the method of surface nanografting developed by Xu et al. was used to inscribe nanopatterns [33]. For these experiments, *n*-alkanethiol SAMs provided an internal calibration tool; essentially, the well-known dimensions of *n*-alkanethiol monolayers furnish an in situ ruler for local measurements of the thickness of molecular films [7,34-36].

Our protocols for nanografting used either dodecanethiol or TMMH as matrix SAMs that were prepared by immersion in ethanolic solutions. Areas of the matrix were selected for nanoshaving or nanografting of patterns to enable a side-by-side comparison of molecular thickness. The steps of experiments were captured with AFM images before and after fabricating nanopatterns within a liquid environment. The same AFM probe was used for writing nanopatterns and for in situ sample characterizations.

A square pattern of octadecanethiol (ODT) was nanografted into a matrix of TMMH, as shown in Figure 5. The bright square consists of densely-packed alkanethiols with methyl-terminated headgroups (Figure 5a). A slightly darker contrast is observed for the nanografted pattern compared to the matrix for the lateral force image of Figure 5b, even though TMMH and ODT are both terminated with methyl groups. The darker contrast could be attributable to differences in packing density: the nanografted pattern appears to be more dense than the surrounding SAM of TMMH, which is consistent with observations from previous studies of tridentate SAMs on gold [19]. The surrounding areas of the TMMH matrix are shorter than ODT. The expected thickness of an octadecanethiol SAM on gold is 2.2 nm, and the octadecanethiol square is approximately 1 nm taller than the TMMH matrix (Figure 5c). Thus, for this example the local thickness of TMMH measures 1.2 ± 0.2 nm.

To acquire additional local measurements of the thickness of TMMH films, nanopatterns of 11-mercaptoundecanoic acid (MUA) were grafted within a matrix of TMMH (Figure 6a). Each of the patterns shown in Figure 6a were inscribed by multiple sweeps across the same selected region, which produced a double-layer thickness for the circles and letter shapes. It has previously been reported that multiple sweeps during nanografting of carboxylic acid-terminated SAMs produced bilayer nanopatterns [36]. The square nanopattern of MUA on the left side of the topography frame measures 200 × 200 nm^2, and reveals a two-tier design with single- and double-layer thickness. Cursor lines were drawn across the top and bottom areas of the MUA nanopatterns (Figure 6b) measuring 0.5 ± 0.2 and 2.0 ± 0.2 nm above the TMMH matrix for the single and double layers, respectively. The profile across the monolayer region of the pattern (Figure 6b, red line) measuring ~0.5 nm above the matrix indicates that the SAM derived from TMMH is ~1 nm thick. The areas of the pattern

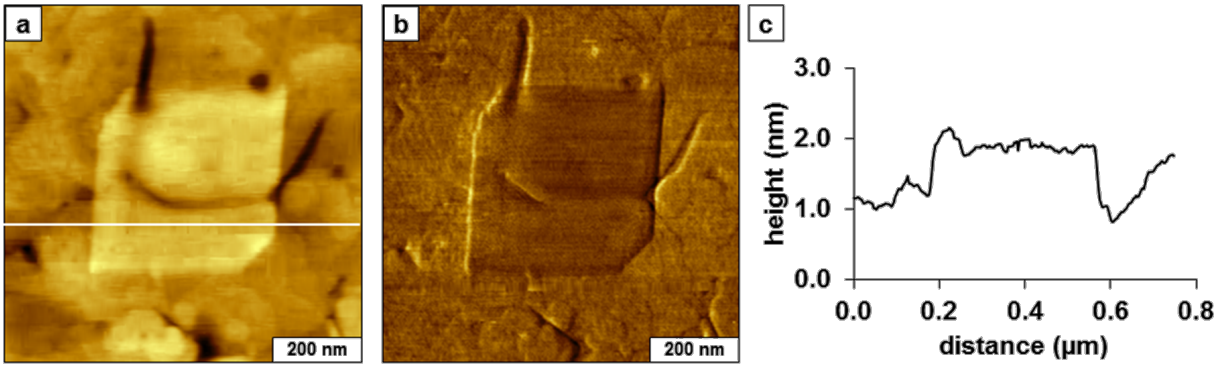

Figure 5: Nanografting of octadecanethiol (ODT) within a densely-packed TMMH matrix. (a) Topography image acquired in contact mode; (b) corresponding lateral force image. (c) Height profile taken across the square pattern in (a).

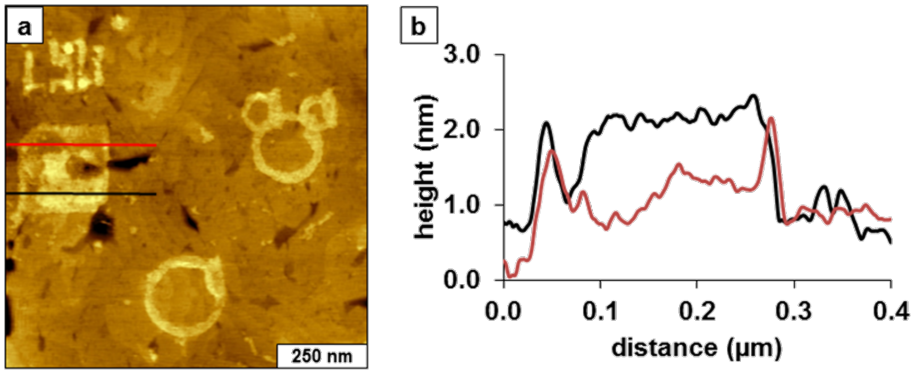

Figure 6: Nanografting of 11-mercaptoundecanoic acid (MUA) within a matrix of TMMH. (a) Topography view of multiple patterns that were nanografted within an 800 × 800 nm^2 region. (b) Cursor profiles across the terrace square of (a).

with a double layer (Figure 6b, black line) are 2 ± 0.2 nm taller than the TMMH matrix. Since a double layer of MUA would be 3.0 nm thick, this analysis likewise indicates a height of ~1 nm for the SAM derived from TMMH.

Further experiments were conducted with nanografting of TMMH nanopatterns within a methyl-terminated dodecanethiol SAM (Figure 7). The dodecanethiol SAM was prepared from 1 mM ethanolic solution, and the TMMH nanografted patterns were prepared with 0.01 mM solution. The expected thickness of a dodecanethiol SAM is 1.5 nm, as a reference for evaluating the thickness of TMMH nanostructures. Four nanopatterns were written within the methyl-terminated SAM (Figure 7a,b). The height of the TMMH squares is shorter than the surrounding matrix SAM of dodecanethiol. The difference in thickness ranges from 0.6–0.9 nm, which corresponds to a thickness of 0.7 ± 0.3 nm for nanografted patterns of TMMH (Figure 7c). The simultaneously acquired lateral force image (Figure 7b) reveals the edges of the nanopatterns as well as the step edges of the underlying gold substrates. The surface density of TMMH within the nanografted regions is not homogeneous; for example, the top right square seems to have a greater density of TMMH than the patterns on the left side of the frame. The pattern at the top right side has patches of brighter and darker shades, which correspondingly have different thickness measurements within the nanofabricated area. Further experiments are planned to evaluate how the physical parameters for nanofabrication (line speed, line density) influence the thickness of TMMH patterns.

When nanografting *n*-alkanethiols, the molecules attach to the gold surfaces directly in a standing-up configuration due to the effects of spatial confinement [37]. However, the tridentate molecules have a larger headgroup, which influences the packing density [19]. The thickness values derived from each of the different AFM experiments are summarized in Table 1, and are in fair agreement for measurements at the nanoscale.

Unlike our earlier observations from unconstrained surface assembly (Figure 1) that several hours were required for TMMH to bind to gold surfaces to form a SAM, nanografting experiments disclosed that TMMH attached immediately

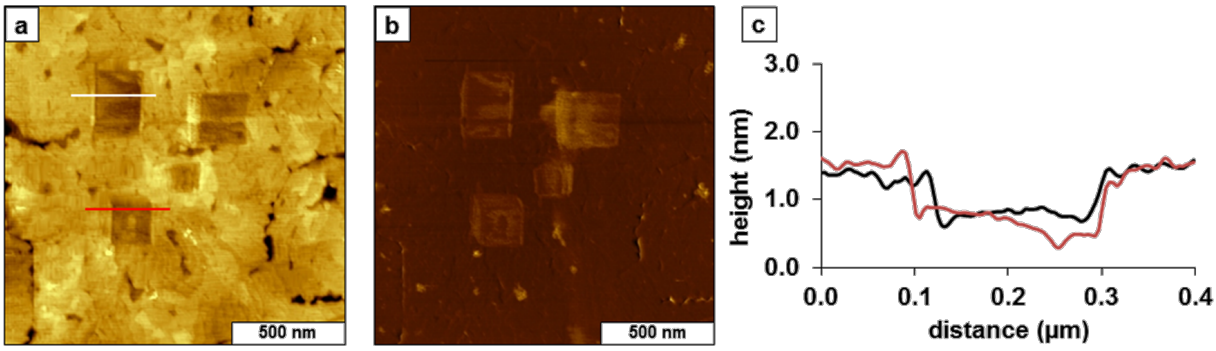

Figure 7: Nanografted patterns of TMMH within a dodecanethiol SAM. (a) Topograph of squares of TMMH (1.5 × 1.5 µm^2); (b) lateral force image for (a); (c) height profile across two TMMH nanopatterns in (a).

Table 1: Thickness measurements of TMMH on gold substrates.

AFM protocol	TMMH[a] thickness (nm)	Example
Time-lapse AFM study, upright adsorbates on gold	1.0 ± 0.2	Figure 2
Nanoshaving of mature SAM of TMMH	1.0 ± 0.2	Figure 4
Nanografted ODT within TMMH matrix SAM	1.2 ± 0.2	Figure 5
Nanografted MUA within TMMH matrix SAM	1.0 ± 0.2	Figure 6
Nanografted TMMH within dodecanethiol SAM	0.7 ± 0.3	Figure 7

[a]The error is estimated to be at least 0.2 nm from the thickness of a gold step.

following the scanning track of the AFM tip (Figure 7). However, the shorter height suggests a less-dense packing arrangement for the nanografted patterns of TMMH with the bigger foot (i.e., larger molecule). The height of nanografted patterns is shorter than that expected for an upright configuration of TMMH, likely attributable to the dilute conditions of the experiment. This may be attributable to an incomplete surface assembly of all three sulfurs of the tridentate group, with only one or two sulfur atoms attaching to the substrate during nanografting protocols.

For the nanografting experiments with TMMH as the matrix monolayer, the overall film thickness indicates a tilted configuration. Using the value of 1.0–1.2 nm as the thickness of a mature TMMH SAM from Table 1, the heptadecane backbone would be tilted ~59–64° with respect to surface normal, compared to the well-known 30° tilt of *n*-alkanethiol SAMs. The interplay of a wider intermolecular spacing between adjacent backbones and the larger geometry of the tridentate "foot" provide the rationale for a less dense arrangement of TMMH films. The tridentate adsorbates formed a monolayer in which the alkyl chains are highly disordered on the surface as compared to SAMs derived from monodentate *n*-alkanethiols reported from studies with sum frequency generation imaging microscopy [38]. The packing density followed the trend monodentate > bidentate > tridentate. There is a possibility that only one or two of the sulfur groups bind to the substrate which would likewise contribute to a tilted orientation for TMMH. Previous studies of the thermal stability of tridentate SAMs show increased stability for tridentate alkanethiols compared to *n*-alkanethiols [3,17]; thus for our model we propose that three sulfurs are anchored to the substrate. In future experiments, we plan to evaluate the parameters of concentration and solvents for producing SAMs of TMMH, and will investigate the stability of multidentate films with exposure to heat, UV-irradiation and oxidation.

Conclusion

Using dilute ethanolic solutions, the surface self-assembly of TMMH onto Au(111) was imaged with time-lapse AFM for 6 h. With higher concentration, multilayers of TMMH were produced. Protocols of nanografting and nanoshaving were used to compare the heights of TMMH with *n*-alkanethiol SAMs using side-by-side AFM views. The films of TMMH formed from relatively dilute conditions (0.01 mM) were less densely packed than for *n*-alkanethiol SAMs that were prepared at mM concentration.

Experimental

Materials and reagents. Ethanol (200 proof) was obtained from AAper Alcohol and Chemical Co. (Shelbyville, KY). Flame-annealed gold films on mica substrates (150 nm thick-

ness) were obtained from Agilent Technologies (Phoenix, AZ). Template-stripped gold films were prepared on glass slides using Epotek 377, as previously described by Wagner et al [39]. Octadecanethiol and dodecanethiol were purchased from Sigma Aldrich (St. Louis, MO) and used as received. The tridentate molecule 1,1,1-tris(mercaptomethyl)heptadecane (TMMH) was synthesized as described below and is illustrated in Scheme 1 in a similar manner as previously reported [5,40].

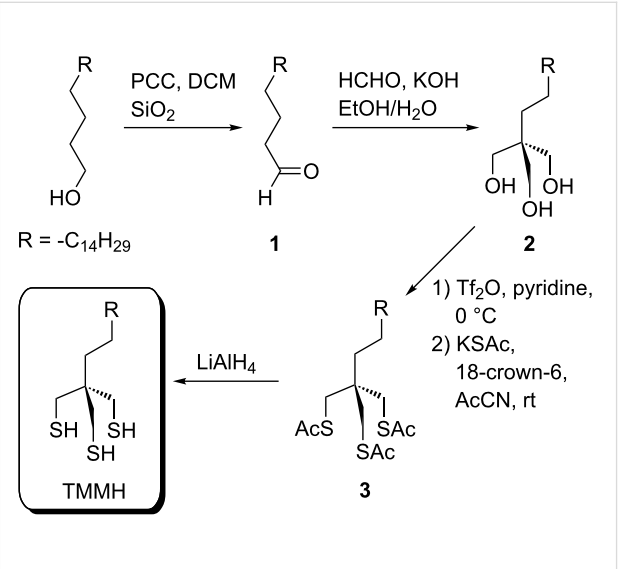

Scheme 1: Strategy used to prepare 1,1,1-tris(mercapto-methyl)heptadecane (TMMH).

For the synthetic procedures, all organic solvents were dried with calcium hydride (CaH_2) and distillated before use. Pyridinium chlorochromate (PCC) and lithium aluminum hydride ($LiAlH_4$) were purchased from Alfa Aesar. 1-Octadecanol (ReagentPlus®, 99%), formaldehyde (37 wt % in H_2O), trifluoromethanesulfonic anhydride (≥99%), 18-crown-6 (≥99.9%), pyridine (anhydrous, 99.8%), potassium thioacetate (98%), and anhydrous acetonitrile (AcCN) were purchased from Sigma-Aldrich. All other reagents were used without further purification.

Octadecanal (1). The aldehyde was synthesized by using a modification of literature methods [5,41]. Specifically, pyridinium chlorochromate (26.89 g, 124.7 mmol) and silica gel (30 mg) were mixed and suspended in 100 mL of dry CH_2Cl_2. The solution of 1-octadecanol (20.13 g, 74.42 mmol) in CH_2Cl_2 was added into the stirred mixture. Stirring was continued for 4 h at rt, and the black chromium compounds were removed by passage through a short pad of silica gel. The filtrate was concentrated to dryness and purified by column chromatography on silica gel, eluting with 4% diethyl ether in hexanes to afford octadecanal **1** (16.25 g, 60.53 mmol, 81%). ^{1}H NMR (500 MHz, $CDCl_3$) δ 0.88 (t, J = 7.0 Hz, 3H, CH_3), 1.20–1.36 (m, 28 H), 1.59–1.66 (m, 2H, CH_2CH$_2$CHO), 2.42 (td, J = 1.9, 7.4 Hz, 2H, CH_2CHO), 9.76 (t, J = 1.9 Hz, 1H, CHO).

1,1,1-Tris(hydroxymethyl)heptadecane (2) [42]. Octadecanal (10.25 g, 38.18 mmol) and aqueous formaldehyde (37 wt % in H_2O, 30 mL, excess) were dissolved in 60 mL of aqueous ethanol (50%). To this stirred mixture was added a solution of potassium hydroxide (3.59 g, 64.0 mmol) in 60 mL of aqueous ethanol (50%). The reaction mixture was stirred for 4 h at rt and heated to 60 °C for 6 h. The ethanol was removed by rotary evaporation, and the residue was extracted with diethyl ether (3 × 100 mL). The combined organic phases were washed with water (3 × 100 mL), dried over $MgSO_4$, and concentrated to dryness. The crude products were purified by column chromatography on silica gel, eluting with 4% methanol in CH_2Cl_2 to give a white solid (4.05 g, 12.3 mmol, 32%). ^{1}H NMR (500 MHz, $CDCl_3$) δ 0.88 (t, J = 7.0 Hz, 3H, CH_3), 1.10–1.33 (m, 30H), 2.53 (t, J = 5.1 Hz, 3H, 3OH), 3.74 (d, J = 4.7 Hz, 6H, 3CH_2OH).

1,1,1,-Tris(acetylthiomethyl)heptadecane (3). Pyridine (30 mL, 0.49 mol) was added to a solution of triol **2** (3.89 g, 11.8 mmol) in dry CH_2Cl_2 (50 mL) at 0 °C and stirred for 15 min. Afterward, trifluoromethanesulfonic anhydride (15 mL, 94 mmol; Tf_2O) in dry and cold CH_2Cl_2 (30 mL) was added dropwise to the reaction solution over a period of 20 min. The reaction mixture was then stirred at 0 °C for 4 h. The mixture was diluted with CH_2Cl_2 (150 mL), washed with 2 M HCl and 5% $NaHCO_3$, and dried with $MgSO_4$. The solvent was removed under reduced pressure to give the crude tritriflate (5.25 g). This intermediate was used without further purification in the next step. A solution of crude tritriflate (5.25 g), 18-crown-6 (24.88 g, 94.15 mmol), and potassium thioacetate (10.75 g, 94.15 mmol) in anhydrous acetonitrile (120 mL) was stirred at rt for 8 h. The resulting precipitate was removed by filtration, and the filtrate washed with 5% NaCl (300 mL) and dried with $MgSO_4$. The organic phase was concentrated in vacuo. The residue was purified by column chromatography on silica gel, eluting with hexanes/ethyl acetate (7:1) to afford **3** (4.86 g, 9.63 mmol, 82% yield). ^{1}H NMR (500 MHz, $CDCl_3$) δ 0.87 (t, J = 7.0 Hz, 3H), 1.18–1.35 (m, 30H), 2.34 (s, 9H, $CH_2SC(O)CH_3$), 2.98 (s, 6H, $CH_2SC(O)CH_3$).

1,1,1-Tri(mercaptomethyl)heptadecane (TMMH). A solution of **3** (2.80 g, 5.55 mmol) in dry THF (80 mL) was added dropwise to a suspension of $LiAlH_4$ (1.26 g, 33.3 mmol) in dry THF (60 mL). The mixture was stirred at rt for 6 h and then quenched with H_2O and acidified with 2 M HCl under argon (H_2O and 2 M HCl were degassed by bubbling with N_2 gas before use). After stirring for 10 min, the mixture was extracted

with CH_2Cl_2 (3 × 100 mL). The combined organic layers were washed with H_2O and brine. After drying the solution with Na_2SO_4, the solvent was removed by rotary evaporation, and the resulting residue was chromatographed on silica gel with hexanes/ethyl acetate (3:1) to afford TMMH (1.60 g, 4.22 mmol, 76% yield). ^{1}H NMR (500 MHz, $CDCl_3$) δ 0.88 (t, J = 7.0 Hz, 3H), 1.17 (t, J = 8.7 Hz, 3H), 1.21–1.33 (m, 28H), 1.35–1.41 (m, 2H), 2.56–2.60 (m, 6H, 3CH_2SH); ^{13}C NMR (125 MHz, $CDCl_3$) δ 14.13, 22.71, 23.27, 29.05, 29.27, 29.36, 29.53, 29.68, 30.04, 30.09, 31.94, 32.42, 41.39.

Atomic force microscopy. Either a model 5500 or 5420 scanning probe microscope (Agilent Technologies, Chandler, AZ) equipped with PicoView v1.8 software was used for the AFM characterizations and scanning probe lithography. Images were acquired using contact mode in a liquid cell, which can hold up to 1 mL of solution. Imaging and fabrication were accomplished with silicon nitride tips, which had an average spring constant of 0.5 N/m (Bruker Instruments, Camarillo, CA). Digital images were processed and analyzed with Gwyddion v.2.25 software [43]. Analysis of surface coverage was accomplished by manually selecting a threshold value to convert images to black and white data sets, and counting pixels using the UTHSCSA *ImageTool* program (developed at the University of Texas Health Science Center at San Antonio, Texas and available from the Internet by anonymous FTP from maxrad6.uthscsa.edu).

AFM study of the self-assembly of TMMH from solution. A piece of template-stripped gold on glass was placed in the liquid cell and imaged continuously. Initially, the sample was imaged in ethanolic media to obtain a representative view of the gold substrate. Next, a solution of TMMH (0.01 mM) in ethanol was injected into the liquid cell to monitor the growth of TMMH in situ. A relatively low concentration of TMMH (0.01 mM) was selected to enable surface assembly at a sufficiently slow rate to enable monitoring with time-lapse AFM images. After introducing TMMH solution into the sample cell, images were acquired every 15 min for 3 h for the same area. The liquid cell was replenished with fresh TMMH solution at 90 minute intervals because the ethanol evaporates over time. After 3 h, the tip was moved for imaging a new area to minimize the effects of perturbing the surface by the scanning probe. Images were acquired at 30 min intervals during the later stages of the experiment.

Scanning probe lithography (nanoshaving and nanografting). Nanoshaving experiments were accomplished by applying a high force (2–5 nN) to sweep a selected area ten times with 256 lines/frame in ethanolic media. The nanoshaved patterns could be imaged in situ using the same probe by returning to a lower force setting. Nanografting experiments were accomplished by sweeping an area under high force in a liquid cell containing an ethanolic solution of the molecule to be patterned. Multiple cursor profiles were acquired for measuring the thickness of nanopatterns. The error term was estimated to be at least the height of a monatomic gold step (0.2 nm). Solutions of either octadecanethiol or dodecanethiol solutions were prepared at a concentration of 1 mM for nanografting. A dodecanethiol SAM was prepared by immersing a piece of template-stripped gold in a 1 mM ethanolic solution for 12 h. A monolayer film of TMMH was prepared by immersing a piece of template-stripped gold in a 0.01 mM ethanolic solution for 72 h. A lower concentration was used for TMMH to prevent forming multilayer films.

Supporting Information

Additional AFM images are provided that include lateral force frames and images acquired at other selected time points during surface self-assembly (Figures S1, S2, S3 and S4).

Supporting Information File 1

Additional AFM images.
[http://www.beilstein-journals.org/bjnano/content/supplementary/2190-4286-5-3-S1.pdf]

Acknowledgements

This research was supported by the National Science Foundation (DMR-0906873), by the American Chemical Society Petroleum Research Fund New Directions Program, and the Camille Dreyfus Teacher-Scholar award. Additional support for work performed at the University of Houston was provided by the Robert A. Welch Foundation (grant no. E-1320), the National Science Foundation (DMR-0906727) and the Texas Center for Superconductivity at the University of Houston. The authors thank Professor George Stanley of LSU for technical assistance with graphics.

References

1. Chinwangso, P.; Jamison, A. C.; Lee, T. R. *Acc. Chem. Res.* **2011,** *44,* 511–519. doi:10.1021/ar200020s
2. Srisombat, L.; Jamison, A. C.; Lee, T. R. *Colloids Surf., A* **2011,** *390,* 1–19. doi:10.1016/j.colsurfa.2011.09.020
3. Srisombat, L.-o.; Zhang, S.; Lee, T. R. *Langmuir* **2010,** *26,* 41–46. doi:10.1021/la902082j
4. Srisombat, L.-o.; Park, J.-S.; Zhang, S.; Lee, T. R. *Langmuir* **2008,** *24,* 7750–7754. doi:10.1021/la800511g
5. Park, J.-S.; Vo, A. N.; Barriet, D.; Shon, Y.-S.; Lee, T. R. *Langmuir* **2005,** *21,* 2902–2911. doi:10.1021/la0475573

6. Park, J.-S.; Smith, A. C.; Lee, T. R. *Langmuir* **2004,** *20,* 5829–5836. doi:10.1021/la036424z
7. Yang, G.; Garno, J. C.; Liu, G.-Y. Scanning Probe-Based Lithography for Production of Biological and Organic Nanostructures on Surfaces. In *Comprehensive Nanoscience and Technology;* Andrews, D.; Scholes, G.; Wiederrecht, G., Eds.; Elsevier, B. V.: Amsterdam, 2010.
8. Garno, J. C.; Batteas, J. D. Nanofabrication with Self-Assembled Monolayers by Scanning Probe Lithography. In *Applied Scanning Probe Methods, Industrial Applications;* Bhushan, B.; Fuchs, H., Eds.; Springer-Verlag: Berlin, Heidelberg, 2006; Vol. IV.
9. Schreiber, F. *J. Phys.: Condens. Matter* **2004,** *16,* R881–R900. doi:10.1088/0953-8984/16/28/R01
10. Ebbens, S.; Hutt, D.; Liu, C. *IEEE Trans. Compon. Packag. Technol.* **2010,** *33,* 251–259. doi:10.1109/TCAPT.2010.2041779
11. Hakamada, M.; Takahashi, M.; Furukawa, T.; Tajima, K.; Yoshimura, K.; Chino, Y.; Mabuchi, M. *Phys. Chem. Chem. Phys.* **2011,** *13,* 12277–12284. doi:10.1039/c0cp02553d
12. Ito, E.; Kang, H.; Lee, D.; Park, J. B.; Hara, M.; Noh, J. *J. Colloid Interface Sci.* **2013,** *394,* 522–529. doi:10.1016/j.jcis.2012.12.035
13. Li, J.; Ang, X. F.; Lee, K. H.; Romanato, F.; Wong, C. C. *J. Nanosci. Nanotechnol.* **2010,** *10,* 4624–4628. doi:10.1166/jnn.2010.1685
14. Ramin, L.; Jabbarzadeh, A. *Langmuir* **2011,** *27,* 9748–9759. doi:10.1021/la201467b
15. Rodríguez, L. M.; Cristina, L. J.; Alarcón, L. S.; Blum, B.; Salvarezza, R. C.; Xi, L.; Lau, W. M.; Sánchez, E. A.; Gayone, J. E.; Grizzi, O. *Nucl. Instrum. Methods Phys. Res., Sect. B* **2011,** *269,* 924–931. doi:10.1016/j.nimb.2010.12.051
16. Stettner, J.; Winkler, A. *Langmuir* **2010,** *26,* 9659–9665. doi:10.1021/la100245a
17. Subramanian, S.; Sampath, S. *Anal. Bioanal. Chem.* **2007,** *388,* 135–145. doi:10.1007/s00216-007-1184-4
18. Willey, T. M.; Vance, A. L.; van Buuren, T.; Bostedt, C.; Terminello, L. J.; Fadley, C. S. *Surf. Sci.* **2005,** *576,* 188–196. doi:10.1016/j.susc.2004.12.022
19. Tam-Chang, S.-W.; Biebuyck, H. A.; Whitesides, G. M.; Jeon, N.; Nuzzo, R. G. *Langmuir* **1995,** *11,* 4371–4382. doi:10.1021/la00011a033
20. Bain, C. D.; Troughton, E. B.; Tao, Y. T.; Evall, J.; Whitesides, G. M.; Nuzzo, R. G. *J. Am. Chem. Soc.* **1989,** *111,* 321–335. doi:10.1021/ja00183a049
21. Porter, M. D.; Bright, T. B.; Allara, D. L.; Chidsey, C. E. D. *J. Am. Chem. Soc.* **1987,** *109,* 3559–3568. doi:10.1021/ja00246a011
22. Poirier, G. E.; Tarlov, M. J.; Rushmeier, H. E. *Langmuir* **1994,** *10,* 3383–3386. doi:10.1021/la00022a004
23. Zhang, S.; Leem, G.; Srisombat, L.-o.; Lee, T. R. *J. Am. Chem. Soc.* **2008,** *130,* 113–120. doi:10.1021/ja0724588
24. Schwartz, D. K. *Annu. Rev. Phys. Chem.* **2001,** *52,* 107–137. doi:10.1146/annurev.physchem.52.1.107
25. Schreiber, F. *Prog. Surf. Sci.* **2000,** *65,* 151–257. doi:10.1016/S0079-6816(00)00024-1
26. Buck, M.; Grunze, M.; Eisert, F.; Fischer, J.; Trager, F. *J. Vac. Sci. Technol., A* **1992,** *10,* 926–929. doi:10.1116/1.577879
27. Xu, S.; Cruchon-Dupeyrat, S.; Garno, J. C.; Liu, G.-Y.; Jennings, G. K.; Yong, T.-H.; Laibinis, P. E. *J. Chem. Phys.* **1998,** *108,* 5002–5012. doi:10.1063/1.475908
28. Debono, R. F.; Loucks, G. D.; Della Manna, D.; Krull, U. J. *Can. J. Chem.* **1996,** *74,* 677–688. doi:10.1139/v96-073
29. Lyles, V. D.; Serem, W. K.; Garno, J. C. In *Surface Analytical Techniques;* Bracco, G.; Holst, B., Eds.; Springer, 2013.
30. Zhang, J.; Parlak, Z.; Bowers, C. M.; Oas, T.; Zauscher, S. *Beilstein J. Nanotechnol.* **2012,** *3,* 464–474. doi:10.3762/bjnano.3.53
31. Hansma, P. K.; Cleveland, J. P.; Radmacher, M.; Walters, D. A.; Hillner, P. E.; Bezanilla, M.; Fritz, M.; Vie, D.; Hansma, H. G.; Prater, C. B.; Massie, J.; Fukunaga, L.; Gurley, J.; Elings, V. *Appl. Phys. Lett.* **1994,** *64,* 1738–1740. doi:10.1063/1.111795
32. Liu, G.-Y.; Xu, S.; Qian, Y. *Acc. Chem. Res.* **2000,** *33,* 457–466. doi:10.1021/ar980081s
33. Xu, S.; Miller, S.; Laibinis, P. E.; Liu, G.-Y. *Langmuir* **1999,** *15,* 7244–7251. doi:10.1021/la9906727
34. Tian, T.; LeJeune, Z. M.; Serem, W. K.; Yu, J.-J.; Garno, J. C. Nanografting: A Method for Bottom-up Fabrication of Designed Nanostructures. In *Tip-Based Nanofabrication;* Tseng, A. A., Ed.; Springer Science: New York, 2011; pp 167–205. doi:10.1007/978-1-4419-9899-6_5
35. Brower, T. L.; Garno, J. C.; Ulman, A.; Liu, G.-Y.; Yan, C.; Gölzhäuser, A.; Grunze, M. *Langmuir* **2002,** *18,* 6207–6216. doi:10.1021/la020084k
36. Kelley, A. T.; Ngunjiri, J. N.; Serem, W. K.; Lawrence, S. O.; Yu, J.-J.; Crowe, W. E.; Garno, J. C. *Langmuir* **2010,** *26,* 3040–3049. doi:10.1021/la9026128
37. Xu, S.; Laibinis, P. E.; Liu, G.-Y. *J. Am. Chem. Soc.* **1998,** *120,* 9356–9361. doi:10.1021/ja981938j
38. Hernandez, M.; Chinwangso, P.; Cimatu, K.; Srisombat, L.-o.; Lee, T. R.; Baldelli, S. *J. Phys. Chem. C* **2011,** *115,* 4688–4695. doi:10.1021/jp1111795
39. Wagner, P.; Hegner, M.; Guentherodt, H.-J.; Semenza, G. *Langmuir* **1995,** *11,* 3867–3875. doi:10.1021/la00010a043
40. Singhana, B.; Rittikulsittichai, S.; Lee, T. R. *Langmuir* **2013,** *29,* 561–569. doi:10.1021/la303101x
41. Corey, E. J.; Suggs, J. W. *Tetrahedron Lett.* **1975,** *16,* 2647–2650. doi:10.1016/S0040-4039(00)75204-X
42. Weibull, B.; Matell, M. *Acta Chem. Scand.* **1962,** *16,* 1062.
43. Nečas, D.; Klapetek, P. *Cent. Eur. J. Phys.* **2012,** *10,* 181–188. doi:10.2478/s11534-011-0096-2

License and Terms

Beilstein Journal of Nanotechnology

Study of mesoporous CdS-quantum-dot-sensitized TiO_2 films by using X-ray photoelectron spectroscopy and AFM

Mohamed N. Ghazzal[*1,2], Robert Wojcieszak[1,3], Gijo Raj[1] and Eric M. Gaigneaux[*1]

Full Research Paper

Open Access

Address:
[1]Institute of Condensed Matter and Nanoscience – Molecules, Solids and Reactivity (IMCN/MOST), Université Catholique de Louvain, Croix du Sud 2/17, 1348 Louvain-La-Neuve, Belgium, [2]Université de Namur, Technology Transfert Office, rue de Bruxelles 61 - 5000 Namur, Belgique and [3]Institute of Chemistry, University of Sao Paulo, USP, São Paulo, 05508-000, SP, Brazil

Email:
Mohamed N. Ghazzal[*] - g_nawfel@yahoo.fr; Eric M. Gaigneaux[*] - eric.gaigneaux@uclouvain.be

* Corresponding author

Keywords:
AFM; CdS; heterojunction; particle size; quantum dots; TiO_2; XPS

Beilstein J. Nanotechnol. **2014,** *5,* 68–76.
doi:10.3762/bjnano.5.6

Received: 03 September 2013
Accepted: 12 December 2013
Published: 20 January 2014

This article is part of the Thematic Series "Advanced atomic force microscopy techniques II".

Guest Editors: T. Glatzel and T. Schimmel

Abstract

CdS quantum dots were grown on mesoporous TiO_2 films by successive ionic layer adsorption and reaction processes in order to obtain CdS particles of various sizes. AFM analysis shows that the growth of the CdS particles is a two-step process. The first step is the formation of new crystallites at each deposition cycle. In the next step the pre-deposited crystallites grow to form larger aggregates. Special attention is paid to the estimation of the CdS particle size by X-ray photoelectron spectroscopy (XPS). Among the classical methods of characterization the XPS model is described in detail. In order to make an attempt to validate the XPS model, the results are compared to those obtained from AFM analysis and to the evolution of the band gap energy of the CdS nanoparticles as obtained by UV–vis spectroscopy. The results showed that XPS technique is a powerful tool in the estimation of the CdS particle size. In conjunction with these results, a very good correlation has been found between the number of deposition cycles and the particle size.

Introduction

To sensitize the photocatalyst TiO_2 with cadmium sulfide quantum dots (QDs-CdS) is a well-established concept that is of great relevance in different applications. The most popular of these applications are photosensitized solar cells with high quantum yields [1-4] and the photocatalytic degradation of pollutants [5,6]. CdS, currently used as an efficient visible-light sensitizer, is a semiconductor that possesses a small band gap (2.4 eV) and suitable potential energies. The electron transfer

between QDs-CdS and TiO_2 is due to the different energy levels of the different conduction and valence bands [7]. This transfer takes place if an exciton is generated by the absorption of an incident photon. If the conduction band energy of CdS is higher than that of TiO_2 the electron can be ejected [6].

Several studies reported the strong dependence of the photovoltaic conversion yield and photocatalytic efficiency on the particle size TiO_2 sensitized with QDs-CdS [3,8]. Varying the size of the CdS particles allows for a tuning of the band gap energy of the QDs-CdS in order to reach the required value to sensitize TiO_2. The suitable positions of the potential energies allow for an easy transfer of the exciton between the semiconductors. Not only does that help to optimize the charge separation by reducing the recombination of charges, it also allows for an extension of the photoresponse of the photocatalyst in the visible range. In general, the conventional methods that are used to estimate the average particle size of QDs-CdS are transmission electron microscopy (TEM) [4,8] or X-ray diffraction (XRD) [6], and UV–vis [9] spectroscopy to some extent. The main difficulty when working with very small particles (below 10 nm) is the determination of their exact size [9]. Because of the different morphology, the heterogeneous distribution on the surface and also the support effect some techniques are limited in their use for determination of size. While XRD is restricted by several factors such as the weight fraction or the crystallinity of the sample, TEM is limited by contrast effects between active phase and support [10]. Moreover, in order to get a correct size distribution several images of the same sample at different sites need to be analyzed and a huge number (about 1000) of particles need to be counted [9]. In the case of spectroscopy techniques such as UV–vis spectroscopy combined with effective mass approximation the values of particle size are usually strongly overestimated [11]. However, this technique could be useful in explaining the dependence of the band gap on quantum size effects [9,11-13].

In this study, X-ray photoelectron spectroscopy (XPS) was used for the first time, to the best of our knowledge, to estimate the particle size of QDs-CdS grown on a mesoporous TiO_2 film. The successive ionic layer adsorption and reaction processes, which are defined as deposition cycles, have been applied to get QDs-CdS with variable particle sizes. For the purpose of validation, the results of the particle sizes obtained from XPS are compared to the results obtained from AFM analysis, and to the evolution of the band gap energy of CdS nanoparticles.

Experimental

TiO_2 Film preparation

Mesoporous TiO_2 films were prepared following the procedure reported elsewhere [14]. An adequate amount of titanium(IV) tetraethoxide (TEOT, $Ti(OC_2H_5)_4$, 95% Aldrich) was dissolved under vigourous stirring (20 min) in concentrated hydrochloric acid (37%) at room temperature. In parallel, the hybrid solution was obtained by the addition of dissolved polyethylene glycol hexadecyl ether (denoted Brij 56, $C_{16}H_{33}(OCH_2CH_2)_nOH$, $n \approx 10$, Aldrich) into 1-butanol (BuOH, >99.4%, Alfa Aesar). The final molar ratio of the solution was TEOT/HCl/1-butanol/Brij 56 1:2–4:9:0.05. The solutions were subsequently aged under magnetic stirring at room temperature for 3 h before the films were spin-coated onto soda lime glass (SLG). Prior to use, the substrates were cleaned by ultrasonication (detergent, distilled water, acetone, ethanol, for 15 min in each medium) to remove hydrophobic contaminants at the surface and then air-dried at 150 °C. After the SLG was spin-coated with the hybrid sol with a spin speed of 2000 rpm, the coating was aged at room temperature for 12 h under atmospheric conditions. The xerogel was finally dried at increasing temperatures (6 h at 70 °C, 3 h at 150 °C and 2 h at 200 °C). Mesoporous titania films (degradation of the template agent and inorganic network consolidation) were then obtained by calcination in air at 400 °C over 2 h with a rising step of 1 °C min^{-1}.

Preparation of QDs-CdS-sensitized TiO_2

QDs-CdS were prepared following the procedure previously described by Besson et al. [9]. Briefly, the titania films were dipped for 1 min into a saturated nitrate solution of Cd^{2+} and washed with water for several times in order to eliminate excess reactive species. The deposition of Cd^{2+} was performed under controlled pH (≈10), which was adjusted by adding NaOH solution at 1 M. The chemical process enables a homogeneous adsorption of cationic species in $Ti{-}O^-$ walls [9]. The resulting film was put in a sealed quartz tube under Argon flux, and gaseous H_2S was injected slowly until $P_{H2S} = P_{atm}$. These two steps (impregnation and precipitation) were repeated until the film was saturated. From here on, this procedure will be referred to as one coating; particles of different sizes were obtained by repeating the cycle of the coating procedure. The film impregnated with Cd^{2+} was colorless. After the first H_2S treatment, the film became a light yellow color, and the color intensity increased during the following cycles.

Films characterization

TEM analysis was performed by using a LEO922 electron microscope operating at 200 keV. The film was scratched off from the substrate, dispersed in ethanol and subsequently deposited on copper grids coated with a porous carbon film. The solvent was evaporated in air prior to the analysis of the samples. AFM experiments were performed analogously to [15] by using a Nanoscope V multimode AFM (NanoSurfaces Business, Bruker Corporation, Santa Barbara, CA) in tapping mode (TM-AFM). Etched Si tapping mode cantilevers (TESP type,

Bruker AFM probes), with a nominal curvature radius of 8 nm were used for imaging under ambient conditions (23 °C and 56% relative humidity). Samples were glued onto a magnetic stainless steel disc by using double-face adhesive tape and mounted on the "J" type piezoelectric scanner. The tapping engage set point was set to 1 in order to apply a minimal force to prevent sample deformation during imaging. The images where recorded at a scan rate of 0.5 Hz. The captured raw images were analyzed by using the Nanoscope scan analysis software (Bruker) and flattened to the 0th order to remove any underlying surface curvature. Similarly as described in [16], diffuse reflectance spectra of CdS/titania films were recorded by using an UV–vis spectrophotometer (Carry 5), which was equipped with an integrating sphere. The baseline was set by $BaSO_4$ in the diffuse reflectance mode. The spectra were recorded at room temperature in the spectral range of interest 200–550 nm. XPS analysis was performed on Kratos Axis-ultra spectrometer. Similarly as described in [10], the analysis chamber was operated under ultrahigh vacuum conditions with an approximate pressure of 5×10^{-7} Pa and the sample was irradiated with a monochromatic Al Kα (1486.6 eV) radiation (10 kV; 22 mA). Charge stabilization was achieved by using an electron flood gun adjusted at 8 eV and placing a nickel grid 3 mm above the sample. Pass energy for the analyzer was set to 160 eV for wide scan. The analyzed area was approximately 1.4 mm^2 and the pass energy was set to 50 eV for recording high resolution peaks. In these conditions, the full width at half maximum (FWHM) of the Au $4f_{7/2}$ peak of a clean gold standard sample was about 1.1 eV. The surface atomic concentrations were calculated by correcting the intensities with theoretical sensitivity factors based on Scofield cross-sections [6] and the mean free path varying according to the 0.7th power of the photoelectron kinetic energy. Peak deconvolution was performed by using curves with a 70% Gaussian type and a 30% Lorentzian type, and a Shirley non-linear sigmoid-type baseline. The following peaks were used for the quantitative analysis: O 1s, C 1s, Ti 2p and Cd 3d, Cd 4s and Cd 3s. The Cl 2p, S 2p and N 1s peaks were also monitored and C 1s to check for charge stability as a function of time. CdS (from Fluka, 99.9% analytical grade) was used as the reference material for the study of the prepared materials. For Kratos measurements, (i) sample powders were pressed into small stainless steel troughs mounted on a multi specimen holder; (ii) the C−(C,H) component of the C 1s peak of adventitious carbon was fixed to 284.8 eV to set the binding energy scale; (iii) the data were analyzed using the CasaXPS software (CasaSoftware Ltd, UK).

Results and Discussion

AFM and TEM images

Figure 1a shows the AFM height image of the TiO_2 film with a root mean square (rms) roughness of less than 1 nm. The pore openings are relatively well distributed on the surface with an average size of ca. 6 nm. Figure 1b shows the TEM micrographs of the TiO_2 films obtained by using Brij 56 as template agent. The film shows a homogeneous mesoporous size partially with ordered–disordered regions. The pore size is fairly comparable to that observed in AFM.

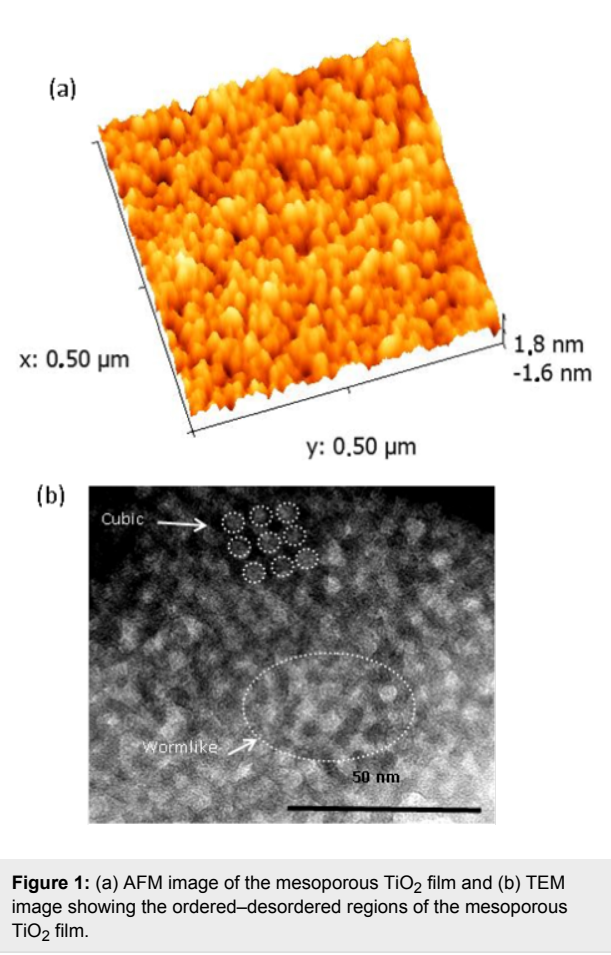

Figure 1: (a) AFM image of the mesoporous TiO_2 film and (b) TEM image showing the ordered–desordered regions of the mesoporous TiO_2 film.

The mesoporous TiO_2 films were exposed to Cd^{2+} and S^{2-} ions by successive immersions in a solution of $Cd(NO_3)_2$, H_2S and water. In order to assess the deposition/growth process, we followed the CdS deposition on mesoporous TiO_2 film by monitoring the absorption spectra, AFM images and XPS (as a new technique to efficiently evaluate the particle size of CdS) at different stages. The successive layers of CdS were deposited onto the TiO_2 film for up to 15 deposition cycles (1, 3, 5, 7, 9 and 15). The deposition time was fixed at 60 s, which was reported as the necessary duration of the nucleation stage [17]. The formation of a $Cd(OH)_2$ thin layer occurs during this stage and the CdS layer grows on it after exposure to H_2S. Upon completion of each cycle, CdS nanoparticles are deposited onto the TiO_2 surface as a layer [3] or localized into the mesoporous structure [9].

AFM analysis performed after 1 to 3 deposition cycles (result not shown) did not show the presence of CdS nanoparticles at the surface of the titanium dioxide films. This result contradicts that obtained by using XPS surface analysis performed on the films, which confirmed the presence of CdS nanoparticles (Table 1, see below). The formation of CdS inside the films pores could explain the discrepancy. Consequently, until up to 3 deposition cycles, CdS nanoparticles probably grow inside the pores of the films and no nanoparticles are observed on the surface. After 3 deposition cycles, AFM images show the presence of CdS nanoparticles on the surface of TiO_2 films. The size of the particles increased with the number of the deposition cycles (5, 7 and 15 deposition cycles). Two kinds of crystals were observed for five deposition cycles ($5\times CdS/TiO_2$) (Figure 2a): separately dispersed CdS nanocrystal behind the very small CdS particles regrouped in aggregates. The formation of the aggregates could result from the accumulation of separated CdS crystals. The size of isolated crystals was smaller than 5 nm as measured from AFM cross-section. With the increase of CdS deposition cycles, the average particle size increased to 8 nm for $7\times CdS/TiO_2$ (Figure 2b), and 10 nm for $15\times CdS/TiO_2$ (Figure 2c). Of note is that despite the presence of few isolated crystallites (5 nm high), the lateral size of the crystals after 15 deposition cycles was remarkably larger than after 7 deposition cycles. This shows that increasing the number of deposition cycles leads to the growth of CdS nanocrytals in two forms; 1) the formation of new crystallites at each depositing cycle, and 2) the growth of pre-deposited crystallites into large aggregates.

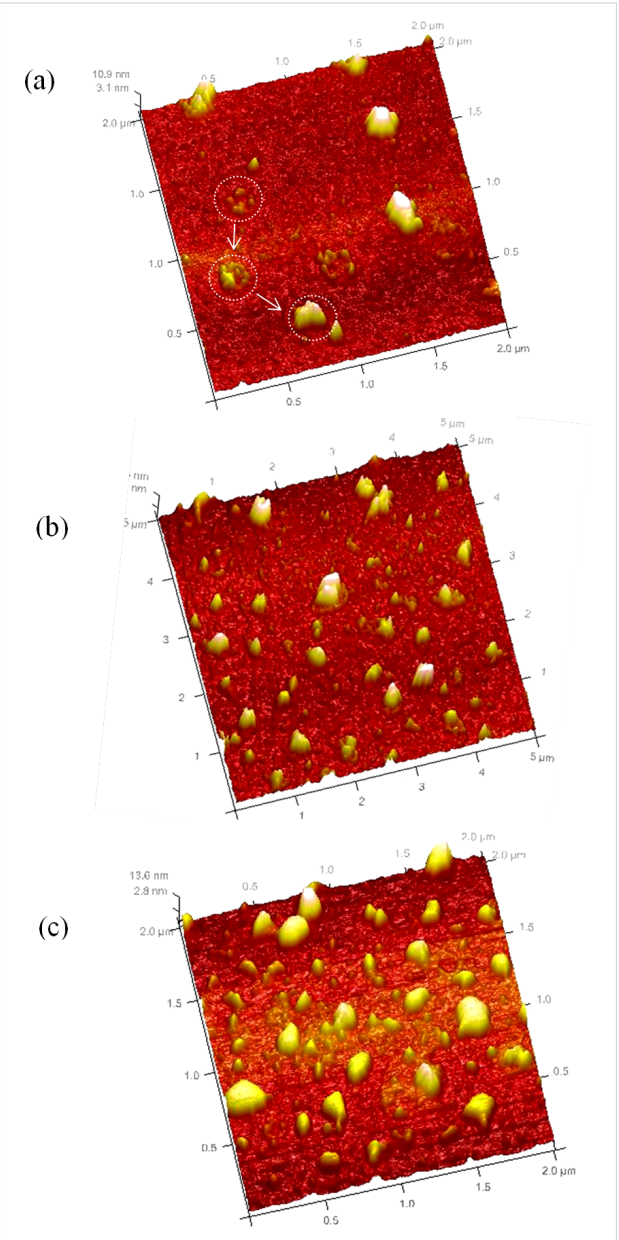

Figure 2: AFM images showing size evolution of CdS particles grown on mesoporous TiO_2 with different number of deposition cycles (a) $5\times CdS/TiO_2$, (b) $7\times CdS/TiO_2$ and (c) $15\times CdS/TiO_2$.

TEM analysis was performed for the $15\times CdS/TiO_2$ sample (Figure 3). It was found that the majority of CdS nanoparticles have a nearly spherical shape with an average particle size of about 10 nm. The TEM study showed the presence of aggregates as a result of spherical particles accumulation, which confirmed our previous hypothesis. The aggregates remain separated from each other, and grow to a diameter of approx. 20 nm. Our data indicate that the growth of the particles inside the pores and the formation of aggregates make the estimation of the average particle size of the CdS nanoparticles by AFM very challenging and result in overestimated values.

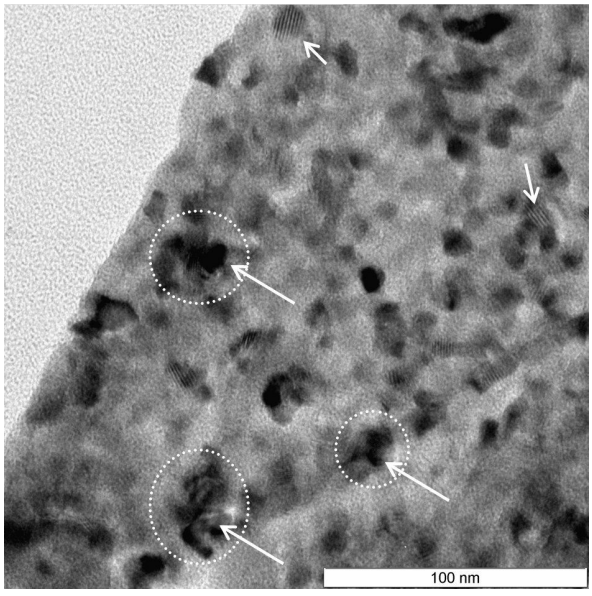

Figure 3: TEM image of the for $15\times CdS/TiO_2$ sample.

UV–vis diffuse reflectance spectroscopy

The absorption spectra recorded for various increasing deposition cycles of CdS quantum dots are shown in Figure 4. The TiO_2 film absorbs only in the UV range ($\lambda < 375$ nm) whereas the absorption edge is shifted to red with successive CdS deposition cycles. The CdS-sensitized TiO_2 film exhibits an absorbance at wavelengths higher than 400 nm, which corresponds to a decrease in the band gap energy. The increase in the absorbance observed for successive deposition cycles confirms the growth of the CdS particles. No significant increase in the absorbance was observed after 15 deposition cycles.

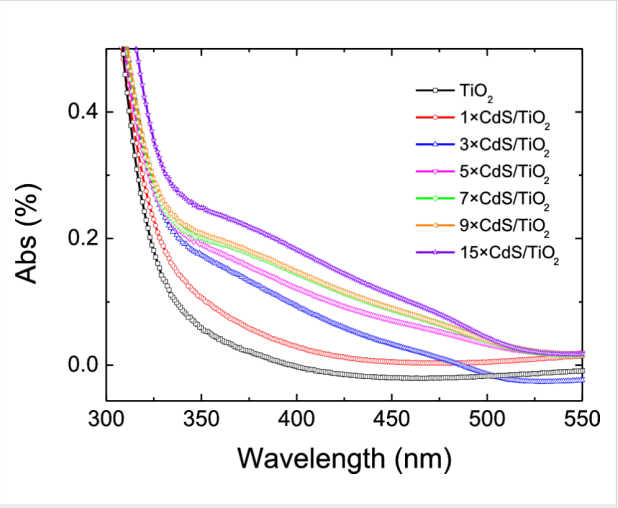

Figure 4: Absorption spectra of the CdS-sensitized titanium dioxide films after different numbers of deposition cycles.

The band gap of the films was determined by extrapolating the fitting line of the onset light absorption to zero. We have assumed that the sensitivity $\alpha \cdot d$ (with α being the absorption coefficient and d being the film thickness) should be of the order of unity or $d \approx 1/\alpha$ and that the scattering was negligible. The band gap of the TiO_2 film is 3.08 eV, which is larger than that of bulk CdS (E_g = 2.4 eV) [1]. Increasing the number of deposition cycles leads to the onset absorption of the films being red-shifted from 333 to 518 nm, indicating a decrease of the band gap energy. The band gap decreases gradually and reaches 2.46 eV for 7×CdS/TiO_2 and further decreases to 2.39 eV for 15×CdS/TiO_2, which is close to the band gap of bulk CdS. The band gap of CdS decreases with the number of deposition cycles used to grow CdS on TiO_2. This result confirms that CdS particles prepared by successive deposition cycles do possess a quantum confinement effect.

XPS analysis of QDs-CdS/TiO_2 films

Elemental analysis

The analysis was carried out on pure TiO_2 and QDs-CdS/TiO_2 samples. The XPS spectra of the principal elements are shown in Figure 5. The spin–orbit components ($2p_{3/2}$ and $2p_{1/2}$) of the Ti 2p peak were well deconvoluted into two curves at 458.5 and 464.2 eV. The measured separation between the Ti $2p_{3/2}$ and Ti $2p_{1/2}$ peaks was 5.7 eV, which is consistent with the binding energy separation observed for stoichiometric TiO_2 [16]. The O 1s peak was deconvoluted into three peaks at 529.8, 530.7 and 532.2 eV for all samples. These can be assigned to oxygen in the O−Ti bonds and O−H bonds of the hydroxy groups and in O−C. The deconvolution of C 1s peak results in four peaks. The one centered at 284.8 and attributed to hydrocarbon is related to the residual carbon coming from the decomposition of the titanium(IV) tetraethoxide precursor and some surface pollution during the XPS analysis. The other peaks are attributed to oxidized forms of carbons, which are usually detected (286.2 eV (C–O); 287.8 eV (C=O, O–C–O) and 288.6 eV (COO) [18]. The Cd $3d_{5/2}$ and Cd $3d_{3/2}$ were found at 411.3 and 404.6 eV respectively for QDs−CdS/TiO_2 and were attributed to Cd^{2+} in CdS [19]. The difference between the binding energies of Cd $3d_{5/2}$ and Cd $3d_{3/2}$ is 6.7 eV, which corresponds to the presence of the oxidation state +2 of Cd 3d at the surface [20]. The S $2p_{3/3}$ peak (Figure 5) was found at 161.8 eV and is attributable to S^{2-} in CdS [21]. The presence of other oxidation states is shown by the peak observed at 167.5 eV, which is due to the presence of sulfate at the surface. The molar concentration of these oxidized states does not exceed 0.6%. Furthermore, no significant variation of the molar concentration of the oxidized states was observed after each step of the deposition cycles. The survey of Cl 2p and N 1s showed only the traces of nitrogen and small quantities of chlorine ions, the molar concentrations of which vary from 1.8 to 2.3% depending on the deposition cycle.

Determination of the QDs-CdS particle size

X-ray photoelectron spectroscopy is usually used to determine the chemical composition of the prepared samples and the valence states of the various species present. In this study we used XPS to determine the particle size of the CdS nanocrystals that were deposited on the TiO_2 films. In the literature, there is evidence that the use of XPS signals could be a useful tool for size measurements of metallic particles [22]. The sizes of nanoparticles can be estimated from the XPS elemental intensity ratios by using an adequate modeling of the signal. Different XPS models could be applied for the estimation of average particle size [10,23,24]. Based on the diamond-shaped support-particles model described by Davis [25], (parameters reported in Table 1), which was used in this study, the average size of metallic nanoparticles was determined by evaluating the intensity ratio between two peaks of the analyzed sample.

However, these two peaks should come from two different electronic levels sufficiently separated in energy. In this work the

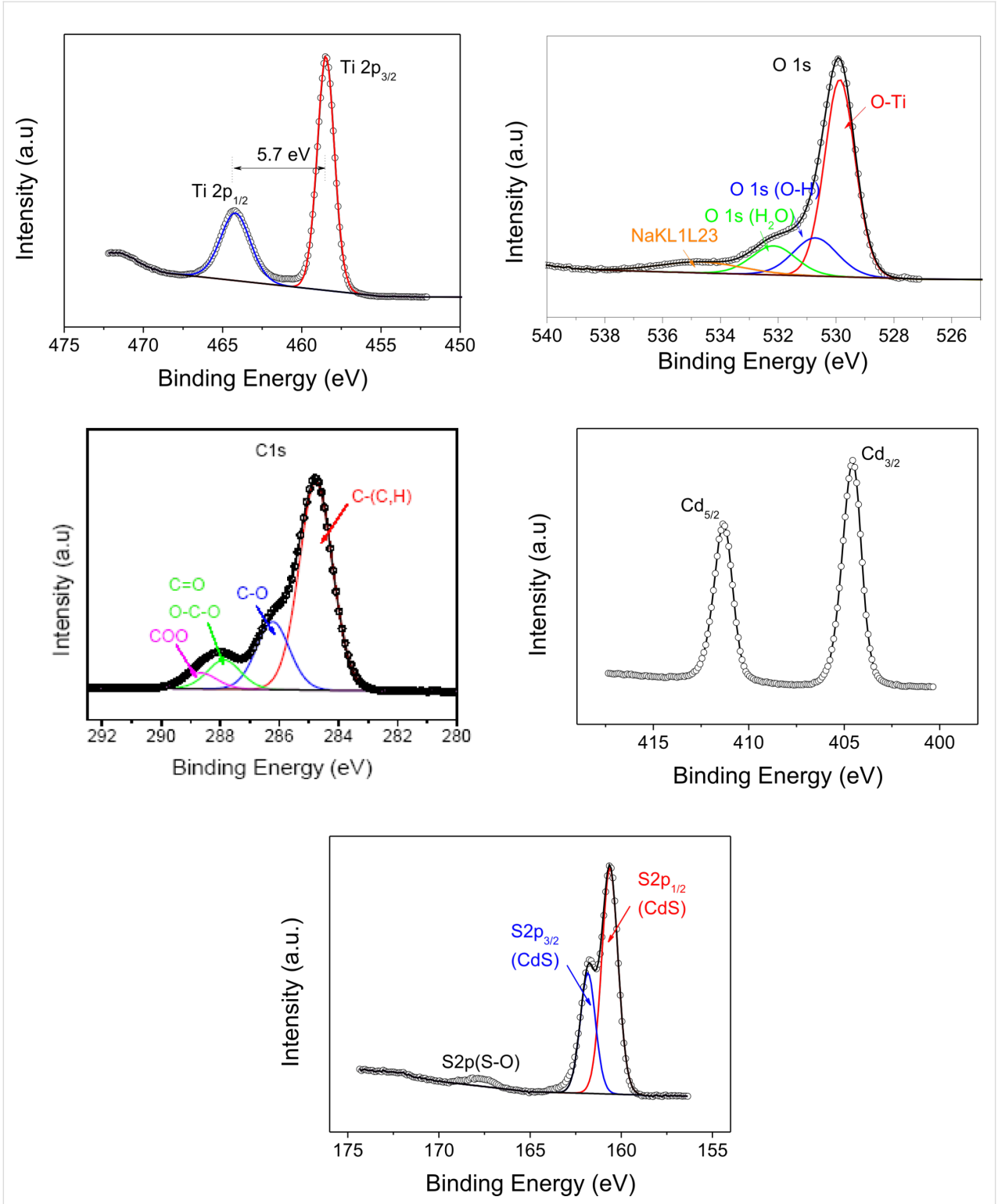

Figure 5: XPS analysis. Spectra of Ti 2p, O 1s, C 1s, Cd 3d and S 2p, and core peaks for 15×CdS/TiO2 sample.

Cd 3s and Cd 4s peaks were chosen as reported in Table 1. This model assumes that the electrons leave the sample under an emission angle of 45° and is more appropriate to determine the size of very small and very big particles [10]. The main advantage in using this model is a certain independence from the physical properties of the sample, such as density, pore struc-

Table 1: Binding energy and peak area ratio of Cd 3s and Cd 4s used for the Davis model.

sample	Cd 3s BE | [eV]	Cd 4s BE [eV]	ratio 3s/4s	particle size [Å]
CdS1	770.7	109.0	3.288	7.0
CdS2	770.4	108.8	3.165	9.0
CdS3	770.4	108.7	2.831	16.0
CdS4	770.4	108.7	2.468	28.0
CdS5	770.3	108.6	2.378	33.0
CdS6	770.3	108.7	2.017	80.0
CdS reference	770.2	108.6	1.886	—

ture or CdS loadings. The influence of the particle shape and surface roughness could be studied by using two different peaks of the same dispersed phase the intensity ratio of which is given in Equation 1:

$$\frac{I_1(d)}{I_2(d)} = \frac{\sigma_1 T_1 \lambda_1 \beta(d,\lambda_1)}{\sigma_2 T_2 \lambda_2 \beta(d,\lambda_2)}, \quad (1)$$

where σ is the photoionization cross section, T is an instrumental transmission function that reflects the basic detection efficiency, λ is the inelastic mean free path (IMFP) of the primary photoelectrons, and β is an attenuation factor, which is dependent on the particle shape and IMFP. The subscripts correspond to the two XPS peaks. Easily derived for different particle sizes by using the relation given by Davis (Equation 2), the attenuation factor (β) strongly depends on the particle shape. In this work the attenuation factor for spherical particles was used as shown in Equation 2, where d is the particle size and could be obtained by iteration [10].

$$\beta(d,\lambda) = 1-(2\lambda^2/d^2)[1-\exp(-d/\lambda)] + (2\lambda/d)\exp(-d/\lambda) \quad (2)$$

The results obtained for CdS plotted by using Equation 1 and Equation 2 are shown in Figure 6a. The normalized intensity ratio (NIR) was calculated from the intensity ratio of pure CdS and the prepared samples. The main parameters are shown in Table 2. The most important parameters for applying the Davis model are the XPS peak areas and the inelastic mean free path length (λ). In our study the values of IMFP were calculated by using the Tougaard Quases-IMFP-TPP2M program [26], which is based on the algorithm proposed by Tanuma [27]. Other essential parameters such as compounds energy band gaps and the Scofield cross sections were taken from [28] and [29] respectively.

Table 2: XPS Parameters used in the Davis model.

	IMFP [nm]		Scofield cross section [eV]	
	λ_{3s}	λ_{4s}	Cd 3s	Cd 4s
Cd	0.959	2.047	3.040	0.692
CdS	1.556	2.557	—	—

The very small CdS particles were observed for the 1×CdS/TiO_2 and 3×CdS/TiO_2 samples (smaller than 1 nm). In contrast, the 15×CdS/TiO_2 sample (15 deposition cycles) showed the biggest particle size (8 nm). It could be concluded that the final size of the particles could be controlled by the preparation method. Indeed, as deduced from the XPS measurements, the final CdS particle size depends on the number of deposition cycles. The smallest particles were formed on 1×CdS/TiO_2 sample after one deposition cycle, whereas the biggest particles were prepared with 15 deposition cycles. A good correlation between CdS particle size and number of deposition cycles was observed (Figure 6b). We propose that the TiO_2 films are covered by spherical grains, the size of which increases with the number of deposition cycles, which is in concordance with UV–vis spectroscopy and AFM studies. The small particles fill the pores of the TiO_2 layer and then cover the surface of the substrate, which leads to a homogeneous layer. In order to illustrate the quantum size effect, the relationship between the optical band gap and the average particle size of CdS made by a different number of deposition cycles is shown in Figure 6c. As deduced from the band-gap and particle-size correlation curves, the smaller the particle size, the larger the band gap. This clearly demonstrates the quantum confinement characteristics of the CdS nanoparticles. The dependence of the optical band gap on the particle size observed in this study is consistent with previously reported data [12].

Conclusion

This article has placed emphasis on the formation of the CdS particles on TiO_2 films and characterizes those by using different methods. We used the XPS model for the first time, to estimate the average particle sizes of CdS quantum dots. Our results confirmed the very good dependence of the CdS particle

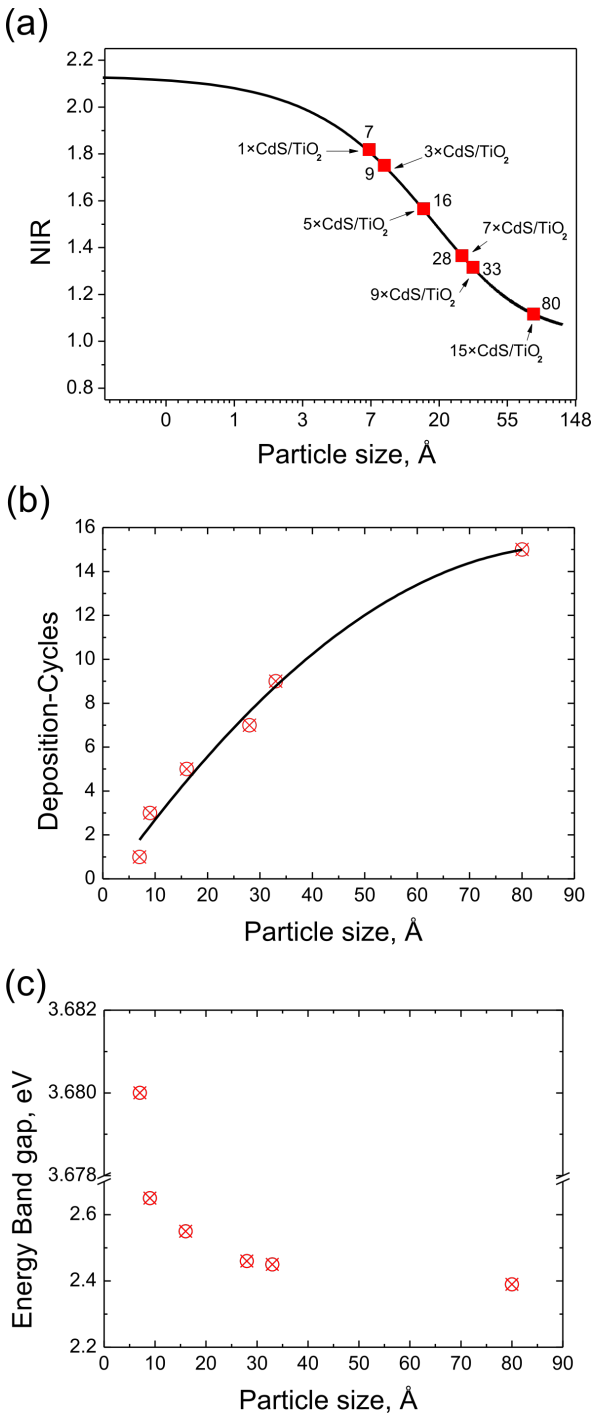

Figure 6: (a) CdS particle size calculated by Davis model vs NIR (normalized intensity ratio calculated from the intensity ratio of pure metal foil and studied material). Particle size evolution vs (b) number of deposition cycles and (c) the band gap energy.

size on the number of successive deposition cycles. Moreover, a very good correlation was observed between results obtained from XPS, AFM and UV-vis. It confirms that XPS is a powerful method for the estimation of the average particle size of CdS quantum dots. We propose that the TiO_2 films are covered by spherical CdS nanoparticles, the size of which increases proportionally to the number of deposition cycles. The small particles accumulated continuously in the pores of the TiO_2 layer and then covered the surface of the substrate, which leads to a homogeneous layer. After each deposition cycle the particles grew following a heterogeneous formation mechanism due to ion-by-ion deposition.

Acknowledgements

The authors are grateful to the ‘‘Région Wallonne’’ (Belgium) for its financial support. M.N.G. is grateful to Pr. J.J. Pireaux and to L. Akhabir for their valuable comments on the manuscript.

References

1. Vogel, R.; Hoyer, P.; Weller, H. *J. Phys. Chem.* **1994,** *98,* 3183–3188. doi:10.1021/j100063a022
2. Jin-nouchi, Y.; Naya, S.; Tada, H. *J. Phys. Chem. C* **2010,** *114,* 16837–16842. doi:10.1021/jp1062226
3. Baker, D. R.; Kamat, P. V. *Adv. Funct. Mater.* **2009,** *19,* 805–811. doi:10.1002/adfm.200801173
4. Lee, H.-J.; Leventis, H. C.; Moon, S.-J.; Chen, P.; Ito, S.; Haque, S. A.; Torres, T.; Nüesch, F.; Geiger, T.; Zakeeruddin, S. M.; Grätzel, M.; Nazeeruddin, M. K. *Adv. Funct. Mater.* **2009,** *19,* 2735–2742. doi:10.1002/adfm.200900081
5. Malashchonak, M. V.; Poznyak, S. K.; Streltsov, E. A.; Kulak, A. I.; Korolik, O. V.; Mazanik, A. V. *Beilstein J. Nanotechnol.* **2013,** *4,* 255–261. doi:10.3762/bjnano.4.27
6. Bessekhouad, Y.; Chaoui, N.; Trzpit, M.; Ghazzal, N.; Robert, D.; Weber, J. V. *J. Photochem. Photobiol., A* **2006,** *183,* 218–224. doi:10.1016/j.jphotochem.2006.03.025
7. Yu, P.; Zhu, K.; Norman, A. G.; Ferrere, S.; Frank, A. J.; Nozik, A. J. *J. Phys. Chem. B* **2006,** *110,* 25451–25454. doi:10.1021/jp064817b
8. Ahmed, R.; Will, G.; Bell, J.; Wang, H. *J. Nanopart. Res.* **2012,** *14,* 1140–1153. doi:10.1007/s11051-012-1140-x
9. Besson, S.; Gacoin, T.; Ricolleau, C.; Jacquiod, C.; Boilot, J.-P. *Nano Lett.* **2002,** *2,* 409–414. doi:10.1021/nl015685v
10. Wojcieszak, R.; Genet, M. J.; Eloy, P.; Ruiz, P.; Gaigneaux, E. M. *J. Phys. Chem. C* **2010,** *114,* 16677–16684. doi:10.1021/jp106956w
11. Lippens, P. E.; Lannoo, M. *Phys. Rev. B* **1989,** *39,* 10935–10942. doi:10.1103/PhysRevB.39.10935
12. Wang, Y.; Herron, N. *Phys. Rev. B* **1990,** *42,* 7253–7255. doi:10.1103/PhysRevB.42.7253
13. Wang, Y.; Suna, A.; Mahler, W.; Kasowski, R. *J. Chem. Phys.* **1987,** *87,* 7315–7322. doi:10.1063/1.453325
14. Ghazzal, M. N.; Kebaili, H.; Joseph, M.; Debecker, D. P.; Eloy, P.; De Coninck, J.; Gaigneaux, E. M. *Appl. Catal., B* **2012,** *115,* 276–284. doi:10.1016/j.apcatb.2011.12.016
15. Raj, G.; Swalus, C.; Guillet, A.; Devillers, M.; Nysten, B.; Gaigneaux, E. M. *Langmuir* **2013,** *29,* 4388–4395. doi:10.1021/la400055t
16. Ghazzal, M. N.; Chaoui, N.; Genet, M.; Gaigneaux, E. M.; Robert, D. *Thin Solid Films* **2011,** *520,* 1147–1154. doi:10.1016/j.tsf.2011.08.097
17. Mazón-Montijo, D. A.; Sotelo-Lerma, M.; Rodríguez-Fernández, L.; Huerta, L. *Appl. Surf. Sci.* **2010,** *256,* 4280–4287. doi:10.1016/j.apsusc.2010.02.015

18. Miller, D. J.; Biesinger, M. C.; McIntyre, N. S. *Surf. Interface Anal.* **2002,** *33,* 299–305. doi:10.1002/sia.1188
19. Xu, F.; Yuan, Y.; Han, H.; Wu, D.; Gao, Z.; Jiang, K. *CrystEngComm* **2012,** *14,* 3615–3622. doi:10.1039/c2ce06267d
20. Yang, G.; Yang, B.; Xiao, T.; Yan, Z. *Appl. Surf. Sci.* **2013,** *283,* 402–410. doi:10.1016/j.apsusc.2013.06.122
21. Bhide, V. G.; Salkalachen, S.; Rastog, A. C.; Rao, C. N. R.; Hegde, M. S. *J. Phys. D: Appl. Phys.* **1981,** *14,* 1647–1656. doi:10.1088/0022-3727/14/9/012
22. Kerkhof, F. P. J. M.; Moulijn, J. A. *J. Phys. Chem.* **1979,** *83,* 1612–1619. doi:10.1021/j100475a011
23. Cimino, A.; Gazzoli, D.; Valigi, M. *J. Electron Spectrosc. Relat. Phenom.* **1999,** *104,* 1–29. doi:10.1016/S0368-2048(98)00300-4
24. Jablonski, A.; Powell, C. J. *Surf. Interface Anal.* **1993,** *20,* 771–786. doi:10.1002/sia.740200906
25. Davis, S. M. *J. Catal.* **1989,** *117,* 432–446. doi:10.1016/0021-9517(89)90353-9
26. QUASES-IMFP-TPP2M program, S. Tougaard. Copyright (c) 2000–2002 Quases-Tougaard Inc.
27. Tanuma, S.; Powell, C. J.; Penn, D. R. *Surf. Interface Anal.* **1994,** *21,* 165–176. doi:10.1002/sia.740210302
28. Strehlow, W. H.; Cook, E. L. *J. Phys. Chem. Ref. Data* **1973,** *2,* 163–199. doi:10.1063/1.3253115
29. Scofield, J. H. *J. Electron Spectrosc. Relat. Phenom.* **1976,** *8,* 129–137. doi:10.1016/0368-2048(76)80015-1

License and Terms

Beilstein Journal of Nanotechnology

Nanoscale patterning of a self-assembled monolayer by modification of the molecule–substrate bond

Cai Shen[1,2] and Manfred Buck[*1]

Full Research Paper

Open Access

Address:
[1]EaStCHEM School of Chemistry, University of St Andrews, St Andrews KY16 9ST, United Kingdom and [2]Ningbo Institute of Materials Technology & Engineering, Chinese Academy of Sciences, Ningbo, 315201, China

Email:
Manfred Buck[*] - mb45@st-andrews.ac.uk

* Corresponding author

Keywords:
copper; electrodeposition; gold adatoms; nanolithography; negative resist

Beilstein J. Nanotechnol. **2014,** *5,* 258–267.
doi:10.3762/bjnano.5.28

Received: 21 November 2013
Accepted: 06 February 2014
Published: 10 March 2014

This article is part of the Thematic Series "Advanced atomic force microscopy techniques II".

Guest Editors: T. Glatzel and T. Schimmel

Abstract

The intercalation of Cu at the interface of a self-assembled monolayer (SAM) and a Au(111)/mica substrate by underpotential deposition (UPD) is studied as a means of high resolution patterning. A SAM of 2-(4'-methylbiphenyl-4-yl)ethanethiol (BP2) prepared in a structural phase that renders the Au substrate completely passive against Cu-UPD, is patterned by modification with the tip of a scanning tunneling microscope. The tip-induced defects act as nucleation sites for Cu-UPD. The lateral diffusion of the metal at the SAM–substrate interface and, thus, the pattern dimensions are controlled by the deposition time. Patterning down to the sub-20 nm range is demonstrated. The difference in strength between the S–Au and S–Cu bond is harnessed to develop the latent Cu-UPD image into a patterned binary SAM. Demonstrated by the exchange of BP2 by adamantanethiol (AdSH) this is accomplished by a sequence of reductive desorption of BP2 in Cu free areas followed by adsorption of AdSH. The appearance of Au adatom islands upon the thiol exchange suggests that the interfacial structures of BP2 and AdSH SAMs are different.

Introduction

The applications of organic adsorbates for the electrodeposition of metals range from tuning the chemistry [1,2] to templating [3,4]. Contrasting the former where random assemblies are used, the latter relies on highly organised layers that comprise supramolecular networks [5,6] or self-assembled monolayers (SAMs) [3,4,7-18]. Exploiting variations in the interfacial charge transfer, SAMs are convenient systems to control the electrodeposition in a potential range both negative (overpotential deposition, OPD) and positive (underpotential deposition [19], UPD) of the Nernst potential. For the more common OPD, SAMs patterned by, for example, e-beam lithography [3,9], electrochemical printing [17], or colloidal masks [18] enable the selective deposition of metal structures and even their transfer to other substrates [4,12].

In contrast, UPD on SAM-modified electrodes yields a mono- or bilayer of metal, which is intercalated at the SAM–substrate interface [20-24]. The interest in this process arises from the alteration in the strength of the S–substrate bond. Following the order Au < Ag < Cu [25] patterning is enabled by a localised UPD of Cu or Ag on Au and the subsequent reductive desorption of the less tightly bound thiol molecules in the UPD-free Au areas to yield either nanoporous SAMs or binary SAMs in the case of backfilling with a second type of thiol [11]. So far, however, this approach has been lacking control as UPD is mediated by random defects [24,26,27] which, using standard SAMs such as alkanethiols, results in the arrangement of pores or domains of different thiols in a statistical fashion, thus, prohibiting patterning and controlling dimensions.

In order to overcome this bottleneck, SAMs are required that exhibit a structural perfection to an extent that UPD does not occur in the case of the native layer but only at defects introduced a posteriori by using lithographic techniques. In previous studies of our group it was found that SAMs of ω-(4'-methylbiphenyl-4-yl)alkanethiols (CH_3-C_6H_4-C_6H_4-$(CH_2)_n$SH, BP*n*) can form layers of exceptional structural perfection [24,28-30], as a consequence of the specific molecular architecture characterised by an aromatic moiety linked to the thiol head group by a short aliphatic chain (see Figure 1a). Designing the molecules such that different factors that determine the enthalpy of the system compete to some extent [28], these SAMs can undergo phase transitions to structures that exhibit the required blocking of UPD. On Au substrates this is the case if the aliphatic spacer chain consists of an even number of methylene units. Two properties of the BP*n* SAMs are decisive for a patterned UPD process. The first one is that imperfections intrinsic to these layers, i.e., defects that cannot be eliminated such as domain boundaries and atomic steps in the underlying substrate, do not impede the passivation of these SAMs against UPD. More substantial defects such as impurities already present on the substrate prior to SAM formation or explicit damaging of the SAM are required. The second one refers to the mechanism of UPD, which is illustrated in Figure 1a. Different from what has been reported for alkanethiols [22,27] the UPD process starts at defects and proceeds via lateral diffusion of the metal atoms at the SAM–substrate interface. Most importantly, the UPD metal is exclusively supplied through the defects, not only in the initial stages of the process but until the whole surface is covered [24]. A crucial feature of the process is that the intercalation of the metal does not affect the passivating properties of the SAM. It is this defect- and diffusion-controlled UPD mechanism that forms the basis for the work presented here as patterned deposition becomes possible by a localised break down of the passivation and control over dimensions of UPD patterns will be exerted through the deposition time and/or the size of defects introduced.

While a range of lithographic techniques involving photons [31], electrons [32], ions [33], or scanning probes [30,34-36] is available for the high-resolution modification of SAMs, the modification by a tip of a scanning tunneling probe was chosen for practical reasons as patterning and characterisation can be conveniently done by the same instrument without altering the experimental setup. This is crucial for enabling the studies presented here, because to find isolated sub-100 nm structures reproducibly would become too tedious otherwise. It is,

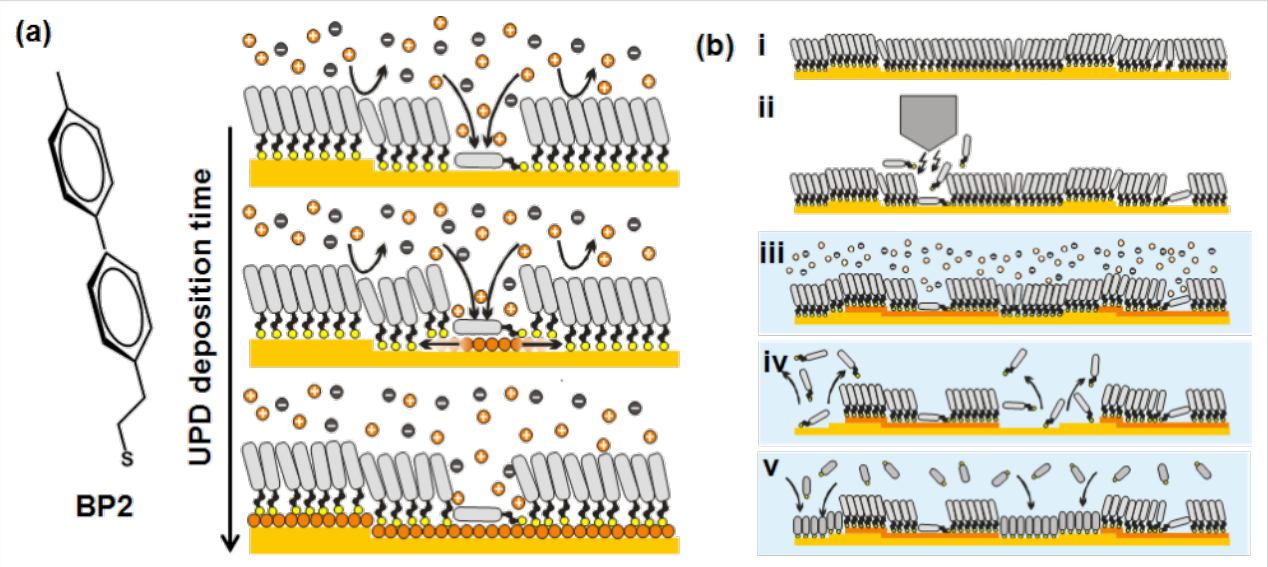

Figure 1: (a) Mechanism of Cu-UPD onto a BP2-modified Au(111) surface with the deposition starting at defects and the UPD proceeding by lateral diffusion of the metal atoms at the SAM–substrate interface. (b) Scheme illustrating the steps in UPD-based patterning. For details see text.

however, noted that this restriction does not apply if one is not interested in mechanistic in situ studies.

The overall process is outlined in Figure 1b. Starting from a high quality SAM (i) defects are introduced (ii) under ambient conditions by applying voltage pulses to the tip [7,8,37,38]. Subsequently, the sample is exposed to the electrolyte that contains the metal ions and UPD is performed (iii). Since, as illustrated in Figure 1a, UPD proceeds via diffusion of the Cu atoms and the deposition rate increases with higher cathodic potentials, the lateral dimensions are determined by controlling deposition time and potential. The UPD-modified SAM can then be further processed by removing the first thiol and then backfill the empty areas by a second thiol (iv), thus, creating a patterned binary SAM (v). It is noted that steps iv/v can be conveniently performed in one setup by reductively desorbing the first thiol in the cathodic sweep of a voltammetric cycle and adsorb the other thiol during the anodic sweep.

Results and Discussion

Patterned UPD

STM images of the UPD of copper on a BP2-modified Au substrate are shown in Figure 2. The typical topography of the SAM-covered substrate is seen in Figure 2a. Due to the thermal treatment of the BP2 layer the smaller terraces are free of vacancy islands (VIs) and those present on more extended terraces are significantly bigger and less dense compared to samples prepared at room temperature. While Ostwald ripening accounts to some extent for this, the phase transition involved in the annealing is another process likely to contribute as discussed further below.

Defects in the SAM are introduced by pulsing the STM tip. The extent of damage depends on the voltage, and a value of 4.5 V was used in this example, which generates defects about 6 nm in size. As seen from Figure 2b the process yields pits of rather uniform size. A look at the line profile reveals that the depth of the depressions is typically 3–4 Å, which is somewhat larger than the 2.5 Å of the step height of the Au substrate. Taking previous studies into account [39] it is likely that thiols are removed together with gold atoms. Due to the lateral mobility thiols also diffuse from areas of the pristine SAM into modified regions. Therefore, the measured height changes are a superposition of topographical changes in the substrate and the SAM. After generation of the pattern in ambient environment the sample is exposed to the $CuSO_4$ electrolyte and the UPD process is monitored in situ by electrochemical STM (EC-STM). According to the mechanism that is illustrated in Figure 1a [24] UPD starts at the defects and spreads radially. The EC-STM image of Figure 2c shows the surface after the growth of the Cu-UPD patterns for about 30 min at +0.275 V. After this period of time the circular UPD features have a diameter in the range of 12–20 nm. The rather anodic potential was applied to slow down the UPD process in order to allow in situ studies of the growth process. It is noted that if one is only interested in the generation of the UPD pattern the process can be significantly accelerated by depositing at more negative potentials or even extending into the OPD region. The features encircled in Figure 2b are interesting as they represent defects right at the edge of a VI and at a substrate step, respectively. They demonstrate that the presence of a step in the substrate does not affect the UPD process, i.e., even in close vicinity of the damaged SAM the passivation of the BP2 SAM across steps

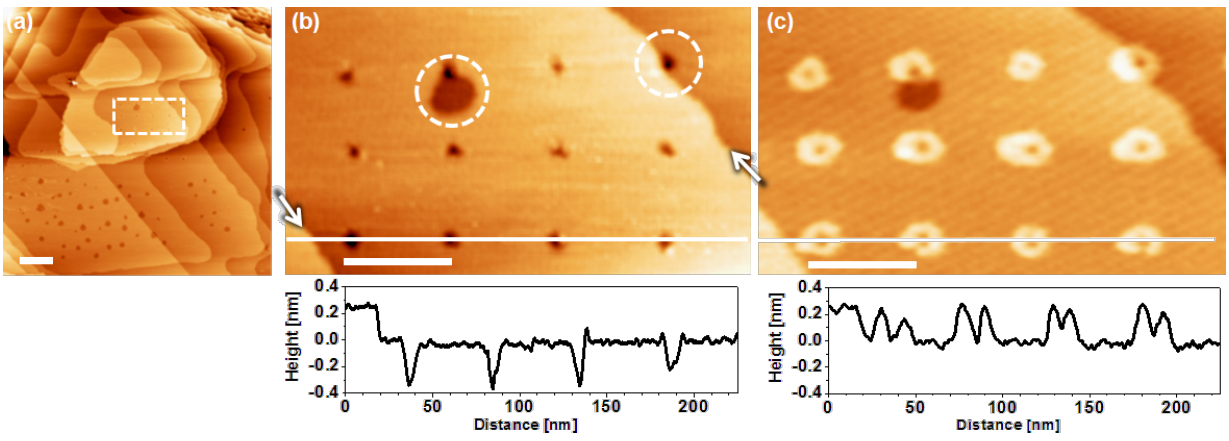

Figure 2: Cu-UPD on Au templated by a patterned BP2 SAM. a) Large scale STM image of the surface before deposition recorded in air. (b) Magnified image of area marked in (a) revealing an array of point defects created by voltage pulses of 4.5 V applied to the STM tip for 50 ms. Steps in the Au substrate are highlighted by the arrows. Dashed circles mark defects at the edge of a vacancy island and step, respectively. (c) In situ electrochemical STM image of the same area after Cu-UPD of 30 min at 0.275 V vs Cu^{2+}/Cu. Height scales in the line profiles are normalised to the Au step height of 2.5 Å. All scale bars 50 nm.

is not affected to the extent that the passivation against UPD breaks down. There is no UPD outside the damaged areas, which confirms the excellent quality of the BP2 SAM.

In experiments, in which we varied the spot size of the damage we noticed that this significantly affects the rate of the UPD process. In agreement with the mechanism established for this type of SAMs [24] this is expected since the growth rate scales with the flux of Cu ions integrated across the defect area. Interestingly, a minimum size of the defect was observed to be required. For defects smaller than 5 nm, it is difficult to trigger the UPD, or even if the UPD starts, the UPD can easily be blocked during the UPD process. This further corroborates that, after removal of thiols by pulsing, thiols diffuse back into the defect from the surrounding area. Obviously, the SAM can bear a certain level of disorder/defects before the passivation against UPD breaks down. Even though it was not a focus of the present study we note that the partial passivation of the defect by SAM molecules also requires substantially more cathodic potentials to initiate the deposition of bulk metal into these holes as compared to a clean Au substrate.

An obvious feature of the UPD mechanism on BP2-modified substrates is to control the dimensions of the deposited metal through the deposition time. This is illustrated in the sequence of STM images depicted in Figure 3, which also illustrates the reproducibility of the process. After generation of the matrix of defects (Figure 3b) by using voltage pulses of 3.8 V/50 ms to yield defects in the range of 7 ± 3 nm, the continued deposition yields growing circular islands (Figure 3c,d) about 10–50 nm in diameter. Figure 3c shows a pattern of Cu-UPD that was formed after 176 min by progressively changing the sample potential from +0.4 V to +0.2 V during this period of time. All UPD islands exhibit a circular shape, with small contour varia-

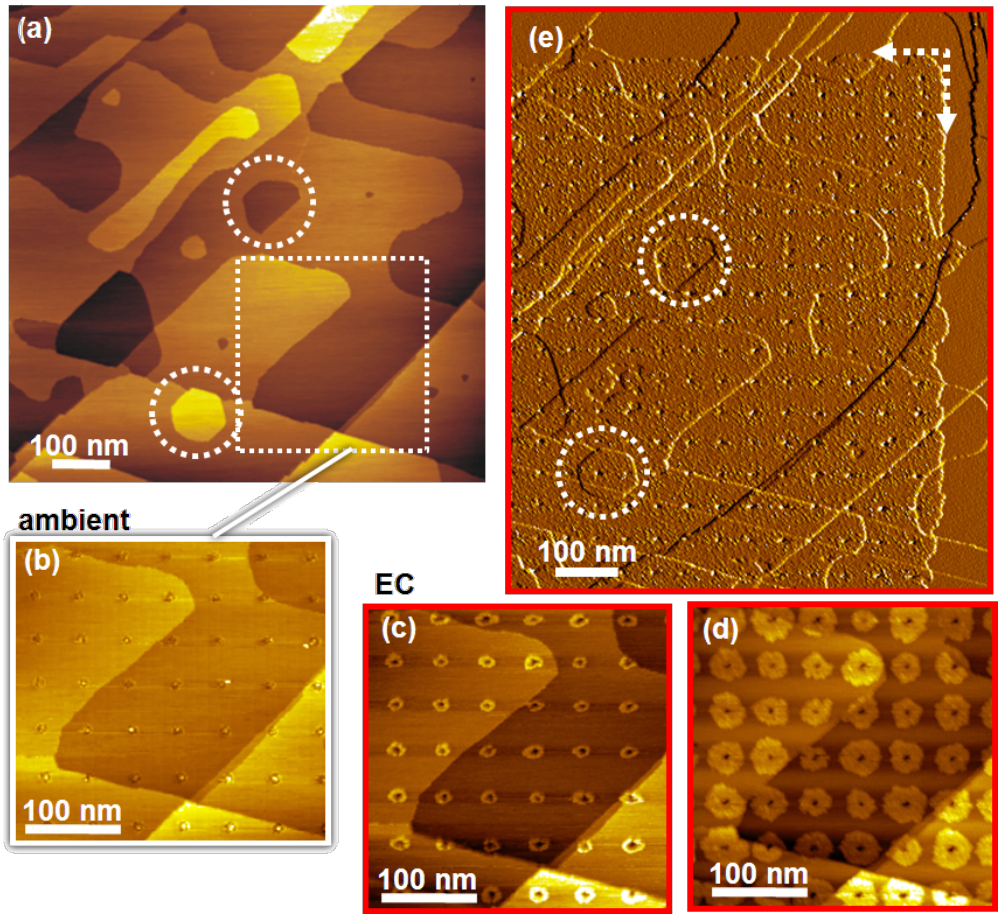

Figure 3: Temporal evolution of Cu-UPD. (a) Large scale ambient STM image of a native BP2 SAM on Au. (b) Magnified image of the area marked by the square in (a) after patterning with voltage pulses of 3.8 V for 50 ms. (c,d) EC-STM images of the area shown in (b) after different periods of UPD, 176 min (c) and 329 min (d) with the sample potential decreased from initially 0.4 V to 0.2 V vs Cu^{2+}/Cu. (e) Large scale STM image after the UPD islands have coalesced to a uniform area. Circles in (a,e) mark identical areas. The dashed arrows in (e) mark boundary between UPD areas and passivated areas. (a–d) show constant current images, in (e) the derivative is shown for better visual differentiation between native and UPD modified areas.

tions at the edges. As the deposition continues the UPD islands grow as evidenced by Figure 3d, which shows the pattern formed after 329 min. The islands are about 30–50 nm in size. Their circular shape is still maintained, which demonstrates that these Cu patterns were formed by the Cu^{2+} ions diffusing radially out from the defects initially created by the STM tip. Ultimately the island coalesce to form a uniform UPD area (Figure 3e), which in the example displayed was accomplished after 486 min at 200 mV. In order to make the uniform deposition more easily visible, the derivative of the current is displayed in Figure 3e. The boundaries between the UPD and unmodified areas are marked by the dashed arrows and the features marked by the dashed circles provide the reference to the large scale image acquired in air prior to UPD.

The procedure is not limited to point like defects as illustrated by Figure 4. By using a bias of 4.2 V and a tip speed of 0.75 µm/s continuous lines such as the letters are written. As for the matrix of point defects, the UPD progresses until areas merge (Figure 4d). A salient feature of this example is the appearance of additional steps during the metal deposition, which is highlighted by the height profiles along the lines shown in Figure 4b and 4c and reflected by an integral step height of 1 nm and 2.5 nm prior and during deposition, respectively. Marked by arrows in the line profile of Figure 4c, the six additional steps that emerge during the electrodeposition are identical in height to the 2.5 Å of the Au steps present on the native substrate, thus, strongly suggesting that the Cu-UPD gives rise to dislocations in the Au surface. The tensile stress introduced by the Cu-UPD [40,41] adds to the stress already present in the substrate as a result of the preparation process and of defects in the mica substrate [42]. Obviously, the additional stress introduced by the UPD of Cu exceeds the threshold required to trigger a substrate relaxation by generating steps. As it can clearly be seen from Figure 4c and Figure 4d there is neither a penetration of UPD metal at newly created steps nor a preferen-

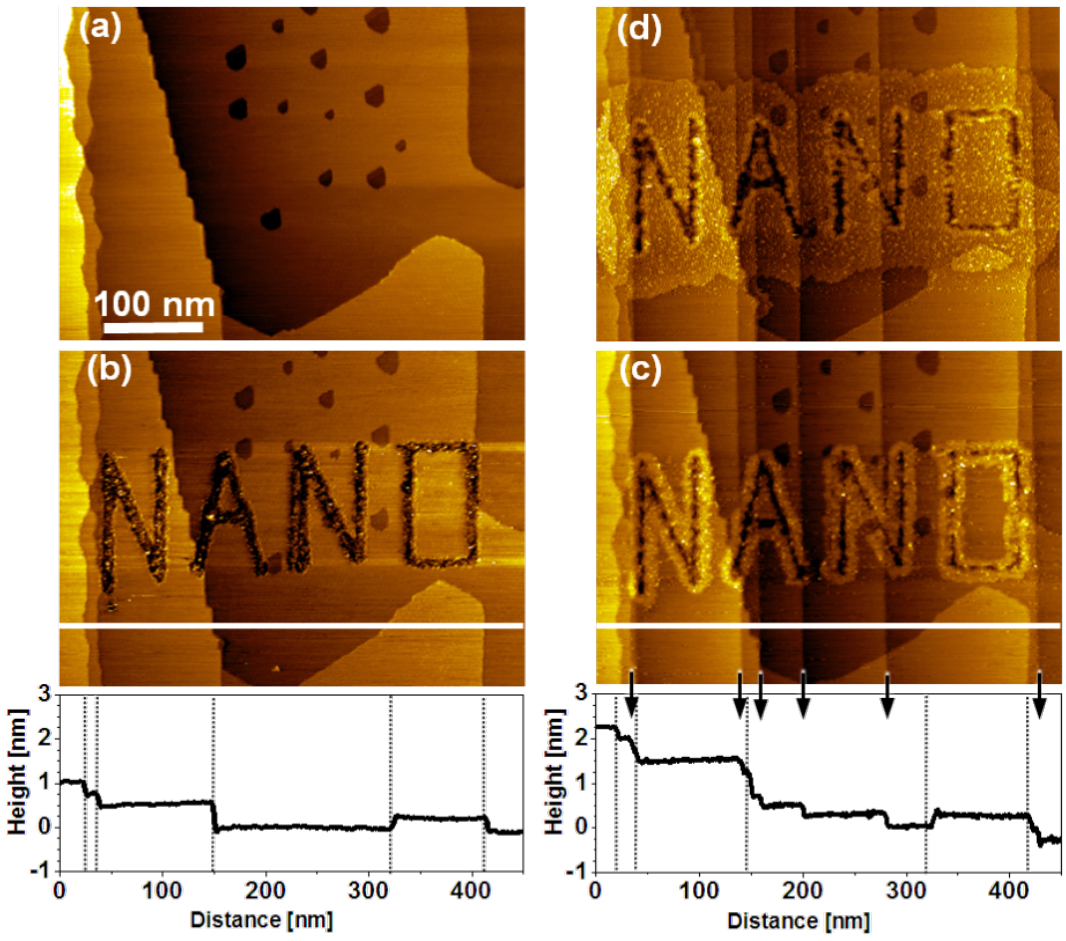

Figure 4: Templated Cu-UPD illustrating tolerance of the process against substrate dislocations. (a) Native substrate with uniform BP2 SAM. (b) Lithographic pattern formed in air by using a tip bias of 4.2 V and a tip speed of 0.75 µm/s. (c) EC-STM images of Cu-UPD after 11 min at 0.16 V vs Cu^{2+}/Cu. (d) Uniform UPD area after 32 min. Dotted lines and arrows in height profiles along lines shown in (b,c) mark substrate steps present in the native substrate and generated during UPD, respectively.

tial diffusion of UPD metal along those steps. Thus, possible structural differences between a BP2 SAM that covers a native step in the initial preparation procedure and one being generated during the UPD process are too small to alter the UPD mechanism. This is essential for the exploitation of this process on the nanoscale as the UPD pattern and, thus, its spatial resolution is not impeded by processes that cannot be eliminated.

The ruggedness of the BP2 SAM structure against the generation of Au steps, which is induced by the UPD, is in line with the preserved passivation of the monolayer at steps of Cu-UPD islands intercalated at the SAM–substrate interface [24]. However, the distinct generation of Au steps in the example presented above suggests that the STM patterning itself has an influence. While for a small point-shaped damage dislocations in the substrate occur rarely (none in Figure 2, one in Figure 3 intersecting the encircled island in the lower half of image (e)) the more extensive damage of the SAM by writing continuous lines (here in the form of letters) gives rise to a substantial number of substrate dislocations. This can be rationalized by considering that at least the topmost Au layer is affected, which includes the removal of Au atoms together with thiol molecules.

Conversion of UPD pattern into binary SAM structure

The SAM modified by the UPD pattern corresponds to a latent image, which has to be developed by, for example, conversion into a pattern that exhibits heterogeneous surface properties as illustrated in Figure 1b. As mentioned above this is conveniently done by exploiting the differences in the strength of the S–metal bond between Au and Ag and Cu [25]. While the selective removal of thiols from UPD-free Au areas has been exploited for the generation of nanoporous SAMs [11], the process lacked control as UPD occurred at defects present in the native monolayer. The approach based on the SAMs used here, which perfectly block UPD, allows for the exploitation of this principle for the controlled patterning on the nanoscale.

The concept is demonstrated in Figure 5, which shows a series of STM images that comprise the native (a), STM patterned (b),

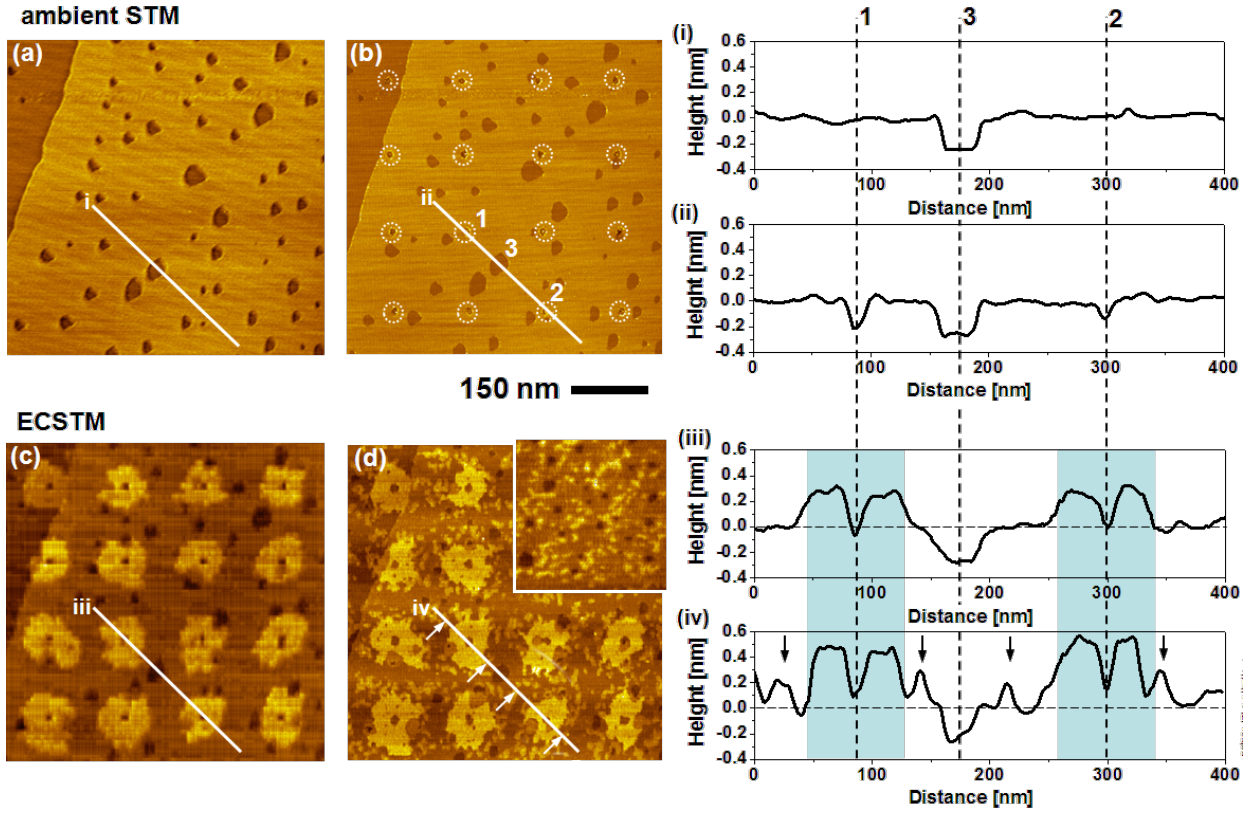

Figure 5: Sequence of STM images showing the UPD-based conversion of a BP2 SAM into a patterned binary SAM of BP2 and AdSH. Left: (a) Native BP2 SAM. b) Array of defects (encircled) created by STM lithography while using voltage pulses of 3.5 V and 50 ms duration. (c) Pattern of Cu-UPD generated by holding the sample potential at +0.3 V vs Cu^{2+}/Cu for 10 seconds. (d) Binary SAM structure after reductive desorption of BP2 and adsorption of AdSH. The inset shows an area of the sample, which had not been modified by Cu-UPD. Right: Compilation of height profiles along lines shown in the STM images illustrating the evolution of topography. Protrusions marked by arrows in (iv) reflect AdSH covered Au islands. For details see text.

and UPD modified BP2 SAM (c), as well as the binary SAM (d), where BP2 adsorbed on Au has been replaced by adamantanethiol (AdSH). The exchange was accomplished by performing a voltammetric cycle, in which the reductive desorption of BP2 and the adsorption of AdSH occured during the cathodic and anodic sweeps, respectively. In the present experiment a basic solution of AdSH in EtOH was used. The successful exchange of the thiol is probed by a second cyclic voltammogram. An anodic shift of the desorption potential by about 35–40 mV (see Figure S1 in Supporting Information File 1) is characteristic for the difference in stability between the two thiols [43]. The exchange is also evidenced by characteristic differences seen in the STM images recorded before (Figure 5c) and after (Figure 5d) the replacement of BP2 in the areas, which were not covered by UPD islands. The most obvious one is that the contours of the islands become rather ill-defined and protrusions appear in between the UPD islands. While, at first glance, this seems like a serious deterioration of the shape of the islands, a closer look reveals that the contours of the islands such as shape asymmetries and irregularities are rather well preserved. The topographical changes are mainly due to the restructuring of the Au surface upon desorption of BP2. The fact that exactly the same topographical changes occur in areas of the sample where the SAM has not been patterned (inset in Figure 5d) proves that these features are not related to Cu-UPD. The formation of the protrusions agrees well with other studies of thiol desorption [44,45] and is explained by the formation of Au islands from Au adatoms present at the SAM–Au interface [46-48]. There is, however, a difference between the present study and other studies, in which island formation has been observed. Any Au islands formed during the desorption of BP2 should be consumed again when the other thiol is adsorbed. The extent to which this occurs is dependent on how similar the structures of the SAM–substrate interface are for the two thiols. Since the adamantanethiol packs less dense compared to BP2 (≈40 $Å^2$ per molecule compared to ≈29 $Å^2$) it is expected that Au islands remain after the adsorption of the adamantanethiol. However, the integrated area covered by the islands is unexpectedly large. Assuming that the number of Au adatoms involved is identical for BP2 and AdSH and that the same bonding configuration discussed for alkanethiols is adopted involving either one Au adatom per molecule or shared between two thiols, the area covered by islands should be about 3.5–7.0% of a monolayer after the exchange. This is significantly smaller than the experimentally observed area covered by islands, which amounts to at least 20%. It is noted that this rough estimation assumes i) a full monolayer of AdSH, ii) a packing density of atoms in the islands equal to that of bulk Au, and iii) a negligible effect of the tip shape on the measured island area. While a full monolayer might not have been formed (see CV) the coverage is not that low that it can account for the difference in numbers. Even though this conclusion is tentative and has to be backed by a separate, more detailed study it raises the question to what extent the structures of the SAM–substrate interface discussed for alkane thiols are realised in thiol SAMs whose packing densities are rather different. It is noted at this point that it has been argued that the pronounced phase transitions observed in BP*n* SAMs with *n* = even are hard to understand without a substantial restructuring of the SAM–Au interface [28,29].

The exchange of BP2 by AdSH is also reflected by a change in the relative height of the UPD islands. For the sample uniformly covered by BP2 (profile iii in Figure 5) the islands exhibit a height of 2.5–3.0 Å, which is in agreement with previous studies for this system [24]. After replacement the height has increased to 4–5 Å (profile iv), which is expected considering the smaller size of AdSH compared to BP2 and the aliphatic nature compared to the aromatic system.

Conclusion

Thiol SAMs based on a molecular architecture, which combines structure determining factors in a competing manner [28], can be prepared in a polymorph, in which defects are eliminated to the extent that a gold electrode is completely passivated against UPD of Cu. This introduces new opportunities for the structuring of SAM on the nanoscale, as the deposition of copper is not determined anymore by randomly distributed defects that are usually present in a native SAM [11]. Instead, patterns of Cu-UPD can be freely defined by generating defects in a controlled fashion. Additional degrees of freedom are provided by the rate of the Cu deposition, which is determined by the size of the defects, and the deposition time, through which the extent of lateral diffusion of Cu at the SAM-substrate interface and, thus, the size of features is defined. In contrast to other patterning schemes, in which the final structure is a replica of the lithographic pattern, this allows to enlarge features and, thus, reduce the effort in the lithographic step, which is of advantage in high resolution patterning that use serial tip or beam based techniques.

The local modification of the sulfur–substrate bond by intercalation of Cu at the Au–substrate interface yields a latent image, which is straightforwardly developed into a patterned binary SAM. Harnessing the significant difference in the strength of the S–Au and S–Cu bond this involves a potential-controlled reductive desorption of the thiol in areas that are not modified by Cu-UPD followed by the adsorption of a second thiol. As such it is a negative resist technique and, thus, complementary to other lithography based schemes such as grafting [35], in which the replacement takes place in the written areas.

While patterning on a scale down to less than 20 nm has been demonstrated it has to be seen how far this patterning scheme can be extended towards the bottom end of the nanoscale. The factors that limit resolution and accuracy at present are related to the precision, at which defects in the SAM can be made and how well the diffusion of both the thiols and the intercalated Cu can be controlled. The use of, for example, an ion beam for SAM patterning instead of the voltage induced generation of defects is anticipated to further improve the accuracy and reproducibility of the Cu-UPD. The timing in the thiol substitution is another parameter to be optimised in order to minimise the blurring of contours by the diffusion of species. While UPD-based patterning has been demonstrated here for the generation of a binary SAM the scope of this scheme reaches further. In particular, the contrast in charge-transfer properties between the passivating UPD-modified SAM islands and the active electrode areas, which are generated by reductive desorption of thiols, makes the scheme attractive for electrodeposition on the nanoscale. An extension to other metals, which include catalytically active or magnetic metals deposited at both underpotential and overpotential, or to semiconductors makes the present scheme interesting for the generation of functional nanostructures. Furthermore, a deposition in the overpotential range at the defects offers the possibility to generate well-defined arrays of metal clusters provided the size of the defects in the SAM can be precisely controlled.

Experimental

SAM preparation. 2-(4'-Methylbiphenyl-4-yl)ethanethiol (BP2) was synthesized as described previously [49]. Adamantanethiol (Sigma-Aldrich) and absolute ethanol (BDH) were used as received. Substrates (300 nm Au film on mica) were purchased from Georg Albert PVD, Heidelberg, Germany and flame annealed prior to the preparation of the SAMs. BP2 SAMs were prepared by following a procedure described elsewhere [50]. The samples were immersed into solutions of 1 mM BP2 in ethanol at 345 K for about 15 h. After rinsing and blowing dry with nitrogen, the samples were annealed in a sealed container under nitrogen atmosphere at 418 K for about 10 h. The annealing transforms the SAM structure that was obtained at room temperature into the highly ordered δ-phase [50], which is used in the experiments.

STM. Structural characterisation and patterning was done with a PicoPlus microscope (Molecular Imaging) including a bipotentiostat and PicoLITH software. The tips were fabricated by chemically etching a Pt/Ir (80:20, GoodFellow) wire in a 2 M KSCN/0.5 M KOH mixture applying an AC current. Subsequently, they were coated with polyethylene to minimize Faradaic currents. Typical tunneling parameters were in the range of 50 pA, 0.5 V for imaging in air, and 50 pA, 0.17–0.30 V for EC-STM.

Patterning and deposition. For patterning of the BP2 SAM and the subsequent Cu-UPD, the sample was mounted on a sample plate inside a custom-built EC-STM Teflon cell and positioned in the STM. After patterning under ambient atmosphere the electrochemical cell was filled without moving the sample. For Cu-UPD an aqueous solution of 50 mM $CuSO_4$/50 mM H_2SO_4, and Pt and Cu wires serving as counter and reference electrodes were used. All potentials are referenced to Cu^{2+}/Cu. Before filling in the electrolyte, the sample potential was set to +0.4 V. UPD was performed at potentials in the range of 0–300 mV, depending on the desired deposition rate.

Generation of binary SAM. The exchange of BP2 by AdSH was done in a 0.1 M KOH ethanol solution containing 1 mM AdSH. In a single voltammetric cycle BP2 was desorbed in the cathodic sweep and AdSH adsorbed during the anodic sweep. The scan rate was set to 0.1 V/s. The successful exchange was verified by a second cycle, which showed a cathodic shift in the desorption potential (see Figure S1 in Supporting Information File 1), in accordance with the lower stability of an AdSH SAM compared to a BP2 SAM [43]. It is noted that the smaller peak area of the AdSH peak arises from the lower packing density of the AdSH molecules compared to BP2. The thiol exchange experiments were performed by removing the sample holder from the STM after Cu-UPD, then replace the Cu electrolyte by the AdSH containing electrolyte and swap the Cu reference electrode for Pt. To find the submicrometer patterns again after remounting the sample in the STM, a custom-made base plate was used with indentations that allow for a reproducible repositioning of the sample. However, due to the limited precision a scanner with a larger range (100 × 100 μm^2) was used, in contrast to the experiments involving only patterning and UPD, which were also possible with a small range scanner (1.5 × 1.5 μm^2).

Supporting Information

A sequence of two linear sweep voltammograms is presented, which show the anodic shift in the reductive desorption peak of the thiol upon replacement of BP2 by AdSH.

Supporting Information File 1

Further experimental data.
[http://www.beilstein-journals.org/bjnano/content/supplementary/2190-4286-5-28-S1.pdf]

Acknowledgements

Financial support by the EU (STRP032109) and EPSRC (EP/D048761/1) is gratefully acknowledged.

References

1. Moffat, T. P.; Josell, D. *Isr. J. Chem.* **2010,** *50,* 312–320. doi:10.1002/ijch.201000029
2. Hai, N. T. M.; Krämer, K. W.; Fluegel, A.; Arnold, M.; Mayer, D.; Broekmann, P. *Electrochim. Acta* **2012,** *83,* 367–375. doi:10.1016/j.electacta.2012.07.036
3. Sondag-Huethorst, J. A. M.; van Helleputte, H. R. J.; Fokkink, L. G. J. *Appl. Phys. Lett.* **1994,** *64,* 285–287. doi:10.1063/1.111182
4. She, Z.; DiFalco, A.; Hähner, G.; Buck, M. *Beilstein J. Nanotechnol.* **2012,** *3,* 101–113. doi:10.3762/bjnano.3.11
5. Allred, D. B.; Sarikaya, M.; Baneyx, F.; Schwartz, D. T. *Nano Lett.* **2005,** *5,* 609–613. doi:10.1021/nl047967b
6. Silien, C.; Räisänen, M. T.; Buck, M. *Angew. Chem., Int. Ed.* **2009,** *48,* 3349–3352. doi:10.1002/anie.200806267
7. Schoer, J. K.; Ross, C. B.; Crooks, R. M.; Corbitt, T. S.; Hampden-Smith, M. J. *Langmuir* **1994,** *10,* 615–618. doi:10.1021/la00015a002
8. Zamborini, F. P.; Crooks, R. M. *J. Am. Chem. Soc.* **1998,** *120,* 9700–9701. doi:10.1021/ja9821955
9. Felgenhauer, T.; Yan, C.; Geyer, W.; Rong, H.-T.; Gölzhäuser, A.; Buck, M. *Appl. Phys. Lett.* **2001,** *79,* 3323–3325. doi:10.1063/1.1415771
10. Cavalleri, O.; Gilbert, S. E.; Kern, K. *Chem. Phys. Lett.* **1997,** *269,* 479–484. doi:10.1016/S0009-2614(97)00317-5
11. Oyamatsu, D.; Kanemoto, H.; Kuwabata, S.; Yoneyama, H. *J. Electroanal. Chem.* **2001,** *497,* 97–105. doi:10.1016/S0022-0728(00)00459-9
12. Thom, I.; Hähner, G.; Buck, M. *Appl. Phys. Lett.* **2005,** *87,* 024101. doi:10.1063/1.1991992
13. Baunach, T.; Ivanova, V.; Kolb, D. M.; Boyen, H.-G.; Ziemann, P.; Büttner, M.; Oelhafen, P. *Adv. Mater.* **2004,** *16,* 2024–2028. doi:10.1002/adma.200400409
14. Langerock, S.; Ménard, H.; Rowntree, P.; Heerman, L. *Langmuir* **2005,** *21,* 5124–5133. doi:10.1021/la050078z
15. Pesika, N. S.; Radisic, A.; Stebe, K. J.; Searson, P. C. *Nano Lett.* **2006,** *6,* 1023–1026. doi:10.1021/nl060368f
16. Pesika, N. S.; Fan, F.; Searson, P. C.; Stebe, K. J. *J. Am. Chem. Soc.* **2005,** *127,* 11960–11962. doi:10.1021/ja050955n
17. Nelson, J. B.; Schwartz, D. T. *Langmuir* **2007,** *23,* 9661–9666. doi:10.1021/la701014u
18. Wang, J.; Duan, G.; Li, Y.; Liu, G.; Dai, Z.; Zhang, H.; Cai, W. *Langmuir* **2013,** *29,* 3512–3517. doi:10.1021/la400433z
19. Herrero, E.; Buller, L. J.; Abruña, H. D. *Chem. Rev.* **2001,** *101,* 1897–1930. doi:10.1021/cr9600363
20. Nishizawa, M.; Sunagawa, T.; Yoneyama, H. *Langmuir* **1997,** *13,* 5215–5217. doi:10.1021/la970545f
21. Cavalleri, O.; Bittner, A. M.; Kind, H.; Kern, K. *Z. Phys. Chem.* **1999,** *208,* 107–136. doi:10.1524/zpch.1999.208.Part_1_2.107
22. Epple, M.; Bittner, A. M.; Kuhnke, A.; Kern, K.; Zheng, W.-Q.; Tadjeddine, A. *Langmuir* **2002,** *18,* 773–784. doi:10.1021/la0109819
23. Hagenström, H.; Esplandiú, M. J.; Kolb, D. M. *Langmuir* **2001,** *17,* 839–848. doi:10.1021/la001140p
24. Silien, C.; Buck, M. *J. Phys. Chem. C* **2008,** *112,* 3881–3890. doi:10.1021/jp710947r
25. Oyamatsu, D.; Kuwabata, S.; Yoneyama, H. *J. Electroanal. Chem.* **1999,** *473,* 59–67. doi:10.1016/S0022-0728(99)00104-7
26. Sun, L.; Crooks, R. M. *J. Electrochem. Soc.* **1991,** *138,* L23–L25. doi:10.1149/1.2086000
27. Oyamatsu, D.; Nishizawa, M.; Kuwabata, S.; Yoneyama, H. *Langmuir* **1998,** *14,* 3298–3302. doi:10.1021/la970984e
28. Cyganik, P.; Buck, M.; Strunskus, T.; Shaporenko, A.; Wilton-Ely, J. D. E. T.; Zharnikov, M.; Wöll, C. *J. Am. Chem. Soc.* **2006,** *128,* 13868–13878. doi:10.1021/ja0640647
29. Cyganik, P.; Buck, M. *J. Am. Chem. Soc.* **2004,** *126,* 5960–5961. doi:10.1021/ja049146e
30. Shen, C.; Buck, M. *Nanotechnology* **2009,** *20,* 245306. doi:10.1088/0957-4484/20/24/245306
31. Leggett, G. J. *Chem. Soc. Rev.* **2006,** *35,* 1150–1161. doi:10.1039/b606706a
32. Turchanin, A.; Gölzhäuser, A. *Prog. Surf. Sci.* **2012,** *87,* 108–162. doi:10.1016/j.progsurf.2012.05.001
33. Ada, E. T.; Hanley, L.; Etchin, S.; Melngailis, J.; Dressick, W. J.; Chen, M.-S.; Calvert, J. M. *J. Vac. Sci. Technol., B* **1995,** *13,* 2189–2196. doi:10.1116/1.588102
34. Wilhelm, T.; Wittstock, G. *Electrochim. Acta* **2001,** *47,* 275–281. doi:10.1016/S0013-4686(01)00566-7
35. Liu, M.; Amro, N. A.; Liu, G.-y. *Annu. Rev. Phys. Chem.* **2008,** *59,* 367–386. doi:10.1146/annurev.physchem.58.032806.104542
36. Krämer, S.; Fuierer, R. R.; Gorman, C. B. *Chem. Rev.* **2003,** *103,* 4367–4418. doi:10.1021/cr020704m
37. Mizutani, W.; Ishida, T.; Tokumoto, H. *Langmuir* **1998,** *14,* 7197–7202. doi:10.1021/la9804379
38. Fuierer, R. R.; Carroll, R. L.; Feldheim, D. L.; Gorman, C. B. *Adv. Mater.* **2002,** *14,* 154–157. doi:10.1002/1521-4095(20020116)14:2<154::AID-ADMA154>3.0.CO;2-B
39. Keel, J. M.; Yin, J.; Guo, Q.; Palmer, R. E. *J. Chem. Phys.* **2002,** *116,* 7151–7157. doi:10.1063/1.1464816
40. Haiss, W.; Sass, J.-K. *Langmuir* **1996,** *12,* 4311–4313. doi:10.1021/la9602224
41. Kongstein, O. E.; Bertocci, U.; Stafford, G. R. *J. Electrochem. Soc.* **2005,** *152,* C116–C123. doi:10.1149/1.1854093
42. Lüssem, B.; Karthäuser, S.; Haselier, H.; Waser, R. *Appl. Surf. Sci.* **2005,** *249,* 197–202. doi:10.1016/j.apsusc.2004.11.082
43. Silien, C.; Räisänen, M. T.; Buck, M. *Small* **2010,** *6,* 391–394. doi:10.1002/smll.200901909
44. Taylor, R.; Torr, N.; Huang, Z.; Li, F.; Guo, Q. *Surf. Sci.* **2010,** *604,* 165–170. doi:10.1016/j.susc.2009.10.034
45. Kautz, N. A.; Kandel, S. A. *J. Am. Chem. Soc.* **2008,** *130,* 6908–6909. doi:10.1021/ja8011325
46. Maksymovych, P.; Yates, J. T., Jr. *J. Am. Chem. Soc.* **2008,** *130,* 7518–7519. doi:10.1021/ja800577w
47. Chaudhuri, A.; Odelius, M.; Jones, R. G.; Lee, T.-L.; Detlefs, B.; Woodruff, D. P. *J. Chem. Phys.* **2009,** *130,* 124708. doi:10.1063/1.3102095
48. Chesneau, F.; Zhao, J.; Shen, C.; Buck, M.; Zharnikov, M. *J. Phys. Chem. C* **2010,** *114,* 7112–7119. doi:10.1021/jp100522n
49. Rong, H.-T.; Frey, S.; Yang, Y.-J.; Zharnikov, M.; Buck, M.; Wühn, M.; Wöll, C.; Helmchen, G. *Langmuir* **2001,** *17,* 1582–1593. doi:10.1021/la0014050
50. Cyganik, P.; Buck, M.; Strunskus, T.; Shaporenko, A.; Witte, G.; Zharnikov, M.; Wöll, C. *J. Phys. Chem. C* **2007,** *111,* 16909–16919. doi:10.1021/jp073979k

Beilstein Journal of Nanotechnology

Control theory for scanning probe microscopy revisited

Julian Stirling

Full Research Paper

Open Access

Address:
School of Physics and Astronomy, The University of Nottingham, University Park, Nottingham, NG7 2RD, United Kingdom

Email:
Julian Stirling - Julian.Stirling@nottingham.ac.uk

Keywords:
AFM; control theory; feedback; scanning probe microscopy

Beilstein J. Nanotechnol. **2014,** *5,* 337–345.
doi:10.3762/bjnano.5.38

Received: 25 November 2013
Accepted: 20 February 2014
Published: 21 March 2014

This article is part of the Thematic Series "Advanced atomic force microscopy techniques II".

Guest Editors: T. Glatzel and T. Schimmel

Abstract

We derive a theoretical model for studying SPM feedback in the context of control theory. Previous models presented in the literature that apply standard models for proportional-integral-derivative controllers predict a highly unstable feedback environment. This model uses features specific to the SPM implementation of the proportional-integral controller to give realistic feedback behaviour. As such the stability of SPM feedback for a wide range of feedback gains can be understood. Further consideration of mechanical responses of the SPM system gives insight into the causes of exciting mechanical resonances of the scanner during feedback operation.

Introduction

Scanning probe microscopy (SPM) imaging relies on feedback loops to maintain a constant interaction between the tip and the sample [1,2]. Many well known artefacts can arise from improper feedback settings [3-5]. Thus, for reliable SPM operation and analysis the characteristics and behaviour of such feedback loops must be considered [6,7]. SPM feedback loops usually employ a proportional-integral (PI) controller, equivalent to the common proportional-integral-differential (PID) controller with the differential gain set to zero to avoid amplification of noise. Other groups have successfully modelled and implemented proportional-differential controllers [8], but these are not commonly used. Previous work has used control theory to analyse the behaviour of PI and PID feedback loops in the context of SPM [9-12], and these models are still being applied in the current literature [13]. However, the details of the operation of the feedback loop have been incorrectly modelled, which results in a decreased stability and an exaggerated ringing at the resonant frequency of the piezoelectric actuator (*z*-piezo). Due to these errors, the feedback controller often cannot maintain tracking without a high derivative component [13], which is

entirely at odds with experimental observations. This paper employs analysis of specific SPM PI controllers to provide a more appropriate method for modelling such systems.

Results and Discussion

When modelling an SPM feedback loop we must first consider the workings of the PI controller under perfect conditions. First, assume that the tip is stationary above a sample at a position Z, and that the z-piezoelectric actuator for tip positioning is extended by X (Figure 1). For this perfect model X is considered to be directly the output of the PI controller; consideration of amplifier bandwidths and mechanical resonances is added later. For our original simplified model we will consider a generic SPM which tracks to a set-point tip–sample distance (Note that the exact mechanism to detect this distance is not relevant). Referring to the set-point distance as P, and the tip–sample distance as $Z - X$, then the error signal input to the PI controller, E, is equal to

$$E = Z - (X + P). \tag{1}$$

After a time t in feedback the output of a standard PI controller would be

$$X(t) = K_p E(t) + K_i \int_0^t E(\tau)\mathrm{d}\tau, \tag{2}$$

where K_p and K_i are the proportional and integral gains of the PI controller respectively and τ is a dummy integration variable. For this standard PI controller the output of the first term is proportional to the instantaneous error, and the output of the second term is proportional to the error that was integrated since the start of the experiment. It is clear that such a system is intrinsically unstable, by considering the case that $E(t_0) = 0$. As the tip–sample distance is equal to the set-point distance there should be no movement. However, evaluating Equation 2 the output to the piezo $X(t_0 + \mathrm{d}t)$ will be zero (where the $\mathrm{d}t$ is used to clarify that the system was not initiated at 0 but the first output after initiation will be zero.). Thus, the tip will return to the zero piezo extension position, rather than stay static (because the error signal is zero). At the next time step, there will be a large error signal and the tip will move back towards its correct position. This rudimentary problem has apparently gone unnoticed to date because it has been 'disguised' by the more complicated modelling of the response of the various other electrical and electromechanical components of the SPM (amplifiers, piezoelectric actuators).

It is helpful to draw an analogy with the most commonly considered control system, namely a temperature controller. A conventional PI controller in essence calculates the heat to be added to the system under control. If the set-point matches the measured temperature an output of zero is required. However, an SPM directly controls the extension of the piezoelectric actuator, which is analogous to directly controlling the temperature. To correct for this one must consider that the output of a PI controller in an SPM is the *change* in the extension. Thus, for the final output of the feedback controller to be the extension we must integrate the PI controller output since the start of the experiment (with $X(0) = 0$):

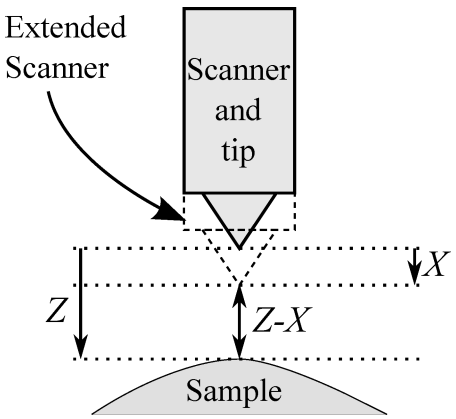

Figure 1: Schematic showing coordinates for sample position, Z, and scanner extension, X. The tip–sample distance can then be calculated as $Z - X$.

$$X(t) = K_p \int_0^t E(t^*)\mathrm{d}t^* + K_i \int_0^t \int_0^{t^*} E(\tau)\mathrm{d}\tau\mathrm{d}t^*, \tag{3}$$

where t^* is another dummy integration variable. This integration effectively stores all previous feedback response. Comparing to Equation 2 we see that if initiated under the same conditions, where $X(0) = 0$, the integral term does store previous response as a proportional controller (i.e., the second term of Equation 2 is equivalent to the first term of Equation 3). Thus, the controller implemented by Equation 2 would perform as a proportional-differential controller.

Figure 2 directly compares the response of Equation 2 and Equation 3 to a unit step, analytically solved by using a Laplace transform with a set-point of zero. For a PI controller, Figure 2a, modelled by using Equation 2 there is a discontinuity in the extension at the time of the step, this results from the incorrectly modelled proportional controller that acts as a derivative controller. This discontinuity can go unnoticed if the equations are solved numerically, if a frequency cut-off is modelled [9], or if the mechanical response of the z-piezo is

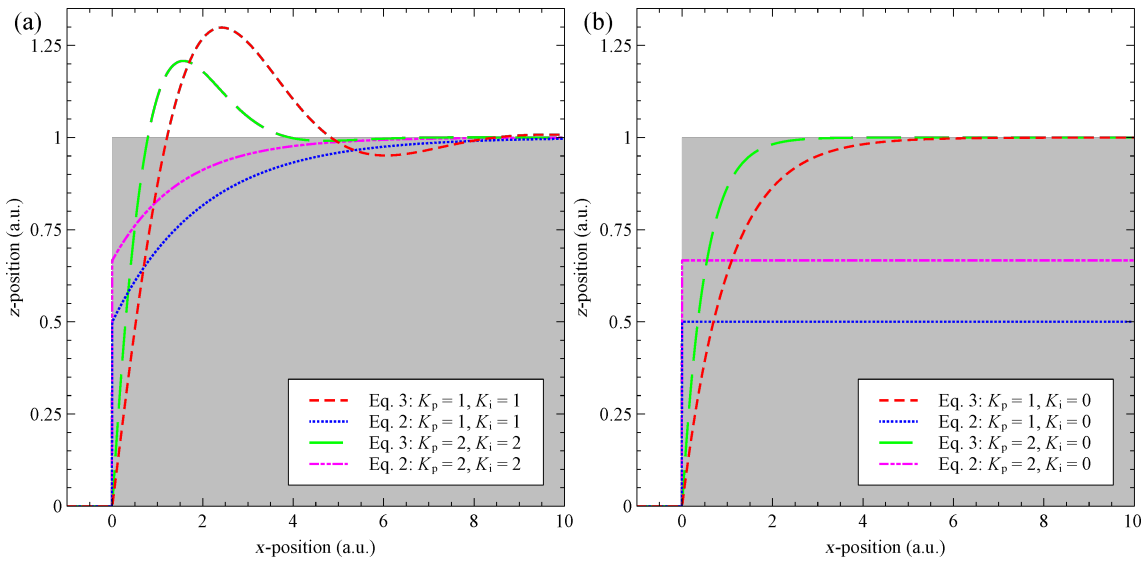

Figure 2: Direct comparison of our model (Equation 3, red and green lines) with the model from the current literature (Equation 2, blue and pink lines), without modelling of electrical or mechanical components. The comparison is performed for a full PI controller (a) and a simple proportional controller (b), where the grey area represents the surface being tracked with a set-point of 0. Equation 2 shows unexpected discontinuities and does not tract the set-point for a proportional controller. Instead it only reacts to the initial impulse. Equation 3 produces the expected results from elementary control theory. All gain units are arbitrary.

modelled. Additionally, the controller modelled by using Equation 2 does not experience the expected overshoot of the set-point for a PI controller, this can also go unnoticed when mechanical response of the *z*-piezo is modelled as its resonance can be mistaken for feedback ringing [9]. By further examining Equation 2 for a proportional controller (K_i = 0), we see (Figure 2b) that in addition to the discontinuity the controller settles to a value that is a $1/(K_p + 1)$ of the required extension. This has previously been mistaken as a steady-state error common to proportional controllers [9]. However, when plotted without any modelling of other components it becomes clear that it results from the controller that only acts to the initial impulse.

From Figure 2b it becomes apparent that there will be no steady-state offset when evaluating the response of Equation 3 to a static surface ($Z(t) = E + X + P$ = constant), for a simple proportional controller (K_i = 0). This initially appears at odds with both experiments and elementary control theory. However, this is due to the simplicity of the system we are modelling. Again considering our analogous temperature controller it is well known that the cause of the steady-state error is the fact that the heat input into the system is equal to the heat lost to (or gained from) outside the system. Now we see that steady-state errors in SPM feedback result from a sample drift in the *z*-direction or from scanning a sample with a tilt. Thus, any system that does not model *z*-drift or sample tilt should not expect a steady-state error.

Complete model of SPM feedback

Before running simulations of our simplified SPM system we will first derive the model for the full SPM feedback system, and then set the transfer functions of unmodelled components to unity, to reduce the possibility for errors following their introduction. To avoid unnecessary generalisations we will discuss the feedback loop as it applies to the scanning tunnelling microscope (STM). The results are, however, equally applicable to other forms of SPM. For analysis of the full feedback loop of an STM (Figure 3) we start by considering that at any time *t* the tip will be above a particular area of the sample with height *Z*. Thus, the tip encounters the topography as a of the time $Z(t)$. By using the extension of the z-axis of the piezoelectric scanner (*z*-piezo), $X(t)$ (note that when modelling a complete SPM $X(t)$ is no longer simply the output of the PI controller, as described in Equation 7), we can express the tip–sample distance, $D(t)$, as

$$D(t) = Z(t) - X(t)\,. \tag{4}$$

The measured tunnelling current is a function of the distance $D(t)$, and also of the properties of the current-to-voltage (I–V) amplifier of the STM. As the tunnel current depends exponentially on the tip–sample distance the logarithm of the tunnel current is used for the feedback to improve the linearity of the feedback response. We shall refer to this log tunnel current as

$$I(t) = \hat{H}_{\mathrm{IV}}(t)D(t)\,, \tag{5}$$

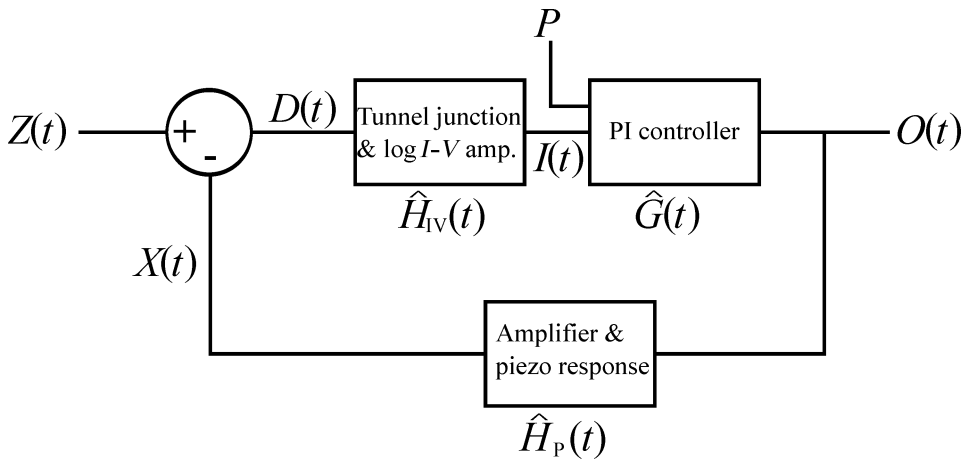

Figure 3: Schematic of an STM feedback loop. $Z(t)$ and $X(t)$ represent the sample height and z-piezo extension at time t respectively, and P is the set-point current. Other SPM systems can be modelled using the same feedback system by replacing the operator $\hat{H}_{IV}$, with an operator that describes the tip–sample interaction and signal amplification of the SPM to be modelled.

where $\hat{H}_{IV}(t)$ is the time dependent operator fully describing the tunnel junction, the I–V amplifier, and the logarithm operation.

The feedback controller then compares $I(t)$ with a set-point, P, and tries to correct for discrepancies by modifying the output, $O(t)$, to the z-piezo. We can write the feedback controller as the time-dependent operator $\hat{G}(t)$, and hence

$$O(t) = \hat{G}(t)\big[P - I(t)\big]. \tag{6}$$

Finally, we can link the z-piezo extension to the feedback controller output with an operator, $\hat{H}_P(t)$. This describes both the high voltage amplifier use for the piezoelectric actuator and the mechanical response of the z-piezo itself:

$$X(t) = \hat{H}_P(t)O(t). \tag{7}$$

As the set-point acts as only a linear offset to the system we can set $P = 0$. Thus, combining Equation 5 and Equation 6 under this condition we get

$$O(t) = -\hat{H}_{IV}(t)\hat{G}(t)D(t). \tag{8}$$

Combining this with Equation 7 gives

$$\begin{aligned} X(t) &= -\hat{H}_{IV}(t)\hat{H}_P(t)\hat{G}(t)D(t) \\ &= -\hat{H}_{IV}(t)\hat{H}_P(t)\hat{G}(t)\big[Z(t) - X(t)\big]. \end{aligned} \tag{9}$$

Here we apply a Laplace transform so that the transfer functions of the feedback components can be easily combined. This gives

$$\tilde{X}(s) = -\tilde{H}_{IV}(s)\tilde{H}_P(s)\tilde{G}(s)\big[\tilde{Z}(s) - \tilde{X}(s)\big], \tag{10}$$

where $\tilde{X}(s) = \mathcal{L}\{X(t)\}$ and $\mathcal{L}$ is the Laplace transform. Some minor rearrangement gives

$$\tilde{X}(s) = \frac{-\tilde{H}_{IV}(s)\tilde{H}_P(s)\tilde{G}(s)\tilde{Z}(s)}{1 - \tilde{H}_{IV}(s)\tilde{H}_P(s)\tilde{G}(s)}. \tag{11}$$

We are interested, however, in the output signal to the z-piezo, not its physical extension, as this is what the SPM controller records for the image. By simply considering the Laplace transform of Equation 7 ($\tilde{X}(s) = \tilde{H}_P(s)\tilde{O}(s)$) we arrive at a final result of

$$\tilde{O}(s) = \frac{-\tilde{H}_{IV}(s)\tilde{G}(s)}{1 - \tilde{H}_{IV}(s)\tilde{H}_P(s)\tilde{G}(s)}\tilde{Z}(s). \tag{12}$$

For this paper we are working in arbitrary units. Thus, the simulation needs to provide the relative response to change in gain settings rather than a response in physical units. Thus, we can set $\hat{H}_{IV}(t) = -1$ ($\tilde{H}_{IV}(s) = -1$) as the logarithm should cancel the exponential dependence of the tunnel junction, and the gain of the I–V amplifier is simply linear, which is irrelevant if we are working in arbitrary units. To specifically consider the effect of the bandwidth of the SPM pre-amplifier, the func-

tional form of $\hat{H}_{\mathrm{IV}}(t)$ must be considered in more detail. More detail on modelling of such electrical components is given in the final section. Under this condition we can simplify Equation 12 to

$$\tilde{O}(s)=\frac{\tilde{G}(s)}{1+\tilde{H}_{\mathrm{P}}(s)\tilde{G}(s)}\tilde{Z}(s)\,. \tag{13}$$

By applying the same argument used to derive Equation 3 we can write the operator for the PI-controller acting on an arbitrary function $f(t)$ as

$$\hat{G}(t)=K_p\int_0^t f(t^*)\mathrm{d}t^*+K_i\int_0^t\int_0^{t^*} f(\tau)\mathrm{d}\tau\mathrm{d}t^*\,, \tag{14}$$

and thus in s-space this becomes

$$\tilde{G}(s)=\frac{K_p}{s}+\frac{K_i}{s^2}\,. \tag{15}$$

Feedback performance without mechanical modelling

Initially we will study the stability of the STM feedback without modelling the mechanical resonances of the SPM system. For this we can substitute $\tilde{H}_{\mathrm{P}}(s)$ = 1 and Equation 15 into Equation 13. The feedback behaviour has been studied for four simulated surfaces:

$$Z(t)=1\,, \tag{16}$$

$$Z(t)=1+t/10\,, \tag{17}$$

$$Z(t)=t/10\,, \tag{18}$$

$$Z(t)=\sin(t)\exp(-t)\,, \tag{19}$$

which correspond to a unit step, a ramp added to a unit step, a ramp, and a smooth topographical feature respectively. The results for a range of different feedback parameters are plotted in Figure 4. As the system is modelled in arbitrary units, time and x-position are equivalent if the tip is moving at a constant speed in x. It is clear from Figure 4 that the system behaves as expected. Steady state offsets appear for proportional only controllers if there is a z-ramp present, but is corrected by an integral controller.

When discussing the stability of the system, qualitatively one can see that tracking is maintained for a wide range of proportional and integral gains. For large integral gains the system oscillates, as expected. For all plotted gains oscillations always ring-off, never resulting in positive feedback. To further investigate the stability in the case of the unit step (Equation 16) the full system output in s-space can be analysed for poles. The final output in s-space is:

$$\tilde{O}(s)=\frac{K_p s+K_i}{s(s^2+K_p s+K_i)}\,, \tag{20}$$

which results in three poles:

$$s=0\,,\quad s=\frac{-K_p\pm\sqrt{K_p^2-4K_i}}{2}\,. \tag{21}$$

From this it is clear that if K_p and K_i are always positive (true for a feedback loop) no pole ever has a positive real value, and thus the system is always stable. We can also calculate that the feedback output will not oscillate if $4K_i \le K_p^2$.

Feedback performance with mechanical and electrical modelling

For a more realistic model of SPM feedback one should also model the response of electrical and mechanical components. Equations for such extra components should be tested individually and added sequentially to reduce the possibility of error as equations in s-space are rarely intuitive. To build up a full electrical and mechanical model of an arbitrary system is of little use when discussing stability as the system becomes too complicated to analytically derive the poles. Instead the above equations should be used in conjunction with real physical values from a SPM system to understand its stability.

As an example we will include a mechanical resonance for the z-piezo relative to its equilibrium position at its input voltage

$$\tilde{H}_{\mathrm{P}}(s)=\frac{1}{1+\dfrac{s}{Q\omega_0}+\dfrac{s^2}{\omega_0^2}}\,, \tag{22}$$

where Q is the quality factor of the resonance and ω_0 is the angular eigenfrequency. It is important to note that this equation differs from that used in Reference [9], as this text mistakenly uses the mechanical response to a force rather than to a coupled mechanical offset. It is possible to model the transfer function of the z-piezo for an input voltage by replacing the numerator with the relevant piezoelectric coefficient. This is not done as it has no effect for a model in arbitrary units, and also as in this form Equation 22 can equally be used as the response of an AFM cantilever. It is, however, important to note that for

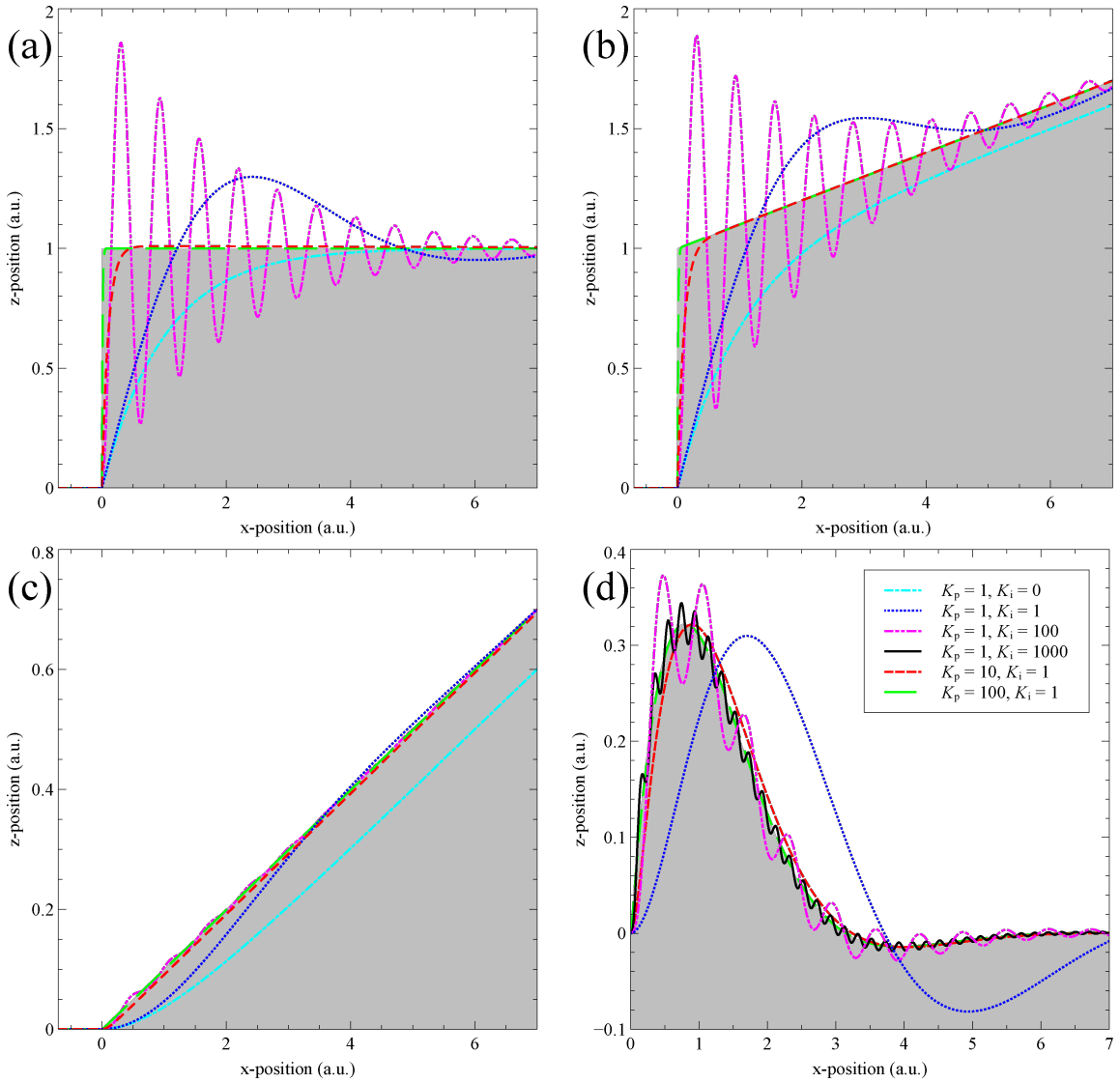

Figure 4: The feedback response of an SPM, without the inclusion of mechanical resonances, calculated for four different topographies, and for a range of feedback gains. Topographies in (a)–(d) correspond to Equation 16–Equation 19 respectively. Not all gains are plotted for all topographies to avoid overcrowding.

some geometries of piezoelectric scanners, such as the tube scanner, the motion of the principle eigenmode is perpendicular to the z-axis [14], and thus cannot be included into our one dimensional model.

Substituting Equation 22 and Equation 15 into Equation 13, along with the equation for a unit step, the response of the full system in s-space is given by

As the denominator is fifth order there are five poles. One pole at $s = 0$ shows the final response to the step. The functional form of the other four poles is too long to be qualitatively useful. However, the trend in pole positions can be qualitatively understood. Two poles correspond to the ringing oscillations from the system without the mechanical resonance, though the frequency and decay times are affected by the modelled resonance. Two further poles represent the excitation of the

$$\tilde{O}(s) = \frac{K_p Q s^3 + (K_i Q + K_p \omega_0) s^2 + (K_i \omega_0 + K_p Q \omega_0^2) s + K_i Q \omega_0^2}{s(Q s^4 + \omega_0 s^3 + Q \omega_0^2 s^2 + K_p Q \omega_0^2 s + K_i Q \omega_0^2)}. \quad (23)$$

mechanical resonance. These poles can move into the unstable region if excited by high gains. The system can be made stable under higher gains by increasing the eigenfrequency or decreasing the Q of the resonator. For these reasons components with a high quality factor and a low resonant frequency are unsuitable as part of the SPM scanners.

In Figure 5a the PI controller output for a range of mechanical eigenfrequencies with a constant quality factor is plotted against time. Arbitrary units are used for both time and the PI output as the evolution under increasing eigenfrequency is valid for any magnitude. The y-axis is labelled PI output, not extension, as these are no longer equivalent when mechanical resonance is modelled. For all plotted outputs the bandwidth of the high voltage (HV) amplifier driving the z-piezo was assumed to be infinite, and hence Equation 22 was used without modification.

The evolution of the output under varying Q of the mechanical resonance is shown in Figure 5b. Again, in agreement with the polar analysis, the stability increases for lower Q. For higher Q the resulting instability can be diminished or eradicated by reducing the bandwidth of the HV amplifier. The transfer function of an amplifier with a finite bandwidth can be accurately modelled as a first order low-pass filter [15]

$$\tilde{H}_{\text{amp}}(s) = \frac{1}{s/\omega_c + 1}, \tag{24}$$

where ω_c is the cut-off angular frequency (3-dB point) of the amplifier. As we are working in arbitrary units this amplifier has a gain of 1, the numerator of the transfer function can be replaced with the desired gain if needed. Including this, the full transfer function of the amplifier and piezo becomes

$$\tilde{H}_{\text{P}}(s) = \frac{1}{(s/\omega_c + 1)\left(1 + \dfrac{s}{Q\omega_0} + \dfrac{s^2}{\omega_0^2}\right)}. \tag{25}$$

The cyan line in 5b shows the significant improvement in stability resulting from a cut-off frequency just above that of the mechanical eigenfrequency. This, however, comes at the cost of an increased overshoot. One also must be careful not to lower the cut-off frequency below the resonance, nor to used an overdamped ($Q < 1/2$) mechanical component as this can introduce a significant phase lag, causing new instabilities. The MATLAB code used to generate the data for Figure 4 and Figure 5 is included as Supporting Information File 1. This can be used to further explore the parameter space of the SPM PI controller.

The only component in Figure 3 that is not modelled, is the tunnel junction and the logarithmic amplifier, $\hat{H}_{\text{IV}}(t)$. Considering the tunnel junction as an exponential decay with distance produces a current that is first amplified by an I–V preamplifier with a finite bandwidth. The logarithm of this output voltage is

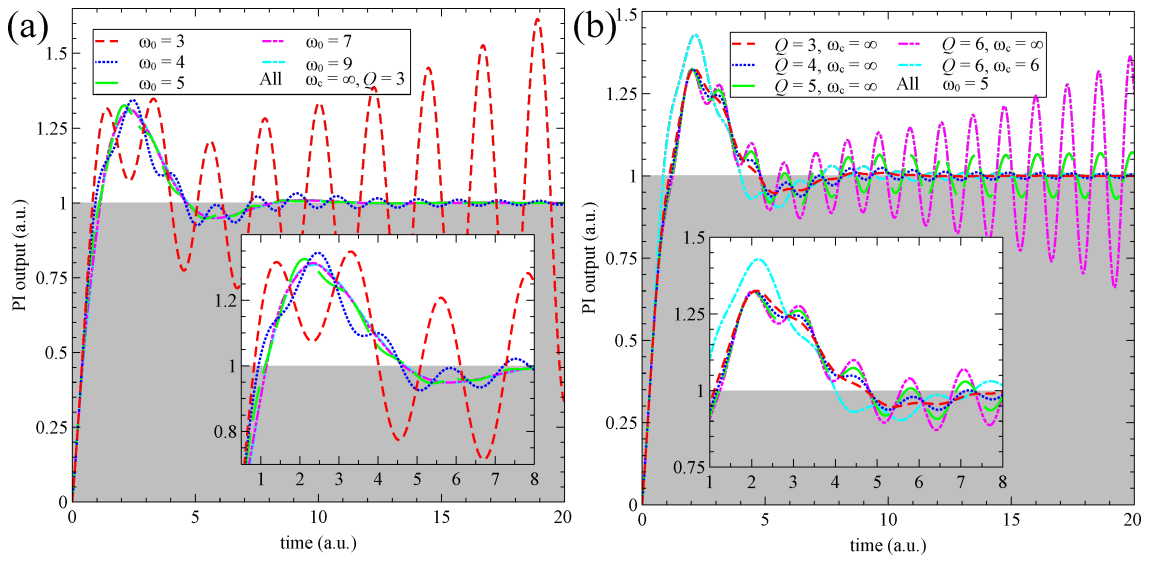

Figure 5: The feedback response of an SPM, including mechanical resonance. (a) Shows the evolution of the feedback output for varying eigenfrequency of the mechanical resonance. The stability improves for increasing resonant frequency. For all plots the bandwidth of the HV amplifier is infinite and the Q of the resonance does not vary. (b) Shows similar evolution in feedback output for varying Q of the resonance at a constant eigenfunction, with lower Q values stabilising the output. The cyan line shows the same resonance properties as the pink line, however by limiting the bandwidth of the HV amplifier to near that of the resonance, the stability is improved significantly. Both insets are zooms of the most important region of their respective plots.

then taken either by a logarithmic amplifier or calculated numerically by the SPM controller. This results in a functional form for the time-domain operator action on the tunnel gap $D(t)$ being

$$\hat{H}_{\mathrm{IV}}(t) = \log\left(\hat{H}_{\mathrm{amp}}\left[\exp\left\{-\kappa D\left(t\right)\right\}\right]\right), \qquad (26)$$

where κ is the characteristic decay length of the tunnel junction, and $\hat{H}_{\mathrm{amp}}$ is the time-domain operator corresponding to the transfer function in Equation 24.

To calculate the *s*-space transfer function of Equation 26, one would need to calculate the Laplace transform of the exponential of an arbitrary function $D(t)$. This may be possible for the specific functional forms of $D(t)$ but is not generally applicable. One can approximate $\hat{H}_{\mathrm{IV}}(t)$ under the approximation that the logarithm and $\hat{H}_{\mathrm{amp}}$ commute:

$$\hat{H}_{\mathrm{IV}}(t) \sim \hat{H}_{\mathrm{amp}}\left(\log[\exp\{-\kappa D(t)\}]\right) = \hat{H}_{\mathrm{amp}}\left(-\kappa D(t)\right). \qquad (27)$$

In arbitrary units, κ can be ignored and the transfer function of the tunnel junction approximates to $\tilde{H}_{\mathrm{IV}}(s) = -\tilde{H}_{\mathrm{amp}}(s)$. Under this approximation we ignore the effect of higher harmonics of frequencies present in $D(t)$ being generated by the exponential dependence in the tunnel junction.

Conclusion

We have derived an appropriate updated model to understand SPM feedback in the context of control theory. This model shows the intrinsic stability of the SPM feedback controller in an ideal environment. We further discuss methods to include modelling of mechanical resonances showing low frequency and high Q components to cause instabilities. By introducing amplifiers with bandwidths just above the mechanical eigenfrequency these instabilities can be controlled. The method presented here uses arbitrary units to show a generalised approach. The equations presented, however, can be used with real parameters from SPM systems to understand and model performance under a range of conditions.

Supporting Information

Supporting Information File 1

MATLAB code used to simulate the presented feedback model.
[http://www.beilstein-journals.org/bjnano/content/supplementary/2190-4286-5-38-S1.zip]

Acknowledgements

The author would like to thank P. Moriarty for his suggestions. This work was financially supported by a doctoral training grant from the EPSRC.

References

1. Binnig, G.; Quate, C. F.; Gerber, C. *Phys. Rev. Lett.* **1986,** *56,* 930–933. doi:10.1103/PhysRevLett.56.930
2. Binnig, G.; Rohrer, H.; Gerber, C.; Weibel, E. *Phys. Rev. Lett.* **1982,** *49,* 57–61. doi:10.1103/PhysRevLett.49.57
3. Cesbron, Y.; Shaw, C. P.; Birchall, J. P.; Free, P.; Lévy, R. *Small* **2012,** *8,* 3714–3719. doi:10.1002/smll.201001465
4. Yu, M.; Stellacci, F. *Small* **2012,** *8,* 3720–3726. doi:10.1002/smll.201202322
5. Lenihan, T. G.; Malshe, A. P.; Brown, W. D.; Schaper, L. W. *Thin Solid Films* **1995,** *270,* 356–361. doi:10.1016/0040-6090(95)06747-7
6. Wutscher, T.; Niebauer, J.; Giessibl, F. J. *Rev. Sci. Instrum.* **2013,** *84,* 073704. doi:10.1063/1.4812636
7. Payton, O.; Champneys, A. R.; Homer, M. E.; Picco, L.; Miles, M. J. *Proc. R. Soc. A* **2010,** *467,* 1801–1822. doi:10.1098/rspa.2010.0451
8. Leang, K. K.; Devasia, S. *IEEE Trans. Control Syst. Technol.* **2007,** *15,* 927–935. doi:10.1109/TCST.2007.902956
9. Park, S.; Barrett, R. C. Design Considerations for an STM System. In *Scanning Tunneling Microscopy;* Stroscio, J. A.; Kaiser, W. J., Eds.; Methods in Experimental Physics, Vol. 27; Academic Press: Boston, MA, USA, 1993; pp 31–76.
10. Oliva, A. I.; Anguiano, E.; Denisenko, N.; Aguilar, M.; Peña, J. L. *Rev. Sci. Instrum.* **1995,** *66,* 3196. doi:10.1063/1.1145551
11. Anguiano, E.; Oliva, A. I.; Aguilar, M. *Rev. Sci. Instrum.* **1998,** *69,* 3867. doi:10.1063/1.1149191
12. Nony, L.; Baratoff, A.; Schär, D.; Pfeiffer, O.; Wetzel, A.; Meyer, E. *Phys. Rev. B* **2006,** *74,* 235439. doi:10.1103/PhysRevB.74.235439
13. Biscarini, F.; Ong, Q. K.; Albonetti, C.; Liscio, F.; Longobardi, M.; Mali, K. S.; Ciesielski, A.; Reguera, J.; Renner, C.; De Feyter, S.; Samorì, P.; Stellacci, F. *Langmuir* **2013,** *29,* 13723–13734. doi:10.1021/la403546c
14. Schitter, G.; Stemmer, A. *IEEE Trans. Control Syst. Technol.* **2004,** *12,* 449–454. doi:10.1109/TCST.2004.824290
15. Glisson, T. H., Jr.. Introduction. *Introduction to Circuit Analysis and Design;* Springer: New York, 2011; pp 1–17.

Beilstein Journal of Nanotechnology

Impact of thermal frequency drift on highest precision force microscopy using quartz-based force sensors at low temperatures

Florian Pielmeier*, Daniel Meuer, Daniel Schmid, Christoph Strunk and Franz J. Giessibl

Letter

Open Access

Address:
Institute of Experimental and Applied Physics, University of Regensburg, D-93053 Regensburg, Germany

Email:
Florian Pielmeier* - florian1.pielmeier@ur.de

* Corresponding author

Keywords:
AFM; frequency drift; length extensional resonator; needle sensor; qPlus sensor; quartz

Beilstein J. Nanotechnol. **2014,** *5,* 407–412.
doi:10.3762/bjnano.5.48

Received: 16 January 2014
Accepted: 11 March 2014
Published: 04 April 2014

This article is part of the Thematic Series "Advanced atomic force microscopy techniques II".

Guest Editors: T. Glatzel and T. Schimmel

Abstract

In frequency modulation atomic force microscopy (FM-AFM) the stability of the eigenfrequency of the force sensor is of key importance for highest precision force measurements. Here, we study the influence of temperature changes on the resonance frequency of force sensors made of quartz, in a temperature range from 4.8–48 K. The sensors are based on the qPlus and length extensional principle. The frequency variation with temperature T for all sensors is negative up to 30 K and on the order of 1 ppm/K, up to 13 K, where a distinct kink appears, it is linear. Furthermore, we characterize a new type of miniaturized qPlus sensor and confirm the theoretically predicted reduction in detector noise.

Findings

Frequency modulation atomic force microscopy [1] has become an essential tool for surface scientist's to study chemical and magnetic interactions at the atomic scale [2-6]. In FM-AFM the frequency shift $\Delta f = f - f_0$ of a mechanical oscillator with stiffness k upon tip–sample interaction is measured, while the oscillation amplitude A is kept constant. For quantitative force measurements the uncertainty in the force gradient is crucial [7]. Frequency shift and force gradient are related via

$$\Delta f = \frac{f_0}{2k}\langle k_{\mathrm{ts}}\rangle, \tag{1}$$

where $\langle k_{\mathrm{ts}}\rangle$ is the averaged force gradient between tip and sample, which can be deconvolved into k_{ts} [8]. Four noise contributions limit the accuracy of the Δf measurement, which are inherent to FM-AFM [7]. Deflection detector noise [1,9-11] is proportional to the measurement bandwidth B with $B^{1.5}$,

thermal [1] and oscillator noise [11] are proportional to $B^{0.5}$. At higher bandwidths (e.g., B > 100 Hz), deflection detector noise is usually the dominant noise contribution [10]. If the measurement bandwidth B can be set sufficiently small, e.g., at low temperatures, these noise contributions are significantly reduced and imaging with millihertz resolution becomes possible [12]. In turn, when B is small the stability of the eigenfrequency f_0 is particularly important, because frequency drift noise is proportional to $1/\sqrt{B}$ [7]. The main cause of frequency drift are changes in f_0 with temperature T, which are material dependent. Even for experiments conducted at liquid helium temperatures, temperature drift limits the achievable resolution. Changes in ambient pressure affect the boiling temperature of helium, e.g., the vapor pressure of He^4 at 4.4 K changes at a rate of $\approx 10^5$ Pa/K [13]. Typical changes in ambient pressure are between 100–500 Pa/day, leading to temperature changes in the range of 1–5 mK/day.

Since the introduction of the AFM by Binnig et al. [14] mainly force sensors made of silicon are in use [10]. In the last decade force sensors based on quartz resonators became more attractive, with quartz tuning forks (TF) in the "qPlus" configuration (Figure 1c–f) [15] and length extensional resonators (LER) as the so called "needle sensor" (Figure 1a) [16]. Quartz resonators are usually designed and characterized for room temperature applications. Their remarkable frequency stability in comparison to silicon cantilevers results in a significantly smaller frequency drift at room temperature [7,10]. The frequency variation with temperature resembles an inverted parabola centered around the turnover temperature, which is usually tuned to about 25 °C [17]. On the other hand, quartz-based force sensors are often used in a low temperature environment, but little is known about the frequency variation with temperature in this regime.

Hembacher et al. evaluated the relative frequency change $\varepsilon = \delta f/f_0$ of an encapsulated quartz TF over a large temperature range from 300 K down to 4.2 K, where ε decreases monotonically with T [18]. At 300 K and 4.2 K ε is almost zero, hence the influence of temperature variations should be minimized here. In a more detailed measurement, Rychen et al. measured the frequency change of a quartz TF from 1.5 K to 50 K at a constant pressure of 10 mbar, here f_0 is not increasing monotonically with T but shows a local minimum around 20 K [19]. This resembles qualitatively the temperature dependence of the Grüneisen parameter γ, which relates thermal expansion to vibrational properties [20]. The calculated values for γ show a maximum around 30 K decreasing sharply to lower temperatures and gradually to higher ones [20,21]. Additionally the anisotropic thermal expansion coefficients of quartz, $\alpha_{\parallel}$ and $\alpha_{\perp}$, parallel and perpendicular to the optical axis also show a non

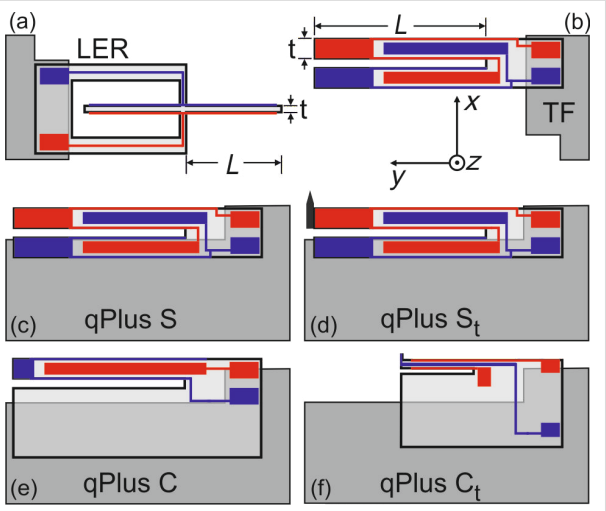

Figure 1: (Color online). Geometry of length extensional resonator (a), tuning fork (b), standard qPlus sensors (c,d) and custom made qPlus sensors (e,f). The two coupled oscillators (LER and TF) are fixed to the substrate at their base, both prongs oscillate, no additional mass or tip is attached. Standard qPlus sensors (S and S_t) are based on quartz TFs, one prong is fixed to the substrate, in (d) a tip is added to the free prong. Custom designed qPlus sensors consist only of a single prong with a larger base, which is fixed to the substrate, unnecessary electrodes are removed to reduce capacity. The beam dimensions of sensor C (e) are the same as for sensors S and S_t. Sensor C_t (f) has a shorter and thinner beam, see Table 1 for details. Note, the *z*-axis (optical axis) is not exactly perpendicular to the oscillation of the beams, but off by ≈2°.

linear behavior with temperature [22]. Here, $\alpha_{\perp}$ increases monotonically with T, whereas $\alpha_{\parallel}$ is negative below ≈12 K [21].

The eigenfrequency f_0 of a beam oscillating in a bending mode is given via

$$f_0 = 0.162 \frac{t}{L^2} \cdot v_s, \tag{2}$$

where L is the length, t the thickness of the beam, and $v_s = \sqrt{E/\rho}$ the velocity of sound with E being Young's modulus and ρ mass density of quartz. In case of the LER one obtains [7]

$$f_0 = \frac{v_s}{4L} \cdot \tag{3}$$

Hence, f_0 changes, when the dimensions of the beam or v_s changes due to thermal expansion. The orientation of the beams of the quartz sensors deviate slightly from a perpendicular orientation to the optical axis (*z*-axis, Figure 1). This is due to the crystal cut, which is not exactly along the optical axis, but off by about 2° (+2° *X*-cut). Hence, the direction of L is off by 2° and t is perpendicular to the optical axis. The thermal expansion along these directions is mainly determined by $\alpha_{\perp}$, which

increases monotonically from 4 K up to room temperature [21]. Neglecting this small deviation in L direction one obtains from Equation 2 for the frequency change with temperature of TF and qPlus sensors

$$\begin{aligned}\frac{\partial f_0}{\partial T} &= f_0\left(\frac{1}{t}-\frac{2}{L}\frac{\partial L}{\partial T}+\frac{1}{v_s}\frac{\partial v_s}{\partial T}\right)\\ &= f_0\left(\alpha_\perp-2\alpha_\perp+\frac{1}{v_s}\frac{\partial v_s}{\partial T}\right)\\ &= f_0\left(-\alpha_\perp+\frac{1}{v_s}\frac{\partial v_s}{\partial T}\right).\end{aligned} \tag{4}$$

The same result is obtained for the LER geometry. For X cut crystalline quartz no change in v_s within a precision of 0.1 ppm was observed below 10 K [23-25]. The measured values of $\alpha_\perp$ below 10 K are in the order of 0.01 ppm/K [21]. According to Equation 4, the variation of ε with T is therefore expected to be in the range of 0.1 ppm/K below 10 K and similar for TF, qPlus and LER geometry.

In this work, we measure the frequency change with temperature from 4.8 K to 48 K for quartz based force sensors. Six different quartz resonators were investigated to directly evaluate and compare the influence of thermal frequency drift on the force gradient noise. Two coupled oscillators, a LER (Figure 1a) and a TF (Figure 1b) both without tip, were used for direct comparison. Two standard qPlus sensors were built with quartz TFs, one without tip (S, Figure 1c) and one with a tip (S_t, Figure 1d). Finally, custom designed quartz cantilevers, are used to build qPlus sensors with standard and smaller beam dimensions (C and C_t, Figure 1e, Figure 1f). At the end of the prong of sensor C_t is a small appendix for easier accommodation of tips, which acts effectively as an additional mass, see Figure 1f. The advantages of the custom designed sensors in contrast to the standard qPlus sensors will be briefly discussed at the end of this letter. In Table 1 the relevant parameters of the sensors are summarized. All quartz resonators were glued with non-conductive epoxy to an aluminum oxide substrate which is commonly used for our qPlus sensors, the electrodes are then contacted with conductive epoxy. For the low temperature measurements the substrates where glued again with non-conductive epoxy onto a piece of copper. The copper piece serves as a thermal anchor and can be mounted on a He^4 stick, usually used for transport measurements. The stick is equipped with a heater resistor and a Si diode to measure T. The sensors were excited electrically with a constant amplitude A and the deflection signal was measured with a commercial charge amplifier [26]. Finally, the frequency shift was determined by a digital phase locked loop stabilized by an oven-controlled quartz resonator with a precision of 1 ppb/day [27]. For the measurements, the temperature setpoint was increased at a rate of 0.5 K/min and the change in eigenfrequency was monitored. At this rate the maximum deviation of the actual temperature from the setpoint temperature was below 0.1 K.

The results of the low temperature measurements are shown in Figure 2, where the relative frequency change ε is plotted against T. As the He^4 stick is not equipped with a vibration isolation system, there are some sharp peaks in the curves for the qPlus sensors caused by mechanical excitations of the sensors. This is not an issue for the coupled oscillators, and also for the sensor C_t, which has a higher resonance frequency and is therefore less affected by external vibrations. Obviously, there is a difference in ε for the various types of sensors used. Overall, the relative change is smallest for the LER followed by the TF and the custom qPlus sensors (C, C_t), the standard qPlus sensors (S, S_t) show the strongest change of f_0 with T. The curves for S and S_t lie exactly on top of each other and start to split up at around 33 K. For the two custom sensors ε is also quite similar and they split up at around 40 K. For sensors S and C, without an additional mass at the end of the prong, ε changes its sign earlier than in case of S_t and C_t. All curves show a fairly linear decrease of ε up to 13 K where a distinct kink appears, which might be due to the sign change in $\alpha_{||}$. After this kink, ε still decreases for all types of sensors. In case of the LER the sign of $\partial\varepsilon/\partial T$ changes from negative to positive at around 30 K,

Table 1: Dimensions (length L, thickness t and width w), resonance frequency f_0 and stiffness k of the different types of sensors investigated. The highest Q values are obtained with the custom qPlus sensors. The values for f_0 and Q are obtained from resonance curves measured at 4.2 K.

	L (μm)	t (μm)	w (μm)	f_0 (Hz)	k (N/m)	Q
qPlus S	2400	214	130	32680	1800	264000
qPlus S_t	2400	214	130	19658	1800	179000
qPlus C	2400	214	130	32884	1800	397000
qPlus C_t	992	85	145	73303	1830	312000
TF	2400	214	130	32742	1800	140000
LER	1340	70	130	998148	530000	202000

this agrees qualitatively with the temperature dependence of the Grüneisen parameter γ. For tuning fork based sensors, ε still decreases, and $\partial\varepsilon/\partial T$ changes its sign at temperatures between 40–47 K.

In the temperature range from 5–12 K the slopes η can be obtained from a linear fit to the data in Figure 2. The determined values for η are all in the order of 1 ppm/K and summarized in Table 2. This is much higher than expected from the change in v_s or $\alpha_\perp$, as discussed above. From neutron irradiation it is known, that the change of v_s with T depends strongly on the quality of the crystal, the rate of change increases linearly with the defect density [24,25,28]. Because the quartz resonators studied in this work are not from the same wafer and manufacturer, one might argue that the differences in $\partial\varepsilon/\partial T$ can be caused by different crystal quality and material processing. But there are two important observations from the measurements presented in Figure 2, which are contradictory to that. First, the difference between the standard qPlus sensors (S, S_t) and the tuning fork is somewhat unexpected, because tuning forks from the same batch were used to build these sensors. Second, the striking similarity between sensors C and C_t, which have different beam dimensions and are not even from the same manufacturer. Hence, the influence of different crystal quality or material processing on the frequency variation with temperature, is expected to be largest for these two types of sensors. Obviously, this is not the case and suggests that the difference between the tuning fork and the standard qPlus sensors is due to the different geometry and the mechanical coupling of the beam to the support. This could also explain the smaller values of ε and η for the coupled oscillators, because they are less influenced by the mechanical coupling of the quartz oscillator to the support than the qPlus sensors.

For qPlus sensors, the resonance frequency f_0 can also be expressed as $f_0 = 1/(2\pi)\sqrt{k/m_{\text{eff}}}$, where m_{eff} = 0.24 m is the effective mass of the oscillating prong. Hence, $\partial\varepsilon/\partial T$ can be interpreted as a variation of the stiffness with temperature, implying m_{eff} remains unchanged. The similarity of $\partial\varepsilon/\partial T$ for sensors S and S_t up to a temperature of around 33 K, leads to the conclusion that there is no significant influence of the additional mass of the tip on the effective stiffness of sensor S_t, compared to sensor S.

So far, only the relative frequency change with temperature was discussed. The influence on the measured force gradient $\partial k_{ts}/\partial T$ is obtained by multiplying the slopes η with the according value of 2 × k [7]. The values for $\partial k_{ts}/\partial T$ are also given in Table 2, due to the much higher stiffness of the LER, $\partial k_{ts}/\partial T$ is more than two orders of magnitude higher than in case of the tuning fork and qPlus sensors. In a previous study we have already

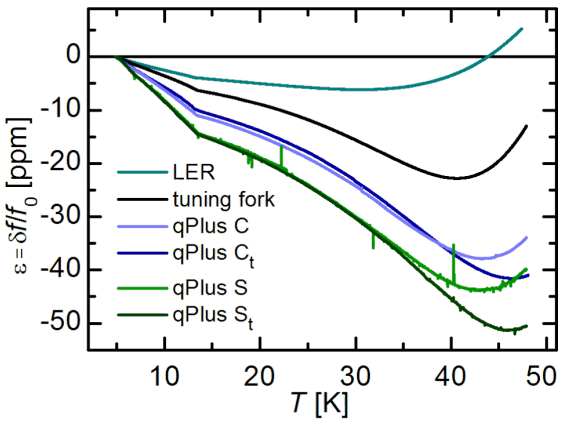

Figure 2: (Color online). Relative frequency change of quartz based AFM sensors from 4.8–48 K. The coupled oscillators show less relative frequency change with temperature as the qPlus sensors. For custom made qPlus sensors ε is smaller as for the standard ones. The spikes in the curves of the qPlus sensors arise from mechanical excitations of the sensors due to external vibrations or sound.

discussed the influence of thermal frequency drift theoretically [7], there the frequency drift for LER and qPlus sensors was assumed to be about 1 ppm/K as estimated from Figure 2a in [19]. Actually, the LER shows only about half of this value whereas for qPlus sensors the frequency drift is about a factor of 1.5 higher. Resulting in a force gradient drift noise, which scales with k, that is 160–240 times higher for LER sensors than for tuning fork or qPlus sensors. This is illustrated in Figure 3, where $\partial k_{ts}/\partial T$ is displayed for the tuning fork and the qPlus sensors (Figure 3a) and the LER (Figure 3b). Again, the wiggles in the curves for the qPlus sensors are caused by external excitations due to a lacking damping system. The kink around 13 K from Figure 2 shows up as a clear step. In temperature dependent measurements it might therefore be beneficial for a stable operation of the force sensor to avoid temperatures around 13 ± 0.5 K.

Table 2: Slopes η from linear fits to the data in a temperature range from 5–12 K. For conversion of frequency shift to force gradient, the corresponding k values from Table 1 were used, in case of TF and LER the stiffness was multiplied with a factor of 2 [7].

	η(ppm/K)	$\partial k_{ts}/\partial T$ (mN/m/K)
qPlus S	−1.69	6.1
qPlus S_t	−1.63	5.9
qPlus C	−1.25	4.5
qPlus C_t	−1.11	4.3
TF	−0.70	5.0
LER	−0.46	960

In the last part, the benefits of the custom designed qPlus sensors C and C_t are briefly discussed. They exhibit higher and

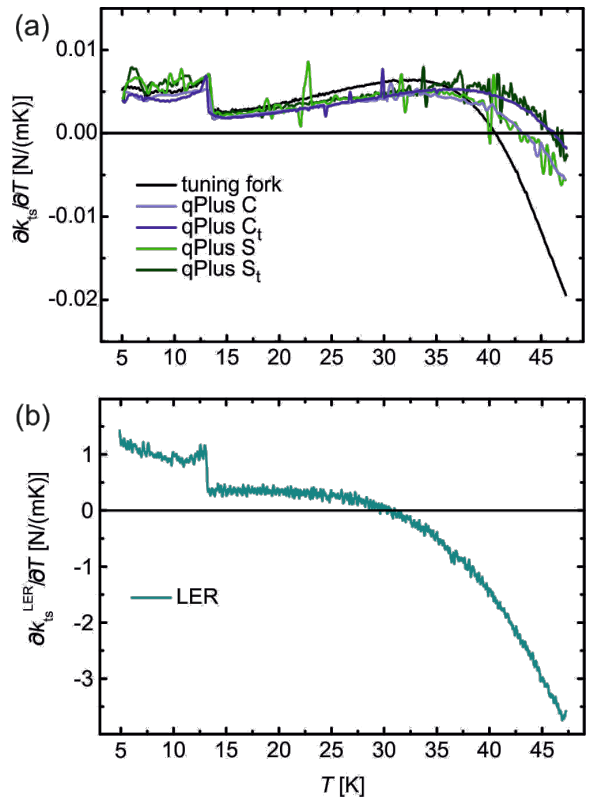

Figure 3: (a) Numerical derivative $\partial k_{ts}/\partial T$ for all tuning fork and qPlus sensors from 5–47 K. (b) $\partial k_{ts}/\partial T$ for LER. Note, the *y* scale is different for (a) and (b).

more reliable Q values, this is attributed to the larger base of the sensor. The clamping point of the beam, where the mechanical strain is highest, is now further away from the glued part as in case of tuning fork based qPlus sensors, see Figure 1. With the qPlus sensors of type C_t, Q values exceeding 1,300,000 have been achieved [6]. The design of sensor C_t is based on an analysis of the signal-to-noise ratio of quartz sensors, which showed that deflection detector noise decreases with decreasing beam thickness t [7]. While reducing simply t would lead to a decrease in k as well, the length L was also decreased to keep k in the optimal stiffness range for atomic resolution imaging [29]. These custom made sensors have now length L = 0.922 mm and thickness t = 85 µm. On the upper and lower side of the prong are etched grooves which lead to a more idealized electric field distribution [7]. For quartz-based force sensors, detector noise is proportional to

$$\delta k_{ts}^{det} \sim \frac{k n_q}{f_0 A} \sim \frac{k n_{amp}}{f_0 S A} \sim \frac{n_{amp} t}{A}, \qquad (5)$$

where $n_q = n_{amp}/S$ is the deflection noise density, n_{amp} the electrical noise density of the preamplifier, S the sensitivity of the sensor and A the oscillation amplitude [7]. For fixed values of n_{amp} and A one expects an improvement for sensor C_t in detector noise by a factor of t^C / t^{C_t} = 214 µm/85 µm = 2.5. Before we can compare δk_{ts}^{det} for sensors with different beam thickness we have to determine the stiffness k for the custom designed sensor C_t. This is done by measuring its resonance frequency f_0 at room temperature and calculate k from $k = (2\pi f_0)^2(m_{eff} + m_{app})$, where m_{app} is the mass of the appendix at the end of the prong. The masses are calculated via $m = \rho V$, where ρ is the mass density of quartz and the volume V is determined by measuring the dimensions of the beam with an optical microscope. Finally, taking the additional mass m_{app} at the end into account gives a stiffness of k = 1830 N/m with a relative error of ±10%. For the determination of n_q one can use thermal excitation spectra of the sensors C and C_t at room temperature analogous to previous studies [7,15,30]. For this purpose the sensors C and C_t were put into a metal box for shielding, one of the electrodes was grounded, whereas the second electrode was connected via a BNC feedthrough to the charge amplifier [26]. The output signal of the charge amplifier was measured with a spectrum analyzer (Agilent 35670A Dynamical Analyzer). The measured thermal excitation spectra at room temperature are shown in Figure 4. From there, the values of n_q for sensors C and C_t are determined as n_q^C = 55 fm/$\sqrt{\text{Hz}}$ and $n_q^{C_t}$ = 45 fm/$\sqrt{\text{Hz}}$. With the values for k from Table 1 and f_0 from Figure 4 for sensors C and C_t the ratio of the deflection noise is given as $\delta k_{ts}^{det,C} \Big/ \delta k_{ts}^{det,C_t} = \left(k^C n_q^C f_0^{C_t}\right) \Big/ \left(k^{C_t} n_q^{C_t} f_0^C\right) = 2.7$. The reduction in detector noise by a factor of 2.7 is even more than the expected value of 2.5 from the decrease in t. We attribute this is to a better performance (lower n_{amp}) of the preamplifier at higher resonance frequencies.

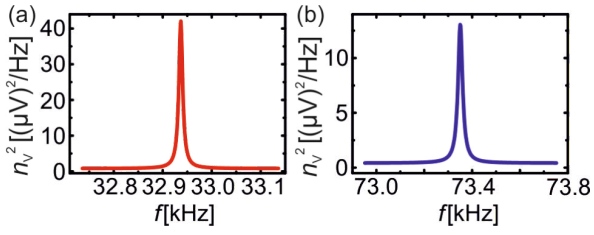

Figure 4: Thermal excitation spectra for sensors C (a) and C_t (b). The center frequency in (a) is f_0 = 32.939 kHz and the frequency range is 400 Hz, in (b) f_0 = 73.351 kHz and the range is 800 Hz. The sensitivities, determined from the area under the peaks, are S^C = 16.3 µV/pm and S^{C_t} = 14.1 µV/pm. The electrical noise densities are n_{amp}^C = 892 nV/$\sqrt{\text{Hz}}$ and $n_{amp}^{C_t}$ = 636 nV/$\sqrt{\text{Hz}}$, resulting in n_q^C = 55 fm/$\sqrt{\text{Hz}}$ and $n_q^{C_t}$ = 45 fm/$\sqrt{\text{Hz}}$.

In summary, the variation of f_0 with T for qPlus, tuning fork and LER sensors was measured at low temperatures and the resulting influence on the force gradient noise was determined. For temperature changes in the order of 1mK the minimum

detectable force gradient is about 1 mN/m for the LER and about 5 μN/m for qPlus sensors. Furthermore, the decreased deflection detector noise of custom qPlus sensors of type C_t was discussed, which is due to the reduced thickness *t* of the beam.

Acknowledgements

We acknowledge financial support from the Deutsche Forschungsgemeinschaft (Grant No. SFB 689 and GRK 1570).

References

1. Albrecht, T. R.; Grütter, P.; Horne, D.; Rugar, D. *J. Appl. Phys.* **1991,** *69,* 668–673. doi:10.1063/1.347347
2. Lantz, M. A.; Hug, H. J.; Hoffmann, R.; van Schendel, P. J. A.; Kappenberger, P.; Martin, S.; Baratoff, A.; Güntherodt, H.-J. *Science* **2001,** *291,* 2580–2583. doi:10.1126/science.1057824
3. Sugimoto, Y.; Pou, P.; Abe, M.; Jelinek, P.; Pérez, R.; Morita, S.; Custance, O. *Nature* **2007,** *446,* 64–67. doi:10.1038/nature05530
4. Kaiser, U.; Schwarz, A.; Wiesendanger, R. *Nature* **2007,** *446,* 522–552. doi:10.1038/nature05617
5. Gross, L.; Mohn, F.; Moll, N.; Liljeroth, P.; Meyer, G. *Science* **2009,** *325,* 1110–1114. doi:10.1126/science.1176210
6. Pielmeier, F.; Giessibl, F. J. *Phys. Rev. Lett.* **2013,** *110,* 266101. doi:10.1103/PhysRevLett.110.266101
7. Giessibl, F. J.; Pielmeier, F.; Eguchi, T.; An, T.; Hasegawa, Y. *Phys. Rev. B* **2011,** *84,* 125409. doi:10.1103/PhysRevB.84.125409
8. Giessibl, F. J. *Appl. Phys. Lett.* **2001,** *78,* 123–125. doi:10.1063/1.1335546
9. Dürig, U.; Steinauer, H. R.; Blanc, N. *J. Appl. Phys.* **1997,** *82,* 3641–3651. doi:10.1063/1.365726
10. Giessibl, F. J. *Rev. Mod. Phys.* **2003,** *75,* 949–983. doi:10.1103/RevModPhys.75.949
11. Kobayashi, K.; Yamada, H.; Matsushige, K. *Rev. Sci. Instrum.* **2009,** *80,* 043708. doi:10.1063/1.3120913
12. Schneiderbauer, M.; Wastl, D.; Giessibl, F. J. *Beilstein J. Nanotechnol.* **2012,** *3,* 174–178. doi:10.3762/bjnano.3.18
13. Worley, R. D.; Zemansky, M. W.; Boorse, H. A. *Phys. Rev.* **1954,** *93,* 45–46. doi:10.1103/PhysRev.93.45
14. Binnig, G.; Quate, C. F.; Gerber, C. *Phys. Rev. Lett.* **1986,** *56,* 930–933. doi:10.1103/PhysRevLett.56.930
15. Giessibl, F. J. *Appl. Phys. Lett.* **2000,** *76,* 1470–1472. doi:10.1063/1.126067
16. An, T.; Eguchi, T.; Akiyama, K.; Hasegawa, Y. *Appl. Phys. Lett.* **2005,** *87,* 133114. doi:10.1063/1.2061850
17. Microcrystal. Micro Crystal Product Brochure, Micro Crystal AG, Grenchen, Switzerland.
18. Hembacher, S.; Giessibl, F. J.; Mannhart, J. *Appl. Surf. Sci.* **2002,** *188,* 445–449. doi:10.1016/S0169-4332(01)00976-X
19. Rychen, J.; Ihn, T.; Studerus, P.; Herrmann, A.; Ensslin, K.; Hug, H. J.; van Schendel, P. J. A.; Güntherodt, H. J. *Rev. Sci. Instrum.* **2000,** *71,* 1695–1697. doi:10.1063/1.1150521
20. Lager, G. A.; Jorgensen, J. D.; Rotella, F. J. *J. Appl. Phys.* **1982,** *53,* 6751–6756. doi:10.1063/1.330062
21. White, G. K. *Cryogenics* **1964,** *4,* 2–7. doi:10.1016/0011-2275(64)90029-3
22. Barron, T. H. K.; Collins, J. G.; White, G. K. *Adv. Phys.* **1980,** *29,* 609–730. doi:10.1080/00018738000101426
23. Blinick, J. S.; Maris, H. J. *Phys. Rev. B* **1970,** *2,* 2139–2146. doi:10.1103/PhysRevB.2.2139
24. Vanelstraete, A.; Laermans, C. *Phys. Rev. B* **1989,** *39,* 3905–3908. doi:10.1103/PhysRevB.39.3905
25. Vanelstraete, A.; Laermans, C. *Mater. Sci. Eng., A* **1989,** *122,* 77–81. doi:10.1016/0921-5093(89)90775-2
26. Femto HQA-15M-10T, Femto Messtechnik GmbH, Berlin, Germany.
27. OC4 - Nanonis Oscillation Controller, Specs Zurich GmbH, Zurich, Switzerland.
28. Parshin, M. A.; Laermans, C. *Phys. Status Solidi C* **2004,** *1,* 2892–2895. doi:10.1002/pssc.200405296
29. Giessibl, F. J.; Bielefeldt, H.; Hembacher, S.; Mannhart, J. *Appl. Surf. Sci.* **1999,** *140,* 352–357. doi:10.1016/S0169-4332(98)00553-4
30. Welker, J.; de Faria Elsner, F.; Giessibl, F. J. *Appl. Phys. Lett.* **2011,** *99,* 084102. doi:10.1063/1.3627184

License and Terms

Beilstein Journal of Nanotechnology

The softening of human bladder cancer cells happens at an early stage of the malignancy process

Jorge R. Ramos[1,2], Joanna Pabijan[3], Ricardo Garcia[*1] and Malgorzata Lekka[*3]

Full Research Paper

Open Access

Address:
[1]Instituto de Ciencia de Materiales de Madrid, CSIC, Sor Juana Inés de la Cruz 3, 28049 Madrid, Spain, [2]Centro de Estudios Avanzados de Cuba, Carretera de San Antonio de los Baños, km 1 ½, Valle Grande, La Habana, Cuba and [3]The Henryk Niewodniczański Institute of Nuclear Physics, Polish Academy of Sciences, Radzikowskiego 152, 31-342 Kraków, Poland

Email:
Ricardo Garcia[*] - r.garcia@csic.es; Malgorzata Lekka[*] - Malgorzata.Lekka@ifj.edu.pl

* Corresponding author

Keywords:
actin filaments; atomic force microscopy (AFM); bladder cells; cytoskeleton; elastic properties of cells; malignancy degree of cancer cells

Beilstein J. Nanotechnol. **2014,** *5,* 447–457.
doi:10.3762/bjnano.5.52

Received: 20 December 2013
Accepted: 11 March 2014
Published: 10 April 2014

This article is part of the Thematic Series "Advanced atomic force microscopy techniques II".

Guest Editors: T. Glatzel and T. Schimmel

Abstract

Various studies have demonstrated that alterations in the deformability of cancerous cells are strongly linked to the actin cytoskeleton. By using atomic force microscopy (AFM), it is possible to determine such changes in a quantitative way in order to distinguish cancerous from non-malignant cells. In the work presented here, the elastic properties of human bladder cells were determined by means of AFM. The measurements show that non-malignant bladder HCV29 cells are stiffer (higher Young's modulus) than cancerous cells (HTB-9, HT1376, and T24 cell lines). However, independently of the histological grade of the studied bladder cancer cells, all cancerous cells possess a similar level of the deformability of about a few kilopascals, significantly lower than non-malignant cells. This underlines the diagnostic character of stiffness that can be used as a biomarker of bladder cancer. Similar stiffness levels, observed for cancerous cells, cannot be fully explained by the organization of the actin cytoskeleton since it is different in all malignant cells. Our results underline that it is neither the spatial organization of the actin filaments nor the presence of stress fibers, but the overall density and their 3D-organization in a probing volume play the dominant role in controlling the elastic response of the cancerous cell to an external force.

Introduction

During oncogenic progression, many cancer-related alterations change both the internal structures of cells and also their surroundings, i.e., the extracellular matrix (ECM). During last two decades, much research has been carried out that demonstrated a larger deformability of living cancerous cells, which is in contradiction to the macroscopically detected stiffening of

various tumors. Several papers demonstrated the possible influence of the ECM surrounding cancerous cells in the tumor progression [1,2]. The best example is breast cancer, whose solid tumors are detectable in macroscale by palpation whereas single cells show a larger deformability [3]. In this context, it has also been proposed that tumorigenesis in breast tissues is driven by changes in the mechanical properties of the extracellular matrix [2,4]. Remarkably, in this case the ECM of the malignant cells is stiffer (reflected by a higher Young's modulus) as compared to the ECM of non-malignant tissues [2]. Those studies underline the connection between changes in the mechanical properties of the cell and the extracellular matrix, and the presence or development of progressive diseases. However, the specific role of the mechanical properties of the cells and the extracellular matrix in pathogenesis such as tumor progression remain poorly understood at best. The relationship between mechanics at the cellular level and tumorigenesis represents a new perspective for which many issues need to be addressed.

The studies of cell mechanics have gained great importance with the advent of AFM measurements, which demonstrated the capability to probe single cells and underlining a correlation between cell mechanics, in particular elasticity, and cancer [5,6]. The first measurements showed that cancerous human bladder cells were softer than non-malignant bladder cells. Further measurements of cancerous cells have confirmed that a lowering of the elastic modulus of the cells is a general feature of cancer transformation [6-12]. This change is probably associated with the enhanced capability to migrate and to adapt to changing environments, which is observed in metastasis. Importantly, these results are valid for other cell lines, such as ovary or prostate cancers [10], and can be extended also to primary cells [6,13] and tissue sections [5,12] that were collected from human patients. For example, a comparison of the elastic properties of normal and benign breast tissues gives a wide distribution of the Young's modulus, in which a peak at lower values characterizes malignant tissues. It has also been found that the Young's modulus distribution in cancerous cells is narrower than the distribution found in non-malignant cells [4,6]. However, the elements of the cell that contributes to its mechanical response as measured by the AFM need to be clarified.

AFM studies on cells are often combined with the use of drugs that modify the mechanical response of the cell [14,15]. The influence of the different elements of the cytoskeleton on the force response can be monitored by selectively inhibiting the formation of some of them [16-19]. By disaggregation of actin filaments with the use of different types of cytochalasin, Rotsch and Radmacher have reported a decrease of the Young's modulus of fibroblasts [16]. Similar findings regarding the role of actin filaments have been reported in other types of cells such as lymphocyte and Jurkat cells [19]. The role of the microtubules (MT) in AFM measurements remains open. Pelling et al. performed immunofluorescence and AFM studies in order to determine the influence of the MT on the cell membrane in response to serum conditions and nocodazole [17]. Their results show that the stiffness depends on the interplay between dynamically different types of MT configurations (unstable and stable) and intermediate filaments (IF), which all act to impart a distinct cellular type of transient metastability. On the other hand, it has been reported that the disassembly of the MT of fibroblasts by using colchicine and colcemide does not lead to a softening of the cell [16]. The abovementioned research shows that disruption of cytoskeletal filaments is useful for assesing the link between the elastic properties of cells and the structure of the cytoskeleton. It is also worth mentioning that such an approach can be used for studying the influence of certain such compounds as chitosan [14] or cisplatin [20] on the mechanics of single cells, while pointing out that studies on the correlation between the mechanical properties and the structure of the actin cytoskeleton are particularly important for developing and monitoring cancer therapies.

It is well established that actin filaments are mostly responsible for the mechanical properties of cells that are measured by the AFM. Therefore, there have been several attempts trying to show the correlation between the 2D-organization of actin filaments and cells stiffness in relation to cancer invasion. The relation between the stiffness of cancer cells and the 2D-organization of the actin cytoskeleton has been reported for breast [3], thyroid [11] and ovarian [21] cancers. For stiffer cells, the actin filaments distribution usually revealed two types of filament organization, i.e., an actin cortex and well-formed linear actin bundles (i.e., stress fibers) that span over a whole cell. For softer cells, the actin filaments were less organized. Mostly, short filaments were observed. If F-actin bundles were present, they were shorter and randomly oriented. In particular for ovarian cancer, the correlation between the migratory behavior of cells and their stiffness has been demonstrated [21]. In other studies, the larger deformability of the mouse ovarian cells has been correlated with the dysregulation of actin (stress) fibers, which influences both fiber thickness and organization, as shown by confocal microscopy of early and late stages of ovarian cancer progression [22].

Here, we study the correlation between the elastic properties and the expression and organization of the actin cytoskeleton in human bladder cancer cells. We have chosen four cell lines with various histological grades. Those lines differ in terms of the organization of the cytoskeleton (presence/absence of stress

fibers, distinct actin expression level) and the elastic properties measured by force spectroscopy. The cancerous cells are more compliant with respect to the non-malignant cells. Regardless of histological grades, the deformability of the cancerous cells reaches a similar level but the organization of actin filaments remains dependent on the cell type. These data underlines the complexity of the remodeling process in actin filaments in cancers that is expressed in the elastic properties of cells. Our findings show that in human bladder cancer cells, both the expression level of actin (in particular, β-actin) and its 3D-organization in the probing volume govern the elastic properties. The organization of actin filaments present on the surface of a cell as probed by AFM and fluorescence microscopy is not sufficient to fully explain the cellular stiffness. Additionally, the presence of actin fibers (stress fibers) is not a prerequisite for a deformability of cancer bladder cells. Moreover, the observed sudden drop of stiffness is a clear indication of cancer-related changes in human bladder cells, which strongly supports the usefulness of cell deformability in detecting cancer-related changes in bladder cancer. Such a relation has not been observed so far for any other cells measured by AFM in which usually a gradual drop of stiffness was observed.

Results

Cell morphology

Force spectroscopy experiments were performed on living cells, which were located on an inverted optical microscope (Figure 1). The optical microscope was also used to estimate the position of the AFM probe (tip) along the cell. Once a position was selected (close to the cell nuclei), the tip was approached towards the cell surface until a repulsive force reached the set point value of 100 pN.

The AFM images were taken over an area of 20 × 20 μm^2 with 512 pixels per line. The scan rate was varied from 0.5 to 1.0 Hz depending on the cell type. Figure 2 shows the AFM topography, error signal, single cross-sections and the fluorescence images of the cell lines studied here, non-malignant HCV29 and the malignant cells HTB-9, HT-1376, and T24, respectively. The AFM error image (panels A, E, I, and M) enables to visualize the cell cytoskeleton that lies beneath the cell membrane. The filaments observed by AFM correspond to the actin filaments. Although, they are dispersed throughout the whole cell, they are mainly concentrated close to the cell membrane to form the so called actin-cortex. The AFM error image shows that these filaments are organized in two groups: (i) short actin filaments and (ii) and bundles of long acting filaments (stress fibers). The presence of these two groups in the AFM image depends on the cell type. In the non-malignant HCV29 cells both short actin filaments and stress fibers are visible. Similarly, both structures are present in cancerous T24 cells (transitional cell carcinoma). However, the other types of malignant cells, HTB-9 (grade II, carcinoma) and HT-1376 (grade III, carcinoma) do not show the presence of stress fibers. These results are consistent with fluorescence microscopy images of actin filaments stained by using phalloidin that was labeled with Alexa Fluor 488 dye (Figure 2, panels D, H, L, P and Figure S1 in Supporting Information File 1). Similarly to the AFM images the stress fibers are only visible in the non-malignant HCV29 cells and the cancerous T24 cells.

The cross-sections along the marked lines on the AFM topography (Figure 2, panels C, G, K, and O) show the apparent height differences between two positions along the cell surface. One located above the nucleus and the other close to the cell edge. The height ranges from 3 to 4 μm depending on the cell type. The highest values were observed for HTB-9 cells (≈4 μm). The others cell types had similar height of about 3 μm. We note that the size of the nucleus does not seem to correlate with the observed height. For example, the HTB-9 cell has the

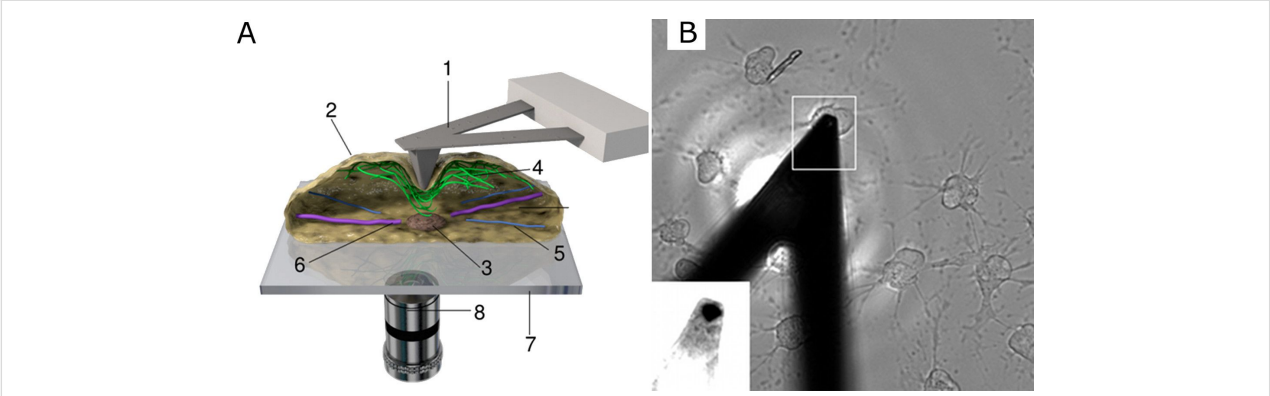

Figure 1: (A) Scheme of experimental setup. (1) V-shaped cantilever-tip ensemble; (2) cell membrane; (3) cell nucleus; (4) actin filaments; (5) intermediate filaments; (6) microtubules; (7) cover slip; (8) optical microscope lens. (B) Optical image of the cantilever positioned on top of the cell treated with cytochalasin D. After being treated with cytochalasin D, the cells shrink to a circular form.

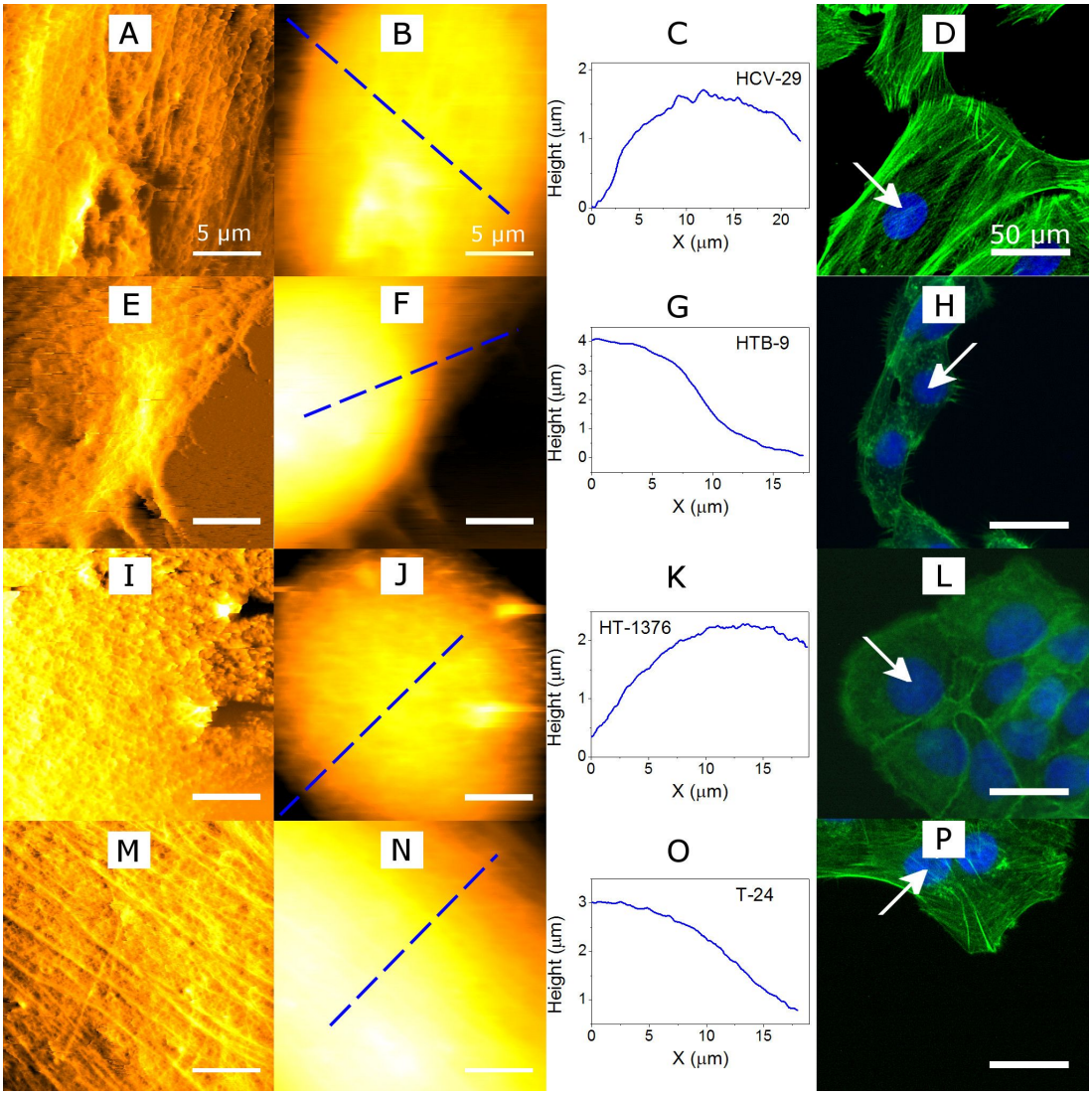

Figure 2: Force and fluorescence microscopy images of bladder cells. (A–D) Non-malignant cells, HCV29; (E–H), HTB-9 cells, grade 2; (I–L) HT-1376 cells, grade 3; (M–P) T24, grades 3 and 4. The AFM measurements were performed on regions centered over the cell nucleus marked with an arrow in the fluorescence images. The 1st column (panels A, E, I and M panels) is the AFM error signal. The 2nd column (B, F, J and N) shows the topography (AFM). The 3rd column (C, G, K and O) shows the apparent height profile. The 4th column (D, H, L and P) shows the fluorescence microscopy images. The arrows indicate the cells where the AFM images were recorded (blue: cell nucleus; green: actin cytoskeleton).

smallest nucleus; however, it has the largest height as measured from the substrate baseline.

Expression of actin

Actin is a globular protein that forms microfilaments. It exists in α, β, and γ isoforms. The α-actin was found in muscle tissues, the β- and γ-actins coexist in most cell types as components of the cytoskeleton [23-25]. Moreover, the transition from the epithelial to the mesenchymal phenotype reported for cancer progression requires a remodeling of the actin cytoskeleton [26]. This phenomenon is visible in the fluorescence and AFM images obtained for the four studied human bladder cell lines.

In order to verify whether changes in the organization of the actin filaments are accompanied with the different expressions of actin, we have used the Western blot (Figure 3). The analysis was performed for the same number of cells (i.e., 2.56×10^6 cells/mL) for each studied cell line. This analysis exhibited two bands at 42 and 43 kDa. The used antibody targets all the known actin isoforms with a molecular mass of 42 kDa in globular and fibrous forms. The band of 43 kDa probably corresponds to cytoplasmic actin isomers of 43 kDa that possess similar epitopes as those of 42 kDa.

The obtained results showed the higher amount of actin in non-malignant HCV29 cells and the lowest in cancerous HT-1376

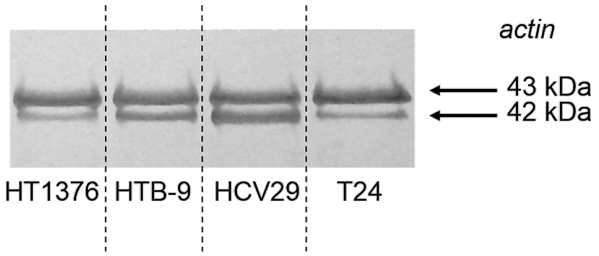

Figure 3: Total expression of actin in human bladder cells. The used antibody targets all known actin isoforms with a molecular mass of 42 kDa (globular actin and fibrous actin). The upper band (43 kDa) probably corresponds to cytoplasmic actin isomers with 43 kDa that possess the similar epitopes as those of 42 kDa.

(grade III, carcinoma) and T24 (transitional cell carcinoma) cells. To quantify the expression, the ImageJ program was used to determine the area under each band. The largest area corresponds to the HCV29 cells. The band area of the cancerous cells with respect to HCV29 was 73%, 35% and 42% for the HTB-9, HT-1376 and T24 cell lines, respectively. The results show that when cells with increasing tumor grading are measured, the amount of actin decreases in the cancerous cells as compared to non-malignant ones.

Determination of the Young's modulus

The elastic properties of the cells were determined by using Sneddon's model for a conical shape of the tip [27]. First, the force curves were converted into force-versus-indentation curves and those curve were fitted to Equation 1 (see section Experimental: Force spectroscopy on living cells). Because the Young's modulus of the tip is about 160 GPa (seven orders of magnitude larger than that of the cells), we can assume that Young's modulus of the interface is $E_{\text{eff}} \approx E_{\text{cell}}/(1 - \nu^2)$. Figure 4A shows a typical force curve obtained on a HT-1376 bladder cell together with a force curve obtained on a stiff surface (glass). For a given deflection (or force), the difference between the piezo displacement for the stiff and compliant surface gives the indentation (Equation 2, see section Experimental: Force spectroscopy on living cells). Figure 4B shows the force-versus-indentation curve derived from Figure 4A and the fit obtained with the Sneddon's model assuming a conical AFM tip with half-angle of 20°. The Young's modulus obtained from the fit was 6.1 kPa. The force spectroscopy data has been acquired in the region of the cell above the nucleus. The experimental force curves show some deviations from a parabola. Consequently, the parameters of the fitting will depend on the fitting length (indentation). For that reason, any conclusion derived from the data has to be verified for all the indentation depths studied here. On the other hand, the relative error in the determination of the contact point will decrease for larger indentations.

The results obtained for all recorded cell lines yielded the corresponding distributions of the Young's moduli. Figure 5 shows the Young's modulus values collected from the four bladder cell lines of this study and calculated for the indentation from 0 to 300 nm. Depending on the cell type distinct features are observed in the histograms. For the non-malignant cells (panel A), the observed distribution can be decomposed in two Gaussians, the larger one centered at 16.0 ± 0.9 kPa and the smaller centered at 33.0 ± 2.0 kPa. For HTB-9 (panel B) cells most of the data is centered at 3.0 ± 0.1 kPa with a small tail centered at 6.4 ± 0.5 kPa; for T24 (panel D) cells the dominant peak is centered at 2.9 ± 0.5 kPa while the secondary contribution has its maximum at 6.2 ± 0.6 kPa. The histogram for HT-1376 (panel C) cells shows a single maximum centered at 5.2 ± 0.1 kPa. We also observe that the histograms are narrower for all cancerous cells. This is in agreement with previous

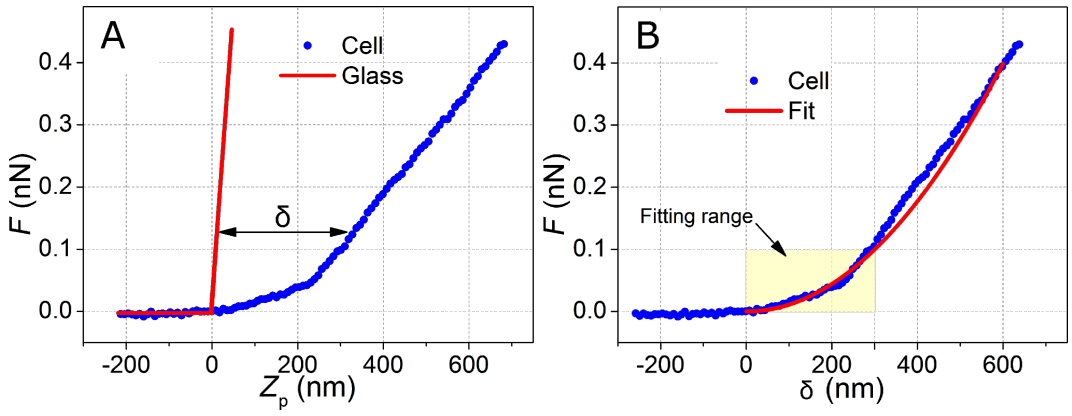

Figure 4: (A) Exemplary force curve recorded on a HT-1376 cell (blue dots). The red solid line represents a curve taken on a hard glass surface (calibration curve). The indentation δ is the horizontal difference between these curves (see Equation 2). The contact point is chosen as the origin. (B) Force-versus-indentation curve (blue dots) fitted with Sneddon's equation for a conical tip (red line).

results that showed that the distribution of the Young's modulus becomes narrower for metastatic cells [4,14].

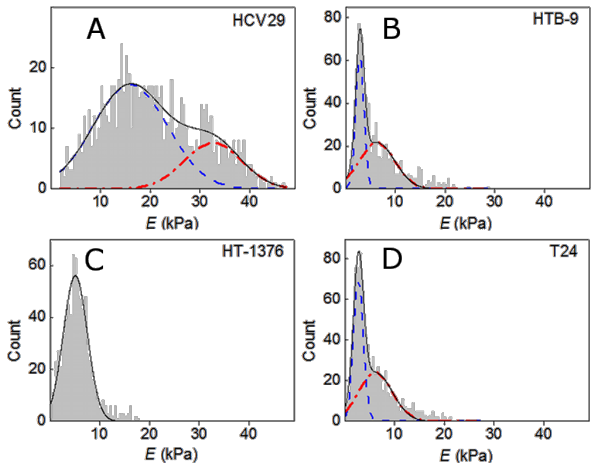

Figure 5: Distribution of Young's moduli determined by fitting the curves within the indentation range up to 300 nm. The elasticity histogram is broader for the non-malignant cells (HCV29) than for the HTB-9 and the T24 cancerous cells. Histogram bin width of 500 Pa.

Figure S2 (Supporting Information File 1) shows the Young's moduli of the same cell lines, but in this case the fitting has been extended up to an indentation depth of δ = 500 nm. Two main conclusions are derived with respect to the data obtained at δ = 300 nm. First, the maxima of the distributions are shifted to lower values. Second, the distribution width is smaller. Those results apply for all bladder cell lines of this study.

Depth-dependent changes of the Young's modulus

Figure 6A presents the changes of the Young's modulus as a function of the indentation depth between 100 and 500 nm. For the non-malignant HCV29 cells the modulus goes from 50 kPa at 100 nm to 10 kPa at 500 nm. For the malignant cells the Young's modulus decreases from about 15 kPa at 100 nm to 5 kPa at 500 nm. The decrease of the Young's modulus with δ has been previously reported [18] although this effect is still not fully understood [5,18,19].

Effect of cytochalasin D on the elasticity of the cells

In order to verify the influence of the actin filaments and their structure on E_{cell}, some of the cell lines were treated with cytochalasin D (Cyt-D), which is known to depolymerize the actin filaments. This results in a reduction of the Young's modulus [16]. However, Cyt-D does not affect the structure of MT or IF. Figure S3 (Supporting Information File 1) shows the Young's moduli of the HCV29 cell line before and after exposure to Cyt-D measured at δ = 300 nm. The actin cytoskeleton of HCV29 cells is composed of short actin filaments and stress fibers. The stress fibers are visible in Figure 2 and Figure S1 (Supporting Information File 1) for the cell lines HCV29 and T24. After adding Cyt-D, the modulus drops from 21 to 2 kPa. We note that the differences between treated and non-treated cells are preserved across the different individual cells and cell locations. The Young's moduli measured on different cells of the same cell line are similar (Figure S3, Supporting Information File 1). In fact the variability observed for each cell type could be attributed to local changes in the region around the cell where the measurement has been performed. The measurement in each of the panels of Supplementary Figure S3 has taken over 4 h.

The actin cytoskeleton structure of HTB-9 cells is mainly composed of short actin filaments. In these cells, there are virtually no stress fibers to be seen. In this cell line a treatment with

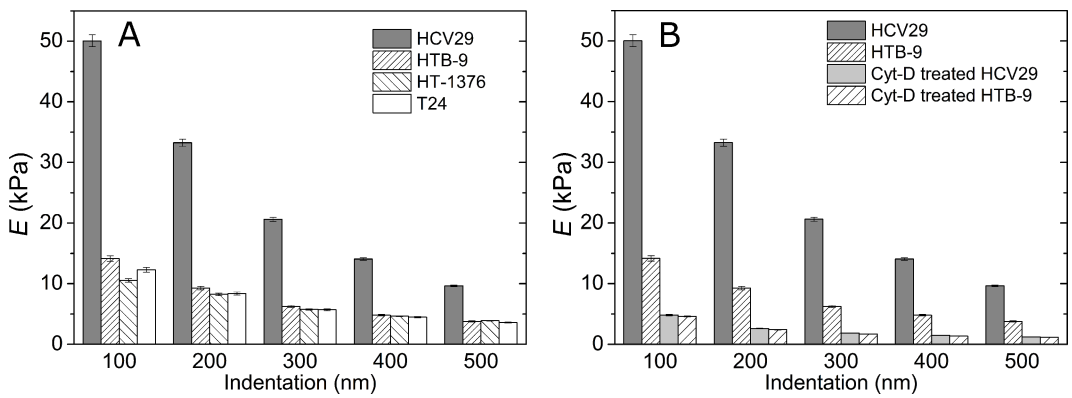

Figure 6: (A) Elasticity of living bladder cells as a function of the indentation depth. The data is presented as mean ± SD. (B) Comparison of the elasticity of the cells before and after treatment with cytochalasin D (Cyt-D). The data is presented as mean ± SD.

Cyt-D causes a decrease of E_{cell} from 15 kPa to 5 kPa (δ = 100 nm) and from 6 kPa to 2 kPa (δ = 300 nm). Figure 6B shows the change of the Young's moduli for HCV29 and HTB-9 cells before and after exposure to Cyt-D for different indentations. Interestingly, the elastic response of non-malignant and malignant cells is almost identical after exposure to Cyt-D.

Statistical significance of the cells Young's modulus

The statistical significance of the Young's modulus measurements for the different cell lines was verified by applying the Tukey–Kramer method [28]. Here the test was performed at a significance level of $P = 0.05$ (Table 1). The test shows statistically significant differences between the Young's modulus values of HCV29 non-malignant cells and those obtained on cancerous cells. Similarly, relevant statistical differences are found between the values measured before and after the treatment with cytochalasin D. It also shows that among cancerous cells (HTB-9, HT-1376 and T24) there are no statistical differences in their values, at least for indentation depths between 200 and 400 nm. It is worth to mention that cells treated with Cyt-D had similar Young's moduli for both cell lines (HCV29 and HTB-9).

Table 1: Tukey–Kramer multiple comparison test of the results shown in Figure 6 with significance level $P = 0.05$ for all indentation depths.[a]

cell type	HTB-9	HT-1376	T24	HCV29 + Cyt-D	HTB-9 + Cyt-D
HCV29	***	***	***	***	***
HTB-9		ns	ns[b]	***	***
HT-1376			ns[b]	***	***
T24				***	***
HCV29 + Cyt-D					ns

[a]*** $P < 0.001$; ns: no significant differences between samples; [b]There are two exceptions for the data represented: for HTB-9–T24 at 100 nm $P < 0.01$ and for HT-1376–T24 at 500 nm $P < 0.05$.

Discussion

The integration of force and fluorescence microscopies enables one to obtain comprehensive information about the morphology of the cells. The latter provides the information about fluorescently labeled structures while AFM delivers the topology and the mechanical properties of the sample. In our studies, the fluorescent images of actin filaments were compared with the surface topography. The cytoskeleton is important for a normal cell function, however, cancer progression changes its role by using it as a tool to alter cell growth, stiffness, movement and invasiveness [26]. The actin cytoskeleton serves as a scaffold for signaling, as a connection to the extracellular environment, and as a mechanosensor. However, there is no general evidence that changes in the expression or organization of actin promotes or inhibits cancer metastasis. It seems that cancerous cells reorganize the actin cytoskeleton to alter the growth or adhesion or the mechanical properties to enhance their survival rate during various phases of tumor progression and metastatic spreading. This reorganization process involves both re-arrangements of actin filaments in the cell and also changes in the actin expression [27]. Our results on human bladder cancer cells showed that the level of actin (a component of the cell cytoskeleton and also a mediator of internal cell motility) in non-malignant HCV29 cells is the highest. Its drops as follows: HTB-9 (grade II, carcinoma) > T24 (transitional cell carcinoma) > HT-1376 (grade III, carcinoma) cells. Moreover, in non-muscles cells, the actin cytoskeleton in cells can be divided into two groups: short actin filaments forming a cortex and long stress fibers that consist of bundles of single actin filaments. The actin cortex is located beneath the cell membrane while the actin stress fibers span over the whole cell. The results obtained on human bladder cells (non-malignant HCV29 and three cancerous lines HTB-9, HT-1376 and T24) showed various organizations of the actin cytoskeleton as observed by fluorescence microscopy. In non-malignant HCV29 cells, both short actin filaments and stress fibers are visible. Similarly, both structures are present in cancerous T24 cells (transitional cell carcinoma). The two other cancerous cells, HTB-9 cells (grade II, carcinoma) and HT-1376 (grade III, carcinoma) only show the presence of short actin filaments. In recent decades, a novel functionality of the AFM, i.e., stiffness tomography, has been demonstrated [29,30] for neurons to deliver a 3D recording of the Young's modulus. The results have shown the presence of hard structures, which are attributed to cortical actin cytoskeleton. However, the organization and mechanical properties of single actin filaments stress fibers have not been shown by this technique. Nevertheless, the imaging of the cell surface by using AFM in contact mode can convey information about the superficial layers of the actin cytoskeleton. In our case the topography of each studied cell lines correlates with the images of phalloidin stained actin filaments, which were recorded by using fluorescence microscopy.

The actin cytoskeleton has been reported to play the main role in the mechanical properties of living cells [15,31]. The observed increase of cellular deformability, which is induced by cytochalasin D, relates to the mechanical properties of the cytoskeleton with the actin network lying beneath the cell membrane. However, it cannot be specified, which form of spatial organization of actin filaments dominates. The highest expression of actin and the most abundant presence of stress

fibers, which is observed in HCV29 cells, were accompanied by a large value of the Young's modulus. It is clearly visible that a lower expression of actin, which is observed in malignant cells (HTB-9, HT-1376 and T24), is associated with a lower Young's modulus. All malignant cells showed similar values of the Young's modulus. However, the elastic properties of the cancerous cells seem to be independent of the presence/absence of stress fibers. The stress fibers are present in T24 cancerous cells (transitional cell carcinoma) but not in HTB-9 (grade II, carcinoma) and the HT-1376 (grade III, carcinoma).

The altered elastic properties of single cells is nowadays almost believed to be a general feature of cancer progression, which has been already shown in various measurements performed by using atomic force microscopy. The examples encompass human bladder [5,32], breast [3], colon [31], prostate [10,32], thyroid [11] and cervical cells [33]. A similar relationship was obtained in previous studies for human bladder cancer cells [5]. The non-malignant HCV29 cells were significantly stiffer than the cancerous ones. It should be also pointed out that these measurements are in agreement with the data reported earlier, in which the stiffness of both HCV29 and T24 cells was measured by force spectroscopy [5,14]. This observation is particularly important since these cells were grown previously on a glass coverslip covered with poly-L-lysine. In the present studies no glass surface modification was introduced. Thus, substrate chemical properties do not change the relationship between non-malignant HCV29 and cancerous T24 cells. The comparison performed in the previous studies showed that two non-malignant cell lines (HCV29 and Hu609) were significantly stiffer than three cancerous ones, i.e., Hu456 (grade I, carcinoma), T24 (transitional cell carcinoma), BC3726 (HCV29 cells transformed with v-*ras* oncogene). However, in the studies from 1999 [5], there was no fluorescence microscopy involved to show the organization of actin filaments in the studied cell lines. In our work we have observed the same relation. Independently of the histological grade, the cancerous cells are more deformable. This point out the usefulness of the AFM to detect bladder cancer cells –regardless of the state of cancer progression– soft cells indicate a malignant phenotype.

The fluorescent images of the actin filaments, obtained in the present study, showed surprisingly that the 2D-organization of these filaments on the cell surface is not solely responsible for the observed stiffness of all malignant cells. It seems that in our case, the elastic properties are governed by both the expression level of F-actin and its 3D-organization in the probing volume.

The dependence of the Young's modulus on the indentation depth represents another important element of the presented data. In the range studied here between 100 and 500 nm, the Young's modulus decreases with the indentation depth (Figure 6A). The decrease of the Young's modulus with the indentation depth indicates little influence of the solid support on the measurements [34]. Here we are focused on the ability to distinguish cells of different malignancy degrees. Consequently, in order to visualize the variations across the different cells lines we have normalized the Young's modulus of the different cells to the one obtained at the same indentation for the non-malignant cells. Two main observations are obtained from the normalized plot. First, non-malignant bladder cells are stiffer than malignant cells. Second, for the cell lines studied here, the histologically determined tumor grade does not seem to be reflected in the elastic properties of the cells.

The treatment of cells with cytochalasin D resulted in a marked decrease of their Young's modulus (Figure 6B). The Cyt-D inhibits the actin polymerization by binding to the fast growing plus ends of the microfilaments and blocking both the assembly and the disassembly of individual actin monomers from the bound end. It has been reported that the results of its action is a drop of the overall cell elasticity [16,33]. The correlation between the reduction of the Young's modulus and the depolymerization of the actin filaments supports a predominant role of these filaments on the stiffness of the cells. In order to verify how the organization of the actin cytoskeleton influences the mechanical properties, HCV29 and HTB-9 cells were treated with 5 μM Cyt-D. The observed decrease of the elastic modulus confirms the pre-dominant influence of actin filaments on the elastic properties. The results was independent of both the 2D organization of actin filaments and on the expression level of actin (similar values were obtained 1.8 ± 0.1 kPa and 1.7 ± 0.1 kPa for HCV29 and HTB-9, respectively). The deformability of all studied cancerous cells is slightly larger than that of the cell treated with cytochalasin D. This points out to partial but extensive changes in actin cytoskeleton structure induced by cancer progression.

The relation between the cell deformability and the degree of invasiveness has attracted attention almost from the beginning of the elasticity measurements of cancerous cells. The comparison between various cell lines of the same origin like breast, prostate, bladder, thyroid, and ovarian cancers, only shows such a relation for ovarian cancers [21]. In the other research either only a comparison between only two cell lines has been done or such correlation could not be shown clearly. In our case, for bladder cancer, the first results from 1999 showed a significant difference between non-malignant and cancerous cells without any consideration of their degree of invasiveness. The results presented here, now clearly demonstrate that most probably, in human bladder cancers, cells acquiring a more invasive phenotype become more deformable at early stages of cancer progres-

sion. This makes the cell stiffness a powerful biomarker for detecting cancer-related alterations in human bladder tumors.

Conclusion

Nanomechanical measurements performed with a force microscope at the single cell level have been applied to characterize the elastic properties of human bladder cancer cells. All malignant bladder cells have Young's moduli about 2–3 times lower that those non-malignant cells. The low Young's modulus (higher cellular deformability) seems to occur at an earlier stage of cancer progression and it does not seem to evolve with the metastatic phenotype. It correlates with a partial lack and/or depolymerization of the actin filaments. The data implies that the elastic response is dominated by the expression of F-actin. However, the presence of actin stress fibers (observed in non-malignant HCV29 and cancerous T24 cells) is not a prerequisite for a smaller cellular deformability of cancer bladder cells. The stress fibers observed in T24 cells produce a rather small increase of the Young's modulus. This strongly suggests that the deformability of cancer cells is mainly related to the 3D-organization of actin filaments (both short filaments, and stress fibers) together with their density. The elastic properties of cancerous cells (HTB-9, HT-1376 and T24) were independent of the cell line, the stage of cancer progression, and the cell cycle. Therefore, they underline the usefulness of atomic force microscopy to detect bladder cancer cells because regardless on the state of cancer progression, softer cells indicate a malignant phenotype.

Experimental

Cell lines: Four bladder cell lines with epithelial origin have been studied: non-malignant transitional epithelial cells of the ureter (HCV29, Institute of Experimental Therapy, Wroclaw, Poland), which serve as a reference; urinary bladder cell carcinoma (HTB-9, grade II, ATCC, LGC Standards); urinary bladder cell carcinoma (HT-1376, grade III, ATCC, LGC Standards) and transitional cell carcinoma (T24, ATCC, LGC Standards).

The HCV29 and the T24 cells were grown in RPMI-1640 medium (Sigma) supplemented with 10% Fetal Bovine Serum (FBS, Sigma). The HTB-9 cells were grown in RPMI-1640 supplemented with 10% FBS, 1% HEPES (4-(2-hydroxyethyl)-1-piperazineethanesulfonic acid, Sigma) and 1% sodium pyruvate (Sigma). Finally, the HT-1376 cells were grown in Eagle's medium (EMEM, LGC Standards) supplemented with 10% FBS (LGC Standards). The cells were cultured on glass coverslips placed inside plastic Petri dishes at 37 °C in a 95% air/5% CO_2 atmosphere. The relative humidity was kept above 98%. The cells were measured 3 to 4 days after seeding. The cells treated with cytochalasin D (Sigma) were first rinsed with RPMI-1640 medium and then they were immersed in a 5 μM Cyt-D solution in RPMI-1640 medium for 1 h at 37 °C.

Actin expression in bladder cells: The expression of β-actin in the studied human bladder cells was determined by using Western blot analysis, performed in analogous way as in [35]. Briefly, for this analytical technique, which uses gel electrophoresis to separate native proteins, the same number of cells of about 2.56×10^6 cells per mL for each cell line was lysed and loaded on 12% gels for SDS-PAGE and afterwards transferred to a polyvinylidene difluoride membrane (Roche). After blocking with casein solution, the membranes were then incubated overnight with the primary antibody against actin (1:10000, 0.025 μg/mL, BD Biosciences).

Force spectroscopy of living cells: Force spectroscopy measurements were performed by using a commercial AFM (model XE120, Park Systems, South Korea). We used v-shaped silicon nitride cantilevers terminated with a silicon tip (MLCT-C, Bruker, USA). Those cantilevers are characterized by a nominal spring constant $k = 0.01$ N/m while the length of the tip length is about 3 μm long, with a half-angle of 20° and a radius of 20 nm. The sensitivity of the photodiode was calibrated on a rigid glass surface.

Force-versus-distance curves (force curves hereafter) were acquired in a 25-μm^2 region centered above the nucleus of the cell. The curves were acquired in 64 different positions separated by about 600 nm. The maximum indentation depth was established by the value of the peak force; in this case, it was set to 1 nN. The curves were acquired with a speed of 5 μm/s. The force-versus-indentation curves were obtained by subtracting the force curves recorded on a stiff glass surface from the ones recorded on the cell surfaces. The elastic modulus (Young's modulus) was determined by fitting the force-indentation curve (approach section) to the Sneddon's model [27,36] while assuming a conical tip. Then, the indentation depth and the effective Young's modulus E_{eff} are related by

$$F = \frac{2\tan\theta}{\pi} E_{\text{eff}} \delta^2 \approx \frac{2\tan\theta}{\pi} \frac{E_{\text{cell}}}{1-\nu^2} \delta^2 , \qquad (1)$$

where F is the loading force, θ is the half-angle of the cone, ν is the Poisson coefficient of the cells (0.5 in this study), and δ is the indentation depth. The indentation is determined from the displacement z_p of the piezo-scanner, the initial contact distance z_0, and the deflection given by a hard wall F/k,

$$\delta = z_p - z_0 - \frac{F}{k} \qquad (2)$$

All experiments were performed at room temperature in a culture medium RPMI-1640 supplemented with 10 mM HEPES. For the cells treated with Cyt-D the buffer was 5 μM Cyt-D in RPMI-1640 medium.

Statistical analysis: We have analyzed 10 to 16 cells for each cell line (about 700 individual force curves per cell line). The Tukey–Kramer test ($P = 0.05$) was used to confirm statistical differences between Young's modulus of different cell lines.

Fluorescence microscopy: The cells grown on a coverslip were washed with a RPMI-1640 medium supplemented with 10 mM HEPES. Next the cells were fixed by adding a 3.7% paraformaldehyde solution in PBS (phosphate buffered saline, Sigma) for 10 min and then washed with PBS buffer. The cell membrane was permeabilized by incubating the cells with a 0.2% Triton X-100 (Sigma) in PBS solution for 5 min. Finally, cells were rinsed with PBS buffer. Such prepared coverslips with cells were fluorescently labeled. The actin filaments were stained with phalloidin fluorescently labeled with Alexa Fluor 488 (Invitrogen) dissolved in PBS buffer (1:200) for 30 min. Then, the sample was washed with PBS buffer and the cell nuclei were stained with Hoechst stain (Invitrogen) in PBS buffer (1:5) for 15 min. The coverslips containing the cells were washed with PBS buffer, sealed using nail polish, and stored at 4 °C in the dark for 24 to 48 h before image recording.

Force and fluorescence microscopy imaging of the cells: The AFM is integrated with the inverted optical microscope equipped with fluorescent functionality. This enables to image the same region with both techniques and to correlate AFM and fluorescence data. The fluorescence microscopy was performed by using an Olympus IX71 inverted microscope (Olympus, Japan) equipped with a 100 W mercury lamp and U-MWIB2 and U-MWIG2 filters used for actin filaments (Alexa Fluor 488) and cell nuclei (Hoechst stain) visualization, respectively. For image recording, the Olympus XC10 digital camera (resolution 1376 × 1032 pixels) was used. Images were recorded using the program CellSens Dimension (Olympus). The AFM is equipped with a liquid cell sitting on a *x*–*y* piezoscanner with a range of 100 × 100 μm^2. The approach and retraction of the AFM probe is realized using a separate piezoscanner with a *z*-range of 10 μm. The AFM images were obtained in contact mode by applying a maximum force of 100 pN. The imaging scan line rate was between 0.5 to 1.0 Hz with a length between 20 to 50 μm. Each image has 512 × 512 pixels.

Western blot method: The Western blot technique is a standard technique used in cell biology to detect specific proteins in the sample. It follows through two steps. First, an electrophoresis is performed to separate proteins from a cell extract. Second, proteins are transferred to a membrane, on which they are stained using monoclonal antibodies. Each band correspond to a specific protein with a particular molecular mass.

Supporting Information

Supporting Information File 1

Additional experimental details.
[http://www.beilstein-journals.org/bjnano/content/supplementary/2190-4286-5-52-S1.pdf]

Acknowledgements

We thank A. Ruiz for sharing with us her knowledge of statistical analysis. This work was supported by the Ministerio de Economía y Competitividad (Consolider Force-For-Future, CSD2010-00024, MAT2009-08650), the project NCN DEC-2011/01/M/ST3/00711 (Poland), and the Cost Action TD1002.

References

1. Lu, P.; Weaver, V. M.; Werb, Z. *J. Cell Biol.* **2012,** *196,* 395–406. doi:10.1083/jcb.201102147
2. Goetz, J. G.; Minguet, S.; Navarro-Lérida, I.; Lazcano, J. J.; Samaniego, R.; Calvo, E.; Tello, M.; Osteso-Ibáñez, T.; Pellinen, T.; Echarri, A.; Cerezo, A.; Klein-Szanto, A. J. P.; Garcia, R.; Keely, P. J.; Sánchez-Mateos, P.; Cukierman, E.; Del Pozo, M. A. *Cell* **2011,** *146,* 148–163. doi:10.1016/j.cell.2011.05.040
3. Li, Q. S.; Lee, G. Y. H.; Ong, C. N.; Lim, C. T. *Biochem. Biophys. Res. Commun.* **2008,** *374,* 609–613. doi:10.1016/j.bbrc.2008.07.078
4. Ludwig, T.; Kirmse, R.; Poole, K.; Schwarz, U. S. *Pfluegers Arch.* **2008,** *456,* 29–49. doi:10.1007/s00424-007-0398-9
5. Lekka, M.; Laidler, P.; Gil, D.; Lekki, J.; Stachura, Z.; Hrynkiewicz, A. Z. *Eur. Biophys. J.* **1999,** *28,* 312–316. doi:10.1007/s002490050213
6. Lekka, M.; Gil, D.; Pogoda, K.; Dulińska-Litewka, J.; Jach, R.; Gostek, J.; Klymenko, O.; Prauzner-Bechcicki, S.; Stachura, Z.; Wiltowska-Zuber, J.; Okoń, K.; Laidler, P. *Arch. Biochem. Biophys.* **2012,** *518,* 151–156. doi:10.1016/j.abb.2011.12.013
7. Cross, S. E.; Jin, Y.-S.; Rao, J.; Gimzewski, J. K. *Nat. Nanotechnol.* **2007,** *2,* 780–783. doi:10.1038/nnano.2007.388
8. Cross, S. E.; Jin, Y.-S.; Tondre, J.; Wong, R.; Rao, J.; Gimzewski, J. K. *Nanotechnology* **2008,** *19,* 384003. doi:10.1088/0957-4484/19/38/384003
9. Reich, A.; Meurer, M.; Eckes, B.; Friedrichs, J.; Muller, D. J. *J. Cell. Mol. Med.* **2009,** *13,* 1644–1652. doi:10.1111/j.1582-4934.2008.00401.x
10. Faria, E. C.; Ma, N.; Gazi, E.; Gardner, P.; Brown, M.; Clarke, N. W.; Snook, R. D. *Analyst* **2008,** *133,* 1498–1500. doi:10.1039/b803355b
11. Prabhune, M.; Belge, G.; Dotzauer, A.; Bullerdiek, J.; Radmacher, M. *Micron* **2012,** *43,* 1267–1272. doi:10.1016/j.micron.2012.03.023
12. Plodinec, M.; Loparic, M.; Monnier, C. A.; Obermann, E. C.; Zanetti-Dallenbach, R.; Oertle, P.; Hyotyla, J. T.; Aebi, U.; Bentires-Alj, M.; Lim, R. Y. H.; Schoenenberger, C.-A. *Nat. Nanotechnol.* **2012,** *7,* 757–765. doi:10.1038/nnano.2012.167

13. Remmerbach, T. W.; Wottawah, F.; Dietrich, J.; Lincoln, B.; Wittekind, C.; Guck, J. *Cancer Res.* **2009,** *69,* 1728–1732. doi:10.1158/0008-5472.CAN-08-4073
14. Lekka, M.; Laidler, P.; Ignacak, J.; Łabędź, M.; Lekki, J.; Struszczyk, H.; Stachura, Z.; Hrynkiewicz, A. Z. *Biochim. Biophys. Acta, Mol. Cell Res.* **2001,** *1540,* 127–136. doi:10.1016/S0167-4889(01)00125-2
15. Wakatsuki, T.; Schwab, B.; Thompson, N. C.; Elson, E. L. *J. Cell Sci.* **2001,** *114,* 1025–1036.
16. Rotsch, C.; Radmacher, M. *Biophys. J.* **2000,** *78,* 520–535. doi:10.1016/S0006-3495(00)76614-8
17. Pelling, A. E.; Dawson, D. W.; Carreon, D. M.; Christiansen, J. J.; Shen, R. R.; Teitell, M. A.; Gimzewski, J. K. *Nanomedicine* **2007,** *3,* 43–52. doi:10.1016/j.nano.2006.11.006
18. Pogoda, K.; Jaczewska, J.; Wiltowska-Zuber, J.; Klymenko, O.; Zuber, K.; Fornal, M.; Lekka, M. *Eur. Biophys. J.* **2012,** *41,* 79–87. doi:10.1007/s00249-011-0761-9
19. Cai, X.; Xing, X.; Cai, J.; Chen, Q.; Wu, S.; Huang, F. *Micron* **2010,** *41,* 257–262. doi:10.1016/j.micron.2009.08.011
20. Sharma, S.; Santiskulvong, C.; Bentolila, L. A.; Rao, J.; Dorigo, O.; Gimzewski, J. K. *Nanomedicine* **2012,** *8,* 757–766. doi:10.1016/j.nano.2011.09.015
21. Xu, W.; Mezencev, R.; Kim, B.; Wang, L.; McDonald, J.; Sulchek, T. *PLoS One* **2012,** *7,* No. e46609. doi:10.1371/journal.pone.0046609
22. Dos Remedios, C. G.; Chhabra, D.; Kekic, M.; Dedova, I. V.; Tsubakihara, M.; Berry, D. A.; Nosworthy, N. J. *Physiol. Rev.* **2003,** *83,* 433–473. doi:10.1152/physrev.00026.2002
23. Ketene, A. N.; Schmetz, E. M.; Roberts, P. C.; Agah, M. *Nanomedicine* **2012,** *8,* 93–102. doi:10.1016/j.nano.2011.05.012
24. Huber, M. A.; Kraut, N.; Beug, H. *Curr. Opin. Cell Biol.* **2005,** *17,* 548–558. doi:10.1016/j.ceb.2005.08.001
25. Yilmaz, M.; Christofori, G. *Cancer Metastasis Rev.* **2009,** *28,* 15–33. doi:10.1007/s10555-008-9169-0
26. Hanahan, D.; Weinberg, R. A. *Cell* **2011,** *144,* 646–674. doi:10.1016/j.cell.2011.02.013
27. Sneddon, I. N. *Int. J. Eng. Sci.* **1965,** *3,* 47–57. doi:10.1016/0020-7225(65)90019-4
28. Montgomery, C. D. *Design and Analysis of Experiments,* 3rd ed.; John Wiley & Sons: Hoboken, NJ, USA, 1991.
29. Roduit, C.; Sekatski, S.; Dietler, G.; Catsicas, S.; Lafont, F.; Kasas, S. *Biophys. J.* **2009,** *97,* 674–677. doi:10.1016/j.bpj.2009.05.010
30. Roduit, C.; Saha, B.; Alonso-Sarduy, L.; Volterra, A.; Dietler, G.; Kasas, S. *Nat. Methods* **2012,** *9,* 774–775. doi:10.1038/nmeth.2112
31. O'Callaghan, R.; Job, K. M.; Dull, R. O.; Hlady, V. *Am. J. Physiol.: Lung Cell. Mol. Physiol.* **2011,** *301,* L353–L360. doi:10.1152/ajplung.00342.2010
32. Lekka, M.; Pogoda, K.; Gostek, J.; Klymenko, O.; Prauzner-Bechcicki, S.; Wiltowska-Zuber, J.; Jaczewska, J.; Lekki, J.; Stachura, Z. *Micron* **2012,** *43,* 1259–1266. doi:10.1016/j.micron.2012.01.019
33. Dokukin, M. E.; Guz, N. V.; Gaikwad, R. M.; Woodworth, C. D.; Sokolov, I. *Phys. Rev. Lett.* **2011,** *107,* 028101. doi:10.1103/PhysRevLett.107.028101
34. Gavara, N.; Chadwick, R. S. *Nat. Nanotechnol.* **2012,** *7,* 733–736. doi:10.1038/nnano.2012.163
35. Lekka, M.; Gil, D.; Dąbroś, W.; Jaczewska, J.; Kulik, A. J.; Lekki, J.; Stachura, Z.; Stachura, J.; Laidler, P. *J. Mol. Recognit.* **2011,** *24,* 833–842. doi:10.1002/jmr.1123
36. Pharr, G. M.; Oliver, W. C.; Brotzen, F. R. *J. Mater. Res.* **1992,** *7,* 613–617. doi:10.1557/JMR.1992.0613

License and Terms

The definitive version of this article is the electronic one which can be found at:
doi:10.3762/bjnano.5.52

Beilstein Journal of Nanotechnology

Scale effects of nanomechanical properties and deformation behavior of Au nanoparticle and thin film using depth sensing nanoindentation

Dave Maharaj and Bharat Bhushan*

Full Research Paper

Open Access

Address:
Nanoprobe Laboratory for Bio-& Nanotechnology and Biomimetics (NLBB), The Ohio State University, 201 W.19th Avenue, Columbus, Ohio 43210-1142, USA

Email:
Bharat Bhushan* - Bhushan.2@osu.edu

* Corresponding author

Keywords:
gold (Au); Hall–Petch; hardness; nanoindentation; nano-objects

Beilstein J. Nanotechnol. **2014,** *5,* 822–836.
doi:10.3762/bjnano.5.94

Received: 14 January 2014
Accepted: 14 May 2014
Published: 11 June 2014

This article is part of the Thematic Series "Advanced atomic force microscopy techniques II".

Guest Editors: T. Glatzel and T. Schimmel

Abstract

Nanoscale research of bulk solid surfaces, thin films and micro- and nano-objects has shown that mechanical properties are enhanced at smaller scales. Experimental studies that directly compare local with global deformation are lacking. In this research, spherical Au nanoparticles, 500 nm in diameter and 100 nm thick Au films were selected. Nanoindentation (local deformation) and compression tests (global deformation) were performed with a nanoindenter using a sharp Berkovich tip and a flat punch, respectively. Data from nanoindentation studies were compared with bulk to study scale effects. Nanoscale hardness of the film was found to be higher than the nanoparticles with both being higher than bulk. Both nanoparticles and film showed increasing hardness for decreasing penetration depth. For the film, creep and strain rate effects were observed. In comparison of nanoindentation and compression tests, more pop-ins during loading were observed during the nanoindentation of nanoparticles. Repeated compression tests of nanoparticles were performed that showed a strain hardening effect and increased pop-ins during subsequent loads.

Introduction

The characterization of mechanical properties is crucial for a fundamental understanding of materials behavior during contact. Mechanical properties of interest comprise hardness, Young's modulus of elasticity, bulk modulus, elastic–plastic deformation, scratch resistance, residual stresses, time-dependent creep and relaxation properties, fracture toughness, fatigue and yield strength.

With the advent of the atomic force microscope (AFM) and specialized commercial depth-sensing indenters, the probing of mechanical properties on the micro- and nanoscale under ultra-low loads has become possible [1,2]. In particular, the use of a nanoindenter with depth sensing is ideal, as mechanical properties such as hardness and Young's modulus of elasticity can be directly obtained as a function of depth. This can be done

with a high degree of accuracy, not easily obtained with an AFM. This advancement in technology has proven useful for understanding the mechanical behavior of micro- and nano-objects that are continually being developed and incorporated into a wide variety of macro- to nanoscale systems [3]. With the depth-sensing nanoindenter, indentation studies with a sharp three-sided pyramidal Berkovich tip and compression studies with a flat punch have been performed. The sharp tip allows for the study of localized deformations and the flat punch allows for the study of deformations of entire micro- or nano-objects. Knowledge of their mechanical properties is crucial for predicting deformation behavior under various loading regimes, which is important for long term use. Research has shown that mechanical properties on the micro- to nanoscale are different from bulk and are scale-dependent as was observed in studies of bulk solid surfaces, surface thin films and micro- to nano-objects. Mechanical properties can either be reduced or enhanced. There are many theories and mechanisms used to explain the state of mechanical properties and deformation behavior of materials on the macro- to nanoscale. Evaluation of each along with experimental conditions is necessary to explain and place new research in context.

Reduced mechanical properties have been observed in some studies of micro/nano-objects where decreasing diameters results in a reduction of yield strength and hardness [4-6]. This has been explained according to the inverse Hall–Petch effect, which means that mechanical properties, below a critical grain size, decreases as grain sizes becomes smaller resulting in reduced properties. Jang and Greer [6], for example reported for Ni micropillars (0.1–2.5 μm) under compression, that the yield strength was reduced as the diameter was decreased with a critical grain size of 60 nm. Of particular interest are cases in which properties are enhanced leading to the 'smaller is stronger' phenomenon. An overview of several of these studies, in which mechanical properties improve as scale is reduced, is presented in Table 1. Also presented are material dimensions and associated theories.

In studies of bulk solid surfaces [7-13] and thin films [14-17] made of various materials including Al, Au, Ag, Cu, GaAs, GaP, Si, Ti, ZnSe and Ni, scale effects on hardness with respect to the depth of penetration or indentation size effect (ISE) and decreasing film thickness have been reported. Pharr and Oliver [9] and Bhushan et al. [11], for example, found that a

Table 1: Review of studies of enhanced scale-dependent mechanical properties of bulk solid surfaces, thin films and various nano-objects. For thin films, the thicknesses are given and for nano-objects, the diameters are given. Pillars described in the studies have low aspect ratios (2–20) compared to wires (>20).

material	method	result	theories
solid surfaces			
Ag, Au, Cu, GaAs, GaP, Ni, Si, Ti, ZnSe	indentation [7-13]	hardness higher than bulk; hardness inversely proportional to indentation depth	strain gradient plasticity [29,30]
thin films			
Al (210–1090 nm)	indentation [14]	hardness inversely proportional to film thickness	Hall–Petch [31-34], dislocation constraint [45]
Ag, Au (100–2000 nm)	indentation [15]		Hall–Petch [31-34]
Au (31–858 nm)	indentation [16]		
Ni (50–700 nm)	indentation [17]	hardness higher than bulk	dislocation constraint [45]
nano-objects			
Cu/Nb microwires (1–10 μm)	indentation [18]	hardness inversely proportional to diameter	Hall–Petch [31-34]
Au micropillars (0.4–7.5 μm)	compression [19]	yield stress higher than bulk; yield stress inversely proportional to diameter	dislocation starvation [19]
Au nanowires (40–250 nm)	bending [20]	yield strength inversely proportional to diameter and greater than bulk	Hall–Petch [31-34]
Ni nanopillars (150–400 nm)	compression [21]	yield stress inversely proportional to diameter	dislocation starvation [19]
Au nanopillars (150–1000 nm)	compression [22]	yield strength inversely proportional to diameter	Hall–Petch [31-34]
Au nanoparticles (200–1000 nm)	compression [26]	smaller nanoparticles yield at higher stress	dislocation entanglement [26]

decreasing indentation depth resulted in higher hardness of Ag and Si surfaces, respectively. In both cases the hardness of the nano-objects was higher than that of the bulk material. Other studies revealed the relationship between film thickness and hardness. Cao et al. [15] and Dietiker et al. [16], for example, demonstrated that as the film thickness decreased for Ag and Au (10–2000 nm) and solely Au (31–858 nm), respectively, hardness increased. The dependence of the hardness on the film thickness can be explained by either the Hall–Petch effect or dislocation constraint, where the hard substrate limits the movement of dislocations. Large strain gradients observed in the ISE also contribute to the material hardness. Scale dependence is also seen in studies of various micro/nano-objects. Enhanced mechanical properties were observed in nano-objects [18-23] made of various materials including Au, Cu, Nb and Ni, for which decreasing diameters result in an increase in micro/nano-object yield stress and hardness. Indentation tests of Cu/Nb microwires (1–10 μm) by Thilly et al. [18] showed that a lower diameter resulted in higher yield stress following the 'smaller is stronger' phenomenon. In compression studies involving Au (0.4–7.5 μm) micropillars a similar observation was made and higher yield strengths were observed compared to bulk with decreasing micropillar diameter [19]. For a thorough review, see Palacio and Bhushan [24]. The increase in yield strength or hardness seen with nano-objects has been explained by the dislocation starvation model or the Hall–Petch effect for single crystalline and polycrystalline nano-objects, respectively. In the dislocation starvation model, the absence of dislocations in the interior of the nano-object does not allow for plastic deformation to occur. Similar to thin films, for indentation of micro and nano-objects, there is also a contribution to hardening due to the occurrence of large strain gradients at shallow depths for both single and polycrystalline materials. Details of the mechanisms which lead to enhanced hardness with polycrystalline bulk solids, surface thin films and nano-objects are presented in the next section. These mechanisms are explained to aid in understanding of mechanical properties and deformation behavior of materials.

Nanoparticles made of Au are of interest since they are used in tribological applications on the macro- to nanoscale and applications requiring controlled manipulation and targeting [25]. In these environments the nanoparticles can be deformed locally or the entire nanoparticle can be compressed. Knowledge of the mechanical properties and deformation mechanisms involved when subjected to an applied load is important for determining their suitability for various applications. Studies have been previously performed on Au nanoparticles by doing indentation experiments to look at the effect of lateral dimension (elongation) on strength [26] and by doing compression experiments to study the effect of overall particle size on strength [23]. Studies that directly compare indentation (local deformation) with compression (global deformation) with nanoparticles of the same size and geometry to understand the differences in deformation modes are lacking. In addition to indentation studies of Au nanoparticles, it is of interest to study thin Au films. As the size of the nanoparticle decreases there is less contact with the tip due to the curvature of both the tip and nanoparticle and this can lead to inaccuracies in determining the contact area. This results in errors during obtaining the mechanical properties. Thin films, due to their flat surfaces, eliminate this problem and provide an opportunity to further investigate scale effects of mechanical properties of a material at smaller dimensions. This is due to a more accurate determination of the contact area than would be possible with a nanoparticle of similar size.

In this paper, 500 nm Au nanoparticles and a 100 nm thick Au film were investigated to determine scale effects of mechanical properties and deformation behavior. Various normal loads were applied through nanoindentation with a sharp tip (local deformation) and compression with a flat punch (global deformation). Data from the nanoindentation studies were compared with bulk to study scale effects on hardness. The effects of the penetration depth on hardness were investigated for nanoparticles and thin films. For the films, creep and strain rate tests were also studied. Load effects were compared between loading methods to understand the mechanisms involved during deformation. Repeated compression tests of nanoparticles were performed to study nanoscale strain hardening.

Mechanisms

In this section, mechanisms for the observed enhanced mechanical properties of polycrystalline materials on the nanoscale are described. Explanations of the various mechanisms are important to aid in discussing and understanding the current research. In some cases one or multiple explanations can account for the observed mechanical properties and deformation behavior. It is necessary to understand the details of these mechanisms to determine which ones apply and best explains the results. As physical dimensions reach the nanoscale, an increase in yield stress or hardening is observed compared to the macroscale. These changes are driven by the presence or absence of sets of atoms that disrupt the regular atomic arrangements in the lattice planes, the so called dislocations.

Figure 1 shows for a polycrystalline material, as an example, dislocations in the grain originating from the grain boundary and the grain interior, from a multiplication of existing dislocations during loading or from geometrically necessary dislocations (GNDs) generated to accommodate strain gradient in nanoindentation at low penetration depths.

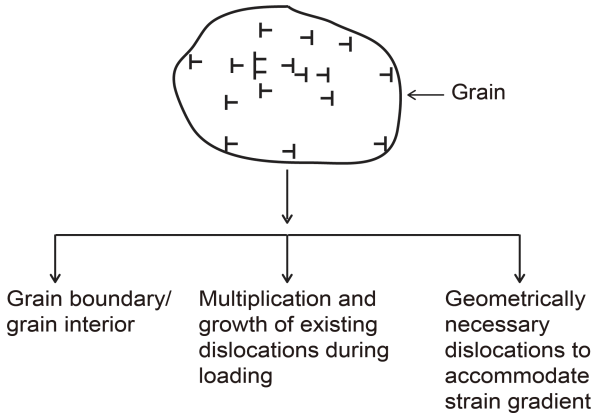

Figure 1: Flowchart illustrating dislocation sources, in a grain, from the grain boundary and the grain interior, from multiplication and growth of an existing dislocation and from geometrically necessary dislocations needed to accommodate strain gradient.

Movement of dislocations by slip allows for plastic deformation to occur [27]. After an initial slip, as more dislocations are generated there is an increase in yield stress or hardness as the dislocations interact with each other or at the grain boundaries in polycrystalline material. These interactions are responsible for the trend of enhanced mechanical properties with reduction in size or the 'smaller is stronger' phenomenon. They help to explain certain observable effects such as the ISE and Hall–Petch effect. The mechanisms of each are given in the following sections. In the case of the ISE, contributions to enhanced hardness can occur in either single or polycrystalline nano-objects.

Indentation size effect: Strain gradient plasticity

Indentation of materials with a sharp tip at shallow depths leads to large strain gradients, which results in formation of GNDs. This allows for the accommodation of plastic deformation of the material beneath the indenter, as depicted in Figure 2. The GNDs along with dislocations which are formed in the absence of strain gradients, known as statistically stored dislocations (SSD), hinder the formation and movement of new dislocations. As indentation depths decreases larger strain gradients lead to an increase in the density of dislocations. This results in a strengthening effect [28-30] and accounts for the observed increase in hardness at shallower indentation depths. This phenomenon was first modeled by Nix and Gao [30] according to the following relation

$$H/H_0 = \left(1 + h^*/h\right)^{1/2} \quad (1)$$

where H is the hardness at a given indentation depth h, with H_0 being the hardness at a large indentation depth and h^* is a characteristic length, which is dependent on the indenter shape, the shear modulus and H_0. The ISE contributes to increased hardness in bulk solid surfaces, thin films and nano-objects.

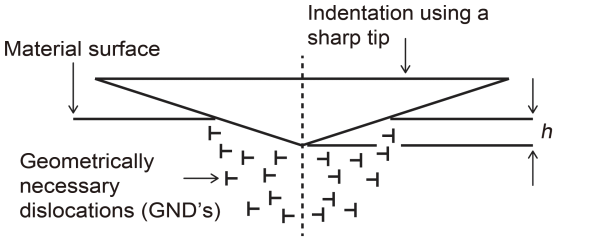

Figure 2: Illustration of the strain gradient plasticity theory in which high strain gradients occur at shallow indentation depths with a sharp tip. This leads to geometrically necessary dislocations (GNDs) being generated to accommodate for the strain gradient and a subsequent permanent deformation. The GNDs entangle and impede further movement of existing dislocations as well as the formation and movement of new dislocations.

Hall–Petch effect

The generation of dislocations leads to the Hall–Petch effect through the dislocation pile up mechanism or the dislocation density mechanism and are described in subsequent sections. In both mechanisms as the grain size is reduced, the yield stress increases resulting in higher hardness in the case of indentation as stated previously [31-34]. It should be noted that the strengthening effect can also be the result of a combination of mechanisms.

Dislocation pile-up mechanism

As the nanoscale is approached, polycrystalline thin films and nano-objects by virtue of their physical dimensions will be composed of materials that have a nanocrystalline structure, i.e., nanometer size grains; as compared to the coarse grained bulk materials, in which grain sizes can vary from 10–300 μm [35]. In the pile-up mechanism illustrated in Figure 3a, for a given applied stress τ, on the grains illustrated by the vertical arrows, dislocations are generated along slip lines, as depicted by the dashed lines, and eventually pile up against the grain boundary. The stress at the grain boundary is called the pile up stress, given as

$$\tau_p = n\left(\tau - \tau_i\right) \quad (2)$$

where τ_i is the friction stress opposing the movement of the dislocations. The number of dislocations in the pile up in grain A (n_{1A}) is greater than in grain C (n_{2C}) due to the larger size

which leads to a greater τ_p. For a slip to occur across the grain boundary, τ_p must be greater than the critical stress, $\tau_{critical}$. A higher initial τ is therefore required on grain C before the critical stress is reached to allow slip to occur and plastic deformation to continue, which results in a higher yield stress compared to grain A [31-34].

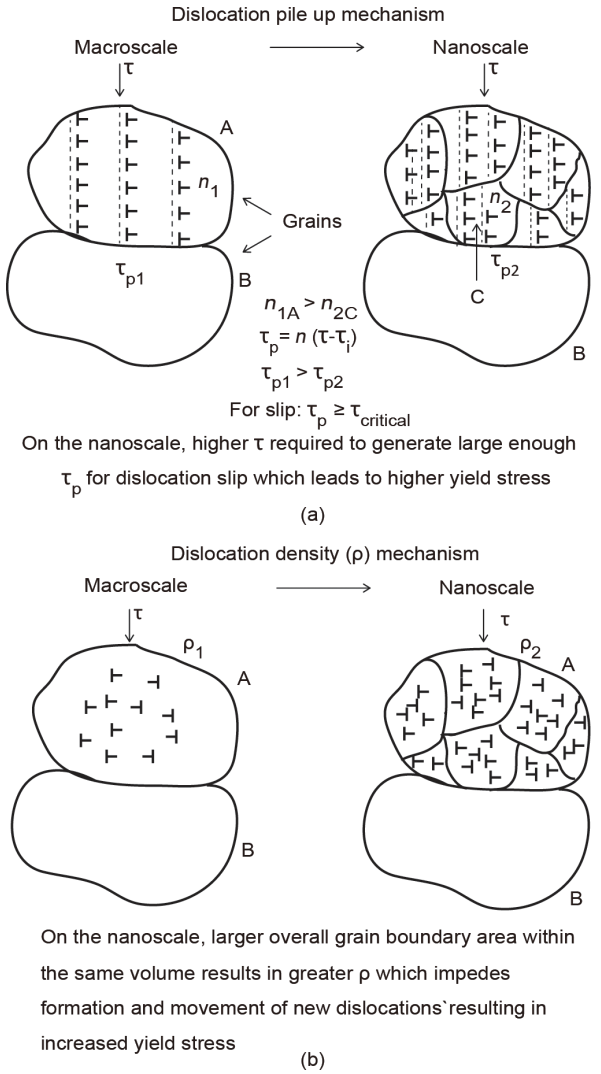

Figure 3: Illustration of (a) Hall–Petch effect by the dislocation pile-up mechanism, where dislocations pile up against the grain boundary under an applied stress τ. The stress at the boundary τ_p (pile up stress) which is a function of τ and τ_i (internal stress) of the dislocations is larger for a bigger grain size (A) on the macroscale due to the larger number of dislocations compared to that for a smaller grain size (C) on the nanoscale. The number of dislocations (*n*) within the grain on the nanoscale is smaller compared to the macroscale, requiring a larger τ to create a pile up stress ($\tau_{critical}$) high enough for dislocation slip and plastic deformation which results in a higher yield stress. (b) Dislocation density mechanism where there is a larger overall grain boundary area as grains become smaller within the same volume, resulting in a greater density of dislocations which impede the formation and motion of new dislocations to accommodate strain gradients and results in higher yield stress.

Dislocation density mechanism

As mentioned earlier, dislocations can be generated from different sources as shown in Figure 1. As the grain size becomes smaller, shown in Figure 3b, there is a larger overall grain boundary area within the same volume on the nanoscale (right) compared to the macroscale (left), resulting in a greater number of dislocations per unit area or density (ρ). This entanglement of dislocations impedes the formation and motion of new dislocations and multiplication of existing dislocations necessary to accommodate strain gradient and subsequent deformation. This results in greater resistance to deformation and increased yield stress [28,36,37].

Experimental

Materials and sample preparation

Si(100) wafers with a native oxide layer (University Wafers, Boston, MA) were ultrasonically cleaned in deionized (DI) water, followed by isopropyl alcohol (IPA) and finally acetone for 15 min each. Polycrystalline Au nanoparticles (Alfa Aesar, Ward Hill, MA) with nominal diameters of 500 nm to be referred to as "Au 500" henceforth, were chosen for the nanoparticle experiments. The 500 nm diameter was the largest size commercially available. It was necessary to use nanoparticles sufficiently larger than the Berkovich indenter tip of radius 100 nm to provide as flat a surface as possible for nanoindentation. This allows for a more accurate determination of the contact area and mechanical properties.

Figure 4 shows a scanning electron microscopy (SEM) image (S-4300 SEM, Hitachi HTA Inc., Pleasanton, CA) of the nanoparticles. For the nanoparticle experiments conducted, several droplets of Au nanoparticles suspended in DI water were deposited onto the clean Si(100) substrates by using a syringe. A solution concentration of 0.01 mg/mL was used. The substrate was then placed on a hot plate and heated to a temperature of about 70–80 °C and left until the water was evaporated.

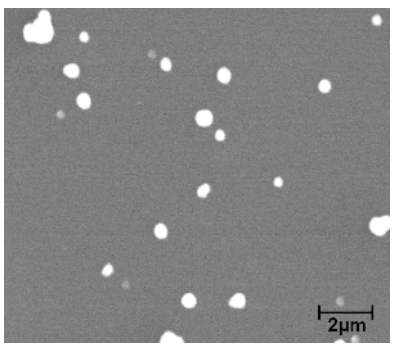

Figure 4: SEM image of spherical Au nanoparticles approximately 500 nm in diameter which are referred to as Au 500.

For thin film experiments, a polycrystalline Au film of approximately 100 nm thickness was deposited onto the surface of the Si(100) substrate by thermal evaporation at an operating pressure of about 0.001 Pa, substrate temperature of 100 °C at a rate of approximately 0.4 nm/s. To observe the grains within the Au film and nanoparticles, focused ion beam (FIB) milling and transmission electron microscopy (TEM) were employed. Cross-sections of samples were cut out by FIB milling (Nova NanoLab 600, FEI, Hillsboro, OR) by using a Ga^+ ion beam accelerated at a voltage of 30 kV with currents ranging from 0.03 to 28 nA. A Pt coating was deposited on both sets of samples to protect the surfaces during milling. The cross-sections were then lifted out by using a micro manipulator and placed in a holder and observed using a TEM system (Tecnai F20, FEI, Hillsboro, OR, USA) operated at a voltage of 200 kV with a current of 1 nA. Figure 5 shows typical TEM images of both the Au film and Au nanoparticles. Figure 5a shows the Au film (100 nm) on a silicon substrate (left) with a magnified view of the section highlighted by the dashed lines shown on the right. In the magnified view the dashed lines highlight the grains. Figure 5b shows several Au 500 nanoparticles (left) with a magnified view of a single nanoparticle highlighted by the dashed lines. The view on the right shows grains highlighted by the dashed lines. The average grain diameters were found by first importing the TEM images into an image processing and analysis software (ImageJ, National Institute of Health, Bethesda, MD). Second, the outlines of the grains were traced and the enclosed area was determined. The outlines were visible due to the difference in color from one grain to the next as a result of the misalignment of atoms at the grain boundary. Using the area, the diameter of a circle of equivalent area is found and this is taken as the grain diameter. The average grain diameters from the representative images were found to be 40 ± 9 nm for the film and 96 ± 30 nm for the nanoparticle.

Nanomechanical characterization

Nanoindentation

All experiments were carried out by using a probe-based scanning nanoindenter head TS 75 Trboscope, (Hysitron, Inc., Minneapolis, MN) attached to an AFM (Bruker Dimension 3100, Santa Barbara, CA) with a diamond tip. For nanoindentation experiments a three-sided diamond pyramidal Berkovich tip of approximately 100 nm in radius was used as shown in Figure 6a (left). Hardness and elastic modulus were obtained as a function of contact depth for the 100 nm thin film by indenting at maximum loads of 20, 40, 60 and 80 μN. The 20 μN load was the lowest load that was possible to produce well defined load–displacement curves for analysis. The 80 μN load was the maximum load possible without the substrate influencing the values of hardness. Effects of creep were studied at 40 and 80 μN by using a hold period of 200 s at the maximum loads. Strain rate effects were investigated at a load

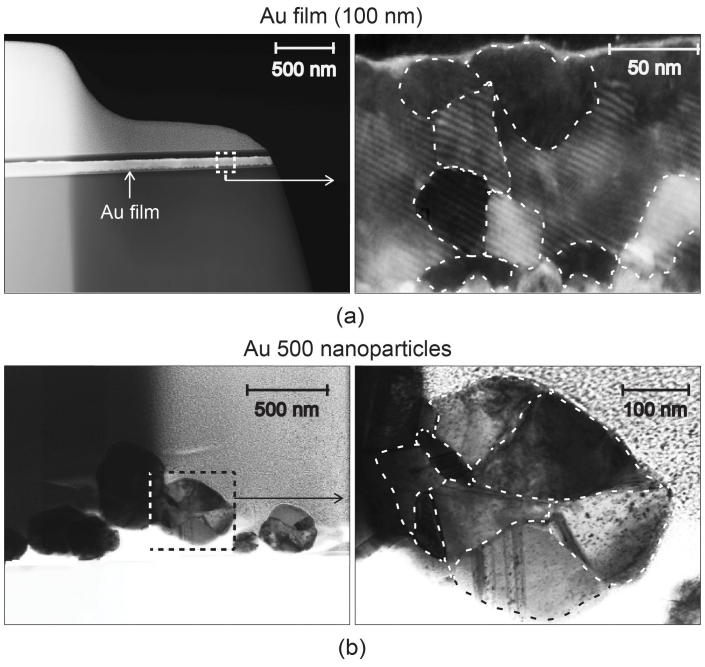

Figure 5: TEM images showing (a) Au film (100 nm) (left) with a magnified view of the section highlighted by the dashed lines shown on the right. In the magnified view, the dashed lines are used to highlight the grains within the film which have an average diameter of 40 ± 9 nm, and (b) several Au 500 nanoparticles (left) with a magnified view of a single nanoparticle with the grains highlighted by the dashed lines (right). The average grain diameter was found to be 96 ± 30 nm.

of 80 μN for loading and unloading times of 20 and 200 s. The creep and strain rate data gives an indication of whether the experiments are sensitive to hold times and loading–unloading rates and helps to further characterize material behavior which is important for determining suitability for various applications.

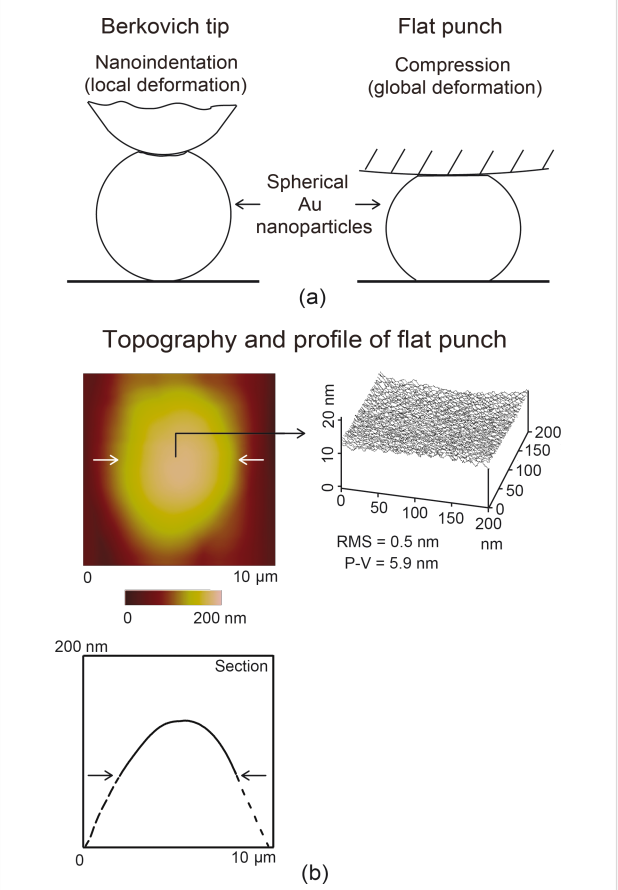

Figure 6: (a) Schematic showing method of deformation by using a Berkovich tip for nanoindentation (local deformation) and flat punch for compression (global deformation) with Au nanoparticles. (b)Topography map (top) and 2-D profile (bottom) of flat punch at the section shown by the pairs of horizontal arrows along with a typical line plot (right) of a 200 nm × 200 nm section indicated by the single horizontal arrow.

Au 500 nanoparticles were indented at maximum loads of 20, 40, 60 and 80 μN similar to the thin film. The Oliver and Pharr [38] method was used to obtain the hardness and the elastic modulus. By using this method the Young's modulus of elasticity and Poisson's ratio for diamond were taken as 1140 GPa and 0.07, respectively. Poisson's ratio for Au was taken as 0.42. The data from these experiments is the average of five measurements on five different nanoparticles for each load. For each Au nanoparticle, further indentation experiments were carried out at intermediate and high loads. These loads were 500 and 1000 μN. Intermediate loads are defined as loads that allow for indents to approximately half the nanoparticle height or more, without fracturing or crushing the nanoparticle. High loads are defined as loads that crush or fracture the nanoparticle. These loads were selected to understand how the nanoparticle deforms under various loading conditions. The duration for loading and unloading was 20 s for all experiments (unless otherwise stated) to prevent the nanoparticle from slipping under the indenter during more rapid and unstable loading. Topography images were also taken before and after indentation with the same tip used for indentation. All experiments were performed at room temperature (23 °C) and 50–55% relative humidity.

Compression

For compression experiments a spherical diamond tip of approximately 3.5 μm in radius was used as shown in Figure 6a (right). This can be considered to be a flat punch due to the large radius of the diamond tip compared to the nanoparticles. Figure 6b shows the topography map (top left) and corresponding 2-D profile (bottom left) of the flat punch. The pairs of arrows indicate the section on which the profile is taken. The dashed lines represent the sides of the holder on which the tip is glued. The single arrow points to a representative 200 nm × 200 nm section on the punch that is illustrated by the 3-D map (right). The root mean squared roughness (RMS) is 0.5 nm and the peak to valley (P-V) roughness is 5.9 nm. The low roughness allows for an overall compression of the nanoparticles without indentation due to any large asperities that may be present on the surface.

Three different maximum loads were applied to the nanoparticles. The lowest load for all three cases was 80 μN similar to indentation. This was done to compare the deformation between the two methods. The intermediate and high loads were 1000 and 1500 μN. These loads are similarly defined as those used in indentation. Repeated compression loading experiments, during which several loads are applied to a single nanoparticle, were also performed. Experiments were carried out to explore strain hardening effects on the nanoscale as well as pop-in behavior. The range was 50–250 μN and loads were applied in increasing increments of 50 μN to obtain enough load–displacement curves to clearly observe strain hardening. The range was limited by the nanoparticle either being pushed during imaging or stuck to the diamond tip during compression. This makes imaging and location of the nanoparticle impossible for further compression. The duration for loading and unloading was 20 s for all experiments similar to nanoindentation. Topography images were also taken before and after indentation with the same tip used for compression. To ensure repeatability, each experiment was performed five times and representative data are shown in the results section. All experiments were performed at room temperature (23 °C) and 50–55% relative humidity.

Macromechanical characterization

For comparison to the macroscale, data from polycrystalline bulk Au was used from experiments presented by Lozinskii [39]. The Vickers hardness was obtained by using a four sided diamond tip under a load of 1 kg. Typical samples were disc shaped with a diameter of 14.8 mm and thickness of 5 mm. The Young's modulus for bulk was obtained through resonance of transverse vibrations of a cylindrical specimen which was typically 100 mm in length and 6–8 mm in diameter [39].

Results and Discussion

In this section, first, hardness, creep and strain rate data are shown for a thin Au film (100 nm). Next, results for nanoindentation using a Berkovich tip and compression using a flat punch are given for Au nano-objects. For both deformation methods, representative load–displacement curves are presented for low, intermediate and high loads. Morphological characterization, before and after deformation, is also presented. Finally load–displacement curves for repeat compression tests using the flat punch are presented.

Nanoindentation with a Berkovich tip – Indentation of thin films

Indentation with a Berkovich tip was used to determine the mechanical properties and investigate the creep and strain rate behavior of a 100 nm thick Au film as shown in Figure 7.

In Figure 7a the mechanical properties for the thin film are illustrated by the bold diamond and squares, while the open diamonds and squares represent the properties of the bulk material. The hardness and Young's modulus for the thin film were found at maximum loads of 20, 40, 60, and 80 μN. The Young's modulus, as a function of the contact depth, is constant for the thin film and similar to that of bulk with little variation. The thin film hardness is greater than that of bulk, which is not believed to be due to the hardness of the substrate. It is generally accepted that the substrate affects the hardness if the depth of penetration is greater than 30% [1] and this limit is not exceeded. Figure 7a shows an ISE where the hardness is greater for shallower penetration depths. This effect was also observed by Bhushan et al. [11] and other researchers as outlined in Table 1. A detailed analysis of the phenomenon was performed by Nix and Gao [30] and explained. As discussed in section Mechanisms, the GNDs along with dislocations that are formed in the absence of strain gradients, known as statistically stored dislocations (SSD), hinder the formation and movement of new dislocations [28-30]. This results in a hardening effect and accounts for the observed increase in hardness at shallower contact depths for the Au film. The higher hardness compared to bulk also has a contribution from the Hall–Petch effect. In this case an increase in yield stress or hardening is observed

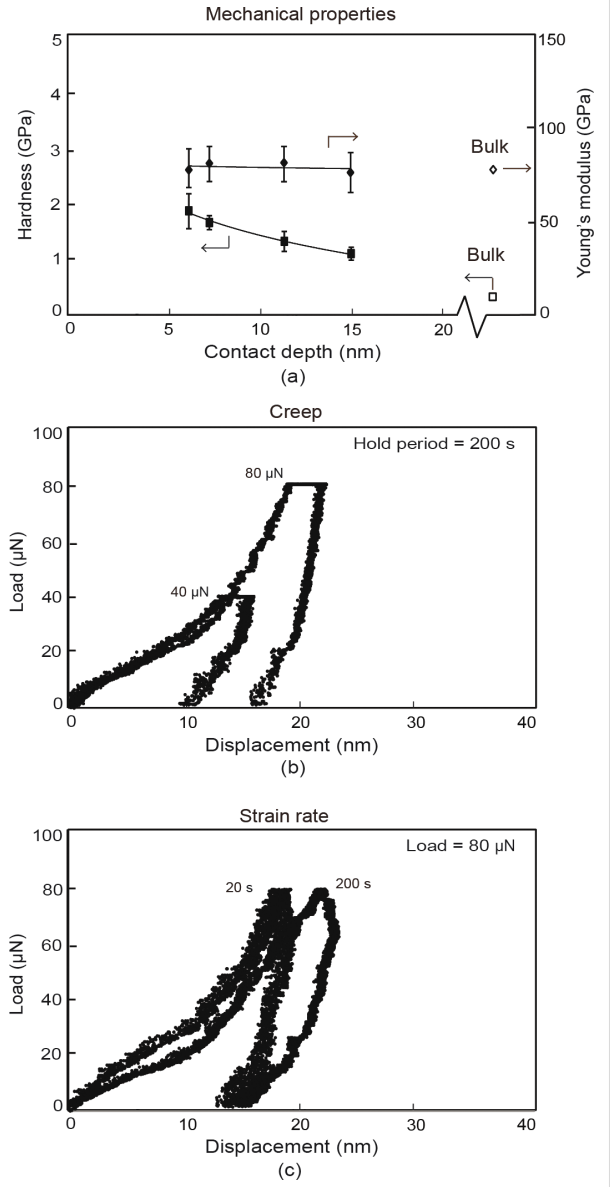

Figure 7: (a) Mechanical properties of thin films with hardness and Young's modulus as a function of contact depth represented by bold square and diamond datum points, respectively, with corresponding open diamond and square datum points representing bulk mechanical properties. Typical load displacement curves showing (b) creep at maximum loads of 40 and 80 μN with a hold period of 200 s, and (c) effects of varying strain rate at a maximum load of 80 μN for loading–unloading periods of 20 and 200 s.

compared to the macroscale due to the smaller grain sizes inherent in the thin film compared to bulk. The grain diameters in the representative image for the film shown in Figure 5a were found to be 40 ± 9 nm. The hardening can occur through dislocation density mechanism and pile-up mechanism outlined in section Mechanisms and illustrated in Figure 3a,b. However, due to the submicron thickness of the film, the nanosized grains limit the number of dislocation pile-ups. It is believed the dislo-

cation density mechanism is primarily responsible for the higher hardness.

Figure 7b shows creep for typical load–displacement curves with maximum loads of 40 and 80 μN with a hold period of 200 s. Figure 7c shows indentation–displacement curves for different strain rates with a maximum load of 80 μN for loading and unloading times of 20 and 200 s. As mentioned in section Experimental, the creep and strain rate data gives an indication of whether the experiments are sensitive to hold times and loading and unloading rates. For the creep data there is there is very little difference in the displacement during the holding times at a load of 40 μN compared to 80 μN. The strain rate data also shows a small amount of displacement from a loading and unloading time of 20–200 s. Both experiments were performed at room temperature. Since Au is inert and does not form an oxide layer it is not believed that the increased displacement at longer holding and loading times is caused by a contaminant layer. According to analysis of experimental data from several research groups by Li et al. [40], creep can occur in most materials, even at room temperature. In materials with small grain sizes (smaller than 0.3–0.4 μm) indentation creep is dominated by grain boundary (cobble) diffusive creep, which occurs by addition or removal of atoms from the boundary between two grains [40,41]. This diffusional creep is believed to be responsible for increased displacements observed for creep and strain rate data. The low sensitivity of Au to creep and strain rate is useful in tribological applications on the nanoscale in situations where constant load or varying loading rates occur. This prevents the film from deforming easily.

Similar experiments were not performed on the Au 500 nanoparticles since over longer hold and loading and unloading times the possibility of nanoparticles rotating and sliding is increased and results in the nanoparticles slipping out from under the indenter.

Nanoindentation with a Berkovich tip – Localized deformation on Au nanoparticles

For probing of mechanical properties of the polycrystalline Au 500 nanoparticles, indentation was performed at a maximum load of 80 μN. Figure 8 shows a typical load–displacement curve for indents at a maximum load of 80 μN, with topography maps of the nanoparticles over a 10 μm × 10 μm scan area and 2-D profiles before and after indentation. The topography maps of the nanoparticles appear not totally circular due to tip shape convolution effects, however they are used to confirm the indentation of the nanoparticle and that the nanoparticle did not slip during loading and unloading. The vertical arrows on the load–displacement curves point to pop-in events during indentation. The horizontal white arrows indicate the nanoparticle of interest along with the section on which the profiles were taken. The pop-in events correspond to generation of new dislocations and multiplication of existing dislocations within the grain boundaries, which leads to an increase in displacement at a constant load. The eventual hardening is due to the dislocation density mechanism and possibly the pile-up mechanism, as discussed in section Mechanisms. Similar to the thin film, it is believed that the submicron size of the Au nanoparticles, limits the number of pile-ups and the dislocation density mechanism is primarily responsible for the increase in hardness. This process repeats and results in subsequent slip and generation and multiplication of dislocations in a neighboring grains [42-44] resulting in further pop-ins. Figure 8c shows the mechanical properties for the Au 500 nanoparticles as illustrated by the bold diamond and squares, while the open diamonds and squares represent the properties of the bulk material. The hardness and Young's modulus for nanoparticles were found at maximum loads of 20, 40 60, and 80 μN. The Young's modulus, as a function of contact depth, is constant for the nanoparticles and slightly lower than that of bulk with little variation. An ISE for the hardness is also observed, similar to the thin film due to higher strain gradients at shallower depths. The hardness is also higher for the nanoparticles compared to bulk Au. This follows the 'smaller is stronger' phenomenon. The average grain diameter for the nanoparticle as shown in Figure 5b was found to be 96 ± 30 nm. It is believed that the nanometer-sized grains are responsible for enhanced hardness. This is based on the mechanisms described in the Hall–Petch effect, for which the dislocation density mechanism provides a greater contribution to hardness than the pile-up mechanism. The decreasing grain sizes leads to higher yield stress and results in an increased hardness as observed.

Table 2 presents data for hardness and Young's modulus of elasticity, in addition to the contact depth during indentation at a representative load of 80 μN for the Au nanoparticles and film. The hardness of the nanoparticles was found to be lower than the thin film. This is expected since the film thickness of 100 nm is less than the diameter of Au 500 and has smaller grains with diameters of 40 ± 9 nm compared to 96 ± 30 nm and higher resistance to yield. Both scales (100 nm and 500 nm) show a higher hardness compared to bulk. This expands the possible uses of nanoscale Au in harsh environments where resistance to deformation under loading is important for reduced friction and wear.

Figure 9 shows examples of load–displacement curves at intermediate and high loads (left) along with topography maps of the nanoparticles over a 10 μm × 10 μm scan area and 2-D profiles before and after indentation (right). The intermediate and high loads were 500 and 1000 μN, respectively. The horizontal white

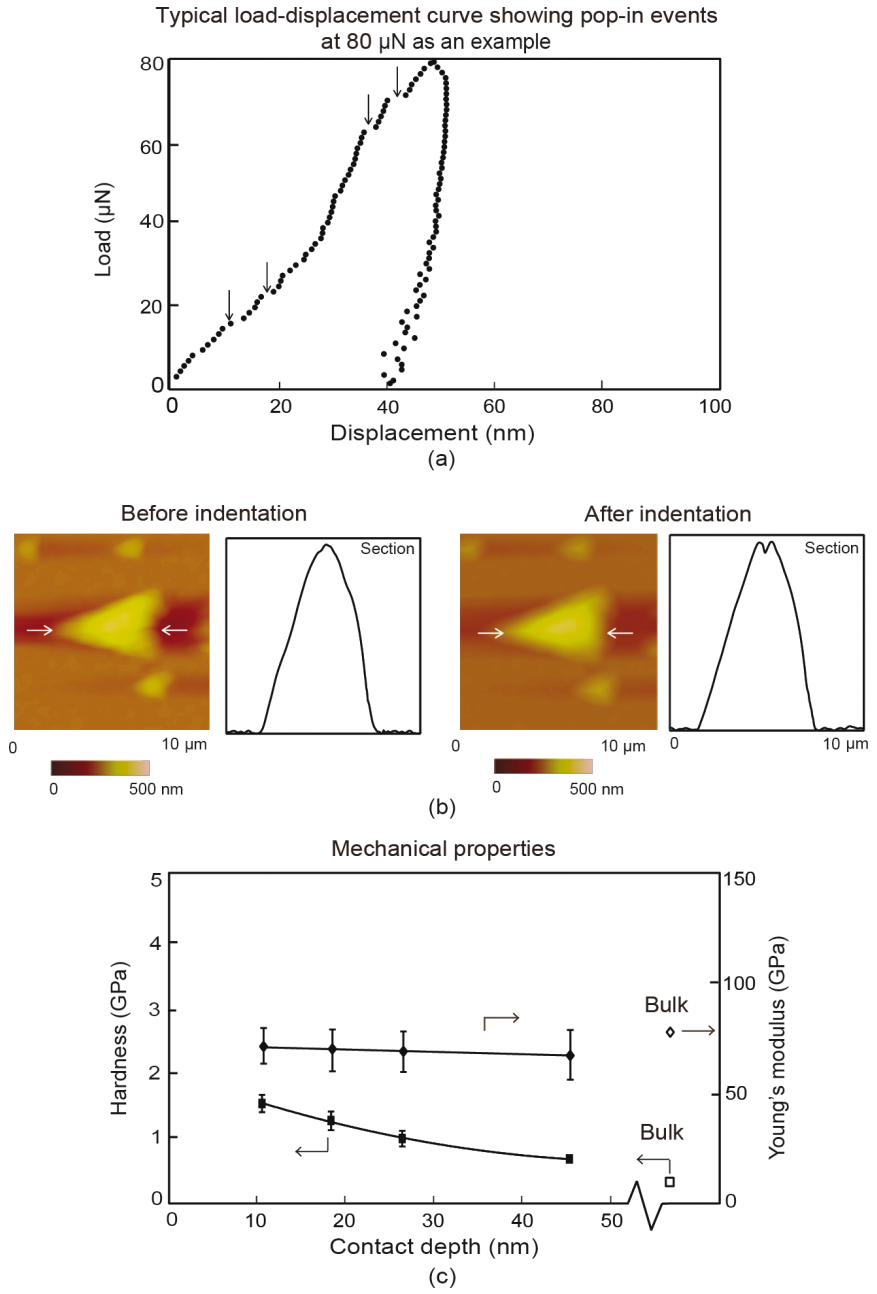

Figure 8: (a) Typical load displacement indentation curve at a maximum load of 80 μN with vertical arrows showing pop-in events and (b) topography maps and 2-D profiles at sections shown by the horizontal arrows before indentation and after indentation. (c) Mechanical properties of Au 500 nanoparticles with hardness and Young's modulus as a function of contact depth represented by bold square and diamond datum points, respectively, with corresponding open diamond and square datum points representing bulk mechanical properties.

Table 2: Nanomechanical properties of Au nanoparticles and thin film at a maximum load of 80 μN compared to bulk Au.

	nanoparticle diameter/ Film thickness (nm)	contact depth (nm)	hardness (GPa)	Young's modulus (GPa)	explanation for enhanced hardness
Au 500	513 ± 38	45 ± 4	0.7 ± 0.1	70 ± 11	Hall–Petch, strain gradient plasticity
Au thin film (100 nm)	100	15 ± 1	1 ± 0.1	76 ± 11	Hall–Petch, strain gradient plasticity
Bulk Au [46]			0.22	78	

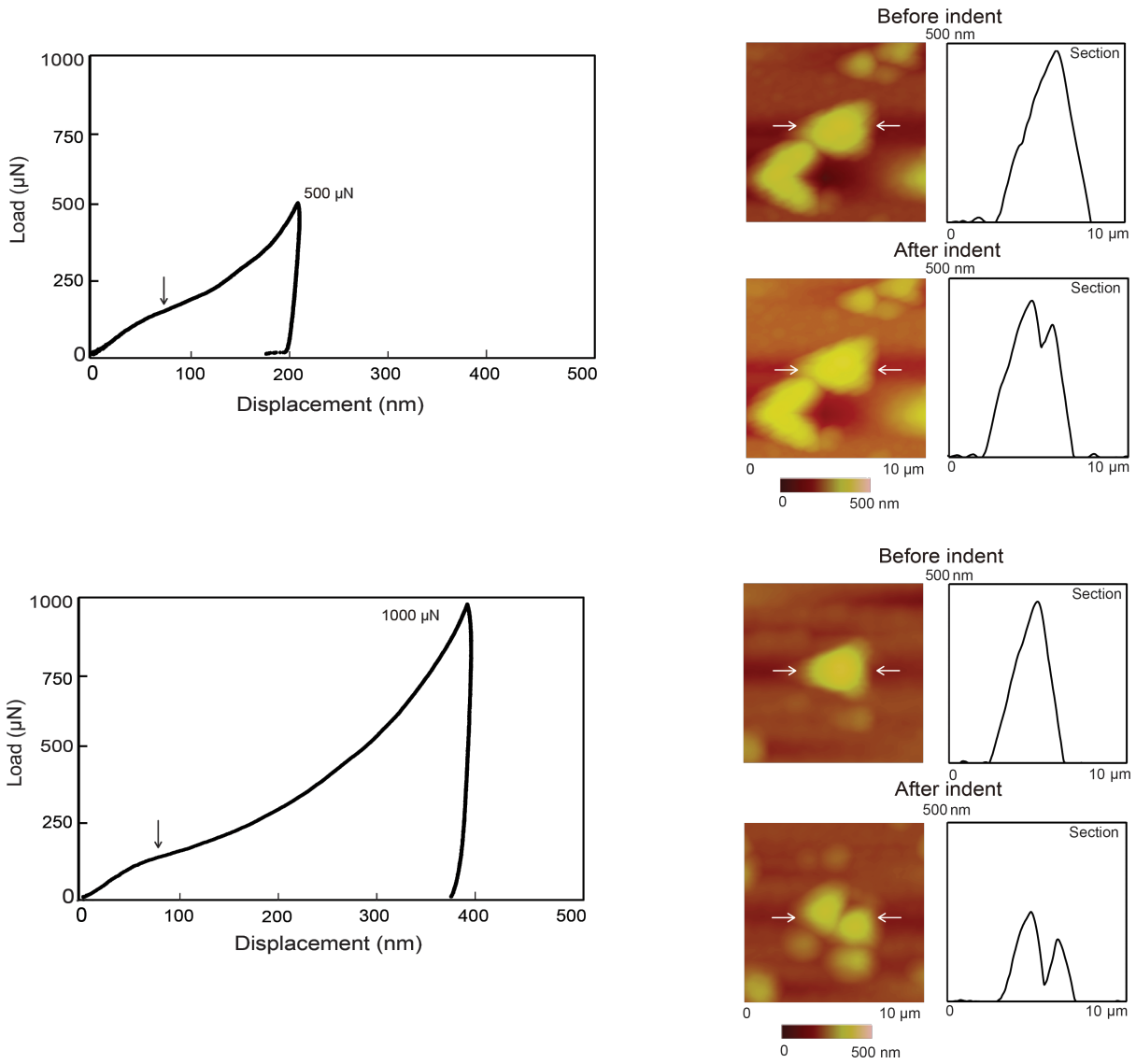

Figure 9: Load displacement curves for intermediate loads 500 μN and high loads 1000 μN for Au 500 with the vertical arrows depicting slip events (left), and topography maps and 2-D profiles, at sections indicated by the horizontal arrows before indentation (first row) and after indentation (second row) (right).

arrows in the topography maps indicate the nanoparticle of interest along with the section on which the profiles were taken. The vertical arrows shown in the load–displacement curves (left) point to slip events where the nanoparticles start to break apart during indentation leading to displacement of material below the Berkovich tip.

Compression with a flat punch – Deformation of entire Au nanoparticle

Nanoparticles were compressed to examine the differences between local deformation (nanoindentation) and global deformation (compression). Compression tests, as well as indentation tests, simulate the types of contacts nanoparticles encounter during different friction and wear conditions. For this purpose, a tip approximately 3.5 μm in radius was used to carry out compression tests. Figure 10 shows a typical load displacement curve for compression at a maximum load of 80 μN, along with topography maps of the nanoparticles over a 10 μm × 10 μm scan area and 2-D profiles before and after compression. The topography maps of the nanoparticles appear not completely circular because of tip-shape convolution effects, however, they are used to confirm the compression of the nanoparticles. The vertical arrows point to pop-in events during indentation. In Figure 10b the horizontal white arrows indicate the nanoparticle of interest along with the section on which the profiles were taken. Pop-in events due to dislocations were observed as

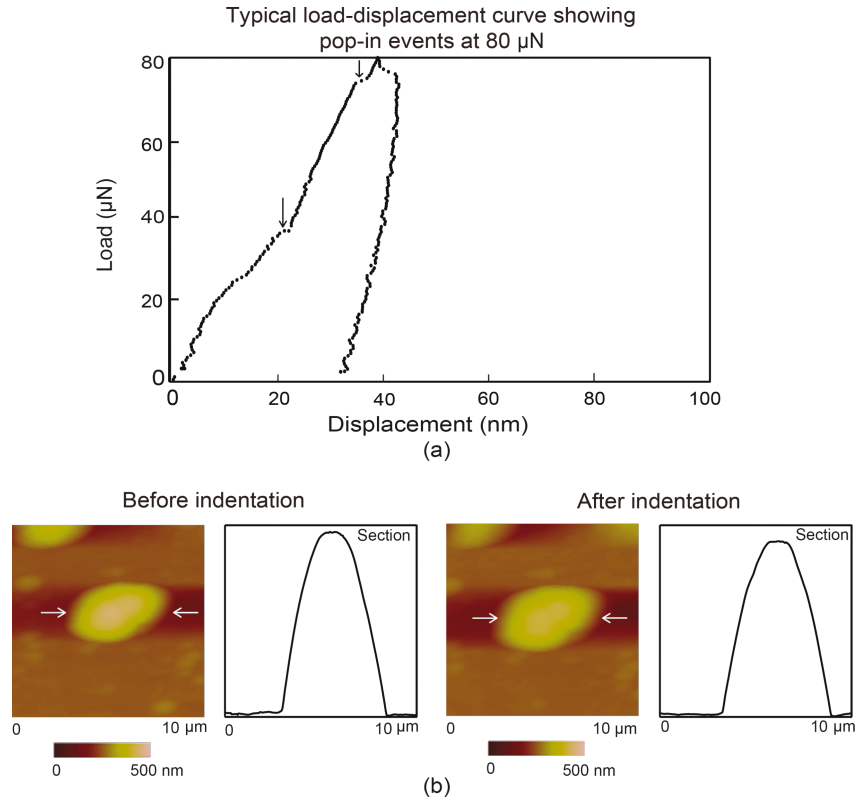

Figure 10: (a) Typical load displacement compression curve at a maximum load of 80 μN for Au 500 with vertical arrows showing pop-in events and (b) topography maps and 2-D profiles at sections shown by the arrows before compression (first row) and after compression (second row).

with nanoindentation. These occur in the latter half of the loading curve unlike with indentation, which shows pop-ins throughout the loading curve. Larger contact area of the flat punch compared to the sharp tip for nanoindentation results in a lower contact pressure. During the early stages of loading, the low pressure does not generate a sufficient internal stress for dislocation nucleation, multiplication and slip to occur which prevents a sudden displacement of material or pop-in.

Figure 11 shows examples of load–displacement curves at intermediate and high loads (left) along with along with 2-D topography maps of the nanoparticles over a 10 μm × 10 μm scan area and profiles before and after compression (right). The intermediate and high loads were 1000 and 1500 μN. The horizontal white arrows in the topography maps indicate the nanoparticle of interest along with the section on which the profiles were taken. No slip events were observed as during nanoindentation. In this case the entire volume of the nanoparticle is being compressed and material does not slip out from under the flat punch.

Repeated compression test were also performed with increasing loads. This provides an opportunity to study strain hardening on the nanoscale and to further investigate pop-in behavior as the loads are increased. Figure 12 shows load–displacement curves for repeated loads for the nanoparticles. Loads were applied with increments of 50 μN for a range 50–250 μN. Initially as the load increases the displacement increases until a load of 150 μN. For the 200 and 250 μN loads, the displacements are almost the same as the 50 μN load and less than the 100 and 250 μN loads. This indicates a hardening effect. Higher loads were not possible as the nanoparticles would either adhere to the indenter tip or slip out, resulting in the nanoparticle not being found during subsequent imaging. It is believed that the dislocations generated either continue to pile up or the already existing dislocations created during the previous loading phase prevents the movement of new dislocations resulting in strain hardening. A larger number of pop-in events were observed especially at 200 and 250 μN which would indicate that the high stress generated by the accumulated dislocations from previous compressions along with newly formed dislocations results in multiple slip events during loading. The hardening observed with the repeated compression can be useful in situations in which repeated contacts with surfaces occur such as tribological systems on the macro- to nanoscale.

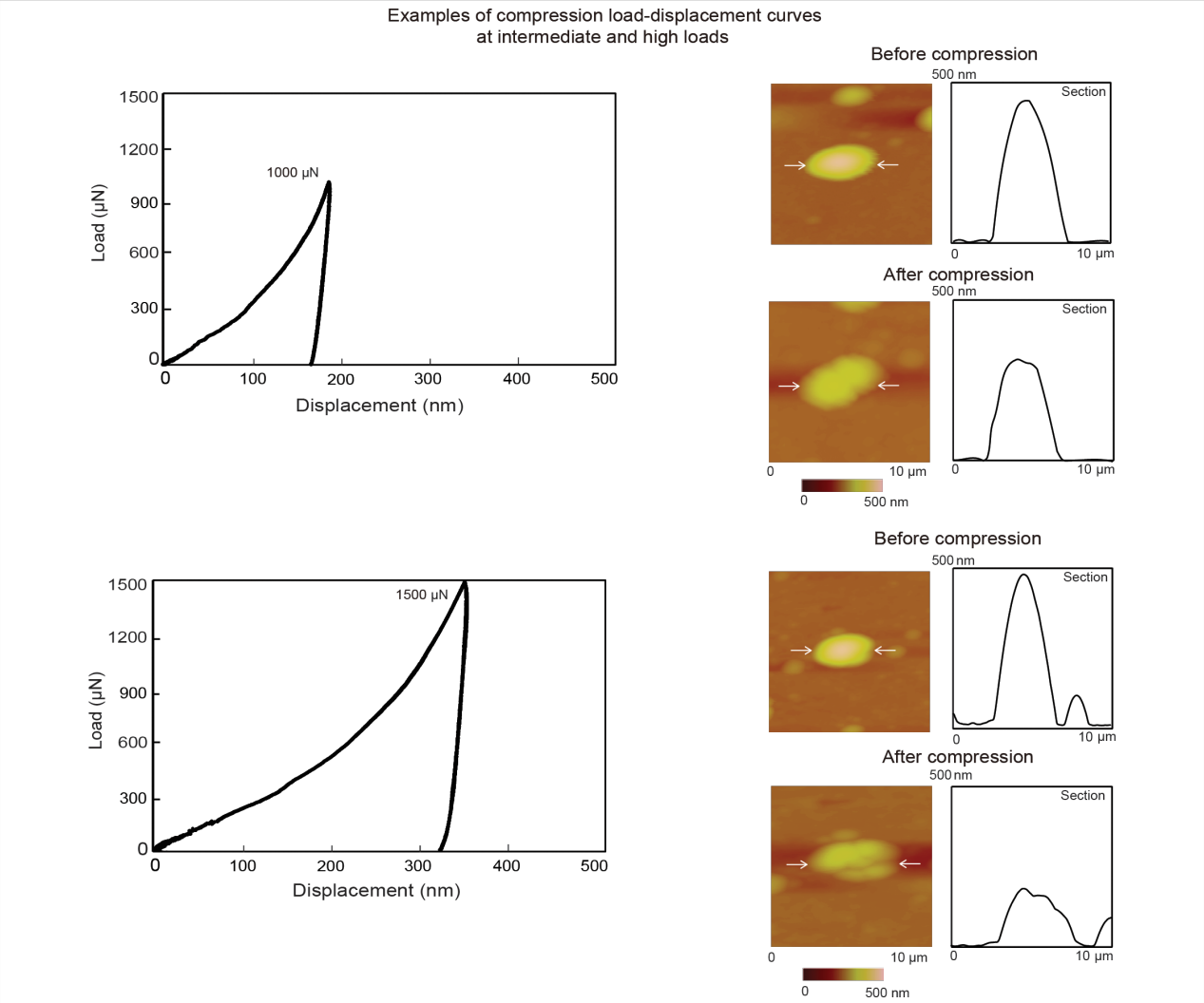

Figure 11: Load–displacement curves for intermediate loads 1000 μN and high loads 1500 μN with topography maps and 2-D profiles at sections shown by the arrows, before compression (first row) and after compression (second row).

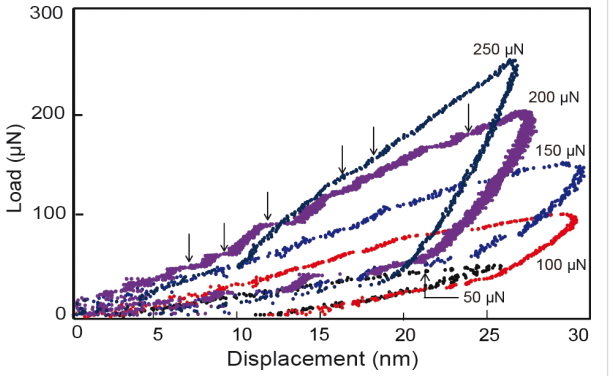

Figure 12: Examples of repeat load–displacement curves for Au 500 nanoparticles with the corresponding maximum loads for each compression event. Vertical arrows point to pop-in events. Increments of 50 μN were applied in a range of 50–250 μN. Evidence of strain hardening can be seen where successive loads after 150 μN result in the displacement being the same or less after unloading.

Conclusion

Au nanoparticles 500 nm in diameter along with a 100 nm thick film were investigated to determine their mechanical properties on the nanoscale and to investigate scale effects. Nano-object studies provided the opportunity to compare local deformation (nanoindentation) with a sharp tip and global deformation (compression) with a flat punch by using a nanoindenter. This was performed under three loading regimes, described as low, intermediate and high. Strain hardening compression was also performed by repeated loading. For the thin film, creep and strain rate behavior was also investigated.

For indentation with a sharp tip, an indentation size effect (ISE) was observed and the hardness of Au 500 and Au film increased due to higher strain gradients at shallower penetration depths. The hardness of the film was higher than that of the nanoparticles with both being higher than that of the bulk because of the

Hall–Petch effect, which was explained by using the dislocation density mechanism and the pile-up mechanism with a greater contribution to the hardness coming from the dislocation density mechanism. TEM analysis confirmed the smaller grain sizes of the film compared to the nanoparticles. The large strain gradients also contributed to an increased hardness compared to bulk Au. Load displacement curves for Au 500 at low loads revealed pop-in effects, which occur due to generation and slip of dislocations. For the thin film, creep and strain rate tests showed displacements of a few nanometers for the hold period and increased loading–unloading times. This is believed to be due to diffusion creep associated with grain boundary translation.

For compression pop-in effects from the sudden displacement of material as a result of accumulation and slip of dislocations, were observed during loading similar to nanoindentation. Repeat compression tests showed a strain hardening effect with each subsequent load. The resulting displacement at each new load was either the same or lower than the previous. This was due to increased resistance to deformation as a result of a greater density of dislocations restricting the creation and movement of new dislocations being formed. Several pop-in effects were observed during repeat compression tests at increasing loads due to accumulation of dislocations from previous loads and formation of new dislocations.

Further studies would include characterizing the sub-micron structure of the film and nanoparticles in terms of grain size and dislocation content and behavior. This would give a more precise determination of the relative contributions of dislocation mechanisms responsible for enhanced hardness. The knowledge gained will have far reaching effects when designing macro- to nanoscale systems that incorporate materials with nano-dimensions.

Acknowledgements

The financial support of this research was provided by a grant from the National Science Foundation, Arlington, VA (Grant # CMMI-1000108) and the ACS Petroleum Research Fund, Washington D.C. (Grant # 52388-ND5)

References

1. Bhushan, B.; Li, X. *Int. Mater. Rev.* **2003,** *48,* 125–164. doi:10.1179/095066003225010227
2. Bhushan, B., Ed. *Nanotribology and Nanomechanics, I and II,* 3rd ed.; Springer: Heidelberg, Germany, 2011.
3. Bhushan, B., Ed. *Springer Handbook of Nanotechnology,* 3rd ed.; Springer: Heidelberg, Germany, 2010. doi:10.1007/978-3-642-02525-9
4. Schaefer, D. M.; Patil, A.; Andres, R. P.; Reifenberger, R. *Appl. Phys. Lett.* **1993,** *63,* 1492–1494. doi:10.1063/1.109666
5. Chen, B.; Zhang, H.; Dunphy-Guzman, K. A.; Spagnoli, D.; Kruger, M. B.; Muthu, D. V. S.; Kunz, M.; Fakra, S.; Hu, J. Z.; Guo, Q. Z.; Banfield, J. F. *Phys. Rev. B* **2009,** *79,* 125406. doi:10.1103/PhysRevB.79.125406
6. Jang, D.; Greer, J. R. *Scr. Mater.* **2011,** *64,* 77–80. doi:10.1016/j.scriptamat.2010.09.010
7. Gane, N.; Cox, J. M. *Philos. Mag.* **1970,** *22,* 881–891. doi:10.1080/14786437008221059
8. Pethicai, J. B.; Hutchings, R.; Oliver, W. C. *Philos. Mag. A* **1983,** *48,* 593–606. doi:10.1080/01418618308234914
9. Pharr, G. M.; Oliver, W. C. *J. Mater. Res.* **1989,** *4,* 94–101. doi:10.1557/JMR.1989.0094
10. Bhushan, B.; Koinkar, V. N. *Appl. Phys. Lett.* **1994,** *64,* 1653–1655. doi:10.1063/1.111949
11. Bhushan, B.; Kulkarni, A. V.; Bonin, W.; Wyrobek, J. T. *Philos. Mag. A* **1996,** *74,* 1117–1128. doi:10.1080/01418619608239712
12. Mante, F. K.; Baran, G. R.; Lucas, B. *Biomaterials* **1999,** *20,* 1051–1055. doi:10.1016/S0142-9612(98)00257-9
13. Grillo, S. E.; Ducarroir, M.; Nadal, M.; Tournié, E.; Faurie, J.-P. *J. Phys. D: Appl. Phys.* **2003,** *36,* L5. doi:10.1088/0022-3727/36/1/102
14. Doerner, M. F.; Gardner, D. S.; Nix, W. D. *J. Mater. Res.* **1986,** *1,* 845–851. doi:10.1557/JMR.1986.0845
15. Cao, Y.; Allameh, S.; Nankivil, D.; Sethiaraj, S.; Otiti, T.; Soboyejo, W. *Mater. Sci. Eng., A* **2006,** *427,* 232–240. doi:10.1016/j.msea.2006.04.080
16. Dietiker, M.; Nyilas, R. D.; Solenthaler, C.; Spolenak, R. *Acta Mater.* **2008,** *56,* 3887–3899. doi:10.1016/j.actamat.2008.04.032
17. Knapp, J. A.; Follstaedt, D. M. *J. Mater. Res.* **2004,** *19,* 218–227. doi:10.1557/jmr.2004.19.1.218
18. Thilly, L.; Lecouturier, F.; von Stebut, J. *Acta Mater.* **2003,** *51,* 5049–5065. doi:10.1016/S1359-6454(02)00543-8
19. Greer, J. R.; Oliver, W. C.; Nix, W. D. *Acta Mater.* **2005,** *53,* 1821–1830. doi:10.1016/j.actamat.2004.12.031
20. Wu, B.; Heidelberg, A.; Boland, J. J. *Nat. Mater.* **2005,** *4,* 525–529. doi:10.1038/nmat1403
21. Shan, Z. W.; Mishra, R. K.; Asif, S. A. S.; Warren, O. L.; Minor, A. M. *Nat. Mater.* **2008,** *7,* 115–119. doi:10.1038/nmat2085
22. Dietiker, M.; Buzzi, S.; Pigozzi, G.; Löffler, J. F.; Spolenak, R. *Acta Mater.* **2011,** *59,* 2180–2192. doi:10.1016/j.actamat.2010.12.019
23. Mordehai, D.; Lee, S.-W.; Backes, B.; Srolovitz, D. J.; Nix, W. D.; Rabkin, E. *Acta Mater.* **2011,** *59,* 5202–5215. doi:10.1016/j.actamat.2011.04.057
24. Palacio, M. L. B.; Bhushan, B. *Mater. Charact.* **2013,** *78,* 1–20. doi:10.1016/j.matchar.2013.01.009
25. Maharaj, D.; Bhushan, B. *Beilstein J. Nanotechnol.* **2012,** *3,* 759–772. doi:10.3762/bjnano.3.85
26. Mordehai, D.; Kazakevich, M.; Srolovitz, D. J.; Rabkin, E. *Acta Mater.* **2011,** *59,* 2309–2321. doi:10.1016/j.actamat.2010.12.027
27. Hull, D.; Bacon, D. J. *Introduction to dislocations,* 4th ed.; Butterworth-Heinemann: Woburn, Massachusetts, 2001.
28. Ashby, M. F. *Philos. Mag.* **1970,** *21,* 399–424. doi:10.1080/14786437008238426
29. Fleck, N. A.; Hutchinson, J. W. *J. Mech. Phys. Solids* **1993,** *41,* 1825–1857. doi:10.1016/0022-5096(93)90072-N
30. Nix, W. D.; Gao, H. *J. Mech. Phys. Solids* **1998,** *46,* 411–425. doi:10.1016/S0022-5096(97)00086-0
31. Hall, E. O. *Proc. Phys. Soc., London, Sect. B* **1951,** *64,* 747.
32. Petch, N. J. J. *Iron Steel Inst., London* **1953,** *174,* 25–28.
33. Li, J. C. M. *Philos. Mag.* **1969,** *19,* 189–198. doi:10.1080/14786436908217773

34. Abson, D. J.; Jonas, J. J. *Met. Sci.* **1970,** *4,* 24–28. doi:10.1179/msc.1970.4.1.24
35. Meyers, M. A.; Mishra, A.; Benson, D. J. *Prog. Mater. Sci.* **2006,** *51,* 427–556. doi:10.1016/j.pmatsci.2005.08.003
36. Gracio, J. J. *Scr. Metall. Mater.* **1994,** *31,* 487–489. doi:10.1016/0956-716X(94)90024-8
37. Conrad, H.; Jung, K. *Mater. Sci. Eng., A* **2005,** *391,* 272–284. doi:10.1016/j.msea.2004.08.073
38. Oliver, W. C.; Pharr, G. M. *J. Mater. Res.* **1992,** *7,* 1564–1583. doi:10.1557/JMR.1992.1564
39. Lozinskii, M. G. *High Temperature Metalloraphy;* Pergamon Press: New York, 1961.
40. Li, W. B.; Henshall, J. L.; Hooper, R. M.; Easterling, K. E. *Acta Metall. Mater.* **1991,** *39,* 3099–3110. doi:10.1016/0956-7151(91)90043-Z
41. Stevens, R. N. *Philos. Mag.* **1971,** *23,* 265–283. doi:10.1080/14786437108216383
42. Gerberich, W. W.; Mook, W. M.; Perrey, C. R.; Carter, C. B.; Baskes, M. I.; Mukherjee, R.; Gidwani, A.; Heberlein, J. P.; McMurry, H.; Girshick, S. L. *J. Mech. Phys. Solids* **2003,** *51,* 979–992. doi:10.1016/S0022-5096(03)00018-8
43. Yang, B.; Vehoff, H. *Mater. Sci. Eng., A* **2005,** *400–401,* 467–470. doi:10.1016/j.msea.2005.01.077
44. Faghihi, D.; Voyiadjis, G. Z. *Mech. Mater.* **2012,** *44,* 189–211. doi:10.1016/j.mechmat.2011.07.002
45. Nix, W. D. *Metall. Trans. A* **1989,** *20,* 2217–2245. doi:10.1007/BF02666659
46. Samsonov, G. V., Ed. *Handbook of the Physiochemical Properties of the Elements;* Plenum: New York, 1968. doi:10.1007/978-1-4684-6066-7

License and Terms

BEILSTEIN JOURNAL OF NANOTECHNOLOGY

Trade-offs in sensitivity and sampling depth in bimodal atomic force microscopy and comparison to the trimodal case

Babak Eslami[1], Daniel Ebeling[1,2] and Santiago D. Solares[*1,§]

Full Research Paper

Open Access

Address:
[1]Department of Mechanical Engineering, University of Maryland, College Park, MD 20742, USA and [2]present address: Institute of Applied Physics, Justus Liebig University of Giessen, 35392 Giessen, Germany

Email:
Santiago D. Solares[*] - ssolares@umd.edu

* Corresponding author
§ Phone: (301) 405-5035 Fax: (301) 314-9477

Keywords:
amplitude modulation; bimodal; multifrequency atomic force microscopy; indentation depth modulation; Nafion; open loop; proton exchange membranes; trimodal

Beilstein J. Nanotechnol. **2014,** *5,* 1144–1151.
doi:10.3762/bjnano.5.125

Received: 28 February 2014
Accepted: 27 June 2014
Published: 24 July 2014

This article is part of the Thematic Series "Advanced atomic force microscopy techniques II".

Guest Editors: T. Glatzel and T. Schimmel

Abstract

This paper presents experiments on Nafion® proton exchange membranes and numerical simulations illustrating the trade-offs between the optimization of compositional contrast and the modulation of tip indentation depth in bimodal atomic force microscopy (AFM). We focus on the original bimodal AFM method, which uses amplitude modulation to acquire the topography through the first cantilever eigenmode, and drives a higher eigenmode in open-loop to perform compositional mapping. This method is attractive due to its relative simplicity, robustness and commercial availability. We show that this technique offers the capability to modulate tip indentation depth, in addition to providing sample topography and material property contrast, although there are important competing effects between the optimization of sensitivity and the control of indentation depth, both of which strongly influence the contrast quality. Furthermore, we demonstrate that the two eigenmodes can be highly coupled in practice, especially when highly repulsive imaging conditions are used. Finally, we also offer a comparison with a previously reported trimodal AFM method, where the above competing effects are minimized.

Introduction

Since its invention in the early 1980s [1], atomic force microscopy (AFM) has become one of the most widely used characterization tools in nanotechnology and a wide range of imaging modes is now available, each with its own capabilities and applications. Among them, a family of techniques known as multifrequency AFM [2-11] has expanded considerably since the introduction of the first bimodal method by Rodriguez and Garcia in 2004 [12]. In multifrequency AFM the cantilever probe is driven simultaneously at more than one frequency, with the objective of creating additional channels of information in order to provide a more complete picture of the sample morphology and properties [2].

In the original method of Garcia and coworkers [12,13] the first eigenmode of the cantilever is driven using the amplitude modulation scheme (AM-AFM [14]) while a higher eigenmode is simultaneously driven at or near its resonance frequency with constant amplitude and frequency (i.e., in "open loop") in order to track its phase with respect to the excitation signal. Since the higher eigenmode is not directly subject to the amplitude modulation control loop that governs the acquisition of the topography, the user has freedom in selecting its operating parameters, thus allowing it to explore a wider range of tip–sample interactions. Additionally, since its amplitude is generally smaller than that of the fundamental mode, it can be made more sensitive to compositional contrast, as previously discussed by Rodriguez and Garcia [12]. The two eigenmodes can also be driven using the frequency modulation scheme (FM-AFM [4,15-17]), and it is also possible to simultaneously drive more than two eigenmodes. In a recently introduced trimodal method, two eigenmodes are used for topographical imaging and compositional mapping, respectively, and a third one is used to modulate the tip indentation depth during imaging [9]. The modulation of the indentation depth is accomplished through changes in the amplitude of the highest driven eigenmode, which has the highest dynamic force constant (the higher stiffness of higher eigenmodes has also been advantageous in subsurface imaging applications in contact resonance AFM [18]). In this paper we show that indentation depth modulation can also be accomplished when using bimodal AFM, although without the flexibility to independently optimize the sensitivity of the compositional mapping process. We discuss the trade-offs involved and provide an illustration of the dynamics complexities, including strong eigenmode coupling in some cases. Finally, we also offer a comparison to the trimodal method [9]. Note that in this paper we use the word sensitivity to *qualitatively* describe the ability of an eigenmode observable (e.g., phase shift) to detect small changes in the tip–sample forces, which in turn are governed by the surface properties. Since much of the discussion is based on the cantilever dynamics, the term can also be understood as the ability of a given cantilever eigenmode to be perturbed by small changes in the external forces when it is oscillating under the specified parameters. Our discussion and conclusions are based on the ideal case where noise is not a limitation.

Results and Discussion

Repulsive vs attractive imaging

In general, nanoscale surfaces can be imaged with AFM in either the attractive or repulsive imaging regime [14]. In the attractive regime the overall interaction between the cantilever tip and the sample surface is not affected by forces originating from physical contact. Instead, changes in the non-contact tip–sample interactions, which include van der Waals, electrostatic and magnetic forces, establish the basis for mapping sample topography and properties. In fact, the first bimodal AFM implementation of Rodriguez and Garcia was for imaging in the attractive regime [12,13]. In the repulsive imaging regime the cantilever tip intermittently impacts the sample and thus the images are governed by contact forces that are a consequence of elastic, plastic, viscous or adhesive surface behaviors, in addition to the noncontact forces. Figure 1 provides an example of single-mode attractive and repulsive images of a Nafion® fuel cell membrane (these images were acquired by using the standard amplitude modulation method [14]). A difference between the two images can be seen in terms of contrast inversion, feature sizes, shapes and patterns, which have been previously attributed by others to the competing effects of membrane functionality and contact mechanics on the cantilever response [19].

In cases in which the mechanics of the subsurface are of interest, it is necessary to operate the AFM in a way that the indentation depth can be controlled. This could be achieved in single-mode operation in a number of ways, including the use of cantilevers with different spring constants (see Figure 2a and Figure 2b), the use of cantilevers with different quality factors (Figure 2c), changes in the amplitude setpoint, or changes in the free oscillation amplitude. The first option is not practical since it requires a cantilever changeover. The second option is feasible using the Q-control method but requires additional electronics [20,21]. The third option does not work indefinitely since indentation and peak forces vary in a non-monotonic fashion as the cantilever is lowered towards the surface, as illustrated by all plots in Figure 2 [9]. The fourth option is also relatively limited in the additional indentation depth that can be accomplished as shown in Figure 2d (black, blue, red and dotted black traces).

Indentation depth modulation with bimodal AFM

Figure 2d shows that the second eigenmode is much more effective in accomplishing additional indentation depth than the fundamental eigenmode for the same change in amplitude (note how a 10 nm increase in the second mode amplitude is significantly more effective in increasing the indentation depth under the conditions illustrated than a 75 nm increase in the first mode amplitude), although the level of penetration into the sample can exhibit non-smooth behavior due to the non-steady state behavior of multifrequency oscillations [9,22], especially as the cantilever is brought very close to the surface (in these simulations the curves become smoother if one considers a larger number of taps for every cantilever height in the construction of the graphs). As previously reported, the greater indentation capability of higher eigenmodes with respect to the fundamental mode can be understood by inspecting the dimensionless equation of motion of a damped harmonic oscillator [9].

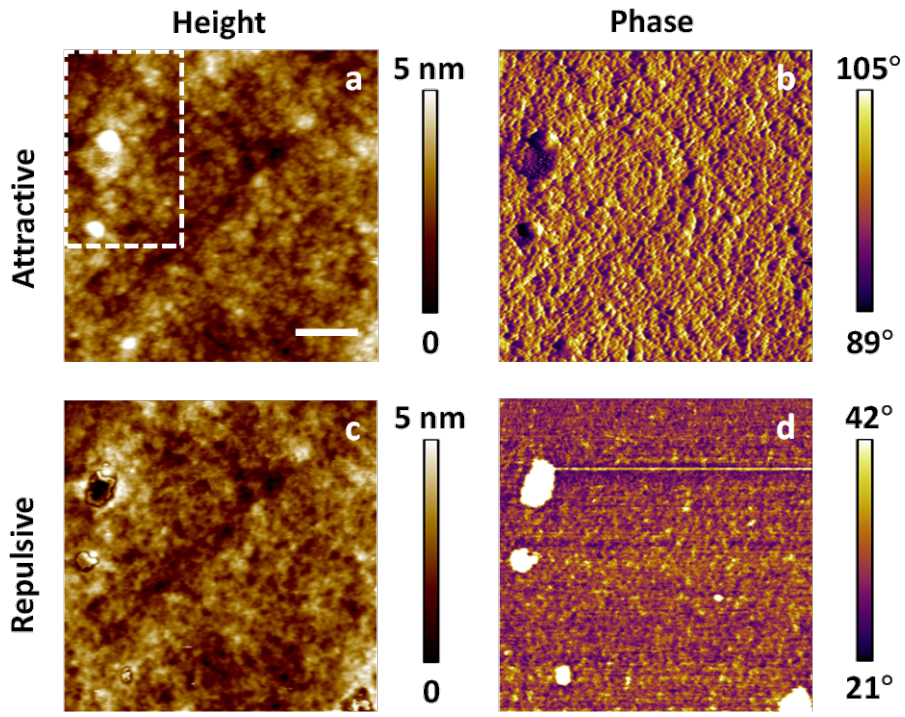

Figure 1: (a) and (b) topography and phase images, respectively, of a Nafion® membrane acquired in the attractive regime; (c) and (d) corresponding images acquired in the repulsive regime. The scale bar is 100 nm. The morphology of the region in the dashed rectangle in (a) is discussed below in Figure 6. The free oscillation amplitude in both cases was 17 nm, with an amplitude setpoint of 80% for attractive regime imaging and 50% for repulsive regime imaging.

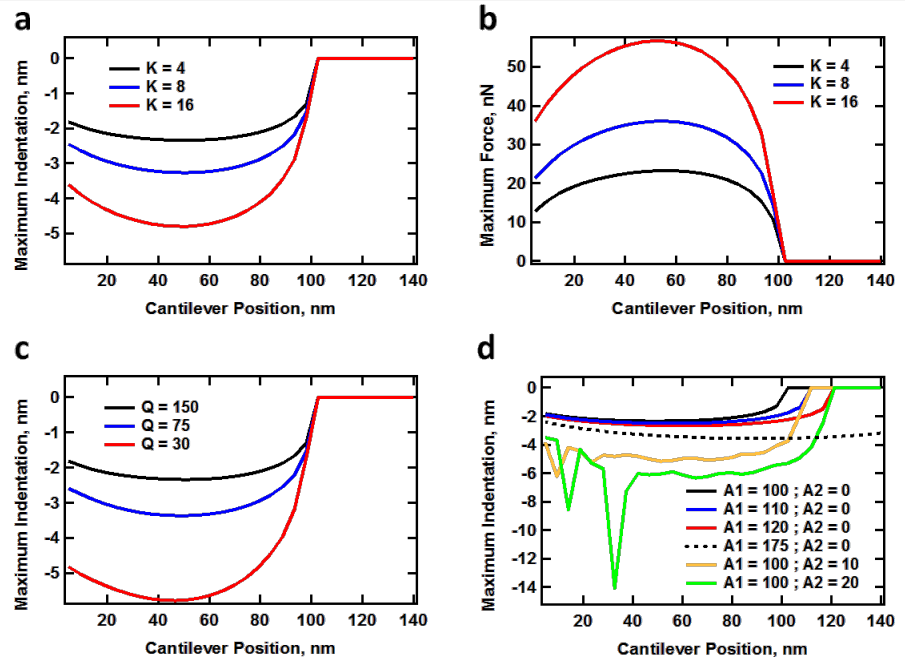

Figure 2: Simulations of maximum indentation and peak force (see section Methods below for details on the numerical simulations of the cantilever dynamics as well as the tip–sample force model used): (a) maximum indentation depth vs cantilever force constant; (b) peak forces corresponding to (a); (c) maximum indentation vs cantilever quality factor, *Q* (unrealistically low values of *Q* were chosen to illustrate the effect of high damping); (d) maximum indentation vs first and second eigenmode free amplitudes. The first eigenmode free amplitude in these simulations was 100 nm, unless otherwise indicated. The cantilever and force model parameters are provided in section Methods. The irregular behavior of the indentation for the lowest two traces at small cantilever–sample separations in (d) is a consequence of the non-steady state behavior of multi-eigenmode oscillations [9,22].

$$\frac{d^2\underline{z}}{d\underline{t}^2} = -\underline{z} + \frac{1}{Q}\left[-\frac{d\underline{z}}{d\underline{t}} + \cos(\underline{t})\right] + \frac{F_{ts}(\underline{z}_{ts})}{kA_o} \quad (1)$$

where A_o is the free amplitude, $\underline{z} = z(t)/A_o$ is the dimensionless tip position with respect to the cantilever base, $\underline{z}_{ts} = z_{ts}/A_o$ is the dimensionless tip–sample distance ($z_{ts} = z + z_{eq}$, where z_{eq} is the position of the cantilever above the sample), $\underline{t} = \omega_o t$ is the dimensionless time, k is the cantilever force constant and F_{ts} is the tip–sample interaction force. We have made the substitution $A \approx A_o = F_o Q/k$ [14], where F_o is the amplitude of the excitation force, and we have combined the damping and excitation terms with the factor $1/Q$. The last term on the right hand side indicates that the tip–sample forces are normalized by the product of the force constant times the free amplitude. Thus, the external forces influence the dynamics more or less when the product kA_o becomes smaller or larger, respectively. As the product kA_o decreases, the oscillator is more easily perturbed by the tip–sample forces (i.e., it is more sensitive to external forces), whereas the perturbations are less significant when this product increases. Thus, if the objective is to obtain the greatest gain in controlling indentation for a given cantilever, one should choose for this purpose the highest available eigenmode, which has the highest dynamic force constant and thus the largest product kA_o for a given value of A_o (the dynamic force constants of the cantilever eigenmodes increase with the square of their eigenfrequency – see Table 1 in [2]). However, one must be mindful that increasing indentation in this manner comes with a loss in sensitivity. In other words, since greater indentation is being accomplished by driving the cantilever in a way in which it is less able to be perturbed by the tip–sample forces (greater repulsive forces are required to perturb it, which leads to greater penetration into the repulsive part of the tip–sample potential), it can also be more difficult to detect small changes in the behavior of the tip–sample forces, which are related to the sample properties. The choice depends on what the user's highest priority is – indentation depth or sensitivity in compositional mapping.

Since each eigenmode is governed by an equation similar to Equation 1 (except that there are additional cosine driving force terms, one for each driven eigenmode) and the tip–sample forces are the same for all equations, the various eigenmodes are coupled and the degree of coupling becomes more noticeable in the dynamics as the higher eigenmode amplitude increases. This is illustrated in Figure 3, in which each row represents a separate experiment for a given free oscillation amplitude of the second eigenmode. The scale bar for each respective phase (first or second) is the same for all experiments. One can easily see that as the second eigenmode amplitude increases and the indentation increases according to Figure 2d, the first eigenmode phase changes drastically indicating a more repulsive interaction (the values decrease for each successive row, which corresponds to higher and higher second mode amplitudes). The first eigenmode has the lowest dynamic force constant, so it is more easily perturbed by the dynamics of the second eigenmode. In contrast, the phase values of the second eigenmode increase for successive rows (which would indicate a less repulsive regime since the values are closer to the 90° phase shift of the unperturbed oscillator).

To understand the above result we have to consider the two competing effects that are at play. As the second mode amplitude increases, this eigenmode becomes less sensitive (more difficult to perturb), which leads to larger phase values (closer to the neutral phase value of 90°, which is observed when no

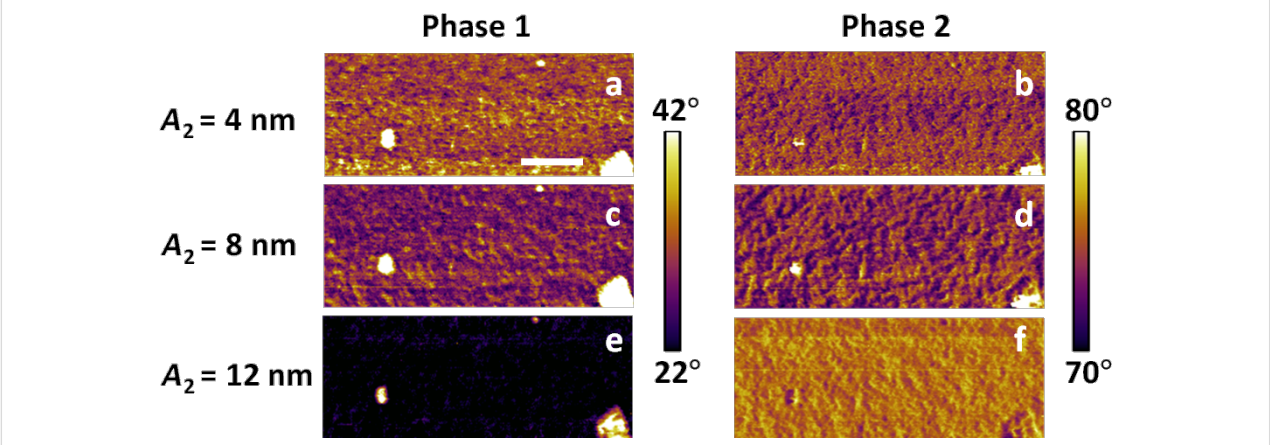

Figure 3: Bimodal experiments with varying second eigenmode amplitude for a Nafion® membrane (the images correspond to the lower portion of those shown in Figure 1). The left and right columns provide, respectively, the phase of the first and second eigenmode. Each row is a separate experiment using the second mode free amplitude indicated on the left. The second amplitude was increased in the downward direction to increase indentation, according to Figure 2d. The first eigenmode free amplitude was 17 nm with a setpoint of 45%. The scale bar is 100 nm.

tip–sample forces are present and the eigenmode is driven at the natural frequency). However, since the relationship between the tip–sample forces and the phase and amplitude is very difficult to establish [23], and the amplitude is not constant for successive rows in the experiments of Figure 3, increasing phase values are not an unambiguous criterion that one can use to conclude that the repulsive forces for this eigenmode are becoming smaller. Additionally, the decrease in sensitivity leads to greater indentation and thus to larger and steeper tip–sample forces, which would have the opposite effect of lowering the phase further away from 90° (see Figure 4b). Depending on the sample and the tip, which govern the behavior of the forces as a function of tip position and velocity, one of these two effects will dominate. In this particular case, the loss in sensitivity dominates and the phase values increase (see also reference [24] for a similar type of experiment on a polystyrene–polybutadiene diblock copolymer). This result may or may not be desirable, depending on what information is sought (surface contrast, high-indentation surface morphology, etc.). Furthermore, as indentation is modulated through free amplitude changes, it is important to consider whether the phase response is in the high or low contrast region (the low contrast regions are those where the phase response becomes nearly flat with respect to changes in the external force gradient, as indicated in Figure 4b). Although the tip–sample force model is not generally available during an experiment, it is also important to consider at least conceptually whether the changes in imaging conditions lead to more or less sensitive phase response for a given type of sample. Figure 5a shows an illustration of the (simulated) phase behavior for the standard linear solid model used here (see section Methods for further details). Clearly the phase response as a function of the cantilever position becomes flatter with respect to the cantilever position above the surface when the first eigenmode amplitude is increased, whereas Figure 5b shows that the phase curve slope behaves similarly for different values of the quality factor (although the cantilever quality factor cannot be arbitrarily changed, the *effective* quality factor can vary significantly during the measurement due to the dissipative tip–sample interactions, which also cause a decrease

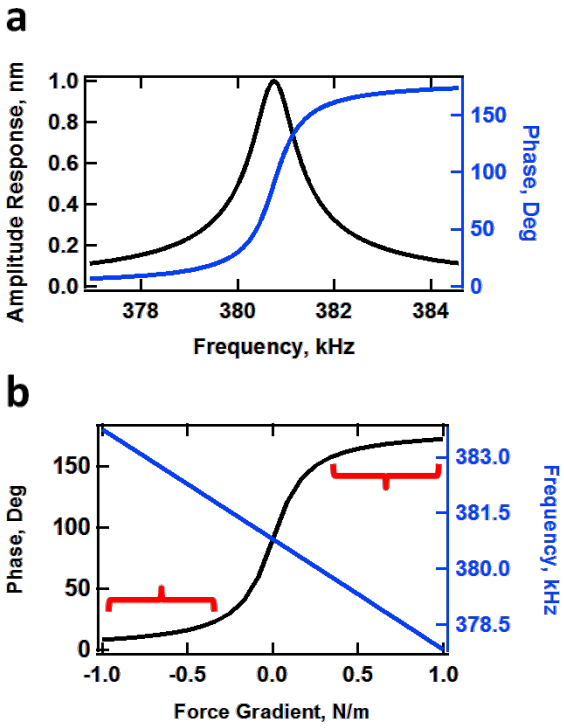

Figure 4: Illustration of the ideal response of a harmonic oscillator [22]. (a) Amplitude and phase vs excitation frequency (at the resonance frequency the phase is 90 degrees); (b) phase and effective frequency shift vs external force gradient (at zero force gradient the phase is 90 degrees and the frequency is equal to the resonance frequency). In general, the force gradient becomes more negative (the force curve becomes steeper in the repulsive region) as the tip–sample indentation increases, leading to lower phase values. The red brackets in (b) indicate regions of low contrast, where the phase response is relatively flat with respect to changes in the force gradient. Measurements under these conditions lead to lower quality contrast in the images.

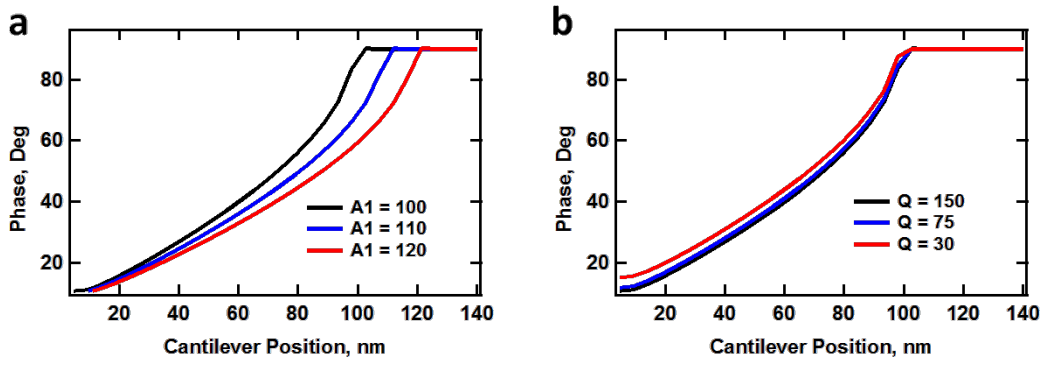

Figure 5: Simulated behavior of the first eigenmode phase as a function of free amplitude (a) and cantilever quality factor (b). See Figure 2 for the corresponding behavior of the indentation.

in amplitude that leads to additional changes in eigenmode sensitivity [22]). In general, steeper responses of the imaging variables are desired with respect to changes in the imaging conditions (e.g., phase vs cantilever height, or equivalently, phase vs amplitude setpoint, in the case of Figure 5).

An important consequence of the phenomena discussed above is that when a user 'optimizes' the imaging conditions in bimodal AFM to obtain the topography with the first eigenmode and to carry out compositional contrast with the higher eigenmode, changes in the higher mode amplitude lead not only to changes in the contrast sensitivity but also to changes in what region of the sample is actually being sampled (sampling region here refers to the volume of material between the surface skin and the lowest point reached by the tip during maximum indentation). Thus, images with drastically different parameters are not necessarily comparable to one another. Figure 6 illustrates the corresponding changes in the acquired topography for the feature highlighted in Figure 1a, for the single-mode attractive and repulsive imaging experiments (Figure 1) and the three sets of experiments shown in Figure 3, and Figure 7 gives the corresponding scan line profiles for four of the images along the dashed line indicated on Figure 6a. Clearly the topography and morphology can change significantly as more repulsive imaging conditions are sought, and these changes become more significant as the sample stiffness decreases (see also indentation-dependent measurements for a soft polymer film embedded with nanoparticles in [9]).

It may appear from the above discussion that the user has little control on what aspect or region of the sample is being characterized, but this is not necessarily the case. The observations presented here simply highlight the need for acquiring complementary information, especially through simulation, in order to carry out a sound interpretation of the results.

Comparison to trimodal AFM

As already stated, in the AM-OL (amplitude modulation – open loop) bimodal method the 'optimization' of compositional contrast mapping and indentation depth modulation is accom-

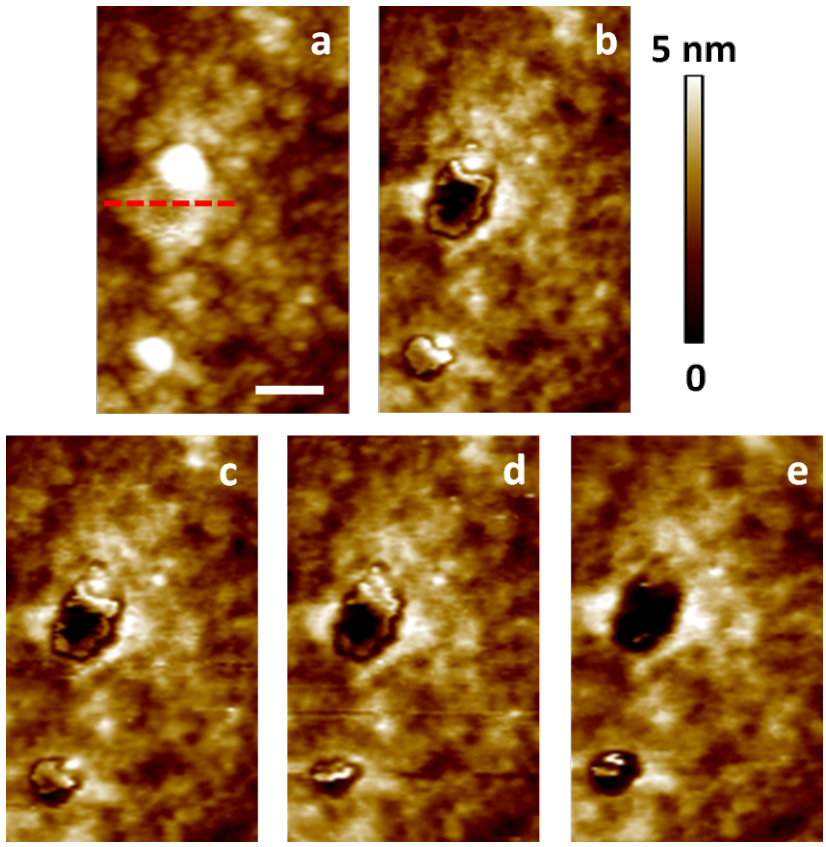

Figure 6: Morphology change of the topographical feature highlighted in Figure 1a for different imaging conditions. (a) and (b) show results taken from the images shown in Figure 1a and 1c, respectively. The panels (c–e) show results acquired during the three experiments shown in Figure 3 with increasing indentation (from the top row to the bottom row in Figure 3). This behavior is initially reversible but becomes irreversible after repeated imaging under highly repulsive conditions. The scan line profiles along the dashed red line for (a), (b), (c) and (e) are provided in Figure 7. The scale bar is 50 nm.

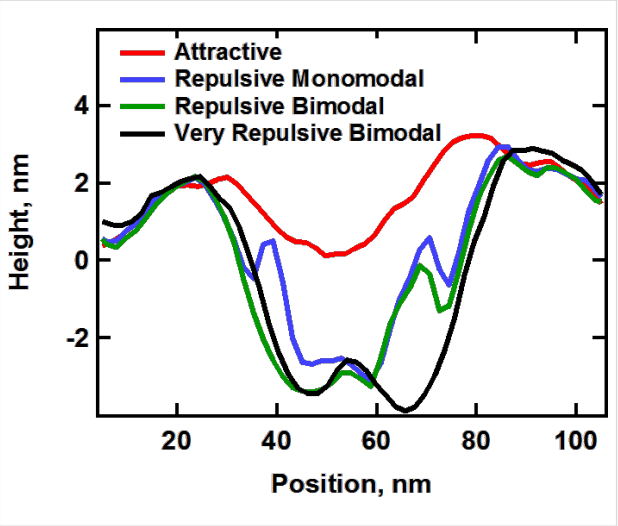

Figure 7: Scan line profiles along the dashed line indicated in Figure 6a for the images shown in Figure 6a (attractive), Figure 6b (repulsive monomodal), 6c Figure (repulsive bimodal) and Figure 6e (very repulsive bimodal).

plished with the same higher eigenmode, which does not allow the user to control them independently. Furthermore, these two objectives can compete against one another since greater indentation is accomplished by driving the cantilever in a way in which it is less likely to be perturbed by the tip–sample forces (i.e., in a way in which it is less sensitive). In contrast, in trimodal AFM each function is accomplished by a separate eigenmode: the fundamental mode is used for topographical acquisition, a higher mode is used for compositional mapping, and an even higher mode is used to modulate indentation [9]. Since the spectroscopy eigenmode can be optimized nearly independently through changes in its free amplitude, the non-responsive regions of the phase response (indicated by brackets in Figure 4b) can be avoided. Not only are all functions accomplished with separate modes, but the user is also able to space those modes as much as is desired. For example, since increasingly higher modes have increasingly larger force constants, one could use the second mode for compositional mapping while modulating indentation with the fourth or an even higher mode for a very stiff sample, whereas one would use the first three modes for a soft sample.

Conclusion

We have examined through experiment and simulation the trade-offs between the optimization of compositional contrast and the modulation of tip–sample indentation for bimodal AFM combining amplitude modulation for topographical acquisition and open-loop drive for compositional mapping [12,13]. In general, it is possible to increase indentation in this mode of operation by increasing the amplitude of the higher mode, but this usually comes with a loss in sensitivity. We demonstrate that changes in sensitivity and indentation cannot be separated within this method. We have also illustrated the coupling of the two eigenmodes, whereby highly repulsive imaging conditions resulting from the choice of higher mode parameters can have a drastic effect in the response of the fundamental mode. Finally, we offer a comparison to a previously reported trimodal AFM method, whereby the modulation of indentation and the optimization of compositional contrast are carried out with separate eigenmodes, thus minimizing the above competing effects. Despite the limitations discussed, however, the AM-OL bimodal method remains an attractive alternative due to its relative simplicity, robustness and commercial availability. Furthermore, an in-depth knowledge of the dynamics and trade-offs involved can allow an experienced user to reach a favorable compromise between versatility and sensitivity.

Methods

Experimental

The experimental measurements were carried out on an Asylum Research (Santa Barbara, CA, USA) MFP3D-SA microscope, which is equipped with bimodal imaging modes. We used a Bruker (Santa Barbara, CA, USA) MPP-33120 cantilever with first two resonance frequencies at 45.99 and 284.39 kHz, respectively, fundamental force constant of 7.3 N/m and fundamental quality factor of 236. The amplitude of the first eigenmode was calibrated by using amplitude–distance curves and the amplitude of higher eigenmodes was estimated by using their respective optical sensitivity factors (see Table 1 in [2]).

The experimental sample consisted of the proton exchange membrane Nafion® 115, purchased from Ion Power, Inc. (New Castle, DE, USA). The product was received in H^+ form and no further treatment was performed, except for a routine cleaning procedure. Sections of the membrane of the size of 1 × 1 cm^2 were rinsed with DI-water followed by 5 min of ultrasonication in DI-water and a second rinse step prior to equilibration in a closed container. During the experiments reported in this paper, the air in the AFM chamber was monitored to be at 23 °C and 17% relative humidity.

Computational

For the numerical simulations the first three eigenmodes of the AFM cantilever were modeled by using individual equations of motion for each, coupled through the tip–sample interaction forces as in previous studies [9]. The first two eigenmodes were excited through respective sinusoidal tip forces of constant amplitude, with the drive frequencies matching the resonance frequencies. The equations of motion were integrated numerically and the amplitude and phase of each eigenmode were calculated using the customary in-phase (I_i) and quadrature (K_i) terms:

$$I_i = \int_{N\tau} z_i(t)\cos(\omega t)dt \quad (2)$$

$$K_i = \int_{N\tau} z_i(t)\sin(\omega t)dt \quad (3)$$

where $z_i(t)$ is the i-th eigenmode response in the time domain, N is the number of periods over which the phase and amplitude were averaged (we rounded N to the integer closest to 25 times the ratio of each eigenmode's frequency to the fundamental frequency), ω is the excitation frequency, and τ is the *nominal* period of one oscillation. The amplitude and phase were calculated, respectively, as:

$$A_i = \frac{\omega}{\pi N}\sqrt{I_i^2 + K_i^2} \quad (4)$$

$$\varphi_i = \tan^{-1}(K_i / I_i) \quad (5)$$

The repulsive tip–sample forces were accounted for through a standard linear solid (SLS) model [9] having force constants of 7.5 N/m for the two linear springs and a dashpot constant of 1×10^{-5} Ns/m. The long-range attractive interactions were included through the Hamaker equation [14] for a tip radius of curvature of 10 nm and a Hamaker constant of 2×10^{-19} J.

Acknowledgements

This work was supported by the U.S. Department of Energy, Office of Science, Basic Energy Sciences, under Award #DESC0008115.

References

1. Binnig, G.; Quate, C. F.; Gerber, Ch. *Phys. Rev. Lett.* **1986,** *56,* 930–933. doi:10.1103/PhysRevLett.56.930
2. Garcia, R.; Herruzo, E. T. *Nat. Nanotechnol.* **2012,** *7,* 217–226. doi:10.1038/nnano.2012.38
3. Proksch, R. *Appl. Phys. Lett.* **2006,** *89,* 113121. doi:10.1063/1.2345593
4. Kawai, S.; Glatzel, T.; Koch, S.; Such, B.; Baratoff, A.; Meyer, E. *Phys. Rev. Lett.* **2009,** *103,* 220801. doi:10.1103/PhysRevLett.103.220801
5. Naitoh, Y.; Ma, Z.; Li, Y. J.; Kageshima, M.; Sugawara, Y. *J. Vac. Sci. Technol., B* **2010,** *28,* 1210–1214. doi:10.1116/1.3503611
6. Platz, D.; Thólen, E. A.; Pesen, D.; Haviland, D. B. *Appl. Phys. Lett.* **2008,** *92,* 153106. doi:10.1063/1.2909569
7. Jesse, S.; Kalinin, S. V.; Proksch, R.; Baddorf, A. P.; Rodriguez, B. J. *Nanotechnology* **2007,** *18,* 435503. doi:10.1088/0957-4484/18/43/435503
8. Rodriguez, B. J.; Callahan, C.; Kalinin, S. V.; Proksch, R. *Nanotechnology* **2007,** *18,* 475504. doi:10.1088/0957-4484/18/47/475504
9. Ebeling, D.; Eslami, B.; Solares, S. D. J. *ACS Nano* **2013,** *7,* 10387–10396. doi:10.1021/nn404845q
10. Guo, S.; Solares, S. D.; Mochalin, V.; Neitzel, I.; Gogotsi, Y.; Kalinin, S. V.; Jesse, S. *Small* **2012,** *8,* 1264–1269. doi:10.1002/smll.201101648
11. Sahin, O.; Magonov, S.; Su, C.; Quate, C. F.; Solgaard, O. *Nat. Nanotechnol.* **2007,** *2,* 507–514. doi:10.1038/nnano.2007.226
12. Rodríguez, T. R.; García, R. *Appl. Phys. Lett.* **2004,** *84,* 449–451. doi:10.1063/1.1642273
13. Martinez, N. F.; Patil, S.; Lozano, J. R.; Garcia, R. *Appl. Phys. Lett.* **2006,** *89,* 153115. doi:10.1063/1.2360894
14. García, R.; Pérez, R. *Surf. Sci. Rep.* **2002,** *47,* 197–301. doi:10.1016/S0167-5729(02)00077-8
15. Giessibl, F. J. *Rev. Mod. Phys.* **2003,** *75,* 949–983. doi:10.1103/RevModPhys.75.949
16. Ebeling, D.; Solares, S. D. *Beilstein J. Nanotechnol.* **2013,** *4,* 198–207. doi:10.3762/bjnano.4.20
17. Herruzo, E. T.; Perrino, A. P.; Garcia, R. *Nat. Commun.* **2014,** *5,* No. 3126. doi:10.1038/ncomms4126
18. Killgore, J. P.; Kelly, J. Y.; Stafford, C. M.; Fasolka, M. J.; Hurley, D. C. *Nanotechnology* **2011,** *22,* 175706. doi:10.1088/0957-4484/22/17/175706
19. O'Dea, J. R.; Buratto, S. K. *J. Phys. Chem. B* **2011,** *115,* 1014–1020. doi:10.1021/jp108821j
20. Ebeling, D.; Hölscher, H.; Anczykowski, B. *Appl. Phys. Lett.* **2006,** *89,* 203511. doi:10.1063/1.2387122
21. Hölscher, H.; Ebeling, D.; Schwarz, U. D. *J. Appl. Phys.* **2006,** *99,* 084311. doi:10.1063/1.2190070
22. Solares, S. D.; Chawla, G. *Meas. Sci. Technol.* **2010,** *21,* 125502. doi:10.1088/0957-0233/21/12/125502
23. Hölscher, H. *Appl. Phys. Lett.* **2006,** *89,* 123109. doi:10.1063/1.2355437
24. Gigler, A. M.; Dietz, C.; Baumann, M.; Martinez, N. F.; Garcia, R.; Stark, R. W. *Beilstein J. Nanotechnol.* **2012,** *3,* 456–463. doi:10.3762/bjnano.3.52

License and Terms

BEILSTEIN JOURNAL OF NANOTECHNOLOGY

Multi-frequency tapping-mode atomic force microscopy beyond three eigenmodes in ambient air

Santiago D. Solares*[1,2,§], Sangmin An[2,3] and Christian J. Long[2,3]

Full Research Paper

Open Access

Address:
[1]Department of Mechanical Engineering, University of Maryland, College Park, Maryland 20742, United States; current address: Department of Mechanical and Aerospace Engineering, George Washington University, Washington, DC 20052, United States, [2]Maryland NanoCenter, University of Maryland, College Park, Maryland 20742, United States and [3]Center for Nanoscale Science and Technology, National Institute of Standards and Technology (NIST), Gaithersburg, Maryland 20899, United States

Email:
Santiago D. Solares* - ssolares@gwu.edu

* Corresponding author
§ Phone: +1 (202) 994-0372

Keywords:
amplitude-modulation; bimodal; frequency-modulation; multi-frequency atomic force microscopy; multimodal; open loop; trimodal

Beilstein J. Nanotechnol. **2014,** *5,* 1637–1648.
doi:10.3762/bjnano.5.175

Received: 24 April 2014
Accepted: 31 August 2014
Published: 25 September 2014

This article is part of the Thematic Series "Advanced atomic force microscopy techniques II".

Guest Editors: T. Glatzel and T. Schimmel

Abstract

We present an exploratory study of multimodal tapping-mode atomic force microscopy driving more than three cantilever eigenmodes. We present tetramodal (4-eigenmode) imaging experiments conducted on a thin polytetrafluoroethylene (PTFE) film and computational simulations of pentamodal (5-eigenmode) cantilever dynamics and spectroscopy, focusing on the case of large amplitude ratios between the fundamental eigenmode and the higher eigenmodes. We discuss the dynamic complexities of the tip response in time and frequency space, as well as the average amplitude and phase response. We also illustrate typical images and spectroscopy curves and provide a very brief description of the observed contrast. Overall, our findings are promising in that they help to open the door to increasing sophistication and greater versatility in multi-frequency AFM through the incorporation of a larger number of driven eigenmodes, and in highlighting specific future research opportunities.

Introduction

Multi-frequency atomic force microscopy (AFM) refers to a family of techniques in which the microcantilever probe is driven simultaneously or sequentially at more than one frequency [1]. Often these frequencies correspond to different cantilever eigenmodes [2-12], but there are also methods involving single-eigenmode multi-frequency excitation [13-15]

and spectral inversion methods in which the cantilever is driven at a single frequency but the response is analyzed for a range of frequencies [16-18]. Generally speaking, the dynamics of the tip motion become increasingly complex in the case of *simultaneous* multi-frequency excitation, as has been previously reported for multi-eigenmode methods [19-22], which are of particular interest since their purpose is to carry out multiple characterization functions at the same time. Specifically, bimodal AFM methods were developed to perform simultaneous topographical imaging and compositional mapping [2,3], and trimodal methods were later introduced to add imaging depth modulation capability to the bimodal schemes [9]. Although there is not yet an obvious need for methods involving more than three eigenmodes, and although a number of challenges are expected in terms of cantilever quality and drive systems performance (see Figure 1 for an example of non-ideal amplitude vs frequency responses for different eigenmodes), signal processing instrumentation (higher eigenmodes have higher frequencies and require faster electronics as well as tip tracking systems with higher performance), and dynamic complexity [19-22], it is important to explore the feasibility of imaging with multimodal drives since the rapid growth of multi-frequency methods suggests they will soon be of interest [1] (in this paper we use the term multimodal to designate imaging schemes involving more than three eigenmodes).

In general, multimodal imaging can be accomplished with similar equipment to that used for bimodal and trimodal methods [9], except that one needs to include a larger number of oscillation controllers according to the number of active eigenmodes. While the instrumentation is already available, the key open question is whether this type of operation is stable and meaningful. In this paper we explore tetramodal (4-eigenmode) imaging experimentally by using a thin polytetrafluoroethylene (PTFE) film sample and simulate pentamodal (5-eigenmode) cantilever dynamics and spectroscopy computationally (hardware, detection bandwidth and data acquisition limitations prevent us from using the same number of eigenmodes and range of eigenfrequencies in the experiments as in the simulations). We focus on the case of large amplitude ratios between the fundamental eigenmode (used for topographical imaging) and the higher eigenmodes, as in previously validated bimodal and trimodal methods [2-9]. Although the dynamics of multimodal tapping-mode AFM can be quite complex, we find that imaging can be remarkably stable and that the cantilever eigenmodes, in general, exhibit the predicted behavior [20]. We focus our results and discussion section on five different topics, namely tip response in time and frequency space, amplitude and phase response, eigenmode frequency sweep response, imaging, and optimization of the tip–sample impact. We discuss primarily the dynamics and stability of the method and do not offer an interpretation of the additional contrast channels in

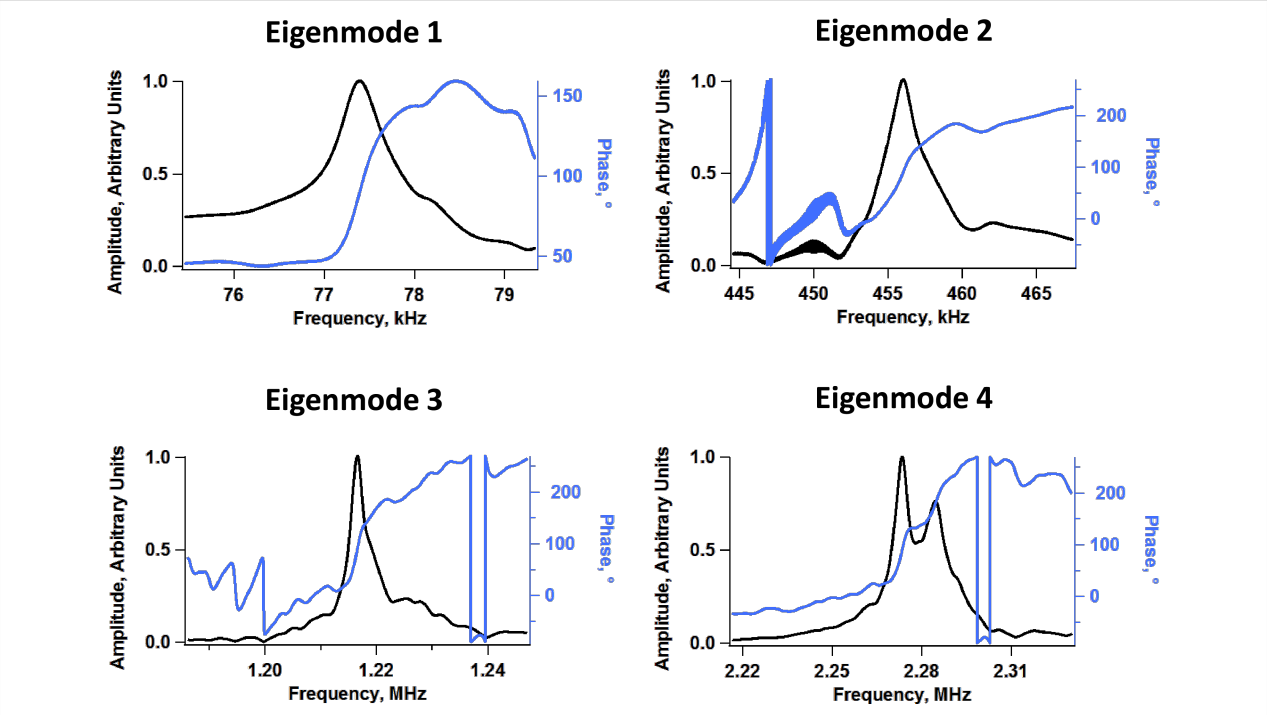

Figure 1: Example of measured frequency response of the first four eigenmodes of one of the rectangular cantilevers used in our experiments, which have nominal fundamental resonance frequency and force constant of 70 kHz and 2 N/m, respectively. As the mode order increases the shape of the peak increasingly deviates from the ideal response of a damped harmonic oscillator.

terms of material properties, as there still remain important open questions even for the bimodal and trimodal methods [20-23]. Overall, our findings are promising and open the door to increasing sophistication and greater versatility in multi-frequency AFM through the inclusion of a larger number of driven eigenmodes along with the corresponding additional contrast channels.

Results and Discussion

Tip response in time- and frequency-space

The dynamic challenges encountered in multimodal tapping-mode imaging are best appreciated by analyzing the time-dependent trajectory of the tip and individual eigenmodes through simulation of ideal cantilevers. Figure 2a illustrates typical tip trajectories simulated for pentamodal operation when imaging a polymer sample. Here the first eigenmode free amplitude is 80 nm and the higher mode free amplitudes are set to either 3 or 8 nm, as indicated on the graphs, which correspond to typical amplitude ratios used in bimodal and trimodal AFM. As the higher mode amplitudes are increased, the tip trajectory has the appearance of becoming increasingly noisy, which occurs in part because the various eigenfrequencies are generally not integer multiples of one another [1]. Figure 2b shows several successive tip trajectories for the same cases, for typical tapping-mode imaging conditions (only the lowest portion of the oscillation is shown, near the sample), illustrating how the tip can penetrate into the surface to different depths every successive impact, which is not surprising given the irregular tip

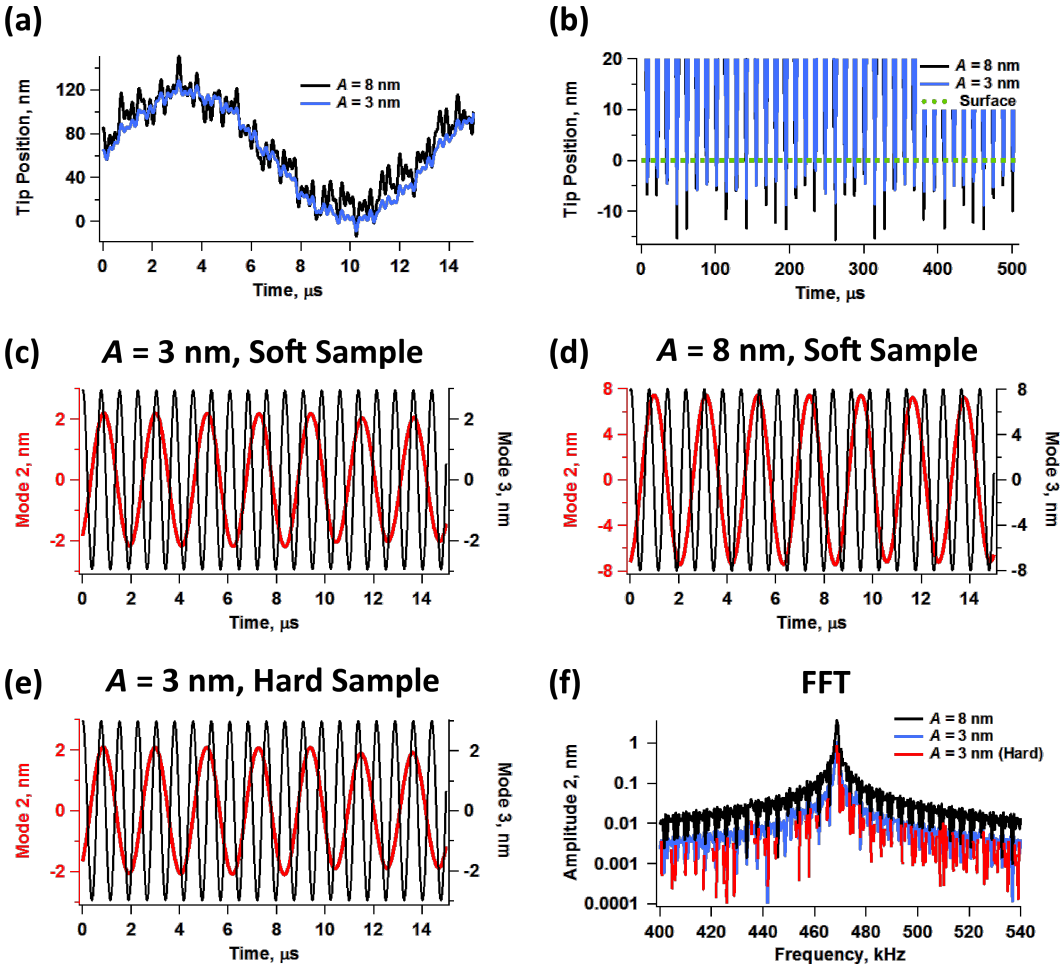

Figure 2: Simulated tip and eigenmode responses for pentamodal tapping-mode AFM: (a) tip trajectories for two different higher eigenmode amplitudes over one fundamental cycle; (b) tip trajectories for two different higher eigenmode amplitudes over multiple fundamental cycles (only the lowest portion of the trajectory is shown, closest to the surface); (c–e) second and third eigenmode trajectories for different free amplitudes and sample parameters; (f) second eigenmode spectra for different free amplitudes. The surface properties were accounted for through a standard linear solid model (see methods section) with K_0 = 7.5 N/m, K_{inf} = 7.5 N/m and C_d = 1 × 10^{-5} N·s/m for the "soft" sample and K_0 = 15 N/m, K_{inf} = 15 N/m and C_d = 3 × 10^{-5} N·s/m for the "hard" sample. The cantilever parameters are v_1 = 75 kHz, k_1 = 4 N/m, Q_1 = 150, Q_2 = 3 Q_1, Q_3 = 5 Q_1, Q_4 = 7 Q_1 and Q_5 = 9 Q_1. The free oscillation amplitudes were A_1 = 80 nm, and A_2 = A_3 = A_4 = A_5 = 3 or 8 nm, as indicated on the graphs. The higher mode frequencies and dynamic force constants were scaled by using the eigenfrequency ratios of ideal rectangular beams [1]. The cantilever height was kept fixed at 60 nm above the surface. The responses of modes 2 & 3 are color coded with their respective axes in figures (c) through (e).

trajectory. Furthermore, the graph shows that impacts become less regular as the higher mode amplitude increases, which is also as expected. Such irregular impacts constantly generate new transients that in turn lead to non-steady-state tip oscillations. These unsettled oscillations are problematic in the development of generalized theories that relate the measurement observables (amplitudes, phases, frequency shifts, etc.) to material properties because the transients depend on the particular sample, probe and parameters used, as well as on noise levels and non-linear intermodal interactions. However, Figures 2c through 2e show that the oscillation of the individual eigenmodes remains remarkably undisturbed. In fact, the perturbation in the third eigenmode (black traces) is not evident to the naked eye. There is a reduction in the amplitude of the second eigenmode (red traces), which is more significant for smaller free oscillation amplitudes, but it is not excessive in any of the cases considered. Some minor irregularity is observed from one oscillation of the second eigenmode to the next one for stiffer samples (Figure 2e), as was the case in previous studies [20], but the response is still well behaved. This is further confirmed by the oscillation spectrum of this eigenmode, shown in Figure 2f, which exhibits a distinct resonance in all cases. Figures 2c through 2e show only the second and third eigenmode responses, since these are the higher modes with the lowest dynamic force constant [1], which makes them more perturbable than the much stiffer and hardly affected fourth and fifth modes.

Amplitude and phase response

Simulations of the amplitude and phase behavior for the cases illustrated in Figure 2 show that these key observables also follow the expected trends, as seen in Figure 3 [24]. Figure 3a and Figure 3b provide, respectively, the amplitude and phase response vs cantilever position for pentamodal operation by using higher eigenmode amplitudes of 3 nm, and Figure 3c and Figure 3d provide the corresponding results for higher eigenmode amplitudes of 8 nm (the fundamental free amplitude was set to 100 nm in both cases). The oscillation amplitude of each eigenmode decreases with increasing tip–sample interaction (shorter distance between the cantilever and the sample) and the corresponding phase decreases and deviates increasingly from 90°, indicating in this example a predominantly repulsive interaction [24]. The results also agree with previously known trends [9,19,20] in that the phase and amplitude responses become less

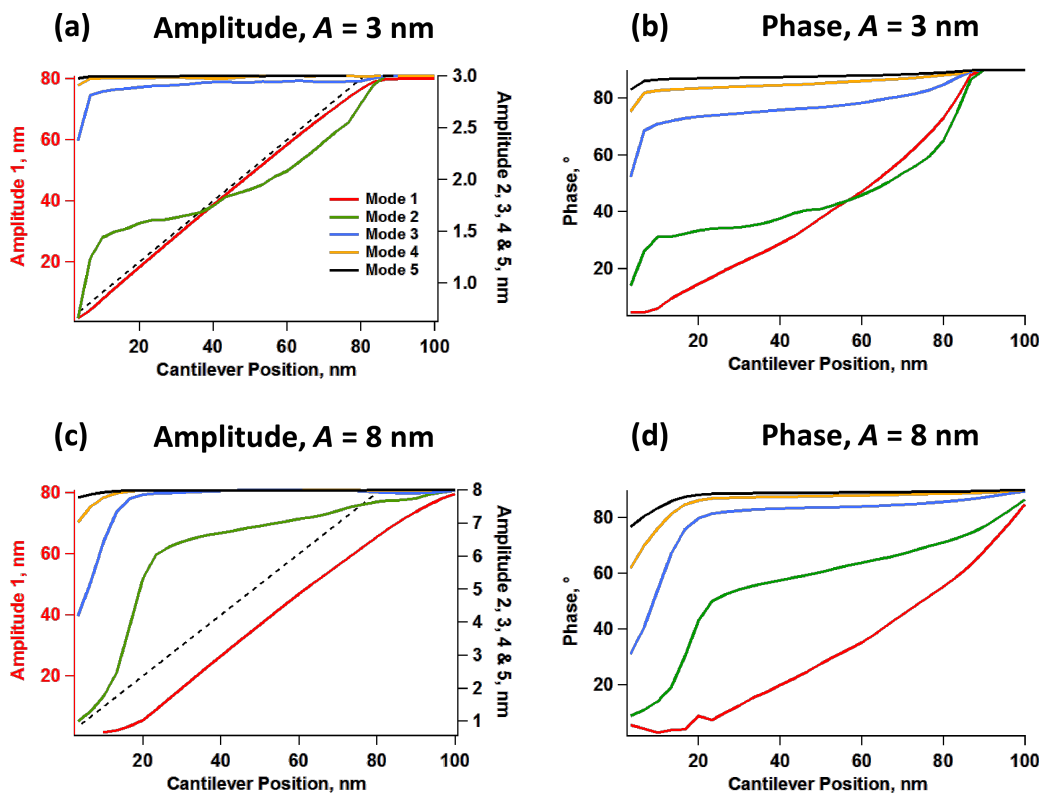

Figure 3: Simulations of amplitude and phase response for two different free amplitudes of the higher eigenmodes. All higher eigenmodes were driven at the same free amplitude in both cases, with the magnitude indicated at the top of the graphs (A = 3 nm or 8 nm), while the fundamental free amplitude was set to 80 nm. The simulation parameters are the same as for Figure 2, except that the cantilever position was varied from 100 nm to zero. The dashed lines in graphs (a) and (c) have slope unity and contain the origin, and are provided for guidance.

and less sensitive as the eigenmode order increases (that is, the magnitude of the phase and amplitude shifts of the higher eigenmodes is in general smaller than for the lower eigenmodes, for the same free oscillation amplitude), and the sensitivity, defined as the rate of change in these observables with respect to a change in cantilever position, also decreases as the higher mode free oscillation amplitude is increased (as discussed in detail in [20] for the trimodal case). This observation is important in terms of signal-to-noise ratio, since the amplitude, phase or frequency shifts, depending on the mode of operation used, could fall below the noise floor for very high (less sensitive) eigenmodes due to their small magnitudes. It is also important to note that although the response curves for different modes exhibit some similarity with one another, they do not necessarily contain the same spectroscopic information, as the shape and curvature can vary significantly from one eigenmode to another, especially for the lowest ones. Different eigenmodes may give different trends in their response variables either due to being able to oscillate in different regimes (attractive or repulsive) with respect to one another or due to nonlinear interactions between them [20-22] (see also Figure 4c and Figure 4d below, which offer an experimental example in which not all eigenmodes oscillate in the same regime). As a result, the spectroscopy theory previously developed for bimodal AFM [25,26] is not necessarily applicable to multimodal AFM. The results of Figure 3 also highlight subtleties in the amplitude curve that could be important depending on the sample and the type of information sought. Specifically, the results show that the amplitude curve for the first eigenmode, which is the basis of the amplitude modulation method [24], is not a straight line as it is in single-mode operation (for guidance, the dashed line in Figure 3a and Figure 3c is a straight line of slope unity, containing the origin). Furthermore, the curvature differs for different higher mode amplitudes (compare the red traces in Figures 3a and 3c) and the curve shifts to the right for larger amplitudes of the higher modes, since the range of oscillation of the tip is the sum of the oscillation ranges of all active eigenmodes.

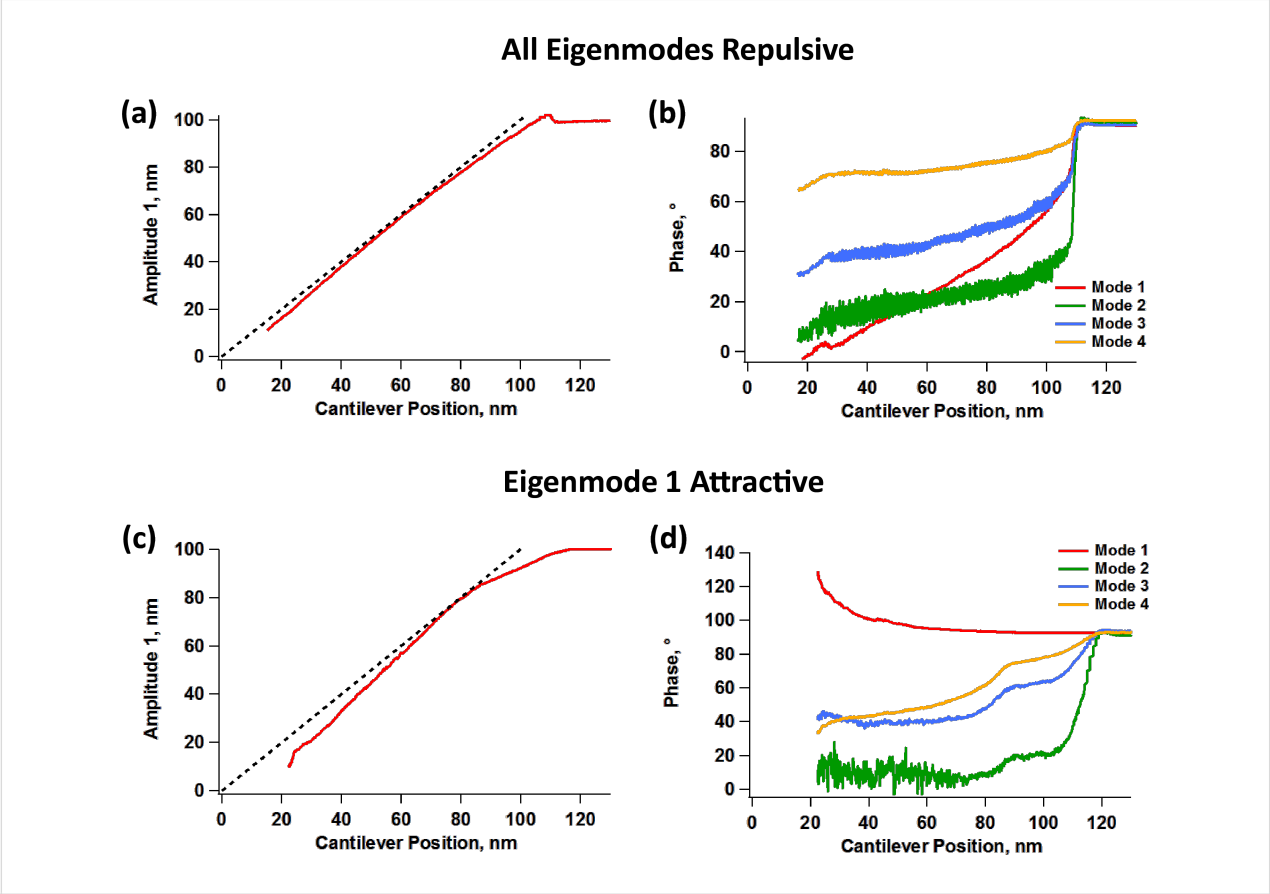

Figure 4: Experimental fundamental amplitude (a, c) and phase responses (b, d) vs cantilever position for tetramodal imaging by using a cantilever similar to the one whose response is illustrated in Figure 1. (a) and (b) correspond to an experiment in which all eigenmodes oscillated in the repulsive imaging regime, similar to the simulations of Figure 3, while (c) and (d) correspond to an experiment in which the fundamental eigenmode oscillated in the attractive imaging regime (the phase of this mode is greater than 90°) while all other eigenmodes oscillated in the repulsive imaging regime. The free oscillation amplitudes for the four eigenmodes were set to approximately 100, 2.9, 1.8, and 1.3 nm, respectively. The dashed lines in graphs (a) and (c) have slope unity and contain the origin, and are provided for guidance.

Figure 4 shows experimental curves analogous to those of Figure 3, but for tetramodal imaging. Since the instrument used has a limited number of acquisition channels, we focused our study on the fundamental amplitude and the four phase responses. Furthermore, since higher eigenmodes have increasingly higher optical detection sensitivity [1], it is possible in an experiment to use smaller physical amplitudes (in units of length) for the highest mode oscillations while still being able to obtain relatively large amplitude readings at the photodetector (in units of voltage), which is also advantageous in terms of making these modes more sensitive [20]. In our experiments we set the free fundamental amplitude to approximately 100 nm and the next three modes to free amplitudes of approximately 2.9, 1.8, and 1.3 nm, respectively. With these settings the amplitude reading at the photodetector for all higher modes was approximately 10% of the reading for the fundamental eigenmode despite the comparatively small physical amplitude of the higher modes. Figure 4a and Figure 4b correspond to an experiment in which all eigenmodes remained in the repulsive regime (as in Figure 3) and Figure 4c and Figure 4d show similar data for an experiment in which the first eigenmode remained in the attractive regime while all others remained in the repulsive regime. Although the simulations assume ideal eigenmode behavior, which is not the case for an experiment (see Figure 1), they do predict important features that were also observed in the experiments. Firstly, non-linear amplitude curves can occur both when the topographical acquisition mode is in the repulsive and in the attractive regime, which as discussed above, has implications for the accuracy of topographical measurement. Second, there is a decrease in the magnitude of the contrast signal (phase shift) as the higher mode order increases, although we did not observe cases in which the highest eigenmode contrast signals fell below the noise floor. Notice also that the second and third phases are noisier than the other two, which is in agreement with the greater propensity of the lower eigenmodes to be perturbed by external forces. Finally, the experimental results illustrate that the curvature of the amplitude or phase response is not necessarily preserved for different eigenmodes (this is especially true when not all eigenmodes operate in the same imaging regime, as illustrated in Figure 4d).

Engaged frequency response

A key consideration regarding the acquisition of meaningful results with multimodal AFM imaging is the quality of the amplitude vs frequency curve of the higher eigenmodes while the cantilever and sample are engaged [20] (this is similar to the usual tuning curve, but with the cantilever and sample engaged). Specifically the degree to which these curves resemble the response of a damped harmonic oscillator, determines the degree to which previous interpretations of the observables and calculated quantities (e.g., phase and amplitude contrast, calculated dissipated power, calculated virial, etc. [25,26]) are applicable. This consideration is also important in cases in which higher modes are excited by using constant drive frequency and amplitude without any feedback (i.e., in 'open loop' [2,3]). In such cases, as long as the oscillation is not chaotic, the user will generally be able to obtain an image, but imaging stability does not guarantee that the results are physically meaningful, since it does not guarantee that the contrast eigenmodes conform to the assumed ideal response. In contrast, if frequency modulation methods are used to drive the higher modes [5,7,27], it is necessary that the frequency response be well behaved both to ensure the stability of the controls scheme and to guarantee physically meaningful results. Our simulations show that the highest (least perturbable) eigenmodes retain their ideal response even in multimodal operation. However, it is possible that the response of the lowest eigenmode, excluding the fundamental eigenmode, will be perturbed enough to compromise the stability of a frequency modulation drive. Figure 5 illustrates the amplitude response of the second eigenmode within pentamodal operation when using conditions that are close to those used to construct Figure 2 and Figure 3, for different amplitudes of the higher eigenmodes (Figure 5a), for different cantilever positions above the sample (Figure 5b – the trace for Z_c = 120 nm is the free response), and for different amplitudes of the second eigenmode, while eigenmodes 3 to 5 were driven with a free oscillation amplitude of 3 nm. In the first case (Figure 5a) we observe that the effective resonance frequency of the second eigenmode (location of the peak in each curve) shifts to the left as the amplitude is increased, which is as expected since the influence of the tip–sample forces on the dynamics diminishes for larger amplitudes [20] (here the repulsive tip–sample forces shift the instantaneous resonance frequency of this eigenmode to the right, but this effect diminishes for larger amplitudes, which decrease eigenmode sensitivity [9]). However, the level of perturbation does not change significantly for the range of conditions explored (it only improves slightly for larger amplitudes). In the second case (Figure 5b), we see that the level of perturbation increases, accompanied by a greater frequency shift (due to a greater influence of the repulsive forces in the range of conditions considered), as the cantilever is lowered towards the sample. Additionally, the frequency response curve gradually deviates from the ideal curve, suggesting that the stability of frequency modulation operations may be compromised unless slower scanning speeds are used, which permit greater averaging in the signals. Finally, the results of Figure 5c show that the eigenmode frequency shift increases as its free amplitude is decreased while keeping the other higher amplitudes constant, in agreement with previous results [20] and with Figure 5a, although the shape of the response curve remains distorted for most of the

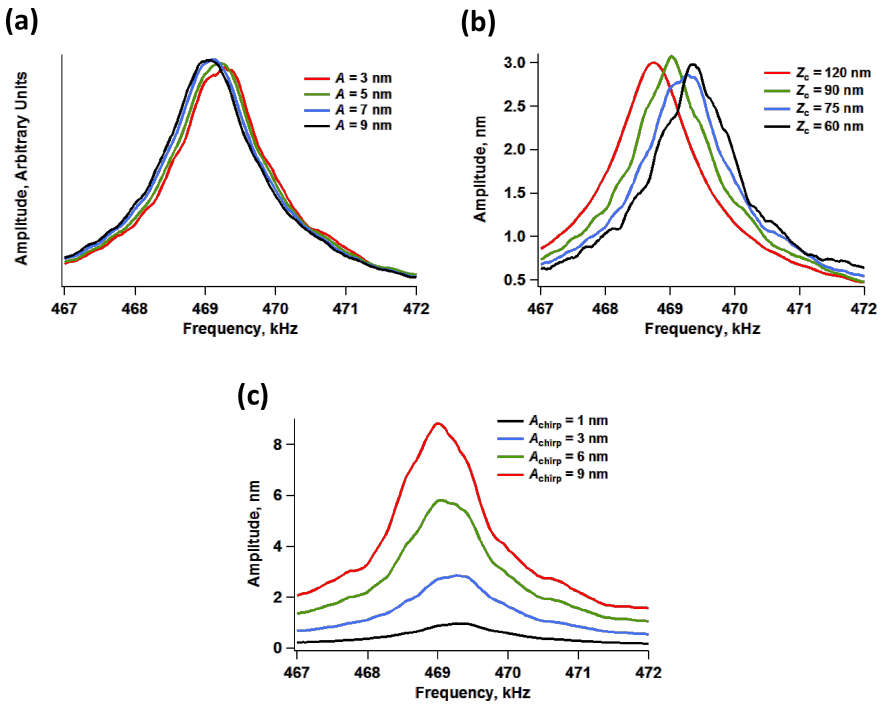

Figure 5: Simulated amplitude vs frequency response of the second eigenmode in pentamodal operation, calculated by sweeping the frequency by using chirp drive functions while the cantilever and sample remained engaged [28]. The simulation parameters are similar to those provided for Figure 2, except that the first eigenmode free amplitude was set to 100 nm. (a) Effect of higher mode free amplitude (A_2 = A_3 = A_4 = A_5 = 3, 5, 7, or 9 nm – Note: the various traces shown are normalized by the free amplitude in each case); (b) effect of cantilever position, Z_c (A_2 = A_3 = A_4 = A_5 = 3 nm); (c) effect of second eigenmode peak chirp response amplitude (A_{chirp} = 1, 3, 6, or 9 nm) for constant amplitude of the highest eigenmodes (A_3 = A_4 = A_5 = 3 nm).

range of amplitudes considered. Despite the nonidealities, the distortions are not extremely drastic for the examples considered, suggesting that frequency modulation drives could still be stable under these conditions as previously shown for trimodal imaging [20]. We recall also that the higher mode responses become more and more regular as the mode order increases (since they are perturbed to a lesser extent by the sample), so the user can in principle select a higher and higher mode whose behavior is close enough to that of an ideal damped harmonic oscillator, in order to enable stable controls. In practice, however, this may not always be feasible or useful in light of the results of Figure 1 which illustrate the typical decline in the quality of the higher eigenmode responses due to tip shaker and cantilever nonidealities.

Imaging

By using the same settings as for Figure 4, imaging of the PTFE film was carried out by using typical scan rates for tapping mode AFM with an amplitude setpoint ratio of 50 to 60%. Similar to the spectroscopy results of Figure 4, it was possible to image the surface with the fundamental eigenmode operating in the repulsive imaging regime (Figure 6 and Figure 7) as well as in the attractive imaging regime (Figure 8), although there was little control on the selection of the regime. In general, higher free amplitudes, lower amplitude setpoints, and drive frequencies lower than the natural frequency favor the repulsive regime, but the result is also strongly determined by the cleanness and sharpness of the tip. Cleaner and sharper tips undergo smaller tip–sample attraction due to their smaller effective radius of curvature. Therefore, they are more amenable to imaging in the repulsive regime, which in general gives sharper topographical contrast since it is governed by contact as opposed to long-range forces which are more likely to cause tip broadening artifacts [29].

For characterization in the repulsive regime (see Figure 6) the phase images generally resembled one another for all eigenmodes, although differences and even contrast inversion between eigenmodes emerged on certain regions of the sample as the imaging conditions were changed. Additionally, the varying range of phase values observed for each eigenmode (phase range decreasing with increasing mode order) confirms the decreasing sensitivity of higher eigenmodes, even though higher modes were driven with smaller amplitudes (see parameters in the caption of Figure 4). This is better illustrated in Figure 7, where all phase images from Figure 6 are plotted

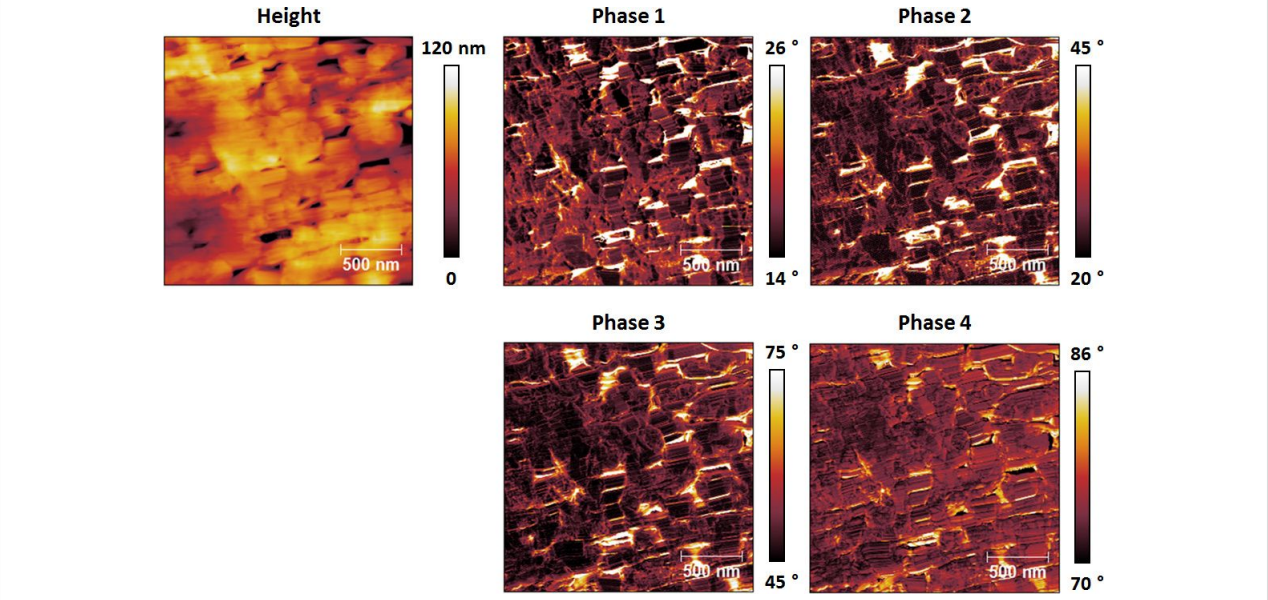

Figure 6: Tetramodal imaging of a thin PTFE film sample by using a cantilever similar to the one whose response is shown in Figure 1. The range of each phase image was chosen such that the contrast is easily discernible. A small percentage of pixels in each image have values that are outside the chosen range. For comparison, Figure 7 shows all phase images of this figure plotted using the same scale. In this experiment all eigenmodes oscillated in the repulsive imaging regime (all phase values are below 90°).

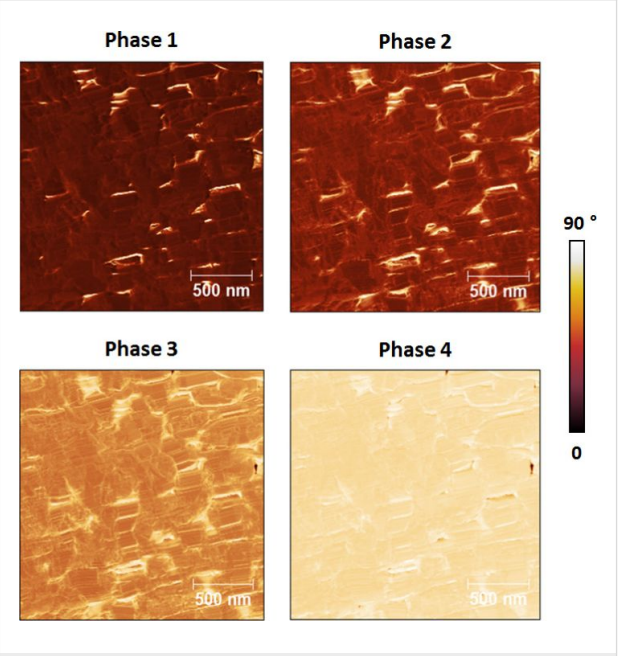

Figure 7: Phase images of Figure 6 plotted using the same scale. As discussed in the text, the phase shifts generally decrease with increasing eigenmode order.

using the same scale. Clearly the highest modes exhibit the smallest phase shift from 90°. In contrast, the phase images acquired driving the fundamental eigenmode in the attractive regime almost always exhibited partial contrast inversion with respect to one another. For example, some bright spots in the first phase image of Figure 8 look dark in the fourth phase image and vice versa. The observed contrast inversion may be related to the mechanism previously identified for bimodal imaging, which was related to the energy content in each eigenmode [20-22], or may be the result of nonlinear interactions between the eigenmodes, given the complexity of the multimodal tip–sample impact.

Optimization of the tip–sample impact

Despite the stability with which imaging can be carried out and the apparent robustness of our results, the non-uniformity of successive tip–sample impacts, the nonlinear coupling of the various eigenmodes, as well as time-dependent tip–sample behaviors such as viscoelasticity suggest that unless single-cycle techniques [16,18,30] can be implemented accurately for multimodal imaging, it may not be possible to carry out fully quantitative measurements of the surface properties. As already discussed, the tip trajectories for a tetramodal or pentamodal operation are even more complex than the already complex bimodal [19] and trimodal [20] trajectories. Furthermore, the variation of the impact shape from one fundamental oscillation to the next one results in non-steady-state dynamics which may not only require lower scanning speeds in order to properly characterize each location on the surface, but which may also preclude the application of spectroscopy theories based on ideal responses and the recording of observables averaged over multiple cantilever cycles [25,26]. However, our simulations also show that the regularity of the tip–sample impact can be

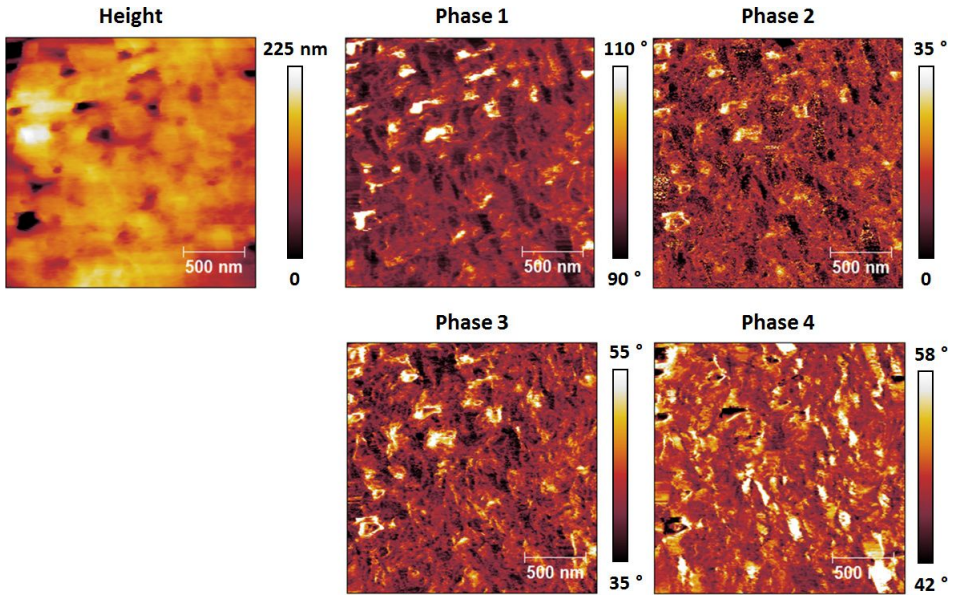

Figure 8: Imaging results analogous to those of Figure 6, but with the first eigenmode oscillating in the attractive regime (the phase values of this mode are greater than 90°).

significantly improved by choosing non-consecutive eigenmodes with relatively high frequency ratios among them, as illustrated in Figure 9 for the trimodal case (the regularity of the impact depends on the frequency spacing between each pair of active eigenmodes, so similar arguments can be made for other multimodal cases). Figure 9a compares the trajectories of a trimodal oscillation using eigenmodes 1, 2 and 3 vs using eigenmodes 1, 4 and 9. It is clear that the successive impacts shown differ significantly in the former case, but not in the latter (see also Figure 9b, which shows a close-up view of the lowest portion of the tip trajectories of Figure 9a, illustrating a more symmetric and regular impact when the eigenmode spacing is greater). Figure 9c shows the force trajectory for a large number of impacts, confirming that successive tip–sample interactions become more similar with greater eigenmode spacing. Notice how the peak forces over a large number of fundamental oscillations in Figure 9c are similar in both cases, but the dynamics are less steady for the case when the first three eigenmodes are used. Note also that in order to improve the regularity of the multimodal tip–sample impact, it is necessary to increase the frequency ratio for each pair of adjacent eigenmodes. For the case discussed here, for example, using eigenmodes 1, 8 and 9 would not be as effective as using eigenmodes 1, 4 and 9. Although the spacing between the first two active eigenmodes would be large in the former case, the frequency ratio of the highest two eigenmodes (8 and 9) would only be about 1.3. The results of Figure 9 suggest that it could in some cases be advantageous to maximize the frequency ratios when selecting the active eigenmodes, although this may not always be possible due to bandwith limitations in the electronics and cantilever and shaker non-idealities (see Figure 1). As stated above, the use of very high eigenmodes can also result in low signal-to-noise ratios due to the decreasing sensitivity in the spectroscopic observables (e.g., small phase shifts, etc.) with increasing mode order, despite the higher optical sensitivity in tracking the tip response [1].

Conclusion

We have explored experimentally and computationally the dynamics and stability of multimodal tapping-mode atomic force microscopy when using more than three active cantilever eigenmodes. We have illustrated the increase in complexity with a larger number of eigenmodes, as well as its indirect effect on the topographical measurement and the response of the spectroscopic observables. We have also shown that stable imaging is possible, although contrast differences emerging from the nonlinear interaction of the eigenmodes are also expected. Overall our findings are positive and encourage further development of multimodal techniques, as well as fundamental research on the probe dynamics and on the measurement process itself. We take the opportunity to remind the reader that our results are only applicable to measurements performed in air environments, corresponding to fundamental quality factors of a few hundreds, and that the work reported here represents by no means an exhaustive study. High-damping environments may offer even greater complexities [31] and our amplitude-modulation/open-loop results are not directly applicable to vacuum environments [24,32].

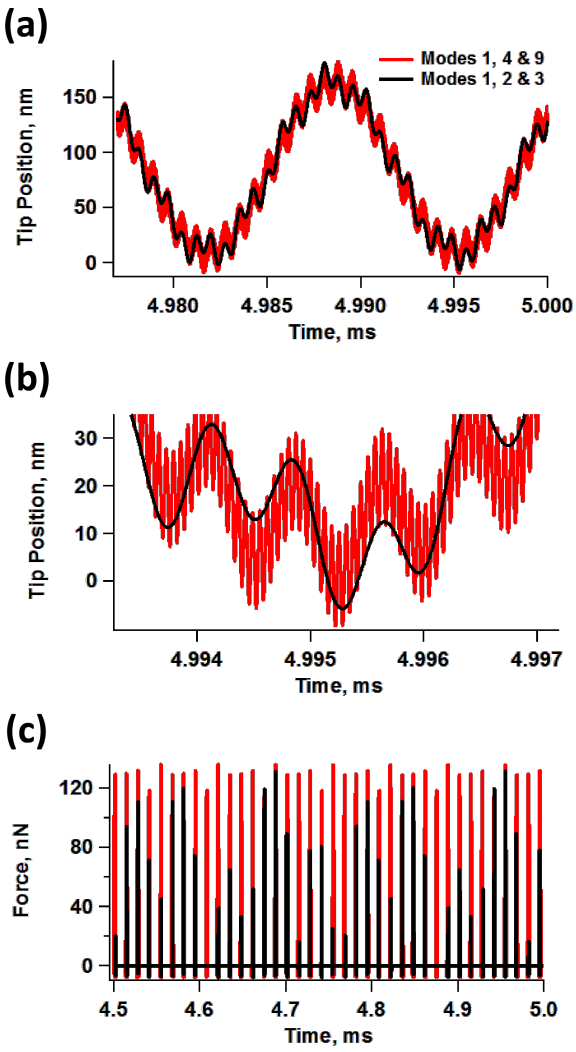

Figure 9: (a) Comparison of tip trajectories for trimodal oscillations using the first three eigenmodes (A_1 = 100 nm, A_2 = A_3 = 3 nm) and eigenmodes 1, 4 and 9 (A_1 = 100 nm; A_4 = A_9 = 3 nm) with $A_{setpoint}$ ≈ 80%; (b) close-up of the lowest portion of the tip trajectory for the above cases; (c) illustration of force trajectories for the above cases (notice how the peak forces in successive impacts become more similar to one another as eigenmode spacing increases). The sample and cantilever parameters are the same as for Figure 2.

Methods

Experimental

The tetramodal experiments were performed using a Cypher AFM (Asylum Research, Santa Barbara, CA), driving all four modes through the internal lock-ins of the instrument (see disclaimer below). Since the number of signals that could be recorded was limited to six, we recorded all the eigenmode phases along with the fundamental amplitude during the experiments. Images were acquired with a resolution of 512 × 512 pixels at a scan rate of 1 Hz in the fast direction. We used a commercial cantilever having a nominal fundamental resonance frequency of 70 kHz and a nominal fundamental force constant of 2 N/m. The sample consisted of PTFE pipe thread seal tape (nominal thickness ca. 0.1 mm) stretched onto the back of single-sided scotch tape, which was adhered sticky side down onto a metal substrate. This type of polymer sample was chosen in order to obtain high contrast in the phase signals.

Computational

For the numerical simulations five eigenmodes of the AFM cantilever were modeled by using individual equations of motion for each, coupled through the tip–sample interaction forces as in previous studies [8,20]. Driven eigenmodes were excited through a sinusoidal tip force of constant amplitude, and frequency equal to the natural frequency. Chirp excitation functions [8,28] were used to construct the engaged amplitude vs frequency curves of Figure 5. The equations of motion were integrated numerically and the amplitude and phase of each eigenmode were calculated using the customary in-phase (I_i) and quadrature (Q_i) terms:

$$I_i = \int_{N\tau} z_i(t)\cos(\omega t)dt \tag{1}$$

$$Q_i = \int_{N\tau} z_i(t)\sin(\omega t)dt \tag{2}$$

where $z_i(t)$ is the spatial response of the ith eigenmode in the time domain, N is the number of periods over which the phase and amplitude were averaged, ω is the excitation frequency, and τ is the nominal period of one oscillation. The amplitude (A_i) and phase (ϕ_i) were calculated, respectively, as:

$$A_i = \frac{\omega}{\pi N}\sqrt{I_i^2 + Q_i^2} \tag{3}$$

$$\phi_i = \tan^{-1}\left(Q_i / I_i\right) \tag{4}$$

The repulsive tip–sample forces were accounted for through a standard linear solid (SLS) model [9] which exhibits both stress relaxation and creep (see Figure 10 and notice the variety of force and surface trajectories for the single and multiple impacts observed in multimodal tapping-mode imaging [20]). Long-range attractive interactions were included via the Hamaker equation [24] for a tip radius of curvature of 10 nm and a Hamaker constant of 2 × 10^{-9} J.

Disclaimer

Certain commercial equipment, instruments or materials are identified in this document. Such identification does not imply recommendation or endorsement by the National Institute of

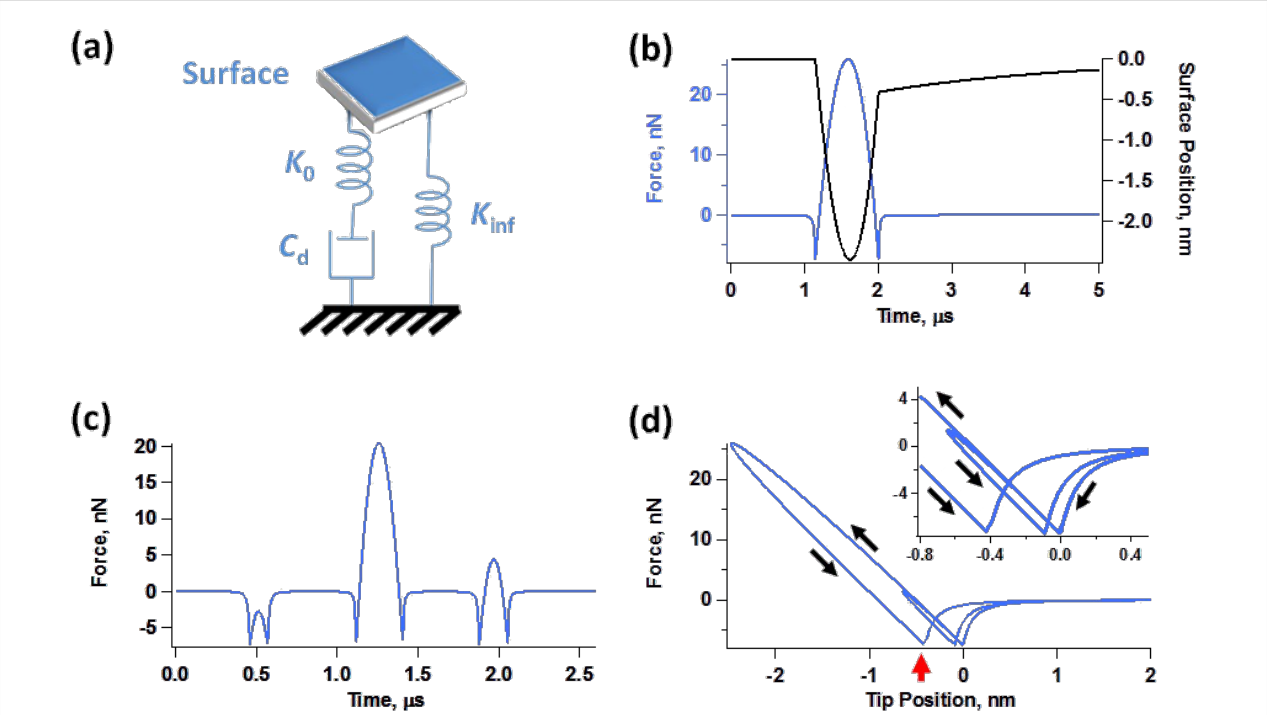

Figure 10: (a) Standard linear solid (SLS) model [9]; (b) illustration of the force trajectory for a single tip–sample impact along with the relaxation trajectory of the surface (notice how the surface remains temporarily indented and gradually recovers after the impact); (c) illustration of a triple impact within a single cycle of the fundamental oscillation for a multimodal imaging case (see also the discussion on multiple impacts in reference [20]); (d) force curve (force vs tip position) for a double-impact, illustrating also the temporary depression of the surface due to relaxation of the SLS model (the red arrow illustrates the depressed position of the surface where tip–sample contact is lost after the first impact).

Standards and Technology, nor does it imply that the products identified are necessarily the best available for our purposes.

Acknowledgements

Work by SDS was supported by the U.S. Department of Energy, Office of Science, Basic Energy Sciences, under Award # DESC0008115. SA acknowledges the Basic Science Research Program through the National Research Foundation of Korea (NRF), funded by the Ministry of Education, Science and Technology (Grant No. 2013R1A6A3A03063900). SA and CJL acknowledge support under the Cooperative Research Agreement between the University of Maryland and the National Institute of Standards and Technology Center for Nanoscale Science and Technology, award 70NANB10H193, through the University of Maryland.

References

1. Garcia, R.; Herruzo, E. T. *Nat. Nanotechnol.* **2012,** *4,* 217–226. doi:10.1038/nnano.2012.38
2. Rodríguez, T.; García, R. *Appl. Phys. Lett.* **2004,** *84,* 449–451. doi:10.1063/1.1642273
3. Martinez, N. F.; Patil, S.; Lozano, J. R.; Garcia, R. *Appl. Phys. Lett.* **2006,** *89,* 153115. doi:10.1063/1.2360894
4. Martinez, N. F.; Lozano, J.; Herruzo, E. T.; Garcia, F.; Richter, C.; Sulzbach, T.; Garcia, R. *Nanotechnology* **2008,** *19,* 384011.
5. Kawai, S.; Glatzel, T.; Koch, S.; Such, B.; Baratoff, A.; Meyer, E. *Phys. Rev. Lett.* **2009,** *103,* 220801. doi:10.1103/PhysRevLett.103.220801
6. Li, Y. J.; Takahashi, K.; Kobayashi, N.; Naitoh, Y.; Kageshima, M.; Sugawara, Y. *Ultramicroscopy* **2010,** *110,* 582–585. doi:10.1016/j.ultramic.2010.02.014
7. Naitoh, Y.; Ma, Z. M.; Li, Y. J.; Kageshima, M.; Sugawara, Y. *J. Vac. Sci. Technol., B* **2010,** *28,* 1210–1214. doi:10.1116/1.3503611
8. Guo, S.; Solares, S. D.; Mochalin, V.; Neitzel, I.; Gogotsi, Y.; Kalinin, S. V.; Jesse, S. *Small* **2012,** *8,* 1264–1269. doi:10.1002/smll.201101648
9. Ebeling, D.; Eslami, B.; Solares, S. D. *ACS Nano* **2013,** *7,* 10387–10396. doi:10.1021/nn404845q
10. Herruzo, E. T.; Perrino, A. P.; Garcia, R. *Nat. Commun.* **2014,** *5,* 3126. doi:10.1038/ncomms4126
11. Garcia, R.; Proksch, R. *Eur. Polym. J.* **2013,** *49,* 1897–1906. doi:10.1016/j.eurpolymj.2013.03.037
12. Dick, A. J. *J. Comput. Theor. Nanosci.* **2011,** *9,* 1744–1750. doi:10.1166/jctn.2011.1877
13. Platz, D.; Tholén, E. A.; Pesen, D.; Haviland, D. B. *Appl. Phys. Lett.* **2008,** *92,* 153106. doi:10.1063/1.2909569
14. Jesse, S.; Kalinin, S.; Proksch, R.; Baddorf, A. P.; Rodriguez, B. J. *Nanotechnology* **2007,** *18,* 435503. doi:10.1088/0957-4484/18/43/435503
15. Rodriguez, B. J.; Callahan, C.; Kalinin, S. V.; Proksch, R. *Nanotechnology* **2007,** *18,* 475504. doi:10.1088/0957-4484/18/47/475504

16. Stark, M.; Stark, R. W.; Heckl, W. M.; Guckenberger, R. *Proc. Natl. Acad. Sci. U. S. A.* **2002,** *99,* 8473–8478. doi:10.1073/pnas.122040599
17. Legleiter, J.; Park, M.; Cusick, B.; Kowalewski, T. *Proc. Natl. Acad. Sci. U. S. A.* **2006,** *103,* 4813–4818. doi:10.1073/pnas.0505628103
18. Sahin, O.; Magonov, S.; Su, C.; Quate, C. F.; Solgaard, O. *Nat. Nanotechnol.* **2007,** *2,* 507–514. doi:10.1038/nnano.2007.226
19. Stark, R. W. *Appl. Phys. Lett.* **2009,** *94,* 063109. doi:10.1063/1.3080209
20. Solares, S. D.; Chawla, G. *Meas. Sci. Technol.* **2010,** *21,* 125502. doi:10.1088/0957-0233/21/12/125502
21. Chakraborty, I.; Yablon, D. *Nanotechnology* **2013,** *24,* 475706. doi:10.1088/0957-4484/24/47/475706
22. Kiracofe, D.; Raman, A.; Yablon, D. *Beilstein J. Nanotechnol.* **2013,** *4,* 385–393. doi:10.3762/bjnano.4.45
23. Yablon, D. G.; Grabowski, J.; Chakraborty, I. *Meas. Sci. Technol.* **2014,** *25,* 055402. doi:10.1088/0957-0233/25/5/055402
24. García, R.; Pérez, R. *Surf. Sci. Rep.* **2002,** *47,* 197–301. doi:10.1016/S0167-5729(02)00077-8
25. Lozano, J. R.; Garcia, R. *Phys. Rev. Lett.* **2008,** *100,* 076102. doi:10.1103/PhysRevLett.100.076102
26. Lozano, J.; Garcia, R. *Phys. Rev. B* **2009,** *79,* 014110. doi:10.1103/PhysRevB.79.014110
27. Chawla, G.; Solares, S. D. *Appl. Phys. Lett.* **2011,** *99,* 074103. doi:10.1063/1.3626847
28. Kareem, A. U.; Solares, S. D. *Nanotechnology* **2012,** *23,* 015706. doi:10.1088/0957-4484/23/1/015706
29. Chen, L.; Cheung, C. L.; Ashby, P. D.; Lieber, C. M. *Nano Lett.* **2004,** *4,* 1725–1731. doi:10.1021/nl048986o
30. Santos, S.; Gadelrab, K.; Font, J.; Chiesa, M. *New J. Phys.* **2013,** *15,* 083034. doi:10.1088/1367-2630/15/8/083034
31. Solares, S. D. *Beilstein J. Nanotechnol.* **2014,** *5,* 298–307. doi:10.3762/bjnano.5.33
32. Giessibl, F. J. *Rev. Mod. Phys.* **2003,** *75,* 949–983. doi:10.1103/RevModPhys.75.949

License and Terms

BEILSTEIN JOURNAL OF NANOTECHNOLOGY

Probing viscoelastic surfaces with bimodal tapping-mode atomic force microscopy: Underlying physics and observables for a standard linear solid model

Santiago D. Solares[1,2,§]

Full Research Paper

Open Access

Address:
[1]Department of Mechanical Engineering, University of Maryland, College Park, MD 20742, USA and [2]Department of Mechanical and Aerospace Engineering, George Washington University, Washington, DC 20052, USA

Email:
Santiago D. Solares - ssolares@gwu.edu

§ Phone: +1 (202) 994-0372

Keywords:
amplitude-modulation; bimodal; dissipation; frequency modulation; multi-frequency atomic force microscopy; viscoelasticity; standard linear solid

Beilstein J. Nanotechnol. **2014,** *5,* 1649–1663.
doi:10.3762/bjnano.5.176

Received: 21 March 2014
Accepted: 31 August 2014
Published: 26 September 2014

This article is part of the Thematic Series "Advanced atomic force microscopy techniques II".

Guest Editors: T. Glatzel and T. Schimmel

Abstract

This paper presents computational simulations of single-mode and bimodal atomic force microscopy (AFM) with particular focus on the viscoelastic interactions occurring during tip–sample impact. The surface is modeled by using a standard linear solid model, which is the simplest system that can reproduce creep compliance and stress relaxation, which are fundamental behaviors exhibited by viscoelastic surfaces. The relaxation of the surface in combination with the complexities of bimodal tip–sample impacts gives rise to unique dynamic behaviors that have important consequences with regards to the acquisition of quantitative relationships between the sample properties and the AFM observables. The physics of the tip–sample interactions and its effect on the observables are illustrated and discussed, and a brief research outlook on viscoelasticity measurement with intermittent-contact AFM is provided.

Introduction

Atomic force microscopy (AFM) has developed considerably since its introduction in the mid-1980s, and today constitutes one of the most powerful and versatile tools in nanotechnology [1-3]. Besides topographical imaging, it is also commonly used to map conservative and dissipative interactions across nanoscale surfaces, from which compositional contrast can be inferred. For soft samples the contrast is often associated with viscoelasticity for which measurements are most commonly carried out by using contact resonance techniques [4-8], whereby classical properties are approximated by using contact models under small-amplitude oscillatory deformations. Such characterization is much more challenging to carry out by using

intermittent-contact techniques due to the non-linear behavior of the probe–sample forces, although significant progress has already been achieved by using multi-frequency methods [9]. The contact models used so far are not true viscoelastic models, since they do not exhibit time-dependent stress and strain relaxation, but they have been shown to be applicable and useful for certain types of samples [9]. The purpose of this paper is to explore computationally the expected physics and the response of the observables for a viscoelastic contact model that exhibits both creep compliance and stress relaxation. Thus, the standard linear solid model (SLS [10]) is used and its complexities and non-idealities are simulated within bimodal AFM, which has become a popular multi-frequency method since its introduction ten years ago [11,12]. The SLS is a simple model that does not fully reproduce the behavior of true surfaces, but since it exhibits the correct qualitative behavior for creep compliance and stress relaxation, its study can highlight the range of open issues that remain in the development of surface viscoelasticity measurement methods based on intermittent-contact AFM. This paper begins with a background section providing a very brief description of multi-frequency AFM, a summary of previous viscoelastic characterization works, a brief introduction to a few viscoelasticity models previously used in AFM and a brief discussion on non-viscoelastic dissipative interactions. The background section is followed by the most relevant results for single-mode and bimodal tip–sample interactions, including force trajectories and discussions on the key observables, after which a brief discussion and a conclusions section are offered. Finally, a short section describing the simulation methods is provided.

Background

Multi-frequency atomic force microscopy – multimodal operation

Multi-frequency AFM [13] is a family of techniques in which the cantilever probe is driven simultaneously at more than one frequency with the purpose of expanding the amount and type of information that can be acquired during each scan. Most commonly this is accomplished by driving simultaneously more than one cantilever eigenmode (multimodal characterization), such that the contrast signals from each eigenmode serve different purposes. For example, within the first multi-frequency technique, proposed by Rodriguez and Garcia in 2004 [11,12], the fundamental cantilever eigenmode is driven by using the conventional amplitude-modulation scheme (AM-AFM, tapping-mode [2]) to obtain the topography, while the second eigenmode is excited with constant drive amplitude and frequency. Compositional contrast is extracted from the response amplitude and phase of the second eigenmode (in this paper this mode of operation is referred to as AM-OL since the first mode is driven by using amplitude-modulation and the second mode is driven in 'open loop'). Since the settings of the higher eigenmode are not controlled by the AM-AFM loop, its excitation amplitude (and in principle also the drive frequency) can be adjusted almost at will to explore a wider range of interactions with high sensitivity. There currently exists a variety of other multi-frequency techniques that use multi-eigenmode excitation with two or three drive signals [9,11,12,14-20], discrete multi-frequency excitation for a single eigenmode [21,22], band excitation single- or dual-mode characterization [23,24] and techniques based on the observation of higher harmonics and their inversion to obtain force distance curves [25,26]. Most of the discussion in this paper is based on the AM-OL method of Rodriguez and Garcia [11,12], which is the most common, but some of the discussion is also applicable to bimodal methods involving frequency-modulation (FM-AFM [3,9,18,27].

Characterization of viscoelastic surfaces with AFM

Viscoelastic characterization is generally performed with contact-mode-based methods involving a sinusoidal displacement of the sample or the cantilever. One of the oldest reports is the force modulation method [28], whereby the sample is driven sinusoidally, causing an analogous response in the cantilever, such that its oscillation amplitude and phase can be used to approximately calculate the sample storage and loss moduli. Similarly, in contact resonance methods [4-8] the user generally measures the cantilever frequency response to small amplitude excitations, from which an effective resonance frequency and quality factor can be computed and post-processed to also give the storage and loss moduli. These moduli are classical bulk quantities, but AFM measurements can exhibit relatively good correlation with results obtained from bulk measurements [6,7]. Analogous measurements can be performed by using the band excitation method [23,29], within which the cantilever is driven in contact mode by using a band of frequencies such that the Fourier transform of the tip response can be fit to a Lorentzian curve that readily yields the effective resonance frequency and quality factor, which in turn yield the desired moduli. A third method that provides similar observables is the dual-amplitude resonance tracking technique [6,7,21], in which the cantilever is also driven in contact mode, but by using only two sinusoidal excitations around the effective resonance frequency.

In recent years, intermittent-contact methods have also been used to gain understanding of the conservative and dissipative tip–sample interactions, simultaneously while topographical imaging is being carried out, although direct mathematical relationships between the observables and actual viscoelastic properties have, in general, not yet been developed. The main obsta-

cles have generally been the non-linear behavior of the tip–sample forces and the non-ideal shape of the tip trajectory during impact, both of which make mathematical analyses extremely difficult (these complexities are further discussed in the Results section). In amplitude modulation AFM (tapping-mode, AM-AFM), Cleveland et al. [30] and Garcia et al. [31] proved mathematically that when tip–sample energy dissipation is absent, the phase shift remains unchanged even if the elastic properties of the sample are non-uniform across the surface. This enables the user to directly map variations in energy dissipation based on the phase contrast. In addition, one can more rigorously describe the conservative and dissipative interactions by quantifying them in terms of the virial (V_{ts}) and average dissipated power (P_{ts}), for which equations have been previously published for use within amplitude- [30,32,33] and frequency-modulation [34-36] methods. Within multi-frequency AFM, Lozano et al. analyzed the behavior of V_{ts} and P_{ts} for the original bimodal AFM method, which uses an open loop drive to excite the higher eigenmode [32,37]. Naitoh and coworkers reported bimodal experiments by using FM-AFM to drive both eigenmodes, in order to simultaneously acquire the topography and quantify the elasticity of a Ge(001) surface with high resolution [17]. Li and coworkers used a bimodal method in which the first eigenmode was driven by using the phase modulation scheme and the higher mode was driven in open loop, which allowed them to obtain images of the sample topography, energy dissipation and elasticity of polymer surfaces immersed in a liquid environment [16]. We have also reported experiments in which images of V_{ts} and P_{ts} were compared for different control schemes applied to the higher mode, including open loop, constant-excitation FM-AFM and constant-amplitude FM-AFM [27]. Even more recently Herruzo et al. [9] succeeded for the first time in inverting the conservative tip–sample interaction force curve along with a depth-dependent, direction-independent tip–sample dissipation coefficient by using bimodal FM-AFM with constant amplitudes for both eigenmodes.

There also exist methods for the real-time acquisition of force curves, from which conservative and dissipative interactions can be studied. Specifically, the spectral inversion method, originally introduced by Stark et al. [25] and later improved by Sahin et al. by using T-shaped cantilevers [26] uses the spectral response of one of the cantilever eigenmodes (the first torsional mode in the method of Sahin et al.) to invert the force curve without making any assumptions about the tip–sample contact model. The method has been demonstrated extensively on soft samples, but becomes subject to low-signal-to-noise ratio limitations as the sample becomes stiffer [38]. Finally, the peak-force AFM method [39], a hybrid between contact- and intermittent-contact AFM, also measures the tip–sample force in real time during approach and retract of the tip by modulating the cantilever base position above the sample with a large amplitude and with a frequency that is much lower than the fundamental frequency. This method also has the advantage that no assumptions need to be made about the tip–sample force model, although it is limited in the range of tip-velocities that can studied and, since it is a deflection-based measurement, it may be limited by low signal-to-noise ratio when small displacements or subtle features in the force curve are being studied.

Viscoelasticity models and the standard linear solid

Viscoelasticity models are used to relate the observables and calculated quantities from the AFM measurement (frequency, phase, amplitude, quality factor, etc.) to the surface properties. In contact resonance typically the Kelvin–Voigt model [40] is used, which consists of a linear spring in parallel with a damper (dashpot). It is incorporated into the solution of the cantilever equations of motion in the form of boundary conditions at the tip [4,5]. This model can reproduce time-dependent creep compliance (time-dependent strain relaxation under a constant stress) with high accuracy, but not stress relaxation (time dependent drop in stress under a constant strain). Another model often used in the study of viscoelasticity, although not commonly used in AFM, is the Maxwell model [40] which consists of the same two elements, a linear spring and a dashpot, but arranged in series. This model reproduces well stress relaxation under constant strain but not creep compliance. Within AFM it has also been common to combine a Hertzian conservative tip–sample model with a position-dependent dissipation coefficient [9,18,34]. This is the approach recently followed by Herruzo et al. [9] to obtain analytical expressions of conservative and dissipative tip–sample interaction forces by using bimodal frequency-modulation AFM. Although the authors show that their approach can be robust for the types of surfaces studied in their work, the characterization of truly viscoelastic surfaces requires being able to capture fundamental viscoelastic behaviors, in particular stress relaxation and creep compliance. The simplest model that meets these conditions is the standard linear solid (SLS), which combines the Kelvin–Voigt and Maxwell models as illustrated in Figure 1a. Figure 1b illustrates typical tip–sample force trajectories during intermittent-contact AFM single- and dual-mode simulations, whereby hysteresis occurs due to relaxation of the surface during the time that the tip and sample are in contact. In fact, for this type of model, the surface can remain temporarily depressed as the tip retracts. This can be inferred from Figure 1b by noting that the position of the maximum attractive (van der Waals) force differs during approach and retract (see blue arrows). In contrast, Figure 1c shows that when a conservative model

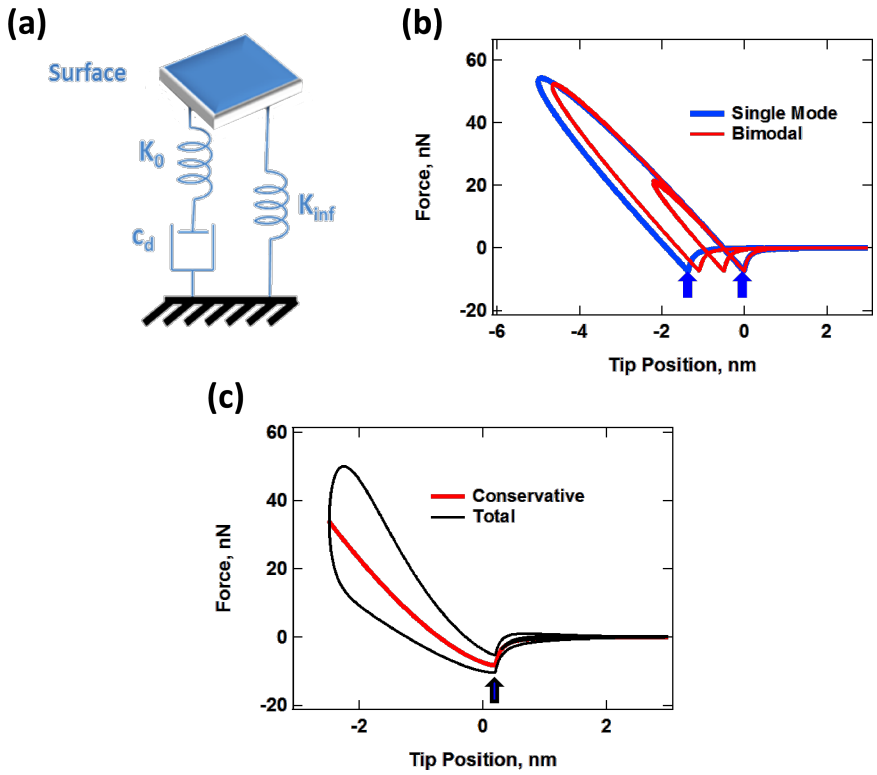

Figure 1: (a) Standard linear solid (SLS) model [10]; (b) simulated tip–sample force trajectories for single- and dual-mode (bimodal) AFM impacts by using the SLS. The key difference between the single- and dual-mode interactions is the possibility of multiple impacts as well as the variation in the shape of successive impacts in the latter [41,42]. The horizontal distance between the two blue arrows indicates the distance that the surface relaxed during the tip–sample contact time for the single-mode case. (c) Simulated tip–sample force trajectory by using a Hertzian contact model with a depth-dependent dissipation coefficient [34,42]. For all force curves shown, the trajectory around the dissipation loops proceeds in the counterclockwise direction.

(e.g., Hertzian) is combined with a dissipation coefficient, there is hysteresis but the location of the force minimum does not differ for the approach and retract. As a result, such models do not fully capture viscoelasticity since the surface does not actually relax, and this has important consequences with regards to the interpretation of the dissipation mechanism. Specifically, the latter models offer a dissipative mechanism in which the tip experiences a 'friction' force opposite to its motion, regardless of the direction in which it travels (upward or downward). In contrast, in the SLS model, the dissipation is a consequence of the simple fact that the work done by the cantilever against the surface during the approach is greater than the work done by the surface on the cantilever during the retract (since the surface relaxes during contact, the amount of work it restores to the cantilever is less than the work received from it). Despite the attractive features of the SLS, however, it is important to note that it is too simple of an approximation to describe the behavior of a real sample under intermittent-contact AFM. For example, since it uses linear springs, it is not able to capture the curvature of the repulsive part of an elastic interaction, which is well reproduced by Hertzian models [2].

The behavior of the SLS under the application of a constant strain is illustrated in Figure 2a. The thick red trace indicates the prescribed position of the surface, which starting at t = 15 μs is depressed and held at a position of −5 nm for the example shown. Immediately the damper begins to relax as indicated by the black dotted line, which results in a relaxation of the force exerted by the surface (blue dashed line). Figure 2b illustrates the behavior of the model after the surface is released, after reaching the final state in Figure 2a. Here the surface immediately relaxes elastically to a position of −2.5 nm (indicated by the position of the green arrow), and then both the position of the surface and the position of the damper gradually relax to the equilibrium state while the force acting on the surface remains at zero. These behaviors are not necessarily critical to reproduce in contact-mode, low-amplitude AFM measurements (e.g., contact-resonance characterization), but are very important in intermittent-contact AFM during which the surface undergoes rapid distortion and relaxation between and during successive interactions with the tip, and where the accurate measurement of viscoelastic properties is much more challenging to carry out [43].

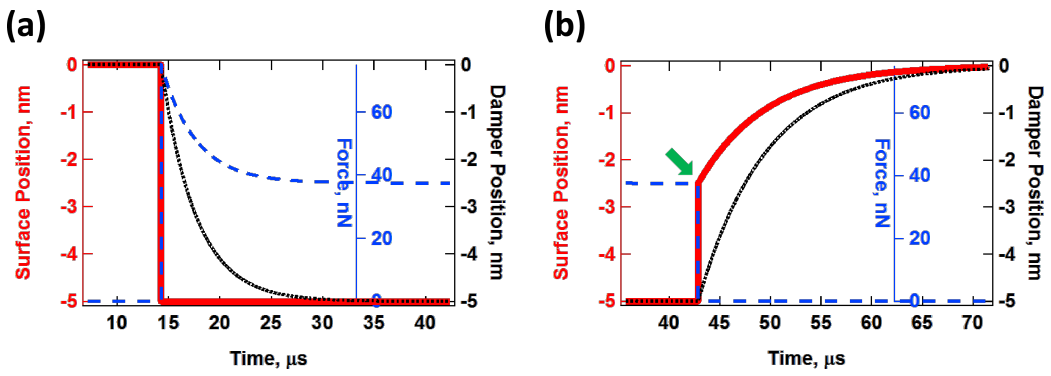

Figure 2: (a) Illustration of stress relaxation and (b) creep (the various traces are color coded with their respective axes). In (a) the surface is depressed and held fixed at a position of 5 nm below its relaxed state, starting at t = 15 µs. Following the simulation described in (a) the surface is released at t = 43 µs and its response is plotted in (b). The magnitude of the immediate elastic relaxation of the surface upon release, indicated by the green arrow in (b), depends on the ratio and magnitudes of the two spring constants, K_{inf} and K_0 (see Figure 1). The simulation parameters were $K_{inf} = K_0 = 7.5$ N/m and $C_{diss} = 2.5 \times 10^{-5}$ N·s/m.

Non-viscoelatic dissipative interactions

The present work studies an AFM tip that is interacting with a clean SLS surface, so no further interactions are included other than attractive van der Waals forces. However, in practice there can be a number of other interactions that can obscure or hinder the measurement of viscoelasticity by using intermittent-contact methods. Well-known interactions of this type include capillary forces [44], plastic behaviors [45], chemical adhesion and topographical artifacts [46] and even geometry-driven physical adhesion artifacts. As illustrated in Figure 3, if the tip indents a cavity into the surface and the surface remains temporarily depressed, the non-bonded interactions during the retract may be greater than during the approach due to the greater sample surface area that is near the tip. This, in turn, would lead to a hysteresis loop in the tip–sample force trajectory, whereby the cantilever would be required to perform additional work in order to break free from the surface. All of the above non-conservative effects influence the observables during measurements of conservative and dissipative interactions with AFM, and it is generally not possible to attribute with certainty the changes in the observables to the variation in surface material properties.

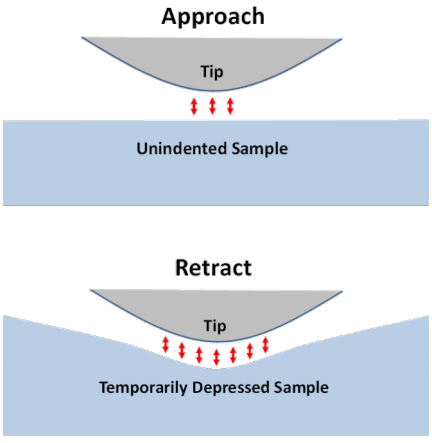

Figure 3: Illustration of tip–sample physical adhesion. In this case the interaction area between tip and sample is greater during the retract than during the approach, due to a change in the non-bonded attractive forces, leading to additional dissipation as the cantilever breaks free from the surface.

Results

This section comprises two main sub-sections. The first sub-section provides an analysis of the tip–sample interaction physics for ideal (prescribed) and numerically computed trajectories of the tip, both for single-mode and bimodal AFM. The second sub-section explores the effect of the SLS model parameters on the observables as well as the prospect for carrying out compositional mapping by using average quantities, such as the virial and dissipated power.

Physics of the tip–sample interaction for the standard linear solid model

Sample response to prescribed sinusoidal trajectories

As starting point, consider the interaction of an SLS surface with a cantilever tip that oscillates along a perfect sinusoidal trajectory. To simulate this, we prescribe that the tip moves along a path defined by $z_{tip}(t) = z_c + A\cdot\cos(\omega t)$, where z_{tip}, z_c, A and ω are, respectively, the tip position as a function of time, the cantilever base position, the oscillation amplitude and the fundamental angular frequency of the probe. If the SLS is relaxed in real time as the tip oscillates, one obtains results similar to those shown in Figure 4. In the first panel (Figure 1a) are depicted tip–sample force trajectories for different cantilever frequencies, ranging from 25 kHz to 156 kHz, which covers a ratio of frequencies of about 6.25, similar to the ratio of the first

two eigenfrequencies of a rectangular cantilever. Figure 4b shows similar information, but plotting the force as a function of the time (notice how the contact time changes due to relaxation of the surface). Figure 4c shows the surface trajectory, including its recovery upon tip retract, and Figure 4d plots the peak repulsive force and the average energy dissipated through the hysteresis loop in the force curve over several cycles. In Figure 4b and Figure 4c the time axis has been normalized by the respective cantilever period. As expected from a viscoelastic system, the amount of surface relaxation (distance between the force minima for a given frequency in Figure 4a) decreases with increasing frequency as the hysteresis loop area also decreases (see Figure 4d). Additionally, the peak force increases. This is because at faster time scales the system behavior becomes more elastic and less viscous. This frequency dependence is an important consideration during a real experiment in which different regions of a viscoelastic sample may have different and multiple relaxation times. For some cantilever frequencies certain regions may not exhibit a measurable viscous behavior, and for other frequencies, regions of different properties may exhibit similar dissipation behaviors. As it can also be inferred from the results presented here, it is not possible to express the tip–sample force curve analytically, since it depends on the sample deformation timescale as well as on the previous history of the surface. The frequency dependence also raises an important issue with regards to the controls schemes used in bimodal AFM. It has been previously found that in order to properly compare the compositional mapping of different regions of the sample it is necessary that the higher eigenmode amplitude remains constant, which requires the use of a constant-response-amplitude method such as constant-amplitude frequency-modulation [27]. However, if the frequency shift is significantly different for different regions, according to the results of Figure 4a, they may not be directly comparable since the interplay of conservative and dissipative interactions may be artificially changed in a different way for each region.

Sample response to prescribed bimodal trajectories

For the simulated interaction of an SLS surface with a tip oscillating along a prescribed bimodal trajectory of the form $z_{tip}(t) = z_c + A_1 \cdot \cos(\omega_1 t) + A_2 \cdot \cos(\omega_2 t)$ we are interested in studying the system response as the amplitude of the second eigenmode changes. One can envision that for small values of A_2, which are smaller than the distance that the sample penetrates into the surface, the SLS will interact with a trajectory having more than one oscillation loop (since the tip will travel up and down according to the second frequency oscillation while still remaining under the sample for a contact time dictated by the first oscillation frequency). However, as A_2 increases and exceeds the penetration depth, the surface will only interact with single-loop oscillations where the tip will dip into and come out of the sample at a frequency dictated by the second oscillation frequency. More than one impact will be possible for every fundamental cycle because the period of the second oscillation is smaller than that of the first oscillation (for the example shown here the ratio of eigenfrequencies was set to

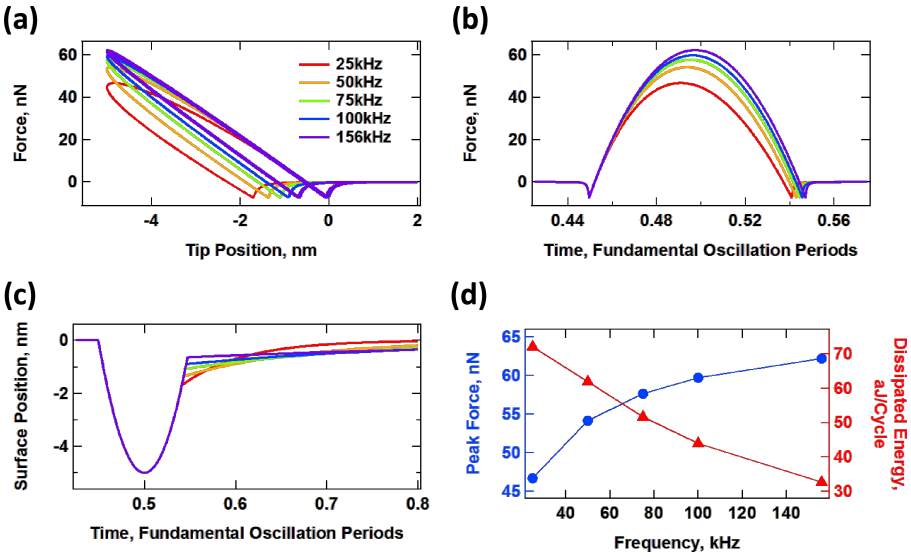

Figure 4: Interaction of an SLS surface with a probe oscillating along a perfectly sinusoidal trajectory given by $z_{tip}(t)$ = 95 nm + (100 nm)·cos(ωt), where ω is equal to 2π times the frequency indicated in the graphs (the relaxed surface is initially located at a height of zero). (a) Force–distance tip trajectory (the trajectory proceeds in the counterclockwise direction); (b) tip–sample force vs normalized time; (c) surface recovery vs normalized time; (d) peak force and dissipated energy per cycle vs cantilever frequency (the two traces are color coded with their respective axes). The SLS parameters were $K_{inf} = K_o$ = 7.5 N/m and C_{diss} = 1 × 10^{-5} N·s/m. The time axes in (b) and (c) have been normalized by the respective fundamental period for each trace.

about 6.21 in order to mimic the first two modes of a rectangular cantilever). As a result, measurements with different levels of penetration and with different amplitude values and ratios may not be directly comparable. Furthermore, in carrying out this ideal comparison of perfectly controllable sinusoidal tip oscillations, there are two extreme behaviors that need to be considered as A_2 increases. First, one could prescribe that the maximum tip–sample penetration remains the same in all cases, such that any increase in the value of A_2 is compensated by an equal increase in the cantilever position, z_c. Alternatively, one could prescribe that the cantilever position remains the same in all cases, such that greater a penetration will be achieved as A_2 increases (as discussed below, the real situation lies in between these extremes, unless FM controls are used with which the penetration is controllable [9]). Figure 5 shows the results for the former case, and Figure 6 shows the results for the latter case. For each figure, panel (a) shows force distance trajectories for different values of A_2 (including $A_2 = 0$) and panel (b)

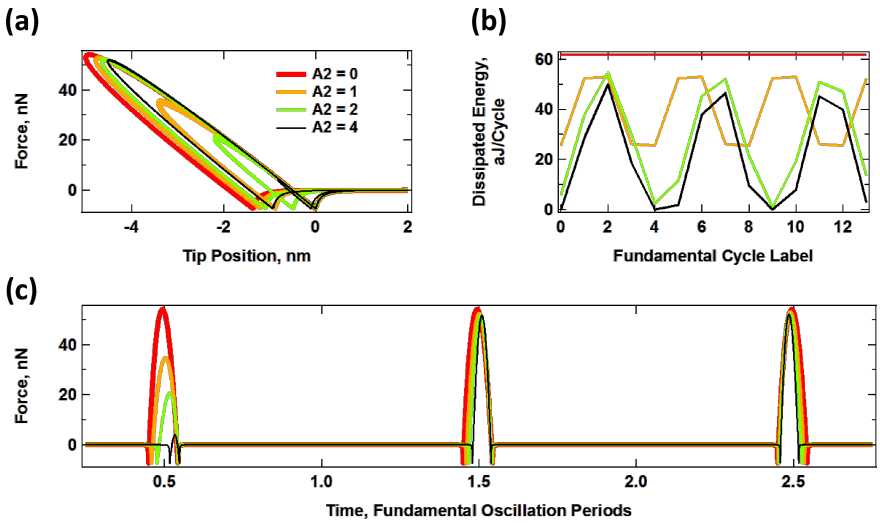

Figure 5: Interaction of an SLS surface with a probe oscillating along a bimodal trajectory of constant maximum penetration, given by $z_{tip}(t)$ = (95 nm + A_2) + (100 nm)·cos($\omega_1 t$) + A_2 cos(6.21·$\omega_1 t$), with $\omega_1 = 2\pi$ (50 kHz), $K_{inf} = K_o = 7.5$ N/m and $C_{diss} = 1 \times 10^{-5}$ N·s/m. (a) Force–distance trajectories for varying A_2; (b) dissipated energy per cycle for successive fundamental cycles and varying A_2; (c) example of successive tip–sample impacts for the same cases. The color code is the same for all plots and the unit of A_2 is nm.

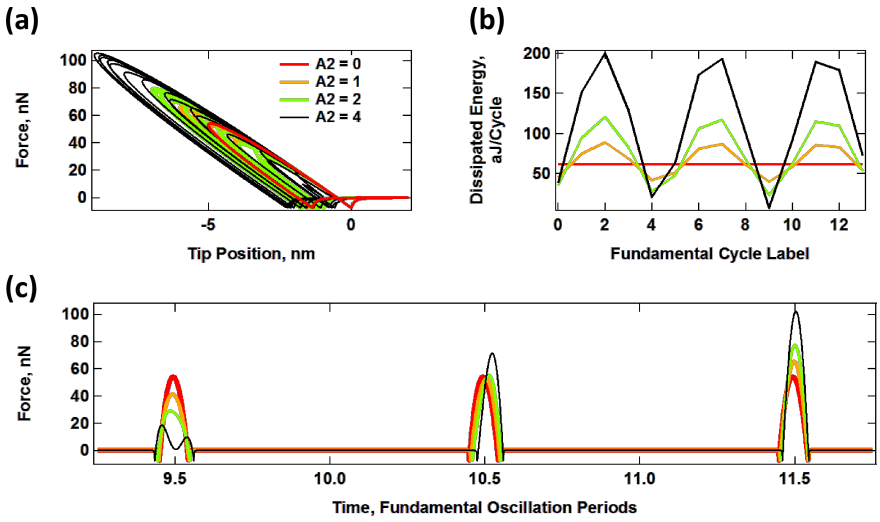

Figure 6: Interaction of an SLS surface with a probe oscillating along a prescribed bimodal trajectory of variable maximum penetration, given by $z_{tip}(t)$ = 95 nm + (100 nm)·cos($\omega_1 t$) + A_2·cos(6.21·$\omega_1 t$), with $\omega_1 = 2\pi$ (50 kHz), $K_{inf} = K_o = 7.5$ N/m and $C_{diss} = 1 \times 10^{-5}$ N·s/m. (a) Force–distance trajectories for varying A_2; (b) dissipated energy per cycle for successive fundamental cycles and varying A_2; (c) example of successive tip–sample impacts for the same cases. The color code is the same for all plots and the unit of A_2 is nm.

shows the energy dissipated during successive tip–sample impacts (this dissipation was calculated by integrating numerically the area of the dissipation loops), and panel (c) shows a few examples of successive tip–sample impacts, illustrated as time-dependent forces. Interestingly, even in the case in which the peak penetration is fixed for different values of A_2, the peak forces still differ considerably for successive impacts since the trajectory is bimodal. Furthermore, there are some impacts during which the interaction between the tip and the sample is almost negligible (see, for example, the first impact for $A_2 = 4$ in Figure 5c). The dissipation loops in the force curves for the case of constant maximum depth (Figure 5a) show a gradual transition from a low frequency response to a high frequency response, qualitatively similar to what is observed for single-eigenmode oscillations (Figure 4a), but with irregular impacts. As A_2 increases, the dissipation loops are dominated more and more by the frequency of the second eigenmode and the average level of dissipation drops (Figure 5b). The irregularity of the impacts is easily noticeable in the irregular oscillation of the dissipated energy for successive impacts (Figure 5b), as well as in the plot describing the force as a function of time (Figure 5c). Finally, it is not surprising that the contact time also decreases gradually as the second eigenfrequency becomes more dominant (compare Figure 5c to Figure 4b). Note: the contact time for each impact can be inferred from the graphs of the tip–sample force vs time by examining the horizontal spacing between the two force minima surrounding each peak in the plots (the first of these minima occurs when the tip approaches the sample and crosses the attractive tip–sample force region and goes into the repulsive region, and the second one occurs during the retract, when the tip leaves the repulsive region and crosses through the attractive region again).

In the case of varying penetration (constant z_c), the dissipation loop areas increase as A_2 increases since the oscillation of the second eigenfrequency does not replace that of the first eigenfrequency, but rather their effects are additive. The effect of the low-frequency oscillation on the surface is always present to the same degree. Therefore, the average surface relaxation distance (distance between the approach and retract tip–sample force minima in Figure 6a) increases with A_2, as does the average level of dissipation (Figure 6b). Similarly, the range of contact time also increases, although as expected, there is high variability for different successive impacts. For example, the contact time increases for the first impact shown in Figure 6c, but decreases for the two subsequent impacts. This is a significant difference with respect to single-mode AM-AFM.

Sample response to simulated bimodal trajectories

A direct comparison of the results for the prescribed trajectories shown in Figure 5 and Figure 6 with realistic trajectories in which the dynamics determine the tip–sample penetration is not straightforward since analytical solutions of the trajectory cannot be obtained. However, it is still possible to make some general observations. In the results of Figure 7, the dynamics of the cantilever have been solved numerically in real time, driving

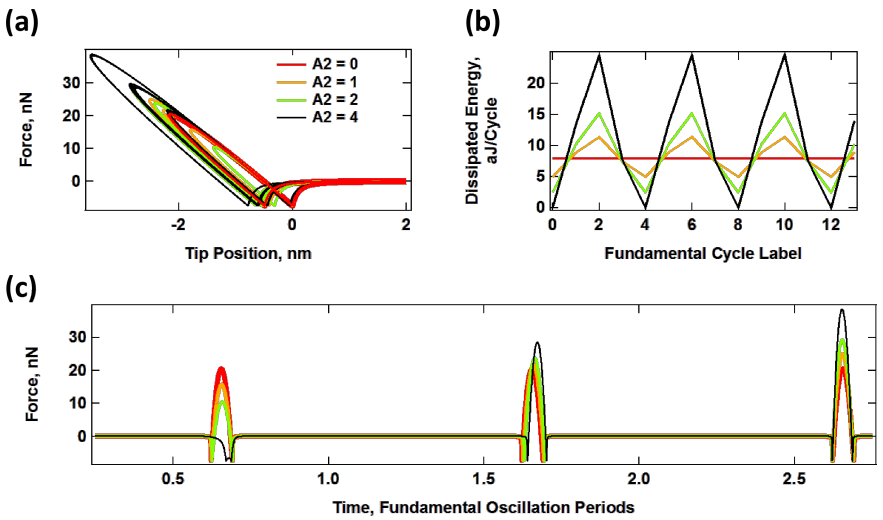

Figure 7: Interaction of an SLS surface with a probe oscillating along a realistic AM-OL bimodal trajectory obtained by simulating the cantilever dynamics. (a) Force–distance trajectories for varying A_2; (b) dissipated energy per cycle for successive fundamental cycles and varying A_2; (c) example of successive tip–sample impacts for the same cases. The first eigenmode free amplitude was 100 nm in all cases and A_2 is the free oscillation amplitude of the second eigenmode (in nm). The cantilever position is z_c = 80 nm. The SLS parameters are the same as in Figure 5 and Figure 6. The eigenfrequency ratio of the first two eigenmodes is 6.25 instead of 6.21, which was used in Figure 5 and Figure 6. This different ratio was chosen to illustrate a different impact periodicity (the periodicity is 4 in this case, whereas it is 100 for Figure 5 and Figure 6). The color coding is the same in all panels.

the first two eigenmodes at their respective natural frequencies, with A_1 = 100 nm and with the values of A_2 indicated on the plots. In general, the results resemble those of Figure 5 and Figure 6. There is overall lower penetration into the surface than for the prescribed trajectories despite the relatively low cantilever position of 80 nm, since the presence of the sample perturbs the cantilever oscillation [2]. Penetration increases with higher values of A_2 (see Figure 7a) as previously reported [42], similar to Figure 6. The average level of dissipation for different fundamental cycles (Figure 7b) follows a more regular pattern due to the use of a slightly different ratio of eigenfrequencies for the first and second mode (see comment in the caption of Figure 7). The time-dependent force trajectories (Figure 7c) are equally rich and a wide variation in the contact time is again observed. Figure 8a compares the trends in dissipated energy as a function of A_2 for the three cases analyzed in Figures 5–7. It shows that the trend for the real case lies in between the results of the prescribed trajectories with constant penetration and the prescribed trajectories of additive penetration for the two eigenmodes, while being qualitatively closer to the latter. That is, dissipation increases with A_2, but in a more gradual fashion than if penetration would increase by the same amount (Figure 8b shows an expanded view of the simulated dynamics trace in Figure 8a). Finally, Figure 8c shows the peak tip penetration as a function of A_2 for a simulation of a spectroscopy curve in which the cantilever is approached towards the surface. The results confirm that there is a gain in penetration as A_2 increases, but the gain in penetration is smaller than the increase in A_2.

As can be inferred from the previous results, the behavior of the dissipated energy and the tip–sample forces is extremely complex and cannot be predicted a priori. In addition, the observables that are available during an AFM experiment can be quite sensitive to the imaging conditions, depending on the imaging mode used. For example, Figure 9 shows the behavior of the normalized second mode amplitude ($A_2/A_{2\text{-free}}$, Figure 9a) and phase (Figure 9b) for AM-OL spectroscopy curves simulated with parameters similar to those of Figure 7, for different values of A_2, including the full dynamics of the first three cantilever eigenmodes. As the various traces show, the trends are not always regular nor follow a simple pattern.

Effect of model parameters on the observables

Conservative and dissipative interactions for varying model parameters

In order to develop methods that recover the contact model parameters, it is necessary to understand the effect of those parameters on the probe response. To this end, Figure 10

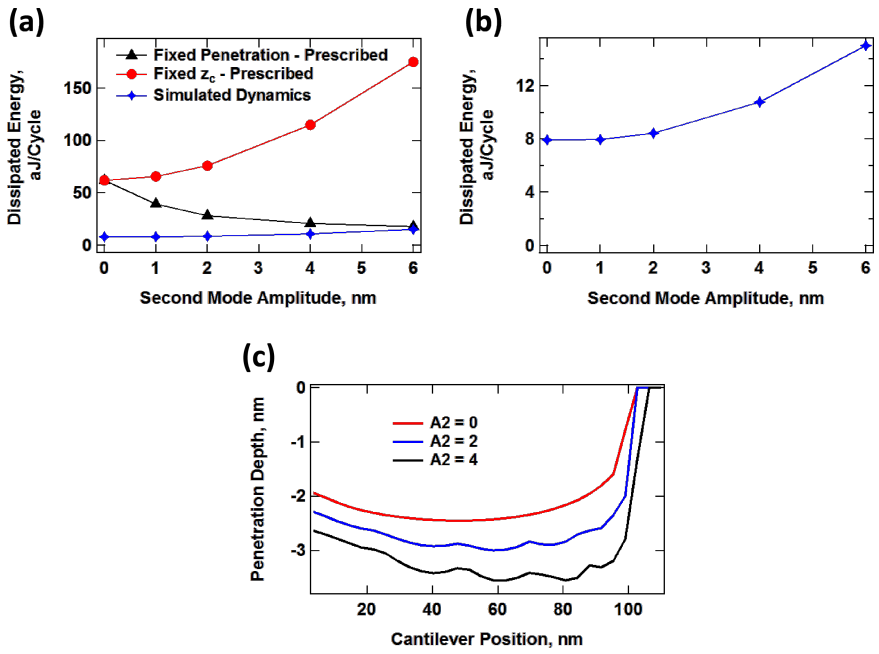

Figure 8: (a) Dissipated energy vs second eigenmode free amplitude for an SLS surface interacting with a tip following a prescribed bimodal oscillation with constant penetration maximum (see Figure 5), a prescribed bimodal oscillation with variable penetration maximum (see Figure 6) and a realistic dynamics trajectory solved in real time for AM-OL operation (see Figure 7); (b) expanded view of the result for the realistic dynamics trajectory (same trace as in (a) but plotted by using a different scale); (c) lowest tip position reached by the tip over 15 fundamental cycles after reaching steady state as a function of cantilever rest position during a simulated spectroscopy measurement for the realistic tip trajectory using the parameters given for Figure 7.

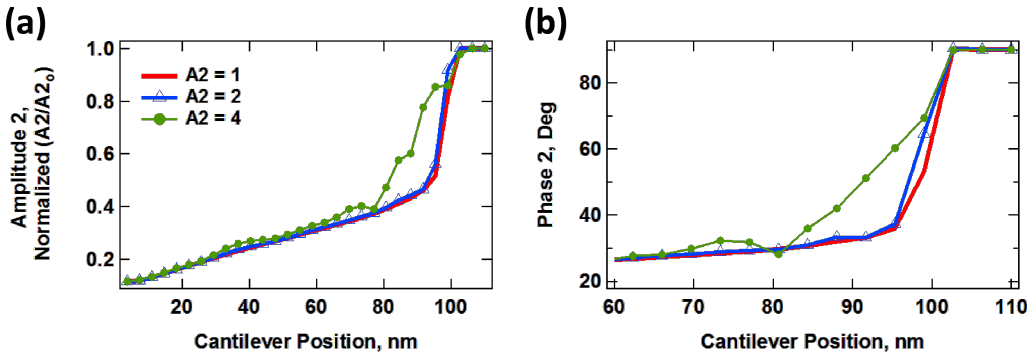

Figure 9: Simulated amplitude and phase spectroscopy curves for realistic cantilever trajectories calculated using parameters similar to those of Figure 7 for AM-OL operation. (a) Normalized amplitude ($A_2/A_{2\text{-free}}$) vs cantilever position; (b) phase vs cantilever position.

provides an example of the changes in the force trajectory as each of the three SLS parameters is varied independently. For this example, Figure 10a serves as a baseline case and all results are plotted by using the same axis scales for easier comparison. Figure 10b shows the trajectory obtained when the stiffness of K_{inf} is increased to about 315% of its original value. Inspection of the SLS model (also provided in Figure 10) suggests that the spring K_{inf} should directly interact with the tip during tip–sample impact, and that increasing its value should result in an overall higher stiffness with smaller penetration (in general steeper force curves lead to smaller penetration for the same AFM parameters [47]). This expectation is confirmed by the force trajectory shown in Figure 10b, which also exhibits a smaller hysteresis area as a result of the shorter contact time, which is a result of shallower tip penetration. In Figure 10c the stiffness of K_0 has been increased to about 315% of its original value. Inspection of the model indicates that the spring K_0 interacts with the tip, but also with the damper. Increasing its stiffness results in the transmission of a larger force from the AFM tip to the damper, which should lead to a faster and greater relaxation of the latter and a correspondingly larger dissipation energy. Again, this expectation is confirmed by Figure 10c. Finally, in Figure 10d, the damper constant, C_{diss}, has been increased to 300% of its original value, which retards its relaxation and leads to a more elastic and less viscous response with a smaller dissipation energy, as confirmed by the result.

The above discussion suggests that one can intuitively predict the behavior of the model as its parameters change. However, the situation is more difficult in an experiment since the number

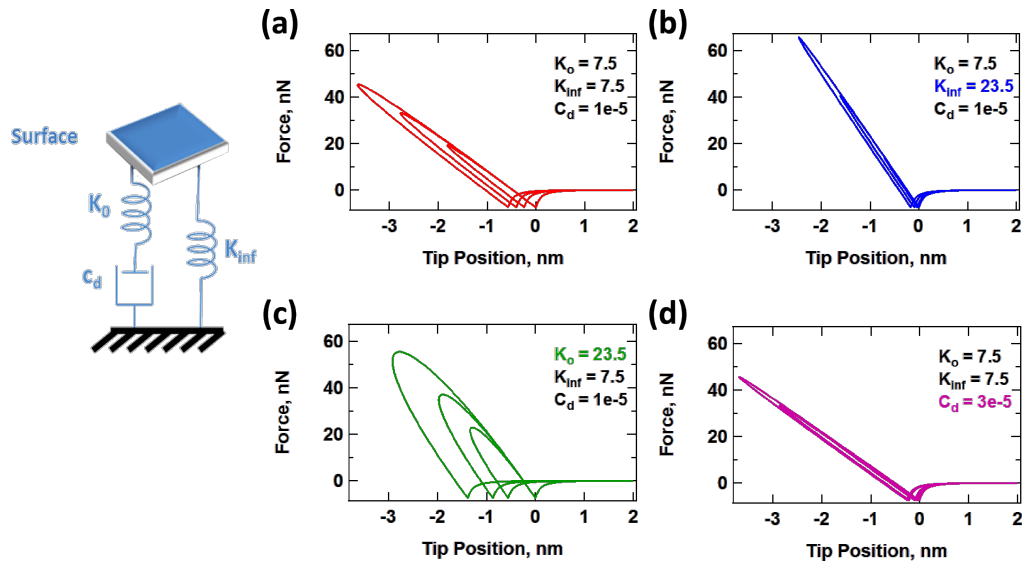

Figure 10: Example of the evolution of force–distance trajectories with changes in the SLS surface parameters: (a) baseline; (b) increase in K_{inf}; (c) increase in K_0; (d) increase in C_{diss}. The parameters are similar to those given for Figure 7, except for $A_{2\text{-free}}$ = 5 nm and any other parameters indicated in the figures.

of observables is limited and the parameters of the model are not known. Furthermore, the observables (eigenmode amplitudes and phases) vary in a non-trivial fashion, as illustrated in Figure 11a, Figure 12a and Figure 13a for a range of values of K_{inf}, K_0 and C_{diss}, respectively. As the results suggest, it is possible for the trends to be non-monotonic and non-smooth, such that simple mappings of these observables do not provide an accurate picture of the variation of material properties across the sample (see comment in the captions of Figure 11 and Figure 12 regarding the origin of the kinks in some of the traces). Additionally, Figure 11b, Figure 12b and Figure 13b suggest that the trends in dissipated energy and peak forces are not unique for each of the three SLS parameters. For example, an asymptotic decrease in the dissipated energy (Figure 11b and Figure 13b) can be caused by a linear increase in the magnitude of K_{inf} or C_{diss}, or a combination of both. Similarly, increases in the peak tip–sample forces can be caused by increases in any of the three SLS parameters.

Compositional mapping based on average quantities

The quantities plotted in panels (b) of Figures 11–13 are important from the physics point of view, but are generally not directly observable in AFM. Instead, the user commonly relies on quantities calculated from the phases and amplitudes of the two active eigenmodes (in the case of AM-OL), namely the average calculated dissipated power (P_{ts}) and the virial (V_{ts}) for each of the modes [27,32,37]. These quantities are plotted in panels (c) and (d), respectively, in Figures 11–13 as a function of the SLS parameters, varying one parameter at a time (the calculated dissipated power was converted to energy per fundamental cycle in order to allow for a comparison with panel (b) of each figure). Inspection of these results suggests that there is no guarantee that the dissipated energy calculated from P_{ts} correlates with the energy that is dissipated due to the nature of the SLS model, calculated by integrating the area of the dissipation loops in the force–position trajectories (compare, for example, the dissipated energy plotted in Figure 12b with the two traces in Figure 12c). Furthermore, there is not always a strong correlation between the results for each of the eigenmodes (see Figure 11c and Figure 12c). Inspection of panels (b) and (d) of Figures 11–13 show that the correlation between V_{ts} and the peak tapping forces can also be weak or even non-existent. V_{ts} is expected to show a negative correlation with the relative importance of the 'conservative interactions' but these are not directly separable from the non-conservative interactions in the SLS model. Rather, they are coupled and there is not a straightforward physical interpretation of V_{ts}. These discrepancies are not surprising in light of this coupling of conservative and dissipative interactions, in light of the non-trivial dissipation mechanism discussed above, which differs from a simple dissipation coefficient, and in light of the complexity of multi-

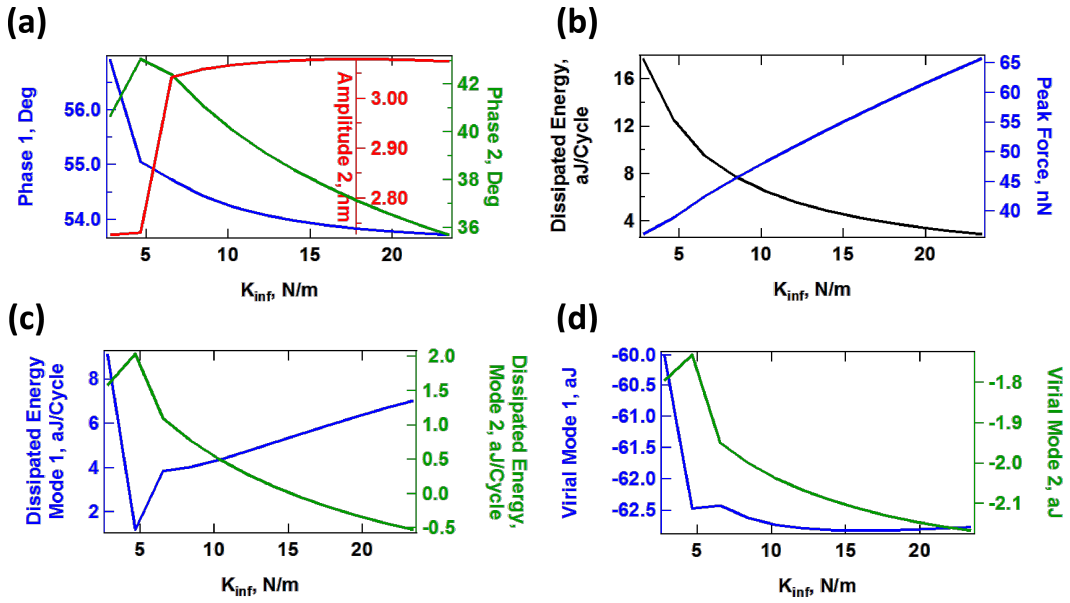

Figure 11: Effect of the SLS parameter K_{inf} on tip–sample interactions and cantilever response. (a) First and second mode phase, and second mode amplitude; (b) dissipated energy calculated from the hysteresis loop of the tip–sample force trajectory and peak impact force; (c) calculated dissipated energy from Equation 5 for the first and second eigenmodes; (d) virial for the first and second eigenmodes. Note that the peak impact force is the largest repulsive force observed over fifteen tip–sample impacts (successive impacts differ, as illustrated in Figure 7c). The parameters other than K_{inf} are the same used to construct Figure 10. The axes are color coded in all cases. The kinks in some of the traces correspond to transitions between dynamic regimes, in some of which the tip skips a tip–sample impact with different frequencies (for example, in one regime the tip may impact the sample every fundamental oscillation, while in another regime the tip may skip every sixth impact [42]).

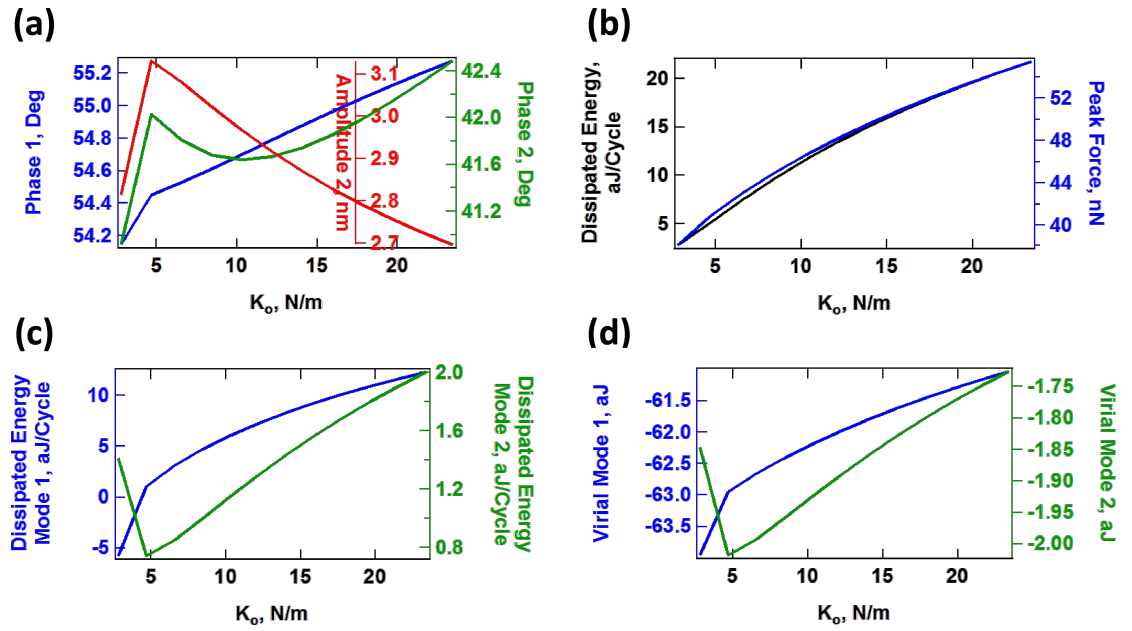

Figure 12: Effect of the SLS parameter K_0 on tip–sample interactions and cantilever response. (a) First and second mode phase, and second mode amplitude; (b) dissipated energy calculated from the hysteresis loop of the tip–sample force trajectory and peak impact force; (c) calculated dissipated energy from Equation 5 for the first and second eigenmodes; (d) virial for the first and second eigenmodes. Note that the peak impact force is the largest repulsive force observed over fifteen tip–sample impacts (successive impacts differ, as illustrated in Figure 7c). The parameters other than K_0 are the same used to construct Figure 10. The axes are color coded in all cases. The kinks in some of the traces correspond to transitions between dynamic regimes, in some of which the tip skips a tip–sample impact with different frequencies (for example, in one regime the tip may impact the sample every fundamental oscillation, while in another regime the tip may skip every sixth impact [42]).

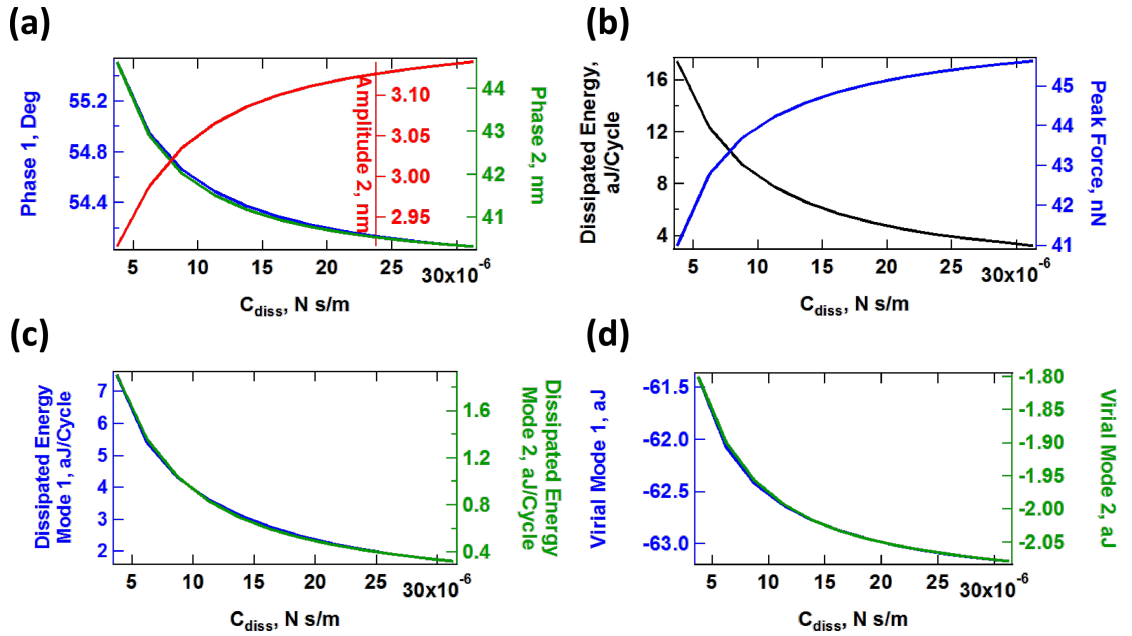

Figure 13: Effect of the SLS parameter C_{diss} on tip–sample interactions and cantilever response. (a) First and second mode phase, and second mode amplitude; (b) dissipated energy calculated from the hysteresis loop of the tip–sample force trajectory and peak impact force; (c) calculated dissipated energy from Equation 5 for the first and second eigenmodes; (d) virial for the first and second eigenmodes. Note that the peak impact force is the largest repulsive force observed over fifteen tip–sample impacts (successive impacts differ, as illustrated in Figure 7c). The parameters other than C_{diss} are the same used to construct Figure 10. The axes are color coded in all cases.

frequency tip–sample interactions, which can lead to a variety of dynamics subtleties, even including severe artifacts such as contrast inversion depending on the imaging conditions [42,48,49].

Discussion

As the results shown in the previous sections illustrate, the interactions of viscoelastic surfaces with the AFM tip can be extremely complex, especially if multi-frequency AFM methods are involved. The relatively large oscillations of the tip in intermittent-contact measurements, as well as the sharp variations in the forces make it necessary to use a tip–sample interaction model that includes the relevant types of attractive and repulsive interactions, as well as the intrinsic behaviors of viscoelastic surfaces, namely creep compliance, stress relaxation and a response that depends on the timescale of application of the stresses or deformations. Despite the simplicity of the SLS model, the richness of the observed phenomena can already seem to be overwhelming when one considers possible means to invert the cantilever response to obtain the surface model parameters. The use of more elaborate models, such as models with multiple relaxation times or nonlinear springs would further complicate matters and would make the inversion even more challenging since the number of observables in an experiment is limited unless the acquired data is enriched through procedures such as volume scanning [50,51]. Nonetheless, one can envision at least two research avenues that should prove very fruitful in this endeavor.

Firstly, the results presented here suggest that it would be advantageous, when characterizing viscoelastic samples, to carry out multiple measurements involving different timescales in order to capture the different relaxation times of the sample. In practice this can be accomplished by sequentially studying the same sample with cantilevers of different fundamental frequency or by using different higher eigenmodes in successive experiments. Even if an inversion methodology is not available, this approach can help to discern between samples of seemingly identical properties at a given timescale, especially if it is combined with volume scanning spectroscopy, which would provide depth-dependent information. Figure 5b, for example, shows that for constant-indentation imaging of the sample with increasing higher mode amplitude (if such a method can be developed) the level of dissipation decreases monotonically, which is as expected, since the SLS has only one characteristic relaxation time (governed by the damper) and the sample deformation is transitioning from a low frequency deformation (governed by the fundamental mode) to a high frequency deformation (governed by the higher mode). However, a real sample may have more than one characteristic relaxation time, which could be probed by gradually increasing the amplitude of different higher eigenmodes in successive experiments, under constant indentation. The analysis could be repeated at different levels of indentation to give a complete picture of the depth-dependent behavior of the sample.

Second, the further development of spectroscopy methods that provide the tip–sample force curve for individual impacts [25,26,52,53] with high accuracy will be extremely beneficial, as it can allow expanded representations of the tip–sample force dependence (for example, representations in which the force is measured with respect to not only position but also velocity [10]). The acquisition of such signatures of the tip–sample interaction force can in turn spur the development of inversion methodologies for different types of models. An example of this type of inversion for an SLS surface is offered in reference [40]. This study demonstrates mathematically that such an inversion is possible even with conventional force–distance curves (force vs distance), although it assumes very high accuracy in the acquisition of the tip–sample force curve through the spectral inversion method [26]. In practice there exist limitations that preclude such accuracy [38]. The development of new real-time spectroscopies remains at the forefront of multi-frequency AFM research [9,26,53-55], although to the knowledge of the author there is not yet a single-cycle, model-free experimental spectroscopy technique that can provide a sufficiently high accuracy to reproduce the sharp turns in the tip–sample force curve, especially around the force minimum dictated by the maximum attractive force. Besides the above two research avenues, further studies on realistic 3D contact models within the specific context of the most recently developed AFM techniques would also be extremely beneficial. In general, a detailed treatment of viscoelasticity within the ever-growing of number of intermittent-contact AFM techniques is in the opinion of the author an extremely important area of opportunity necessitating a combination of strong experimental, analytical and computational efforts.

Conclusion

A numerical simulation study of the interactions observed in single-mode and bimodal AFM characterization of viscoelastic surfaces modeled as standard linear solids (SLSs) is presented. Examples of the extremely complex behavior of the tip–sample forces and observables are provided, along with an illustration of their dependence on the surface model parameters. The SLS model is the simplest that can reproduce stress relaxation and creep compliance, which are important fundamental behaviors observed in real viscoelastic surfaces. Additional opportunities remain in modeling real surfaces, which may require non-linear springs and multiple relaxation times. However, the inversion of the surface parameters from experimental data is an extremely challenging task even with the simple SLS. Further research is

encouraged on single-cycle force spectroscopy measurement as well as inversion methodologies specific for viscoelastic surfaces.

Methods

The numerical simulations of the cantilever dynamics were carried out including three eigenmodes of the AFM cantilever as in previous studies [24,42]. Active eigenmodes, as indicated throughout the paper, were driven at their natural frequency. The surface was modeled in most cases as a SLS (Figure 1a), except for the result of Figure 1c, which uses the combination of a Hertzian contact model with a depth dependent dissipation constant [34,42]. Long-range attractive interactions were included for a tip radius of curvature of 10 nm and a Hamaker constant of 2×10^{-19} J. In some cases, the oscillation of the tip was prescribed along ideal single-mode or bimodal trajectories, as indicated in the text, by relaxing only the SLS in real time. The cantilever force constant was set to $k = 4$ N/m and the first two quality factors to $Q_1 = 150$ and $Q_2 = 450$ in all cases (the frequencies varied and are provided along with the results). The amplitude and phase of each eigenmode, where applicable, were calculated by using the in-phase (I) and quadrature (Q) integrals:

$$I = \int_{N\tau} z(t)\cos(\omega t)dt \tag{1}$$

$$Q = \int_{N\tau} z(t)\sin(\omega t)dt \tag{2}$$

where $z(t)$ is the eigenmode response in the time domain, N is the number of periods over which the phase and amplitude were averaged, ω is the excitation angular frequency, and τ is the nominal period of one oscillation. The amplitude and phase were calculated, respectively, as:

$$A = \frac{\omega}{\pi N}\sqrt{I^2 + Q^2} \tag{3}$$

$$\phi = \tan^{-1}\left(Q/I\right) \tag{4}$$

The average dissipated power (P_{ts}) and virial (V_{ts}) for panels (c) and (d) in Figures 11–13 were calculated as follows (panel (c) of these figures shows the energy dissipated per cycle, which was obtained by multiplying P_{ts} by the fundamental period) [30-32]:

$$P_{ts} = \frac{\pi f_0 k A^2}{Q}\left[\frac{A_{free}}{A}\sin\phi - 1\right] \tag{5}$$

$$V_{ts} = \frac{kA}{2}\left[-\frac{A_{free}\cos\phi}{Q}\right] \tag{6}$$

Acknowledgements

This work was supported by the U.S. Department of Energy, Office of Science, Basic Energy Sciences, under Award # DESC0008115.

References

1. Binnig, G.; Quate, C. F.; Gerber, C. *Phys. Rev. Lett.* **1986,** *56,* 930–933. doi:10.1103/PhysRevLett.56.930
2. García, R.; Pérez, R. *Surf. Sci. Rep.* **2002,** *47,* 197–301. doi:10.1016/S0167-5729(02)00077-8
3. Giessibl, F. J. *Rev. Mod. Phys.* **2003,** *75,* 949–983. doi:10.1103/RevModPhys.75.949
4. Yuya, P. A.; Hurley, D. C.; Turner, J. A. *J. Appl. Phys.* **2008,** *104,* 074916. doi:10.1063/1.2996259
5. Yuya, P. A.; Hurley, D. C.; Turner, J. A. *J. Appl. Phys.* **2011,** *109,* 113528. doi:10.1063/1.3592966
6. Killgore, J. P.; Yablon, D. G.; Tsou, A. H.; Gannepalli, A.; Yuya, P. A.; Turner, J. A.; Proksch, R.; Hurley, D. C. *Langmuir* **2011,** *27,* 13983–13987. doi:10.1021/la203434w
7. Yablon, D. G.; Gannepalli, A.; Proksch, R.; Killgore, J.; Hurley, D. C.; Grabowski, J.; Tsou, A. H. *Macromolecules* **2012,** *45,* 4363–4370. doi:10.1021/ma2028038
8. Stan, G.; King, S. W.; Cook, R. F. *Nanotechnology* **2012,** *23,* 215703. doi:10.1088/0957-4484/23/21/215703
9. Herruzo, E. T.; Perrino, A. P.; Garcia, R. *Nat. Commun.* **2014,** *5,* 3126. doi:10.1038/ncomms4126
10. Williams, J. C.; Solares, S. D. *Beilstein J. Nanotechnol.* **2013,** *4,* 87–93. doi:10.3762/bjnano.4.10
11. Rodríguez, T.; García, R. *Appl. Phys. Lett.* **2004,** *84,* 449–451. doi:10.1063/1.1642273
12. Martinez, N. F.; Patil, S.; Lozano, J. R.; Garcia, R. *Appl. Phys. Lett.* **2006,** *89,* 153115. doi:10.1063/1.2360894
13. Garcia, R.; Herruzo, E. T. *Nat. Nanotechnol.* **2012,** *4,* 217–226. doi:10.1038/nnano.2012.38
14. Proksch, R. *Appl. Phys. Lett.* **2006,** *89,* 113121. doi:10.1063/1.2345593
15. Kawai, S.; Glatzel, T.; Koch, S.; Such, B.; Baratoff, A.; Meyer, E. *Phys. Rev. Lett.* **2009,** *103,* 220801. doi:10.1103/PhysRevLett.103.220801
16. Li, Y. J.; Takahashi, K.; Kobayashi, N.; Naitoh, Y.; Kageshima, M.; Sugawara, Y. *Ultramicroscopy* **2010,** *110,* 582–585. doi:10.1016/j.ultramic.2010.02.014
17. Naitoh, Y.; Ma, Z. M.; Li, Y. J.; Kageshima, M.; Sugawara, Y. *J. Vac. Sci. Technol., B* **2010,** *28,* 1210–1214. doi:10.1116/1.3503611
18. Solares, S. D.; Chawla, G. *J. Appl. Phys.* **2010,** *108,* 054901. doi:10.1063/1.3475644
19. Ebeling, D.; Solares, S. D. *Nanotechnology* **2013,** *24,* 135702. doi:10.1088/0957-4484/24/13/135702
20. Ebeling, D.; Eslami, B.; Solares, S. D. *ACS Nano* **2013,** *7,* 10387–10396. doi:10.1021/nn404845q
21. Rodriguez, B. J.; Callahan, C.; Kalinin, S. V.; Proksch, R. *Nanotechnology* **2007,** *18,* 475504. doi:10.1088/0957-4484/18/47/475504
22. Platz, D.; Tholén, E. A.; Pesen, D.; Haviland, D. B. *Appl. Phys. Lett.* **2008,** *92,* 153106. doi:10.1063/1.2909569

23. Jesse, S.; Kalinin, S. V.; Proksch, R.; Baddorf, A. P.; Rodriguez, B. J. *Nanotechnology* **2007,** *18,* 435503. doi:10.1088/0957-4484/18/43/435503
24. Guo, S.; Solares, S. D.; Mochalin, V.; Neitzel, I.; Gogotsi, Y.; Kalinin, S. V.; Jesse, S. *Small* **2012,** *8,* 1264–1269. doi:10.1002/smll.201101648
25. Stark, M.; Stark, R. W.; Heckl, W. M.; Guckenberger, R. *Proc. Natl. Acad. Sci. U. S. A.* **2002,** *99,* 8473–8478. doi:10.1073/pnas.122040599
26. Sahin, O.; Magonov, S.; Su, C.; Quate, C. F.; Solgaard, O. *Nat. Nanotechnol.* **2007,** *2,* 507–514. doi:10.1038/nnano.2007.226
27. Chawla, G.; Solares, S. D. *Appl. Phys. Lett.* **2011,** *99,* 074103. doi:10.1063/1.3626847
28. Radmacher, M.; Tilman, R. W.; Gaub, H. E. *Biophys. J.* **1993,** *64,* 735–742. doi:10.1016/S0006-3495(93)81433-4
29. Kareem, A. U.; Solares, S. D. *Nanotechnology* **2012,** *23,* 015706. doi:10.1088/0957-4484/23/1/015706
30. Cleveland, J. P.; Anczykowski, B.; Schmid, A. E.; Elings, V. B. *Appl. Phys. Lett.* **1998,** *72,* 2613–2615. doi:10.1063/1.121434
31. Martínez, N. F.; García, R. *Nanotechnology* **2006,** *17,* S167–S172. doi:10.1088/0957-4484/17/7/S11
32. Lozano, J. R.; Garcia, R. *Phys. Rev. Lett.* **2008,** *100,* 076102. doi:10.1103/PhysRevLett.100.076102
33. García, R.; Tamayo, J.; San Paulo, A. *Surf. Interface Anal.* **1999,** *27,* 312–316. doi:10.1002/(SICI)1096-9918(199905/06)27:5/6<312::AID-SIA496>3.0.CO;2-Y
34. Gotsmann, B.; Seidel, C.; Anczykowski, B.; Fuchs, H. *Phys. Rev. B* **1999,** *60,* 11051–11061. doi:10.1103/PhysRevB.60.11051
35. Hölscher, H.; Gotsmann, B.; Allers, W.; Schwarz, U. D.; Fuchs, H.; Wiesendanger, R. *Phys. Rev. B* **2001,** *64,* 075402. doi:10.1103/PhysRevB.64.075402
36. Schirmeisen, A.; Hölscher, H.; Anczykowski, B.; Weiner, D.; Schäfer, M. M.; Fuchs, H. *Nanotechnology* **2005,** *16,* S13–S17. doi:10.1088/0957-4484/16/3/003
37. Lozano, J. R.; Garcia, R. *Phys. Rev. B* **2009,** *79,* 014110. doi:10.1103/PhysRevB.79.014110
38. Solares, S. D.; Hölscher, H. *Nanotechnology* **2010,** *21,* 075702. doi:10.1088/0957-4484/21/7/075702
39. Bruker Corporation. http://www.bruker.com (accessed March 20, 2014).
40. Williams, J. C. Surface characterization of viscoelastic materials through spectral intermittent contact atomic force microscopy. M.S. Thesis, University of Maryland, College Park, USA, 2012.
41. Stark, R. W. *Appl. Phys. Lett.* **2009,** *94,* 063109. doi:10.1063/1.3080209
42. Solares, S. D.; Chawla, G. *Meas. Sci. Technol.* **2010,** *21,* 125502. doi:10.1088/0957-0233/21/12/125502
43. Yablon, D. G.; Grabowski, J.; Chakraborty, I. *Meas. Sci. Technol.* **2014,** *25,* 055402. doi:10.1088/0957-0233/25/5/055402
44. Zitzler, L.; Herminghaus, S.; Mugele, F. *Phys. Rev. B* **2002,** *66,* 155436. doi:10.1103/PhysRevB.66.155436
45. Caron, A.; Arnold, W. *Acta Mater.* **2009,** *57,* 4353–4363. doi:10.1016/j.actamat.2009.05.030
46. Santos, S.; Barcons, V.; Font, J.; Verdaguer, A. *Beilstein J. Nanotechnol.* **2014,** *5,* 268–277. doi:10.3762/bjnano.5.29
47. Solares, S. D.; Matsuda, Y.; Goddard, W. A. *J. Phys. Chem. B* **2005,** *109,* 16658–16664. doi:10.1021/jp052758g
48. Chakraborty, I.; Yablon, D. *Nanotechnology* **2013,** *24,* 475706. doi:10.1088/0957-4484/24/47/475706
49. Kiracofe, D.; Raman, A.; Yablon, D. *Beilstein J. Nanotechnol.* **2013,** *4,* 385–393. doi:10.3762/bjnano.4.45
50. Albers, B. J.; Schwendemann, T. C.; Baykara, M. Z.; Pilet, N.; Liebmann, M.; Altman, E. I.; Schwarz, U. D. *Nat. Nanotechnol.* **2009,** *4,* 307–310. doi:10.1038/nnano.2009.57
51. Stan, G.; Solares, S. D.; Pittenger, B.; Erina, N.; Su, C. *Nanoscale* **2014,** *6,* 962–969. doi:10.1039/C3NR04981G
52. Legleiter, J.; Park, M.; Cusick, B.; Kowalewski, T. *Proc. Natl. Acad. Sci. U. S. A.* **2006,** *103,* 4813–4818. doi:10.1073/pnas.0505628103
53. Santos, S.; Gadelrab, K.; Font, J.; Chiesa, M. *New J. Phys.* **2013,** *15,* 083034. doi:10.1088/1367-2630/15/8/083034
54. Borysov, S. S.; Platz, D.; de Wijn, A. S.; Forchheimer, D.; Tolén, E. A.; Balatsky, A. V.; Haviland, D. B. *Phys. Rev. B* **2013,** *88,* 115405. doi:10.1103/PhysRevB.88.115405
55. Santos, S.; Gadelrab, K. R.; Barcons, V.; Font, J.; Stefancich, M.; Chiesa, M. *J. Appl. Phys.* **2012,** *112,* 124901. doi:10.1063/1.4769434

License and Terms

BEILSTEIN JOURNAL OF NANOTECHNOLOGY

Dynamic calibration of higher eigenmode parameters of a cantilever in atomic force microscopy by using tip–surface interactions

Stanislav S. Borysov[*1,2,3], Daniel Forchheimer[1] and David B. Haviland[1]

Full Research Paper

Open Access

Address:
[1]Nanostructure Physics, KTH Royal Institute of Technology, Roslagstullsbacken 21, SE-106 91 Stockholm, Sweden, [2]Nordita, KTH Royal Institute of Technology and Stockholm University, Roslagstullsbacken 23, SE-106 91 Stockholm, Sweden and [3]Theoretical Division, Los Alamos National Laboratory, Los Alamos, NM 87545, USA

Email:
Stanislav S. Borysov[*] - borysov@kth.se

* Corresponding author

Keywords:
atomic force microscopy; calibration; multimodal AFM; multifrequency AFM

Beilstein J. Nanotechnol. **2014,** *5,* 1899–1904.
doi:10.3762/bjnano.5.200

Received: 10 June 2014
Accepted: 01 October 2014
Published: 29 October 2014

This manuscript is part of the Thematic Series "Advanced atomic force microscopy techniques II".

Guest Editors: T. Glatzel and T. Schimmel

Abstract

We present a theoretical framework for the dynamic calibration of the higher eigenmode parameters (stiffness and optical lever inverse responsivity) of a cantilever. The method is based on the tip–surface force reconstruction technique and does not require any prior knowledge of the eigenmode shape or the particular form of the tip–surface interaction. The calibration method proposed requires a single-point force measurement by using a multimodal drive and its accuracy is independent of the unknown physical amplitude of a higher eigenmode.

Introduction

Atomic force microscopy [1] (AFM) is one of the primary methods of surface analysis with resolution at the nanometer scale. In a conventional AFM an object is scanned by using a microcantilever with a sharp tip at the free end. Measuring cantilever deflections allows not only for the reconstruction of the surface topography but also provides insight into various material properties [2,3]. If deflection is measured near one of the cantilevers resonance frequencies, an enhanced force sensitivity is achieved due to multiplication by the sharply peaked cantilever transfer function. Measurement of response at multiple eigenmodes can provide additional information about the tip–surface interactions [4-11].

The optical detection system [12] common to most AFM systems leverages a laser beam reflected from the cantilever, measuring the slope rather than its vertical deflection. This

underlying principle leads to the measured voltage at the detector being dependent on the geometric shape of the excited eigenmode (Figure 1). While determination of the stiffness and optical lever inverse resposivity (inverse magnitude of the response function of the optical lever [m/V], also known as "inverse optical lever sensitivity") of the first flexural eigenmode can be performed with high accuracy using a few well-developed techniques [13-21], calibration of the higher eigenmode parameters is still a challenging task. The main problem with the existing theoretical approaches based on the calculation of eigenmode shapes [18,22] is that real cantilevers differ form the underlying solid body mechanical models due to the tip mass [23,24], fabrication inhomogeneities and defects [25,26]. In this paper, we propose a method which overcomes these deficiencies.

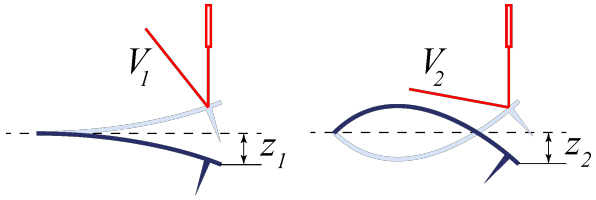

Figure 1: Schematic illustration of the two first flexural eigenmode shapes of a rectangular cantilever and an optical detection system. Measuring of the slope at the free end leads to the situation when the equal vertical tip deflections, $z_1 = z_2$, result in the different detected voltages, $V_1 \neq V_2$. In the case of small deflections, z_n is proportional to V_n with some coefficient α_n called optical lever inverse responsivity.

The method uses the fact that the tip–surface force is equally applied to all eigenmodes. This approximation is suitable unless the characteristic spatial wave length of an eigenmode shape is significantly bigger than the tip–cantilever contact area. Any other force acting on the whole cantilever, e.g., of thermal or electromagnetic nature, should be convoluted with the eigenmode shape, leading to a different definition of the effective dynamic stiffness. Thus, knowledge of the geometry of cantilever is not required to reconstruct the tip–surface force. The framework proposed harnesses a force reconstruction technique inspired by the Intermodulation AFM [27] (ImAFM), which was recently generalized to the multimodal case [28]. It is worth noting that the proposed calibration method is similar to that described in [29], in which stiffness of the second eigenmode is experimentally defined by using consecutive measurements of the frequency shift caused by the tip–surface interaction for different eigenmodes. In contrast, we propose a simultaneous one-point measurement by using a multimodal drive that avoids issues related to the thermal drift [30] and exploits nonlinearities for higher calibration precision.

Results and Discussion

Cantilever model

We consider a point-mass approximation of a cantilever derived from the eigenmode decomposition of its continuum mechanical model, e.g., the Euler–Bernoulli beam theory. Such a reduced system of coupled harmonic oscillators in the Fourier domain has the following form

$$k_n \alpha_n \hat{V}_n(\omega) = \hat{G}_n(\omega)\left[\hat{F}(\omega) + \hat{\mathrm{f}}_n(\omega)\right], \tag{1}$$

where the caret denotes the Fourier transform, ω is the frequency, k_n is the effective dynamic stiffness of the nth eigenmode ($n = 1, \ldots, N$), α_n is the optical lever inverse responsivity, V_n is the measured voltage (corresponding to the eigencoordinate $z_n = \alpha_n V_n$, where total tip deflection is $z = \sum_{n=1}^{N} z_n$),

$$\hat{G}_n = \left[1 + (i/Q_n)(\omega/\omega_n) - (\omega/\omega_n)^2\right]^{-1} \tag{2}$$

is the linear transfer function of a harmonic oscillator with the resonant frequency ω_n and quality factor Q_n, F is a nonlinear tip–surface force and f_n is a drive force. The stiffness is deliberately excluded from the expression for the G_n since the parameters Q_n and ω_n can be found by employing the thermal calibration method [14,17]. Note that if the force amplitudes on the right hand side of Equation 1 are known, one immediately gets k_n and α_n by taking the absolute values in combination with the equipartition theorem

$$k_n \left\langle z_n^2 \right\rangle = k_n \alpha_n^2 \left\langle V_n^2 \right\rangle = k_{\mathrm{B}} T, \tag{3}$$

where $\langle\cdot\rangle$ is a statistical average, k_{B} is the Boltzmann constant and T is an equilibrium temperature.

Spectral fitting method

The task at hand requires reconstruction of the forces on the right hand side of Equation 1 from the measured motion spectrum. Firstly, it is possible to remove the unknown drive contribution, $\hat{\mathrm{f}}_n$, for each n, by means of subtraction of the free oscillations spectrum, $\hat{V}_n^{\mathrm{f}}$ (far from the surface, where $F \equiv 0$), from the spectrum of the engaged tip motion, $\hat{V}_n^{\mathrm{e}}$ (near the surface). It gives the following relationships

$$k_n \alpha_n \Delta\hat{V}_n = \hat{G}_n \hat{F}, \tag{4}$$

where $\Delta\hat{V}_n \equiv \hat{V}_n^{\mathrm{e}} - \hat{V}_n^{\mathrm{f}}$. For the high-$Q$ cantilevers, the measured response near each resonance $\hat{V}_n$ may be separately detected with the high signal-to-noise ratio (SNR). Neglecting possible

surface memory effects, F depends on the tip position z and its velocity $\dot{z}$ only. With this assumption, the force model to be reconstructed has some generic form

$$\tilde{F}(z,\dot{z}) = \sum_{i=0}^{P_z}\sum_{j=0}^{P_z} g_{ij} z^i \dot{z}^j = \sum_{i=0}^{P_z}\sum_{j=0}^{P_z} g_{ij}\left(\sum_{n=1}^{N}\alpha_n V_n^{\mathrm{e}}\right)^i\left(\sum_{n=1}^{N}\alpha_n \dot{V}_n^{\mathrm{e}}\right)^j, \quad (5)$$

with $P = P_z P_z - 1$ unknown parameters g_{ij} (g_{00} is excluded because it corresponds to the static force) which can be found by using the spectral fitting method [31,32]: Substitution of Equation 5 in Equation 4 yields a system of linear equations for g_{ij}. However, this system becomes nonlinear with respect to the unknown k_n and α_n.

Intermodulation AFM

Assuming that α_1 and k_1 are calibrated by using one of the methods mentioned in the Introduction, the resulting system contains $2(N-1)+P$ unknown variables. Use of the equipartition theorem (Equation 3) for each eigenmode gives us $N-1$ equations and the remaining equations should be defined by using Equation 4 for the known response components in the motion spectrum. If the force acting on a tip over its motion domain is approximately linear ($P = 1$), one drive tone at each resonant frequency is enough to determine the system. However, when the force behaves in a nonlinear way ($P > 1$), as is usually the case, more measurable response components in the frequency domain are needed. The core idea of ImAFM relies on the ability of a nonlinear force to create intermodulation of discrete drive tones in a frequency comb. Driving an eigenmode subject to a nonlinear force on at least two frequencies ω_{n1}^{d} and ω_{n2}^{d} gives a response in the frequency domain not only at these drive frequencies and their higher harmonics but also at their linear combinations $n\omega_1^{\mathrm{d}} + m\omega_2^{\mathrm{d}}$ (n and m are integers) called intermodulation products (IMPs). Use of the small base frequency $\delta\omega = \left|\omega_{n1}^{\mathrm{d}} - \omega_{n2}^{\mathrm{d}}\right|$ results in the concentration of IMPs close to the resonance, which opens the possibility for their detection with high SNR. This additional information can be used in Equation 4 for the reconstruction of nonlinear conservative and dissipative forces [28,31-33] with the only restriction that IMPs in the different narrow bands near resonances contain the same information about the unknown force parameters [28].

Calculation details

In the rest of the paper, we consider a bimodal case implying straightforward generalization for $N > 2$ eigenmodes. Equation 1 is integrated by using CVODE [34] for two different sets of cantilever parameters from Table 1. The cantilever is excited by using multifrequency drive (specified below) with frequencies being integer multiples of the base frequency $\delta\omega = 2\pi\cdot 0.1$ kHz. The tip–surface force F is represented by the vdW-DMT model [35] with the nonlinear damping term being exponentially dependent on the tip position [36]

$$F = F^{\mathrm{con}} + F^{\mathrm{dis}},$$
$$F^{\mathrm{con}}(z) = \begin{cases} -\dfrac{HR}{6(z+h)^2}, & z+h \geq a_0 \\ -\dfrac{HR}{6a_0^2} + \dfrac{4}{3}E^*\sqrt{R(a_0-(z+h))}, & z+h < a_0 \end{cases} \quad (6)$$
$$F^{\mathrm{dis}}(z,\dot{z}) = -\gamma_1 \dot{z} e^{-(z+h)/\lambda_z},$$

where h is a reference height. Its conservative part, F^{con}, has four phenomenological parameters: the intermolecular distance $a_0 = 0.3$ nm, the Hamaker constant $H = 7.1\times10^{-20}$ J, the effective modulus $E^* = 1.0$ GPa and the tip radius $R = 10$ nm. The dissipative part, F^{dis}, depends on the damping factor $\gamma_1 = 2.2\times10^{-7}$ kg/s and the damping decay length $\lambda_z = 1.5$ nm. The force (Equation 6) and its cross-sections are depicted in Figure 2.

Calibration by using a nonlinear tip–surface force

In order to find k_2 and α_2 from the nonlinear system (Equation 3 and Equation 4), we first solve the linear system for the force parameters g_{ij}. It is then convenient to compare only the conservative part of the tip–surface force given its non-monotonic behavior. There are two methods to require equality of the reconstructed forces $\tilde{F}^{(1)}$ (using the band near the first eigenmode) and $\tilde{F}^{(2)}$ (near the second eigenmode). The first method is to check the difference between the corresponding parame-

Table 1: Cantilever parameters used for the numerical calculations in the paper. Last column E is a total oscillation energy of a free cantilever with the equal eigenmode amplitudes $A_1 = A_2 = 1$ nm.

cantilever	ω_1 ($(2\pi)^{-1}$ kHz)	ω_2/ω_1	Q_1	Q_2/Q_1	k_1 (N/m)	k_2/k_1	α_2/α_1	E (fJ)
soft	82.7	6.35	220.0	2.9	5.0	40.0	2.0	1.02
stiff	300.0	6.3	400.0	3.0	40.0	50.0	2.0	0.105

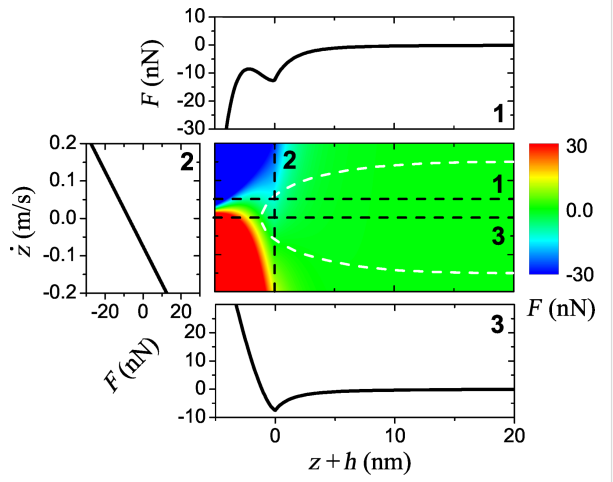

Figure 2: The tip–surface force (Equation 6) used in the simulations. The white dashed line corresponds to a phase space trajectory of the bimodal stiff cantilever with the eigenmode amplitudes $A_1 = A_2 = 12.5$ nm and reference height $h = 17$ nm. Cross-sections for different values of z and $\dot{z}$ are shown: The projections (1) and (2) correspond to the lines $\dot{z} = 0.05$ m/s and $z = 0$ nm respectively; the conservative part (3) corresponds to the line $\dot{z} = 0$ m/s.

ters $g_{ij}^{(1)}$ and $g_{ij}^{(2)}$. However, this approach is not suitable because two completely different sets of coefficients might define very similar functions on the interval of the actual engaged tip motion, $[A^{\min,e}; A^{\max,e}]$, where $A^{\max} = \max A(t) = \max z(t)$. As numerical simulations have shown, the error function does not have a well-defined global minimum and it is highly sensitive to reconstruction errors. An alternative approach is to minimize a mean square error function in real space

$$\int_{A^{\min,e}(\alpha_2)}^{A^{\max,e}(\alpha_2)} \left[\tilde{F}_1\left(z^e(\alpha_2)\right) - \tilde{F}_2\left(z^e(\alpha_2);k_2\right)\right]^2 dz\,, \qquad (7)$$

which in most regimes of the tip motion has only one global minimum lying in the deep valley defined by the curve $\alpha_2^{\text{true}} k_2^{\text{true}}$. Moreover, increasing the reconstructed polynomial power, P_z, makes this valley deeper and hence more resistant to noise. This method allows for the estimation of the product $\alpha_2 k_2$ with higher accuracy than α_2 and k_2 separately.

Figure 3 shows the absolute value of the relative error

$$\eta = 1 - k_2\alpha_2 \big/ k_2^{\text{true}}\alpha_2^{\text{true}} \qquad (8)$$

plotted in the plane of maximum free oscillation energy $E^{\max,f} = \left(k_1\left(A_1^{\max,f}\right)^2 + k_2\left(A_2^{\max,f}\right)^2\right)\big/2$ and the ratio $R = h/A^{\max,f}$. The relative calibration error is small over a wide range of oscillation energy and probe height for both soft (Figure 3a) and stiff (Figure 3b) cantilevers. The regions of lower error correspond to a large value of the ratio $A_1^{\max,f} / A_2^{\max,f}$ (Figure 3c and Figure 3d). Experimentally, one can check the stability of calibration by comparing different probe heights and oscillation energies. Finally, the stiff cantilever has a wider region of low error because a higher oscillation energy effectively weakens the nonlinearity.

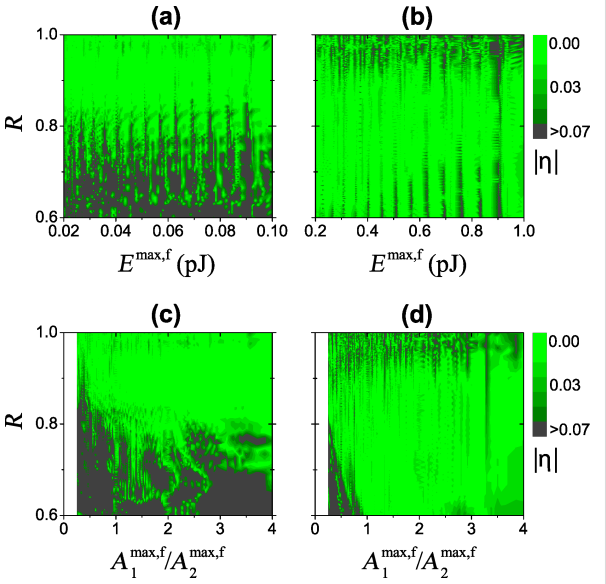

Figure 3: Absolute value of the relative calibration error η of $k_2\alpha_2$ as a function of the ratio $R = h/A^{\max,f}$, total maximum free oscillation energy $E^{\max,f}$ (top row) and the ratio of maximum free amplitudes $A_1^{\max,f}/A_2^{\max,f}$ (bottom row) for the soft (a), (c) and stiff (b), (d) cantilever, respectively.

Calibration by using a linear tip–surface force

When the interval of the engaged tip motion is small, the tip–surface force (Equation 5) can be linearized. In this case, it is possible to obtain the explicit expression for the stiffness by using a linear model $\tilde{F}$ with one unknown parameter g_{10}

$$k_2 = \left|\frac{\hat{G}_1(\omega)}{\hat{G}_2(\omega)}\right|\left|\frac{\Delta\hat{V}_1(\omega)}{\Delta\hat{V}_2(\omega)}\right|k_1\,. \qquad (9)$$

If g_{01} is used instead, k_2 should be additionally multiplied by ω_1/ω_2. As previously mentioned, the multimodal drive at the resonant frequencies ω_1 and ω_2 (more precisely, their discrete approximations defined by $\delta\omega$) produces enough response components to find k_2. The corresponding domain of the engaged tip motion and eigenmode sensitivity to the force are defined by the energy scale factor $k_n^{-1}\hat{G}_n(\omega_n)$. Therefore, calibration of the softer cantilever can be performed with higher accuracy, while for the stiff cantilever, small drive amplitudes are required for acceptable calibration results (Figure 4). Near

the surface, the force is highly nonlinear, making the tip prone to sudden jumps to the contact. From an experimental point of view, probing only the attractive part of the interaction with small oscillation amplitudes protects the tip from possible damage since the dissipation is almost zero in this regime.

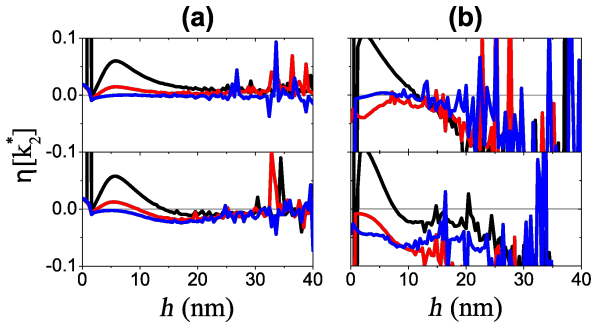

Figure 4: Relative calibration error of the calibrated stiffness k_2, $\eta = 1 - k_2 / k_2^{\text{true}}$, using Equation 9 for two different cantilevers: (a) soft and (b) stiff, with different free eigenmode oscillations amplitudes: A_1^{f} = 1 nm (top), A_1^{f} = 3 nm (bottom), A_2^{f} = 0.1 nm (blue), 1.0 nm (red) and 2.0 nm (black).

Finally, the linear method is dependent on the unknown higher eigenmode free amplitude, A_n^{f}, which must be small for the linear approximation to be valid. Since A_n^{f} is not known a priori, one can use the following formula to try to make a rough guess given the known free amplitude of the first mode for the particular drive voltage amplitude

$$A_n^{\text{f}} = \left| \frac{\hat{G}^{\text{piezo}}(\omega_n)}{\hat{G}^{\text{piezo}}(\omega_1)} \right| \frac{k_1}{kn} \frac{Q_n}{Q_1} A_1^{\text{f}} , \qquad (10)$$

where $\hat{G}^{\text{piezo}}$ is a transfer function of the piezoelectric shaker.

Implementation

Summarizing the ideas presented, an experimental implementation of the proposed calibration would consist of the following steps, with related sources of possible calibration error:

1. *Construct a multimode drive and measure the free motion spectrum of a cantilever*, V^{f}. Since the free motion components can be used instead of the drive force, the real physical amplitude of the cantilever and the transfer function of the piezo shaker do not contribute to the accuracy of the method. However, as numerical calculations have shown, the method is sensitive to SNR of the measurement, performing poorly when the SNR is too small. Therefore, a drive with approximately the same SNR for all eigenmodes would be a good option.
2. *Move the cantilever closer to the surface and measure its engaged motion spectrum*, V^{e}. In principle only one measured spectrum corresponding to a particular probe height is enough for calibration purposes. However, the use of spectra at different probe heights will improve calibration precision. The method may be applied to both soft and stiff cantilevers, but works best when nonlinearities are weak. Thus the amplitude contraction of the engaged cantilever oscillations with respect to the free motion should be about 10–20%.
3. *Choose a particular model for the tip–surface interaction and solve nonlinear system* Equation 4 *for unknown parameters using the measured difference spectrum* $V^{\text{e}} - V^{\text{f}}$. If the exact expression for F is unknown, ImAFM provides enough information to reconstruct it in a generic form, e.g., as power series (Equation 5). As numerical simulations have shown, a more realistic model gives better calibration with the same error function (Equation 7). Making use of any additional prior information about the cantilever also improves the accuracy of the calibration. For instance, ω_n, Q_n and $\alpha_n^2 k_n$ can be estimated by using the thermal calibration method [14,17] and the equipartition theorem (Equation 3).

Theoretically, the method should work in liquid or high-damping environments, however, experimental implementation in liquid will suffer from actuation-related effects, squeeze-film damping close to the surface and spurious resonances. [37].

Conclusion

We outlined a theoretical framework for experimental calibration of cantilever parameters by using the tip–surface force with one-point measurement and a multimodal drive. The proposed approach does not require any knowledge of the geometry of the cantilever or the form of the tip–surface interaction. The method possesses a high calibration accuracy independent of the a priori unknown amplitude of the higher eigenmode.

Acknowledgements

This work is supported by KTH, Nordita, DOE, VR VCB 621-2012-2983 and the Knut and Allice Wallenberg Foundation.

References

1. Binnig, G.; Quate, C. F.; Gerber, C. *Phys. Rev. Lett.* **1986,** *56,* 930–933. doi:10.1103/PhysRevLett.56.930
2. Burnham, N. A.; Colton, R. J.; Pollock, H. M. *Nanotechnology* **1993,** *4,* 64. doi:10.1088/0957-4484/4/2/002
3. Butt, H.-J.; Cappella, B.; Kappl, M. *Surf. Sci. Rep.* **2005,** *59,* 1–152. doi:10.1016/j.surfrep.2005.08.003
4. Stark, R. W.; Heckl, W. M. *Surf. Sci.* **2000,** *457,* 219–228. doi:10.1016/S0039-6028(00)00378-2

5. Gigler, A. M.; Dietz, C.; Baumann, M.; Martinez, N. F.; García, R.; Stark, R. W. *Beilstein J. Nanotechnol.* **2012,** *3,* 456–463. doi:10.3762/bjnano.3.52
6. Proksch, R. *Appl. Phys. Lett.* **2006,** *89,* 113121. doi:10.1063/1.2345593
7. Martinez, N. F.; Patil, S.; Lozano, J. R.; García, R. *Appl. Phys. Lett.* **2006,** *89,* 153115. doi:10.1063/1.2360894
8. Rupp, D.; Rabe, U.; Hirsekorn, S.; Arnold, W. *J. Phys. D: Appl. Phys.* **2007,** *40,* 7136–7145. doi:10.1088/0022-3727/40/22/041
9. Lozano, J. R.; García, R. *Phys. Rev. Lett.* **2008,** *100,* 076102. doi:10.1103/PhysRevLett.100.076102
10. Aksoy, M. D.; Atalar, A. *Phys. Rev. B* **2011,** *83,* 075416. doi:10.1103/PhysRevB.83.075416
11. Martinez-Martin, D.; Herruzo, E. T.; Dietz, C.; Gomez-Herrero, J.; García, R. *Phys. Rev. Lett.* **2011,** *106,* 198101. doi:10.1103/PhysRevLett.106.198101
12. Meyer, G.; Amer, N. M. *Appl. Phys. Lett.* **1990,** *57,* 2089–2091. doi:10.1063/1.103950
13. Cleveland, J. P.; Manne, S.; Bocek, D.; Hansma, P. K. *Rev. Sci. Instrum.* **1993,** *64,* 403–405. doi:10.1063/1.1144209
14. Hutter, J. L.; Bechhoefer, J. *Rev. Sci. Instrum.* **1993,** *64,* 1868–1873. doi:10.1063/1.1143970
15. Sader, J. E.; Larson, I.; Mulvaney, P.; White, L. R. *Rev. Sci. Instrum.* **1995,** *66,* 3789–3798. doi:10.1063/1.1145439
16. Higgins, M. J.; Proksch, R.; Sader, J. E.; Polcik, M.; Ms Endoo, S.; Cleveland, J. P.; Jarvis, S. P. *Rev. Sci. Instrum.* **2006,** *77,* 013701. doi:10.1063/1.2162455
17. Butt, H.-J.; Jaschke, M. *Nanotechnology* **1995,** *6,* 1. doi:10.1088/0957-4484/6/1/001
18. Sader, J. E.; Chon, J. W. M.; Mulvaney, P. *Rev. Sci. Instrum.* **1999,** *70,* 3967–3969. doi:10.1063/1.1150021
19. Stark, R. W. *Rev. Sci. Instrum.* **2004,** *75,* 5053–5055. doi:10.1063/1.1808058
20. Schäffer, T. E. *Nanotechnology* **2005,** *16,* 664. doi:10.1088/0957-4484/16/6/007
21. Liu, Y.; Guo, Q.; Nie, H.-Y.; Lau, W. M.; Yang, J. *J. Appl. Phys.* **2009,** *106,* 124507. doi:10.1063/1.3269703
22. Parkin, J. D.; Hähner, G. *Nanotechnology* **2013,** *24,* 065704. doi:10.1088/0957-4484/24/6/065704
23. Kiracofe, D.; Raman, A. *J. Appl. Phys.* **2010,** *107,* 033506. doi:10.1063/1.3284206
24. Allen, M. S.; Sumali, H.; Penegor, P. C. *J. Dyn. Syst., Meas., Control* **2009,** *131,* 064501. doi:10.1115/1.4000160
25. Burnham, N. A.; Chen, X.; Hodges, C. S.; Matei, G. A.; Thoreson, E. J.; Roberts, C. J.; Davies, M. C.; Tendler, S. J. B. *Nanotechnology* **2003,** *14,* 1. doi:10.1088/0957-4484/14/1/301
26. Lozano, J. R.; Kiracofe, D.; Melcher, J.; Garcia, R.; Raman, A. *Nanotechnology* **2010,** *21,* 465502. doi:10.1088/0957-4484/21/46/465502
27. Platz, D.; Tholén, E. A.; Pesen, D.; Haviland, D. B. *Appl. Phys. Lett.* **2008,** *92,* 153106. doi:10.1063/1.2909569
28. Borysov, S. S.; Platz, D.; de Wijn, A. S.; Forchheimer, D.; Tolén, E. A.; Balatsky, A. V.; Haviland, D. B. *Phys. Rev. B* **2013,** *88,* 115405. doi:10.1103/PhysRevB.88.115405
29. Sugimoto, Y.; Innami, S.; Abe, M.; Custance, O.; Morita, S. *Appl. Phys. Lett.* **2007,** *91,* 093120. doi:10.1063/1.2775806
30. Mokaberi, B.; Requicha, A. A. G. *IEEE Trans. Autom. Sci. Eng.* **2006,** *3,* 199–207. doi:10.1109/TASE.2006.875534
31. Hutter, C.; Platz, D.; Tholén, E. A.; Hansson, T. H.; Haviland, D. B. *Phys. Rev. Lett.* **2010,** *104,* 050801. doi:10.1103/PhysRevLett.104.050801
32. Forchheimer, D.; Platz, D.; Tholén, E. A.; Haviland, D. B. *Phys. Rev. B* **2012,** *85,* 195449. doi:10.1103/PhysRevB.85.195449
33. Platz, D.; Forchheimer, D.; Tholén, E. A.; Haviland, D. B. *Beilstein J. Nanotechnol.* **2013,** *4,* 352–360. doi:10.3762/bjnano.4.41
34. Hindmarsh, A. C.; Brown, P. N.; Grant, K. E.; Lee, S. L.; Serban, R.; Shumaker, D. E.; Woodward, C. S. *ACM Trans. Math. Software* **2005,** *31,* 363–396. doi:10.1145/1089014.1089020
35. Derjaguin, B. V.; Muller, V. M.; Toporov, Yu. P. *J. Colloid Interface Sci.* **1975,** *53,* 314–326. doi:10.1016/0021-9797(75)90018-1
36. Gotsmann, B.; Seidel, C.; Anczykowski, B.; Fuchs, H. *Phys. Rev. B* **1999,** *60,* 11051–11061. doi:10.1103/PhysRevB.60.11051
37. Baró, A. M.; Reifenberger, R. G. *Atomic Force Microscopy in Liquid: Biological Applications;* Wiley, 2012. doi:10.1002/9783527649808

License and Terms

BEILSTEIN JOURNAL OF NANOTECHNOLOGY

Dissipation signals due to lateral tip oscillations in FM-AFM

Michael Klocke and Dietrich E. Wolf*

Full Research Paper

Open Access

Address:
Department of Physics, University of Duisburg-Essen and CeNIDE, D-47048 Duisburg, Germany

Email:
Dietrich E. Wolf* - dietrich.wolf@uni-due.de

* Corresponding author

Keywords:
atomic force microscopy (AFM); frequency-modulated atomic force microscopy (FM-AFM); energy dissipation

Beilstein J. Nanotechnol. **2014,** *5,* 2048–2057.
doi:10.3762/bjnano.5.213

Received: 06 June 2014
Accepted: 01 October 2014
Published: 10 November 2014

This article is part of the Thematic Series "Advanced atomic force microscopy techniques II".

Guest Editors: T. Glatzel and T. Schimmel

Abstract

We study the coupling of lateral and normal tip oscillations and its effect on the imaging process of frequency-modulated dynamic atomic force microscopy. The coupling is induced by the interaction between tip and surface. Energy is transferred from the normal to the lateral excitation, which can be detected as damping of the cantilever oscillation. However, energy can be transferred back into the normal oscillation, if not dissipated by the usually uncontrolled mechanical damping of the lateral excitation. For certain cantilevers, this dissipation mechanism can lead to dissipation rates larger than 0.01 eV per period. The mechanism produces an atomic contrast for ionic crystals with two maxima per unit cell in a line scan.

Introduction

The usage of scanning probe microscopes requires an understanding of the physical processes during the scan, otherwise images can be misinterpreted. Due to the importance of frequency-modulated atomic force microscopy (FM-AFM), the physical processes involved have been studied intensively in the past [1]. This includes the relation between tip–surface interaction and frequency-shift [2], as well as features such as the energy dissipation during the scan [3], which is an interesting side-effect of the FM-AFM principle. The height (the topography) of a point on the surface is measured by shifting the probe such that the resonant frequency of the cantilever oscillation is detuned by a given amount due to surface–tip interactions. The amplitude is kept constant, which requires to drive the oscillation. Energy loss of the oscillation occurs not only due to mechanical damping of the cantilever, but also due to interaction between tip and surface, so that the damping signal can be used for imaging, even with atomic resolution [4].

There is a broad consensus, that the observed dissipation is due to adhesion hysteresis [5]: As the tip approaches the surface, the atomic configuration becomes metastable and at the same time a modified configuration becomes energetically more favorable. When the energy barrier between these two configurations is low enough, a sudden transition into the favorable one happens. The energy difference is dissipated. This mechanism has been found in various systems [6-8].

The ultimate goal would be to extract valuable information about the surface from the rate of the dissipated energy, e.g., the identification of functional groups within molecules [9]. Unfortunately, the effects that take place are far more complex than having just a single hysteresis loop. Depending on the indentation depth of the tip (or the minimum distance between tip and sample), multiple adhesion hysteresis loops might occur [10]. It can also happen that in some of the cycles, there is no adhesion hysteresis loop at all, which leads to complex beating phenomena [11]. Moreover, alternative dissipation effects have been discussed, and it is possible that these effects are additionally at work [12-15]. In this paper, we propose another dissipation mechanism, which can enhance the dissipation signal independently of the presence of adhesion hysteresis.

We show that the bending mode of the cantilever (oscillation normal to the substrate) is coupled to lateral tip oscillations, and connect this coupling to the damping of the cantilever oscillation. The lateral tip oscillations can include torsional or lateral cantilever modes, which also lead to an oscillation of the end of the tip parallel to the surface of the substrate. While torsional cantilever deflections can be detected directly by using techniques similar to the ones used for lateral-force AFM measurements [16-18], this is in general not the case for lateral tip deflections without cantilever torsion. The damping that we are going to describe indicates such deflections.

Up to now, the effect of a lateral displacement of the tip has only been studied for the quasi-static case [19,20]. These studies are valuable for the understanding and correction of certain distortions seen in the actual images. Here, we enhance these studies by taking lateral dynamics of the tip into account and study the effect on the topography as well as on the energy dissipation signal.

It is necessary to distinguish between the terms damping and dissipation. Damping means, that the normal oscillation of the cantilever is reduced. The reason can be irreversible energy dissipation, or a redistribution of energy between normal and lateral modes. In principle, such a redistribution is reversible, but the lateral mode is no perfect energy storage. Mechanical damping is responsible for the dissipation of energy of the macroscopic degrees of freedom. We will therefore address three questions: (i) How large is the damping rate, (ii) is the resulting dissipation rate comparable to adhesion hysteresis, and (iii) what happens to the non-dissipated energy?

The mechanical damping of the normal oscillation mode can be measured directly. It is a common assumption, that the lateral and bending modes of the cantilever are decoupled, but this only holds as long as there are no asymmetries in the mass distribution of the cantilever [21]. We will neglect this kind of coupling, as it is an intrinsic feature of the cantilever and should not be sensitive to the surface potential (we also neglect any kind of direct coupling between different lateral modes [22]). Based on this assumption, we present a simple two-dimensional model for surface-induced coupling between normal and lateral tip oscillations. Later on we use more realistic potential energy landscapes from molecular dynamics calculations. The simulations show, under which circumstances the coupling of normal and lateral modes is strong enough to compete with dissipation rates due to adhesion hysteresis and the effects it has on the imaging process.

Description of the two-dimensional model

We start from the common one-dimensional description of the cantilever dynamics. The tip is described as a single point of mass m_z [23]. The bending mode oscillation of the cantilever is replaced by the oscillation of a harmonic spring with the spring constant k_z. The mass m_z has to be chosen such that the frequency $\omega_z = \sqrt{k_z / m_z}$ matches the frequency of the cantilever [24]. The internal damping of the cantilever motion is experimentally compensated by a driving force. There exist sophisticated models that describe the dynamics of an AFM in great detail by taking into account all electrical and mechanical components [25]. The AFM setup itself can also lead to some sort of spurious dissipation signal [26,27]. These effects can additionally be at work, but will not be considered further as they have been sufficiently elaborated [28]. Instead we focus solely on the proposed effect and therefore use a rather simple yet quite often used approach by neglecting both damping and excitation [29]. It is possible to include dissipation caused by the adhesion hysteresis effect by using non-conservative forces [30], but we do not consider this effect here. We define z to be the position of the end of the tip. z_0 is the equilibrium position, that is the position when there is no cantilever deflection. Let the interaction between tip and sample be given by a potential energy V_{ts}. The equation of motion then reads

$$m_z \ddot{z} + k_z \left(z - z_0 \right) = -\partial_z V_{\mathrm{ts}} = F_z . \tag{1}$$

This model can easily be extended to include additional degrees of freedom. For simplicity we add only a single lateral displacement coordinate, $x - x_0$, in the plane perpendicular to the cantilever axis, where x_0 denotes the equilibrium value of the x-coordinate of the end of the tip in the absence of interaction with the surface, see Figure 1. In analogy to Equation 1 the effective dynamics for the x-coordinate is given by

$$m_x \ddot{x} + \gamma \dot{x} + k_x (x - x_0) = -\partial_x V_{\mathrm{ts}} = F_x . \tag{2}$$

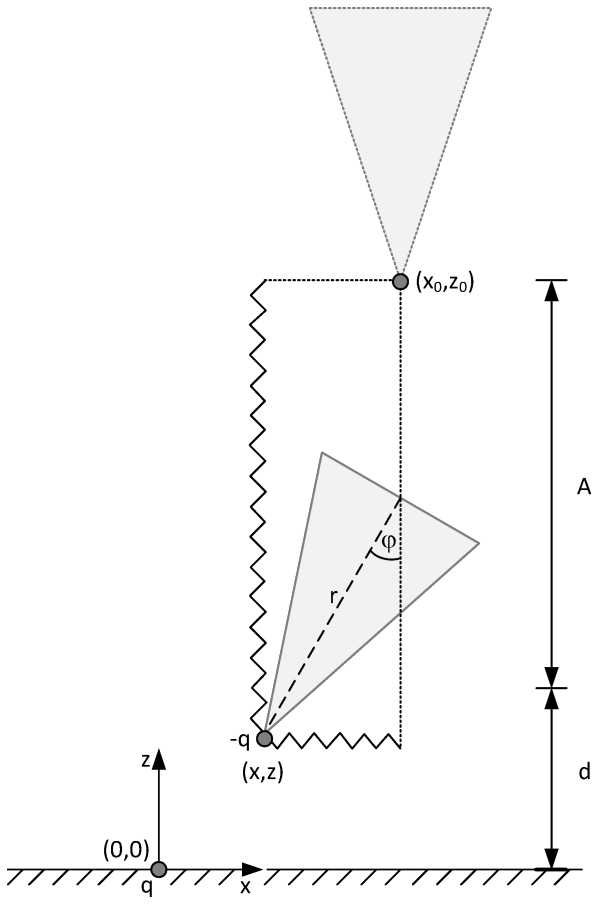

Figure 1: Sketch of the two-dimensional model setup.

For the lateral excitations we include a viscous friction term with the coefficient γ, because these losses are not compensated like they are in the bending mode. Commonly, γ is expressed by the quality factor $Q = (m_x\omega_x)/\gamma$, where $\omega_x = \sqrt{k_x / m_x}$. We only consider damping in the lateral degree of freedom and therefore omit any sort of indexing of damping parameters (such as Q_x). It should be clear that if the damping in the z-direction is explicitly used, one will have to distinguish between Q_x and Q_z.

Without distinguishing further degrees of freedom, these equations of motion describe the combined elastic response of cantilever and tip. A recent innovation in FM-AFM is the use of tuning fork cantilevers. Their spring constants are several orders of magnitude larger than those of ordinary cantilevers. In this case, the lateral displacement is mostly due to elastic deformation of the tip. For illustrative purposes we briefly want to discuss the opposite limit, where the lateral displacement originates from a torsion of the cantilever superimposed on its bending. Then $x - x_0 \approx r\varphi$, where r is the length of the tip and φ the torsional angle of the cantilever. Denoting the moment of inertia of the cantilever by J and the torsional spring constant by k_φ, the equation of motion for φ without the interaction with the substrate would be $J\ddot{\varphi} = k_\varphi\varphi$, which is in agreement with Equation 2, if one identifies $k_x = k_\varphi/r^2$ and $m_x = J/r^2$. The single mass point at (x, z) appears to have an anisotropic mass, as $m_x \neq m_z$.

The interaction between tip and surface can be described by different models [31]. If both the tip and the substrate are ionic crystals, we can imagine a charge q at the surface, which has a fixed position taken as the origin of the coordinate system. The mass point representing the cantilever, including the tip, carries a charge of $-q$. The tip–surface interaction then reads

$$V_{\mathrm{ts}}(x,z) = -\left(q^2/r\right) \text{ with } r = \sqrt{x^2 + z^2}.$$

Although this force model is quite simple and might not be as well justified as commonly used models, it provides an important feature that other models lack of: It couples the normal and the lateral motion. For this reason, it seems to be the simplest, yet sufficient, approach to investigate the proposed effect.

The coupled differential equations in Equation 1 and Equation 2 are solved numerically. We use the symplectic velocity-Verlet scheme [32] implemented with our own code; the timestep is set to $\Delta t = 5\cdot10^{-5}$ (using reduced units in length, frequency and stiffness with $l_0 = 10$ nm, $\omega_0 = 100$ kHz and $k_0 = 0.5$ N/m). At the beginning, we place the tip at the upper turning point of the normal oscillation and at the rest position of the lateral spring (so that initially there is no energy in the lateral degree of freedom) with velocity set to zero. We therefore define the amplitude A with this initial positioning. The set point z_0 can be used for variations of the distance between tip and sample. We will describe variations of z_0 via the nominal distance d, that is the closest distance between tip and sample, if no interaction would take place ($d = z_0 - A$, see Figure 1).

Without the damping term ($\gamma = 0$) in Equation 2, the total energy of the system is conserved. But the total energy is also conserved, if $\gamma \to \infty$, as in this case an excitation of the lateral degree of freedom becomes impossible. For finite γ, energy can be transferred into the lateral degree of freedom, but this energy could partly also be transferred back into the normal degree of freedom. The dissipated energy per normal cycle is just given by the viscous damping term in the lateral degree of freedom,

$$E_{\mathrm{diss}} = \int_0^{2\pi/\omega_z} dt\gamma v_x^2, \text{ with } v_x = \dot{x}. \tag{3}$$

We can estimate the dissipated energy from the energy stored in the lateral spring,

$$E_{\mathrm{l}}(t)=\frac{1}{2}k_x\left(x(t)-x_0\right)^2+\frac{1}{2}m_x v_x^2(t). \tag{4}$$

As long as there is no interaction, $E_{\mathrm{l}}(t)$ is constant. We denote this constant as E_{lat}. Assuming that the damping is low and that $\omega_x >> \omega_z$, we can integrate Equation 3 for one cycle in z with $v_x = v_0 \cos(\omega_x t)$ and $v_0 = \sqrt{2E_{\mathrm{lat}}/m_x}$, which yields

$$E_{\mathrm{diss}} \approx \frac{2\pi\omega_x/\omega_z}{Q}E_{\mathrm{lat}}. \tag{5}$$

If we just consider one oscillation cycle in our numerical simulations, we start at the upper turning point of the normal oscillation but the lateral excitations set in at the lower turning point. Thus the dissipation values will be just half of the values expected from Equation 5. If Q is sufficiently high, some significant amount of energy remains in the lateral degree of freedom after one cycle. This would create a new situation, because it is not clear, how much energy is transferred to the lateral degree of freedom in the succeeding cycles.

In the next two sections (and in Figure 2–Figure 4 and Figure 6) we use the following parameters: k_x = 24 N/m, k_z = 0.5 N/m, $\omega_x/2\pi$ = 600 kHz, $\omega_z/2\pi$ = 100 kHz, Q = 30000. The lateral distance between the tip and the fixed charge is set to x_0 = 0.3 nm, the amplitude A is set to 3.155 nm. We do not give a default value for the nominal distance here. The values for k_x and ω_x are typical for torsional cantilever oscillations. The actual lateral motion is not necessarily torsional, but can for instance be a local tip deformation. Likewise, k_z and ω_z vary significantly for different cantilevers [33]. In fact, for FM-AFM usually much stiffer cantilevers are used ($k_z \approx 40$ N/m) [34] in order to suppress thermal fluctuations and to increase the robustness with respect to snap into contact. This is not so urgent for computer simulations, where the parameters can be explicitly chosen such that the tip keeps oscillating (see e.g. [35]). Then, however, in order to compare with experiments, it is important to show robustness of the simulation results with respect to variations of k_z. The sensitivity with respect to all parameters (including the lateral quality factor Q) will be assessed in the later sections.

Results and Discussion

Dissipation spectroscopy

Energy transfer within one cycle

As a first application of the model, we calculate the energy transfer from the normal into the lateral degree of freedom for different nominal distances. The motion starts at the upper turning point of the normal oscillation. When the cantilever returns to this turning point next time, a part, E_{lat}, of its energy has been diverted from the bending mode into the lateral degree of freedom, and some energy E_{diss} has been dissipated.

Figure 2 shows E_{lat} as a function of the nominal distance. Although the interaction with the substrate monotonously increases the closer the tip gets to the surface, the energy E_{lat} transferred into the lateral degree of freedom shows an oscillatory behavior.

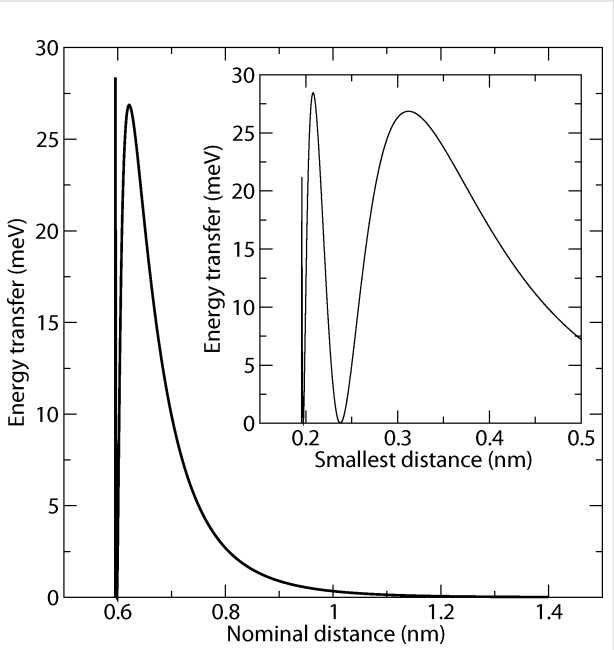

Figure 2: Distance-dependency of the energy transfer after one cycle. As a function of the nominal distance (which would be the closest approach of the tip, if the interaction with the sample was switched off, cf. Figure 1), only one of the oscillations can be resolved. Due to the attraction between tip and sample the tip actually comes closer than the nominal distance. In the inset, which shows the same data, advantage has been taken of the non-linear dependence of the actual minimal distance on the nominal distance in order to resolve a second oscillation.

In order to understand the origin of this oscillating behavior, we will simplify the equations of motion, such that they become analytically solvable. As a first step, the x-dependence of the z-component of the force is neglected by approximating $F_z(x, z) \approx F_z(x_0, z)$. Then the solution $z(t)$ of Equation 1 is independent of Equation 2. This leads to an effectively time-dependent lateral force $F_x(x, z(t))$ for Equation 2.

As the interaction between the surface and the tip is short ranged, the lateral force may be assumed to be non-zero only for the small fraction p of the normal cycle, when the tip is sufficiently close to the surface. We use the following approximation:

$$F_x(t)=\begin{cases}2F_{\mathrm{av}}\left(x_0,d\right)\sin^2\left(\dfrac{\omega_z}{2p}t\right) & \text{for } 0\le t<\dfrac{2\pi}{\omega_z}p=t_{\mathrm{int}}\\ 0 & \text{else}\end{cases}. \quad (6)$$

$F_{\mathrm{av}}(x_0, d)$ is the lateral force averaged over the time interval t_{int}, during which it is non-zero. It increases, the smaller the closest nominal approach d to the surface becomes.

With this approach, the equation of motion

$$m_x\ddot{x}+k_x x=F_x\left(t\right). \quad (7)$$

can be solved analytically. We introduce the dimensionless lateral elongation $\xi = x/\lambda$ by using the length scale $\lambda = F_{\mathrm{av}}/k_x$, the dimensionless time $\tau = \omega_x t$, and abbreviate the dimensionless duration of interaction by $2\pi\alpha = \omega_x t_{\mathrm{int}}$. In these variables, the equation of motion simply reads

$$\frac{d^2\xi}{d\tau^2}+\xi=\begin{cases}1-\cos\dfrac{\tau}{\alpha} & \text{for}\quad 0\le\tau\le 2\pi\alpha\\ 0 & \text{else}\end{cases},$$

which is solved by

$$\xi(\tau)=\begin{cases}0 & \text{for } \tau<0\\ \dfrac{1}{1-\alpha^2}\left(\left(1-\cos\tau\right)-\alpha^2\left(1-\cos\dfrac{\tau}{\alpha}\right)\right) & \text{for } 0\le\tau\le 2\pi\alpha\\ \dfrac{1}{1-\alpha^2}\left(\cos\left(\tau-2\pi\alpha\right)-\cos\tau\right) & \text{for } \tau>2\pi\alpha\end{cases}.$$

The energy transferred into the lateral degree of freedom after one cycle is

$$\begin{aligned}E_{\mathrm{lat}}&=\frac{1}{2}k_x\lambda^2\left(\xi^2+\left(\frac{d\xi}{d\tau}\right)^2\right)\\&=\frac{F_{\mathrm{av}}^2\left(x_0,d\right)}{k_x}\frac{1}{\left(1-\alpha^2\right)^2}\left(1-\cos 2\pi\alpha\right).\end{aligned} \quad (8)$$

In spite of its simplicity, this model can explain a number of qualitative findings for the numerical solution of the coupled Equation 1 and Equation 2.

When the nominal distance d is decreased, the average force F_{av} as well as the fraction of time p with significant lateral interaction, and hence α, increase. While the first leads to a higher amount of transferred energy, varying α leads to oscillations as observed in the numerical solution, Figure 2. For $\alpha = n$ (with any natural number n), the lateral excitation is zero, because the energy transiently transferred from the normal into the lateral mode is reversibly given back, when the tip retreats. Note that due to $p < 1$ the number of these oscillations is limited by $\alpha_{\max} = \omega_x/\omega_z$.

The dependence of the energy transfer in a single cycle on the frequency ratio ω_x/ω_z is shown for the numerical solution as the full curve in Figure 3. Like the simplified result in Equation 8 it starts at 0 for $\omega_x/\omega_z = 0$, then goes through local maxima decreasing in height with increasing ω_x/ω_z (only first maximum shown). Note that the singularity of $(1 - \alpha^2)^{-2}$ in Equation 8 is removed by the zero of the second factor at $\alpha = 1$. The transferred energy vanishes asymptotically for $\omega_x/\omega_z \to \infty$ as expected, because the lateral displacement becomes zero for infinite lateral stiffness.

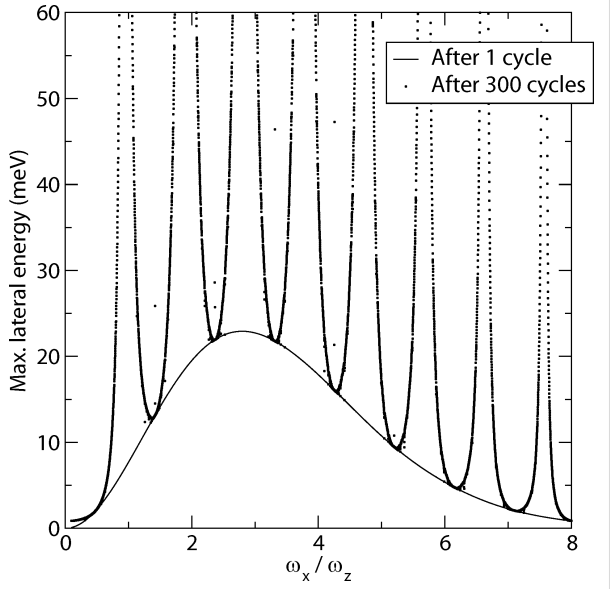

Figure 3: Numerical results of energy in lateral degree of freedom after one cycle (line) and maximum energy in the lateral degree of freedom ($E_{\mathrm{lat}}^{\max}$) over 300 cycles (points) versus frequency ratio ω_x/ω_z.

Energy transfer and dissipation after multiple cycles

After we have discussed the energy transfer into the lateral degree of freedom within one cycle, we can now consider the actual dissipation rate after multiple cycles. We evaluate the dissipation rate by the loss of total energy of the system divided by the number of normal cycles. Compared to the energy transfer per cycle E_{lat} of the previous section, we find values, which are about three orders of magnitude lower, in agreement with Equation 5.

We compare the dissipation rate for one and for 30 cycles. For certain nominal distances, there is only a small observable difference, while for others the dissipation rate for 30 cycles is about five times higher (Figure 4). We also observe the non-monotonic d-dependence corresponding to the one derived for E_{lat} in the previous section. The lateral excitation can be amplified in succeeding cycles, if the normal oscillation is in resonance with it. We therefore evaluated the energy transfer during each cycle (by evaluating the difference between the lateral energies E_{l} in the upper turning point of the normal oscillation for two successive cycles). We found, that the energy transfer oscillates (see inset of Figure 4). As long as it is positive, the lateral oscillation is amplified, but for negative values, energy is transferred back to the normal degree of freedom.

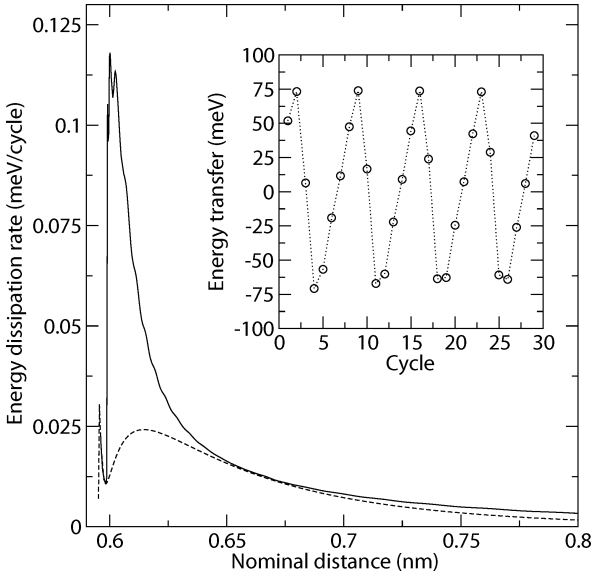

Figure 4: Distance dependency of dissipation rate for one cycle (dashed line) and averaged over 30 cycles (solid line). Inset shows the energy transfer per cycle for the nominal distance d = 0.605 nm.

In the previous section, we found with a simple model, that the energy transfer is essentially given by the phase of the lateral oscillation, when the tip leaves the tip–surface interaction region. If we extend the model to a second cycle, we see that the amplification also depends on the phase when the tip enters the interaction region. In Figure 4, interaction times are such that there is a significant energy transfer per cycle, as well as an amplification in the first cycles. After about three cycles the energy transfer changes sign. What may be called an energy swapping frequency, is therefore about $\omega_z/6$ in this case. By altering the nominal distance, we also alter the interaction times. There are points, where there is no difference between the dissipation rate for one cycle and for multiple cycles. At these points, the whole energy stored in the lateral degree of freedom is transferred back in the next cycle (the energy swapping frequency is then $\omega_z/2$).

Parameter choice

The experimentally observed dissipation rate due to tip–surface interactions in FM-AFM is at least 0.01 eV per cycle. We will now consider the question, what fraction of the observed dissipation rate may be accounted for by the excitation of lateral tip oscillations.

Monte-Carlo study of parameter set

Before we study the influence of single parameters, we want to get a quick overview, what can actually be expected. This is obtained by a Monte Carlo sampling of the parameter space, in which we chose combinations of parameters randomly within a reasonable range.

The normal spring constant k_z of typical cantilevers ranges from 0.004 N/m to 40 N/m (for tuning forks it may be 100 times larger). Values for lateral stiffness k_x ranging from k_z up to $1000k_z$ should cover most cases. For the lateral frequency ω_x we consider a range from ω_z to $30\omega_z$. The Q-value ranges from 100 to 30000. We also vary the values of x_0 and z_0 between 0 and 0.5 nm and between 10 and 12 nm, respectively, in order to have different ratios between lateral and normal force. The amplitude is always equal 10 nm. We discard parameter sets for which the reduced frequency shift [2] lies outside the interval -7 fN m$^{1/2}$ and -0.7 fN m$^{1/2}$. For each parameter set, we calculate 300 cycles.

Figure 5 shows that for most parameter sets the energy dissipation due to coupling between normal and lateral oscillations is below 0.01 eV per cycle, but for (nearly) integer ratios of ω_x/ω_z the dissipation rate becomes rather large due to a resonant excitation of the lateral degree of freedom.

Lateral frequency

The Monte-Carlo study shows, that the dissipation rate depends strongly on the lateral frequency. To study this effect in detail, we use the parameter set given at the end of the Section in which the model is described. The nominal distance is set to d = 0.79 nm, while we vary the lateral frequency ω_x. We perform one simulation with one normal cycle and one with 300 normal cycles.

We evaluate E_{lat} after each cycle (in the upper turning point of a normal oscillation) and take the maximum over all 300 normal cycles, denoted by $E_{\mathrm{lat}}^{\mathrm{max}}$. We found that after the first cycle E_{lat} has a maximum for a frequency ratio of $\omega_x/\omega_z \approx 3$ (Figure 3), which is quite near the frequency ratio of the torsional and normal frequency for many cantilevers [36]. This value can

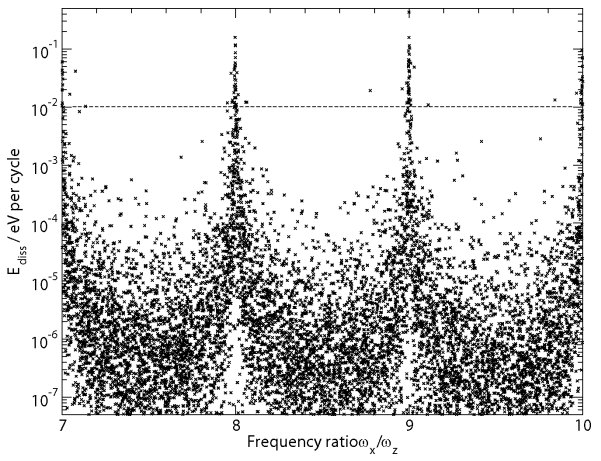

Figure 5: Dissipation rate depending on frequency ratio ω_x/ω_z for different systems. Dashed line indicates the lower bound of experimentally observed values. Dissipation rate is averaged over 300 cycles.

serve as a lower bound for $E_{\text{lat}}^{\max}$ after multiple cycles. There we found resonance-like peaks at nearly integer values of ω_x/ω_z. This indicates that although the dissipation rate after one cycle may be small, higher dissipation rates can be achieved due to further amplification of the lateral oscillation (assuming a relation between $E_{\text{lat}}^{\max}$ and E_{diss} such as in Equation 5). We also observe deviations from a smooth curve, especially at the minima. These are based on a subtle effect, which is caused by the variation of the potential between two consecutive cycles due to the loss of energy in the normal degree of freedom. We will, however, not discuss this effect in detail, as its impact is limited to very narrow ranges of frequency ratios.

Quality factor

We studied the influence of the quality factor on the energy dissipation rate (Figure 6). For high Q-values, the trajectory of the tip in the strong interaction region is nearly unaffected by the damping in the lateral degree of freedom. Therefore, the approximation leading to Equation 5 is applicable, which explains the Q^{-1}-dependence shown in Figure 6. At lower Q-values, the effect on the trajectory becomes stronger. The energy transfer into the lateral degree of freedom slows down and, being limited in time by the normal cantilever oscillation, does not reach the level any more that it had for large Q. E_{lat} decreases with decreasing Q so that E_{diss} no longer increases like Q^{-1}. For weak lateral interaction (d = 1.1) E_{diss} even drops with decreasing Q. Heading towards the overdamped case (Q < 1), the dissipation rate rises again, as a higher fraction of the transferred energy is actually dissipated. For Q = 0 one would not expect any dissipation, as any lateral displacement is suppressed. Figure 6 shows the numerical results for two different nominal distances and the parameter set given at the end of the Section in which the model is described. While the absolute maximum is found for rather low Q-values ($Q \approx 0.6$), a second maximum is found for values of Q of about 10–30. Typical quality factors for the normal cantilever oscillation range from 200 [17] up to 100000 [37]. However, the Q-values for the lateral oscillations may be smaller.

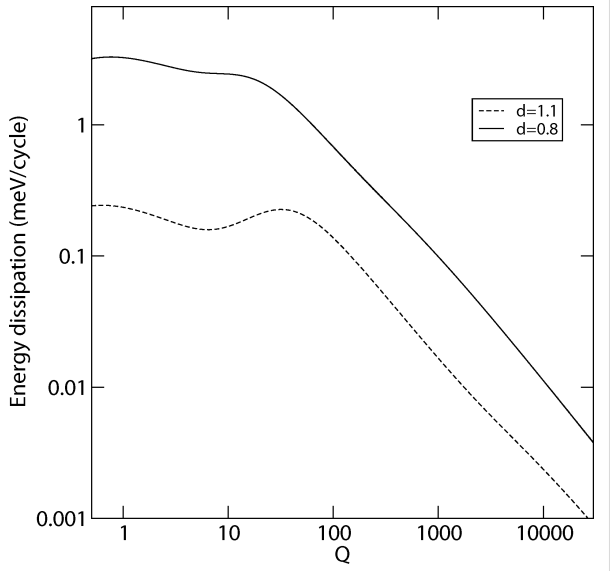

Figure 6: Dissipation rate with respect to the variation of the Q-factor for nominal distances of d = 0.8 nm and d = 1.1 nm. Numerical simulation for 300 normal cycles with the default parameter set.

Realistic potentials

In the previous sections we have used two point charges as a simple model for the tip–surface interaction, which includes coupling between a lateral and a normal component. In order to show that this simple model captures relevant physics, in this section we compare it with the results of a more realistic model, where tip and substrate consist of many atoms. The interaction is given by the summation over pair potentials as they are used in molecular dynamics.

In classical molecular dynamics, atomic bonding is described by empirical potentials. We used the potential of Fumi and Tosi [38] with parameters from [39] and van der Waals parameters from [40] for the ionic bonding of KBr. The tip is a cube of 3 × 3 × 3 unit cells (216 atoms) of a NaCl-lattice, while there are 7 × 7 × 3 unit cells (1176 atoms) for the substrate. Compared to the crystallographic orientation of the substrate, the tip cube is rotated by the Euler angles $\pi/2$, 0, and $\arctan\left(1/\sqrt{2}\right)$, so that its diagonal axis is parallel to the z-axis. In this configuration there is exactly one apex atom closest to the substrate.

In this setup, the dissipation mechanisms of adhesion hysteresis [6] or more rare transitions between a number of tip configura-

tions [14,41] are known to occur. Here, we want to study the possibility of an additional dissipation mechanism caused by the excitation of lateral oscillations. Therefore, we calculate the tip–substrate interaction force only for the approach of the tip, and assume the same force for the retreat, thereby intentionally suppressing the adhesion hysteresis effect as well as configurational changes. In a first step, we put all atoms on ideal NaCl-lattice positions and run a relaxation separately for the tip and the substrate. Then the two subsystems are assembled with fixed atomic positions of the lowest atomic layer of the substrate and the uppermost atom of the tip cube. The other atomic positions are relaxed by using open boundary conditions and the conjugate gradient method. The interaction force between tip and substrate is evaluated for a fine grid of tip positions by repeating the relaxation procedure each time. The forces are interpolated linearly for the use in Equation 1 and Equation 2.

In order to simulate an FM-AFM, we start at a certain position (x_0, z_0) and integrate Equation 1 and Equation 2 for 10 cycles. The usual reduced frequency shift is adjusted to a given value f_{set},

$$\left(\frac{2\pi}{\omega_z T}-1\right)k_z A^{3/2} = f_{\text{set}}\ , \tag{9}$$

by changing z_0 accordingly. Here, T is the actual period of the normal tip oscillation, which due to the attraction by the substrate is larger than $2\pi/\omega_z$. Afterwards, we displace the tip by small amounts Δx_0 and determine the topography signal $z_0(x_0)$ for the same reduced frequency shift. The parameter set for the simulation is given in Table 1.

Table 1: Parameter set for simulations with KBr potential, and ranges for MC parameter sampling.

quantity	AFM simulation	ranges for MC
k_x	10 N/m	0.05–5000 N/m
k_z	0.5 N/m	0.5–500 N/m
$\omega_x/2\pi$	455 kHz	10–1000 kHz
$\omega_z/2\pi$	100 kHz	100 kHz
A	3.0 nm	0.5–6.0 nm
Q	50	10–900
z_0	7.10 nm	4–11 nm
f_{set}	−6.2 fN m$^{1/2}$	
normal cycles	10	200

The atomic contrast in the topography signal can be seen clearly (Figure 7). As we used open boundary conditions for the relaxation of the substrate atoms, we have a small distortion at the boundary of the substrate. The surface is therefore not flat, but convex, which is also visible in the topography signal. Such finite size effects are expected to occur not only in the simulation but for real nanostructured surfaces as well.

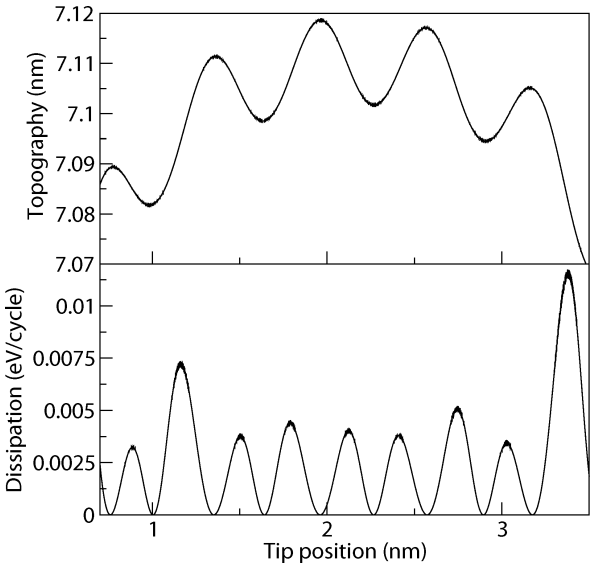

Figure 7: Topography and dissipation for KBr. Scan line along [010]. We observe a doubling in the dissipation signal.

We see a strong contrast in the dissipation signal. The dissipation signal is slightly below the experimentally observed 0.01 eV per cycle. However, it should be noted, that the frequency ratio is chosen such that a moderate resonance is responsible for the rather high dissipation rate (which means that with a slightly detuned frequency, one would exceed the threshold of 0.01 eV per cycle, but one could also get lower values). It shows two maxima to the left and to the right of one maximum in the topography (comparable to the experimental finding in [42]). As the lateral force is responsible for the dissipation here, these maxima occur where the partial derivative of the potential energy in lateral direction is highest. Due to the boundary-induced distortion of the surface, the maxima at the border of the substrate appear much larger, because in addition to the gradient between the atoms, there is also a displacement in z-direction which leads to higher lateral forces.

By choosing a very stiff lateral spring with a high frequency, we can suppress the excitation of lateral oscillations. While the dissipation signal vanishes, the topography is almost unchanged in the present case, because the lateral displacement was smaller than 0.1 nm anyway.

In order to check whether there are higher dissipation rates possible, we performed a Monte-Carlo parameter study again,

but now with the potential for KBr. We place the tip such that we expect a maximum in the dissipation signal. We vary the parameter set according to Table 1.

Figure 8 shows that the dissipation rate increases dramatically by a factor of 10^8, when the nominal distance decreases from 2 nm to 1 nm. The vertical line roughly indicates a threshold for the nominal distance, such that for distances below that threshold it is likely to find dissipation rates above 0.01 eV per cycle. This threshold corresponds to a certain value for the nominal frequency shift of around 8 fN $m^{1/2}$, which is not uncommon for experimental setups.

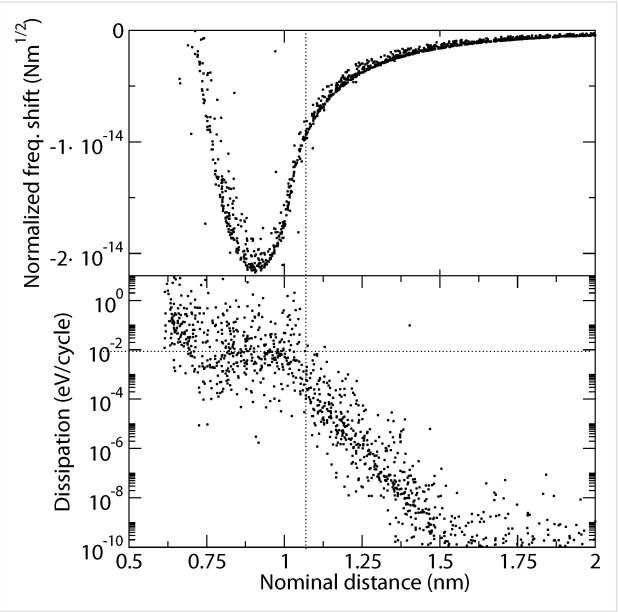

Figure 8: Topography and dissipation for Monte-Carlo parameter-space study.

Conclusion

The dissipation signal is an interesting property of the scanning process, but its interpretation is not trivial. In addition to the adhesion hysteresis mechanism, lateral excitations can be responsible for dissipation rates of the same order of magnitude. The strength of the dissipation depends on the absolute value of the lateral forces. One, therefore, expects high dissipation rates at step edges. If atomic resolution is achieved, this dissipation mechanism would show two maxima accompanying one maximum in the topography signal.

The higher the nominal frequency shift is, the closer the tip gets to the surface and lateral forces increase. The Monte-Carlo study showed, that not all conditions have to be met in order to find dissipation rates higher than 0.01 eV per cycle. There is another condition acting here: The relative phase shift of the lateral oscillation between two successive normal cycles plays an important role. The relative phase shift strongly depends on the frequency and the duration, where lateral forces are significantly acting on the tip. The lateral excitation can be amplified over many successive normal cycles thus leading to much higher dissipation rates.

From Equation 8 it can be concluded that the higher the stiffness of the cantilever is, the smaller the energy dissipation gets. It is therefore less probable for cantilevers with high stiffness, such as tuning forks, that the effect shows up. This is a possible reason, why lateral tip displacements had no effect on the dissipation signal in [43].

Although the origin of this dissipation mechanism is based on lateral forces near the surface, the signal cannot be used to quantitatively determine these forces. Even if all parameters of the lateral oscillator would be known, due to the dependency of the dissipation signal on the phase shift, there is no monotonic dependency of the dissipation signal on the lateral force.

Acknowledgements

This work was supported by the German Research Society (DFG) within SFB 616 “Energy Dissipation at Surfaces”.

References

1. García, R.; Pérez, R. *Surf. Sci. Rep.* **2002,** *47,* 197–301. doi:10.1016/S0167-5729(02)00077-8
2. Giessibl, F. J. *Phys. Rev. B* **1997,** *56,* 16010–16015. doi:10.1103/PhysRevB.56.16010
3. Denk, W.; Pohl, D. W. *Appl. Phys. Lett.* **1991,** *59,* 2171–2173. doi:10.1063/1.106088
4. Lüthi, R.; Meyer, E.; Bammerlin, M.; Baratoff, A.; Howald, L.; Gerber, C.; Güntherodt, H.-J. *Surf. Rev. Lett.* **1997,** *4,* 1025–1029. doi:10.1142/S0218625X9700122X
5. Sasaki, N.; Tsukada, M. *Jpn. J. Appl. Phys.* **2000,** *39,* L1334–L1337. doi:10.1143/JJAP.39.L1334
6. Trevethan, T.; Kantorovic, L. *Nanotechnology* **2004,** *15,* S34–S39. doi:10.1088/0957-4484/15/2/008
7. Kantorovich, L.; Hobbs, C. *Phys. Rev. B* **2006,** *73,* 245420. doi:10.1103/PhysRevB.73.245420
8. Martínez, N. F.; Kamiński, W.; Gómez, C. J.; Albonetti, C.; Biscarini, F.; Pérez, R.; García, R. *Nanotechnology* **2009,** *20,* 434021. doi:10.1088/0957-4484/20/43/434021
9. Langewisch, G.; Kamiński, W.; Braun, D.-A.; Möller, R.; Fuchs, H.; Schirmeisen, A.; Pérez, R. *Small* **2012,** *8,* 602–611. doi:10.1002/smll.201101919
10. Bamidele, J.; Li, Y. J.; Jarvis, S.; Naitoh, Y.; Sugawara, Y.; Kantorovich, L. *Phys. Chem. Chem. Phys.* **2012,** *14,* 16250–16257. doi:10.1039/C2CP43121A
11. Sahagún, E.; Sáenz, J. J. *Phys. Rev. B* **2012,** *85,* 235412. doi:10.1103/PhysRevB.85.235412
12. Gauthier, M.; Tsukada, M. *Phys. Rev. B* **1999,** *60,* 11716. doi:10.1103/PhysRevB.60.11716
13. Volokitin, A. I.; Persson, B. N. J. *Phys. Rev. B* **2002,** *65,* 115419. doi:10.1103/PhysRevB.65.115419

14. Ghasemi, S. A.; Goedecker, S.; Baratoff, A.; Lenosky, T.; Meyer, E.; Hug, H. J. *Phys. Rev. Lett.* **2008,** *100,* 236106. doi:10.1103/PhysRevLett.100.236106
15. Høye, J. S.; Brevik, I. *EPL* **2010,** *91,* 60003. doi:10.1209/0295-5075/91/60003
16. Kunstmann, T.; Schlarb, A.; Fendrich, M.; Paulkowski, D.; Wagner, T.; Möller, R. *Appl. Phys. Lett.* **2006,** *88,* 153112. doi:10.1063/1.2194367
17. Reinstädtler, M.; Kasai, T.; Rabe, U.; Bhushan, B.; Arnold, W. *J. Phys. D: Appl. Phys.* **2005,** *38,* R269–R282. doi:10.1088/0022-3727/38/18/R01
18. Kawai, S.; Sasaki, N.; Kawakatsu, H. *Phys. Rev. B* **2009,** *79,* 195412. doi:10.1103/PhysRevB.79.195412
19. Fremy, S.; Kawai, S.; Pawlak, R.; Glatzel, T.; Baratoff, A.; Meyer, E. *Nanotechnology* **2012,** *23,* 055401. doi:10.1088/0957-4484/23/5/055401
20. Baykara, M. Z.; Dagdeviren, O. E.; Schwendemann, T. C.; Mönig, H.; Altman, E. I.; Schwarz, U. D. *Beilstein J. Nanotechnol.* **2012,** *3,* 637–650. doi:10.3762/bjnano.3.73
21. Reinstaedtler, M.; Rabe, U.; Scherer, V.; Turner, J. A.; Arnold, W. *Surf. Sci.* **2003,** *532-535,* 1152–1158. doi:10.1016/S0039-6028(03)00183-3
22. Song, Y.; Bhushan, B. *J. Appl. Phys.* **2006,** *99,* 094911. doi:10.1063/1.2195021
23. Chen, J.; Workman, R. K.; Sarid, D.; Hoper, R. *Nanotechnology* **1994,** *5,* 199–204. doi:10.1088/0957-4484/5/4/003
24. Rabe, U.; Turner, J.; Arnold, W. *Appl. Phys. A* **1998,** *66,* S277–S282. doi:10.1007/s003390051145
25. Nony, L.; Baratoff, A.; Schär, D.; Pfeiffer, O.; Wetzel, A.; Meyer, E. *Phys. Rev. B* **2006,** *74,* 235439. doi:10.1103/PhysRevB.74.235439
26. Couturier, G.; Boisgard, R.; Dietzel, D.; Aimé, J. P. *Nanotechnology* **2005,** *16,* 1346. doi:10.1088/0957-4484/16/8/061
27. Gauthier, M.; Pérez, R.; Arai, T.; Tomitori, M.; Tsukada, M. *Phys. Rev. Lett.* **2002,** *89,* 146104. doi:10.1103/PhysRevLett.89.146104
28. Trevethan, T.; Kantorovich, L.; Polesel-Maris, J.; Gauthier, S. *Nanotechnology* **2007,** *18,* 084017. doi:10.1088/0957-4484/18/8/084017
29. Gotsmann, B.; Seidel, C.; Anczykowsi, B.; Fuchs, H. *Phys. Rev. B* **1999,** *60,* 11051. doi:10.1103/PhysRevB.60.11051
30. García, R.; Gómez, C. J.; Martinez, N. F.; Patil, S.; Dietz, C.; Magerle, R. *Phys. Rev. Lett.* **2006,** *97,* 016103. doi:10.1103/PhysRevLett.97.016103
31. Krüger, D.; Anczykowski, B.; Fuchs, H. *Ann. Phys.* **1997,** *509,* 341–363. doi:10.1002/andp.19975090502
32. Swope, W. C.; Andersen, H. C.; Berens, P. H.; Wilson, K. R. *J. Chem. Phys.* **1982,** *76,* 637–649. doi:10.1063/1.442716
33. Rabe, U.; Janser, K.; Arnold, W. *Rev. Sci. Instrum.* **1996,** *67,* 3281–3293. doi:10.1063/1.1147409
34. Giessibl, F. J. *Rev. Mod. Phys.* **2003,** *75,* 949–983. doi:10.1103/RevModPhys.75.949
35. Solares, S. D.; Hölscher, H. *Nanotechnology* **2010,** *21,* 075702. doi:10.1088/0957-4484/21/7/075702
36. Green, C. P.; Lioe, H.; Cleveland, J. P.; Proksch, R.; Mulvaney, P.; Sader, J. E. *Rev. Sci. Instrum.* **2004,** *75,* 1988–1997. doi:10.1063/1.1753100
37. Kawai, S.; Kitamura, S.-i.; Kobayashi, D.; Kawakatsu, H. *Appl. Phys. Lett.* **2005,** *87,* 173105. doi:10.1063/1.2112203
38. Fumi, F. G.; Tosi, M. P. *J. Phys. Chem. Solids* **1964,** *25,* 31–43. doi:10.1016/0022-3697(64)90159-3
39. Sangster, M. J. L.; Dixon, M. *Adv. Phys.* **1976,** *25,* 247–342. doi:10.1080/00018737600101392
40. Jain, J. K.; Shanker, J.; Khandelwal, D. P. *Phys. Rev. B* **1976,** *13,* 2692–2695. doi:10.1103/PhysRevB.13.2692
41. Hoffmann, R.; Baratoff, A.; Hug, H. J.; Hidber, H. R.; Löhneysen, H. v.; Güntherodt, H.-J. *Nanotechnology* **2007,** *18,* 395503. doi:10.1088/0957-4484/18/39/395503
42. Canova, F. F.; Kawai, S.; de Capitani, C.; Kan'no, K.-i.; Glatzel, T.; Such, B.; Foster, A. S.; Meyer, E. *Phys. Rev. Lett.* **2013,** *110,* 203203. doi:10.1103/PhysRevLett.110.203203
43. Such, B.; Glatzel, T.; Kawai, S.; Koch, S.; Meyer, E. *J. Vac. Sci. Technol., B: Nanotechnol. Microelectron.: Mater., Process., Meas., Phenom.* **2010,** *28,* C4B1–C4B5. doi:10.1116/1.3382230

License and Terms

BEILSTEIN JOURNAL OF NANOTECHNOLOGY

Nanometer-resolved mechanical properties around GaN crystal surface steps

Jörg Buchwald*[1], Marina Sarmanova[1], Bernd Rauschenbach[1,2] and Stefan G. Mayr*[1,2,3]

Full Research Paper

Open Access

Address:
[1]Leibniz-Institut für Oberflächenmodifizierung e.V. (IOM), Permoserstr. 15, 04318 Leipzig, Germany, [2]Fakultät für Physik und Geowissenschaften, Universität Leipzig, 04103 Leipzig, Germany and [3]Translationszentrum für regenerative Medizin (TRM), Universität Leipzig, 04103 Leipzig, Germany

Email:
Jörg Buchwald* - joerg.buchwald@iom-leipzig.de; Stefan G. Mayr* - stefan.mayr@iom-leipzig.de

* Corresponding author

Keywords:
finite elements; gallium nitride; indentation; mechanical properties; molecular dynamics; nanostructures

Beilstein J. Nanotechnol. **2014,** *5,* 2164–2170.
doi:10.3762/bjnano.5.225

Received: 03 June 2014
Accepted: 29 October 2014
Published: 19 November 2014

This manuscript is part of the Thematic Series "Advanced atomic force microscopy techniques II".

Guest Editors: T. Glatzel and T. Schimmel

Abstract

The mechanical properties of surfaces and nanostructures deviate from their bulk counterparts due to surface stress and reduced dimensionality. Experimental indentation-based techniques present the challenge of measuring these effects, while avoiding artifacts caused by the measurement technique itself. We performed a molecular dynamics study to investigate the mechanical properties of a GaN step of only a few lattice constants step height and scrutinized its applicability to indentation experiments using a finite element approach (FEM). We show that the breakdown of half-space symmetry leads to an "artificial" reduction of the elastic properties of comparable lateral dimensions which overlays the effect of surface stress. Contact resonance atomic force microscopy (CR-AFM) was used to compare the simulation results with experiments.

Introduction

Recently developed scanning probe-based techniques, such as contact resonance atomic force microscopy (CR-AFM) [1,2], allow for the assessment of mechanical properties of soft and hard condensed matter surfaces at the nanoscale. Such developments make it even more compelling to look at nanometer-sized materials from a theoretical point of view to gain a deeper understanding of the physical mechanisms involved in mechanical response. Several studies have focused on the mechanical properties of nanostructures such as nanowires [3,4] or nanosized granular films [5] by using indentation methods. Here, generally two major challenges arise. On the one hand, the varying tip–surface contact area has to be taken into account. On the other hand, the breakdown of half-space symmetry hinders a straightforward analysis, especially when stressfields significantly exceed the sample dimensions or become severely influenced by domain boundaries. Therefore, in the present study, a simple step of several atomic layers height has been studied as a model system in order to gain insight into the rele-

vant physics and/or artifacts caused by a specific measurement technique.

While it is established that surfaces lead to an effective change of the elastic constants, e.g., a reduction due to surface stresses within a thin film [6], mechanical properties around more advanced surface features, including steps, are unclear at this point. The present work addresses the mechanical behavior around a gallium nitride (GaN) step employing a combination of classical molecular dynamics (MD) simulations with a finite element (FEM) approach and CR-AFM experiments. GaN is a material of great interest due to its application as a wide-band-gap semiconductor especially for optoelectronic devices [7,8]. Additionally, it is known that GaN can exhibit terraces ranging from monoatomic to a few lattice parameters in step height [9,10]. In principle, the results of this paper can be generalized, due to the fact that they are based on a general formalism introducing surface stresses in continuum mechanics and since many other materials ranging from ionic crystals [11] to metals [12] are known to form such steps.

Theoretical considerations

A step can be described by the set

$$\mathsf{M} = \left\{ \left(x, y, z \right) \mid z \le h\Theta\left(y \right) \right\}, \tag{1}$$

where h is the step height and Θ the heaviside step function. This paper will focus on how the surface stress at $y = 0$ influences the mechanical properties at a given distance on the top and at the bottom of the step (close to the surface). Therefore, the surface stress of the planes $\{(x,y,h) \mid y \ge 0\}$ and $\{(x,y,0) \mid y \le 0\}$ will be neglected as it is constant along x and y, but its treatment would follow the same procedure concerning surface elasticity and symmetry arguments as depicted in the following approach.

We first sub-divide the material of interest into infinitesimal cubes of the volume dV. The resulting force acting on a partial volume is equal to the sum of all forces acting on each single element. The divergence theorem connects the force acting on a volume element with the stresses at its boundaries:

$$\int \mathcal{F}_i dV = \oint \sigma_{ij} dA_j, \left(i, j = 1,2,3 \right). \tag{2}$$

The force (expressed in terms of force per unit volume $\mathcal{F}$) acting on volume element dV at point p arises from the effective stresses acting on the boundaries of its neighboring volumes. Due to the fact that the tensile stresses are homogeneous along $\{(x,0,z) \mid 0 \le z \le h\}$, the near field behavior of the stress field is a reduction just along its lateral distance y from the step edge. This fact can be expressed by considering the surface stress, which is the variation of the total surface energy as a function of the strain, ε:

$$f_{ij}\left(\varepsilon \right) = \frac{1}{A_0} \frac{d\left(A\left(\varepsilon \right) \gamma\left(\varepsilon \right) \right)}{d\varepsilon_{ij}}, \left(i, j = 1,2,3 \right), \tag{3}$$

where A_0 is the surface area before deformation and γ the surface energy. Therefore, the local stresses $\sigma_{ij}(y_p)$ which are acting on the boundaries of dV can be written in terms of the surface stress f_{ij}:

$$\sigma_{ij}\left(y_p, \varepsilon = 0 \right) = \frac{f_{ij}\left(\varepsilon = 0 \right)}{y_p}, \left(i, j = 1,2,3 \right). \tag{4}$$

By defining the constants $c_{ijkl}(\varepsilon)$ $\varepsilon_{kl} := f_{ij}(\varepsilon) - f_{ij}(\varepsilon = 0)$ and applying Hooke's law, it is possible to calculate local effective elastic constants as a function of their distance y_p from the step edge:

$$C_{ijkl}^{\mathrm{loc}}\left(y_p \right) = C_{ijkl} + \frac{c_{ijkl}}{y_p}, y_p > 0, \left(i, j, k, l = 1,2,3 \right). \tag{5}$$

Analogously, it is also possible to understand the behavior below the step, i.e., for $y < 0$. The stress induced by the step does not only decrease along $-y$, but also along $-z$ due to the fact that from this point of view, the stresses arising from the step are homogeneous along the x-axis only. This can be also expressed by a line tension F_i along the step edge, which defines the non-zero elements of the edge elastic tensor $d_{iijj}(\varepsilon)\varepsilon_{jj} := F_i(\varepsilon) - F_i(\varepsilon = 0)$. As a consequence of the line tension, the stressfield is spread cylindrically from its origin along $-z$ and $-y$. Therefore, the following relation for the elastic constants is obtained:

$$C_{ijkl}^{\mathrm{loc}}\left(y_p \right) = C_{ijkl} + \frac{d_{ijkl}}{y_p^2}, y_p < 0, \left(i, j, k, l = 1,2,3 \right). \tag{6}$$

From linear response theory, it is also possible to derive a microscopic expression for the elastic constants [13]:

$$\begin{aligned} C_{ijkl}^{\mathrm{loc}} = & \left\langle C_{ijkl}^{\mathrm{B}} \right\rangle - \frac{V}{k_{\mathrm{B}}T}\left(\left\langle \sigma_{ij}\sigma_{kl} \right\rangle - \left\langle \sigma_{ij} \right\rangle \left\langle \sigma_{kl} \right\rangle \right) \\ & + \frac{2Nk_{\mathrm{B}}T}{V}\left(\delta_{ik}\delta_{jl} - \delta_{il}\delta_{jk} \right) \left(i, j, k, l = 1,2,3 \right). \end{aligned} \tag{7}$$

The last (kinetic) term can be omitted at low temperatures. The Born-term $C^{B}_{ijkl} = 1/V\partial^2 U/(\partial\varepsilon_{ij}\partial\varepsilon_{kl})$ will just differ for edge atoms, therefore the stress-induced effective change in the elastic properties along y will essentially lead to a change in the stress-fluctuation term. Equation 7 allows us to study the mechanical response at a step by means of MD simulations. Here, the explicit calculation of the elastic constants will be omitted, since the volume per atom V is not uniquely defined in any case. Therefore, these expressions have been used to provide a qualitative understanding of the problem and have been accompanied by explicit indentation simulations to quantitatively describe the elastic response of a step.

Simulation methods

All MD runs were carried out with the LAMMPS code [14]. The GaN step was modeled in the wurtzite crystal structure oriented along the [001] direction by means of a Stillinger–Weber potential [15]. The simulations were carried out in a NVT ensemble utilizing Nosé–Hoover thermostatting at 5 K [16,17], Verlet time integration at constant volume and free boundary conditions along all three axes. We simulated three different step heights: $h = 1c$, $2c$, and $3c$, where $c = 0.521$ nm is the lattice parameter of the wurtzite structure along the z-direction. For the fluctuation method, 10,000 atoms were simulated over a time period of 100 ps. For the indentation experiments, approximately 70,000 atoms were used with a simulation time period of 100 ps as well. In Figure 1, one sees the MD configuration of a GaN step of height $h = 2c$.

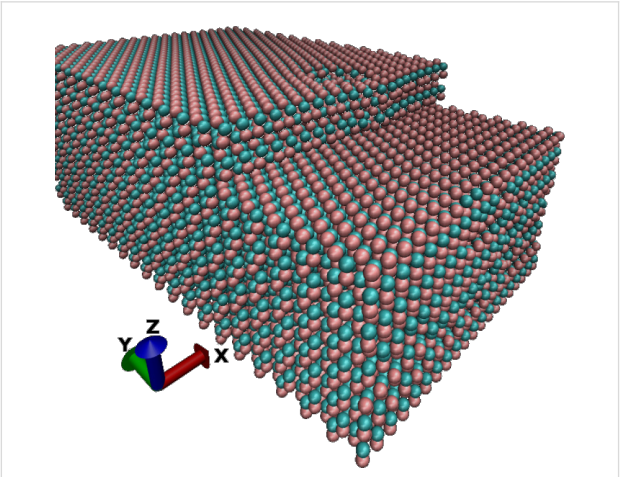

Figure 1: MD configuration of a GaN step with a step height of $h = 2c$ during indentation of surface atoms within a circular area of $A_2 = 1.232$ nm^2. The red spheres denote the gallium and blue spheres the nitrogen atoms.

The FEM simulations were performed by using the COMSOL software package [18] and experimental elastic constants [19]. The model domain was 120 nm × 120 nm × 80 nm large with free boundaries along x and y, with a fixed boundary as the substrate. The tetrahedral mesh consisted of approximately 180,000 elements, including extra refinements at the contact region.

Results and Discussion

Simulation Results

In Figure 2, the yy-component of the stress variance, representing C_{yyyy}, is given in squared energy units due to the fact that the per-atom volume for surface and edge atoms, in particular, is not well defined. At the top of the step, i.e., for $y > 0$ one observes the expected $1/y$ behavior (Equation 5), which is comparable for all step heights due to nearly identical surface stresses, with exception of the first atom particularly for the smallest step height. This can easily be understood by taking into account the interaction of all three surfaces and differences in the per-atom volume at this point. Below the step, the stress fluctuations are nearly constant for all step heights except for the closest atom which feels the stress significantly. This behavior reflects the better convergence properties of $1/y^2$ (Equation 6).

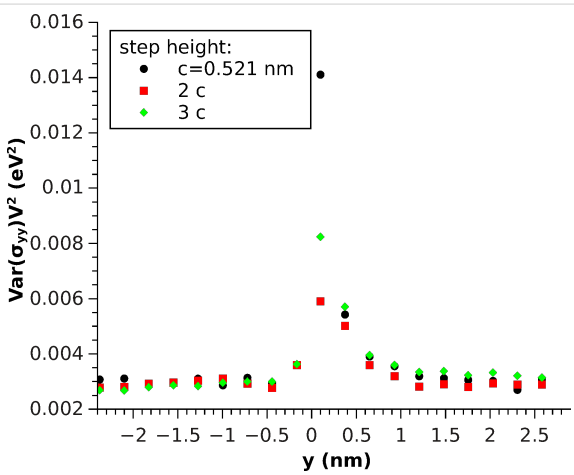

Figure 2: Stress fluctuation multiplied by the squared per-atom volume $\mathrm{Var}(\sigma_{yy})V^2 = V^2(\langle\sigma_{yy}\sigma_{yy}\rangle - \langle\sigma_{yy}\rangle^2)$ along the y-axis of the upper Ga atoms.

From an experimental point of view, it is hardly possible to evaluate the microscopical expressions (Equation 7) for the elastic constants. Therefore, the mechanical properties were investigated in terms of the indentation (or reduced Young's) modulus M by using an indenter acting with a load F on a contact area A of a half-space, thereby causing a displacement u [20]:

$$M = \frac{\sqrt{\pi}}{2\sqrt{A}}\frac{dF}{du} \tag{8}$$

Since the elastic constants can consistently be extrapolated on an atomistic level (Equation 7), we also expect M to give reasonable values at this scale. For simulating a flatpunch indentation, forces of about 10–30 eV/nm were applied directly to each gallium surface atom within a certain radius r_c. As contact area A, the product of the two-dimensional Wigner–Seitz volume and the number of surface atoms within that radius were chosen. The indentation simulations were carried out by using approximately 70,000 atoms on a fixed substrate and free boundaries along the other sides.

The step was investigated by using two contact areas: $A_1 = 0.088$ nm^2 and $A_2 = 1.232$ nm^2 which correspond to one and 14 indented atoms, respectively (Figure 3 and Figure 4). The asymptotic (far from $y = 0$) elastic constants differ for both cases due to the difference in contact area. This difference leads to a change in surface sensitivity and affect the influence of the boundary conditions, which play a more pronounced role for greater contact radii due to the increased extension of the stress field. Under these conditions both values are in reasonable agreement with the experimental value of $M_{lit} = 330$ GPa, which was calculated from the elastic constants [19] by using the formalism presented by Vlassak and Nix [20], who connected the indentation modulus to the Barnett–Lothe tensors for anisotropic materials [21].

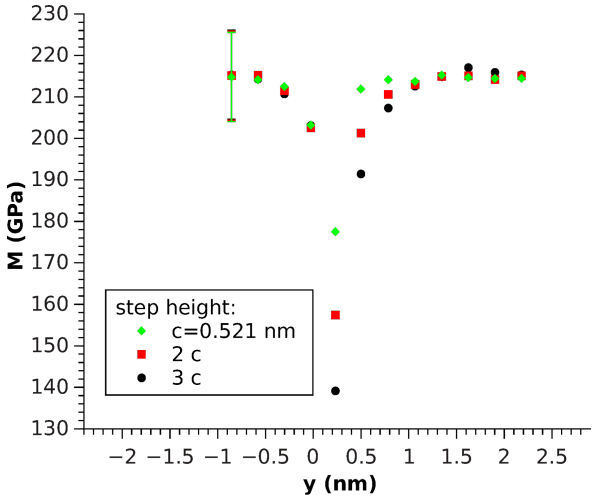

Figure 3: Local [001]-oriented indentation modulus for three different step heights along the y-axis. Measured by indenting a single atom ($A_1 = 0.088$ nm^2). The error bars denote the standard deviation of the displacement and apply to all data points.

For the one-atom indentation, (Figure 3), M behaves similarly to stress fluctuations with better convergence below the step and a similar decrease in the elastic constants on top, approaching the step edge, comparable to the theoretical predictions (Equation 6 and Equation 5) for the elastic constants.

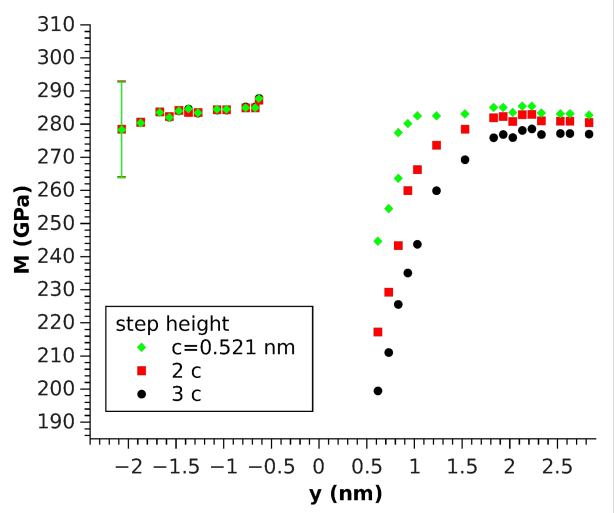

Figure 4: [001]-oriented indentation modulus for three different step heights along y. Measured by indenting a circular region of surface atoms ($A_2 = 1.232$ nm^2). The error bars denote the standard deviation of the displacement and apply to all data points.

Therefore, it can be concluded that one-atom indentation describes the stress distribution quite well, except for the fact that a clear (monotone) difference between different step heights was observed. Indeed, the step seems to soften with increasing step height. This trend is even more pronounced for the greater contact radius (Figure 4). Another matter that is conspicuous in this case is the fact that the softening for $y < 0$ is not measurable anymore, rather, a tiny increase for the smallest distance is observed, independent of the step height. Even on these scales, both facts indicate that the breakdown of half-space symmetry at $y = 0$ plays a non-negligible role.

To estimate the influence of this effect, the same contact radius was used to simulate the indentation in a FEM model (Figure 5) in which surface stresses were omitted. The indentation modulus was calculated by evaluating the contact stiffness $S = dF/du$ of the stationary solution. The flatpunch indenter was modeled by a cylinder of hard material with a contact area A_2 and a force of $|\mathbf{F}| = -F_z = 30$ nN as an initial condition.

As a result, a distinctive step height-dependent increase for $y < 0$ and decrease ($y > 0$ towards the step) were seen, which could be explained by the outreach of the stressfields induced by the indenter over the region that could be treated as a half-space (Figure 6). Comparing these results to the molecular dynamics simulation with the same radius (Figure 4), a similar behavior for the indentation modulus could be found. However, there was an even more pronounced increase for $y < 0$ that was also dependent on the step height, in contrast to our MD simulations results. Nevertheless, the stress-induced softening, observed when using one-atom indentation, and the hardening,

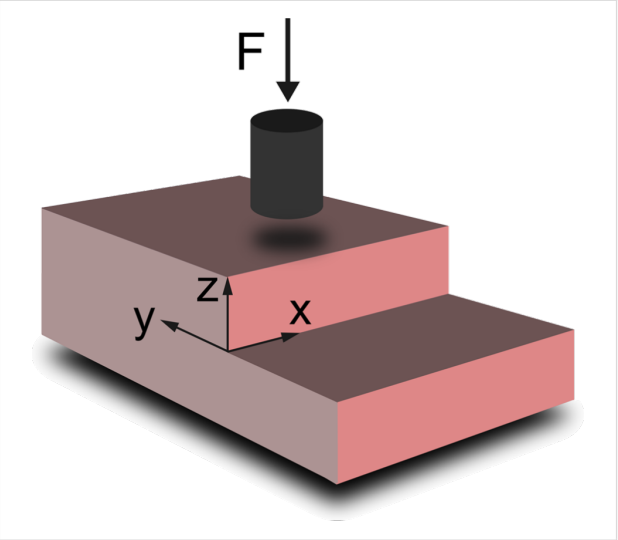

Figure 5: Schematic FEM configuration of the indentation on top of the step by using a flatpunch indenter.

observed in the FEM simulation, seem to nearly compensate in the MD simulation for this contact radius (Figure 4). The decrease of M for $y > 0$ towards the step looks quite similar in Figure 4 and Figure 6, which indicates that it plays a dominant role in Figure 4 in addition to the effects caused by the role of stress.

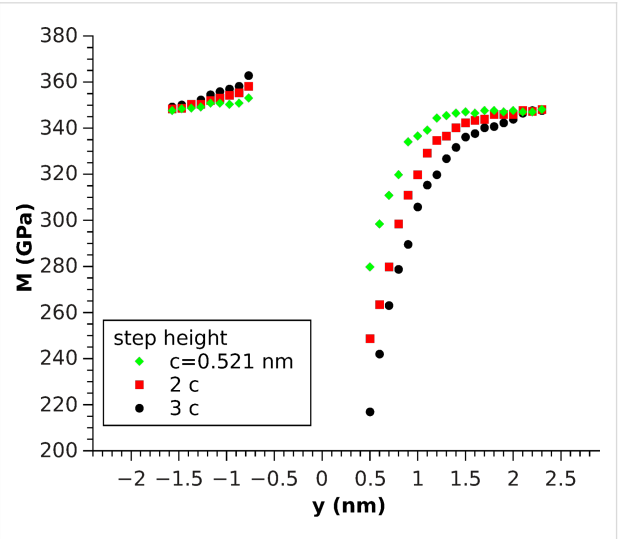

Figure 6: FEM simulation of indentation modulus for three different step heights by using a flatpunch indenter (A_2 = 1.232 nm^2).

The contact area of A_2 corresponds to a radius of r_2 = 0.626 nm, so there are three moduli $M(0 < y < 0.626$ nm) in Figure 6, for which both the stress field in the sample and the contact area are shrinking as y approaches 0, due to the size of the contact area of the indenter. However, in this case, the change in the contact area manifests in a small bend and appears to play a minor role.

Experimental Results

In order to validate the theoretical results, CR-AFM studies on GaN thin films were undertaken. CR-AFM is a technique for evaluating the mechanical properties of a broad range of materials while using one of the highest lateral resolution available, compared to other recent methods [1,2,22,23]. The investigated sample was an epitaxial c-plane GaN film grown on a 6H-SiC substrate by ion beam-assisted molecular beam epitaxy [24]. Measurements for the elastic properties of the GaN film were performed by a CR-AFM, that was custom-built into a commercial Asylum Research MFP-3D AFM [25]. The AFM probe used for CR-AFM imaging was a Si PPP-NCLR (NanoSensors, Switzerland) with a spring constant of 39 N/m. The second resonance mode was used for further analysis. The reduced Young's modulus was measured by using a reference approach with three reference samples: fused silica (M = 75 GPa), silicon (M = 165 GPa) and sapphire (M = 433 GPa), which were demonstrated to be sufficient for quantitative mechanical analysis [26]. From this data, we obtained M = 285 GPa with an uncertainty of 5–10%, typical for CR-AFM measurements.

According to previous investigations, the radius of curvature, R, of the Si-tip hardly remains below 25 nm during elasticity measurements of stiff materials [26]. Considering a spherical contact and a force loading F in the range of 400–500 nN, the resulting contact radius r_c is determined by [22]

$$r_c = \sqrt[3]{\frac{3RF}{4M}} \tag{9}$$

and will be within 4.0–4.5 nm for GaN films. Here, M is the indention modulus of the contact that is given by

$$\frac{1}{M} = \frac{1}{M_{tip}} + \frac{1}{M_s}, \tag{10}$$

where M_{tip} and M_s are the indentation moduli of the tip and the sample, respectively. Since the influence of the step edge only spreads within a distance of several nanometers from the step edge, the measurements should be performed directly on the step. Therefore, the reduction of the contact area when the tip passes the step edge must be taken into account. When the center of symmetry of the tip passes the step edge, the contact area adopts half of its initial value. Therefore, the contact radius can be estimated to be roughly √2 times less than that of a vibrating tip far from the step. From Equation 8, it is obvious that this decrease in contact area leads to an underestimation of the elastic modulus when maintaining a load.

This effect is demonstrated for a GaN step of 5 nm in height (see Figure 7). The step is high enough to theoretically exhibit a visible reduction in the indentation modulus with a sufficiently sharp tip. Simultaneously, with continuous measurements of the contact resonance frequencies by CR-AFM, the topography image was obtained. When comparing both, the frequency and topography images, a small reduction of resonance frequency was detected near the step edge. Taking into account the diminished contact area compared to flat surface contact, calculation of the indentation modulus by using the reduced contact area leads to the same value as far from the step within accuracy of 10%. At the bottom of the step, where one has to take multiple contact areas into account due to the spherical tip, it was not possible to measure any change. Obviously, the radius of the tip was too large to observe any stress dependence in the indentation modulus. One way to solve this problem is through the use of custom-designed probes with much higher stiffness in order to reduce contact area, making it possible to obtain more accurate elasticity values and thereby detecting the reduction in the indentation modulus with nanometer-sized steps.

Conclusion

Tensile stresses lead to a significant local effective reduction in the elastic constants. In the case for a step of several nanometers in height, this effect can lead to considerable changes for lateral distances as large as 1 nm. We showed that this behavior affects the indentation modulus with qualitative differences for various indentation radii. By using FEM simulations in which surface stresses were neglected, it was shown that indentation leads to a softening on the same length scale at the top of the step and to a hardening below the step, which explains these differences in the moduli. As stated before, this result reflects no real mechanical property of the material since this effect is highly dependent on the area and shape of the indenter.

In the case of a flatpunch, this behavior dominates the stress-induced reduction in the elastic constants, even for small tip radii. By using CR-AFM, it was not possible to measure a significant reduction of the indentation modulus close to a step of similar height outside the confidence interval. Hence, it will be an increasingly significant challenge for future measuring devices to advance to regimes that experimentally unravel the stress-induced reduction in the elastic constants. Simulations were carried out for GaN, but the results can be generalized for materials that are known to form sharp steps of comparable height.

Supporting Information

Supporting Information File 1

Information about the influence of finite size effects on the indentation modulus.
[http://www.beilstein-journals.org/bjnano/content/supplementary/2190-4286-5-225-S1.pdf]

Acknowledgements

Fruitful discussions with M. Hennes are gratefully acknowledged. This work was performed within the Leipzig Graduade School of Natural Sciences “Building with Molecules and Nano-objects” (BuildMoNa), established by the German Science Foundation (DFG) within the German Excellence Initiative. A grant of computing time by the Center for Information Services and High Performance Computing (ZIH), TU

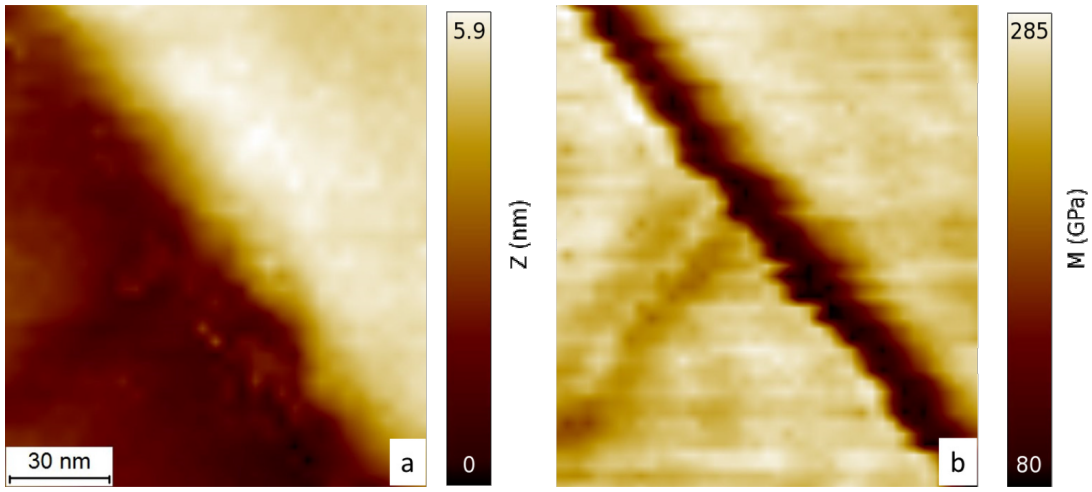

Figure 7: Topography (a) and indentation modulus (b) map of the area around a GaN step.

Dresden, is gratefully acknowledged. This work is funded by the SAW award of the German Leibniz Association (SAW-2011-IOM-2).

References

1. Rabe, U.; Arnold, W. *Appl. Phys. Lett.* **1994,** *64,* 1493–1495. doi:10.1063/1.111869
2. Yamanaka, K.; Ogiso, H.; Kolosov, O. *Appl. Phys. Lett.* **1994,** *64,* 178–180. doi:10.1063/1.111524
3. Stan, G.; Cook, R. Elastic property characterization of oxidized Si nanowires by contact-resonance atomic force microscopy. In *APS March Meeting 2010,* Portland, Oregon, USA, March 15–19, 2010; Pine, D., Ed.; American Physical Society, 2010; pp 95 ff.
4. Stan, G.; Ciobanu, C. V.; Parthangal, P. M.; Cook, R. F. *Nano Lett.* **2007,** *7,* 3691–3697. doi:10.1021/nl071986e
5. Stan, G.; Cook, R. F. *Nanotechnology* **2008,** *19,* 235701. doi:10.1088/0957-4484/19/23/235701
6. Izumi, S.; Hara, S.; Kumagai, T.; Sakai, S. *Thin Solid Films* **2004,** *467,* 253–260. doi:10.1016/j.tsf.2004.03.034
7. Morkoç, H.; Strite, S.; Gao, G. B.; Lin, M. E.; Sverdlov, B.; Burns, M. *J. Appl. Phys.* **1994,** *76,* 1363–1398. doi:10.1063/1.358463
8. Nakamura, S.; Senoh, M.; Mukai, T. *Appl. Phys. Lett.* **1993,** *62,* 2390–2392. doi:10.1063/1.109374
9. Held, R.; Nowak, G.; Ishaug, B. E.; Seutter, S. M.; Parkhomovsky, A.; Dabiran, A. M.; Cohen, P. I.; Grzegory, I.; Porowski, S. *J. Appl. Phys.* **1999,** *85,* 7697–7704. doi:10.1063/1.370574
10. Weyher, J. L.; Brown, P. D.; Zauner, A. R. A.; Müller, S.; Boothroyd, C. B.; Foord, D. T.; Hageman, P. R.; Humphreys, C. J.; Larsen, P. K.; Grzegory, I.; Porowski, S. *J. Cryst. Growth* **1999,** *204,* 419–428. doi:10.1016/S0022-0248(99)00217-1
11. Steiner, P.; Gnecco, E.; Krok, F.; Budzioch, J.; Walczak, L.; Konior, J.; Szymonski, M.; Meyer, E. *Phys. Rev. Lett.* **2011,** *106,* 186104. doi:10.1103/PhysRevLett.106.186104
12. Holland-Moritz, E.; Gordon, J.; Borges, G.; Sonnenfeld, R. *Langmuir* **1991,** *7,* 301–306. doi:10.1021/la00050a017
13. Frenkel, D.; Smit, B. *Understanding Molecular Simulation: From Algorithms to Applications;* Computational Science Series, Vol. 1; Elsevier Science, 2001.
14. Plimpton, S. *J. Comput. Phys.* **1995,** *117,* 1–19. doi:10.1006/jcph.1995.1039
15. Béré, A.; Serra, A. *Philos. Mag.* **2006,** *86,* 2159–2192. doi:10.1080/14786430600640486
16. Nosé, S. *J. Chem. Phys.* **1984,** *81,* 511–519. doi:10.1063/1.447334
17. Hoover, W. G. *Phys. Rev. A* **1985,** *31,* 1695–1697. doi:10.1103/PhysRevA.31.1695
18. *COMSOL Multiphysics;* COMSOL, Inc., 2010.
19. Polian, A.; Grimsditch, M.; Grzegory, I. *J. Appl. Phys.* **1996,** *79,* 3343–3344. doi:10.1063/1.361236
20. Vlassak, J. J.; Nix, W. D. *Philos. Mag. A* **1993,** *67,* 1045–1056. doi:10.1080/01418619308224756
21. Barnett, D.; Lothe, J. *Phys. Norv.* **1975,** *8,* 13–22.
22. Kopycinska-Müller, M. On the elastic properties of nanocrystalline materials and the determination of elastic properties on a nanoscale using the atomic force acoustic microscopy technique. Ph.D. Thesis, Universität des Saarlandes, Saarbrücken, Germany, 2005.
23. Steiner, P.; Roth, R.; Gnecco, E.; Glatzel, T.; Baratoff, A.; Meyer, E. *Nanotechnology* **2009,** *20,* 495701. doi:10.1088/0957-4484/20/49/495701
24. Neumann, L.; Gerlach, J. W.; Rauschenbach, B. *Thin Solid Films* **2012,** *520,* 3936–3945. doi:10.1016/j.tsf.2012.02.004
25. Jakob, A. M.; Müller, M.; Rauschenbach, B.; Mayr, S. G. *New J. Phys.* **2012,** *14,* 033029. doi:10.1088/1367-2630/14/3/033029
26. Jakob, A. M.; Buchwald, J.; Rauschenbach, B.; Mayr, S. G. *Nanoscale* **2014,** *6,* 6898–6910. doi:10.1039/C4NR01034E

License and Terms